



## Low-cost Pencil-Graphite Multi-electrodes for Simultaneous Detection of Iron and Copper

Tugba OZER<sup>1\*</sup>  

<sup>1</sup> Yildiz Technical University, Department of Bioengineering, Faculty of Chemical and Metallurgical Engineering, Istanbul, 34220, Turkey

**Abstract:** Herein, two novel ion-selective electrodes are reported for simultaneous potentiometric determination of Fe<sup>3+</sup> and Cu<sup>2+</sup> ions. The liquid polymeric membrane components were optimized and the resulting pencil graphite electrodes gave Nernstian slopes of 20.7 mV/decade and 31.2 mV/decade with lower detection of limit of 1×10<sup>-6</sup> mol L<sup>-1</sup> and 2×10<sup>-6</sup> mol L<sup>-1</sup>, and wide pH range of 1.5-3.5 and 2.0-4.7 for Fe<sup>3+</sup> and Cu<sup>2+</sup> ions, respectively. The electrodes exhibited very fast response time (<6 s). In addition, the electrodes exhibited high selectivity for Fe<sup>3+</sup> and Cu<sup>2+</sup> ions against different cations, which were tested by matched potential method. The sensing platform using the optimized electrodes were integrated with the Internet of Things concept are suitable for simultaneous monitoring of Fe<sup>3+</sup> and Cu<sup>2+</sup> in real samples with high accuracy and precision.

**Keywords:** Potentiometric determination, ion selective electrode, copper, iron, internet of things, simultaneous determination.

**Submitted:** June 08, 2021. **Accepted:** November 16, 2021.

**Cite this:** Ozer T. Low-cost Pencil-Graphite Multi-electrodes for Simultaneous Detection of Iron and Copper. JOTCSA. 2022;9(1):1-12.

**DOI:** <https://doi.org/10.18596/jotcsa.949831>.

**\*Corresponding author. E-mail:** [tozer@yildiz.edu.tr](mailto:tozer@yildiz.edu.tr).

### INTRODUCTION

Heavy metals have been widely used in a variety of industries such as petrochemicals, metal processing, organic chemicals, pharmaceuticals, pesticides, and plastics (1). Due to the discharge of industrial effluents into natural waters, heavy metal ions adversely affect environment and human health (2). Among the heavy metals, Fe and Cu are the first and second most widely used industrial metals worldwide (3). Fe<sup>3+</sup> plays a significant role in various metabolic processes including oxygen transport, enzyme catalysis, DNA and RNA synthesis, and hemoglobin synthesis (4). Although Fe<sup>3+</sup> is necessary for living organisms at low concentrations, biological disorders such as Alzheimer's, Parkinson's, and Huntington's diseases and, renal failure are seen with uptake of Fe<sup>3+</sup> at high concentrations (5). Similarly, excess copper causes anemia, bone disorders, diarrhea, infertility, hepatic and renal damages, and neurological

disorders, thus, permissible limits of copper in ground water and drinking water are set as 3 mg L<sup>-1</sup> and 2 mg L<sup>-1</sup>, respectively, by United States Environmental Protection Agency (EPA) and The World Health Organization (WHO) (6). In addition, the concentration of copper should not surpass 100-150 µg dL<sup>-1</sup> (15.7-23.6 µmol L<sup>-1</sup>) in human blood according to WHO. Thus, there is a need for a continuous and simultaneous sensing system for copper and iron to ensure water safety and public health.

There are many conventional techniques such as atomic absorption spectroscopy, atomic fluorescence spectrometry, chromatography, inductively coupled plasma mass spectrometry and ultraviolet-visible spectrophotometry for quantitative determination of heavy metals (7). Although these methods are highly sensitive and selective, they have several disadvantages such as labor-intensive and time-consuming experimental

steps, the need of expensive and bulky instruments and specialized personnel (8). On the other hand, potentiometric method based on ion selective electrodes (ISEs) have been widely employed for quantitative and in-situ determination of target ion activity in aqueous samples owing to their advantages including simplicity, low-cost, rapid response, miniaturization, portability and low energy consumption (9). There have also been various reports of liquid membrane-based ISEs consisting of a plasticizer, a polymer (mostly polyvinyl chloride, PVC), an ionic additive, and an ionophore (10). Due to the semipermeable nature of PVC, it has been widely used for ISEs application (11). While the ionophore complexes with the metal ion of interest, the plasticizer enhances solubility and mobility of the ionophore in the membrane (12). In addition, lipophilic anionic additives such as sodium tetraphenyl borate and potassium tetrakis(4-chlorophenyl)borate (KTChPB) are utilized to enhance ISE sensitivity and selectivity while decreasing membrane resistance (11). Various ionophores such as calixarenes, crown ethers, macrocyclic polyethers, cyclic tetrapeptides, and thiophenes have been applied for the fabrication of  $\text{Cu}^{2+}$  and  $\text{Fe}^{3+}$  selective ISEs (13). Previously reported electrodes have drawbacks including higher limit of detection or interferences from other cations.

Porphyryns, which are a class of heterocyclic macromolecular compounds, can be utilized as ionophores for constructing cation-selective electrodes by grafting functional groups to the porphyrin ring (14). Recently, Chen et al. synthesized Gd-(5,10,15,20-tetrakis (4 carboxyphenyl) porphyrin to detect  $\text{Fe}^{3+}$  using colorimetric and fluorometric methods (15). Although low detection limits were achieved with the use of a polymer-based probe, their methods require bulky instruments an UV-visible spectrometer and fluorescence spectrometer, and they are not suitable for online monitoring of  $\text{Fe}^{3+}$ . In addition, their assay showed a limited linear range of  $10^{-4}$  and  $0.5 \times 10^{-6}$  mol  $\text{L}^{-1}$ . In our study, a new membrane consisting of Fe(III) octaethylporphyrin chloride ( $\text{C}_{36}\text{H}_{44}\text{ClFeN}_4$ ) as an ionophore was used to develop low-cost and disposable ISEs for the first time. Selectivity and detection limits of the fabricated  $\text{Fe}^{3+}$  and  $\text{Cu}^{2+}$  selective electrodes were improved due to the optimization of membrane components including lipophilic additives and plasticizers. The electrodes had fast response time ( $\leq 6$  s) and showed selectivity over various interfering cations. Also, the Internet of Things (IoT) concept was tested for on-site and simultaneous environmental monitoring of  $\text{Cu}^{2+}$  and  $\text{Fe}^{3+}$  using our developed ISEs. The sensing platform exploits the IoT approach to transmit the data to smartphones through a cloud service for the end-users. Furthermore, the characteristics of the electrodes were compared with

the previous literature reports. The developed multi-analyte sensor is advantageous over various methods due to their low-cost, fast response time, ease of fabrication, and applicability for the simultaneous quantification of iron and copper in water samples.

## EXPERIMENTAL SECTION

### Reagents and Chemicals

All chemicals and reagents were of analytical grade and utilized as received. Tetrahydrofuran (THF), KTChPB, Fe (III) octaethylporphyrin chloride, high molecular weight PVC and plasticizers, o-nitrophenyloctyl ether (NPOE), dioctylsebacate (DOS), dibutyl phthalate (DBP), dioctyl phthalate (DOP) were obtained from Fluka (Bucks, Switzerland). An 8B pencil graphite (2 mm, Koh-i Noor) was purchased from a local store and used without any pre-treatment. Ultrapure water ( $\sim 18.2$   $\text{M}\Omega\text{-cm}$ , 25 °C, ELGA LabWater, UK) was utilized to prepare all solutions of metal ions from their nitrate salts. Sodium hydroxide and nitric acid solutions with concentration between 0.1-1 mol  $\text{L}^{-1}$  were used for adjusting solution pH.

### Apparatus

The potentiometric measurements were conducted using a portable multi-channel potentiostat (sensitivity:  $\pm 0.1\text{mV}$ ) connected a smartphone through a WiFi module based on our previous study (16). A Ag/AgCl electrode (MF2052 model, BASi) was used as reference electrode (RE) during electrochemical measurements. Solution pH was tested with HI9126 (Hanna Instruments) portable pH/mV meter. All measurements were carried out at room temperature (25 °C). Debye-Hückel equation was used to calculate the ion activity coefficients (17). The weight loss of the membrane was investigated as a function of temperature using a thermal gravimetric analyzer (TGA-DTA, TA Instruments, New Castle, DE, USA). Electrode holders were 3D printed (Formlab, USA). Modified electrodes and the Ag/AgCl electrode were mounted onto the 3D-printed holder for electrochemical measurements.

### Procedure

To prepare membrane cocktails, the ionophore, KTChPB and DOS, DBP, DOP or NPOE plasticizers were dissolved in THF (18). The cocktail solution was let evaporate at room temperature. 20  $\mu\text{L}$  of membrane cocktail was dropped on the surface of each pencil graphite electrode and left at ambient temperature for 2 h to allow the THF to evaporate. Finally, the electrodes were equilibrated into a  $10^{-2}$  mol  $\text{L}^{-1}$  solution of each ion for 12 h before use. The ion-selective electrodes along with Ag/AgCl reference electrode were assembled using a fabricated 3D-printed holder. The potentiometric sensors and the reference electrode connected to the multi-channel potentiostat were dipped into 10

mL of the test solution in an electrochemical cell to perform potentiometric measurements as shown in Figure 1.

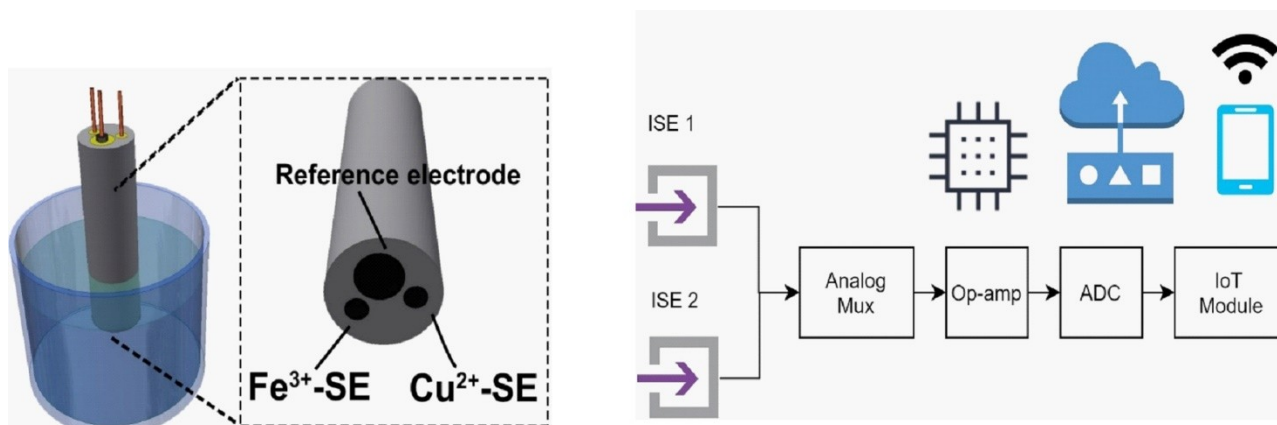


**Figure 1:** Schematic representation of the electrochemical measurement cell and diagram of the IoT data acquisition process.

## RESULTS AND DISCUSSION

To investigate the potentiometric behavior of the electrodes towards different cations, the developed electrodes were submerged into nitrate/chloride solutions of corresponding cations, which were adjusted to pH=3, for overnight. The slopes of the

corresponding potential values versus logarithmic activity of ion plots exhibited much lower than the Nernstian slopes excepting  $\text{Fe}^{3+}$  and  $\text{Cu}^{2+}$  ions, respectively (Figure 2a and 2b). Therefore, Fe(III) octaethylporphyrin chloride was selected for preparation of  $\text{Fe}^{3+}$  and  $\text{Cu}^{2+}$ -selective membranes.

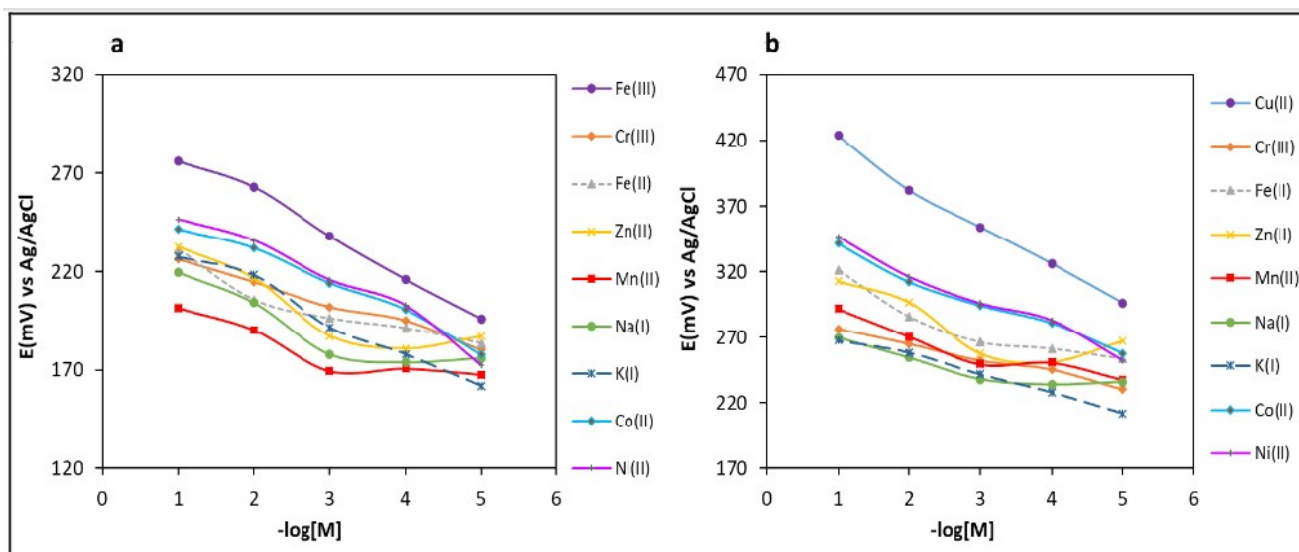


**Figure 2:** The EMF signals of (a)  $\text{Fe}^{3+}$ -selective electrode (b)  $\text{Cu}^{2+}$ -selective electrode towards different ions.

### Optimization of the Proposed Electrodes

The properties and component amounts for the membrane have significant effect on the performance of an ISE due to rapid interfacial reaction of a target metal ion at the membrane-aqueous interface. After various compositions of the membrane were prepared, their potentiometric responses were recorded as a function of primary ions concentration. Ion-selective membrane was prepared using (by weight) 0.3% KTChPB, 1% ionophore, 65.8% plasticizer, and 32.9% PVC in

THF. DOS and NPOE were used as plasticizers for preparation of iron-selective and copper-selective membrane, respectively. 200 mg of the membrane components were mixed in 2 mL of THF in a glass vial and homogenized using an ultrasonicator for 5 min. The optimized membrane composition was used to prepare the electrodes as presented in the experimental section. Then, a Mitutoyo digital micrometer (Japan) was used to measure the thickness of the membrane and was found to be  $0.20 \pm 0.09$  mm.

The potential response values of the electrodes were recorded in different activities of  $\text{Fe}^{3+}$  and  $\text{Cu}^{2+}$  solutions and a calibration curve was plotted for

each ion (Figure 3a and 3b). Nernstian slope, which is the function of different activity of analytes, is shown as the slope of the calibration curve.

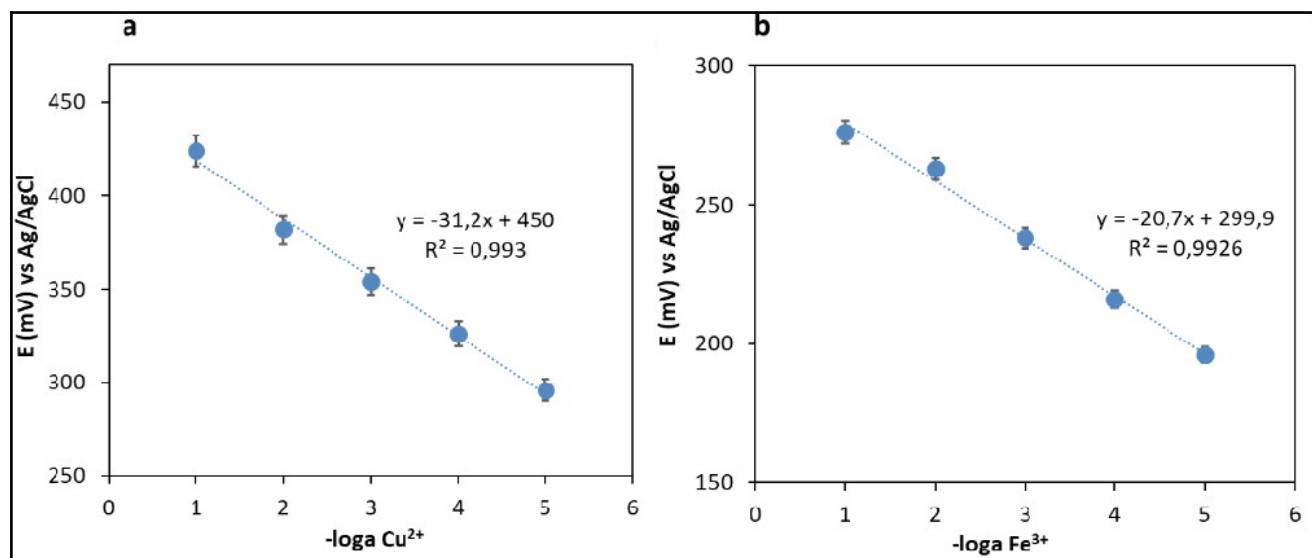


**Figure 3:** Calibration curve of the solid-contact (a)  $\text{Cu}^{2+}$  ISE and (b)  $\text{Fe}^{3+}$  ISE. Each error bar represents one standard deviation for three measurements.

For  $\text{Fe}^{3+}$ -selective electrode, the membrane composition (M5) including 1% ionophore, 65.8% DOS, 0.3% KTChPB and 32.9% PVC showed a slope of 20.7 mV/decade, which shows the ideal Nernstian slope for trivalent ions, and a limit of detection (LOD) of  $1 \times 10^{-6} \text{ mol L}^{-1}$  calculated from intersection of two slope lines. The relationship between the potential response of the  $\text{Cu}^{2+}$ -selective electrode consisting of membrane M7 and logarithm of ion activity was linear from  $1 \times 10^{-5} \text{ mol L}^{-1}$  to  $1 \times 10^{-1} \text{ mol L}^{-1}$  with a slope of 31.2 mV/decade showing Nernstian response and a LOD of  $2 \times 10^{-6} \text{ mol L}^{-1}$ . According to the results presented in Table 1, it was observed that the presence of KTChPB in the membrane enhanced the calibration curve slope.

The Donnan exclusion was improved by increased amount of KTChPB to 30 mol% (19). Plasticizer NPOE is suitable for ISEs for detection of divalent ions (11). Moreover, a polymeric membrane including more polar plasticizer, NPOE ( $\epsilon = 24$ ), exhibited an increased potential response slope and a lower detection limit for  $\text{Cu}^{2+}$  compared to the membrane consisting of PVC-DOS ( $\epsilon = 4.8$ ). Similarly, better sensitivity and enhanced detection limit were obtained using PVC-DOS membrane for  $\text{Fe}^{3+}$  detection compared to membranes containing other types of plasticizers. According to these results, it was observed that the composition of ion selective membrane has significant impact on LOD values and sensitivity of the electrodes.

**Table 1:** Composition and characterization of  $\text{Cu}^{2+}$  ISE and  $\text{Fe}^{3+}$  ISE having PVC:Plasticizer (1:2) Membrane consisting of 1 wt % ionophore and KTChPB (mol %)

Electrode	KTChPB (mol %)	Plasticizer	$\text{Cu}^{2+}$ ISE		$\text{Fe}^{3+}$ ISE	
			Slope (mV/dec)	Detection limit ( $\text{mol L}^{-1}$ )	Slope (mV/dec)	Detection limit ( $\text{mol L}^{-1}$ )
M1	10	NPOE	27.3	$7 \times 10^{-6}$	17.5	$6 \times 10^{-4}$
M2	50	NPOE	35.4	$1 \times 10^{-6}$	18.6	$5 \times 10^{-4}$
M3	10	DOS	23.1	$3 \times 10^{-5}$	18.9	$3.2 \times 10^{-5}$
M4	50	DOS	27.3	$5 \times 10^{-5}$	18.5	$1 \times 10^{-5}$
M5	30	DOS	27.7	$5 \times 10^{-5}$	20.1	$1 \times 10^{-6}$
M6	-	DOS	-	-	15.2	$5.4 \times 10^{-4}$
M7	30	NPOE	31.2	$2 \times 10^{-6}$	18.7	$6.5 \times 10^{-5}$
M8	30	DOP	26.5	$1 \times 10^{-4}$	18.4	$2.3 \times 10^{-4}$
M9	30	DBP	25.3	$1 \times 10^{-4}$	18.2	$5 \times 10^{-4}$
M10	-	NPOE	20.6	$6.2 \times 10^{-4}$	-	-

#### Effect of pH

The pH effect on the potentiometric response of the electrodes was investigated at a fixed concentration



( $1 \times 10^{-3}$  mol L<sup>-1</sup>) in the pH range between 1.0 and 8.0. The potential values are plotted in Figure 4a and 4b. It was observed that the potential response of the electrodes were constant at pH values in the range of 1.5-3.5 and 2.0-4.7, which could be considered as the working pH range of iron- and copper-selective electrodes, respectively. Due to the binding of H<sup>+</sup>/OH<sup>-</sup>, the potential changes might be observed with high acidity or alkalinity of the

solution. Potential responses were not independent at pH lower than 1.5 and pH higher than 3.5 because of protonation of the ionophore and formation of ferric hydroxide in the solution, respectively. Similarly, change in equilibrium potential below 4.7 and above 2.0 could be due to hydrolysis of Cu<sup>2+</sup> resulting in formation of more H<sup>+</sup> ions competing with Cu<sup>2+</sup> (20).

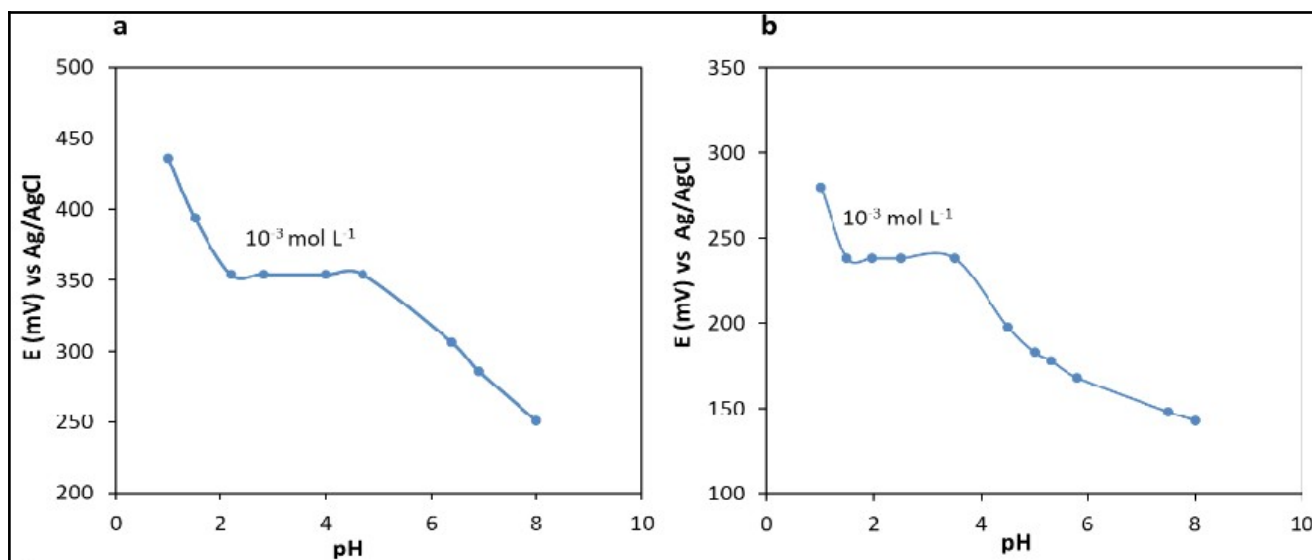


**Figure 4:** pH effect of the solutions to the EMF signals of (a) Cu<sup>2+</sup> ISE and (b) Fe<sup>3+</sup> ISE.

#### Response Time, Repeatability, Reproducibility, and Stability of the Electrodes

Electrodes response times were recorded with the time required to achieve 95% of final equilibrium electromotive force (EMF) signal after successive immersion of the test solutions within the concentration from  $1.0 \times 10^{-6}$  mol L<sup>-1</sup> to  $1.0 \times 10^{-2}$  mol L<sup>-1</sup>. The electrode response times were obtained as 6 s and 4 s for detection of Fe<sup>3+</sup> and Cu<sup>2+</sup>, respectively (Figure 5a and 5b), which is suitable for *in-situ* detection. The short response time of the electrodes was the result of the fast exchange kinetics between association and dissociation of ions with the porphyrin derivative ionophore at the membrane surface. It is necessary to obtain consistent performance after utilization of the

electrodes repeatedly for real-time monitoring water. Thus, the repeatability and reproducibility tests (n=5) of the electrodes were performed in  $1.0 \times 10^{-3}$  mol L<sup>-1</sup> Fe<sup>3+</sup> and Cu<sup>2+</sup> solutions. While RSDs (relative standard deviations) have been calculated as 2.4% and 2.7% for repeatability of Fe<sup>3+</sup> and Cu<sup>2+</sup> selective electrodes, respectively, RSDs were found as 3.2% and 3.0% for reproducibility of the electrodes. Moreover, long-term stability of the electrodes were investigated using same electrodes during eight weeks and the calibration plot slopes were decreased by 5% and 7% for Fe<sup>3+</sup> and Cu<sup>2+</sup> selective electrodes, respectively. Since the change were not significant, they could be used during this period.

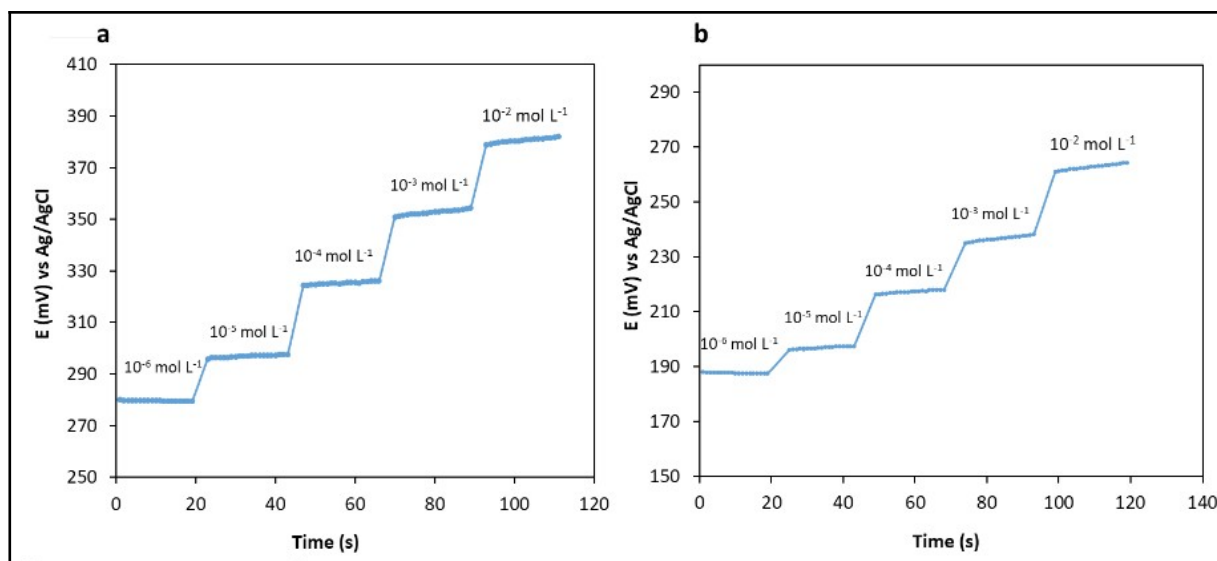


**Figure 5:** Response time of (a)  $\text{Cu}^{2+}$  ISE and (b)  $\text{Fe}^{3+}$  ISE for step change in concentrations.

### Interference Study

The interference effect of other cations to the response of developed electrodes were investigated since selectivity coefficient represent the ability of the electrode to discriminate the target ion in the presence of interfering ions. For determination of the selectivity coefficients, the matched potential method (MPM) was used (21). The potential response ( $\Delta E$ ) value was recorded while the activity of primary ions changed from  $a_A = 5 \times 10^{-4} \text{ mol L}^{-1}$  to  $a_{A'} = 5 \times 10^{-3} \text{ mol L}^{-1}$ . Until the same  $\Delta E$  was obtained,  $0.1 \text{ mol L}^{-1}$  solution of the interfering ion

( $a_B$ ) was added to primary ion solution. The values of the sensor selectivity coefficient are evaluated using the equation (Equation 1) and presented in Table 2.

$$K_{A,B} = (a'_A - a_A) / a_B \quad (1)$$

It can be seen in Table 2 that interferences with metal ions including  $\text{Na}^+$ ,  $\text{K}^+$ ,  $\text{Mn}^{2+}$ ,  $\text{Zn}^{2+}$ ,  $\text{Ni}^{2+}$ ,  $\text{Co}^{2+}$ ,  $\text{Fe}^{2+}$ , and  $\text{Cr}^{3+}$  are negligible for the developed electrodes since the selectivity coefficient values were lower than 1 (22).

**Table 2:** Potentiometric selectivity coefficients of the developed ISEs.

Ion	Log $K_{i,j}^a$	Log $K_{i,j}^a$
	$\text{Cu}^{2+}$ ISE	$\text{Fe}^{3+}$ ISE
$\text{Na}^+$	-3.6	-4.3
$\text{K}^+$	-3.8	-4.4
$\text{Mn}^{2+}$	-2.8	-2.4
$\text{Zn}^{2+}$	-2.5	-2.4
$\text{Fe}^{2+}$	-3.0	-3.2
$\text{Cu}^{2+}$	-	-3.5
$\text{Ni}^{2+}$	-2.8	-2.9
$\text{Co}^{2+}$	-2.7	-2.2
$\text{Fe}^{3+}$	-3.5	-
$\text{Cr}^{3+}$	-4.5	-3.1

<sup>a</sup>Average value obtained from the three corresponding pairs of concentrations of  $\text{Cu}^{2+}$ ,  $\text{Fe}^{3+}$  and the respective interfering cation.

### Thermogravimetric Analysis

The results of the thermal analysis of the PVC/ionophore/NPOE and PVC/ionophore/DOS membranes are presented in Figure 6a and Figure 6b, respectively. Weight loss of the membranes started to be seen at 293 and 295 °C, respectively. At temperatures which the initial mass loss was observed, the loss of mass was equal to 11.68% and 14.59% for the slow decomposition of the material in the TGA measurement. The inorganic contents of the component underwent degradation

based on the curve which was at 455 °C onwards. A single large peak was found at ~295 °C, which indicate the exothermic reaction in the composite in the DTGA curve (Figure 6b). The thermal decomposition of the polymeric membrane showed the similar general weight loss pattern to the reported values of 200-350 °C and 450-600 °C (23). These results include that the membranes are thermally stable and can be used at higher temperatures.

**Analytical Applications**

10 mL aliquot samples of tap water were spiked with standard Fe<sup>3+</sup> or Cu<sup>2+</sup> solutions at pH=3. For each increment, the concentration of Fe<sup>3+</sup> or Cu<sup>2+</sup> sample solution was calculated using the change in potential responses (mV). Next, the environmental water sample was used for application of the developed sensing platform integrated with WiFi to an IoT based web server (ThingSpeak.com) and the real-time data was validated with standard addition method and exhibited in Table 3. In addition, the

electrodes were utilized to determine Fe<sup>3+</sup> and Cu<sup>2+</sup> ion concentration in spiked tap water with standard addition method (Table 3). There were no significant differences between the determination results of the developed electrodes. Since the results obtained using Fe<sup>3+</sup>-ISE and Cu<sup>2+</sup>-ISE are in good agreement with added values, the proposed methodology has great promise for accurate and simultaneous quantification of Fe<sup>3+</sup> and Cu<sup>2+</sup> ions in water samples.

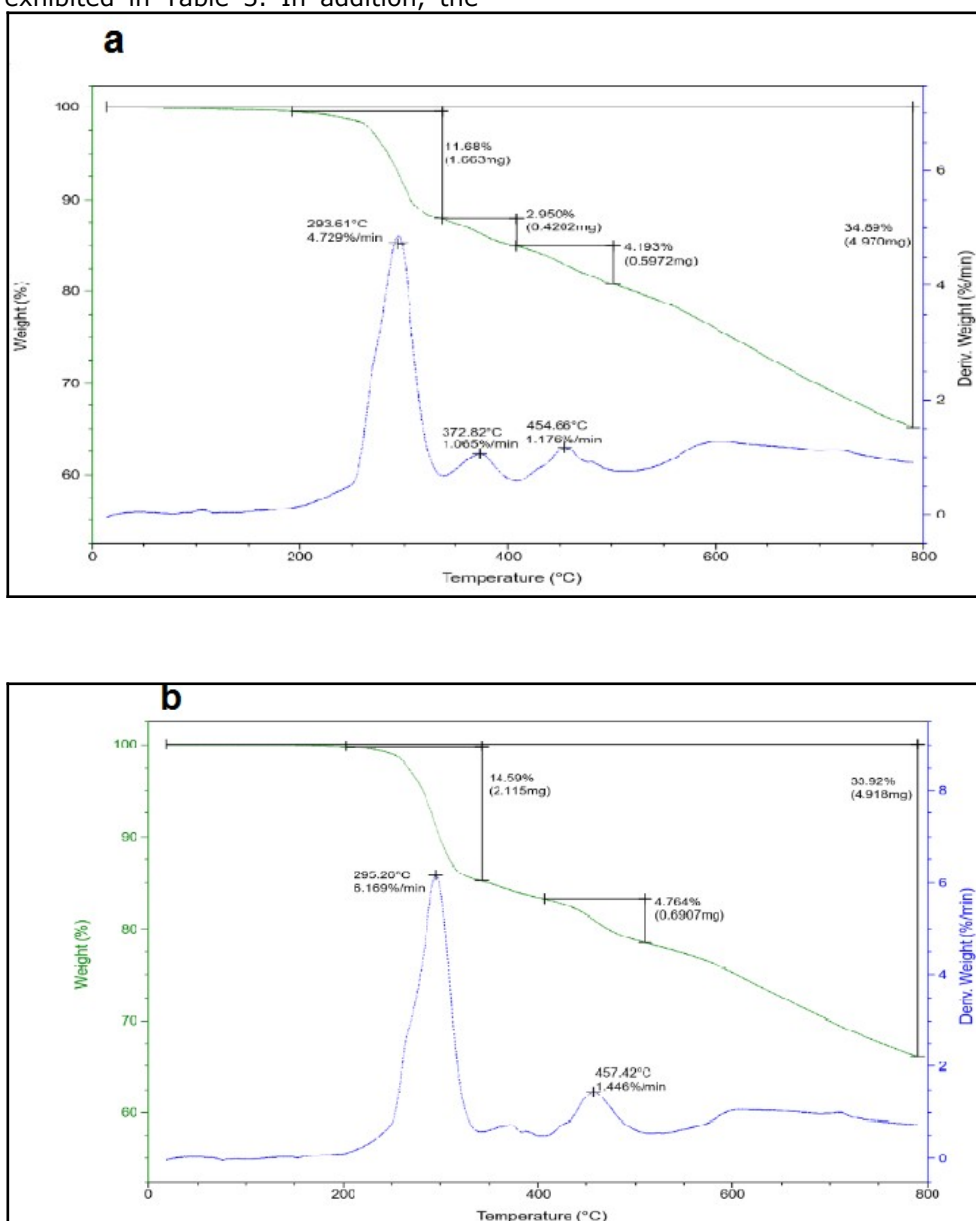


**Figure 6:** TGA spectra of (a) PVC/ionophore/NPOE and (b) PVC/ionophore/DOS up to 800 °C in nitrogen atmosphere.

**Table 3:** The results for the simultaneous detection of  $\text{Cu}^{2+}$  and  $\text{Fe}^{3+}$  in water samples using developed ISEs.

Sample	Added ( $\mu\text{mol L}^{-1}$ )	$\text{Cu}^{2+}$ ISE (measured value, $\mu\text{mol L}^{-1}$ )	Recovery (%)	$\text{Fe}^{3+}$ ISE (measured value, $\mu\text{mol L}^{-1}$ )	Recovery (%)
Tap water 1	10	10.06±0.09	100.6	10.08±0.09	100.8
Tap water 2	20	20.3±0.1	101.5	19.9±0.1	99.5
Tap water 2	50	49.3±0.1	98.6	50.1±0.2	100.2
Environmental water	50	49.40±0.1	98.8	49.8±0.2	99.6

### Comparison of the $\text{Fe}^{3+}$ and $\text{Cu}^{2+}$ Ion-Selective Electrodes with other ISEs

The response characteristics of other  $\text{Fe}^{3+}$  and  $\text{Cu}^{2+}$ -ISEs in the literature ions are compared with the proposed electrodes in Tables 4 and 5. Consequently, the developed electrodes for detection of  $\text{Fe}^{3+}$  and  $\text{Cu}^{2+}$  ions show better LOD and wider linear concentration ranges compared to the most of previous works.

### CONCLUSION

It is important to detect metal ions in environmental samples to protect human health and ecosystem. The routine analysis of iron and copper are typically performed using bulky instruments such as atomic absorption spectroscopy, inductively coupled plasma-optical emission spectrophotometry, inductively coupled plasma mass spectrometry, and spectrophotometry, which require trained personnel to operate, large amount of samples/reagents and transportation of samples to the laboratory. On the other hand, the electrochemical sensors integrated with IoT provide autonomous decisions along with the obtained data, allowing rapid response time of sensing platforms in a user-friendly manner. The

utilization of smart technology is crucial for in-field applications of environmental samples.

In this study, a new low-cost IoT-based sensing platform using disposable pencil graphite electrodes is developed for simultaneous and sensitive detection of  $\text{Fe}^{3+}$  and  $\text{Cu}^{2+}$  ions. Fe (III) octaethylporphyrin chloride was used as ionophore for the polymeric membrane  $\text{Fe}^{3+}$ -ISE and  $\text{Cu}^{2+}$ -ISE for the first time. The membrane components were optimized and resulted in improved Nernstian responses towards  $\text{Fe}^{3+}$  and  $\text{Cu}^{2+}$ , slope of 20.7 mV/decade and 31.2 mV/decade with LOD of  $1 \times 10^{-6}$  mol  $\text{L}^{-1}$  and  $2 \times 10^{-6}$  mol  $\text{L}^{-1}$ , respectively. The results demonstrate that the fabricated ISEs are able to be employed in a pH range of 1.5-3.5 and 2.0-4.7 for  $\text{Fe}^{3+}$  and  $\text{Cu}^{2+}$  ions respectively, with rapid response, good reversibility, and a long-time stability. The electrodes had no interference in the presence of common ions. High thermal membrane stability was observed in TGA studies. Furthermore, the ISEs were successfully used to detect  $\text{Fe}^{3+}$  and  $\text{Cu}^{2+}$  in spiked and real water samples with good recoveries. The proposed system is suitable for real-time monitoring of  $\text{Fe}^{3+}$  and  $\text{Cu}^{2+}$  ions in water.

**Table 4:** The developed Fe<sup>3+</sup>-selective electrode compared to other electrodes in the literature.

<b>Ionophore</b>	<b>Linear Range (mol L<sup>-1</sup>)</b>	<b>LOD (mol L<sup>-1</sup>)</b>	<b>Response time (s)</b>	<b>pH range</b>	<b>Ref.</b>
1) Phosphorylated Calix-6-Arene Derivative	1.0×10 <sup>-2</sup> - 1.0×10 <sup>-4</sup>	1.0 × 10 <sup>-5</sup>	5	4.0-7.0	(24)
2) norfloxacin	1.0×10 <sup>-1</sup> - 1.0×10 <sup>-5</sup>	5.0×10 <sup>-6</sup>	10	3.0-8.0	(25)
3) morin-Fe <sup>2+</sup> schiff-base complex	1.0×10 <sup>-1</sup> - 1.0×10 <sup>-6</sup>	4.5×10 <sup>-7</sup>	<10	5.0-10.0	(26)
4) Iron (II) Phthalocyanines	1.0×10 <sup>-1</sup> - 1.0×10 <sup>-6</sup>	1.8×10 <sup>-7</sup>	<7	3.5-5.7	(18)
5) Iron(III) phosphate and silver sulfide	1.0×10 <sup>-2</sup> - 3.97×10 <sup>-5</sup>	2.41×10 <sup>-5</sup>	Not tested	1	(27)
6) Fe(III) octaethylporphyrin chloride	1.0×10 <sup>-1</sup> - 1.0×10 <sup>-5</sup>	1×10 <sup>-6</sup>	6	1.5-3.5	This work

**Table 5.** The developed Cu<sup>2+</sup>-selective electrode compared to other electrodes in the literature.

<b>Ionophore</b>	<b>Linear Range (mol L<sup>-1</sup>)</b>	<b>LOD (mol L<sup>-1</sup>)</b>	<b>Response time (s)</b>	<b>pH range</b>	<b>Ref.</b>
1) 1-ethyl-3-methyl imidazolium chloride	1.0×10 <sup>-1</sup> - 1.0×10 <sup>-7</sup>	3.2×10 <sup>-8</sup>	5-10	2.5-6.0	(28)
2) Rhodamine 6g	1.0×10 <sup>-2</sup> - 4.3×10 <sup>-7</sup>	4.3×10 <sup>-7</sup>	15	4.0-7.5	(3)
3) phenanthroline-tetraphenyl borate	1.0×10 <sup>-2</sup> - 1.0×10 <sup>-6</sup>	1.0×10 <sup>-6</sup>	8	3.8 - 5	(29)
4) thiohydrazone and thiosemicarbazone ligands	1.0×10 <sup>-2</sup> - 1.0×10 <sup>-5</sup>	2.5×10 <sup>-6</sup>	2-18	-	(30)
5) cyclic tetrapeptide derivatives	1.0×10 <sup>-2</sup> - 3.1.0×10 <sup>-6</sup>	2.1×10 <sup>-6</sup>	<15	4.5 - 7	(31)
6) Fe (III) octaethylporphyrin chloride	1.0×10 <sup>-1</sup> - 1.0×10 <sup>-5</sup>	2×10 <sup>-6</sup>	4	2.0-4.7	This work

## CONFLICT OF INTEREST

The author declares that they have no known competing financial interests or personal relationships that could have appeared to influence the work reported in this paper.

## ACKNOWLEDGEMENTS

This work was supported by Yildiz Technical University Scientific Research Projects Coordination Unit under project number FBA-2021-4389. I would like to thank Prof. Dr. Charles S. Henry for editing English language throughout the manuscript.

## REFERENCES

1. Ghasemi Z, Mohammadi A. Sensitive and selective colorimetric detection of Cu (II) in water samples by thiazolylazopyrimidine-functionalized TiO<sub>2</sub> nanoparticles. *Spectrochimica Acta Part A: Molecular and Biomolecular Spectroscopy*. 2020 Oct;239:118554. <DOI>.
2. Kaur I, Sharma M, Kaur S, Kaur A. Ultra-sensitive electrochemical sensors based on self-assembled chelating dithiol on gold electrode for trace level detection of copper(II) ions. *Sensors and Actuators B: Chemical*. 2020 Jun;312:127935. <DOI>.
3. Paul A, Nair RR, Chatterjee PB, Srivastava DN. Fabrication of a Cu(II)-Selective Electrode in the Polyvinyl Chloride Matrix Utilizing Mechanochemically Synthesized Rhodamine 6g as an Ionophore. *ACS Omega*. 2018 Nov 30;3(11):16230–7. <DOI>.
4. Tang S, Chang Y, Shen W, Lee HK. Selective extraction by dissolvable (nitriloacetic acid-nickel)-layered double hydroxide coupled with reaction with potassium thiocyanate for sensitive detection of iron(III). *Talanta*. 2016 Jul;154:416–22. <DOI>.
5. Zhao Y, Ouyang H, Feng S, Luo Y, Shi Q, Zhu C, et al. Rapid and selective detection of Fe (III) by using a smartphone-based device as a portable detector and hydroxyl functionalized metal-organic frameworks as the fluorescence probe. *Analytica Chimica Acta*. 2019 Oct;1077:160–6. <DOI>.
6. Di Masi S, Pennetta A, Guerreiro A, Canfarotta F, De Benedetto GE, Malitesta C. Sensor based on electrosynthesised imprinted polymeric film for rapid and trace detection of copper(II) ions. *Sensors and Actuators B: Chemical*. 2020 Mar;307:127648. <DOI>.
7. Akhond M, Absalan G, Pourshamsi T, Ramezani AM. Gas-assisted dispersive liquid-phase microextraction using ionic liquid as extracting solvent for spectrophotometric speciation of copper. *Talanta*. 2016 Jul;154:461–6. <DOI>.
8. Yasukawa T, Kiba Y, Mizutani F. A Dual Electrochemical Sensor Based on a Test-strip Assay for the Quantitative Determination of Albumin and Creatinine. *Anal Sci*. 2015;31(7):583–9. <DOI>.
9. Soloviev V, Varnek A, Babain V, Polukeev V, Ashina J, Legin E, et al. QSPR modeling of potentiometric sensitivity towards heavy metal ions for polymeric membrane sensors. *Sensors and Actuators B: Chemical*. 2019 Dec;301:126941. <DOI>.
10. Mahanty B, Satpati AK, Kumar S, Leoncini A, Huskens J, Verboom W, et al. Development of polyvinyl chloride (PVC)-based highly efficient potentiometric sensors containing two benzene-centered tripodal diglycolamides as ionophores. *Sensors and Actuators B: Chemical*. 2020 Oct;320:127961. <DOI>.
11. Bakker E, Bühlmann P, Pretsch E. Carrier-Based Ion-Selective Electrodes and Bulk Optodes. 1. General Characteristics. *Chem Rev*. 1997 Dec 1;97(8):3083–132. <DOI>.
12. Pungor E, Tóth K. Ion selective electrodes. A review. *Anal Sci*. 1987;3(5):387–93. <DOI>.
13. McQuade DT, Pullen AE, Swager TM. Conjugated Polymer-Based Chemical Sensors. *Chem Rev*. 2000 Jul 1;100(7):2537–74. <DOI>.
14. Qi Z-L, Cheng Y-H, Xu Z, Chen M-L. Recent Advances in Porphyrin-Based Materials for Metal Ions Detection. *IJMS*. 2020 Aug 14;21(16):5839. <DOI>.
15. Chen X, Wang Y, Zhao X, Liu B, Xu Y, Wang Y. A gadolinium(III)-porphyrin based coordination polymer for colorimetric and fluorometric dual mode determination of ferric ions. *Microchim Acta*. 2019 Feb;186(2):63. <DOI>.
16. Agir I, Yildirim R, Nigde M, Isildak I. Internet of Things Implementation of Nitrate and Ammonium Sensors for Online Water Monitoring. *Anal Sci*. 2021 Jul 10;37(7):971–6. <DOI>.
17. Manov GG, Bates RG, Hamer WJ, Acree SF. Values of the Constants in the Debye–Hückel Equation for Activity Coefficients 1. *J Am Chem Soc*. 1943 Sep;65(9):1765–7. <DOI>.
18. Ozer T, Isildak I. A New Fe (III)-Selective Membrane Electrode Based on Fe (II) Phthalocyanine. *J Electrochem Sci Technol*. 2019 Sep 30; 321-8. <DOI>.
19. Li L, Zhang Y, Du P, Qian Y, Zhang P, Guo Q. Polymeric Membrane Electrodes Using Calix[4]pyrrole Bis/Tetra-Phosphonate Cavitands as Ionophores for Potentiometric Acetylcholine Sensing with High Selectivity. *Anal Chem*. 2020 Nov 3;92(21):14740–6. <DOI>.



20. Mahajan RK, Sood P. Novel Copper (II)-selective electrode based on 2, 2': 5', 2''-terthiophene in PVC matrix. *Int J Electrochem Sci.* 2007;2:832–47.
21. Umezawa Y, Umezawa K, Sato H. Selectivity coefficients for ion-selective electrodes: Recommended methods for reporting  $K_{A,B}^{pot}$  values (Technical Report). *Pure and Applied Chemistry.* 1995 Jan 1;67(3):507–18. [<DOI>](#).
22. K. Mittal S, Kumar S, Kaur N. Enhanced Performance of CNT-doped Imine Based Receptors as Fe(III) Sensor Using Potentiometry and Voltammetry. *Electroanalysis.* 2019 Jul;31(7):1229–37. [<DOI>](#).
23. Khan A, Khan AAP, Hussein MA, Neppolian B, Asiri AM. Preparation of new and novel wave like poly(2-anisidine) zirconium tungstate nanocomposite: Thermal, electrical and ion-selective studies. *Chinese Journal of Chemical Engineering.* 2019 Feb;27(2):459–66. [<DOI>](#).
24. Zareh MM, Zordek W, Abd-Alhady A. Iron-Selective Electrode Based on Phosphorylated Calix-6-Arene Derivative. *JST.* 2014;04(04):186–94. [<DOI>](#).
25. Yari A. A Novel Iron(III) Potentiometric Sensor Based on (E)-N'-((2-hydroxynaphthalen-3-yl)methylene)benzohydrazide. *Int J Electrochem Sci.* 2016 Aug;6597–608. [<DOI>](#).
26. Gupta VK, Singh AK, Al Khayat M, Gupta B. Neutral carriers based polymeric membrane electrodes for selective determination of mercury (II). *Analytica Chimica Acta.* 2007 May;590(1):81–90. [<DOI>](#).
27. Paut A, Prkić A, Mitar I, Bošković P, Jozić D, Jakić M, et al. Potentiometric Response of Solid-State Sensors Based on Ferric Phosphate for Iron(III) Determination. *Sensors.* 2021 Feb 25;21(5):1612. [<DOI>](#).
28. Wardak C, Lenik J. Application of ionic liquid to the construction of Cu(II) ion-selective electrode with solid contact. *Sensors and Actuators B: Chemical.* 2013 Dec;189:52–9. [<DOI>](#).
29. Ali TA, Mohamed GG, El-Dessouky MMI, Abou El-Ella SM, Mohamed RTF. Modified Screen-Printed Electrode for Potentiometric Determination of Copper(II) in Water Samples. *J Solution Chem.* 2013 Jul;42(6):1336–54. [<DOI>](#).
30. Jesús Gismera M, Antonia Mendiola M, Rodriguez Procopio J, Teresa Sevilla M. Copper potentiometric sensors based on copper complexes containing thiohydrazone and thiosemicarbazone ligands. *Analytica Chimica Acta.* 1999 Apr;385(1–3):143–9. [<DOI>](#).
31. Hassan S, Elnemma E, Mohamed A. Novel potentiometric copper (II) selective membrane sensors based on cyclic tetrapeptide derivatives as neutral ionophores. *Talanta.* 2005 May 15;66(4):1034–41. [<DOI>](#).





## Alterations in Antioxidant Defense Systems and Metal Profiles in the Liver of Rats with Metabolic Syndrome Induced with High-Sucrose Diet

Özlem Alptekin<sup>1\*</sup>  , S. Seyhan Tükel<sup>2</sup> , Belma Turan<sup>3</sup> , Yurdun Kuyucu<sup>4</sup> 

<sup>1</sup>University of Cukurova, Faculty of Pharmacy, Department of Biochemistry, Adana, Turkey

<sup>2</sup>University of Cukurova, Faculty of Arts & Sciences, Department of Chemistry, Adana, Turkey

<sup>3</sup>University of Lokman Hekim, Faculty of Medicine, Department of Biophysics, Ankara, Turkey

<sup>4</sup>University of Cukurova, Faculty of Medicine, Department of Histology and Embryology, Adana, Turkey

**Abstract:** Metabolic syndrome (MetS) is a combination of several different metabolic disorders and considered one of the major public health problems worldwide. The underlying causes of MetS include being overweight and obesity, physical inactivity, and genetic factors. We aimed to examine the alterations in the levels of biomarkers of oxidative stress, activities of antioxidant defense enzymes, and metal contents of the liver in rats with MetS. Rats in control and MetS groups were fed with standard rat chow-drinking water and standard rat chow - 32% sucrose solution (instead of drinking water) *ad libitum* for 16 weeks, respectively. Following the confirmation of MetS, antioxidant enzyme activities and malondialdehyde (MDA), 3-nitrotyrosine (3-NT), phospho-Akt (pSer473) levels were measured in the homogenates of the liver. Distributions of elements in the liver were also analyzed. The stained hepatic tissue slides were examined by light microscopy. The activities of catalase and glutathione-S-transferase were significantly decreased in MetS-group (about 15% and 29%, respectively) compared to the control group, while the glutathione reductase activity and MDA and 3-NT levels were significantly increased (as the levels of 78%, 26%, and 67%, respectively) ( $p < 0.05$ ). The hepatocytes in the MetS group showed mild diffuse microvesicular steatosis. Furthermore, Cu, Fe, and Mn levels were significantly high in MetS-group while Zn level was significantly low compared to the control group. Our results showed increased oxidative stress, impaired antioxidant defense enzyme activities, and altered metals' metabolisms which may have an important role in the pathogenesis of MetS.

**Keywords:** Metabolic syndrome, liver, antioxidants, oxidative stress, metals

**Submitted:** September 23, 2021. **Accepted:** November 16, 2021.

**Cite this:** Alptekin Ö, Tükel SS, Turan B, Kuyucu Y. Alterations in Antioxidant Defense Systems and Metal Profiles in the Liver of Rats with Metabolic Syndrome Induced with High-Sucrose Diet. JOTCSA. 2022;9(1):13-20.

**DOI:** <https://doi.org/10.18596/jotcsa.945582>.

**\*Corresponding author. E-mail:** [oyalptekin@cu.edu.tr](mailto:oyalptekin@cu.edu.tr).

### INTRODUCTION

Metabolic syndrome (MetS) is a cluster of metabolic conditions, such as insulin resistance, abnormal glucose tolerance, abdominal obesity, hypertension, hypertriglyceridemia, hyperinsulinemia, hyper low-density lipoproteins, prothrombotic and/or pro-inflammatory states. Those are accepted risk factors that increase the incidence of type 2 diabetes mellitus (T2DM), non-alcoholic fatty liver disease (NAFLD), cardiovascular disease (CVD), and renal

disease (1). MetS affects a significant percentage of the population and is increasingly more prevalent in developing countries, such as Turkey, where the prevalence was 26.8% in men and 38.3% in women in 2018 (2).

The pathogenesis of MetS is very complex and the underlying mechanisms of how the risk factors are affecting are not known very well yet. Imbalance of oxidant/antioxidant status may play a key role in its manifestations (3,4). Oxidative damage is resulted

from oxidative stress and disrupts redox signaling. The levels of biomarkers which are oxidative damage products from lipids, proteins and DNA are often measured for determination of the status of oxidative stress (5). The malondialdehyde (MDA) and 3-nitrotyrosine (3-NT) are the main products of oxidative damage of lipids and amino acids, respectively. Modification of protein tyrosine can result in changes of protein structure, function, and catalytic activity. The formation of reactive oxygen or nitrogen species (ROS or RNS) and repair of oxidative damage in cells can be controlled by the antioxidant system that consists of non-enzymatic and enzymatic antioxidants (6). Superoxide dismutase (SOD), catalase (CAT), glutathione reductase (GR) and glutathione peroxidase (GPx) are the antioxidant enzymes. SOD is a metalloenzyme containing Cu/Zn in cytosol or Mn in mitochondria catalyzes the formation of hydrogen peroxide from the superoxide anion radical. CAT is also a metalloenzyme containing Fe catalyzing the decomposition of hydrogen peroxide to molecular oxygen and water. GR catalyzes the reduction of glutathione disulfide (GSSG) to glutathione (GSH) by the NADPH-dependent mechanism and plays a critical role in GSH metabolism. GPx containing Se plays an important role in the reduction of hydrogen peroxide and peroxide radicals. Glutathione S-transferase (GST), that is important for detoxification of oxidative products of oxidative stress, catalyzes the conjugation of GSH to xenobiotic substrates for the cellular detoxification and excretion (7).

The major tasks of the liver include maintaining systemic glucose and lipid homeostasis through a complex hormonal system, control of transcription factors and signalling pathways. Moreover, it is especially susceptible to the damage of oxidative stress (8). Akt (PKB) is a serine/threonine-specific protein kinase and plays an important role in cell growth, survival, proliferation, and metabolism (9). Furthermore, Akt signaling plays a central role in insulin-stimulated glucose uptake in both muscle and adipose tissue in that time it inhibits glucose release from hepatocytes (10). Akt can affect further processes associated with MetS and its long-term consequences.

Experimental animal models mimicking the disease state in humans are very important to evaluate the pathophysiology of MetS in human. Genetic modification, drugs and dietary manipulation were used to induce MetS in animal models in many pieces of research (11). Diet affects whole-body metabolism so a single type of diet (high-sucrose, high-fructose or high-fat) or a combination of diets (high-sucrose/high-fat or high-fructose/high-fat) were used to induce MetS. Rat model that is the most used to investigate metabolic diseases displays the closest criterion to human MetS was induced by diet.

In some studies of MetS in humans, metal levels have been measured in biological samples such as whole blood, plasma, serum, and urine (12-15). Animal model studies are also important to determine possible changes in metal levels in different organs or tissues as early and direct indicators of many syndromes. The roles of the metals, antioxidant enzymes and products of ROS and RNS in MetS are not clear yet. In the literature, there were different experimental studies related to the MetS in which CAT and SOD activities, MDA or some metals status in serum, liver, or other tissues were measured (16-21). However, all above mentioned parameters and additionally GPx, GR and GST activities and 3-NT and phospho-Akt (pSer473) levels in the liver were not evaluated simultaneously. This study will contribute to the more accurate explanation of the mechanisms related to MetS in the liver. To the best of our knowledge, there is not any similar experimental study in the literature that determine all the above-mentioned parameters in the liver of male Wistar rats in which MetS is induced with a 32% sucrose solution. In the present study, we aimed to investigate the possible association between MetS and the altered antioxidant status in terms of enzymatic activities, the levels of oxidative stress biomarkers, and morphological changes of hepatic tissue and to assess the levels of metals in the liver of rats with sucrose induced MetS.

## MATERIALS AND METHODS

### Experimental Animals

In this study, 2-month-old male Wistar rats (n=16) were randomly separated into two groups: control (n = 6); and MetS (n = 10). Initial bodily weight of the rats was approximately 200–220 g in each group. They were kept on a 12-light/12-h dark cycle at  $20 \pm 2$  °C, 30–70% humidity. All experimental procedures approved by The Local Ethics Committee on Animal Experiments of Ankara University (2019-5-50) and they performed according to institutional guidelines.

### Induction and Validation of Mets in Rats

Rats in the control group were fed with standard rat chow-drinking water and in the MetS group they fed standard rat chow-32% sucrose solution *ad libitum* for 16 weeks. Bodily weight of each animal was recorded at the beginning of experimental studies then at the end of 16 weeks. Glucose tolerance and insulin resistance tests were made for control and MetS groups at the 16<sup>th</sup> week. Fasting blood glucose and serum insulin levels were measured in blood samples were taken from the tail vein, using a glucometer (Accu-check Nano Performa, Roche, Mannheim, Germany) and an insulin (rat) enzyme immunoassay kit (A05105; SPIBIO, Montigny le Bretonneux, France), respectively. Homeostatic Model Assessment for Insulin Resistance (HOMA-IR) was calculated according to the formula: fasting

insulin ( $\mu\text{U/L}$ )  $\times$  fasting glucose ( $\text{mmol/L}$ )/22.5 (22).

The oral glucose tolerance test (OGTT) was performed to rats fasted for 12 h. Glucose solution (40% (w/v)) was loaded into the stomach by a gastric catheter at a dose of 2 g/kg bodily weight of rats. Blood glucose and serum insulin levels were measured at 0, 15, 30, 60, and 120 min after glucose loading and results were calculated from the area under the curve (AUC) of insulin and glucose.

#### Harvesting of the Liver and Preparation of the Tissue Homogenate

Rats were sacrificed after intraperitoneal injection of pentobarbital sodium (30 mg/kg) and then the livers were immediately excised. Some small pieces of the hepatic tissue samples were fixed in 10% formalin for histomorphological examination and remaining parts were stored at  $-80\text{ }^{\circ}\text{C}$  until using for biochemical analysis.

The liver homogenates were prepared according to our previous study (16). The homogenates were centrifuged at 10,000 g (Hettich Universal 30 RF, Tuttlingen, Germany) for 30 min at  $+4\text{ }^{\circ}\text{C}$ . The supernatants were separated from precipitates then their protein concentrations were determined according to Lowry et al. by using bovine serum albumin solution as a standard (23). Before measuring SOD, CAT, GPx, GR and GST activities, the protein concentrations of supernatants were adjusted to 1 mg/mL.

#### Determination of MDA, 3-NT, and Phospho-Akt (pSer473) Levels

The MDA level was assessed according to the method of Buege and Aust (24). The results were given as  $\mu\text{mol}$  MDA per milligrams of protein in supernatants. For determination of 3-NT and phospho-Akt (pSer473) levels in the liver ELISA (Enzyme linked immunosorbent assay) kits (ab116691, Abcam and RAB0011, Sigma-Aldrich) were used according to the manufacturer's instructions. The relative amount of phospho-Akt (pSer473) was calculated in the MetS group as compared to the control group.

#### Determination of SOD, CAT, GPx, GR, and GST Activities

SOD, CAT, GPx, GR and GST activities were determined according to Sun et al. (25), Aebi (26), Paglia and Valentine (27), Carlberg and Mannervik (28) and Habig et al. (29) by spectrophotometric means, respectively. One SOD unit was defined as the amount of enzyme that inhibits the rate of nitro blue tetrazolium (NBT) reduction by 50%. The CAT activity was expressed as  $\mu\text{mol}$  of  $\text{H}_2\text{O}_2$  decomposed per mg protein per minute. The GPx and GR activities were expressed as nmol oxidized NADPH per mg of protein per minute. The GST activity was given as nmol 1-chloro-2,4-dinitrobenzene (CDNB)-glutathione conjugate per mg protein per minute.

#### Light Microscopic Examination

The hepatic tissue samples were fixed in 10% formalin for 72 h and dehydrated for paraffin embedding. The paraffin piece was cut into sections, at 5  $\mu\text{m}$  thickness using a microtome, then they were stained with hematoxylin and eosin (H&E). Slides were examined and photographed with the Olympus BX 53 light microscope (Olympus Corp., Tokyo, Japan).

#### Determination of Metallic Levels in the Liver

The weighed liver samples were dried at  $105\text{ }^{\circ}\text{C}$  for 120 h, then dried tissues were digested with a  $\text{HClO}_4/\text{HNO}_3$  (1:2; v/v) acidic mixture at  $100\text{ }^{\circ}\text{C}$  for 5 h. The levels of Ca, Cu, Fe, Mg, Mn, and Zn were determined using inductively coupled plasma optical emission spectrometry (ICP-OES; Optima 2100 DV; Perkin Elmer, Shelton, CT, USA) and  $\mu\text{g}$  elements per gram of dry tissue were calculated.

#### Statistics

The Sigma Plot software for Windows version 12.0 (Systat Software, San Jose, CA, USA) was used for the statistical analysis of the results. The results are given as mean  $\pm$  standard deviation (SD). Statistical significance was evaluated using one-way ANOVA followed by Duncan's post hoc test for comparisons between groups. A  $p$ -value  $< 0.05$  was considered to be statistically significant.

## RESULTS AND DISCUSSION

Bodily weight, fasting blood glucose, plasma insulin, OGTT levels, and HOMA-IR score were measured in both control and MetS groups as indicators of MetS. As shown in Figure 1 (a-b), sucrose administration caused significant ( $p < 0.05$ ) increases in the following parameters: bodily weight (15%) (a), fasting blood glucose (43%) (b), serum insulin level (80%) (c), HOMA-IR score (162%) (d) and OGTT level (51%) (e). These results indicate that the metabolic syndrome was successfully induced in rats.

As shown in Figure 2, MDA and 3-NT levels determined in the hepatic tissue from the MetS group were significantly higher than those of the control group as 26% and 67%, respectively (a and b). The phospho-Akt (pSer473) level of the MetS group was similar that of the control group (Figure 2c). The elevated levels of MDA and 3-NT together with observed mild diffuse microvesicular steatosis could be associated with hepatic fibrosis and mitochondrial dysfunction, which represent critical initiating events for the development of NAFLD in the liver of MetS-rats (15,17). In the literature, some studies reported that the increased 3-NT was related to steatosis in the liver which may indicate a possible involvement of peroxynitrite in the development of MetS complications (18,30). In the present study, the level of phospho-Akt (pSer473) did not change significantly in the liver of rats with

MetS compared to that of controls. Although the difference was not significant, however, a tendency to increase may be noted in the MetS group. In the literature, increased basal phospho-Akt (pSer473)

level was associated with decreased mitochondrial production and increased ectopic fat accumulation and oxidative stress in the liver of mice under the high-fat-diet was reported (31).

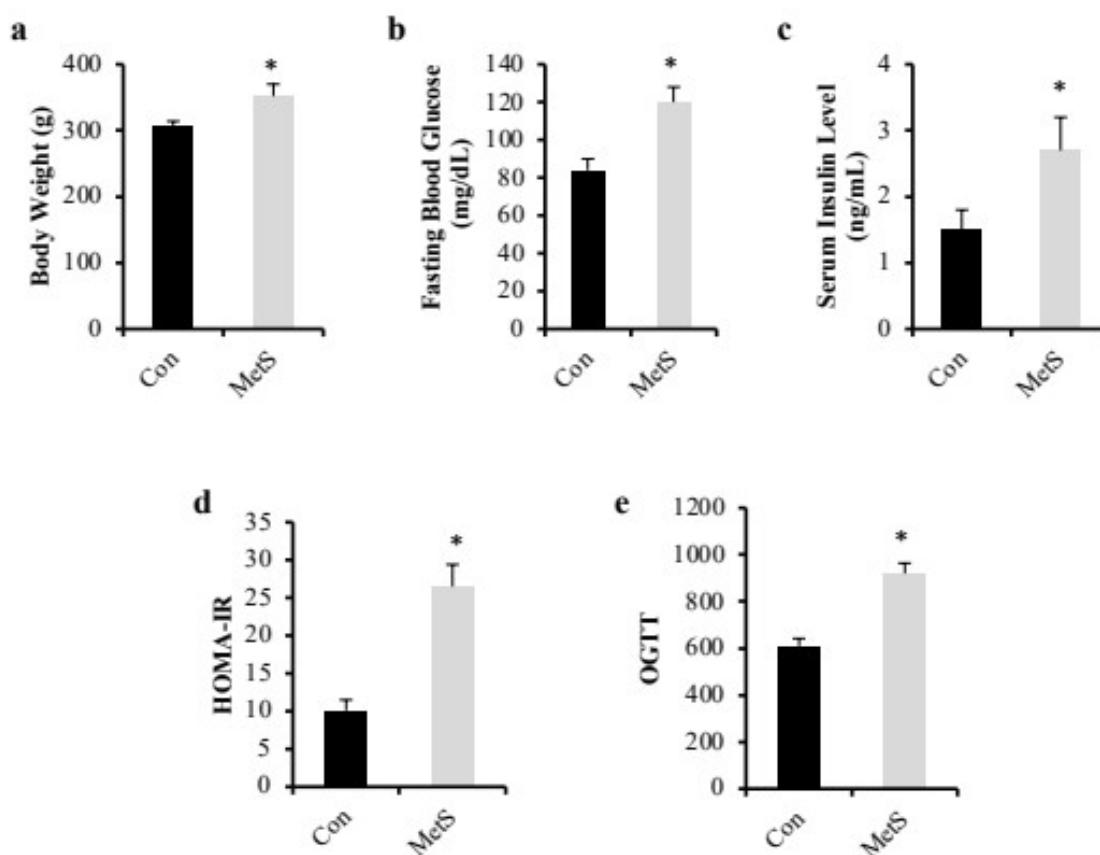


**Figure 1:** Bodily weight (a), fasting blood glucose concentration (b), plasma insulin level (c), HOMA-IR score (d), OGTT level (e) in control (Con) and metabolic syndrome (MetS) groups. \* $p < 0.05$  vs. Con group.

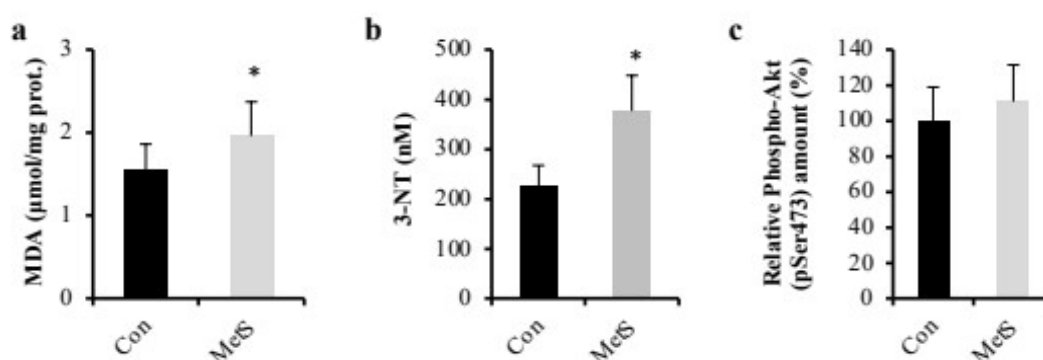


**Figure 2:** The levels of MDA (a), 3-NT (b), phospho-Akt (pSer473) (c) in the liver of control (Con) and metabolic syndrome (MetS) groups. \* $p < 0.05$  vs. Con-group.

The activities of SOD and GPx in the hepatic tissue were found similar in both MetS and control groups (Figure 3a and 3b). However, the CAT and GST activities were significantly low in the MetS group as a level of 15% and 29% when compared to the

control group, respectively (Figure 3c and 3d). On the other hand, the GR activity was significantly high in the MetS group (by 78%) than that of the control group (Figure 3e). In this study, decreased CAT, GST activities and increased GR activity



demonstrated oxidative stress in the MetS group. The change of antioxidant enzyme activities can be explained with (i) increasing of ROS and RNS production (20), the enzymes nitration (21), and the glycation products (3) (ii) reduced antioxidant capacity and (iii) increasing or decreasing the enzymes expressions (8, 32). Increased GR activity also indicated that GSH metabolism was affected from MetS. In our previous study, activities of SOD, CAT, GPx, GR were all significantly decreased in the masseter muscles of rats with MetS (16). These results demonstrated that the effects of MetS on different tissues varied depending on the metabolic functions of the tissues. In the literature, there were different results regarding changes in antioxidant enzyme activities in rats with the MetS group.

Nestorov et al. reported an increased expression of Mn-SOD but the lack of correlation between Mn-SOD activity and its protein level due to inactivation of the enzyme by glycation (33). However, Rubio-Rubiz et al. reported decreased SOD activity in the liver of rats with MetS (34). Moreover, Jarukamjorn et al. reported that mRNA expression and enzymatic activity of SOD, CAT, and GPx were increased in the liver of mice fed with the high-fat high-fructose diet for 2–8 wks (35). Al Mamun et al. reported decreased CAT and SOD activities in the liver of high-carbohydrate/high-fat (HCHF) diet-fed rats (36). Although hepatic tissue with MetS was investigated, different diet, age, and animal models that were used in these studies made it difficult to compare the results directly.

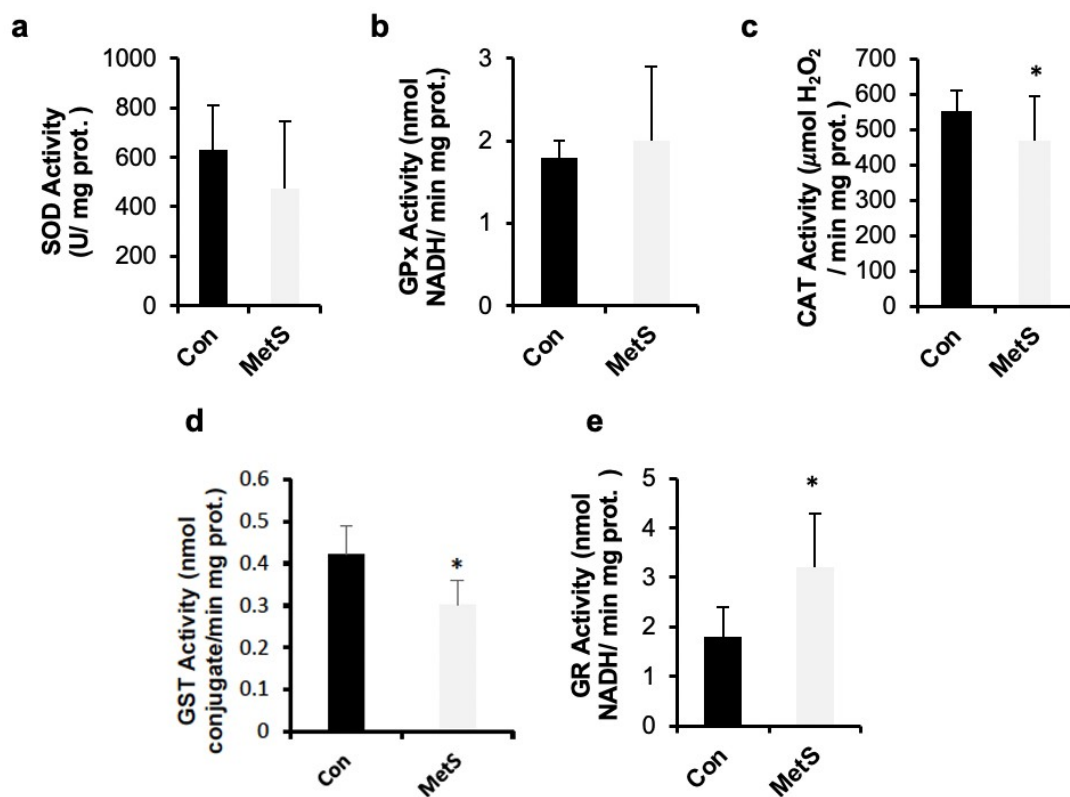


**Figure 3:** Antioxidant enzyme activities determined in the hepatic tissues from metabolic syndrome (MetS) group compared to the control (Con) group. SOD (a), GPx (b), CAT (c), GST (d) and GR (e) activities. \* $p < 0.05$  vs. Con group.

Hepatic parenchyma in the control group was consisted of stacks of anastomosing plates of hepatocytes, which were one cell thick and were separated by sinusoidal capillaries. Hepatocytes, with vesicular nucleus and the hepatocyte cytoplasm, were seen normal. Sinusoidal capillaries, the vascular channels between the plates of

hepatocytes, perisinusoidal spaces, the central vein, the portal areas with hepatic artery, portal vein, and the bile duct were seen normal (Figure 4a and 4b). However, hepatocytes in the MetS group showed mild diffuse microvesicular steatosis (Figure 4c and 4d).

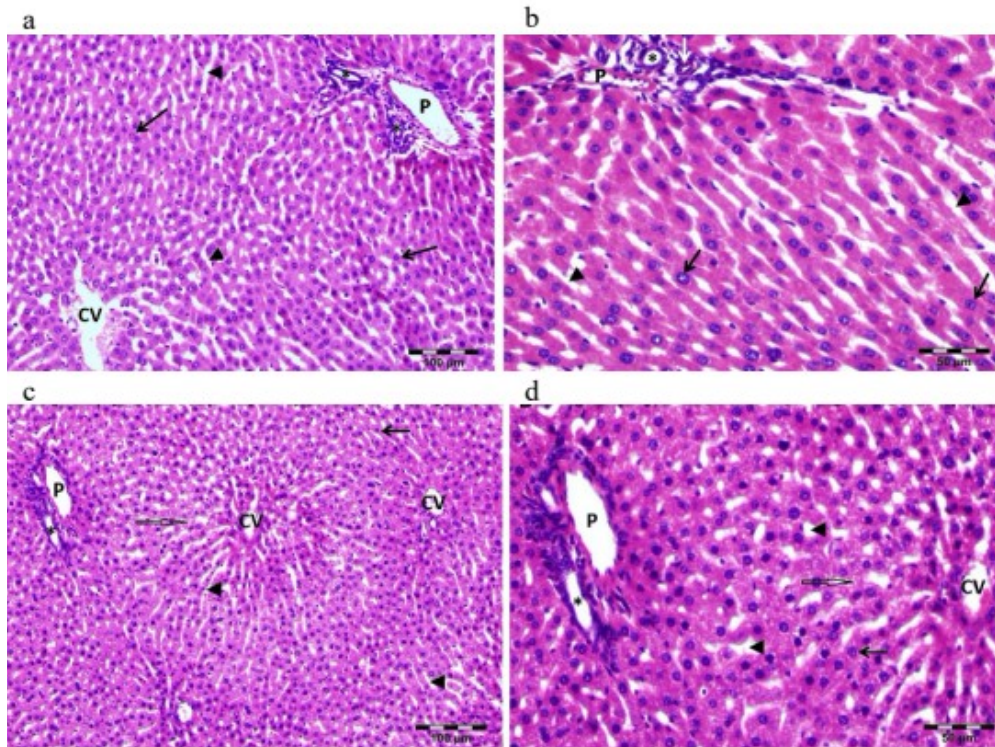


**Figure 4:** Control Group (4a and 4b). Metabolic Syndrome Group (4c and 4d). Hepatocytes (black arrows), sinusoidal capillaries (arrow heads), central veins (CV), portal veins (P), hepatic arteries (white arrows) and the bile ducts (\*) are seen. Microvesicular lipid storage is indicated (empty arrows). Bars: 100 µm(4a and 4c) and 50 µm (4b and 4d).

**Table 1:** Levels of metals in the hepatic tissues of rats.

Name of the Metals	Metals Levels (µg/g dried tissue)	
	Con Group	MetS Group
Ca	40.7±26.5	55.0±47.1
Cu	4.4±0.9	5.6±1.6*
Fe	269.1±95.1	356.6±126.2*
Mg	269.3±42.7	288.8±56.4
Mn	0.4±0.3	3.0±0.8**
Zn	42.4±6.3	35.9±8.6*

The male Wistar rats in the group that had metabolic syndrome (MetS; n=10 rats) induced with a high-sucrose diet by comparison with the normal control (Con; n=6 rats) group. Data are presented as mean±SD. \* $p < 0.05$  and \*\* $p < 0.01$  compared with the Con group.

As shown in Table 1, the levels of Ca and Mg were similar among these two groups. However, the levels of Cu, Fe, and Mn determined in the hepatic tissues were significantly high in MetS group compared to the control group as 1.3, 1.3 and 7.0-fold, respectively. The level of Zn was significantly low in MetS group compared to the control group. In our study, elevated Cu, Fe, and Mn concentrations were indicated that MetS significantly related to their status in the liver of rats and they could lead to changes in the balance of oxidant/antioxidant status. The increased Cu and Fe levels in the liver of rats with MetS support the increased oxidative stress. Because Cu and Fe as redox-cycling metals are involved in the formation of ROS; the catalytic function of  $Fe^{2+}/Fe^{3+}$  and  $Cu^+/Cu^{2+}$  in Fenton reactions mediated generation of hydroxyl radical from  $H_2O_2$  should be mentioned. As a result of

Fenton reactions,  $H_2O_2$  concentration may be reduced and this may be another factor in the reduction of CAT activity in the liver of rats with MetS. Increased Mn level may disrupt normal mitochondrial function by altering membrane permeability, inhibiting ATP production, and increasing ROS (37). In the liver, formation of oxidative stress, alteration of enzymatic antioxidant defense systems, and significant changes in metal metabolism may be the cause of insulin resistance by interfering with the ability of insulin to suppress hepatic glucose production. This may result in mitochondrial dysfunction with time and finally, cause MetS. In our previous study, we found that Cu level increased in the masseter muscle of rats with MetS while Fe and Mn levels were like those of controls (16). In the literature, increased Fe and Cu levels and decreased Mn and Zn levels were

reported in liver of rats fed a high carbohydrate-high fat diet for up to 16 weeks (38). Flores et al. reported the increased Cu level in serum and urine in T2DM patients as a result of the possibility of removing Cu from tissues (13). However, decreased plasma Cu level in a subject with MetS was reported by Parades et al. (14).

## CONCLUSION

Our data have shown that the activities of antioxidant defense enzymes such as CAT and GST were significantly low in the liver of MetS-rats than that of control rats, although the levels of MDA and 3-NT were significantly high in the liver of MetS-rats. However, the GR activity in the liver of MetS-rats was markedly high in that group compared to that of control rats. The light microscopy analysis of the livers showed mild diffuse microvesicular steatosis in the MetS group. Furthermore, the tissue levels of Cu, Fe, and Mn were significantly high in MetS group while Zn level was significantly low compared to the control group. The impaired carbohydrate, lipid, metal and glutathione metabolisms may have important roles in the pathogenesis and progression of MetS. Increased Cu, Fe and Mn levels and decreased Zn level may also play an important role in imbalance of oxidant/antioxidant status in the liver of rats with MetS. Considering oxidative stress as signaling markers for any dysfunction of organs in certain circumstances, its control signifies a rational curative strategy to prevent and cure hepatic diseases in MetS.

## CONFLICT OF INTEREST

All authors declare no conflict of interest.

## REFERENCES

- Nicolson GL. Metabolic syndrome and mitochondrial function: Molecular replacement and antioxidant supplements to prevent membrane peroxidation and restore mitochondrial function. *J Cell Biochem.* 2007 Apr 15;100(6):1352-69. <DOI>.
- Abacı A. Data on prevalence of metabolic syndrome in Turkey: Systematic review, meta-analysis and meta-regression of epidemiological studies on cardiovascular risk factors. *Arch Turk Soc Cardiol.* 2018; 46(7): 591-601. <DOI>.
- Vona R, Gambardella L, Cittadini C, Straface E, Pietraforte D. Biomarkers of Oxidative Stress in Metabolic Syndrome and Associated Diseases. *Oxidative Medicine and Cellular Longevity.* 2019 May 5;2019:1-19. <DOI>.
- Rochlani Y, Pothineni NV, Kovelamudi S, Mehta JL. Metabolic syndrome: pathophysiology, management, and modulation by natural compounds. *Therapeutic Advances in Cardiovascular Disease.* 2017 Aug;11(8):215-25. <DOI>.
- Rytz CL, Pialoux V, Mura M, Martin A, Hogan DB, Hill MD, et al. Impact of aerobic exercise, sex, and metabolic syndrome on markers of oxidative stress: results from the Brain in Motion study. *Journal of Applied Physiology.* 2020 Apr 1;128(4):748-56. <DOI>.
- Matés JM, Pérez-Gómez C, De Castro IN. Antioxidant enzymes and human diseases. *Clinical Biochemistry.* 1999 Nov;32(8):595-603. <DOI>.
- Townsend DM, Tew KD. The role of glutathione-S-transferase in anti-cancer drug resistance. *Oncogene.* 2003 Oct;22(47):7369-75. <DOI>.
- Meng R, Zhu D-L, Bi Y, Yang D-H, Wang Y-P. Anti-oxidative effect of apocynin on insulin resistance in high-fat diet mice. *Ann Clin Lab Sci.* 2011;41(3):236-43. PMID: 22075506.
- Zhu C, Schwarz P, Abakumova I, Aguzzi A. Unaltered Prion Pathogenesis in a Mouse Model of High-Fat Diet-Induced Insulin Resistance. *Ma J, editor. PLoS ONE.* 2015 Dec 14;10(12):e0144983. <DOI>.
- Mackenzie R, Elliott B. Akt/PKB activation and insulin signaling: a novel insulin signaling pathway in the treatment of type 2 diabetes. *DMSO.* 2014 Feb;55. <DOI>.
- Wong SK, Chin K-Y, Suhaimi FH, Fairus A, Ima-Nirwana S. Animal models of metabolic syndrome: a review. *Nutr Metab (Lond).* 2016 Dec;13(1):65. <DOI>.
- Kazi TG, Afridi HI, Kazi N, Jamali MK, Arain MB, Jalbani N, et al. Copper, Chromium, Manganese, Iron, Nickel, and Zinc Levels in Biological Samples of Diabetes Mellitus Patients. *Biol Trace Elem Res.* 2008 Apr;122(1):1-18. <DOI>.
- Flores CR, Puga MP, Wrobel K, Garay Sevilla MaE, Wrobel K. Trace elements status in diabetes mellitus type 2: Possible role of the interaction between molybdenum and copper in the progress of typical complications. *Diabetes Research and Clinical Practice.* 2011 Mar;91(3):333-41. <DOI>.
- Paredes S, Matta-Coelho C, Monteiro A, Fernandes V, Marques O, Alves M. Copper levels, calcium levels and metabolic syndrome. *Rev Port Diabetes.* 2016;11:99-105. <URL>.
- Freitas E, Cunha A, Aquino S, Pedrosa L, Lima S, Lima J, et al. Zinc Status Biomarkers and Cardiometabolic Risk Factors in Metabolic Syndrome: A Case Control Study. *Nutrients.* 2017 Feb 22;9(2):175. <DOI>.
- Tükel HC, Alptekin Ö, Turan B, Delilbaşı E. Effects of metabolic syndrome on masseter muscle of male Wistar rats. *Eur J Oral Sci.* 2015 Dec;123(6):432-8. <DOI>.
- Noeman SA, Hamooda HE, Baalash AA. Biochemical Study of Oxidative Stress Markers in the Liver, Kidney and Heart of High Fat Diet Induced Obesity in Rats. *Diabetol Metab Syndr.* 2011 Dec;3(1):17. <DOI>.
- Ucar F, Sezer S, Erdogan S, Akyol S, Armutcu F, Akyol O. The relationship between oxidative stress and nonalcoholic fatty liver disease: Its effects on the development of nonalcoholic steatohepatitis. *Redox Report.* 2013 Jul;18(4):127-33. <DOI>.

19. Roncal-Jimenez CA, Lanaspá MA, Rivard CJ, Nakagawa T, Sanchez-Lozada LG, Jalal D, et al. Sucrose induces fatty liver and pancreatic inflammation in male breeder rats independent of excess energy intake. *Metabolism*. 2011 Sep;60(9):1259–70. [<DOI>](#).
20. Moreno-Fernández S, Garcés-Rimón M, Vera G, Astier J, Landrier J, Miguel M. High Fat/High Glucose Diet Induces Metabolic Syndrome in an Experimental Rat Model. *Nutrients*. 2018 Oct 14;10(10):1502. [<DOI>](#).
21. Ghosh S, Sulistyoningrum DC, Glier MB, Verchere CB, Devlin AM. Altered Glutathione Homeostasis in Heart Augments Cardiac Lipotoxicity Associated with Diet-induced Obesity in Mice. *Journal of Biological Chemistry*. 2011 Dec;286(49):42483–93. [<DOI>](#).
22. Matthews DR, Hosker JP, Rudenski AS, Naylor BA, Treacher DF, Turner RC. Homeostasis model assessment: insulin resistance and  $\beta$ -cell function from fasting plasma glucose and insulin concentrations in man. *Diabetologia*. 1985 Jul;28(7):412–9. [<DOI>](#).
23. Lowry OH, Rosebrough NJ, Farr AL, Randall RJ. Protein measurement with the Folin phenol reagent. *Journal of biological chemistry*. 1951;193:265–75.
24. Buege JA, Aust SD. [30] Microsomal lipid peroxidation. In: *Methods in Enzymology* [Internet]. Elsevier; 1978 [cited 2021 Nov 20]. p. 302–10. [<URL>](#).
25. Sun Y, Oberley LW, Li Y. A simple method for clinical assay of superoxide dismutase. *Clinical Chemistry*. 1988 Mar 1;34(3):497–500. [<DOI>](#).
26. Aebi H. [13] Catalase in vitro. In: *Methods in Enzymology* [Internet]. Elsevier; 1984 [cited 2021 Nov 20]. p. 121–6. Available from: [<URL>](#).
27. Paglia DE, Valentine WN. Studies on the quantitative and qualitative characterization of erythrocyte glutathione peroxidase. *The Journal of laboratory and clinical medicine*. 1967;70(1):158–69. [<URL>](#).
28. Carlberg I, Mannervik B. Purification and characterization of the flavoenzyme glutathione reductase from rat liver. *Journal of Biological Chemistry*. 1975 Jul;250(14):5475–80. [<DOI>](#).
29. Habig WH, Pabst MJ, Jakoby WB. Glutathione S-Transferases. *Journal of Biological Chemistry*. 1974 Nov;249(22):7130–9. [<DOI>](#).
30. Mercuri F, Tonutti L, Taboga C, Ceriello A, Assaloni R, Motz E, et al. Detection of nitrotyrosine in the diabetic plasma: evidence of oxidative stress. *Diabetologia*. 2001 Jul 1;44(7):834–8. [<DOI>](#).
31. Liu H-Y, Hong T, Wen G-B, Han J, Zuo D, Liu Z, et al. Increased basal level of Akt-dependent insulin signaling may be responsible for the development of insulin resistance. *American Journal of Physiology-Endocrinology and Metabolism*. 2009 Oct;297(4):E898–906. [<DOI>](#).
32. Pereira ENG da S, Silvaes RR, Flores EEI, Rodrigues KL, Ramos IP, da Silva IJ, et al. Hepatic microvascular dysfunction and increased advanced glycation end products are components of non-alcoholic fatty liver disease. Gracia-Sancho J, editor. *PLoS ONE*. 2017 Jun 19;12(6):e0179654. [<DOI>](#).
33. Nestorov J, Gliban AM, Mijušković A, Nikolić-Kokić A, Elaković I, Veličković N, et al. Long-term fructose-enriched diet introduced immediately after weaning does not induce oxidative stress in the rat liver. *Nutrition Research*. 2014 Jul;34(7):646–52. [<DOI>](#).
34. Rubio-Ruiz M, Guarner-Lans V, Cano-Martínez A, Díaz-Díaz E, Manzano-Pech L, Gamas-Magaña A, et al. Resveratrol and quercetin administration improves antioxidant defenses and reduces fatty liver in metabolic syndrome rats. *Molecules*. 2019 Apr 3;24(7):1297. [<DOI>](#).
35. Jarukamjorn K, Jearapong N, Pimson C, Chatuphonprasert W. A High-Fat, High-Fructose Diet Induces Antioxidant Imbalance and Increases the Risk and Progression of Nonalcoholic Fatty Liver Disease in Mice. *Scientifica*. 2016;2016:1–10. [<DOI>](#).
36. Mamun MdAA, Faruk Md, Rahman MdM, Nahar K, Kabir F, Alam MA, et al. High Carbohydrate High Fat Diet Induced Hepatic Steatosis and Dyslipidemia Were Ameliorated by Psidium guajava Leaf Powder Supplementation in Rats. *Evidence-Based Complementary and Alternative Medicine*. 2019 Feb 3;2019:1–12. [<DOI>](#).
37. Li L, Yang X. The Essential Element Manganese, Oxidative Stress, and Metabolic Diseases: Links and Interactions. *Oxidative Medicine and Cellular Longevity*. 2018;2018:1–11. [<DOI>](#).
38. Kalita H, Hazarika A, Devi R. Withdrawal of High-Carbohydrate, High-Fat Diet Alters Status of Trace Elements to Ameliorate Metabolic Syndrome in Rats With Type 2 Diabetes Mellitus. *Canadian Journal of Diabetes*. 2020 Jun;44(4):317–326.e1. [<DOI>](#).





## Spectral Outputs of Yb<sup>3+</sup>/Pr<sup>3+</sup> Doped Tellurite Glasses for Solid-State Lighting

Murat Erdem<sup>1\*</sup> , Anıl Doğan<sup>1</sup> 

<sup>1</sup>Physics Department, Faculty of Science and Letters, Marmara University, 34722, Istanbul, Turkey

**Abstract:** Downconversion processes which include visible and near-infrared luminescence at high energy excitation have been investigated in Yb<sup>3+</sup>/Pr<sup>3+</sup> doped TeO<sub>2</sub>-ZnO-BaO glasses. The decrease of the DC emission intensities of Pr<sup>3+</sup> ions with increasing mol% amount of Pr<sup>3+</sup> ions is attributed to the concentration quenching. The CIE chromaticity coordinates of the perceived emission of Pr<sup>3+</sup> ions shifted from orange to the red region depending on the increase in the pumping power. Consequently, Yb<sup>3+</sup>/Pr<sup>3+</sup> doped TeO<sub>2</sub>-ZnO-BaO glasses could be used as functional optical materials for solid-state lighting applications.

**Keywords:** Downconversion, tellurite glasses, color parameters, lighting.

**Submitted:** September 09, 2021. **Accepted:** November 19, 2021.

**Cite this:** Erdem M, Doğan A. Spectral Outputs of Yb<sup>3+</sup>/Pr<sup>3+</sup> Doped Tellurite Glasses for Solid-State Lighting. JOTCSA. 2022;9(1):21-8.

**DOI:** <https://doi.org/10.18596/jotcsa.993096>.

**\*Corresponding author. E-mail:** [merdem@marmara.edu.tr](mailto:merdem@marmara.edu.tr).

### INTRODUCTION

Downconversion (DC), which is known as Quantum Cutting (QC), is a frequency conversion process that a photon at higher energy is cut into two photons at lower energy. This physical energy conversion process has represented by Dexter in the 1950s (1). Energy conversion processes play an important role in studies on rare earth (RE) ion doped materials for assorted areas, for instance, lighting technology, solar cells, optical amplifiers, and solid-state lasers (2-5). Among the RE ions, Pr<sup>3+</sup> ions can exhibit multi-photon emission under a high energy excitation, as an instance of downconversion (6). Besides, the luminescence performance of Pr<sup>3+</sup> ions can be enhanced by contributing the ideal rate of Yb<sup>3+</sup> ions as an acceptor in the energy transfer (ET) processes between both ions (7). Therefore, Yb<sup>3+</sup> ion provides a phonon-assisted non-resonant energy transfer. Also, the phonon structure of the material is important due to the achievement of efficient phonon-assisted energy transfer (8).

Tellurite glasses have common usage in optical fibers, mid-infrared laser applications, and optical sensors (9-11) due to having attractive features such as wide transmission frame, high refractive indices, lower melting temperature, high thermal stability against crystallization, good chemical durability, high devitrification resistance, low phonon energy, and high RE ion solubility (12,13).

With modifier oxides (ZnO, BaO, GeO, Nb<sub>2</sub>O<sub>5</sub>, and B<sub>2</sub>O<sub>3</sub>, etc), the physical properties of tellurite-based glass materials can change. Among them, ZnO indicates that a decrease in the optical band gap, glass density, and thermal stability, whereas an increment in the refractive index, crystallization temperature (T<sub>c</sub>), and glass transition temperature (T<sub>g</sub>) (14,15). BaO also provides higher T<sub>g</sub>, thermal stability, transmission spectra, and the cross-linking network density to glass materials (16,17). Additionally, high BaO concentrations in the Er<sup>3+</sup> doped phosphate glasses give rise to intense red and near-infrared (NIR) emissions (18).

The studies on Pr<sup>3+</sup> and Yb<sup>3+</sup>/Pr<sup>3+</sup> doped glass materials are available in the literature. In the

studies on Pr<sup>3+</sup> doped TeO<sub>2</sub>-Sb<sub>2</sub>O<sub>3</sub>-WO<sub>3</sub> and TeO<sub>2</sub>-ZnO-YF<sub>3</sub>-NaYF<sub>4</sub> glass systems, it is seen that the luminescence intensities of Pr<sup>3+</sup> doped glasses increase with increasing Pr<sup>3+</sup> concentration up to 1.0 mol%, and then decrease over the 1.0 mol%. This decrement is proposed to be due to concentration quenching (19,20). The emission of Pr<sup>3+</sup> ions around 910 nm corresponding to <sup>3</sup>P<sub>0</sub> → <sup>1</sup>G<sub>4</sub> transition decreases down to zero at 6 mol% Yb<sup>3+</sup> ion concentration, and <sup>2</sup>F<sub>5/2</sub> → <sup>2</sup>F<sub>7/2</sub> emission intensity at 978 nm of Yb<sup>3+</sup> ions decrease by increasing Yb<sup>3+</sup> ion concentration due to the reabsorption process of Yb<sup>3+</sup> (21). The range of 1050 nm emission of Pr<sup>3+</sup> ions which is attributed to <sup>1</sup>D<sub>2</sub> → <sup>3</sup>F<sub>3,4</sub> energy transition as an occurrence by the cross-relaxation process of <sup>3</sup>P<sub>0</sub> + <sup>3</sup>H<sub>4</sub> → <sup>3</sup>H<sub>6</sub> + <sup>1</sup>D<sub>2</sub> in Yb<sup>3+</sup>/Pr<sup>3+</sup> co-doped SiO<sub>2</sub>-Nb<sub>2</sub>O<sub>5</sub> nanocomposites had been reported (22). The energy transition from <sup>2</sup>F<sub>5/2</sub> level to <sup>2</sup>F<sub>7/2</sub> level of Yb<sup>3+</sup> ion can be observed at around 1020 nm as seen in our results due to the cross-relaxation between Pr<sup>3+</sup> and Yb<sup>3+</sup> ions correspond to <sup>3</sup>P<sub>0</sub> + <sup>2</sup>F<sub>7/2</sub> → <sup>1</sup>G<sub>4</sub> + <sup>2</sup>F<sub>5/2</sub> (23). Rajesh et. al. reported that the emission intensity of Yb<sup>3+</sup>: <sup>2</sup>F<sub>5/2</sub> → <sup>2</sup>F<sub>7/2</sub> transition decreased with increasing Yb<sup>3+</sup> ion concentration due to the back energy transfer process from <sup>2</sup>F<sub>5/2</sub> level of Yb<sup>3+</sup> to <sup>1</sup>G<sub>4</sub> level of Pr<sup>3+</sup> ions (24). Marcos P. Belançon et. al. was investigated the 612 and 645 nm emissions of Pr<sup>3+</sup> doped TWNN glasses at lower and higher Pr<sup>3+</sup> concentrations and obtained stronger 645 nm and weaker 612 nm emissions at high Pr<sup>3+</sup> concentration due to hypersensitive <sup>3</sup>P<sub>0</sub> → <sup>3</sup>F<sub>2</sub> transition of Pr<sup>3+</sup> ions (25). Seshadri et al. proposed that the Yb<sup>3+</sup>/Pr<sup>3+</sup> co-doped TBZLN glasses are good candidates for photonic devices due to their yellow-orange emissions (26). V. Himamaheswara Rao et.al observed the orange color on Pr<sup>3+</sup> ions doped TeO<sub>2</sub>-Sb<sub>2</sub>O<sub>3</sub>-WO<sub>3</sub> glasses (27). Furthermore, reddish-orange color was observed on the Commission International de L'Eclairage (CIE, France) chromaticity system under 445 nm excitation in Pr<sup>3+</sup> doped ZnO-Na<sub>2</sub>CO<sub>3</sub>-Bi<sub>2</sub>O<sub>3</sub>-B<sub>2</sub>O<sub>3</sub> glasses which are applicable materials for lighting devices (28).

Apart from these studies in the literature, in our study, the DC and tunable color properties of Yb<sup>3+</sup> and Pr<sup>3+</sup> ion-doped TeO<sub>2</sub>-ZnO-BaO (TZB) glasses under 439 nm laser excitation were examined and discussed.

## MATERIALS AND METHODS

Yb<sup>3+</sup>/Pr<sup>3+</sup> ions doped TZB glasses were produced by melt quenching which is the traditional technique for fabricating the glass materials. The powder's purities of oxides are 99.995% TeO<sub>2</sub> and 99.999% BaO by Sigma Aldrich; 99.999% ZnO, 99.9% Pr<sub>2</sub>O<sub>3</sub>, and 99.99% Yb<sub>2</sub>O<sub>3</sub> by Alfa Aesar. The mol percent values of the oxide powers are (76-x)% for tellurium dioxide, 16% for zinc oxide, 5% for

barium oxide, x% for praseodymium oxide, and 3% for ytterbium oxide. The x values of praseodymium oxides are chosen as 0.075 and 0.15 mol and the glass samples are labeled as TZBYP1 and TZBYP2 respectively.

The oxide powders whose amounts were defined and mixed in an agate mortar. The melt of the mixture was obtained in the furnace at 950 °C for 1 h. The molten mixture was poured from a platinum crucible into a stainless-steel mold. To abate the inner stress, the melt was heated at 150 °C in the stainless-steel mold and kept for 30 minutes. After manufacturing, transparent TZBYP glasses were prepared for the optical analyses.

The absorption spectrum of the samples was obtained through A Perkin Elmer Lambda 35 UV/VIS Spectrophotometer at room temperature. The analysis of photoluminescence spectra of the glasses was done via an SP2500i monochromator from Princeton Instruments. To define the emission intensities of the samples, a SI 440-silicon detector from the Acton series was used. A CNI MDL-H-975 model continuous-wave diode laser was used to excite the glass samples. The pump power applied on the glass samples was determined through a FieldMaxII - TOP power meter from Coherent. To specify the chromaticity coordinates of the luminescence of the samples, an AsenseTek Lighting Passport Model illuminance meter was used.

## RESULTS AND DISCUSSIONS

### Absorption Spectra

Figure 1 illustrates the absorption spectra of TZBYP glasses in the range of 400-1100 nm. In the spectra, four absorption peaks are observed at 435, 445, 485, and 628 nm wavelengths correspond to the ground level (<sup>3</sup>H<sub>4</sub>) excitation to the <sup>3</sup>P<sub>2</sub>, <sup>3</sup>P<sub>1</sub>, <sup>1</sup>I<sub>6</sub>, <sup>3</sup>P<sub>0</sub> and <sup>1</sup>D<sub>2</sub> excited energy levels of the Pr<sup>3+</sup> ions, respectively. Additionally, the broad absorption band of Yb<sup>3+</sup> ions is observed around 1065 nm due to the <sup>2</sup>F<sub>7/2</sub> → <sup>2</sup>F<sub>5/2</sub> transitions. Moreover, as seen in the spectra, there is a rise in the absorption band peaks depending on the increasing concentration of Pr<sup>3+</sup> ions.

### Photoluminescence Characteristics

Figure 2 indicates the DC luminescence intensities of two glasses between 400-1100 nm wavelengths. As seen in Figure 2, the peaks of down-converted emissions of Pr<sup>3+</sup> ions centered around 497, 530, 542, 597, 617, 647, 686, 708, and 732 nm at the visible region, and 886 nm at the NIR region. These peaks correspond to the <sup>3</sup>P<sub>0</sub> → <sup>3</sup>H<sub>4</sub>, <sup>3</sup>P<sub>1</sub> → <sup>3</sup>H<sub>5</sub>, <sup>3</sup>P<sub>0</sub> → <sup>3</sup>H<sub>5</sub>, <sup>1</sup>D<sub>2</sub> → <sup>3</sup>H<sub>4</sub>, <sup>3</sup>P<sub>0</sub> → <sup>3</sup>H<sub>6</sub>, <sup>3</sup>P<sub>0</sub> → <sup>3</sup>F<sub>2</sub>, <sup>3</sup>P<sub>1</sub> → <sup>3</sup>F<sub>3</sub>, <sup>3</sup>P<sub>1</sub> → <sup>3</sup>F<sub>4</sub>, <sup>3</sup>P<sub>0</sub> → <sup>3</sup>F<sub>4</sub> transitions at the visible region and <sup>1</sup>D<sub>2</sub> → <sup>3</sup>F<sub>2</sub> transition at the NIR region, respectively. Also, the emission observed around



the 1020 nm is due to  $\text{Yb}^{3+}: {}^2\text{F}_{5/2} \rightarrow {}^2\text{F}_{7/2}$  transitions. The spectral output of the glasses indicates that the down-conversion emission intensities

decreased with increasing mol% of  $\text{Pr}^{3+}$  ions on account of the concentration quenching.

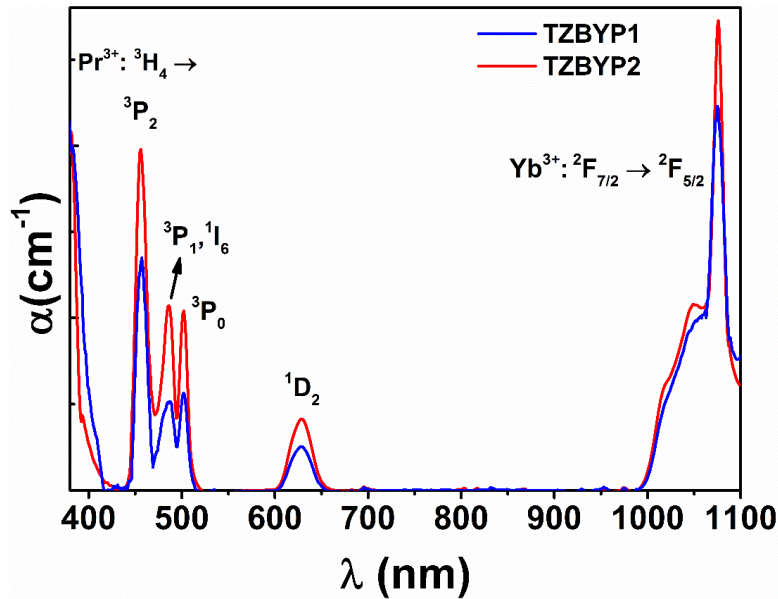


Figure 1: Absorption spectra of TZBYP glasses in 400-1100 nm range.

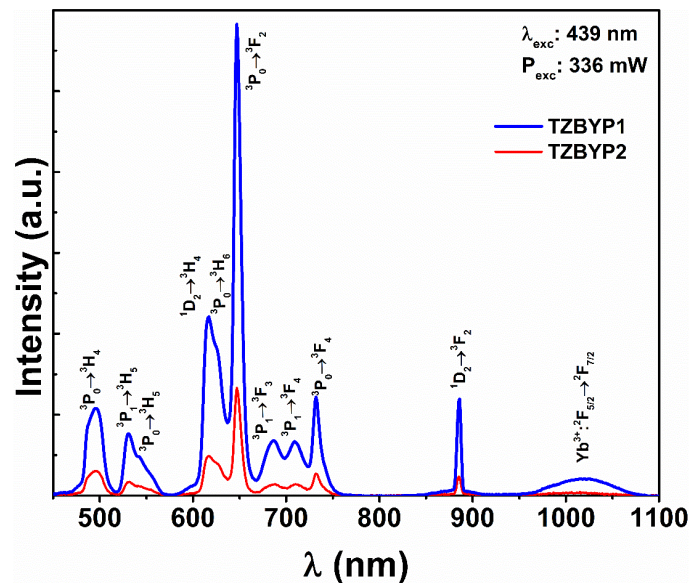


Figure 2: Down-conversion emission intensities depending on the  $\text{Pr}^{3+}$  concentration.

The DC luminescence intensities of the TZBYP glasses were investigated as the function of the pumping power to explain the DC energy transfer process. Figures 3 and 4 (a) represent the DC emission behaviors of the TZBYP1 and TZBYP2 glasses at various pump powers. As clearly seen in Figures 3 and 4 (a), the emission intensities of both glasses increased with an increasing 439 nm laser pumping power. The plots of the emission intensities versus the pumping powers in the logarithmic scale are demonstrated in Figures 3 and 4 (b) to express the photonic absorption

process. The number of photons ( $n$ ) was calculated by the slope of the luminescence intensity vs. power curve ( $I \sim P^n$ ). The slope values of TZBYP1 glass are found to be  $n_{497} = 0.84$ ,  $n_{530} = 0.96$ ,  $n_{617} = 1.04$ ,  $n_{647} = 1.05$ ,  $n_{686} = 0.89$ ,  $n_{708} = 0.82$ ,  $n_{732} = 0.95$ ,  $n_{882} = 0.63$  and  $n_{1020} = 0.52$ , respectively. For TZBYP2 glass, the values are  $n_{497} = 0.91$ ,  $n_{530} = 1.05$ ,  $n_{617} = 1.03$ ,  $n_{647} = 1.03$ ,  $n_{686} = 0.98$ ,  $n_{708} = 0.94$ ,  $n_{732} = 0.96$ ,  $n_{882} = 0.3$  and  $n_{1020} = 0.55$ , respectively. These results indicate that the down-conversion energy process is due to one-photon absorption.

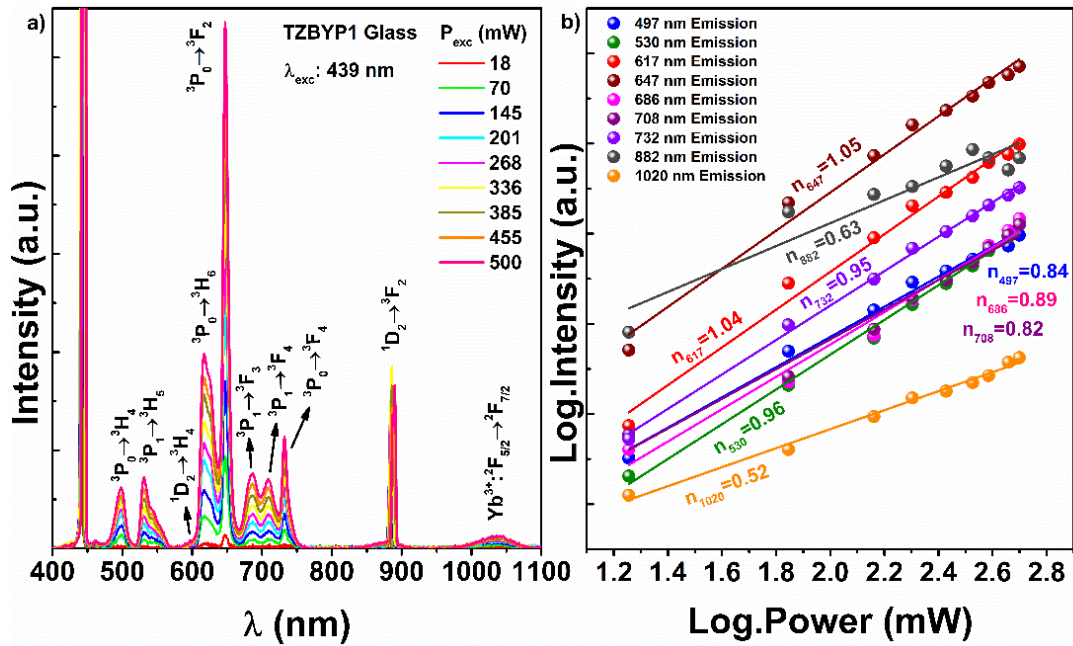


Figure 3: (a) Down-conversion luminescence at different pump powers, and (b) the intensity-power curves for the emissions of TZBYP1.

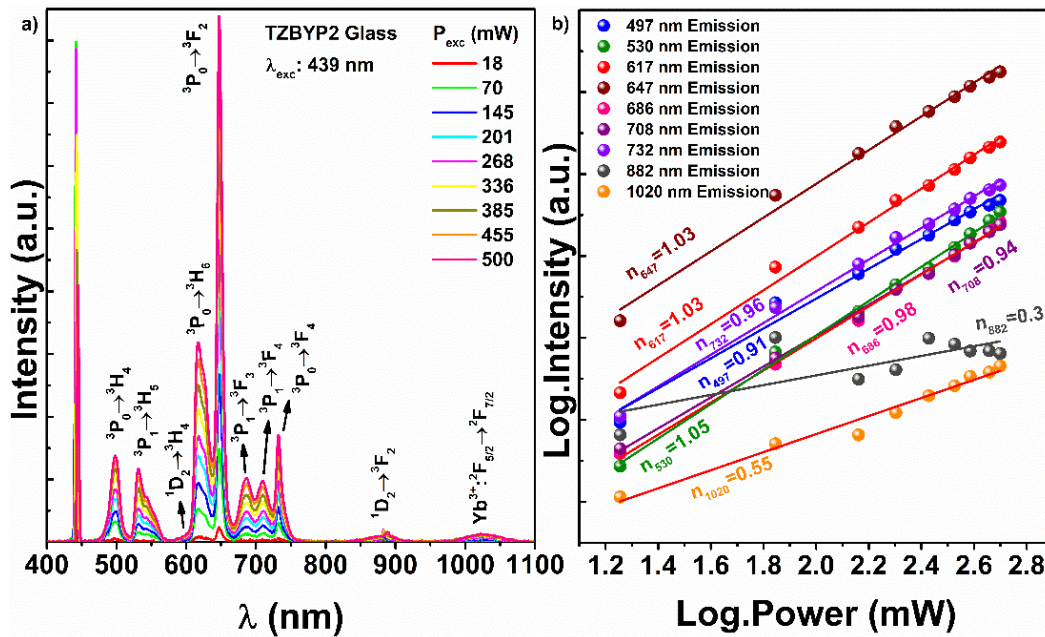


Figure 4: (a) Down-conversion luminescence at different pump powers, and (b) the intensity-power curves for the emissions of TZBYP2.

**Energy Transfer Mechanism**

The schematic representation of the energy levels of Yb<sup>3+</sup> and Pr<sup>3+</sup> ions at visible and NIR regions is given and the possible energy transfers (ET1 and ET2) in the DC process in the Yb<sup>3+</sup>/Pr<sup>3+</sup> doped tellurite glasses are defined in Figure 5. At first, Pr<sup>3+</sup> ions are excited by 439 nm blue photon from the multiplet <sup>3</sup>H<sub>4</sub> ground state to the multiplet <sup>3</sup>P<sub>j</sub> excited state. Nonradiative relaxations (NR) take place from <sup>3</sup>P<sub>2</sub> state to <sup>3</sup>P<sub>0</sub> state that is mostly populated and from <sup>3</sup>P<sub>0</sub> state to <sup>1</sup>D<sub>2</sub> state. The

possible energy transfers between the Pr<sup>3+</sup> and Yb<sup>3+</sup> ions are given by the two-step sequential resonant energy transfer (29) from <sup>3</sup>P<sub>0</sub> <sup>1</sup>G<sub>4</sub> transition of Pr<sup>3+</sup> ions to <sup>2</sup>F<sub>7/2</sub> → <sup>2</sup>F<sub>5/2</sub> transition of Yb<sup>3+</sup> ions and followed by from <sup>1</sup>G<sub>4</sub> → <sup>3</sup>H<sub>4</sub> transition of Pr<sup>3+</sup> ions to <sup>2</sup>F<sub>7/2</sub> → <sup>2</sup>F<sub>5/2</sub> transition of Yb<sup>3+</sup> ions. The energy difference between <sup>3</sup>P<sub>0</sub> and <sup>1</sup>G<sub>4</sub> levels of Pr<sup>3+</sup> ions is close to the energy difference between <sup>2</sup>F<sub>7/2</sub> and <sup>2</sup>F<sub>5/2</sub> levels of Yb<sup>3+</sup> ions. Moreover, the energy gap between the lowest Stark and sub-Stark energy levels of <sup>2</sup>F<sub>5/2</sub> levels of Yb<sup>3+</sup> ion is



small. Therefore, the energy transition from  $\text{Pr}^{3+}$  ion to  $\text{Yb}^{3+}$  ion loads the sub-Stark level of  ${}^2\text{F}_{5/2}$  state of  $\text{Yb}^{3+}$  ion and the energy transfer from the

minimum Stark level of  ${}^2\text{F}_{5/2}$  state to the minimum Stark and sub-Stark levels of  ${}^2\text{F}_{7/2}$  state causes the emission at 1040 nm (30).

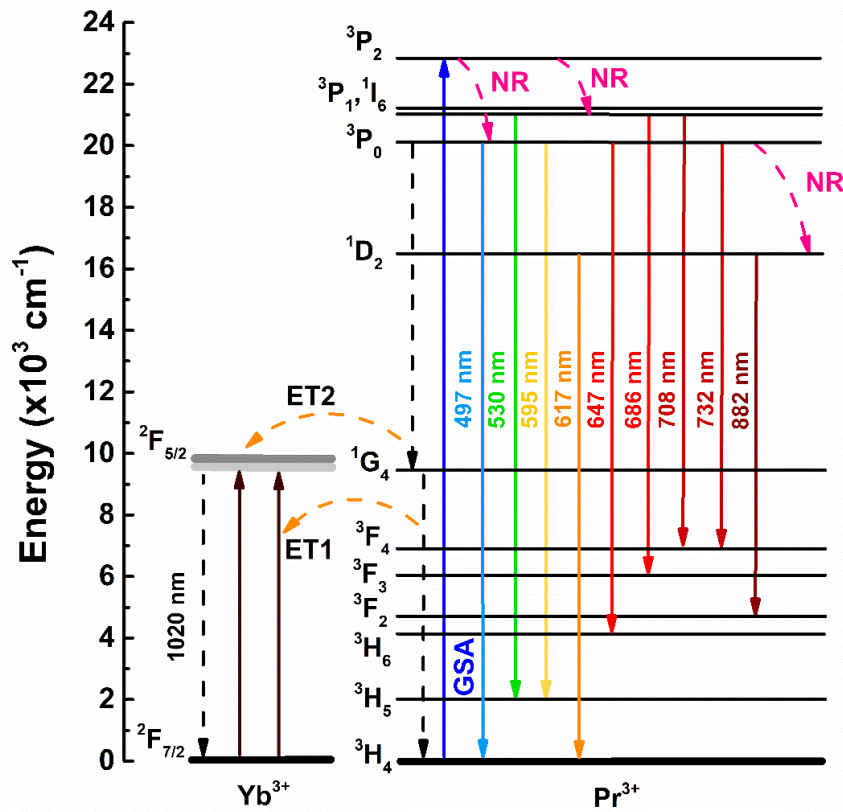
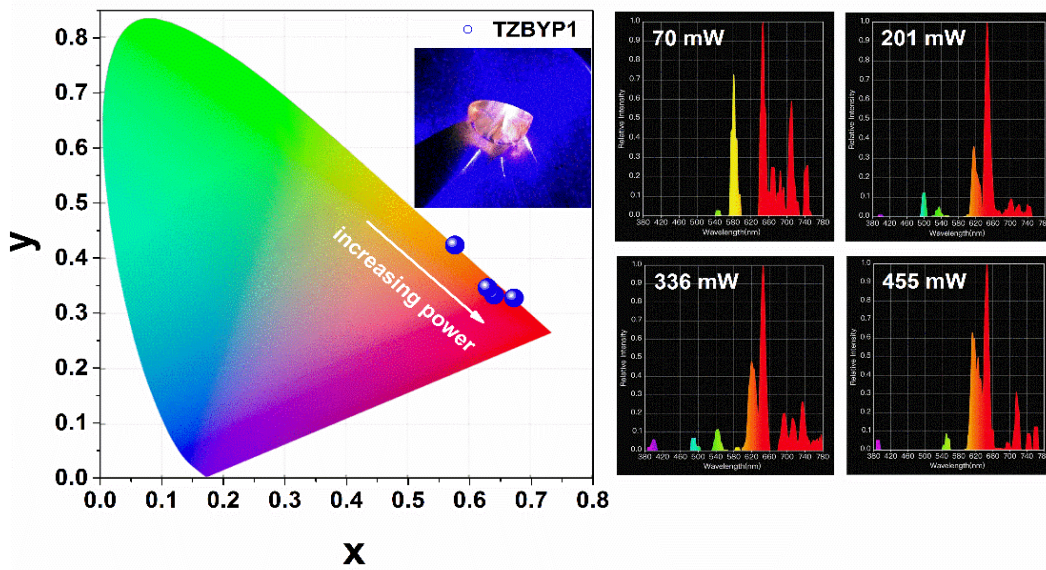


Figure 5: Energy level diagram of  $\text{Pr}^{3+}$  and  $\text{Yb}^{3+}$  ions in the TZB glasses.

**Color Analysis**

Figures 6 and 7 show the photometric analysis supplied from the illuminance meter for the glasses. The insets in Figures 6 and 7 also indicate the camera image of the TZBYP glasses. As seen in the CIE chromaticity diagram of the TZBYP glasses, the color coordinates change with the laser pumping power. While the color coordinate values of TZBYP1 glass were measured as (0.57; 0.42), (0.64; 0.33), (0.63; 0.34) and (0.67; 0.32) for the

related pump power of 70, 201, 336 and 455 mW, respectively. These values of the color coordinates were measured as (0.56; 0.38), (0.54; 0.43) and (0.69; 0.31) for TZBYP2 glass at the pumping power of 201, 336 and 385 mW, respectively. As seen in both figures, remarkable shifts observed in the coordinates with increasing pump power are from the orange to the red region in the CIE diagram.



**Figure 6:** Color coordinates in the CIE diagram and luminescence spectra of TZBYP1 glass at different pumping powers.

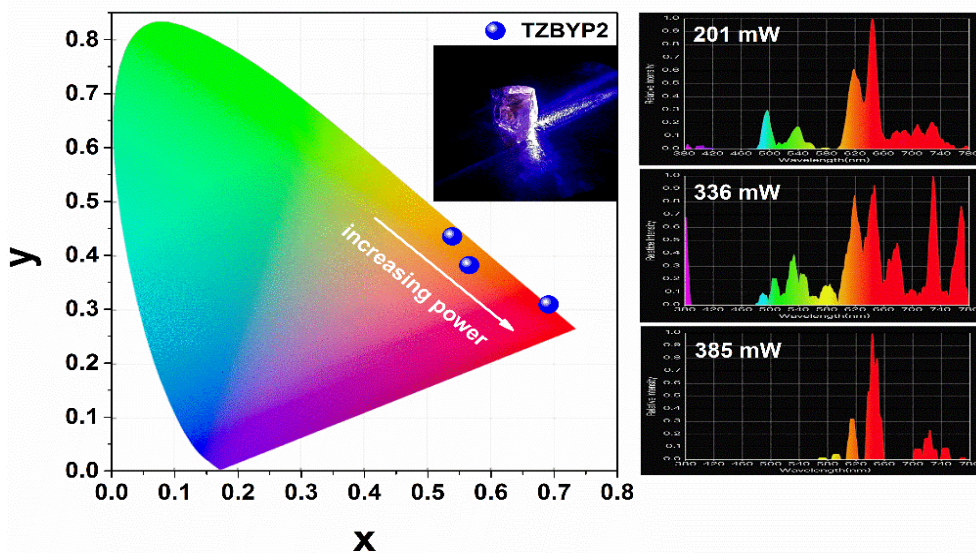


**Figure 7:** Color coordinates in the CIE diagram and luminescence spectra of TZBYP2 glass at different pumping power.

**CONCLUSION**

TeO<sub>2</sub>-ZnO-BaO glasses doped with Yb<sup>3+</sup> and Pr<sup>3+</sup> ions were produced by the traditional melt quenching method. Intense multi-photon downconversion luminescence in the visible region was observed under a 439 nm laser excitation. The spectral output of the glasses indicated that the increment in the Pr<sup>3+</sup> concentration quenches the luminescence intensity of Pr<sup>3+</sup> ions. The color coordinates shifted from the orange region to the red region with increasing excitation power. Consequently, the Yb<sup>3+</sup>/Pr<sup>3+</sup> doped TeO<sub>2</sub>-ZnO-BaO glasses can be useful material for solid-state lighting.

**ACKNOWLEDGMENTS**

The Scientific Research Projects Unit (BAPKO) of Marmara University financially supported this study with the FEN-C-YLP-141118-0600 grant number.

**REFERENCES**

1. Dexter DL. Possibility of Luminescent Quantum Yields Greater than Unity. Phys Rev. 1957 Nov 1;108(3):630-3. <URL>.
2. Caldiño U, Bettinelli M, Ferrari M, Pasquini E, Pelli S, Speghini A, et al. Rare Earth Doped Glasses

for Displays and Light Generation. In 2014 [cited 2021 Nov 21]. p. 174–8. Available from: [<URL>](#).

3. Belançon MP, Marconi JD, Ando MF, Barbosa LC. Near-IR emission in Pr<sup>3+</sup>/single doped and tunable near-IR emission in Pr<sup>3+</sup>/Yb<sup>3+</sup> codoped tellurite tungstate glasses for broadband optical amplifiers. *Optical Materials*. 2014 Apr;36(6):1020–6. [<DOI>](#).

4. Lakshminarayana G, Qiu J. Near-infrared quantum cutting in RE<sup>3+</sup>/Yb<sup>3+</sup> (RE=Pr, Tb, and Tm): GeO<sub>2</sub>-B<sub>2</sub>O<sub>3</sub>-ZnO-LaF<sub>3</sub> glasses via downconversion. *Journal of Alloys and Compounds*. 2009 Jul;481(1–2):582–9. [<DOI>](#).

5. Pask HM, Tropper AC, Hanna DC. A Pr<sup>3+</sup>-doped ZBLAN fibre upconversion laser pumped by an Yb<sup>3+</sup>-doped silica fibre laser. *Optics Communications*. 1997 Jan;134(1–6):139–44. [<DOI>](#).

6. Zhou X, Deng Y, Jiang S, Xiang G, Li L, Tang X, et al. Investigation of energy transfer in Pr<sup>3+</sup>, Yb<sup>3+</sup> co-doped phosphate phosphor: The role of 3P<sub>0</sub> and 1D<sub>2</sub>. *Journal of Luminescence*. 2019 May;209:45–51. [<DOI>](#).

7. Borrero-González LJ, Nunes LAO, Carmo JL, Astrath FBG, Baesso ML. Spectroscopic studies and downconversion luminescence in OH--free Pr<sup>3+</sup>-Yb<sup>3+</sup> co-doped low-silica calcium aluminosilicate glasses. *Journal of Luminescence*. 2014 Jan;145:615–9. [<DOI>](#).

8. Bose S, Debnath R. Strong crystal-field effect and efficient phonon assisted Yb<sup>3+</sup>→Tm<sup>3+</sup> energy transfer in a (Yb<sup>3+</sup>/Tm<sup>3+</sup>) co-doped high barium-tellurite glass. *Journal of Luminescence*. 2014 Nov;155:210–7. [<DOI>](#).

9. Lousteau J, Boetti N, Chiasera A, Ferrari M, Abrate S, Scarciglia G, et al. Er(3+) and Ce(3+) Codoped Tellurite Optical Fiber for Lasers and Amplifiers in the Near-Infrared Wavelength Region: Fabrication, Optical Characterization, and Prospects. *IEEE Photonics J*. 2012 Feb;4(1):194–204. [<DOI>](#).

10. Wang R, Meng X, Yin F, Feng Y, Qin G, Qin W. Heavily erbium-doped low-hydroxyl fluorotellurite glasses for 27 μm laser applications. *Opt Mater Express*. 2013 Aug 1;3(8):1127. [<DOI>](#).

11. Leal JJ, Narro-García R, Flores-De los Ríos JP, Gutierrez-Mendez N, Ramos-Sánchez VH, González-Castillo JR, et al. Effect of TiO<sub>2</sub> on the thermal and optical properties of Er<sup>3+</sup>/Yb<sup>3+</sup> co-doped tellurite glasses for optical sensor. *Journal of Luminescence*. 2019 Apr;208:342–9. [<DOI>](#).

12. Leal JJ, Narro-García R, Desirena H, Marconi JD, Rodríguez E, Linganna K, et al. Spectroscopic properties of tellurite glasses co-doped with Er<sup>3+</sup> and Yb<sup>3+</sup>. *Journal of Luminescence*. 2015 Jun;162:72–80. [<DOI>](#).

13. Wang JS, Vogel EM, Snitzer E. Tellurite glass: a new candidate for fiber devices. *Optical Materials*. 1994 Aug;3(3):187–203. [<DOI>](#).

14. Elkhoshkhany N, Essam O, Embaby AM. Optical, thermal and antibacterial properties of tellurite glass system doped with ZnO. *Materials Chemistry and Physics*. 2018 Aug;214:489–98. [<DOI>](#).

15. Ramamoorthy RK, Bhatnagar AK. Effect of ZnO and PbO/ZnO on structural and thermal properties of tellurite glasses. *Journal of Alloys and Compounds*. 2015 Feb;623:49–54. [<DOI>](#).

16. Manikandan N, Rysanyanskiy A, Toulouse J. Thermal and optical properties of TeO<sub>2</sub>-ZnO-BaO glasses. *Journal of Non-Crystalline Solids*. 2012 Mar;358(5):947–51. [<DOI>](#).

17. Burtan-Gwizdala B, Reben M, Cisowski J, Szpil S, Yousef ES, Lisiecki R, et al. Thermal and spectroscopic properties of Er<sup>3+</sup>-doped fluorotellurite glasses modified with TiO<sub>2</sub> and BaO. *Optical Materials*. 2020 Sep;107:109968. [<DOI>](#).

18. Kuwik M, Pisarska J, Pisarski WA. Influence of Oxide Glass Modifiers on the Structural and Spectroscopic Properties of Phosphate Glasses for Visible and Near-Infrared Photonic Applications. *Materials*. 2020 Oct 23;13(21):4746. [<DOI>](#).

19. Rao VH, Prasad PS, Babu KS. Visible luminescence characteristics of Pr<sup>3+</sup> ions in TeO<sub>2</sub>-Sb<sub>2</sub>O<sub>3</sub>-WO<sub>3</sub> glasses. *Optical Materials*. 2020 Mar;101:109740. [<DOI>](#).

20. Rajesh D. Pr<sup>3+</sup> doped new TZYN glasses and glass-ceramics containing NaYF<sub>4</sub> nanocrystals: Luminescence analysis for visible and NIR applications. *Optical Materials*. 2018 Dec;86:178–84. [<DOI>](#).

21. Maalej O, Boulard B, Dieudonné B, Ferrari M, Dammak M, Dammak M. Downconversion in Pr<sup>3+</sup>-Yb<sup>3+</sup> co-doped ZBLA fluoride glasses. *Journal of Luminescence*. 2015 May;161:198–201. [<DOI>](#).

22. Muscelli WC, Aquino FT, Caixeta FJ, Nunes LRR, Zur L, Ferrari M, et al. Yb<sup>3+</sup> concentration influences UV-Vis to NIR energy conversion in nanostructured Pr<sup>3+</sup> and Yb<sup>3+</sup> co-doped SiO<sub>2</sub>-Nb<sub>2</sub>O<sub>5</sub> materials for photonics. *Journal of Luminescence*. 2018 Jul;199:454–60. [<DOI>](#).

23. Lakshminarayana G, Qiu J. Near-infrared quantum cutting in RE<sup>3+</sup>/Yb<sup>3+</sup> (RE=Pr, Tb, and Tm): GeO<sub>2</sub>-B<sub>2</sub>O<sub>3</sub>-ZnO-LaF<sub>3</sub> glasses via downconversion. *Journal of Alloys and Compounds*. 2009 Jul;481(1-2):582-9. [<DOI>](#).
24. Rajesh D, Dousti MR, Amjad RJ, de Camargo ASS. Quantum cutting and up-conversion investigations in Pr<sup>3+</sup>/Yb<sup>3+</sup> co-doped oxyfluoro-tellurite glasses. *Journal of Non-Crystalline Solids*. 2016 Oct;450:149-55. [<DOI>](#).
25. Belançon MP, Marconi JD, Ando MF, Barbosa LC. Near-IR emission in Pr<sup>3+</sup> single doped and tunable near-IR emission in Pr<sup>3+</sup>/Yb<sup>3+</sup> codoped tellurite tungstate glasses for broadband optical amplifiers. *Optical Materials*. 2014 Apr;36(6):1020-6. [<DOI>](#).
26. Seshadri M, Bell MJV, Anjos V, Messaddeq Y. Spectroscopic investigations on Yb<sup>3+</sup> doped and Pr<sup>3+</sup>/Yb<sup>3+</sup> codoped tellurite glasses for photonic applications. *Journal of Rare Earths*. 2021 Jan;39(1):33-42. [<DOI>](#).
27. Rao VH, Prasad PS, Babu KS. Visible luminescence characteristics of Pr<sup>3+</sup> ions in TeO<sub>2</sub>-Sb<sub>2</sub>O<sub>3</sub>-WO<sub>3</sub> glasses. *Optical Materials*. 2020 Mar;101:109740. [<DOI>](#).
28. Hegde V, Viswanath CSD, Chauhan N, Mahato KK, Kamath SD. Photoluminescence and thermally stimulated luminescence properties of Pr<sup>3+</sup>-doped zinc sodium bismuth borate glasses. *Optical Materials*. 2018 Oct;84:268-77. [<DOI>](#).
29. Zhou X, Wang G, Zhou K, Li Q. Near-infrared quantum cutting in Pr<sup>3+</sup>/Yb<sup>3+</sup> co-doped transparent tellurate glass via two step energy transfer. *Optical Materials*. 2013 Jan;35(3):600-3. [<DOI>](#).
30. Liang L, Mo Z, Ju B, Xia C, Hou Z, Zhou G. Visible and Near-Infrared emission properties of Yb<sup>3+</sup>/Pr<sup>3+</sup> co-doped lanthanum aluminum silicate glass. *Journal of Non-Crystalline Solids*. 2021 Apr;557:120578. [<DOI>](#).





## Laccase-catalyzed Conjugation of BSA Mediated by Gallic Acid: Preparation, Characterization, and Antioxidant Activity

Merve Bat-Özmatara<sup>1</sup> , Fatma Ertan<sup>1</sup> 

<sup>1</sup> Gebze Technical University, Department of Chemistry, Gebze- Kocaeli, Turkey.

**Abstract:** Laccase is one of the enzymes that catalyze the oxidation of phenolic and non-phenolic substrates and show encouraging potential as a biocatalyst in the synthesis of bioactive compounds. It is known that phenolic acids have an antioxidant effect. Bovine serum albumin (BSA) shows gelling activity, and nutraceutical binding ability but it does not show antioxidant activity. In this study, BSA which has no antioxidant activity using laccase, started to show antioxidant activity with gallic acid (GA) conjugation. The synthesized conjugates were analyzed by polyacrylamide gel electrophoresis (PAGE), ultraviolet-visible spectrophotometry (UV-Vis), and Fourier-transform infrared spectroscopy (FTIR). Radical scavenging capacity for antioxidant activity was measured. GA-functionalized-BSA displayed greatly improved 2,2'-azinobis-(3-ethylbenzothiazoline-6-sulfonic acid) (ABTS) and 1,1-diphenyl-2-picryl-hydrazyl (DPPH) radical scavenging capacities, compared with the untreated BSA. Protein-flavonoid conjugates can improve the natural properties of proteins, being promising products to be used in medical, food and polymer fields where antioxidant ability is an essential feature.

**Keywords:** Laccase, bioconjugate, BSA, gallic acid, antioxidant activity.

**Submitted:** June 14, 2021. **Accepted:** November 29, 2021.

**Cite this:** Bat-Özmatara M, Ertan F. Laccase-catalyzed Conjugation of BSA Mediated by Gallic Acid: Preparation, Characterization, and Antioxidant Activity. JOTCSA. 2022;9(1):29-36.

**DOI:** <https://doi.org/10.18596/jotcsa.952065>.

**\*Corresponding author. E-mail:** [mervebatt@gmail.com](mailto:mervebatt@gmail.com).

### INTRODUCTION

It is well known that phenolic compounds exhibit antioxidant and antimicrobial activity and have health benefits. Phenols in foods have been shown to have many biological functions such as anticarcinogens, anti-aging, antimutagenes, antidiabetic and immunostimulatory effects, leading to their recognition as potential nutraceuticals (1,2). Phenolic compounds are simple and naturally occurring compounds containing one or more linked phenolic rings. Various natural phenolic compounds such as gallic acid, hydroxycinnamic acid, hydroxybenzoic acid, ferulic acid, caffeic, p-coumaric acid, vanillin, benzoic acid, catechols are seen in fruits, vegetables and cereals (3). Gallic acid (GA) (3,4,5-trihydroxybenzoic acid), is a powerful antioxidant that protects against oxidative damage caused by reagents such as hydroxyl (HO·), superoxide (O<sub>2</sub><sup>-</sup>)

and peroxy (ROO·) hydrogen peroxide (H<sub>2</sub>O<sub>2</sub>) and hypochlorous acid (HOCl) (4). There are studies in the literature showing that gallic acid has antioxidant and anticancer properties (5,6).

Laccase (benzenediol: oxygen oxidoreductases, EC 1.10.3.2) catalyzes the direct oxidation of an aromatic substrate in the presence of molecular oxygen, which is reduced to water during the reaction. This reaction involves the four single-electron oxidation of the reducing substrate coupled to the four electron reductive cleavage of a dioxygen bond using four Cu atoms distributed between three regions (7). The laccase enzyme has an ability to catalyze a wide variety of substrates such as phenols, aromatic, aliphatic amines, and their derivatives. Laccase was used in the enzymatic polymerization of catechol (8,9). Laccase catalyzed crosslinking of α-lactalbumin and ferulic acid was investigated (10). Some

studies show that phenolic substrates such as caffeic acid, ferulic acid, vanillic acid, gallate, and p-coumaric acid can be used in laccase catalyzed crosslinking of proteins (11,12).

Bovine serum albumin (BSA or "Fraction V") is a serum albumin protein derived from cows. Serum albumin, also known as albumin for short, is the most common protein found in the blood plasma of humans and other mammals. It makes up 60% of the proteins in the blood. It is also found in tissue fluids, particularly muscle and skin, and small amounts of tears, sweat, gastric juices, and bile. 30-40% of the total albumin in the body is in the blood. In addition to carrying fatty acids and various other substances in the blood, its most important function is to balance water between blood and tissue fluids. Bovine serum albumin (BSA) shows gelling activity, surface activity, and nutraceutical binding ability but it does not show antioxidant activity (13,14). In the literature, chitosan and dextran conjugates were made with laccase enzyme (15,16,17). However, no laccase mediated BSA-gallic acid conjugate has been reported.

In this study, the BSA molecule, which has various physiological functions such as contributing to osmotic blood pressure, drug, and other molecule carriers, gained antioxidant activity by conjugating with gallic acid under the effect of laccase.

## EXPERIMENTAL SECTION

### Materials

DPPH, ABTS, Trizma, acrylamide, ammonium persulfate, glycerol, potassium persulfate ( $K_2S_2O_8$ ) and laccase from *Trametes versicolor* were purchased from Sigma. Ethanol, methanol, sodium dodecyl sulfate (SDS), bromophenol blue, 2-mercaptoethanol, Coomassie brilliant blue R250, acetic acid, and sodium acetate were purchased from Merck. All solvents were of analytical grade.

### Laccase activity

The laccase enzyme activity was spectrophotometrically measured by measuring the enzymatic oxidation of 0.5 mM ABTS at 420 nm. Molar extinction coefficient for the oxidation product was  $3.6 \times 10^4 \text{ cm}^{-1} \text{ M}^{-1}$ . A unit laccase (U) defined as the amount of enzyme required to oxidize 1 mol of ABTS per minute at room temperature (18).

### Preparation of acid-protein conjugates

BSA and gallic acid solutions were prepared in 10 mM 4-(2-hydroxyethyl)-1 piperazine-ethanesulfonic acid (HEPES) buffer solution, pH 7.4 with protein concentration at  $5 \text{ mg mL}^{-1}$ . The oxidation reaction was initiated by adding laccase. The sample with 2 different enzyme amounts, 5  $\mu\text{L}$

and 15  $\mu\text{L}$ , was prepared from 11 U/L enzyme. It was left in the shaking incubation at 50 °C for 24 hours (19).

### UV spectroscopy

BSA, gallic acid and conjugates were monitored with a UV-Vis spectrophotometer (SpectraMax Plus 384 Microplate Reader, California, USA). Spectra were collected at room temperature before and after adding laccase.

### FTIR spectroscopy

FT-IR analysis was performed on the BSA, gallic acid, and the conjugate were recorded using the Perkin Elmer FTIR spectrometer. The transmittance values were measured within the spectra between 4000 and  $600 \text{ cm}^{-1}$ .

### SDS PAGE

The molecular weight distribution of BSA, gallic acid and BSA-gallic acid conjugate were analyzed by SDS-PAGE which was carried out on 5% stacking gel and 12% separating gel. The 30  $\mu\text{L}$  of sample was mixed with 10  $\mu\text{L}$  of 4x sample buffer and then heated at 100 °C for 15 min. 10  $\mu\text{L}$  of samples were loaded onto the wells and SDS-PAGE was operated at 120 volts. After electrophoresis, Coomassie Brilliant Blue R250 was adapted to gel staining for thirty minutes followed by decolorization with water overnight.

### Antioxidant Activity

#### DPPH radical scavenging activity

DPPH free radical scavenging activity was measured to evaluate the antioxidant capacity. The Brand-Williams method was used to test whether the sample bleached the stable DPPH radical (20). For this, 0.75 mL of plant extract was added onto 1.50 mL of DPPH solution prepared in ethanol (0.05 mM). After shaking vigorously, the mixture was kept at room temperature for 30 minutes. After 30 minutes, absorbance at 517 nm was measured in a UV-Vis spectrophotometer. The scavenging activity of the DPPH radical was calculated using the formula:

$$\text{DPPH scavenging (\%)} = \left[ \frac{(A_{\text{control}} - A_{\text{sample}})}{A_{\text{control}}} \right] \times 100 \quad (\text{Eq. 1})$$

Herein,  $A_{\text{control}}$  shows the absorbance of the control (DPPH solution without sample) and  $A_{\text{sample}}$  shows the absorbance of the test sample.

#### ABTS radical scavenging activity

This method, developed by Arnao et al., is based on reducing the cationic radical formed by the  $K_2S_2O_8$  oxidation of ABTS with antioxidants. The blue / green colored ABTS  $^{*+}$  radical has a strong absorption at 600-750 nm (21).

For ABTS radical scavenging activity, the 7.4 mM ABTS solution and 2.6 mM potassium persulfate solution were evenly mixed, then kept in the dark

at room temperature for 12 hours. 1 milliliter of the formed ABTS radical solution was diluted with an absorbance of  $1.1 \pm 0.02$  at 734 nm wavelength in the spectrophotometer by adding approximately 60 mL of methanol. Then, 150  $\mu\text{L}$  of sample solution and 2850  $\mu\text{L}$  of ABTS  $^{*+}$  radical solution were left in incubation for 2 hours in the dark. The control solution was prepared using distilled water instead of the sample. Absorbance at 734 nm wavelength was measured in a spectrophotometer. In the calculations, ABTS% radical scavenging effect was found with the formula below.

$$\text{ABTS scavenging (\%)} = \frac{[(A_{\text{control}} - A_{\text{sample}}) / A_{\text{control}}] \times 100}{\text{(Eq. 2)}}$$

Here,  $A_{\text{control}}$  shows the absorbance of the control (ABTS solution without sample) and  $A_{\text{sample}}$  shows the absorbance of the test sample.

## RESULTS AND DISCUSSION

### UV Analysis

The typical UV spectrum chart of the product obtained as a result of our study is shown in Figure 1. Accordingly, it was observed that the peak belonging to gallic acid at higher laccase

concentrations than the two different laccase concentrations applied weakened as in the references and slightly shifted towards the red region. The protein absorption band at 280 nm was seen as a small shoulder of the dense absorption band of gallic acid (at 258 nm). This shoulder peak may mean conjugation has occurred. BSA in this shoulder heteroconjugation is thought to belong to the amino acid tyrosine. That a similar shoulder peak at 280 nm was obtained in conjugation with myoglobin and gallic acid. However, it is difficult to evaluate the extent of complex formation using the density and shear properties of these signals (22). The weaker band at 280 nm suggests that conjugation is hetero-conjugation. This suggests that the amount of laccase present in the medium is not sufficient for homo-conjugation. These results are also supported by the references disclosed. In addition to these, when we examined the prepared samples, no precipitation was observed in the samples prepared at the ratio of BSA: GA (3: 1), while the samples prepared at the ratio of BSA: GA (1: 1) or BSA: GA (1: 3) were observed. It has been observed that the collapse occurs as the amount of BSA decreases. As a result of the reaction, gallic acid, which is oxidized and converted to quinones, binds to tyrosine residues in BSA.

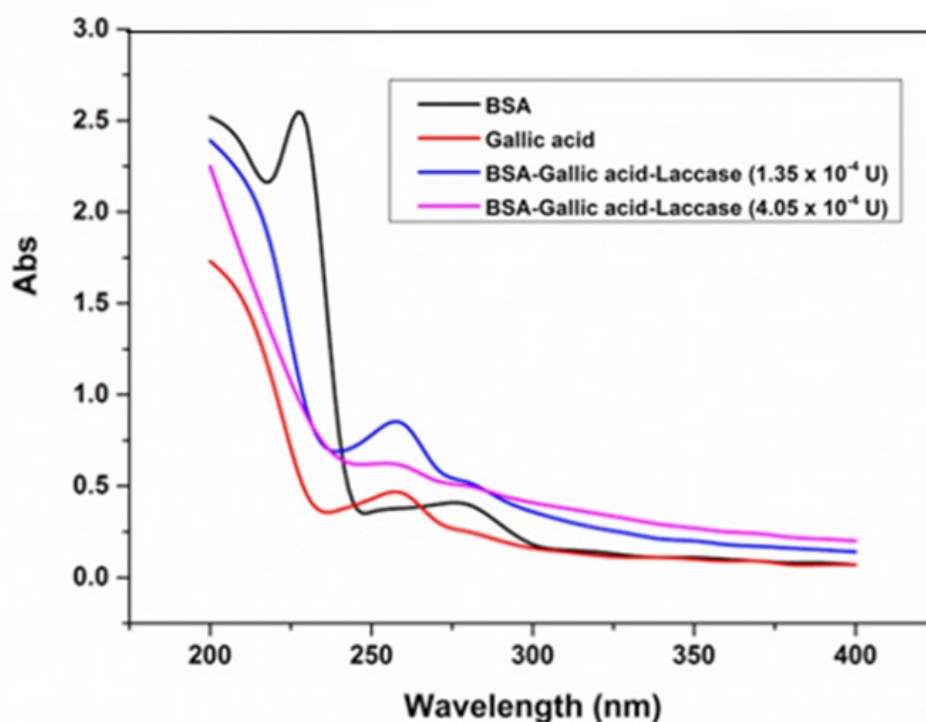


**Figure 1:** UV spectra of BSA, Gallic acid, and conjugates.

### FTIR Analysis

The conjugation of gallic acid with BSA was analyzed by infrared spectroscopy. Polyphenolic characteristics with the existence of a phenolic ring

-OH stretching within the  $3200\text{--}3550\text{ cm}^{-1}$ . Amide band, which is located between  $1700\text{ cm}^{-1}$  and  $1600\text{ cm}^{-1}$ , is composed mainly (around 80%) of the C=O stretching vibration of the peptidic bond

(23). The spectral alterations observed are due to changes in the intensity of the amide band, upon acid interactions with protein C-O, C-N and NH groups (hydrophilic contacts). The amide peak was moved to a lower wavelength due to the decreased  $\alpha$ -helix content of the protein conjugated with gallic acid.

In the protein-flavonoid conjugate study performed by Kim and Paulo, FT-IR microscopy was used to analyze the chemical bonds formed by the conjugate. The study was carried out with  $\alpha$ -casein and BSA proteins. Different peak formation was not observed in the conjugates of casein and BSA protein structures, and a change in the intensities of the peaks present in the protein was observed depending on the protein used (BSA, Casein) (19). Observation of the intensity decrease and shifts in the peaks belonging to the functional groups observed in the FT-IR analysis obtained in our study shows that the conjugate is formed.

In another study by Fan et al., bovine serum albumin (BSA)-caffeic acid (CA) conjugate was prepared by free radical-induced grafting method. In the study, FT-IR spectra of resveratrol, zein, BSA-CA conjugate and resveratrol loaded zein-BSA-CA nanoparticle, FT-IR spectroscopy were also used to analyze the intermolecular interactions between resveratrol and proteins. As a result of the analysis, zein protein and BSA-CA conjugate spectra were observed to be very similar and characteristic absorption bands were determined for both structures. It was stated that resveratrol did not cause new absorption peaks in the loaded zein-BSA-CA nanoparticle, indicating that the proteins and resveratrol were physically linked and did not exhibit any covalent reaction (24). The absence of an absorbance peak of the BSA-GA conjugate we obtained in our study is expressed by the fact that the interaction is not a covalent interaction as supported by the studies in the literature.

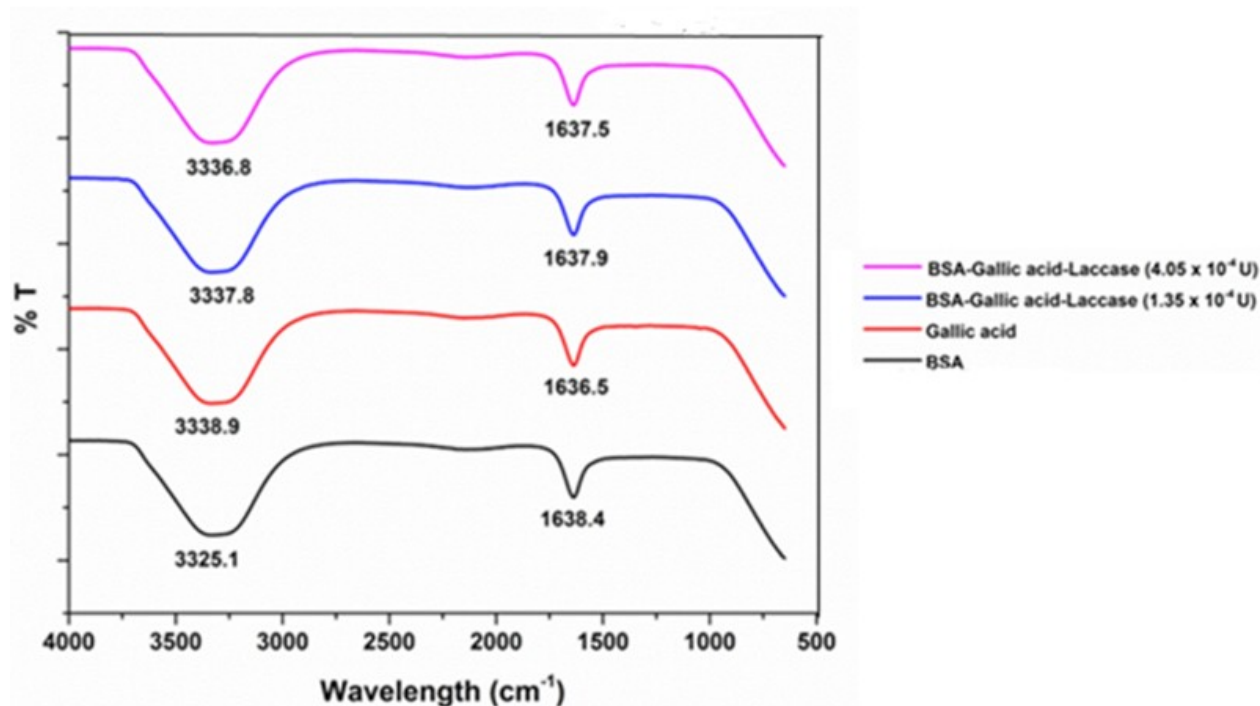


**Figure 2:** FTIR of BSA, Gallic acid, and conjugates.

### SDS PAGE

The molecular weight distributions of pure BSA, GA, and BSA-gallic acid conjugate catalyzed by laccase were performed by SDS-PAGE (Figure 3). BSA-GA 1 represent BSA-gallic acid-laccase ( $1.35 \times 10^{-4}$  U) and BSA-GA 2 represent BSA-gallic acid-laccase ( $4.05 \times 10^{-4}$  U). The band of gallic acid was

hardly detected (line 2) due to its low molecular weight. When both gallic acid and laccase were added to the BSA solution, the band moved slower than that of BSA and appeared higher in the gel because of its high molecular weight. This showed that GA and BSA were bound in the enzymatic process.

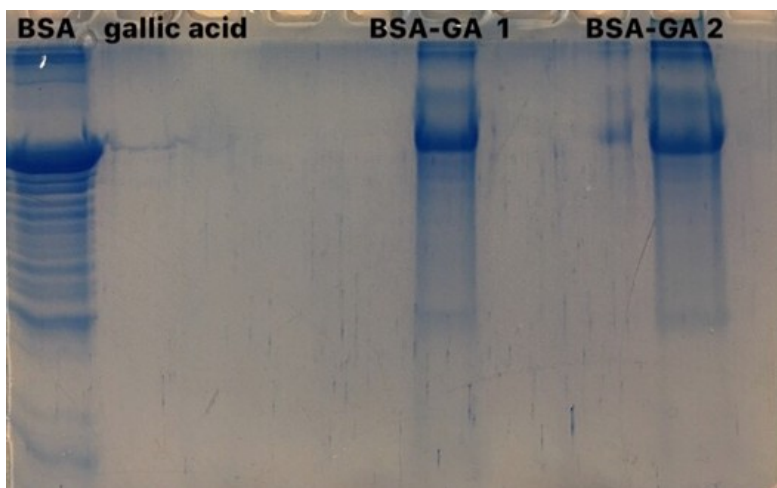


**Figure 3:** SDS-PAGE of BSA, GA, and conjugates.

### Antioxidant Activity

In the DPPH test, the ability of BSA, GA, and conjugates to act as a donor for hydrogen atoms or electrons to reduce DPPH to DPPH-H was measured in a spectrophotometric manner. BSA does not have a DPPH radical scavenging activity. On the other hand, GA shows 94.53% radical inhibition activity. The BSA-GA conjugates formed as a result of the reaction show antioxidant activity. Conjugates showed an inhibitory activity of 86.79% and 81.96%, respectively, depending on the excess amount of enzyme (Figure 4). Excessive amount of enzyme causes more GA-BSA interaction, thus increasing the activity.

In the ABTS test, the reaction between ABTS and potassium persulfate forms the ABTS radical cation (ABTS<sup>+</sup>) and a blue-green color is observed. When the antioxidant is present, the radical reverts to a colorless state. While gallic acid shows 96.57% ABTS radical inhibition activity, BSA does not show an antioxidant activity. The BSA-gallic acid conjugates showed a radical inhibition activity of 84.73% and 82.67% depending on the excess amount of enzyme (Figure 4). As in DPPH radical scavenging, the more enzyme amount increases the activity because it causes more gallic acid BSA interaction.

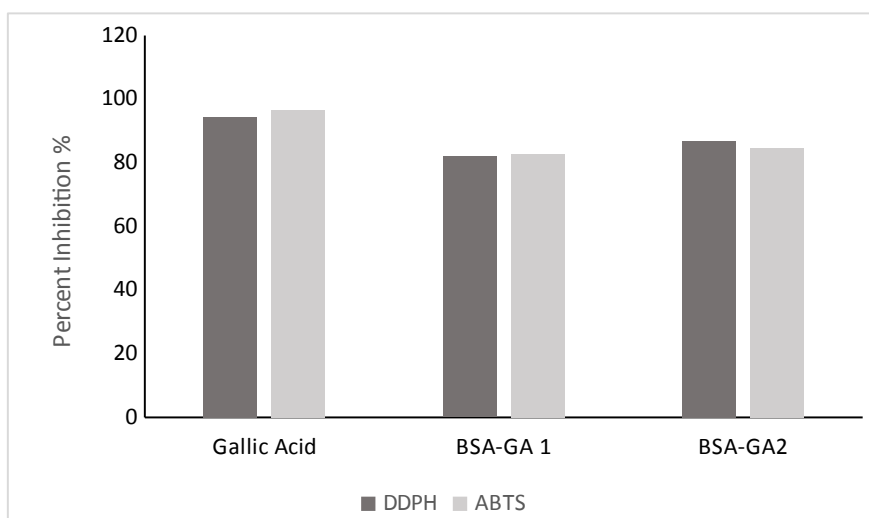


**Figure 4:** Antioxidant activity of Gallic acid, BSA-GA 1, BSA-GA 2.

### CONCLUSION

In the present study, BSA was successfully functionalized with GA, a natural antioxidant, by laccase. The formation of BSA-gallic acid was proved by UV-Vis and FTIR spectra. Importantly, BSA-GA exhibited potent ABTS and DPPH scavenging activities, all of which were stronger

than those of BSA. Protein-flavonoid conjugates can improve the natural properties of proteins, being promising products to be used in medical, food and polymer fields where antioxidant ability is an essential feature.



**CONFLICT OF INTEREST**

The authors declare that they have no conflict of interest.

**REFERENCES**

1. Ls R, Nja S. Anticancer Properties of Phenolic Acids in Colon Cancer – A Review. *J Nutr Food Sci* [Internet]. 2016 [cited 2021 Nov 29];06(02). [<DOI>](#).
2. Weng C-J, Yen G-C. Chemopreventive effects of dietary phytochemicals against cancer invasion and metastasis: Phenolic acids, monophenol, polyphenol, and their derivatives. *Cancer Treatment Reviews*. 2012 Feb;38(1):76–87. [<DOI>](#).
3. Tian R-R, Pan Q-H, Zhan J-C, Li J-M, Wan S-B, Zhang Q-H, et al. Comparison of Phenolic Acids and Flavan-3-ols During Wine Fermentation of Grapes with Different Harvest Times. *Molecules*. 2009 Feb 18;14(2):827–38. [<DOI>](#).
4. Badhani B, Sharma N, Kakkar R. Gallic acid: a versatile antioxidant with promising therapeutic and industrial applications. *RSC Adv*. 2015;5(35):27540–57. [<DOI>](#).
5. Sagdicoglu Celep AG, Demirkaya A, Solak EK. Antioxidant and anticancer activities of gallic acid loaded sodium alginate microspheres on colon cancer. *Current Applied Physics*. 2020 Jul;S1567173920301164. [<DOI>](#).
6. de Cristo Soares Alves A, Mainardes RM, Khalil NM. Nanoencapsulation of gallic acid and evaluation of its cytotoxicity and antioxidant activity. *Materials Science and Engineering: C*. 2016 Mar;60:126–34. [<DOI>](#).
7. Giardina P, Faraco V, Pezzella C, Piscitelli A, Vanhulle S, Sannia G. Laccases: a never-ending story. *Cell Mol Life Sci*. 2010 Feb;67(3):369–85. [<DOI>](#).
8. Su J, Noro J, Fu J, Wang Q, Silva C, Cavaco-Paulo A. Enzymatic polymerization of catechol under high-pressure homogenization for the green coloration of textiles. *Journal of Cleaner Production*. 2018 Nov;202:792–8. [<DOI>](#).
9. Su J, Castro TG, Noro J, Fu J, Wang Q, Silva C, et al. The effect of high-energy environments on the structure of laccase-polymerized poly(catechol). *Ultrasonics Sonochemistry*. 2018 Nov;48:275–80. [<DOI>](#).
10. Jiang Z, Yuan X, Yao K, Li X, Zhang X, Mu Z, et al. Laccase-aided modification: Effects on structure, gel properties and antioxidant activities of  $\alpha$ -lactalbumin. *LWT*. 2017 Jul;80:355–63. [<DOI>](#).
11. Aljawish A, Chevalot I, Jasniewski J, Paris C, Scher J, Muniglia L. Laccase-catalysed oxidation of ferulic acid and ethyl ferulate in aqueous medium: A green procedure for the synthesis of new compounds. *Food Chemistry*. 2014 Feb;145:1046–54. [<DOI>](#).
12. Mattinen M-L, Hellman M, Permi P, Autio K, Kalkkinen N, Buchert J. Effect of Protein Structure on Laccase-Catalyzed Protein Oligomerization. *J Agric Food Chem*. 2006 Nov 1;54(23):8883–90. [<DOI>](#).
13. Livney YD. Milk proteins as vehicles for bioactives. *Current Opinion in Colloid & Interface Science*. 2010 Apr;15(1–2):73–83. [<DOI>](#).
14. Matsudomi N, Rector D, Kinsella JE. Gelation of bovine serum albumin and  $\beta$ -lactoglobulin; effects of pH, salts and thiol reagents. *Food Chemistry*. 1991 Jan;40(1):55–69. [<DOI>](#).
15. Božič M, Gorgieva S, Kokol V. Laccase-mediated functionalization of chitosan by caffeic and gallic acids for modulating antioxidant and antimicrobial properties. *Carbohydrate Polymers*. 2012 Mar;87(4):2388–98. [<DOI>](#).
16. Yu C, Liu X, Pei J, Wang Y. Grafting of laccase-catalysed oxidation of butyl paraben and p-coumaric acid onto chitosan to improve its antioxidant and antibacterial activities. *Reactive and Functional Polymers*. 2020 Apr;149:104511. [<DOI>](#).
17. Božič M, Štrancar J, Kokol V. Laccase-initiated reaction between phenolic acids and chitosan. *Reactive and Functional Polymers*. 2013 Oct;73(10):1377–83. [<DOI>](#).
18. Wolfenden BS, Willson RobinL. Radical-cations as reference chromogens in kinetic studies of one-electron transfer reactions: pulse radiolysis studies of 2,2'-azinobis-(3-ethylbenzthiazoline-6-sulphonate). *J Chem Soc, Perkin Trans 2*. 1982; (7):805–12. [<DOI>](#).
19. Kim S, Cavaco-Paulo A. Laccase-catalysed protein-flavonoid conjugates for flax fibre modification. *Appl Microbiol Biotechnol*. 2012 Jan;93(2):585–600. [<DOI>](#).
20. Brand-Williams W, Cuvelier ME, Berset C. Use of a free radical method to evaluate antioxidant activity. *LWT - Food Science and Technology*. 1995;28(1):25–30. [<DOI>](#).

21. Arnao MB, Cano A, Alcolea JF, Acosta M. Estimation of free radical-quenching activity of leaf pigment extracts. *Phytochem Anal.* 2001 Mar;12(2):138-43. [<DOI>](#).

22. Grigoryan KR, Shilajyan HA. Analysis of the interaction of gallic acid and myoglobin by UV-vis absorption spectroscopy. *Russ J Bioorg Chem.* 2017 May;43(3):255-8. [<DOI>](#).

23. Grdadolnik J. Saturation effects in FTIR spectroscopy: intensity of amide I and amide II bands in protein spectra. *Acta chimica slovenica.* 2003;50(4):777-88.

24. Fan Y, Liu Y, Gao L, Zhang Y, Yi J. Improved chemical stability and cellular antioxidant activity of resveratrol in zein nanoparticle with bovine serum albumin-caffeic acid conjugate. *Food Chemistry.* 2018 Sep;261:283-91. [<DOI>](#).







## A Simple and Feasible Method for the Quantification of Metabolites in the Human Follicular Fluid Using $^1\text{H}$ HR-MAS NMR Spectroscopy

Akin MUMCU<sup>1,2\*</sup>  

<sup>1</sup>Laboratory of NMR, Scientific and Technological Research Centre, Inonu University, Malatya, Turkey

<sup>2</sup>Reproductive Sciences & Advanced Bioinformatics Application & Research Centre, Inonu University, Malatya, Turkey

**Abstract:** This study presents a reliable method for the quantification of metabolite concentrations in follicular fluid with the high-resolution magic angle spinning nuclear magnetic resonance (HR-MAS NMR) spectroscopy and the ERETIC2 (Electronic REference To access In vivo Concentrations) based on PULCON (pulse length based concentration determination) principle. The positive effect of the HR-MAS probe technology on spectral quality and its ability to perform analyses with very low sample amounts were the most important factors of proposing this method. In evaluating the performance of the proposed method, standard creatine solutions in different concentrations containing DSS (2,2-dimethyl-2-silapentane-5-sulfonate sodium salt) as an internal reference standard were analyzed using different pulse programs (cpmgrp1d and zg30). The results obtained with the ERETIC2 were compared with the classical internal standard NMR quantification method (DSS method). The relative standard deviation (RSD) values for ERETIC2 were in the range of 0.3% - 5.7% and recovery values were calculated as minimum 90.3%, while RSD values for DSS method were in the range of 0.1% - 3.1% and recovery values were minimum 97.0%. Besides, it was observed that the metabolite concentration values calculated using the ERETIC2 procedure of follicular fluid samples obtained from the women with endometriosis and healthy controls were compatible with the values those obtained using different methodologies. The obtained results showed that the proposed quantification method based on the HR-MAS spectroscopy can easily be used in biological fluids and therefore it can be utilized as a good alternative to the internal standard method considering its accuracy and precision.

**Keywords:** HR-MAS spectroscopy, quantification, PULCON, ERETIC2, metabolite concentration

**Submitted:** August 24, 2021. **Accepted:** November 29, 2021.

**Cite this:** Mumcu A. A simple and feasible method for the quantification of metabolites in the human follicular fluid using  $^1\text{H}$  HR-MAS NMR spectroscopy. JOTCSA. 2022;9(1):37-56.

**DOI:** <https://doi.org/10.18596/jotcsa.986523>.

**\*Corresponding author. E-mail:** [akinmumcu@gmail.com](mailto:akinmumcu@gmail.com)

### INTRODUCTION

High-resolution magic angle spinning nuclear magnetic resonance (HR-MAS NMR) spectroscopy is a versatile analytical technique and it was developed to obtain high-quality NMR spectra in studies on semi-solid and

heterogeneous systems (1). Nuclear spins in semisolid samples are subject to some interactions resulting in dominant spectral broadening (2). This spectral broadening results from chemical shift anisotropy, magnetic susceptibility, and dipolar-quadrupolar interactions caused by sample heterogeneity

(3). These line broadening effects are reduced by the fast spinning of the sample in the direction of a static magnetic field at the angle of  $54.7^\circ$  in the HR-MAS technique and a high-resolution NMR spectrum is obtained (4,5). With these features, HR-MAS spectroscopy is an analytical tool of increasing importance in the characterization of metabolic structure in heterogeneous samples such as intact tissues and cells (6). Besides, since almost all biological fluids except urine do not fall into the classical definition of aqueous solution due to their protein or macromolecule contents, the broadened NMR signals in these fluids can be reduced by using the HR-MAS technique (7). Metabolic characterization, also called metabolomics, is the systematic identification and quantification of metabolites to obtain important biochemical information from various biological samples or a given organism (8). The ability to measure metabolite concentrations, especially in biological samples, is crucial for examining the pathophysiology and course of a disease, monitoring its response to treatment, and classifying disease states (9). Quantification of metabolite concentrations not only allows us to identify abnormal metabolism but also helps to compare results from different subjects and patient groups (9). In this context, quantitative NMR has been used for many years by different disciplines in determining biochemical pathways of plants and animal species as well as the identification of biomarkers for the diagnosis of diseases (10). There are two main types of quantification with NMR: relative and absolute quantification (11). Although relative quantitation is used in many metabolomics studies, it has a major disadvantage. In this method, concentrations of related metabolites simultaneously change in some disease states. Therefore, absolute quantitation is preferred for clinical diagnosis and determination of metabolite concentrations in physiological studies (12). There are two main NMR methods, depending on whether an internal or external reference standard is used for absolute quantification (11). The internal reference method is simple and easy to use (13). However, it is not always applied in the sample solution, as it is difficult to create the correct combination of the solvent, analyte, and internal standard, without any chemical interaction between them (11). Addition of internal NMR reference chemicals such as DSS (2,2-dimethyl-2-silapentane-5-sulfonate sodium salt) or TSP (trimethylsilyl propionate), which

are mostly used in biological applications, carries the risk of chemical interaction of these substances with biological macromolecules in the sample. Also, quantification becomes difficult due to overlap signal problems (14). The use of the external reference method can avoid these disadvantages of the internal method (11). In the external reference method, the reference compound and sample are prepared as separate solutions and NMR signals are measured simultaneously in two separate NMR tube systems. This method prevents possible interactions between the reference substance and biological macromolecules but requires additional sample preparation time (13). Another disadvantage, since the external reference method depends on concentrations, an additional source of error may occur that can be caused by volume measurements of the solvents used in the preparation of calibration and sample solutions (11). An alternative approach to the external reference method was first introduced by Barantin et al. as a new method in vivo quantification (15). This method, called the ERETIC (Electronic reference to access in vivo concentrations) method, uses an artificial NMR signal produced by a small loop coil that matches the RF coil as a reference signal (12). Since the ERETIC method uses a synthesized RF pulse during the acquisition period when generating a reference signal, (16) there is no need to add any internal reference material to the sample (17). However, the need for some modifications in the spectrometer setup, the requirement additional specialized hardware and the necessity of the ERETIC signal to remain stable regularly are the drawbacks of this method (14). Also, several important quantification methods are available, such as PULCON (PULse-length-based CONcentration determination) and ERETIC2 (Bruker Topspin) (13). PULCON is an internal standard method (18) that relates the absolute intensities of two different spectra and uses the reciprocity principle, which indicates that the  $90^\circ$  or  $360^\circ$  pulse lengths is inversely proportional to the NMR signal intensity (14). This method provides the necessary compensation factors for losses in coil sensitivity originating from dielectric properties in different samples and does not require specialized electronic devices (19). While the development of the PULCON method brought a noticeable convenience to the applicability of quantitative NMR, it also established an infrastructure for the ERETIC2 method which is based on the

PULCON principle. ERETIC2 is the name of a software program developed by Bruker that uses the PULCON principle to determine the absolute concentration of a molecule (20). ERETIC2 does not require specialized NMR tube systems and any additional devices to generate an electronic reference signal. Also, it prevents any interaction between the analyte and the reference compound as well as eliminating the problems caused by peak overlaps (13). With these features, the ERETIC2 is a good alternative to the classical internal standard method due to the convenience provided to researchers in the absolute quantification of the unknown substance (18). This study aims to evaluate the accuracy and precision of the ERETIC2 in the quantification of the metabolite composition of follicular fluid samples obtained from participants with endometriosis and healthy using HR-MAS spectroscopy. Human follicular fluid was chosen because it contains important metabolites that affect oocyte quality, fertilization, and embryonic development and provides important information about folliculogenesis (21,22). Moreover, it is thought that the changes in the metabolic profile of the follicular fluid (FF), which constitutes the microenvironment of oocyte, plays an important role in determining oocyte quality and embryonic quality, and subsequent embryonic development and fertilization (23,24). In recent years, the recognition of the relationship between follicular fluid (FF) and oocyte quality and the ability to obtain follicular fluid easily with oocyte during standard in-vitro fertilization procedures have attracted the interest of omics-based technologies and different disciplines (25,26). To the best of our knowledge, this is the first study in literature that utilizes ERETIC2 and HR-MAS technique for quantification of the metabolite content of follicular fluid. To achieve this, firstly the accuracy of ERETIC2 was compared with the classical internal standard method. For this purpose, different pulse sequences and different concentrations of standard solutions containing DSS as an internal reference standard were used. The ERETIC2 was then applied to follicular fluid samples for metabolite quantification.

## EXPERIMENTAL SECTION

### Preparation of standard solutions

Firstly, a stock solution containing 10 mM creatine and DSS was prepared using 10 mM

phosphate-buffered saline (PBS, pH 7.4) prepared in D<sub>2</sub>O (deuterium oxide). Standard solutions of 10 mM, 5 mM, 3 mM, and 1 mM to be used in the calibration experiments were prepared with dilution weight by volume from 10 mM stock solution. The phosphate buffer salt prepared in D<sub>2</sub>O was used in the dilution process. Chemicals used in this study, such as the creatine monohydrate (%99), D<sub>2</sub>O (%99.9 D atom, 1.11 g/mL), KH<sub>2</sub>PO<sub>4</sub> (%98) and Na<sub>2</sub>HPO<sub>4</sub> (%99) were obtained from Merck, while the DSS (%97), KCl (%99) and NaCl were obtained from Sigma-Aldrich. Sartorius CP225D (readability 0.01 mg) was used for all weight measurements.

### Sample preparation for HR-MAS spectroscopy

Follicular fluids used in HR-MAS analysis were obtained from the patients recruited in İnönü University Faculty of Medicine, Department of Obstetrics and Gynecology. This study was approved by the Human Research Ethics committee of Malatya (No: 2016/113), and participants was enrolled in the study after their written informed consent. The healthy control sample was selected from the patients having intracytoplasmic sperm (ICSI) treatment, while the sample with endometriosis was selected from the patients having in vitro fertilization (IVF) treatment. Thus, this study includes follicular fluid samples collected from a total of 10 patients. Five of the samples were obtained from healthy controls and 5 from patients with endometriosis. The diagnosis of endometrioma in patients with endometriosis was made using transvaginal ultrasonography. The healthy control group was selected only from patients with infertility caused by a strong male factor (severe azoospermia). Individuals participating in the study had good physical and mental health. The criteria for inclusion of individuals with normal pelvic anatomy as a result of ultrasonographic screening were age < 35, BMI (body mass index) < 30 kg/m<sup>2</sup> and FSH (follicle-stimulating hormone) < 10.0 IU/L. As exclusion criteria, age of > 35, BMI > 30 kg/m<sup>2</sup>, FSH > 10.0 IU/L and chronic systemic diseases were chosen. Follicular fluid samples to be NMR analyzed were collected from approximately 20 mm sized follicles during oocyte recovery and added to individual sterile tubes. All samples were centrifuged for 10 min at 2900 rpm to remove possible cell impurities. After these procedures, samples were stored at -80 °C until NMR analysis (27).

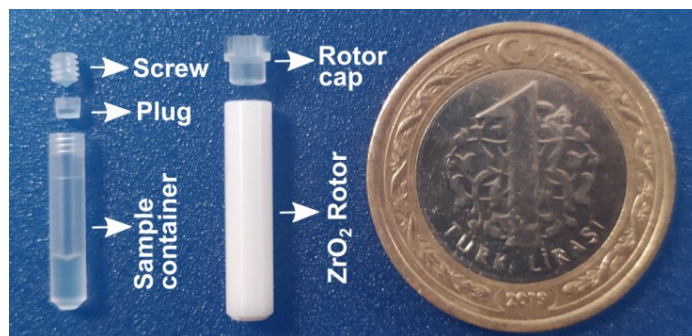


**Figure 1:** 4 mm diameter zirconium rotor and disposable HR-MAS insert consisting of three parts (screw, plug and container). The plug seals the sample inside the sample container. The plug restraining screw holds the plug in position. The assembled insert fits into a standard HR-MAS rotor.

HR-MAS analyses of both standard solutions and follicular fluids were performed in 30  $\mu\text{L}$  volumes in sealed disposable inserts (Bruker) made from biologically inert KEL-F (poly (1-chloro-1,2,2-trifluoroethylene)). Since creatine solutions of different concentrations are prepared in  $\text{D}_2\text{O}$ , samples of 30  $\mu\text{L}$  volume taken from them are placed first in disposable inserts consisting of one sample container, plug, and screw, and then in a 4 mm diameter  $\text{ZrO}_2$  MAS rotor suitable for these inserts (Figure 1). For follicular fluid samples, first 5  $\mu\text{L}$  of  $\text{D}_2\text{O}$  and then 25  $\mu\text{L}$  of FF were added into the disposable insert and after the rotor assembly was completed, samples were transferred to the HR-MAS probe for NMR analysis. A possible error during the assembly of the rotor may cause some spin problems during the analysis or loss of the lock signal as a result of sample leakage. To avoid this, the amount of sample in the rotor was double-checked by weighing before and after the analysis.

#### **$^1\text{H}$ HR-MAS analysis of samples**

All one-dimensional (1D)  $^1\text{H}$  NMR experiments were recorded using a 600 MHz Bruker Avance III HD NMR spectrometer equipped with a 4 mm diameter HR-MAS probe ( $^1\text{H}/^{13}\text{C}/^{15}\text{N}$ ). All samples were spun at 4 kHz using a MAS speed controller. While the probe temperature was controlled using a Bruker cooling unit, instrumental temperature in all experiments was retained constant at 295 K. When the samples were placed in the magnet, HR-MAS probe was manually tuned and matched to reduce radio frequency (RF) reflection before each analysis.  $^1\text{H}$  NMR spectra of each creatine solution samples were acquired using both standard zg30 pulse sequence (RD -  $30^\circ$  - FID)

and Carr-Purcell-Meiboom-Gill (cpmgpr1d) pulse sequence (RD -  $90^\circ$  -  $\{180^\circ - \tau - (\tau - 180^\circ - \tau)_L - \tau - 180^\circ\}$  - FID), whereas  $^1\text{H}$  NMR spectra of follicular fluids (FF) samples were acquired using only cpmgpr1d pulse sequence. During standard zg30 pulse experiments, 64K data points and a spectral width of 12019.2 Hz were applied. For each sample, FID (free induction decay) acquisitions were collected in 8 min using 2.73 sec acquisition time, 128 transients, and a relaxation delay (RD) of 1.0 sec. All CPMG  $^1\text{H}$  NMR spectra were recorded with 32K data points and a spectral width of 7002.8 Hz. Where CPMG echo delay ( $\tau$ ) was 0.7 msec, relaxation delay (RD) was 4.0 sec, and the number of loops ( $L$ ) was 128. The water signal was suppressed with a weak presaturation pulse ( $2.8\text{E}-5$  W) on water peak frequency during the acquisition. FID acquisitions were collected in 27 min using 2.34 sec acquisition time and 256 transients. Bruker Topspin (ver. 3.2.7) was used for the processing of NMR data. Previous to Fourier transform, the exponential line broadening of 0.3 Hz was performed to FID. All spectra were manually phase-corrected and baseline corrected. The chemical shifts of creatine samples were calibrated according to the singlet peak at 0 ppm of the DSS reference. Spectral assignments of follicular fluid metabolites were determined from the published literature and from various resources (28,29).

#### **Comparison experiments of the internal standard method (DSS method) and ERETIC2**

The concentrations of creatine solutions in different concentrations (10 mM, 5 mM, 3 mM, and 1 mM) containing DSS as the internal

reference standard substance was calculated using both the internal standard method (DSS method) and the ERETIC2. First, Equation 1 was used to calculate the concentrations of creatine samples using the internal standard method.

$$[X_{Cr}] = n_{DSS} / n_{Cr} \times A_{Cr} / A_{DSS} \times [DSS] \quad (\text{Eq. 1})$$

In this equation,  $n_{DSS}$  and  $n_{Cr}$  show the proton numbers of the DSS and creatine peaks, respectively. In concentration calculations, 9 proton singlet signals of DSS in the range of 0.02 to - 0.17 ppm and 3 proton methyl signal of creatinine in the range of 3.05 - 2.9 ppm were used.  $A_{Cr}$  and  $A_{DSS}$  show the calculated integral area of the creatinine methyl peaks and the DSS peak.  $[DSS]$  is the concentration of DSS in the sample. Secondly, the quantification module called ERETIC2 developed by Bruker was used in concentration calculations. ERETIC2 was carried out in two steps including calibration and quantification. In the calibration step, a 10 mM DSS solution prepared in  $D_2O$  solvent containing 10 mM phosphate-buffered saline was used as the ERETIC2 reference to generate the synthetic signal. NMR spectrum obtained from ERETIC2 reference sample was recorded using acquisitions parameters such as number of scan ( $ns$ ) and receiver gain ( $rg$ ) specified for this sample. The signals in the DSS spectrum are defined as ERETIC reference from the integration menu of the ERETIC2 module in the software program of TopSpin and the calibration process is completed. In the quantification step, NMR spectra from creatine solutions prepared at different concentrations were recorded using the same experimental parameters as the ERETIC2 reference sample except for receiver gain. The receiver gain and the  $90^\circ$  pulse length were determined individually for each sample. In addition, the same processing parameters were used in both steps (supporting information file Figure S1). The creatine concentrations in the sample were then determined by Equation 2 using the integration menu in the ERETIC2 module (18).

$$C_{Cr} = k \cdot C_{Ref} \frac{A_{Cr} \cdot T_{cr} \cdot \theta_{90}^{Cr} \cdot ns_{Ref}}{A_{Ref} \cdot T_{Ref} \cdot \theta_{90}^{Ref} \cdot ns_{Cr}} \quad (\text{Eq. 2})$$

In the Equation 2 used by the ERETIC2,  $C_{Cr}$  and  $C_{Ref}$  are the concentrations of the creatine and reference samples respectively,  $T$  is the

temperature at which analyses are performed,  $\theta_{90}$   $90^\circ$  is the pulse length,  $ns$  is the number of scans used for experiments, and  $k$  is the correction factor accounts for the experimental differences such as the receiver gain or incomplete relaxation (18). To evaluate the accuracy of both methods, 1D  $^1H$  NMR analyses of all samples were repeated five times (supporting information file Table S1 and Table S2), both in the same samples and in different samples prepared. While the analysis of the same samples was repeated, the samples were removed the magnet and placed back into the magnet each time.

### Metabolite quantification in follicular fluid samples with ERETIC2

Similar to the quantification of creatine solutions, metabolite quantification with the ERETIC2 was also performed in two steps. In the calibration process, for the ERETIC2 reference, the previously obtained NMR spectrum of the 10 mM DSS solution was used. In the quantification step, the NMR spectra of the follicular fluid samples were used for metabolite quantification (supporting information file Figure S2). Also, 1D  $^1H$  NMR analysis of each follicular fluid sample was repeated three times with different samples prepared.

## RESULTS AND DISCUSSION

### Spectral properties and advantages of HR-MAS

The metabolite peaks examined in NMR studies of biological fluids are overlapped by broad signals originated from proteins, lipids, and especially water, which is a predominant component of biological samples (4). Therefore, suppression of the water peak is very important to obtain interpretable NMR spectra (30). Figure 2 shows the NMR spectra recorded utilizing the identical pulse sequences of the same follicular fluid sample with the 4 mm diameter HR-MAS probe (Figure 2b) and the conventional 5 mm diameter liquid state NMR probe (Figure 2a). As seen in Figure 2, water suppression with the HRMAS probe is more successful than the water suppression with the conventional probe. In this way, with a better baseline obtained in the HR-MAS spectrum, the  $\beta$ -glucose (4.55 ppm) and  $\alpha$ -glucose (5.13 ppm) signals located in areas close to the water signal at about 4.7 ppm are more clearly observed. This provides an advantage in the correct quantification of the relevant metabolite peaks. Water suppression is

improved by some experimental and hardware factors. In NMR spectroscopy, some gradient-based suppression techniques (WET, WATERGATE, or CPMG) which can be easily combined with most of the pulse sequences are used to suppress unwanted signals in the spectrum (31). Another important factor for successful water suppression is the homogeneity of the  $B_0$  magnetic field (32). Better  $B_0$  homogeneity can be achieved by reducing the sample volume and keeping the

entire sample within the active volume of the probe (33). However, in conventional 5 mm diameter NMR probes, the receiver coil is shorter than the sample length in the NMR tube, and a solution volume of approximately 600  $\mu\text{L}$  is required to provide the appropriate spectral resolution in these probes. This causes unsuppressed water in the sample to disperse inside or outside the active volume of the probe.

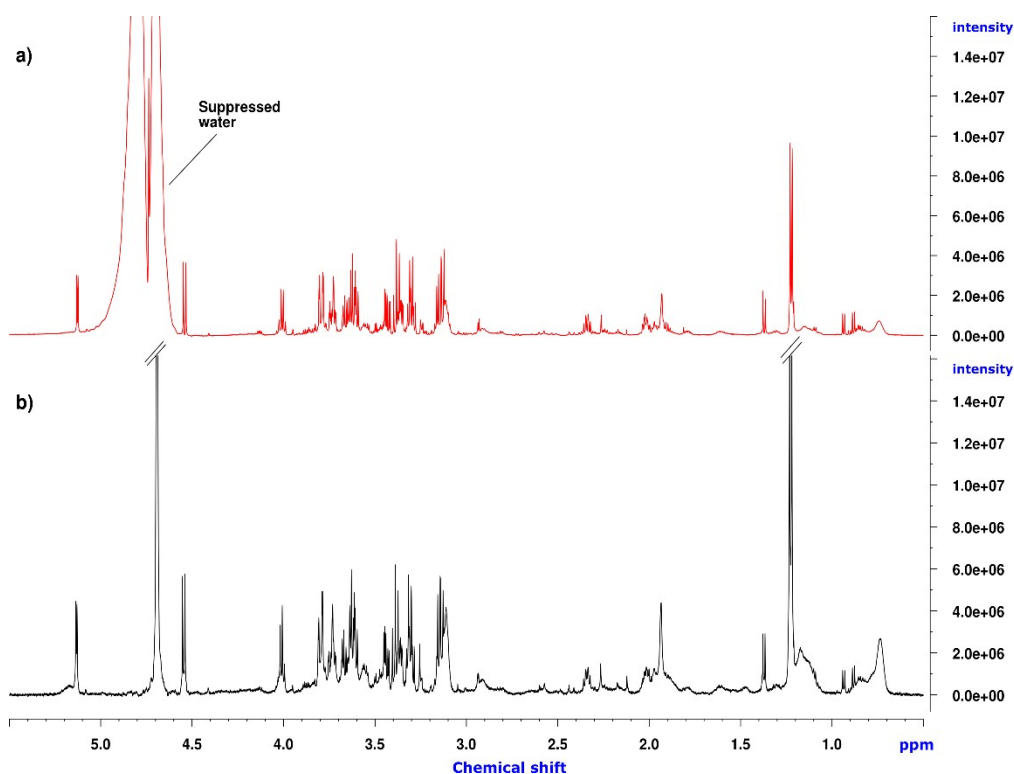


**Figure 2:** Effects of two different probes on solvent suppression using the same follicular fluid sample. 1D  $^1\text{H}$ -NMR spectra acquired at 600 MHz using a) a 5 mm conventional liquid state probe and b) a 4 mm HR-MAS probe. While the watt value was retained between probes for presaturation, different values were used for pulse length and power level for pulse in both probes due to probe design differences. In addition, depending on the differences in the sample requirements of the probes, 400  $\mu\text{L}$  of sample were used for the conventional liquid state probe, while only 25  $\mu\text{L}$  of sample were used for the HR-MAS probe. The difference in metabolite signal intensities in the same follicular fluid sample can be easily seen.

In HR-MAS technology, which allows working with very low sample quantities ( $\leq 40 \mu\text{L}$ ), the receiver coil of the HR-MAS probe head is slightly larger than the sample chamber of the probe, so the entire sample is placed in the coil active volume of the probe (34). This results in better  $B_0$  homogeneity and better water suppression. Also, when Figure 2 is examined, it is seen that the noise level in the spectrum

obtained with the conventional 5 mm diameter probe is slightly better than the HR-MAS probe. However, the intensity of the peaks in the spectrum obtained with the HR-MAS probe are higher. The signal-to-noise (S/N) ratio values of these two spectra in a spectral noise region of approximately 1000 Hz were calculated as 15.9 (Figure 2a) and 12.6 (Figure 2b), respectively. Although this depends on the sensitivity

characteristics of the probes studied (90° pulse in  $\mu\text{s}$ , power level in W, etc.), the detection limit of the HR-MAS technology is slightly better when compared to the conventional 5 mm diameter liquid state NMR probe under the most optimized conditions for the studied sample. It is possible to say that this situation is an advantage for samples with limited quantity, especially considering that a sample amount of approximately 25  $\mu\text{L}$  is used in the HR-MAS technique. However, it should be noted that sample recovery from the HR-MAS rotor is more difficult compared to other small diameter NMR tubes.

### Performance of NMR quantification methods

Quantification results of creatine concentrations in standard creatine solutions of different concentrations determined using DSS method and ERETIC2 are presented in Table 1. In both methods, creatine concentrations were calculated by means of methyl peaks using two different pulse sequences (cpmgpr1d and zg30). Also, the standard deviation ( $\pm$  SD), % recovery, and % relative standard deviation (RSD) values are provided for all results from the same sample and differently prepared samples at each concentration. Recovery was calculated with  $(\{\text{measured value} / \text{actual value}\} \times 100)$ , and the relative standard deviation was calculated with  $(\{\text{standard deviation} / \text{mean value}\} \times 100)$ . In Table 1,

when 5 repeated measurement results of the same samples were examined in both methods, the lowest recovery value was determined as 97.0% in the DSS method for the cpmgpr1d pulse sequence, while the lowest recovery value was determined as 108.0% for the zg30 pulse sequence. In ERETIC2, a 90.3% recovery value was calculated for cpmgpr1d pulse sequence, and the lowest recovery value for zg30 pulse sequence was determined as 102.0%. Likewise, when the results obtained with the DSS method and the ERETIC2 for 5 differently prepared samples were compared, the lowest recovery value for the cpmgpr1d pulse sequence in the DSS method was 98.3%, while this value was determined as 108.0% with the zg30 pulse. In the ERETIC2, the lowest recovery values for cpmgpr1d and zg30 pulse sequences were calculated as 94.3% and 102.0%, respectively. Besides, when the values for the same samples provided in Table 1 are examined, RSD values of 1.2% (for the cpmgpr1d) and 2.4% (for the zg30) or lower were achieved in the DSS method. While in the ERETIC2, RSD values of 2.2% (for the cpmgpr1d) and 1.7% (for the zg30) or lower were obtained. Considering the results obtained from differently prepared samples, the DSS method provided 2.0% (for the cpmgpr1d) and 3.1% (for the zg30) or lower RSD. On the other hand, the ERETIC2 provided RSD values of 5.2% (for the cpmgpr1d) and 5.7% (for the zg30) or lower for these samples.

**Table1:** Quantification results determined using the DSS method and ERETIC2 from standard creatine solutions (C.S) in different concentrations (mM).

Method	Sample type	Pulse program	C.S (mM)	Concentrations (mM)		
				Mean ( $\pm$ SD)	Recovery (%)	RSD (%)
DSS method	from the same sample	cpmgpr1d	10	9.79 ( $\pm$ 0.02)	97.9	0.2
			5	4.99 ( $\pm$ 0.06)	99.8	1.2
			3	2.91 ( $\pm$ 0.02)	97.0	0.7
			1	0.98 ( $\pm$ 0.01)	98.0	1.0
		zg30	10	10.80 ( $\pm$ 0.01)	108	0.1
			5	5.44 ( $\pm$ 0.06)	108.8	1.1
			3	3.42 ( $\pm$ 0.02)	114.0	0.6
			1	1.27 ( $\pm$ 0.03)	127.0	2.4
	from the differently prepared samples	cpmgpr1d	10	9.85 ( $\pm$ 0.13)	98.5	1.3
			5	4.92 ( $\pm$ 0.07)	98.4	1.4
			3	2.95 ( $\pm$ 0.03)	98.3	1.0
			1	1.01 ( $\pm$ 0.02)	101.0	2.0
		zg30	10	10.80 ( $\pm$ 0.01)	108	0.1
			5	5.44 ( $\pm$ 0.04)	108.8	0.7
			3	3.44 ( $\pm$ 0.03)	114.6	0.9
			1	1.28 ( $\pm$ 0.04)	128.0	3.1



ERETIC2	from the same sample	cpmgrp1d	10	9.51 ( $\pm$ 0.04)	95.1	0.4
			5	4.95 ( $\pm$ 0.11)	99.0	2.2
			3	2.71 ( $\pm$ 0.04)	90.3	1.5
			1	0.93 ( $\pm$ 0.02)	93.0	2.1
		zg30	10	10.20 ( $\pm$ 0.07)	102	0.7
			5	5.28 ( $\pm$ 0.06)	105.6	1.1
			3	3.12 ( $\pm$ 0.01)	104.0	0.3
			1	1.18 ( $\pm$ 0.02)	118.0	1.7
	from the different prepared samples	cpmgrp1d	10	9.43 ( $\pm$ 0.16)	94.3	1.7
			5	4.93 ( $\pm$ 0.05)	98.6	1.0
			3	2.90 ( $\pm$ 0.15)	96.6	5.2
			1	0.96 ( $\pm$ 0.03)	96.0	3.1
		zg30	10	10.02 (0.15)	102	1.5
			5	5.32 ( $\pm$ 0.07)	106.4	1.3
			3	3.11 ( $\pm$ 0.04)	103.6	1.3
			1	1.22 ( $\pm$ 0.07)	122.0	5.7

In a study using the PULCON methodology, Watanabe et al. compared the results obtained with the ERETIC2 and the internal standard method using an NMR spectrometer equipped with 5mm diameter conventional probe in the quantification of the isolated okadaic acid compound. When the results of different integral regions in the spectra obtained from the same samples using zg pulse sequence are examined, the maximum RSD values calculated for the internal standard method and the ERETIC2 were reported as 5.16% and 3.77%, respectively (20). Using the ERETIC2 as a fast and precise method in addition to the gravimetric method for the quantitative determination of low molecular weight molecules in natural isolates and reference substances, Frank et al. used an NMR spectrometer with the conventional 5 mm diameter multinuclear probe hardware. They determined the accuracy of the ERETIC2 with the quantification of different concentrations of benzoic acid (1.72, 6.14, and 16.21 mM) and L-tyrosine (2.73, 7.33, and 9.99 mM) using 3.12 mM caffeine solution as their standard solution. Recovery values calculated for benzoic acid were 98.8%, 99.6%, and 99.2%, while recovery values calculated for L-tyrosine were 100.6%, 100.7%, and 100.9% (35). In another study, Selegato et al. evaluated the accuracy of the global spectral deconvolution-based NMR quantification method developed for the quantification of bioactive molecules in microbial cultures with the classical internal standard method and the ERETIC2. In this study, they used an NMR spectrometer equipped with a triple resonance CryoProbe. The reference calibration spectrum required for the ERETIC2 was obtained from the standard

sucrose solution of 2 mM. In their study, the accuracy of the internal standard and ERETIC2 methodologies was determined by the quantification of standard benzyl benzoate solutions of different concentrations. The values obtained for 1 mM benzyl benzoate solution were reported as 0.96 mM for the classical internal standard method and 1.20 mM for the ERETIC2 (36).

In Table 1, it is clear that the quantification results obtained by using the HR-MAS probe exhibit lower RSD and better recovery compared to the literature provided above. This situation could be explained by the fact that the standard HR-MAS probes have higher radiofrequency (rf) field homogeneity compared to the conventional probes (34,37). Also, even if it was optimized for the experimental conditions, an HR-MAS probe properly placed into the NMR magnet can still have an inhomogeneous rf-field. This is a result of probe-independent factors such as the magnetic field induced by the non-spinning components of the NMR probe that are close to the sample, or the presence of temperature gradients within the sample caused by spinning and high radio frequency (38). However, rf-inhomogeneity will affect the internal standard method less than the quantification method based on an electronically generated reference signal (37). As a result, when Table 1 is examined, it is seen that DSS method provides a slightly lower RSD than ERETIC2 from the results obtained from both pulse programs. However, considering the possibility of internal standard substances to chemically interact with analyte molecules in the sample, we can conclude that the ERETIC2 is a more accurate approach for quantification.



Besides, it is an expected result that the accuracy of the results obtained from the same samples will be higher due to some errors that may occur during the preparation of different samples. Also, when the results obtained with both the DSS method and the ERETIC2 were examined, it was observed that the zg30 pulse sequence showed a shorter analysis time and consequently a faster quantification, but higher RSD and lower accuracy compared to the cpmgpr1d pulse sequence. The zg30 pulse sequence used in the quantitative NMR leads broad bands that complicate the integration of the signals in the NMR spectrum, and it decreases the signal-to-noise (S/N) ratio and increases the baseline distortions especially for low sample concentrations. Therefore, some signal resonances are overestimated in the zg30 pulse sequence (39). Additionally, suppressing the solvent resonance at very low

sample concentrations with the appropriate pulse sequence allows the use of maximum receiver gain to improve the signal-to-noise (S/N) ratio of the spectrum and thus increases the accuracy of the quantitation results (10).

### Metabolite concentrations calculated with ERETIC2

ERETIC2 has become a fast and reliable quantification method used in liquid-state NMR spectroscopy to determine the concentrations of target molecules in complex mixtures (35,40). The results obtained from this study showed that ERETIC2 method can be easily adapted to HR-MAS spectroscopy in determining metabolite concentrations of biological samples. Figure 3 shows the one-dimensional  $^1\text{H}$  HR-MAS NMR spectrum obtained from human follicular fluid sample.

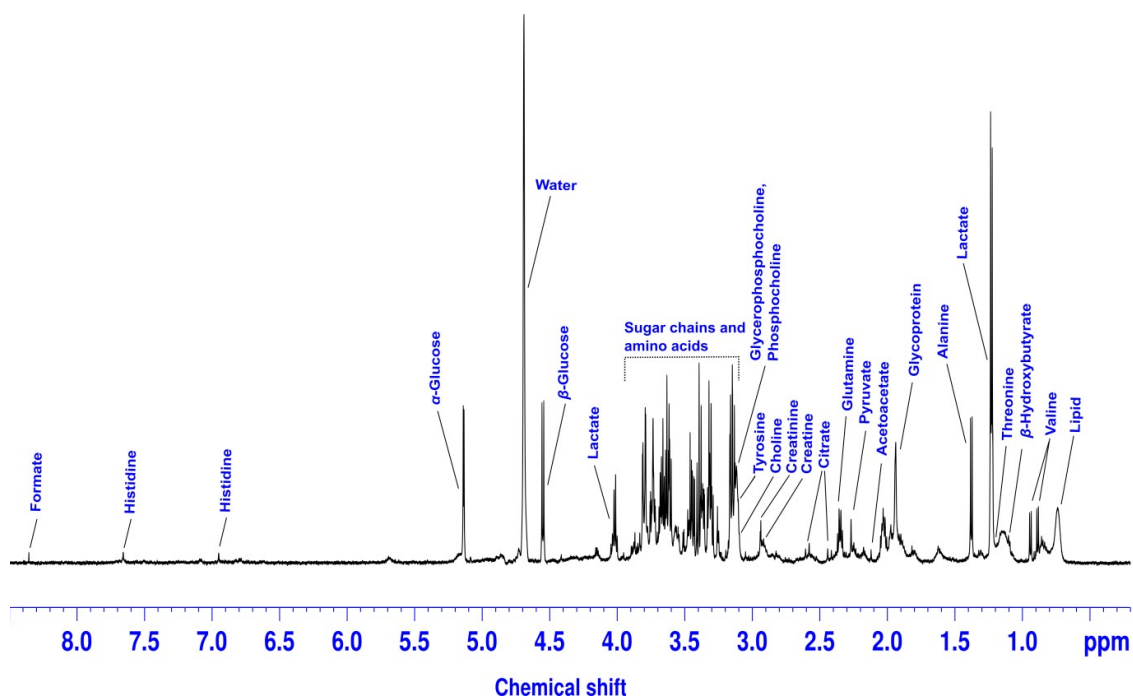


**Figure 3:** 600 MHz  $^1\text{H}$  HR-MAS CPMG (Carr-Purcell-Meiboom-Gill) NMR spectrum recorded at a spin rate of 4 KHz and 295 K of human follicular fluid.

When Figure 3 is examined, it is seen that the signals of some metabolites were quite good resolved in the NMR spectrum of the follicular fluid. Thus, the integration of these metabolite signals can be easily performed. The concentration values of selected metabolites (valine, lactate, alanine, acetoacetate, pyruvate, glutamine, citrate,  $\beta$ -glucose,  $\alpha$ -

glucose) calculated using ERETIC2 method from ten different follicular fluid samples (from healthy control group and group with endometriosis) are given in Table 2.  $^1\text{H}$  NMR experiments repeated three times with different samples obtained from each group. In Table 2, small standard deviation values obtained for the concentration results support the accuracy of

the method. Another method that can be used to evaluate the performance of ERETIC2 combined with HR-MAS spectroscopy in the quantification of follicular fluid metabolites may be to compare the results obtained in this study with those obtained from other methodologies.

However, while studies using NMR spectroscopy in the precise quantification of the metabolite composition of the human follicular fluid are limited in the literature, relative quantitation is currently the focus of many NMR-based metabolomics studies (26,41).

**Table 2.** The absolute concentration values of the various metabolites contained in follicular fluids determined using the ERETIC2 method.

Metabolite	Integrated area (ppm)	Multiplicity	Group	Concentration (mM)	
				Healthy control Mean $\pm$ SD	Endometriosis Mean $\pm$ SD
Valine	0.90-0.87	doublet	$\gamma$ CH <sub>3</sub>	0.23 $\pm$ 0.06	0.22 $\pm$ 0.08
Valine	0.95-0.91	doublet	$\gamma'$ CH <sub>3</sub>	0.17 $\pm$ 0.05	0.16 $\pm$ 0.05
Lactate	1.24-1.21	doublet	$\beta$ CH <sub>3</sub>	3.99 $\pm$ 1.60	5.90 $\pm$ 2.72
Alanine	1.39-1.35	doublet	$\beta$ CH <sub>3</sub>	0.52 $\pm$ 0.14	0.56 $\pm$ 0.16
Acetoacetate	2.13-2.10	singlet	$\gamma$ CH <sub>3</sub>	0.07 $\pm$ 0.07	0.06 $\pm$ 0.02
Pyruvate	2.28-2.25	singlet	$\beta$ CH <sub>3</sub>	0.28 $\pm$ 0.06	0.30 $\pm$ 0.06
Glutamine	2.37-2.31	multiplet	$\gamma$ CH <sub>2</sub>	0.87 $\pm$ 0.23	0.82 $\pm$ 0.30
Citrate	2.45-2.40	doublet	$\alpha$ , $\gamma$ CH	0.29 $\pm$ 0.12	0.29 $\pm$ 0.10
Citrate	2.61-2.56	doublet	$\alpha'$ , $\gamma'$ CH	0.34 $\pm$ 0.15	0.34 $\pm$ 0.11
Lactate	4.06-3.96	quartet	$\alpha$ CH	3.59 $\pm$ 1.38	5.19 $\pm$ 2.30
$\beta$ -glucose	4.57-4.50	doublet	C <sup>1</sup> H	1.64 $\pm$ 0.68	1.44 $\pm$ 0.97
$\alpha$ -glucose	5.17-5.09	doublet	C <sup>1</sup> H	2.29 $\pm$ 0.71	2.07 $\pm$ 1.20

In the early studies, the researchers used different methods other than the NMR to determine the concentrations of metabolites such as glucose and lactate in follicular fluid, which were predicted to be important for oocyte quality. In their studies, Leese and Lenton calculated the glucose concentration in follicular fluid as 3.29  $\pm$  0.09 mM and the lactate concentration as 6.12  $\pm$  0.17 mM where they used an autoanalyzer for glucose and fluorometric method for lactate. They also reported the average pyruvate concentration calculated for some samples as 0.26  $\pm$  0.008 mM (42). In another study, Gull et al. who investigated the glycolysis process in human ovarian follicles, determined the glucose and lactate concentrations in the follicular fluid using glucose analyzer and lactate spectrophotometric analyzer. They calculated the mean glucose and lactate concentrations in follicular fluid as 3.39  $\pm$  0.91 mM and 3.17  $\pm$  0.90 mM, respectively (43). Józsvik et al. reported the glucose concentration as 2.78 mM in their studies by determining the sugar and polyol concentrations in a human follicular fluid using high-performance liquid chromatography (HPLC) method (44). Gosden et al. is the first group to use <sup>1</sup>H NMR spectroscopy to examine the molecular composition of follicular fluid. However, in their studies, they detected low molecular weight metabolites such as acetate,

alanine, creatinine, glycine, D-3-hydroxybutyrate, lactate, and valine in the follicular fluid samples of some farm animals at concentrations exceeding 0.1 mM. In the quantitative determination of the molar concentrations of the metabolites, firstly, lactate concentrations were determined in each sample by an independent lactate dehydrogenase experiment. Next, these lactate values were used to determine metabolite concentrations by considering the NMR signals obtained from other metabolites (45). A detailed analysis of the metabolite composition of the human follicular fluid was first performed by Piñero-Sagredo et al. using a high-resolution liquid-state NMR spectrometer equipped with a 5 mm diameter triple CyroProbe. Although the concentrations of all metabolites determined in this study were not precisely calculated, a linear combination of reference NMR spectra obtained from solutions with known concentrations of both metabolites was used for glucose and lactate quantification. The glucose and lactate concentrations obtained by this method were reported as 2 mM and 5 mM, respectively (28). After Piñero-Sagredo and his group introduced a comprehensive metabolite profile of human follicular fluid into the literature, follicular fluid studies based on NMR spectroscopy focused on determining the relationship between follicular fluid metabolite composition and oocyte

development potential, embryo viability and etiology of diseases (46). Wallace et al. conducted  $^1\text{H-NMR}$  based metabolomics analyzes using liquid-state NMR spectroscopy in follicular fluids collected from in vitro fertilization (IVF) patients. The collected samples were analyzed considering the number of embryo cells and noncleaving oocytes to test the ability of the follicular fluid metabolite composition in the prediction of successful IVF result. In Wallace's study, the metabolite concentrations were determined using a different method (amino acid analyzer) and the glucose concentration in the follicular fluid of two groups was reported as  $3.25 \pm 1.24$  mM and  $2.33 \pm 0.57$  mM (25). In another study, Karaer et al. conducted metabolomics analyzes using an NMR spectrometer with a conventional 5 mm diameter probe equipment to determine whether the change in the metabolite composition of follicular fluids collected from ovarian endometriosis patients was identifiable. In Karaer's study, ERETIC2 was used for the  $^1\text{H}$  NMR-based quantitative analysis of metabolites in the women with ovarian endometriosis and healthy controls. The concentrations (mM) of different metabolites for each group were obtained as lactate ( $2.75 \pm 1.1$  and  $1.6 \pm 5.5$ ),  $\alpha$ -glucose ( $1.72 \pm 0.5$  and  $1.25 \pm 0.2$ ),  $\beta$ -glucose ( $1.25 \pm 0.2$  and  $0.83 \pm 0.3$ ), alanine ( $0.38 \pm 0.11$  and  $0.27 \pm 0.09$ ), pyruvate ( $0.19 \pm 0.04$  and  $0.14 \pm 0.03$ ) and valine ( $0.17 \pm 0.03$  and  $0.12 \pm 0.04$ ) (27). When the results presented in Table 2 are examined, it is seen that lactate, alanine and pyruvate concentration values from the patient group were calculated higher than the healthy control group, similar to the results obtained by Karaer et al. (27). On the other hand, in contrast to Karaer et al.,  $\alpha$ -glucose and  $\beta$ -glucose concentration values were higher in the control group compared to the patient group. Although the relationship between the ratio of glucose and lactate concentrations and the anaerobic metabolism in the hyperstimulated follicle is out the scope of this study, in literature different values related to the ratio between glucose and lactate have been reported. In some studies, this ratio is given approximately 1:2 (42,28) while in others it is given approximately 1:1 (43,27). When the results obtained from this study are examined, it is seen that the ratio between total glucose and lactate is approximately 1:1 for healthy controls and approximately 1:2 in the patient group. It has been shown that, there is a negative correlation between follicle size and

glucose concentration and a positive correlation between follicle size and lactate concentration (43). In this study, the glucose and lactate concentration values calculated from follicular fluid samples collected from follicles with a diameter of about 20 mm are compatible with the concentration values obtained from the follicles of the same size by Gull et al. (43).

## CONCLUSION

NMR spectroscopy has a very important place among quantification methods, as it provides a direct relationship between peak area and absolute concentration as well as providing valuable structural and diagnostic information within short analysis times. Recent advances in PULCON methodology have shown that analyte spectra used in quantitative NMR can be obtained completely without internal standard reference material. In this context, ERETIC2 can be easily applied in determining metabolite concentrations in intact biological fluids. Also, attention should be paid to the use of the same pulse sequence in the analysis of the known reference solution and the subsequent analyte solution, the effects of factors such as solvent and concentration on the acquisition parameters such as relaxation delay and pulse length, and the salt concentration contained in the sample when obtaining the reference spectrum for the ERETIC2 method. Although HR-MAS NMR spectroscopy is generally used in the analysis of heterogeneous sample systems, it can be an excellent alternative in the analysis of limited amounts of biological fluid samples and quantification of unknown species in these samples. Sample leakage that may occur in the rotor system is one of the most important factors that can lead to quantitation errors in HR-MAS studies of biological fluids. However, these errors can be prevented with care and attention to be shown during rotor assembly. Additionally, it should be noted that sample recovery in HRMAS studies is difficult. When the results obtained in this study and previous literature data obtained from other methodologies are compared, it is seen that the ERETIC2 method combined with HR-MAS NMR spectroscopy is reliable and accurate in determining follicular fluid metabolite concentrations.

## CONFLICT OF INTEREST

No potential conflict of interest was reported by the author.

**ACKNOWLEDGMENTS**

I wish to thank Reproductive Sciences & Advanced Bioinformatics Application & Research Centre, Inonu University for its technical support of this study.

**REFERENCES**

- Renault M, Shintu L, Piotta M, Caldarelli S. Slow-spinning low-sideband HR-MAS NMR spectroscopy: delicate analysis of biological samples. *Sci Rep*. 2013 Dec;3(1):3349. [<DOI>](#).
- Moestue S, Sitter B, Frost Bathen T, Tessem M-B, Susann Gribbestad I. HR MAS MR Spectroscopy in Metabolic Characterization of Cancer. *CTMC*. 2011 Jan 1;11(1):2–26. [<DOI>](#).
- Mazzei P, Piccolo A. HRMAS NMR spectroscopy applications in agriculture. *Chem Biol Technol Agric*. 2017 Dec;4(1):11. [<DOI>](#).
- Gogiasvili M, Nowacki J, Hergenröder R, Hengstler JG, Lambert J, Edlund K. HR-MAS NMR Based Quantitative Metabolomics in Breast Cancer. *Metabolites*. 2019 Jan 22;9(2):19. [<DOI>](#).
- Lindon JC, Beckonert OP, Holmes E, Nicholson JK. High-resolution magic angle spinning NMR spectroscopy: Application to biomedical studies. *Progress in Nuclear Magnetic Resonance Spectroscopy*. 2009 Aug;55(2):79–100. [<DOI>](#).
- Swanson MG, Zektzer AS, Tabatabai ZL, Simko J, Jarso S, Keshari KR, et al. Quantitative analysis of prostate metabolites using <sup>1</sup>H HR-MAS spectroscopy. *Magn Reson Med*. 2006 Jun;55(6):1257–64. [<DOI>](#).
- Tilgner M, Vater TS, Habel P, Cheng LL. High-Resolution Magic Angle Spinning (HRMAS) NMR Methods in Metabolomics. In: Gowda GAN, Raftery D, editors. *NMR-Based Metabolomics* [Internet]. New York, NY: Springer New York; 2019 [cited 2021 Dec 1]. p. 49–67. (Methods in Molecular Biology; vol. 2037). [<URL>](#).
- Bharti SK, Roy R. Quantitative <sup>1</sup>H NMR spectroscopy. *TrAC Trends in Analytical Chemistry*. 2012 May;35:5–26. [<DOI>](#).
- Zoelch N, Hock A, Heinzer-Schweizer S, Avdievitch N, Henning A. Accurate determination of brain metabolite concentrations using ERETIC as external reference. *NMR in Biomedicine*. 2017 Aug;30(8):e3731. [<DOI>](#).
- Barding GA, Salditos R, Larive CK. Quantitative NMR for bioanalysis and metabolomics. *Anal Bioanal Chem*. 2012 Sep;404(4):1165–79. [<DOI>](#).
- Cullen CH, Ray GJ, Szabo CM. A comparison of quantitative nuclear magnetic resonance methods: internal, external, and electronic referencing: Comparison of quantitative NMR methods. *Magn Reson Chem*. 2013 Sep. [<DOI>](#).
- Heinzer-Schweizer S, De Zanche N, Pavan M, Mens G, Sturzenegger U, Henning A, et al. In-vivo assessment of tissue metabolite levels using <sup>1</sup>H mrs and the electric reference to access in vivo concentrations (eretic) method: In-Vivo Assessment of Tissue Metabolite Levels Using Eretic. *NMR Biomed*. 2010 May;23(4):406–13. [<DOI>](#).
- Jung Y-S, Hyeon J-S, Hwang G-S. Software-assisted serum metabolite quantification using NMR. *Analytica Chimica Acta*. 2016 Aug;934:194–202. [<DOI>](#).
- Monakhova YB, Kohl-Himmelseher M, Kuballa T, Lachenmeier DW. Determination of the purity of pharmaceutical reference materials by <sup>1</sup>H NMR using the standardless PULCON methodology. *Journal of Pharmaceutical and Biomedical Analysis*. 2014 Nov;100:381–6. [<DOI>](#).
- Barantin L, Pape AL, Akoka S. A new method for absolute quantitation MRS metabolites. *Magn Reson Med*. 1997 Aug;38(2):179–82. [<DOI>](#).
- Albers MJ, Butler TN, Rahwa I, Bao N, Keshari KR, Swanson MG, et al. Evaluation of the ERETIC method as an improved quantitative reference for <sup>1</sup>H HR-MAS spectroscopy of prostate tissue. *Magn Reson Med*. 2009 Mar;61(3):525–32. [<DOI>](#).
- Akoka S, Barantin L, Trierweiler M. Concentration Measurement by Proton NMR Using the ERETIC Method. *Anal Chem*. 1999 Jul 1;71(13):2554–7. [<DOI>](#).
- Anonymous. TopSpin ERETIC 2 [Internet]. Bruker, Corp.; 2016 [cited 2021 Dec 1]. [<URL>](#).
- Farrant RD, Hollerton JC, Lynn SM, Provera S, Sidebottom PJ, Upton RJ. NMR quantification using an artificial signal. *Magn Reson Chem*. 2010 Oct;48(10):753–62. [<DOI>](#).
- Watanabe R, Sugai C, Yamazaki T, Matsushima R, Uchida H, Matsumiya M, et al. Quantitative Nuclear Magnetic Resonance Spectroscopy Based on PULCON Methodology: Application to Quantification of Invaluable Marine Toxin, Okadaic Acid. *Toxins*. 2016 Oct 13;8(10):294. [<DOI>](#).
- Bianchi L, Gagliardi A, Campanella G, Landi C, Capaldo A, Carleo A, et al. A methodological and functional proteomic approach of human follicular fluid en route for oocyte quality evaluation. *Journal of Proteomics*. 2013 Sep;90:61–76. [<DOI>](#).
- O’Gorman A, Wallace M, Cottell E, Gibney MJ, McAuliffe FM, Wingfield M, et al. Metabolic profiling of human follicular fluid identifies potential biomarkers of oocyte developmental competence. *Reproduction*. 2013 Oct;146(4):389–95. [<DOI>](#).

23. Revelli A, Piane LD, Casano S, Molinari E, Massobrio M, Rinaudo P. Follicular fluid content and oocyte quality: from single biochemical markers to metabolomics. *Reprod Biol Endocrinol*. 2009 Dec;7(1):40. [<DOI>](#).
24. Bouet P-E, Chao de la Barca JM, El Hachem H, Descamps P, Legendre G, Reynier P, et al. Metabolomics shows no impairment of the microenvironment of the cumulus-oocyte complex in women with isolated endometriosis. *Reproductive BioMedicine Online*. 2019 Dec;39(6):885-92. [<DOI>](#).
25. Wallace M, Cottell E, Gibney MJ, McAuliffe FM, Wingfield M, Brennan L. An investigation into the relationship between the metabolic profile of follicular fluid, oocyte developmental potential, and implantation outcome. *Fertility and Sterility*. 2012 May;97(5):1078-1084.e8. [<DOI>](#).
26. Castiglione Morelli MA, Iuliano A, Schettini SCA, Petrucci D, Ferri A, Colucci P, et al. NMR metabolic profiling of follicular fluid for investigating the different causes of female infertility: a pilot study. *Metabolomics*. 2019 Feb;15(2):19. [<DOI>](#).
27. Karaer A, Tuncay G, Mumcu A, Dogan B. Metabolomics analysis of follicular fluid in women with ovarian endometriosis undergoing in vitro fertilization. *Systems Biology in Reproductive Medicine*. 2019 Jan 2;65(1):39-47. [<DOI>](#).
28. Piñero-Sagredo E, Nunes S, de los Santos MJ, Celda B, Esteve V. NMR metabolic profile of human follicular fluid. *NMR Biomed*. 2010 Mar 24;23(5):485-95. [<DOI>](#).
29. Fan TW-M. Metabolite profiling by one- and two-dimensional NMR analysis of complex mixtures. *Progress in Nuclear Magnetic Resonance Spectroscopy*. 1996 Jan;28(2):161-219. [<DOI>](#).
30. Kruk J, Doscocz M, Jodłowska E, Zacharzewska A, Łakomiec J, Czaja K, et al. NMR Techniques in Metabolomic Studies: A Quick Overview on Examples of Utilization. *Appl Magn Reson*. 2017 Jan;48(1):1-21. [<DOI>](#).
31. Mumcu A, Karaer A, Dogan B, Tuncay G. Metabolomics analysis of seminal plasma in patients with idiopathic Oligoasthenoteratozoospermia using high-resolution NMR spectroscopy. *Andrologia*. 2020 Mar;8(2):450-6. [<DOI>](#).
32. Juchem C, de Graaf RA. B 0 magnetic field homogeneity and shimming for in vivo magnetic resonance spectroscopy. *Analytical Biochemistry*. 2017 Jul;529:17-29. [<DOI>](#).
33. Cohn BR, Joe BN, Zhao S, Kornak J, Zhang VY, Iman R, et al. Quantitative metabolic profiles of 2nd and 3rd trimester human amniotic fluid using 1H HR-MAS spectroscopy. *Magn Reson Mater Phys*. 2009 Dec;22(6):343-52. [<DOI>](#).
34. Ziarelli F, Peng L, Zhang C-C, Viel S. High resolution magic angle spinning NMR to investigate ligand-receptor binding events for mass-limited samples in liquids. *Journal of Pharmaceutical and Biomedical Analysis*. 2012 Feb;59:13-7. [<DOI>](#).
35. Frank O, Kreissl JK, Daschner A, Hofmann T. Accurate Determination of Reference Materials and Natural Isolates by Means of Quantitative 1 H NMR Spectroscopy. *J Agric Food Chem*. 2014 Mar 26;62(12):2506-15. [<DOI>](#).
36. Selegato DM, Freire RT, Pilon AC, Biasetto CR, de Oliveira HC, de Abreu LM, et al. Improvement of bioactive metabolite production in microbial cultures-A systems approach by OSMAC and deconvolution-based 1 HNMR quantification. *Magn Reson Chem*. 2019 Aug;57(8):458-71. [<DOI>](#).
37. Sitter B, Bathen TF, Singstad TE, Fjøsne HE, Lundgren S, Halgunset J, et al. Quantification of metabolites in breast cancer patients with different clinical prognosis using HR MAS MR spectroscopy: Eretic Quantification in Breast Cancer Tissue. *NMR Biomed*. 2010 May;23(4):424-31. [<DOI>](#).
38. Wong A, Lucas-Torres C. CHAPTER 5. High-resolution Magic-angle Spinning (HR-MAS) NMR Spectroscopy. In: Keun HC, editor. *New Developments in NMR* [Internet]. Cambridge: Royal Society of Chemistry; 2018 [cited 2021 Dec 1]. p. 133-50. [<URL>](#).
39. Bertelli D, Brighenti V, Marchetti L, Reik A, Pellati F. Nuclear magnetic resonance and high-performance liquid chromatography techniques for the characterization of bioactive compounds from *Humulus lupulus* L. (hop). *Anal Bioanal Chem*. 2018 Jun;410(15):3521-31. [<DOI>](#).
40. Paniagua-Vega D, Cavazos-Rocha N, Huerta-Heredia AA, Parra-Naranjo A, Rivas-Galindo VM, Waksman N, et al. A validated NMR method for the quantitative determination of rebaudioside A in commercial sweeteners. *Journal of Food Composition and Analysis*. 2019 Jun;79:134-42. [<DOI>](#).
41. Marianna S, Alessia P, Susan C, Francesca C, Angela S, Francesca C, et al. Metabolomic profiling and biochemical evaluation of the follicular fluid of endometriosis patients. *Mol BioSyst*. 2017;13(6):1213-22. [<DOI>](#).
42. Leese HJ, Lenton EA. Glucose and lactate in human follicular fluid: concentrations and interrelationships. *Human Reproduction*. 1990 Nov;5(8):915-9. [<DOI>](#).
43. Gull I, Geva E, Lerner-Geva L, Lessing JB, Wolman I, Amit A. Anaerobic glycolysis. *European*

Journal of Obstetrics & Gynecology and Reproductive Biology. 1999 Aug;85(2):225-8. [<DOI>](#).

44. Jozwik M, Jozwik M, Teng C, Battaglia FC. Concentrations of monosaccharides and their amino and alcohol derivatives in human preovulatory follicular fluid. Molecular Human Reproduction. 2007 Nov 1;13(11):791-6. [<DOI>](#).

45. Gosden RG, Sadler IH, Reed D, Hunter RHF. Characterization of ovarian follicular fluids of sheep,

pigs and cows using proton nuclear magnetic resonance spectroscopy. Experientia. 1990 Oct;46(10):1012-5. [<DOI>](#).

46. Baskind NE, McRae C, Sharma V, Fisher J. Understanding subfertility at a molecular level in the female through the application of nuclear magnetic resonance (NMR) spectroscopy. Human Reproduction Update. 2011 Mar 1;17(2):228-41. [<DOI>](#).



**Supporting Information**

**A simple and feasible method for the quantification of metabolites in the human follicular fluid using  $^1\text{H}$  HR-MAS NMR spectroscopy**

**Akın MUMCU<sup>1,2\*</sup>**

<sup>1</sup>Laboratory of NMR, Scientific and Technological Research Centre, Inonu University, Malatya, Turkey

<sup>2</sup>Reproductive Sciences & Advanced Bioinformatics Application & Research Centre, Inonu University, Malatya, Turkey

**Table S1:** Concentration values obtained as a result of two different methods and 5 different measurements for same standard creatine solutions at different concentrations. Concentrations of creatine in solutions were calculated from the 9 proton singlet signals of DSS in the range of 0.02 to - 0.17 ppm and the 3 proton methyl signal of creatine in the range of 3.05 - 2.9 ppm using equation 1 and 2.

Method	Std creatine solutions (mM)	Concentration results obtained using two different pulse programs (mM)									
		cpmgrp1d					zg30				
		Expt. 1	Expt. 2	Expt. 3	Expt. 4	Expt. 5	Expt. 1	Expt. 2	Expt. 3	Expt. 4	Expt. 5
DSS method	10	9.80	9.80	9.78	9.77	9.81	10.80	10.81	10.80	10.82	10.79
	5	4.97	5.08	5.03	4.96	4.94	5.47	5.39	5.48	5.37	5.50
	3	2.91	2.89	2.90	2.90	2.95	3.40	3.42	3.44	3.42	3.44
	1	0.98	0.99	0.98	0.97	0.98	1.25	1.28	1.27	1.24	1.31
ERETIC 2	10	9.57	9.53	9.50	9.45	9.51	10.31	10.22	10.18	10.13	10.18
	5	4.98	4.97	5.10	4.86	4.82	5.29	5.27	5.36	5.20	5.29
	3	2.71	2.66	2.66	2.76	2.73	3.12	3.11	3.13	3.12	3.12
	1	0.97	0.94	0.92	0.91	0.92	1.14	1.20	1.18	1.17	1.19

**Table S2:** Concentration values calculated using two different methods as a result of NMR measurements obtained from 5 different samples prepared from each standard creatine solution at different concentrations. In concentration calculations, 9 proton singlet signals of DSS in the range of 0.02 to - 0.17 ppm and 3 proton methyl signal of creatine in the range of 3.05 - 2.9 ppm were used.

Method	Std creatine solutions (mM)	Concentration results obtained using two different pulse programs (mM)									
		cpmgrp1d					zg30				
		Expt. 1	Expt. 2	Expt. 3	Expt. 4	Expt. 5	Expt. 1	Expt. 2	Expt. 3	Expt. 4	Expt. 5
DSS method	10	9.80	9.97	9.99	9.79	9.69	10.80	10.79	10.81	10.81	10.80
	5	4.97	4.81	4.94	4.89	4.98	5.39	5.42	5.44	5.51	5.46
	3	2.90	2.94	2.96	2.97	2.99	3.47	3.40	3.46	3.43	3.45
	1	0.98	1.02	1.01	1.02	1.03	1.25	1.30	1.30	1.32	1.23
ERETIC 2	10	9.57	9.51	9.44	9.15	9.47	10.18	9.94	10.13	9.80	10.04
	5	4.98	4.91	4.93	4.97	4.86	5.27	5.41	5.29	5.39	5.26
	3	2.76	2.73	3.08	2.96	2.98	3.04	3.12	3.12	3.14	3.12
	1	0.92	1.00	0.95	0.97	0.97	1.14	1.32	1.23	1.24	1.19

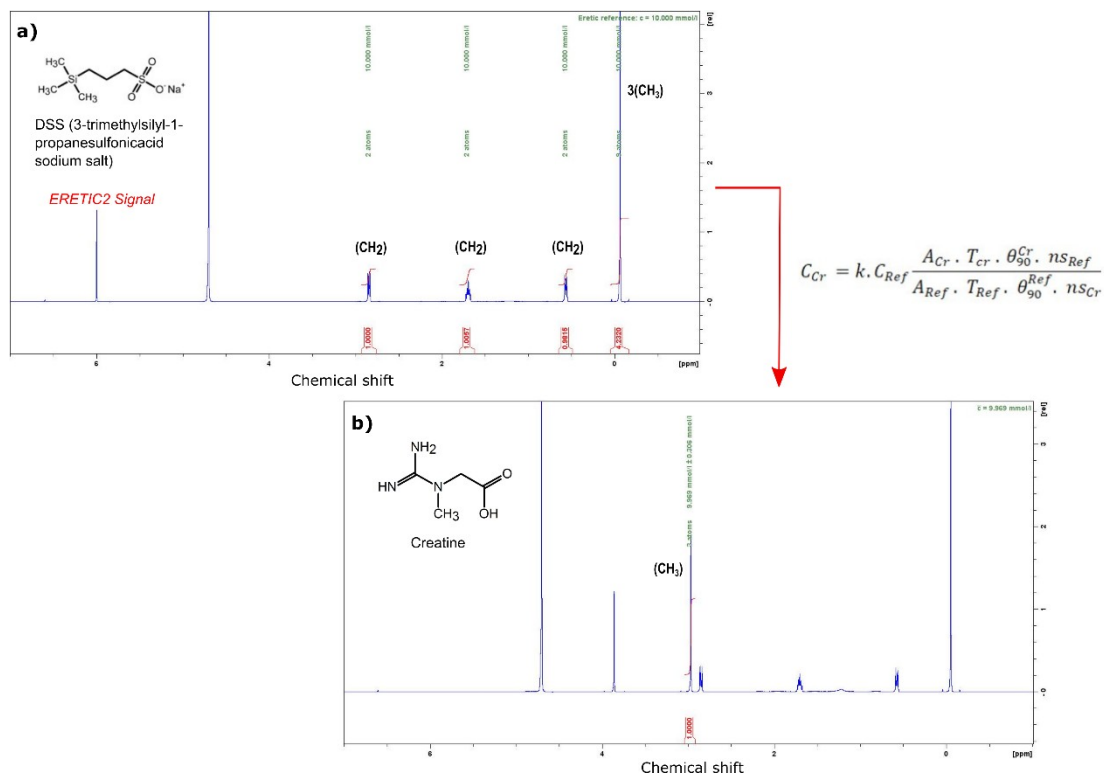


**Figure S1:** Quantification procedure used for the ERETIC2 a) one dimensional  $^1\text{H}$  HR-MAS NMR spectrum of a 10 mM DSS solution (calibration step where the ERETIC2 signal is generated using DSS sample). To determine the  $90^\circ$  pulse ( $\theta_{90} = 5.75 \mu\text{sec}$ ), the command *pulsecal* was used, where relaxation delay was 10 s; number of experiments was 25; and the pulse calibration was performed in 0.5  $\mu\text{sec}$  interval within 2  $\mu\text{sec}$ . b)  $^1\text{H}$  HR-MAS NMR spectrum of 10 mM creatine solution containing internal standard (quantification step in which the concentration of standard creatine solutions in different concentrations is determined). The acquisition parameters given above were used to determine the  $90^\circ$  pulse ( $\theta_{90} = 6.0 \mu\text{sec}$ ). Besides, The FIDs were processed by multiplying with 0.3 Hz line broadening parameter. NMR spectra were phase-corrected manually and the "absn" function was used for the baseline correction.

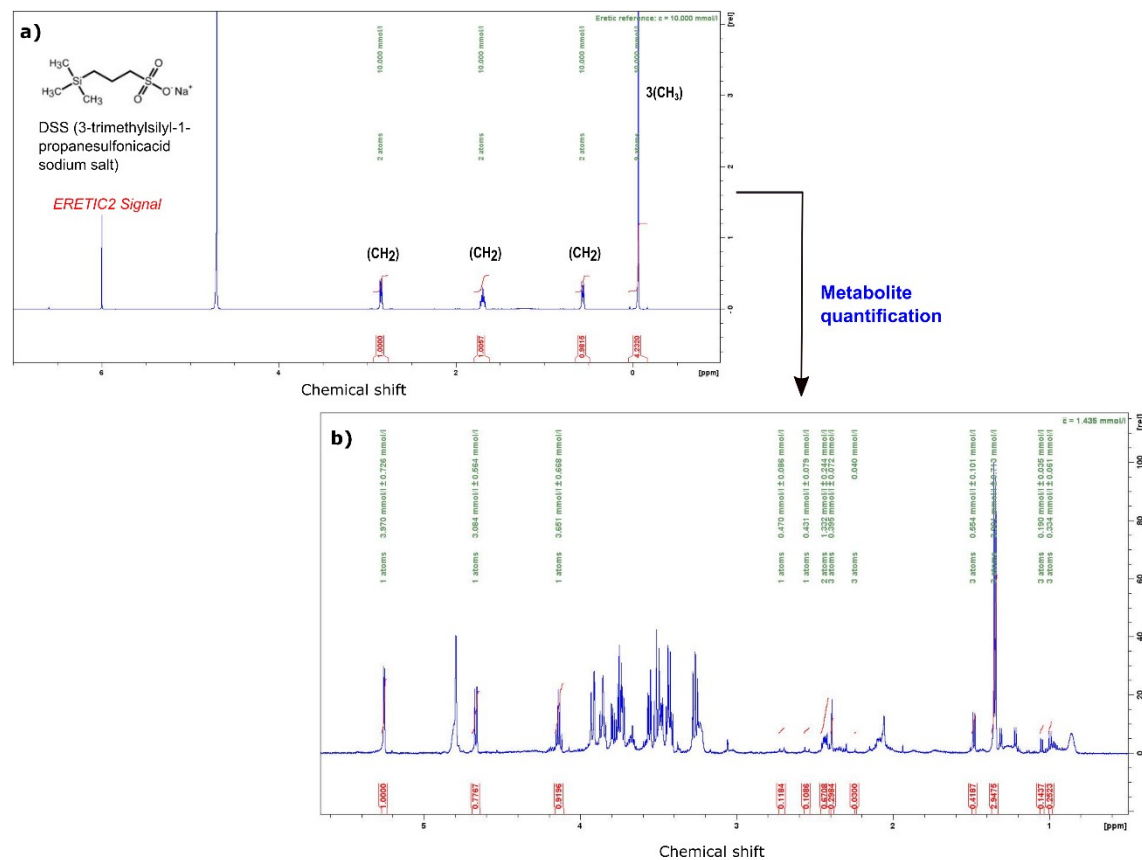


**Figure S2:** Determination of follicular fluid metabolite concentrations (mM) using the ERETIC2 a) one dimensional <sup>1</sup>H HR-MAS NMR spectrum of a 10 mM DSS solution (calibration step where the ERETIC2 signal is generated using DSS sample). b) representative <sup>1</sup>H HR-MAS NMR spectrum of the follicular fluid sample (the relevant metabolite concentrations were determined by means of equation number 2).







## Synthesis of Geranyloxy coumarin Derivatives under Mild Conditions Using $\text{Cs}_2\text{CO}_3$

SuMi Hwang<sup>1</sup>  and EonJoo Roh<sup>2\*</sup>  

<sup>1</sup>Sangji University, Department of Clinical Pathology, Won-ju 26339, Republic of Korea; zzz0722@hanmail.net (S.M.H)

<sup>2</sup>Changwon National University, Interdisciplinary Program in Biotechnology, Graduate School, Changwon 51140, Republic of Korea; medlife99@gmail.com (E.J.R)

**Abstract:** In this study, the synthesis of various geranyloxy coumarin derivatives from hydroxy coumarin was obtained in good yield under mild conditions using  $\text{Cs}_2\text{CO}_3$ . In the synthesis of geranyloxy coumarin derivatives, when 4-hydroxy coumarin reacts with geranyl bromide under mild conditions due to tautomeric keto-enol forms, 4-geranyloxy coumarin (3a), C-alkylated coumarin (3aa) and structure 3ab formed by hydrolysis and decarboxylation from 3aa were formed products. In addition, the alkylation reaction of 3-OH, 5-OH, 6-OH, 7-OH, and 8-OH coumarin except 4-OH group produced a high yield.

**Keywords:** Geranyloxy coumarin derivatives; 4-hydroxy coumarin; tautomeric keto-enol forms; coumarin compounds; geranyl bromide.

**Submitted:** September 18, 2021. **Accepted:** November 23, 2021.

**Cite this:** Hwang S, Roh E. Synthesis of Geranyloxy coumarin Derivatives under Mild Conditions Using  $\text{Cs}_2\text{CO}_3$ . JOTCSA. 2022;9(1):57-66.

DOI: <https://doi.org/10.18596/jotcsa.996363>.

\*Corresponding author. E-mail: [medlife99@gmail.com](mailto:medlife99@gmail.com), [no670@changwon.ac.kr](mailto:no670@changwon.ac.kr). Tel.: +82-10-7247-9996.

### INTRODUCTION

Coumarin and its derivatives are widely used in the synthesis of bioactive molecules (1). The derivatives also show a broad spectrum of beneficial effects, such as anti-inflammatory (2-6), anti-HIV (7-9), anticancer (10-15), antimicrobial (16-18), antitumor (19-23), anti-platelet (24), COX inhibitors (25), antioxidant (26-33), and antibacterial (34,35) activities.

Among them, hydroxylated coumarin secondary metabolites are essential in the synthesis of various derivatives, such as geranyloxy coumarins, with outstanding bioactivities. Well known naturally occurred geranyloxy coumarins are 7-geranyloxy coumarin (auraptene) isolated from *Poncirus trifoliata Rafinesque* and 5-geranyloxy-7-methoxy coumarin, bergamottin (geranyloxy psoralen) isolated from *Citrus*

*aurantifolia* (36).

Coumarin secondary metabolites with hydroxy group are critical in the synthesis of various derivatives with outstanding bioactivity. 4-Hydroxy coumarin and the synthesis of its derivatives first attracted the attention of Shah V.R. et al. in 1960 (36) and 4-hydroxy coumarin has since been used for producing a variety of coumarin derivatives based on its keto-enol tautomeric properties (37). The alkylation of the coumarin without the 4-OH group has also been investigated as a general method of synthesis. The alkylation reaction of the hydroxy coumarins has been investigated as a general method of synthesis of geranyloxy coumarins but, on the best of our view, the reaction strongly depended on the position of the hydroxy group, base additive, and reaction conditions. Interestingly, 4-hydroxy coumarin has since been used for producing a variety of O-4 and C-3 coumarin derivatives based on its keto-enol

tautomeric properties (38).

In this study, the reaction between hydroxycoumarins (1) and geranyl bromide (2) was studied in the synthesis of geranyloxy coumarin derivatives (3), using both weak and strong basic additives such as  $K_2CO_3$ ,  $Cs_2CO_3$ , and  $Ag_2CO_3$ , respectively. The C-3 and O-4 alkylation of the 4-hydroxycoumarin under mild optimized reaction condition has also been investigated.

## EXPERIMENTAL

### General Experimental Procedures

The silica gel 60 (230-400 mesh ASTM, 0.040-0.063 mm) for open chromatography and GF<sub>254</sub> for TLC were purchased from Merck Ltd. (Darmstadt, Germany). All solvents and chemicals used in this study were of analytical grade. For the hydroxycoumarin derivatives with a different substituent (4-hydroxycoumarin, 4-hydroxy-3-nitrocoumarin, 3-hydroxycoumarin, 6-hydroxycoumarin, 7-hydroxycoumarin, 3-phenylumbelliferone, 3-chloro-7-hydroxy-4-methylcoumarin and 6-chloro-7-hydroxy-4-methylcoumarin), the commercially available, 97%–98% pure TCI (Japan) and Alfa Aesar (USA) products were used. The established methods of synthesis were used to obtain 4-methyl-7-hydroxycoumarin (39,41), 6-hydroxy-4-methylcoumarin (39,41), 7-hydroxy-4-trifluoromethylcoumarin (39,41) and 4-methyl-6,7-dihydroxycoumarin (39,41). The alkenyl chain used in the synthesis of geranyloxy coumarin derivatives was 95% geranyl bromide (Aldrich, USA). For the base, NaOH,  $K_2CO_3$ ,  $Cs_2CO_3$ ,  $Ag_2CO_3$  and triethylamine ( $Et_3N$ ) were used, whereas the solvents used in this study were ethyl acetate (EtOAc), acetonitrile, n-hexane, dichloromethane (DCM), ethanol (EtOH), and acetone. Nuclear magnetic resonance spectrometer (NMR spectrometer; BRUKER AVANCE 400 MHz, BRUKER, Germany) was used for analysis.  $CDCl_3$  containing tetramethylsilane (TMS), which is an internal standard, was used as analytical solvent. Chemical shifts ( $\delta$ ) are given in parts per million (ppm), and coupling constants (J) are in hertz (Hz). Residual central signals of  $CDCl_3$  were recorded as follows:  $\delta$  H = 7.26,  $\delta$  C = 77.00. Infrared spectroscopy was performed, in the form of KBr pellets, on FT/IR-4200 (JASCO, Japan) spectrophotometer, to confirm the functional groups in the compound. High-resolution mass spectra were recorded on an SCIEX (Qtrap 3200) liquid-chromatography-mass spectrometer (USA). In addition, the melting point was measured without calibrating the temperature. A thermometer was mounted under a paraffin oil container, and the open glass capillary method was used.

### Common synthesis method of geranyloxy coumarin derivative

To a stirred mixture of hydroxycoumarin 1a (1.0 mmol) and powdered cesium carbonate (1.1 mmol) in acetonitrile (30 mL), geranyl bromide with 95% purity (1.2 mmol) was added, and the stirring was continued at RT for 3 hours. The reaction progress was monitored using TLC. When the reaction finished the solvent was removed under reduced pressure, then DCM (20 mL) was added to the mixture which was filtered off. After the evaporation of the solvent, crude products were purified by column chromatography on silica gel eluted with the mixture of n-hexane:DCM (1:1, v/v) to obtain pure geranyloxy coumarins (E)-4-(3,7-dimethylocta-2,6-dienyloxy)-2Hchromen-2-one (3a), 3,3-bis((E)-3,7-dimethylocta-2,6-dien-1-yl)chromane-2,4-dione (3aa), and (E)-2-((E)-3,7-dimethylocta-2,6-dien-1-yl)-1-(2-hydroxyphenyl)-5,9-dimethyldeca-4,8-dien-1-one (3ab).

### Characterization of (3a) (44)

White powder, Yield: 18%; m.p. 47–48 °C; **IR** (KBr,  $cm^{-1}$ ):  $\nu$  2923 (Aliphatic C-H), 1718 (C=O), 1620, 1371, 1235 (C-O), 1182 (C-O), 1104 (C-O), 923, 817, 764, 751, 500; **<sup>1</sup>H-NMR** (400 MHz,  $CDCl_3$ ):  $\delta$  1.62 (s, 3H,  $CH_3$ ), 1.69 (s, 3H,  $CH_3$ ), 1.77 (s, 3H,  $CH_3$ ), 2.08–2.18 (m, 4H,  $-CH_2CH_2-$ ), 4.71 (d,  $J$  = 6.7 Hz, 2H,  $-CH_2-$ ), 5.08–5.12 (m, 1H, =CH), 5.51 (t,  $J$  = 6.7 Hz, 1H, =CH), 5.69 (s, 1H, H-3), 7.25–7.33 (m, 2H, H-6 and H-8), 7.53–7.57 (m, 1H, H-7), 7.84 (dd,  $J$  = 2.2 Hz, 5.8 Hz, 1H, H-5) ppm; **<sup>13</sup>C-NMR** (100 MHz,  $CDCl_3$ ):  $\delta$  16.82 ( $CH_3$ ), 17.75 ( $CH_3$ ), 25.70 ( $CH_3$ ), 26.19 (CH), 39.50 (CH), 66.27 (CH), 90.64 (CH), 115.92 (C), 116.75 (CH), 117.06 (CH), 123.19 (CH), 123.46 (CH), 123.83 (CH), 132.13 (CH), 132.31 (C), 143.74 (C), 153.35 (C), 163.15 (C), 165.61 (C) ppm; **MS (EIMS)**:  $m/z$  298  $[M]^+$ ; Anal. Calcd for  $C_{19}H_{22}O_3$ : C, 76.48; H, 7.43; Found: C, 76.49; H, 7.40.

### Characterization of (3aa) (43)

Colorless liquid, Yield: 11%; **IR** (KBr,  $cm^{-1}$ ):  $\nu$  2966 (Aliphatic C-H), 2917 (Aliphatic C-H), 2854 (Aliphatic C-H), 1772 (C=O), 1689 (C=O), 1611, 1461, 1288 (C-O), 1142, 755; **<sup>1</sup>H-NMR** (400 MHz,  $CDCl_3$ ):  $\delta$  1.47 (s, 6H, 2 $CH_3$ ), 1.55 (s, 6H, 2 $CH_3$ ), 1.59 (s, 6H, 2 $CH_3$ ), 1.79 (s, 8H, 2( $-CH_2CH_2-$ )), 2.70–2.80 (m, 2H,  $-CH_2-$ ), 2.82–2.89 (m, 2H,  $-CH_2-$ ), 4.86–4.95 (m, 4H, 4 (=CH)), 7.15 (dd,  $J$  = 2.5 Hz, 8.0 Hz, 1H, H-8), 7.21–7.25 (m, 1H, H-5), 7.58–7.63 (m, 1H, H-7), 7.91 (dd,  $J$  = 2.5 Hz, 8.0 Hz, 1H, H-5) ppm; **<sup>13</sup>C-NMR** (100 MHz,  $CDCl_3$ ):  $\delta$  16.21 ( $CH_3$ ), 17.52 ( $CH_3$ ), 25.49 ( $CH_3$ ), 26.33 (CH), 37.62 (CH), 39.65 (CH), 62.24 (C), 116.89 (CH), 117.49 (C), 119.53 (CH), 123.78 (CH), 124.66 (CH), 126.55 (CH), 131.32 (C), 136.82 (C), 140.59 (C), 154.89 (C), 170.56 (C), 194.66 (C) ppm; **MS (EIMS)**:  $m/z$  434  $[M]^+$ ; Anal. Calcd for  $C_{29}H_{38}O_3$ : C, 80.14; H, 8.81; Found: C, 80.09; H, 8.76.

*Synthesis method of (3ab)*

To a stirred mixture of 3aa (2.3 mmol) and powdered cesium carbonate (2.5 mmol) in acetonitrile (30 mL), distilled water (2.6 mmol/6mmol) was added, and the stirring was continued at RT for 9 hours. The reaction progress was monitored using TLC. When the reaction finished the solvent was removed under reduced pressure, then DCM (20 mL) was added to the mixture which was filtered up. After evaporation of the solvent crude products were filtered by column chromatography on silica gel eluted with the mixture of n-hexane:DCM (3:1, v/v) to obtain pure 3ab.

*Characterization of (3ab)*

Colorless liquid, Yield : 35%; IR (KBr,  $\text{cm}^{-1}$ ):  $\nu$  1712 ( $-\text{C}=\text{O}$ );  $^1\text{H-NMR}$  (400MHz,  $\text{CDCl}_3$ ):  $\delta$  1.54 (s, 6H, 2CH<sub>3</sub>), 1.58 (s, 6H, 2CH<sub>3</sub>), 1.62 (s, 6H, 2CH<sub>3</sub>), 1.84–1.98 (m, 8H, 2(-CH<sub>2</sub>CH<sub>2</sub>-)), 2.25–2.32 (m, 2H, -CH<sub>2</sub>-), 2.41–2.48 (m, 2H, -CH<sub>2</sub>-), 3.47–3.54 (m, 1H, -C-H), 4.98–5.03 (m, 2H, 2(=C-H)), 5.06–5.11(m, 2H, 2(=C-H)), 6.86–6.90 (m, 1H), 6.95–6.98 (m, 1H), 7.42–7.46 (m, 1H), 7.76–7.79 (dd,  $J = 1.8$  Hz, 8.2 Hz, 1H), 12.66 (s, 1H, OH, D<sub>2</sub>O exch.) ppm;  $^{13}\text{C-NMR}$  (100MHz,  $\text{CDCl}_3$ ):  $\delta$  16.10 (CH<sub>3</sub>), 17.67 (CH<sub>3</sub>), 25.65 (CH<sub>3</sub>), 26.54 (CH<sub>2</sub>), 30.60 (CH<sub>2</sub>), 39.74 (CH<sub>2</sub>), 46.39 (CH), 118.56 (CH), 118.68 (CH), 119.65 (C), 121.10 (CH), 124.11 (CH), 130.24 (CH), 131.45 (C), 136.20 (CH), 137.59 (C), 162.93 (C), 210.28 ( $-\text{C}=\text{O}$ ) ppm; MS (EIMS):  $m/z$  408 [M]<sup>+</sup>; Anal. Calcd for C<sub>28</sub>H<sub>40</sub>O<sub>2</sub>: C, 82.30; H, 9.87, Found: C, 82.27; H, 8.88.

*Common synthesis method of geranyloxycoumarin derivatives*

To a stirred mixture of hydroxycoumarin 1b-1l (1.0 mmol) and powdered cesium carbonate (1.1 mmol) in acetonitrile (30 mL), 95% geranyl bromide (1.2 mmol) was added, and the stirring was continued at RT for 2.5-34 hours. The reaction progress was monitored using TLC. When the reaction finished the solvent was removed under reduced pressure, then DCM (20 mL) was added to the mixture which was filtered up. After evaporation of the solvent crude products were filtered by column chromatography on silica gel eluted with the mixture of n-hexane:DCM (1:1, v/v) to obtain pure geranyloxycoumarin 3c-3l.

*Characterization of (3c)*

White solid, Yield: 90%; m.p. 62–63 °C; IR (KBr,  $\text{cm}^{-1}$ ):  $\nu$  3077 (Aromatic C-H), 3030 (Aromatic C-H), 2974 (Aliphatic C-H), 2914 (Aliphatic C-H), 2894 (Aliphatic C-H), 1730 (Carbonyl (ester  $-\text{C}=\text{O}$ )), 1609 (C=C bond), 1556, 1516, 1452, 1427, 1400, 1351, 1275, 1215, 1192, 1166, 1137, 1014, 999, 958, 872, 818, 781, 715, 649, 626 ;  $^1\text{H-NMR}$  (400 MHz,  $\text{CDCl}_3$ ):  $\delta$  1.57 (s, 3H, CH<sub>3</sub>), 1.62 (s, 3H, CH<sub>3</sub>), 1.73 (s, 3H, CH<sub>3</sub>), 2.03–2.13 (m, 4H, -CH<sub>2</sub>CH<sub>2</sub>-), 4.59 (d,  $J = 4.0$  Hz, -OCH<sub>2</sub>-), 5.01–5.06 (m, 1H, =CH),

5.40–5.45 (m, 1H, =CH), 6.57 (s, 1H, H-3), 6.83 (d,  $J = 2.5$  Hz, 1H, H-8), 6.88 (dd,  $J = 2.5$  Hz, 9.0 Hz, 1H, H-6), 7.56–7.59 (m, 1H, H-5) ppm;  $^{13}\text{C-NMR}$  (100 MHz,  $\text{CDCl}_3$ ):  $\delta$  16.79 (CH<sub>3</sub>), 17.70 (CH<sub>3</sub>), 25.65 (CH<sub>3</sub>), 26.20 (CH<sub>2</sub>), 39.50 (CH<sub>2</sub>), 65.67 (CH<sub>2</sub>), 102.13 (CH), 106.88 (CH), 112.04 (q,  $^3J_{\text{CF}} = 5.7$  Hz), 113.98 (C), 120.25 (CH), 123.00 (CH), 123.54 (CH), 126.24 (q,  $^3J_{\text{CF}} = 2.0$  Hz, CH), 132.02 (C), 141.61 (q,  $^2J_{\text{CF}} = 32.7$  Hz, CCF<sub>3</sub>), 142.78 (C), 156.31 (C), 159.49 (C), 162.86 (C) ppm;  $^{19}\text{F-NMR}$  (470 MHz, DMSO-d<sub>6</sub>):  $\delta$  63.62 (s, 3F) ppm; MS (EIMS):  $m/z$  366 [M]<sup>+</sup>; Anal. Calcd for C<sub>20</sub>H<sub>21</sub>F<sub>3</sub>O<sub>3</sub>: C, 65.57; H, 5.78, Found: C, 65.54; H, 5.76.

*Characterization of (3d) (44)*

White solid, Yield: 93%; m.p. 66–67 °C; IR (KBr,  $\text{cm}^{-1}$ ):  $\nu$  3082 (Aromatic C-H), 3053 (Aromatic C-H), 2972 (Aliphatic C-H), 2896 (Aliphatic C-H), 2879 (Aliphatic C-H), 2849 (Aliphatic C-H), 2833 (Aliphatic C-H), 1728 (Carbonyl (ester  $-\text{C}=\text{O}$ )), 1611 (C=C bond), 1507, 1452, 1430, 1403, 1369, 1348, 1280, 1234, 1201, 1165, 1126, 1103, 1022, 990, 889, 852, 830, 776, 760;  $^1\text{H-NMR}$  (400 MHz,  $\text{CDCl}_3$ ):  $\delta$  1.60 (s, 3H, CH<sub>3</sub>), 1.66 (s, 3H, CH<sub>3</sub>), 1.75 (s, 3H, CH<sub>3</sub>), 2.06–2.15 (m, 4H, -CH<sub>2</sub>CH<sub>2</sub>-), 4.59 (d,  $J = 6.7$  Hz, 2H, -CH<sub>2</sub>-), 5.05–5.09 (m, 1H, =CH), 5.44–5.48 (m, 1H, =CH), 6.24 (d,  $J = 9.5$  Hz, 1H, H-3), 6.81 (d,  $J = 2.5$  Hz, 1H, H-6), 6.84 (dd,  $J = 2.4$  Hz, 8.4 Hz, 1H, H-8), 7.36 (d,  $J = 8.6$  Hz, 1H, H-5), 7.63 (d,  $J = 9.5$  Hz, 1H, H-4) ppm;  $^{13}\text{C-NMR}$  (100 MHz,  $\text{CDCl}_3$ ):  $\delta$  16.37 (CH<sub>3</sub>), 17.31 (CH<sub>3</sub>), 25.26 (CH<sub>3</sub>), 25.82 (CH<sub>2</sub>), 39.11 (CH<sub>2</sub>), 65.08 (CH<sub>2</sub>), 101.18 (CH), 112.01 (CH), 112.56 (C), 112.84 (CH), 117.99 (CH), 123.20 (CH), 128.26 (CH), 131.57 (C), 141.98 (C), 143.04 (CH), 155.47 (C), 160.90 (C), 161.74 (C) ppm; MS (EIMS):  $m/z$  296 [M]<sup>+</sup>; Anal. Calcd for C<sub>19</sub>H<sub>22</sub>O<sub>3</sub>: C, 76.48; H, 7.43, Found: C, 76.45; H, 7.41.

*Characterization of (3e) (45)*

White solid, Yield: 91%; m.p. 54–55 °C; IR (KBr,  $\text{cm}^{-1}$ ):  $\nu$  3078 (Aromatic C-H), 3028 (Aromatic C-H), 2964 (Aliphatic C-H), 2917 (Aliphatic C-H), 2856 (Aliphatic C-H), 1726 (Carbonyl (ester  $-\text{C}=\text{O}$ )), 1617 (C=C bond), 1508, 1441, 1420, 1390, 1345, 1278, 1257, 1199, 1154, 1134, 1070, 992, 982, 843, 825;  $^1\text{H-NMR}$  (400 MHz,  $\text{CDCl}_3$ ):  $\delta$  1.57 (s, 3H, CH<sub>3</sub>), 1.63 (s, 3H, CH<sub>3</sub>), 1.73 (s, 3H, CH<sub>3</sub>), 2.03–2.13 (m, 4H, -CH<sub>2</sub>CH<sub>2</sub>-), 2.37 (d,  $J = 1.1$  Hz, 3H, CH<sub>3</sub>), 4.57 (d,  $J = 6.5$  Hz, 2H, -CH<sub>2</sub>-), 5.03–5.07 (m, 1H, =CH), 5.42–5.46 (m, 1H, =CH), 6.10 (q,  $J = 1.2$  Hz, 2.4 Hz, 1H, H-3), 6.79 (d,  $J = 2.5$  Hz, 8.8 Hz, 1H, H-8), 6.84 (d,  $J = 2.5$  Hz, 1H, H-6), 7.46 (dd,  $J = 2.6$  Hz, 8.8 Hz, 1H, H-5) ppm;  $^{13}\text{C-NMR}$  (100 MHz,  $\text{CDCl}_3$ ):  $\delta$  16.79 (CH<sub>3</sub>), 17.73 (CH<sub>3</sub>), 18.70 (CH<sub>3</sub>), 25.68 (CH<sub>3</sub>), 26.24 (CH<sub>2</sub>), 39.53 (CH<sub>2</sub>), 65.44 (CH<sub>2</sub>), 101.59 (CH), 111.85 (CH), 112.94 (C), 113.47 (CH), 118.45 (CH), 123.63 (CH), 125.46 (CH), 131.97 (C), 142.35 (C), 152.61 (C), 155.25 (C), 161.41 (C), 161.95 (C) ppm ; MS (EIMS):  $m/z$

312 [M]<sup>+</sup>; Anal. Calcd for C<sub>20</sub>H<sub>24</sub>O<sub>3</sub>: C, 76.89; H, 7.74, Found: C, 76.88; H, 7.72.

#### Characterization of (3f) (46)

Light yellow solid, Yield: 93%; m.p. 136–137 °C; **IR** (KBr, cm<sup>-1</sup>): ν 3076 (Aromatic C-H), 3027 (Aromatic C-H), 2960 (Aliphatic C-H), 2909 (Aliphatic C-H), 2851 (Aliphatic C-H), 1720 (Carbonyl (ester -C=O)), 1604 (C=C bond), 1600 (C=C bond), 1548, 1505, 1453, 1378, 1354, 1262, 1257, 1208, 1169, 1142, 1077, 1008, 946, 873, 818, 753, 583; **<sup>1</sup>H-NMR** (400 MHz, CDCl<sub>3</sub>): δ 1.60 (s, 3H, CH<sub>3</sub>), 1.66 (s, 3H, CH<sub>3</sub>), 1.76 (s, 3H, CH<sub>3</sub>), 2.06–2.17 (m, 4H, -CH<sub>2</sub>CH<sub>2</sub>-), 2.54 (s, 3H, CH<sub>3</sub>), 4.60 (d, *J* = 6.6 Hz, -CH<sub>2</sub>-), 5.05–5.09 (m, 1H, =CH), 5.43–5.48 (m, 1H, =CH), 6.82 (d, *J* = 2.5 Hz, 1H, H-8), 6.90 (dd, *J* = 2.5 Hz, 8.9 Hz, 1H, H-6), 7.51 (d, *J* = 8.9 Hz, 1H, H-5) ppm; **<sup>13</sup>C-NMR** (100 MHz, CDCl<sub>3</sub>): δ 16.12 (CH<sub>3</sub>), 16.74 (CH<sub>3</sub>), 17.66 (CH<sub>3</sub>), 25.62 (CH<sub>3</sub>), 26.18 (CH<sub>2</sub>), 39.46 (CH<sub>2</sub>), 65.50 (CH<sub>2</sub>), 101.44 (CH), 113.10 (CH), 113.56 (C), 117.60 (CH), 118.24 (CH), 123.54 (CH), 125.74 (CH), 131.93 (C), 142.46 (C), 147.96 (C), 153.04 (C), 157.47 (C), 161.82 (C) ppm; **MS (EIMS)**: *m/z* 346 [M]<sup>+</sup>; Anal. Calcd for C<sub>20</sub>H<sub>23</sub>ClO<sub>3</sub>: C, 69.26; H, 6.68, Found: C, 68.70; H, 6.62.

#### Characterization of (3g)

White solid, Yield: 90%; m.p. 95–96 °C; **IR** (KBr, cm<sup>-1</sup>): ν 3078 (Aromatic C-H), 3003 (Aromatic C-H), 2965 (Aliphatic C-H), 2916 (Aliphatic C-H), 2856 (Aliphatic C-H), 2854 (Aliphatic C-H), 1728 (Carbonyl (ester -C=O)), 1609 (C=C bond), 1494, 1414, 1388, 1378, 1320, 1274, 1205, 1157, 1083, 1047, 982, 883, 829; **<sup>1</sup>H-NMR** (400 MHz, CDCl<sub>3</sub>): δ 1.59 (s, 3H, CH<sub>3</sub>), 1.65 (s, 3H, CH<sub>3</sub>), 1.77 (s, 3H, CH<sub>3</sub>), 2.06–2.15 (m, 4H, -CH<sub>2</sub>CH<sub>2</sub>-), 2.38 (d, *J* = 1.2 Hz, 3H, CH<sub>3</sub>), 4.69 (d, *J* = 6.4 Hz, 2H, -CH<sub>2</sub>-), 5.04–5.08 (m, 1H, =CH), 5.44–5.48 (m, 1H, =CH), 6.16 (dd, *J* = 1.4 Hz, 2.6 Hz, 1H, H-3), 6.83 (s, 1H), 7.56 (s, 1H) ppm; **<sup>13</sup>C-NMR** (100 MHz, CDCl<sub>3</sub>): δ 16.89 (CH<sub>3</sub>), 17.73 (CH<sub>3</sub>), 18.65 (CH<sub>3</sub>), 25.65 (CH<sub>3</sub>), 26.19 (CH<sub>2</sub>), 39.50 (CH<sub>2</sub>), 66.63 (CH<sub>2</sub>), 101.57 (CH), 112.74 (CH), 113.65 (C), 118.03 (CH), 119.34 (C), 123.54 (CH), 125.32 (CH), 132.01 (C), 142.66 (C), 151.70 (C), 153.52 (C), 156.93 (C), 160.79 (C) ppm; **MS (EIMS)**: *m/z* 346 [M]<sup>+</sup>; Anal. Calcd for C<sub>20</sub>H<sub>23</sub>ClO<sub>3</sub>: C, 69.26; H, 6.68, Found: C, 69.00; H, 6.64.

#### Characterization of (3h)

White solid, Yield: 92%; m.p. 104–105 °C; **IR** (KBr, cm<sup>-1</sup>): ν 3054 (Aromatic C-H), 3036 (Aromatic C-H), 2965 (Aliphatic C-H), 2909 (Aliphatic C-H), 2851 (Aliphatic C-H), 1707 (Carbonyl (ester -C=O)), 1606 (C=C bond), 1503, 1450, 1443, 1429, 1365, 1272, 1220, 1178, 1123, 1105, 1012, 990, 941, 827, 784, 691, 630; **<sup>1</sup>H-NMR** (400 MHz, CDCl<sub>3</sub>): δ 1.59 (s, 3H, CH<sub>3</sub>), 1.66 (s, 3H, CH<sub>3</sub>), 1.75 (s, 3H, CH<sub>3</sub>), 2.05–2.15 (m, 4H, -CH<sub>2</sub>CH<sub>2</sub>-), 4.60 (d, *J* = 8.0 Hz, 2H, -CH<sub>2</sub>-), 5.05–5.09 (m, 1H, =CH), 5.44–5.48 (m,

1H, =CH), 6.84–6.87 (m, 2H, H-6 and H-8), 7.34–7.44 (m, 4H), 7.65–7.68 (m, 2H), 7.74 (s, 1H, H-4) ppm; **<sup>13</sup>C-NMR** (100 MHz, CDCl<sub>3</sub>): δ 16.76 (CH<sub>3</sub>), 17.69 (CH<sub>3</sub>), 25.64 (CH<sub>3</sub>), 26.20 (CH<sub>2</sub>), 39.48 (CH<sub>2</sub>), 65.47 (CH<sub>2</sub>), 101.12 (CH), 113.19 (CH), 113.39 (CH), 118.38 (CH), 123.58 (C), 124.63 (CH), 128.36 (CH), 128.39 (CH), 128.74 (CH), 131.94 (C), 135.03 (C), 140.06 (C), 142.34 (CH), 155.23 (C), 160.95 (C), 161.88 (C) ppm; **MS (EIMS)**: *m/z* 374 [M]<sup>+</sup>; Anal. Calcd for C<sub>25</sub>H<sub>26</sub>O<sub>3</sub>: C, 80.18; H, 7.00, Found: C, 80.16; H, 6.99.

#### Characterization of (3i) (44,47)

White solid, Yield: 92%; m.p. 95–96 °C; **IR** (KBr, cm<sup>-1</sup>): ν 3067 (Aromatic C-H), 3050 (Aromatic C-H), 2958 (Aliphatic C-H), 2911 (Aliphatic C-H), 2870 (Aliphatic C-H), 2840 (Aliphatic C-H), 1704 (Carbonyl (ester -C=O)), 1566 (C=C bond), 1490, 1443, 1385, 1276, 1175, 1171, 1110, 1017, 922, 882, 816, 706; **<sup>1</sup>H-NMR** (400 MHz, CDCl<sub>3</sub>): δ 1.60 (s, 3H, CH<sub>3</sub>), 1.66 (s, 3H, CH<sub>3</sub>), 1.74 (s, 3H, CH<sub>3</sub>), 2.06–2.16 (m, 4H, -CH<sub>2</sub>CH<sub>2</sub>-), 4.56 (d, *J* = 6.6 Hz, 2H, -CH<sub>2</sub>-), 5.05–5.10 (m, 1H, =CH), 5.45–5.50 (m, 1H, =CH), 6.42 (d, *J* = 9.4 Hz, 1H, H-3), 6.92 (d, *J* = 2.9 Hz, 1H, H-5), 7.12 (dd, *J* = 2.9 Hz, 9.0 Hz, 1H, H-7), 7.26 (d, *J* = 9.0 Hz, 1H, H-8), 7.64 (d, *J* = 9.5 Hz, 1H, H-4) ppm; **<sup>13</sup>C-NMR** (100 MHz, CDCl<sub>3</sub>): δ 16.74 (CH<sub>3</sub>), 17.73 (CH<sub>3</sub>), 25.70 (CH<sub>3</sub>), 26.25 (CH<sub>2</sub>), 39.53 (CH<sub>2</sub>), 65.57 (CH<sub>2</sub>), 111.08 (CH), 117.02 (CH), 117.83 (CH), 118.90 (CH), 119.15 (CH), 120.15 (C), 123.65, 131.95 (C), 141.96 (C), 143.28 (CH), 148.41 (C), 155.34 (C), 161.05 (C) ppm; **MS (EIMS)**: *m/z* 298 [M]<sup>+</sup>; Anal. Calcd for C<sub>19</sub>H<sub>22</sub>O<sub>3</sub>: C, 76.48; H, 7.43, Found: C, 76.46; H, 7.42.

#### Characterization of (3j)

White solid, Yield: 89%; m.p. 57–58 °C; **IR** (KBr, cm<sup>-1</sup>): ν 3040 (Aromatic C-H), 2965 (aliphatic C-H), 2925 (aliphatic C-H), 2884 (aliphatic C-H), 1712 (C=O), 1673, 1571, 1493, 1428, 1386, 1275, 1238 (C-O), 1167, 990, 926, 838; **<sup>1</sup>H-NMR** (400 MHz, CDCl<sub>3</sub>): δ 1.60 (s, 3H, CH<sub>3</sub>), 1.67 (s, 3H, CH<sub>3</sub>), 1.77 (s, 3H, CH<sub>3</sub>), 2.06–2.17 (m, 4H, -CH<sub>2</sub>CH<sub>2</sub>-), 2.41 (d, *J* = 1.2 Hz, 3H, CH<sub>3</sub>), 4.59 (d, *J* = 6.6 Hz, 2H, -CH<sub>2</sub>-), 5.06–5.10 (m, 1H, =CH), 5.47–5.51 (m, 1H, =CH), 6.30 (q, *J* = 1.4 Hz, 2.6 Hz, 1H, H-3), 7.04 (d, *J* = 2.9 Hz, 1H, H-5), 7.13 (dd, *J* = 2.9 Hz, 9.0 Hz, 1H, H-7), 7.27 (d, *J* = 9.0 Hz, 1H, H-8) ppm; **<sup>13</sup>C-NMR** (100 MHz, CDCl<sub>3</sub>): δ 16.74 (CH<sub>3</sub>), 17.72 (CH<sub>3</sub>), 18.74 (CH<sub>3</sub>), 25.68 (CH<sub>3</sub>), 26.27 (CH<sub>2</sub>), 39.55 (CH<sub>2</sub>), 65.56 (CH<sub>2</sub>), 108.82 (CH), 115.44 (CH), 117.89 (CH), 119.00 (CH), 119.32 (C), 120.43 (CH), 123.64 (CH), 131.96 (C), 141.96 (C), 147.84 (C), 152.02 (C), 155.20 (C), 161.03 (C) ppm; **MS (EIMS)**: *m/z* 312 [M]<sup>+</sup>; Anal. Calcd for C<sub>20</sub>H<sub>24</sub>O<sub>3</sub>: C, 76.89; H, 7.74, Found: C, 76.86; H, 7.75.

#### Characterization of (3k)

White solid, Yield: 86%; m.p. 63–64 °C; **IR** (KBr,

cm<sup>-1</sup>):  $\nu$  3065 (Aromatic C-H), 2937 (Aliphatic C-H), 2917 (Aliphatic C-H), 2854 (Aliphatic C-H), 1708 (Carbonyl (ester -C=O)), 1612 (C=C bond), 1562, 1520, 1430, 1384, 1280, 1231, 1164, 984, 822; **<sup>1</sup>H-NMR** (400 MHz, CDCl<sub>3</sub>):  $\delta$  1.59 (s, 6H, 2CH<sub>3</sub>), 1.64 (s, 6H, 2CH<sub>3</sub>), 1.77 (s, 6H, 2CH<sub>3</sub>), 2.06–2.15 (m, 8H, 2(-CH<sub>2</sub>CH<sub>2</sub>-)), 2.37 (d,  $J$  = 1.2 Hz, 3H, CH<sub>3</sub>), 4.67 (d,  $J$  = 6.4 Hz, 4H, 2(-CH<sub>2</sub>-)), 5.04–5.08 (m, 2H, 2(=CH)), 5.44–5.48 (m, 2H, 2(=CH)), 6.15 (dd,  $J$  = 1.4 Hz, 2.64 Hz, 1H, H-3), 6.83 (s, 1H, H-5), 7.55 (s, 1H, H-8) ppm; **<sup>13</sup>C-NMR** (100 MHz, CDCl<sub>3</sub>):  $\delta$  17.04 (CH<sub>3</sub>), 17.17 (CH<sub>3</sub>), 18.01 (CH<sub>3</sub>), 19.14 (CH<sub>3</sub>), 25.95 (CH<sub>3</sub>), 26.52 (CH<sub>3</sub>), 26.59 (CH<sub>3</sub>), 39.81 (CH<sub>2</sub>), 39.86 (CH<sub>2</sub>), 66.63 (CH<sub>2</sub>), 67.16 (CH<sub>2</sub>), 101.75 (CH), 108.76 (CH), 112.37 (C), 112.65 (CH), 119.06 (CH), 119.92 (C), 123.96 (CH), 132.22 (C), 141.50 (C), 141.91 (C), 145.76 (C), 149.76 (C), 152.70 (C), 153.07 (C), 161.95 (C) ppm; **MS (EIMS)**:  $m/z$  464 [M]<sup>+</sup>; Anal. Calcd for C<sub>30</sub>H<sub>40</sub>O<sub>4</sub>: C, 77.55; H, 8.68, Found: C, 77.54; H, 8.66.

#### Characterization of (3l) (44)

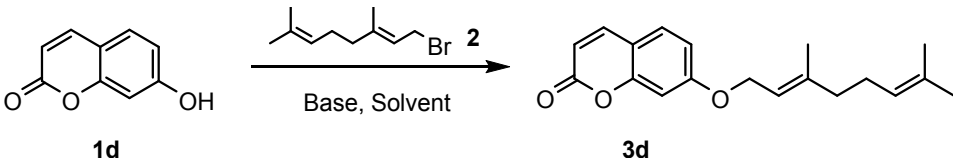
White solid, Yield: 87%; m.p. 72–73 °C; **IR** (KBr, cm<sup>-1</sup>):  $\nu$  3086 (Aromatic C-H), 3052 (Aromatic C-H), 2975 (Aliphatic C-H), 2917 (Aliphatic C-H), 2885 (Aliphatic C-H), 1745 (Carbonyl (ester -C=O)), 1638 (C=C bond), 1585, 1503, 1468, 1446, 1413, 1390, 1331, 1319, 1225, 1218, 1164, 1122, 996, 950, 938, 900, 864, 790, 761, 603; **<sup>1</sup>H-NMR** (400 MHz, CDCl<sub>3</sub>):  $\delta$  1.57 (s, 3H, CH<sub>3</sub>), 1.62 (s, 3H, CH<sub>3</sub>), 1.73 (s, 3H, CH<sub>3</sub>), 2.03–2.13 (m, 4H, -CH<sub>2</sub>CH<sub>2</sub>-), 4.61 (d,  $J$  = 8.0 Hz, 2H, -CH<sub>2</sub>-), 5.02–5.06 (m, 1H, =CH), 5.46–5.51 (m, 1H, =CH), 6.79 (s, 1H, H-4), 7.20–7.28 (m, 2H, H6 and H-8), 7.32–7.37 (m, 2H, H-5 and H-7) ppm; **<sup>13</sup>C-NMR** (100 MHz, CDCl<sub>3</sub>):  $\delta$  16.82

(CH<sub>3</sub>), 17.72 (CH<sub>3</sub>), 25.66 (CH<sub>3</sub>), 26.17 (CH), 39.50 (CH), 66.24 (CH), 113.69 (CH), 116.29 (CH), 117.96 (C), 119.82 (CH), 123.59 (C), 124.64 (CH), 126.37 (CH), 128.33 (CH), 132.00 (CH), 142.51 (C), 143.69 (C), 149.53 (C), 157.77 (C) ppm; **MS (EIMS)**:  $m/z$  298 [M]<sup>+</sup>; Anal. Calcd for C<sub>19</sub>H<sub>22</sub>O<sub>3</sub>: C, 76.48; H, 7.43, Found: C, 76.44; H, 7.42.

## RESULTS AND DISCUSSION

In this study, our first goal was to identify the optimal conditions for obtaining *O*-alkylated geranyloxycoumarin derivatives by reaction between hydroxycoumarin and geranyl bromide (Table 1). At first, the reaction between 7-hydroxycoumarin (1d) and geranyl bromide (2) was performed in the presence of Et<sub>3</sub>N in acetone at RT to give tarry mixture unidentified degradation products (Table 1, Entry 1). Secondly, when changing to K<sub>2</sub>CO<sub>3</sub> instead of TEA, the desired product 3d was obtained in a low 35% yield with 5 hours reaction time (Table 1, Entry 2). Prolonged the reaction time to 26 hours give higher 62% yield of the product 3d, but at solvent reflux temperature we isolated desired product at promising 73% yield (Table 1, Entries 3–4). Then we change solvent to CH<sub>3</sub>CN, at solvent reflux temperature we obtained higher purity product with a little better 74% yield (Table 1, Entry 5). As such, the optimized CH<sub>3</sub>CN solvent was tested using Cs<sub>2</sub>CO<sub>3</sub> additive at 3 hours or 30 min. times, and at RT or under CH<sub>3</sub>CN reflux temperature and geranyloxycoumarin 3d was formed with 93% or 87% yields, respectively (Table 1, Entries 6–7). The change base to more expensive silver(I) carbonate (Ag<sub>2</sub>CO<sub>3</sub>) give also good but low promising 85% yield of the product 3d (Table 1, Entry 8).

**Table 1:** Optimization of the reaction conditions for 7-geranyloxycoumarin (3d) preparation.



Entry	Conditions	Yield (%)
1	Et <sub>3</sub> N, acetone, RT, 12 h	degradation
2	K <sub>2</sub> CO <sub>3</sub> , acetone, RT, 5 h	35
3	K <sub>2</sub> CO <sub>3</sub> , acetone, RT, 26 h	62
4	K <sub>2</sub> CO <sub>3</sub> , acetone, reflux, 1 h	73
5	K <sub>2</sub> CO <sub>3</sub> , CH <sub>3</sub> CN, reflux, 1 h	74
6	Cs <sub>2</sub> CO <sub>3</sub> , CH <sub>3</sub> CN, RT, 3 h	93
7	Cs <sub>2</sub> CO <sub>3</sub> , CH <sub>3</sub> CN, reflux, 30 min	87
8	Ag <sub>2</sub> CO <sub>3</sub> , CH <sub>3</sub> CN, RT, 3 h	85

Geranyloxycoumarin was synthesized in good yield by the reaction of hydroxycoumarin excluding 4-OH group and geranyl bromide under weak base and

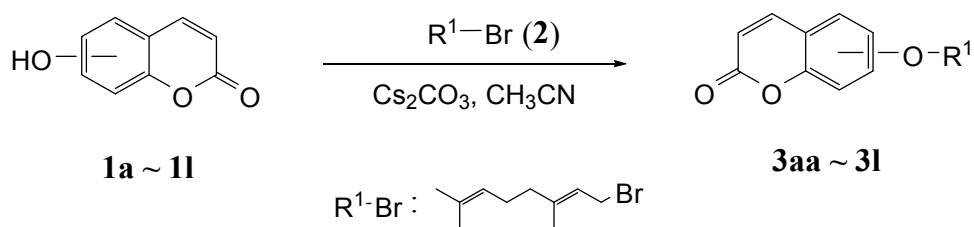
CH<sub>3</sub>CN condition. In the cases where the OH group was positioned on the 3<sup>rd</sup>, 5<sup>th</sup>, 6<sup>th</sup>, 7<sup>th</sup>, or 8<sup>th</sup> carbon of the coumarin structure, the reaction of



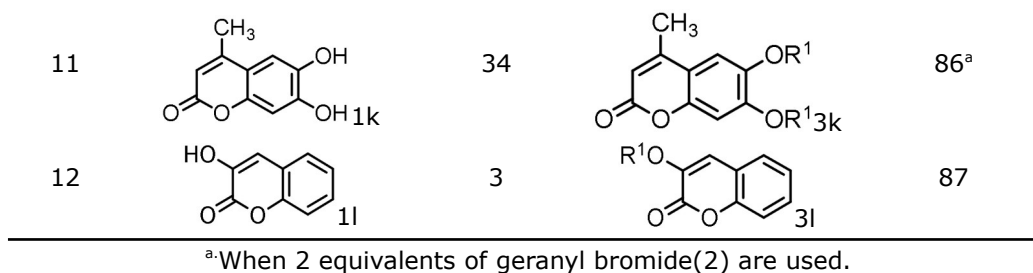
hydroxycoumarin (ex, 6-hydroxycoumarin) and geranyl bromide with cesium carbonate and acetonitrile at RT produced a high yield of *O*-alkylated compounds. In this result, the reaction of

the different types of hydroxycoumarin and geranyl bromide under the given conditions produced various novel coumarin derivatives (Table 2).

**Table 2:** Synthesized geranyloxycoumarin derivatives.



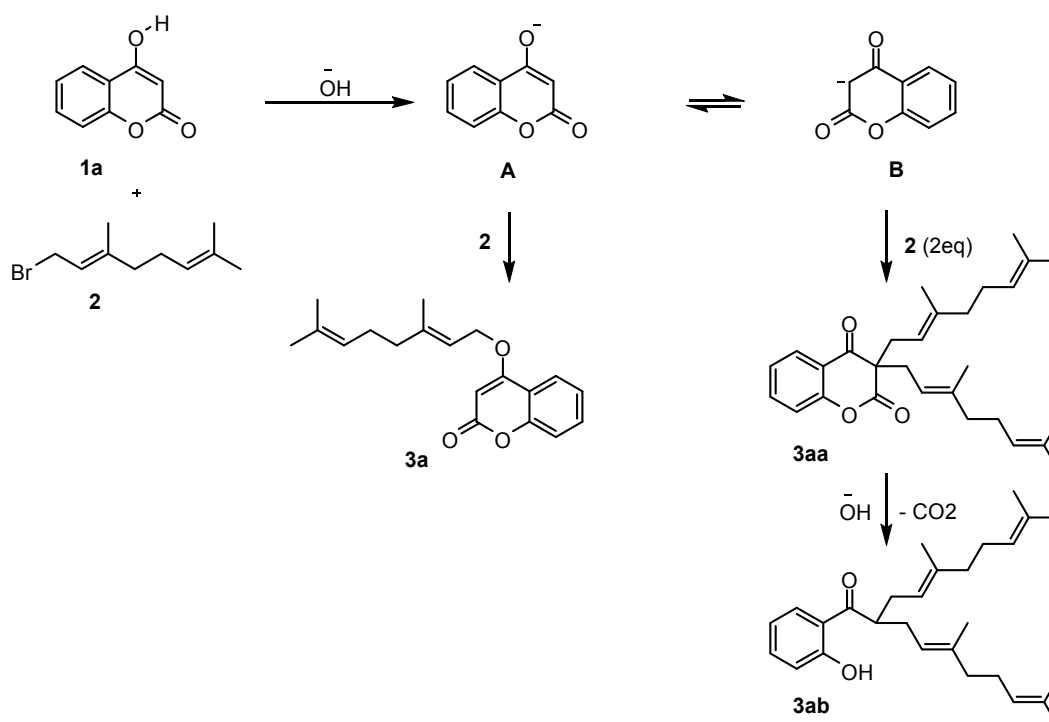
Entry	Coumarin	Time (h)	Product	Yield (%)
1		3		18
2		72		-
3		3.5		90
4		3		94
5		3		91
6		4		93
7		2.5		90
8		3		92
9		3		92
10		3		89



Next, we studied the reaction of 4-hydroxycoumarin (1a) with geranyl bromide (2) to produce *O*-4 and *C*-3 alkylated products. Under optimized reaction conditions for *O*-alkylation, the desired 4-geranyloxy coumarin (3a) was obtained in low 18% yield. This reaction takes place on the tautomer A with the anion located on the oxygen atom in the *C*-4 position.

On the other hand, *C*-3 alkylated coumarin 3aa was formed in the reaction with 2 equivalents of geranyl bromide (2) started on the keto form tautomer B,

with anion localized at *C*-3 carbon atom, with 11% yield. Moreover, compound 3ab was obtained in 35% yield by hydrolysis and decarboxylation from 3aa. We also confirmed that 3ab was obtained by adding 3aa to acetonitrile to which water was added and stirring at RT for 9 hours. These results are reported by Yi-Jen Shue et al. to obtain a *C*-alkylated coumarin and a diallylated product, which was hydrolyzed and then decarboxylated, by reacting 4-hydroxycoumarin and cinnamyl alcohol with water and palladium catalyst (Scheme 1) (37-40).



**Scheme 1:** Reactivity of 4-hydroxycoumarin.

No reaction occurred between 4-hydroxy-3-nitrocoumarin (**1b**) and geranyl bromide (2) in  $\text{Cs}_2\text{CO}_3$ ,  $\text{CH}_3\text{CN}$  for 72 hours at RT or in reflux condition. It is expected that the desired product was not obtained by the reversible structure of 4-hydroxy-3-nitrocoumarin of the nitro and nitrous types.

As can be seen, the alkylation reaction of hydroxycoumarin and geranyl bromide under mild

conditions led to a good yield; however, a new method of synthesis is required to achieve a higher yield of 4-geranyloxy coumarin. In addition, as the *O*-alkylated derivatives of geranyloxy coumarin are predicted to exhibit diverse bioactivities, further studies should be conducted on their synthesis.

## REFERENCES

- Borges F, Roleira F, Milhazes N, Santana L, Uriarte E. Simple Coumarins and Analogues in Medicinal Chemistry: Occurrence, Synthesis and Biological Activity. *CMC*. 2005 Apr 1;12(8):887-916. [<DOI>](#).
- Niu X, Xing W, Li W, Fan T, Hu H, Li Y. Isofraxidin exhibited anti-inflammatory effects in vivo and inhibited TNF- $\alpha$  production in LPS-induced mouse peritoneal macrophages in vitro via the MAPK pathway. *International Immunopharmacology*. 2012 Oct;14(2):164-71. [<DOI>](#).
- Berrino E, Milazzo L, Micheli L, Vullo D, Angeli A, Bozdog M, et al. Synthesis and Evaluation of Carbonic Anhydrase Inhibitors with Carbon Monoxide Releasing Properties for the Management of Rheumatoid Arthritis. *J Med Chem*. 2019 Aug 8;62(15):7233-49. [<DOI>](#).
- Zhao Y-L, Yang X-W, Wu B-F, Shang J-H, Liu Y-P, Zhi-Dai, et al. Anti-inflammatory Effect of Pomelo Peel and Its Bioactive Coumarins. *J Agric Food Chem*. 2019 Aug 14;67(32):8810-8. [<DOI>](#).
- Peperidou A, Bua S, Bozdog M, Hadjipavlou-Litina D, Supuran C. Novel 6- and 7-Substituted Coumarins with Inhibitory Action against Lipoygenase and Tumor-Associated Carbonic Anhydrase IX. *Molecules*. 2018 Jan 12;23(1):153. [<DOI>](#).
- Chen LZ, Sun WW, Bo L, Wang JQ, Xiu C, Tang WJ, et al. New arylpyrazoline-coumarins: Synthesis and anti-inflammatory activity. *European Journal of Medicinal Chemistry*. 2017 Sep;138:170-81. [<DOI>](#).
- Zhu M, Ma L, Wen J, Dong B, Wang Y, Wang Z, et al. Rational design and Structure-Activity relationship of coumarin derivatives effective on HIV-1 protease and partially on HIV-1 reverse transcriptase. *European Journal of Medicinal Chemistry*. 2020 Jan;186:111900. [<DOI>](#).
- Liu Y-P, Yan G, Xie Y-T, Lin T-C, Zhang W, Li J, et al. Bioactive prenylated coumarins as potential anti-inflammatory and anti-HIV agents from *Clausena lenis*. *Bioorganic Chemistry*. 2020 Apr;97:103699. [<DOI>](#).
- Patil AD, Freyer AJ, Eggleston DS, Haltiwanger RC, Bean MF, Taylor PB, et al. The inophyllums, novel inhibitors of HIV-1 reverse transcriptase isolated from the Malaysian tree, *Calophyllum inophyllum* Linn. *J Med Chem*. 1993 Dec;36(26):4131-8. [<DOI>](#).
- Zhao J-W, Wu Z-H, Guo J-W, Huang M-J, You Y-Z, Liu H-M, et al. Synthesis and anti-gastric cancer activity evaluation of novel triazole nucleobase analogues containing steroidal/coumarin/quinoline moieties. *European Journal of Medicinal Chemistry*. 2019 Nov;181:111520. [<DOI>](#).
- Lin M-H, Wang J-S, Hsieh Y-C, Zheng J-H, Cho E-C. NO<sub>2</sub> functionalized coumarin derivatives suppress cancer progression and facilitate apoptotic cell death in KRAS mutant colon cancer. *Chemico-Biological Interactions*. 2019 Aug;309:108708. [<DOI>](#).
- Eker Y, Şenkuytu E, Ölçer Z, Yıldırım T, Çiftçi GY. Novel coumarin cyclotriphosphazene derivatives: Synthesis, characterization, DNA binding analysis with automated biosensor and cytotoxicity. *Journal of Molecular Structure*. 2020 Jun;1209:127971. [<DOI>](#).
- Sanduja M, Gupta J, Singh H, Pagare PP, Rana A. Uracil-coumarin based hybrid molecules as potent anti-cancer and anti-bacterial agents. *Journal of Saudi Chemical Society*. 2020 Feb;24(2):251-66. [<DOI>](#).
- Ahmed EY, Abdel Latif NA, El-Mansy MF, Elserwy WS, Abdelhafez OM. VEGFR-2 inhibiting effect and molecular modeling of newly synthesized coumarin derivatives as anti-breast cancer agents. *Bioorganic & Medicinal Chemistry*. 2020 Mar;28(5):115328. [<DOI>](#).
- Maly DJ, Leonetti F, Backes BJ, Dauber DS, Harris JL, Craik CS, et al. Expedient Solid-Phase Synthesis of Fluorogenic Protease Substrates Using the 7-Amino-4-carbamoylmethylcoumarin (ACC) Fluorophore. *J Org Chem*. 2002 Feb 1;67(3):910-5. [<DOI>](#).
- Koparde S, Hosamani KM, Barretto DA, Joshi SD. Microwave synthesis of coumarin-maltol hybrids as potent antitumor and anti-microbial drugs: An approach to molecular docking and DNA cleavage studies. *Chemical Data Collections*. 2018 Aug;15-16:41-53. [<DOI>](#).
- Ostrowska K. Coumarin-piperazine derivatives as biologically active compounds. *Saudi Pharmaceutical Journal*. 2020 Feb;28(2):220-32. [<DOI>](#).
- Smyth T, Ramachandran VN, Smyth WF. A study of the antimicrobial activity of selected naturally occurring and synthetic coumarins. *International Journal of Antimicrobial Agents*. 2009 May;33(5):421-6. [<DOI>](#).
- Wang H, Xu W. Mito-methyl coumarin, a novel mitochondria-targeted drug with great antitumor potential was synthesized. *Biochemical and Biophysical Research Communications*. 2017 Jul;489(1):1-7. [<DOI>](#).
- Weber US, Steffen B, Siegers CP. Antitumor-activities of coumarin, 7-hydroxy-coumarin and its glucuronide in several human tumor cell lines. *Res Commun Mol Pathol Pharmacol*. 1998 Feb;99(2):193-206. [<URL>](#).
- Liu H, Li Z, Yu L, Zhang Y. Antitumor activity and mechanisms of scoparone. *J Zhong Guo Yao Li Tong Xun*. 2005;22:40-1.
- Liu W, Hua J, Zhou J, Zhang H, Zhu H, Cheng Y, et al. Synthesis and in vitro antitumor activity of novel scopoletin derivatives. *Bioorganic & Medicinal Chemistry Letters*. 2012 Aug;22(15):5008-12. [<DOI>](#).
- Zaragozá C, Monserrat J, Mantecón C, Villaescusa L, Zaragozá F, Álvarez-Mon M. Antiplatelet activity of flavonoid and coumarin drugs. *Vascular Pharmacology*. 2016 Dec;87:139-49. [<DOI>](#).
- Revankar HM, Bukhari SNA, Kumar GB, Qin H-L. Coumarins scaffolds as COX inhibitors. *Bioorganic Chemistry*. 2017 Apr;71:146-59. [<DOI>](#).
- Huang H-Y, Ko H-H, Jin Y-J, Yang S-Z, Shih Y-A, Chen I-S. Dihydrochalcone glucosides and antioxidant activity from the roots of *Anneslea fragrans* var. *lanceolata*. *Phytochemistry*. 2012 Jun;78:120-5. [<DOI>](#).

26. Khan S, Riaz N, Afza N, Malik A, Aziz-ur-Rehman, Iqbal L, et al. Antioxidant constituents from *Cotoneaster racemiflora*. *Journal of Asian Natural Products Research*. 2009 Jan 1;11(1):44–8. [<DOI>](#).
27. Mangasuli SN, Hosamani KM, Managutti PB. Microwave assisted synthesis of coumarin-purine derivatives: An approach to in vitro anti-oxidant, DNA cleavage, crystal structure, DFT studies and Hirshfeld surface analysis. *Heliyon*. 2019 Jan;5(1):e01131. [<DOI>](#).
28. Ambreen, Haque S, Singh V, Katiyar D, Ali Khan MT, Tripathi V, et al. Biotransformation of newly synthesized coumarin derivatives by *Candida albicans* as potential antibacterial, antioxidant and cytotoxic agents. *Process Biochemistry*. 2019 Dec;87:138–44. [<DOI>](#).
29. Kavetsou E, Gkionis L, Galani G, Gkolfinopoulou C, Argyri L, Pontiki E, et al. Synthesis of prenyloxy coumarin analogues and evaluation of their antioxidant, lipoxygenase (LOX) inhibitory and cytotoxic activity. *Med Chem Res*. 2017 Apr;26(4):856–66. [<DOI>](#).
30. Roussaki M, Zelianaios K, Kavetsou E, Hamilakis S, Hadjipavlou-Litina D, Kontogiorgis C, et al. Structural modifications of coumarin derivatives: Determination of antioxidant and lipoxygenase (LOX) inhibitory activity. *Bioorganic & Medicinal Chemistry*. 2014 Dec;22(23):6586–94. [<DOI>](#).
31. Al-Majedy Y, Al-Duhaidahawi D, Al-Azawi K, Al-Amiery A, Kadhum A, Mohamad A. Coumarins as Potential Antioxidant Agents Complemented with Suggested Mechanisms and Approved by Molecular Modeling Studies. *Molecules*. 2016 Jan 23;21(2):135. [<DOI>](#).
32. Yun B-S, Lee I-K, Ryoo I-J, Yoo I-D. Coumarins with Monoamine Oxidase Inhibitory Activity and Antioxidative Coumarino-lignans from *Hibiscus s yriacus*. *J Nat Prod*. 2001 Sep 1;64(9):1238–40. [<DOI>](#).
33. Tamene D, Endale M. Antibacterial Activity of Coumarins and Carbazole Alkaloid from Roots of *Clausena anisata*. *Advances in Pharmacological Sciences*. 2019 Feb 3;2019:1–8. [<DOI>](#).
34. Yang L, Wu L, Yao X, Zhao S, Wang J, Li S, et al. Hydroxycoumarins: New, effective plant-derived compounds reduce *Ralstonia pseudosolanacearum* populations and control tobacco bacterial wilt. *Microbiological Research*. 2018 Oct;215:15–21. [<DOI>](#).
35. Ramírez-Pelayo C, Martínez-Quiñones J, Gil J, Durango D. Coumarins from the peel of citrus grown in Colombia: composition, elicitation and antifungal activity. *Heliyon*. 2019 Jun;5(6):e01937. [<DOI>](#).
36. Shah V, Bose J, Shah R. Communication- New Synthesis of 4-Hydroxycoumarins. *J Org Chem*. 1960 Apr;25(4):677–8. [<DOI>](#).
37. Cravotto G, Nano GM, Palmisano G, Tagliapietra S. 4-Hydroxycoumarin and related systems: Site selectivity of the Mitsunobu reaction with prenyl alcohols. *HETEROCYCLES*. 2003;60:1351–8. [<URL>](#).
38. Patra P. 4-Chloro-3-formylcoumarin as a multifaceted building block for the development of various bio-active substituted and fused coumarin heterocycles: a brief review. *New J Chem*. 2021;45(32):14269–327. [<DOI>](#).
39. Russell A, Frye JR. 2,6-dihydroxyacetophenone. *Org Synth*. 1941;21:22. [<DOI>](#).
40. Shue Y-J, Yang S-C. Activator-free and one-pot C-allylation by simple palladium catalyst in water. *Tetrahedron Letters*. 2012 Mar;53(11):1380–4. [<DOI>](#).
41. Woods LL, Sapp J. A New One-Step Synthesis of Substituted Coumarins. *J Org Chem*. 1962 Oct;27(10):3703–5. [<DOI>](#).
42. Venturella P, Bellino A, Marino M, Maria L. Synthesis of terpenoid coumarins, an approach to the synthesis of Pilocellodan. *Gazz Chim Italiana*. 1982;112(9/10):433–4.
43. Iranshahi M, Jabbari A, Orafaie A, Mehri R, Zeraatkar S, Ahmadi T, et al. Synthesis and SAR studies of mono O-prenylated coumarins as potent 15-lipoxygenase inhibitors. *European Journal of Medicinal Chemistry*. 2012 Nov;57:134–42. [<DOI>](#).
44. Khomenko TM, ZarubaeV VV, Orshanskaya IR, Kadyrova RA, Sannikova VA, Korchagina DV, et al. Anti-influenza activity of monoterpene-containing substituted coumarins. *Bioorganic & Medicinal Chemistry Letters*. 2017 Jul;27(13):2920–5. [<DOI>](#).
45. Orhan IE, Senol Deniz FS, Salmas RE, Durdagi S, Epifano F, Genovese S, et al. Combined molecular modeling and cholinesterase inhibition studies on some natural and semisynthetic O-alkylcoumarin derivatives. *Bioorganic Chemistry*. 2019 Mar;84:355–62. [<DOI>](#).





## Nonlinear Fitting for Estimation of Adsorption Equilibrium, Kinetic and Thermodynamic Parameters of Methylene Blue onto Activated Carbon

Ibrahim Y. Erwa<sup>1</sup> , Omer A. Ishag<sup>1\*</sup>  , Omar A. Alrefaei<sup>1</sup> , Issa M. Hassan<sup>1</sup> 

<sup>1</sup>International University of Africa, Faculty of Pure and Applied Sciences, Department of Applied and Industrial Chemistry (12223), Khartoum, Sudan.

**Abstract:** Adsorption equilibrium, kinetics, and thermodynamics of methylene blue dye (MB) from aqueous solutions onto activated carbon (AC) synthesized from pomegranate peel was conducted in controlled batch systems. The effects of initial MB concentration, AC particle size, contact time, and temperature on adsorption were evaluated. Under the optimized conditions (i.e., contact time 120 min, pH ~ 5, particle size 125  $\mu\text{m}$ , dye concentration 20 mg/L, temperature 333 K, and 0.5 g AC/50 mL MB solution), the removal percentages can achieve ~ 98.28%. The nonlinear method was conducted for estimating the equilibrium and kinetic parameters, where the equilibrium data were fitted to the Langmuir isotherm model. The Langmuir isotherm suggested a maximum monolayer adsorption capacity of 5.03 mg/g at 60 °C. The pseudo-second-order kinetic model provided the best fit to the experimental data compared with the pseudo-first-order. Kinetic studies showed that the adsorption equilibrium was rapidly established, with low activation energy entailed for adsorption ( $E_a$ ; 15.60 kJ/mol). Thermodynamic parameters showed that the adsorption was spontaneous ( $-\Delta G^\circ$  and  $+\Delta S^\circ$ ), endothermic ( $+\Delta H^\circ$ ), and favorable at ambient conditions.

**Keywords:** Methylene blue, adsorption isotherms, kinetics, thermodynamic parameters, nonlinear fitting.

**Submitted:** March 27, 2021. **Accepted:** November 30, 2021.

**Cite this:** Erwa I, Ishag O, Alrefaei O, Hassan I. Nonlinear Fitting for Estimation of Adsorption Equilibrium, Kinetic and Thermodynamic Parameters of Methylene Blue onto Activated Carbon. JOTCSA. 2022;9(1):67-84.

**DOI:** <https://doi.org/10.18596/jotcsa.904311>.

**\*Corresponding author. E-mail:** [adamomer4@gmail.com](mailto:adamomer4@gmail.com).

### INTRODUCTION

Pollution of the aquatic environment resulting from the discharging of insufficiently treated industrial wastes containing relatively large quantities of some chemicals of industrial origin, such as dyes, phenols, coloring materials, pesticides, and fertilizers, into water sources is a growing environmental problem and a direct threat to the life of all living organisms (1). In addition to being a major factor causing a lack of healthy food, disease, and death, water pollution often leads to a persistent shortage of clean drinking water accessible around the world (2). About 75 – 80% of water pollution results from improperly treated industrial wastewater discharges, as waste from

industries such as sugar, textiles, electroplating, and pesticides pollute the water to a large extent (3). Color is one of the most obvious water pollution indicators, and the release of colored effluents can pollute aquatic bodies. These pollutants come from synthetic dyes widely utilized in numerous industries, incorporating dyeing of textiles, paper, and plastics that consume 60%, 10%, and 10% of global pigment production, respectively (4). The textile industry alone uses about  $1.0 \times 10^4$  different types of dyes (5). The world's annual production of dyes is over  $7.0 \times 10^5$  tons (6, 7). It is estimated that 10–15% of the used dye is discarded in the effluent during the dyeing process (8). Wastewater contaminated with highly colored dyes requires appropriate treatment



before release into the environment (9). It is difficult to remedy such wastewater by conventional wastewater treatment methods because the organic dye molecules resist aerobic digestion, and some are stable to light, heat, and oxidation processes. Moreover, some azo dyes and their analogs contain carcinogenic compounds, so treating liquid wastes containing these compounds is important to protect natural waters (4). On the other hand, the chemical treatment method requires large quantities of chemicals, and additional treatment should be taken into account for secondary protection from the reaction products, which increases the cost of the process (10). Therefore, research continues to develop an efficient and environmentally friendly new technology to treat harmful organic pollutants in industrial wastewater. Several methods have been developed, such as coagulation, membrane filtration, adsorption, catalyzed photolysis, aerobic and anaerobic decomposition, advanced oxidation, and ozone treatment to treat waste organic dyes (11-14). Adsorption is considered one of the best techniques used to remove dye from a solution due to its high efficiency, effectiveness, and low cost (15). In this regard, well-known adsorbents, such as activated carbon (16), biomass (17) zeolite, clay materials (18), and polymers (19), are used to remove the contaminating dyes. The adsorption is classified based on the adsorbate-adsorbent interaction and the heat associated with the process. The type and strength of the bonds between the adsorbent and the substrate provide a clear indication of the type of adsorption, beginning with weaker bonds such as van der Waals forces or so-called physical adsorption, and even strong bonds in the case of chemical adsorption, where chemical bonds are established between the substrate and the adsorbent surface (20). The adsorption capacity depends on the relationship between the adsorbent's surface area and the nature and size of the adsorbate. The adsorption process is accompanied by a change in the free energy ( $\Delta G$ ), as well as a decrease in the entropy ( $\Delta S$ ) due to the restriction of the particles that have adsorbed to the adsorbent surface, and in general, the adsorption process is mostly exothermic, and this does not prevent some types of endothermic adsorption from occurring. Activated carbon is a porous carbon material increasingly used due to its exceptional properties in desalination, wastewater treatment plants, and air purification (21). The advantages of activated carbon adsorbents are reasonably priced wastewater treatment, clear process design, fast process application, corrosive resistance, high adsorption ability in gas and liquid purification, and their use as supporting catalysts (22). In general, activated carbon is produced from biomass and agricultural waste in two major steps: pyrolysis or carbonization and activation (23). Many low-cost

waste materials of plant origin have been studied to produce activated carbon because they contain minimum organic matter, long shelf life, and a solid structure that preserves their properties under varying operating conditions. For this purpose, agricultural by-products were used, such as sugarcane bagasse, peanut husks, rice straw, soybean husk, walnut husks, and pecan husks (24). Methylene blue (MB) is a basic or cationic dye, also recognized as methylthionium chloride and other common names; its IUPAC name is (3,7-bis(dimethylamino)-phenothiazin-5-ium chloride). Methylene blue is a dark green crystalline powder. It has a slight odor; it is very soluble in water 43.60 g/L at 25 °C, and it is commonly used as a staining agent in research labs and textile factories and is often used as an adrenaline aid in the ablation process (25, 26). It has a chemical formula ( $C_{16}H_{18}N_3SCl$ ), molecular mass (319.85 g/mol); it absorbs light strongly at wavelengths of 589 and 664 nm (15). MB molecules' highly toxic nature makes them a possible threat to human health and the natural environment (27). Direct contact with MB induces dermatitis and permanent damage to the eyes, and MB-rich water intake results in diarrhea, vomiting, nausea, gastritis, delirium, and heavy sweating (28). This study aims to remove methylene blue (MB) from synthetic wastewater by a batch adsorption process using low-cost activated carbon (prepared from pomegranate peel waste) as an adsorbent and to study the process equilibrium, kinetics, and thermodynamic using the nonlinear regression analysis.

## EXPERIMENTAL SECTION

### Chemicals and Equipment

All chemicals used in this study were of analytical grade, as follows: MB (C.I. 52015, Merck), sodium hydroxide, and hydrochloric acid (NICE, India). A stock aqueous solution of MB (1000 mg/L) was prepared. A water bath (Model 1008, G.F.L.) was used for all the adsorption experiments. For the estimation of MB concentrations, a UV/Visible spectrophotometer (Model CE7200, Aquarius) was used. A muffle furnace (Carbolite) and drying oven (SLW 15 POL-EKO-APARATURA) were used to prepare activated charcoal.

### Carbonization of Pomegranate Peel

About 100 g of well-cleaned, dried, and grounded pomegranate peel was blended with 100 mL of 0.1 M NaOH solution in a closed crucible and carbonized in the muffle furnace (650 °C) for 1 h in the absence of oxygen. The crucible was then removed from the furnace and left to cool at room temperature. The prepared charcoal was washed with distilled water, to remove the excess NaOH, and with 0.1 M HCl solution to remove residues of activating agent which clog the pores, finally

washed with deionized water to remove any surface impurities. The cleaned charcoal sample was dried at 105 °C and subsequently activated at 250 °C for 24 h in an oven, then allowed to cool in the desiccator. The dried sample was powdered and sieved using different micrometers aperture sieve sizes (29, 30).

#### Determination of Bulk Density of the Adsorbent

A pre-weighed dry density bottle was filled with the prepared activated carbon (AC), the spaces between the carbon particles were removed by lightly striking the bottle, then the density bottle and its contents were accurately weighted. The bulk density was calculated using Equation 1:

$$\text{Bulk density} = \frac{\text{weight of charcoal}}{\text{volume}} \quad (1)$$

#### Determination of Moisture Content of the Adsorbent

About 5 g of the AC samples were balanced in a dry and weighed porcelain crucible. Crucible was heated (105 °C) for 2 h in an electric oven. The crucible was cooled in a desiccators then reweighed. The procedure was repeated until achieving a constant weight. The adsorbent moisture content was calculated utilizing Equation 2:

$$\text{Moisture content (\%)} = \frac{w_2 - w_3}{w_2 - w_1} \times 100 \quad (2)$$

Where:  $w_1$  is empty crucible weight;  $w_2$  is crucible and sample weight;  $w_3$  is crucible and sample weight after heating.

#### Determination of Ash Content of the Adsorbent

About 5 g of the prepared AC was weighed into a dry and weighed crucible and transferred to the muffle furnace at 500 °C for 2 h (30), where ash content was calculated utilizing Equation 3:

$$\text{Ash content (\%)} = \frac{\text{weight of ash}}{\text{sample weight}} \times 100 \quad (3)$$

#### Batch Adsorption Study

Batch adsorption experiments were conducted in an isothermal shaker at an agitation speed of 250 rpm utilizing a sequences of 100 mL Erlenmeyer flasks. In all sets of experiments, 50 mL of MB solutions (natural pH = 5.01 without any further adjustment) was added to 0.5 g of AC. The influence of various adsorption parameters, initial concentrations (10, 20, 30, 40, 50, 60, 70, 90, 110, 130, and 150 mg/L), contact time (1 – 120 min), adsorbent particle size (50, 63, 125 and 250 microns) and temperature (20 – 60 °C) was

investigated by varying the parameter under investigation, while all other experimental parameters have remained constant. After equilibrium, the solutions were filtered, and the dye's concentration in the filtrates was determined by measuring the absorbance at 664 nm using a double beam UV-Vis spectrophotometer. The adsorption capacity ( $q_e$ ) and MB removal percentage ( $R\%$ ) was calculated using the following expressions:

$$q_e = \frac{(C_i - C_e)V}{m} \quad (4)$$

$$R(\%) = \frac{C_i - C_e}{C_i} \times 100 \quad (5)$$

Where  $q_e$  is the quantity of MB adsorbed per unit mass of adsorbent (mg/g),  $C_i$  is the initial concentration of MB (mg/L),  $C_e$  is the equilibrium concentration of MB (mg/L),  $V$  is the MB solution volume (L), and  $m$  is the adsorbent mass (g). All measurements were repeated three times, and the mean values were taken.

#### Statistical Analysis

The Origin software version 8.5 was used to compute the kinetic and isotherm models' parameters precisely in batch experiments. The coefficient of determination ( $R^2$ ) of the nonlinear optimization method was calculated utilizing Equation 6. For the assessment of the fit of the equations to the experimental data of the adsorption process a nonlinear ( $R^2$ ), chi-square ( $\chi^2$ ), and the adjusted coefficient of determination ( $R^2_{adj}$ ) (Equations 6 – 8) values were determined.

$$R^2 = 1 - \frac{\sum (q_{e,exp} - q_{e,cal})^2}{\sum (q_{e,exp} - q_{e,mean})^2} \quad (6)$$

$$\chi^2 = \frac{\sum (q_{e,exp} - q_{e,cal})^2}{q_{e,cal}} \quad (7)$$

$$R^2_{adj} = 1 - (1 - R^2) \left( \frac{n_p - 1}{n_p - p - 1} \right) \quad (8)$$

Where  $q_{e,exp}$  (mg/g) is the amount of MB uptake at equilibrium obtained from Equation 4;  $q_{e,cal}$  (mg/g) is the amount of MB adsorbed computed from the model using the Origin software;  $q_{e,mean}$  (mg/g) is the average of  $q_{e,exp}$  values;  $n_p$  is the number of experiments carried out,  $p$  is the number of parameters of the fitted model.

#### Adsorption Isotherm

Two well-known equilibrium isotherm models (Langmuir and Freundlich) were used to describe experimental adsorption data. According to Langmuir, adsorption occurs over a homogenous

surface through monolayer adsorption, where all the adsorption positions are duplicate and energetically equivalent. The nonlinear formula of the Langmuir model shown in Equation 9, and one linear formula of the equation is represented in Equation 10:

$$q_e = \frac{Q_{max} K_L C_e}{1 + K_L C_e} \quad (9)$$

$$\frac{C_e}{q_e} = \frac{1}{Q_{max} K_L} + \frac{C_e}{Q_{max}} \quad (10)$$

Where:  $q_e$  and  $Q_{max}$  are equilibrium adsorption capacity (mg/g) and maximum adsorption capacity (mg/g) of MB on AC, respectively;  $C_e$  is the equilibrium concentration (mg/L);  $K_L$  is the Langmuir constant (L/mg).

The nonlinear and linear forms of the Freundlich model are described in Equation 11 and Equation 12, respectively.

$$q_e = K_F C_e^n \quad (11)$$

$$\log q_e = \log K_F + n \log C_e \quad (12)$$

Where:  $K_F$  and  $n$  are Freundlich constants (31).

### Adsorption Kinetics

Lagergren's nonlinear pseudo-first-order equation (PFO) (Equation 13) and Blanchard et al. nonlinear pseudo-second-order (PSO) (Equation 14) kinetic models were adopted to analyze the experimental results in order to fully understand the adsorption process of MB on the surface of the prepared AC (32).

$$q_t = q_e (1 - e^{-k_1 t}) \quad (13)$$

$$q_t = \frac{q_e^2 k_2 t}{1 + k_2 q_e t} \quad (14)$$

### Adsorption Thermodynamics

An essential element of determining adsorption type (physisorption or chemisorption) is conducting thermodynamic analysis. The functions (thermodynamic) for the adsorption of MB by AC derived from pomegranate peel (33) can be determined utilizing the equations:

$$\Delta G^0 = -RT \ln K_c \quad (15)$$

Where  $\Delta G^0$  is the Gibbs energy change,  $R$  is the universal gas constant (8.314 J/mol.K),  $T$  is the absolute temperature in K, and  $K_c$  (dimensionless) is the equilibrium constant. The equilibrium constant was derived from the value of the best-fit nonlinear isotherm model.  $K_c$  can simply be acquired as a dimensionless constant depending on the appropriate equilibrium unit isotherm constant. Using the Gibbs equation, the relationship between Gibbs energy changes ( $\Delta G^0$ ), enthalpy change ( $\Delta H^0$ ) and entropy changes ( $\Delta S^0$ ) of adsorption can be defined as follows:

$$\Delta G^0 = \Delta H^0 - T \Delta S^0 \quad (16)$$

By substituting Equation 15 into Equation 16, the famous Van't Hoff correlation is derived (Equation 17):

$$\ln K_c = \frac{-\Delta H^0}{R} \times \frac{1}{T} + \frac{\Delta S^0}{R} \quad (17)$$

$\Delta G^0$  is calculated directly from Equation 15, while  $\Delta H^0$  and  $\Delta S^0$  are calculated from the slope and intercept of a plot of  $\ln K_c$  against  $1/T$  (Equation 17).

## RESULTS AND DISCUSSION

### Physical Properties of the Adsorbent

Some properties (bulk density, moisture, and ash content) of the prepared AC were presented in Table 1. These results were consistent with the findings of Dekhyl and Mohamed (29) and Ali and Fatthee (34). Often activated carbon is condensed to obtain a larger storage capacity for the same volume (30), but a density of 0.40 g/cm<sup>3</sup> was obtained for the prepared AC. Some reports relate the bulk density to the rate of adsorption (35). Bulk density may probably have the same effect on the adsorbent used in this study. The value of moisture content was relatively low; according to Moyo, Chikazaza (35), moisture content does not affect adsorption capacity. As shown in Table 1, the ash content was low, indicating that a significant portion of the inorganic materials and ash components were removed during the washing step by NaOH and HCl solutions (36). The low ash level increases the activity of the carbon.

**Table 1:** The physical properties of the prepared charcoal.

Ash content (%)	Moisture content (%)	Density (g/cm <sup>3</sup> )
5.65 ± 0.04	8.05 ± 0.18	0.40 ± 0.01

\*Values are mean ± SD

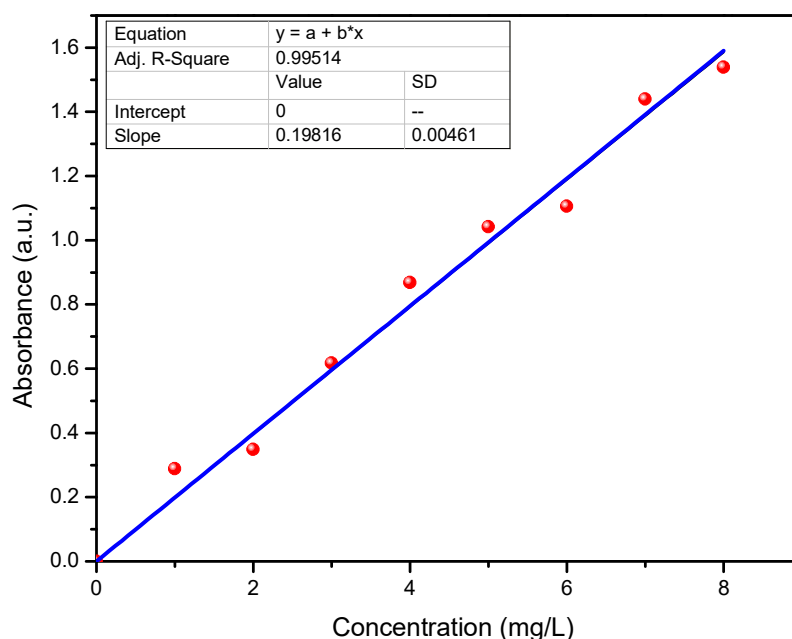
### Standard Calibration Curve for MB

Figure 1 shows the standard calibration curve for MB. The wavelength scanned for the standard

solutions between 450 – 900 nm showed absorption maxima,  $\lambda_{max}$ , at 664 nm. The Beer's law was verified from the calibration curve by

plotting graphs between concentration against absorbance, whereby a linear curve passed through the origin ( $y = 0.19816 x$ ) was obtained.

Beer's law was obeyed in the concentration range 1.00 – 8.00 mg/L.



**Figure 1:** Standard calibration curve for methylene blue.

#### Effect of Initial Solution Concentration

It is obvious that the percentage of removed adsorbate (MB) from aqueous solution by AC derived from pomegranate peel depends on the initial concentration of the dye solution, as shown in Figure 2. The removal% is high (94.45 – 85.87%) at low initial concentrations of MB solution (10 – 50 mg/L). However, the removal percentage decreased gradually from 61.74% to 6.66% at higher dye concentrations, corresponding to the concentration range of 60 – 150 mg/L. At low concentrations, the dye is adsorbed by the empty active adsorption sites on the adsorbent's surface, while at higher concentrations, the adsorption rate decreases due to the saturation of adsorption sites. The accumulation of MB dye molecules on the surface of the activated charcoal may be attributed to the lack of sufficient surface area to accommodate much more dye molecules available in the solution (37, 38). However, utilization of removal% to express adsorption capacity should be utilized cautiously as it is very approximate and can cause ambiguous assumptions about relative adsorption performance (39). So utilization removal% in the study of adsorption equilibria can lead to inaccurate observations and conclusions. The substrate's

quantity adsorbed onto an adsorbent depended on the equilibrium concentrations of dye's ( $q_e$ ), the pH of solution, and temperature. Thus, adsorption isotherm should be assumed as a relationship between dye ( $C_e$ ) equilibrium concentration and the equilibrium adsorbed amounts per unit mass of adsorbent ( $q_e$ ) at carefully controlled environmental parameters of the system, namely the pH of the solution and temperature. The results demonstrate that adsorption performance of MB on AC derived from pomegranate peel depends on the equilibrium concentration of the dye solution, as in Figure 5. The maximum adsorption performance of MB ( $q_e = 5.03$  mg/g) at 60 °C was observed in the MB dye initial concentration of 90 mg/L, where  $C_e$  is 40.00 mg/L. At 25 °C, the adsorption uptakes of MB at equilibrium increased from 1.84 to 4.32 mg/g as the equilibrium dye concentration was increased from 1.62 to 46.82 mg/L. In contrast, the saturation of the active positions on the surface occurs in this case (40), the ratio of MB molecules in solution to unoccupied active positions of adsorbent becomes large, and subsequently, the quantity of adsorbate adsorbed at equilibrium ( $q_e$ ; mg/g) becomes independent of MB concentration (41, 42).

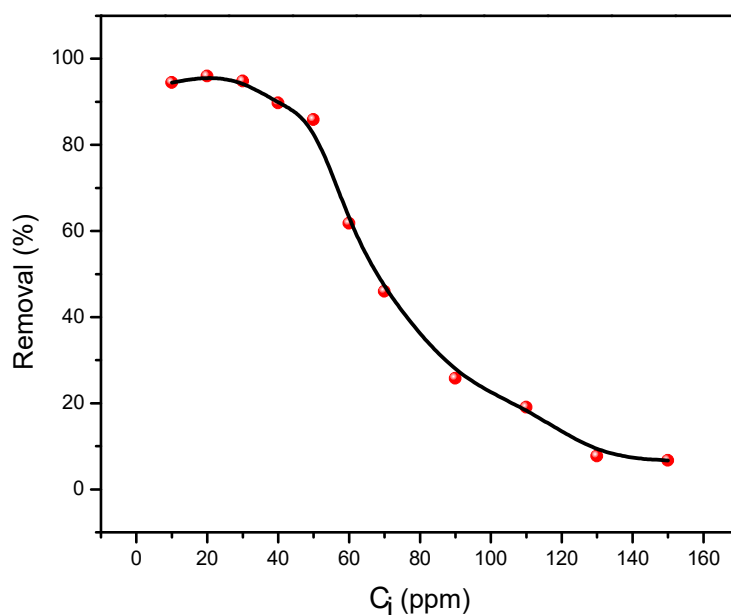


**Figure 2:** The effect of initial concentration on adsorption of MB on activated charcoal at 30°C

#### Effect of Contact Time

In order to study the effect of contact time on the MB uptake, 50 mL of MB solutions with an initial concentration of 20 mg/L was shaken with 0.5 g of AC for different time periods ranging from 1 minute to 120 minutes at constant temperatures of 35 °C and 60 °C separately, with a rotation speed of 120 rpm, and the solution pH was kept original without any pH adjustment. It is evident from Figure 6 that the adsorption capacity of MB increased with a contact time quickly at the beginning, and after that, the rate was gradually lowered, and finally, the curve becomes parallel to the time axis when the system attained equilibrium. Based on the result, suggestion adsorption occurs quickly at the initial stage on the adsorbent's external surface, followed by a slower internal diffusion process, which is perhaps the rate-determining step (32). Moreover, the rapid adsorption at the initial stage may also be because a large number of surface sites are available for adsorption, but after a lapse of time, the remaining surface positions are challenging to be occupied. It was found that the equilibrium state was reached

after about 50 minutes with a removal% of > 96.5%. This result agrees with that reported by many authors (43).

#### Effect of Temperature

The temperature of the solution is an essential factor that affects the absorption efficiency; Figure 3 exhibits the correlation between the solution temperature and the percentage of MB removal at temperatures of 20, 30, 40, 50, and 60 °C when the initial dye concentration was 20 mg/L, as shown, increasing solution temperature from 20 to 60 °C leads to an increase in the equilibrium adsorption capacity, this suggests that the adsorption process, in this case, is endothermic (44) as confirmed by the thermodynamic parameter values, determined later. This increase in adsorption capacity may suggest that increasing the kinetic energy of MB molecules with increasing temperature contributes to an increase in the adsorption rate on the adsorbent surface by increasing the number of molecules that obtain adequate energy to adsorb to the active positions on the surface.

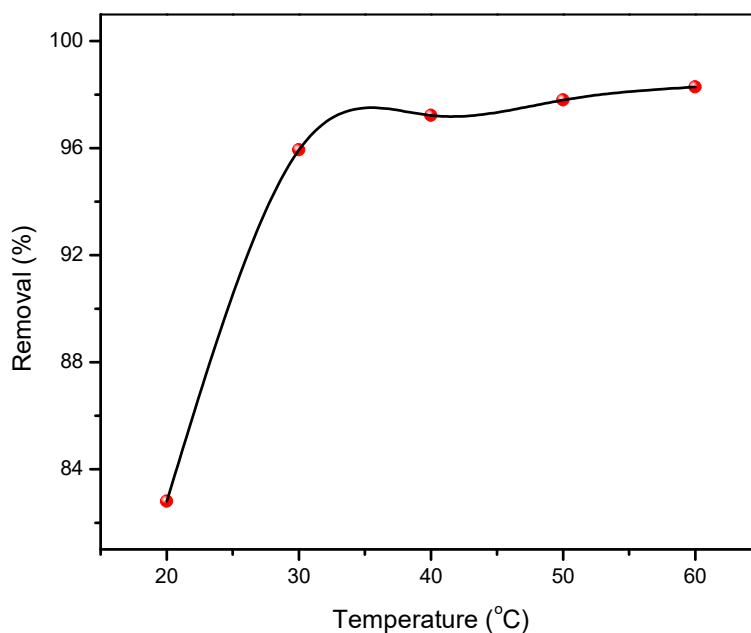


**Figure 3:** Effect of solution temperature on MB adsorption onto AC at constant other parameters.

#### Effect of Particle Size

The MB removal percentages of 250, 125, 63, and 50 mesh particles at the contact time of 2 h were 87.51, 95.94, 87.64, and 80.45%, respectively (Figure 4). The effect of particle size on the adsorption process was studied using a fixed concentration of MB solutions (20 mg/L) and a constant weight (0.5 g) of the adsorbent material. It is evident from the obtained results that particle size influences the adsorption efficiency, and there is a direct relative association between particle size

and surface area. The adsorption increases until it attains a maximum at a particle size of 125  $\mu\text{m}$ , which has the highest available surface area for adsorption and an ideal number and size of pores; thus, the ratio of active sites to volume increases relatively, and then begins to decrease with the increase in particle size due to the decrease in surface area compared to volume, this observation is consistent with what was reported by Emad and Stephen (45).

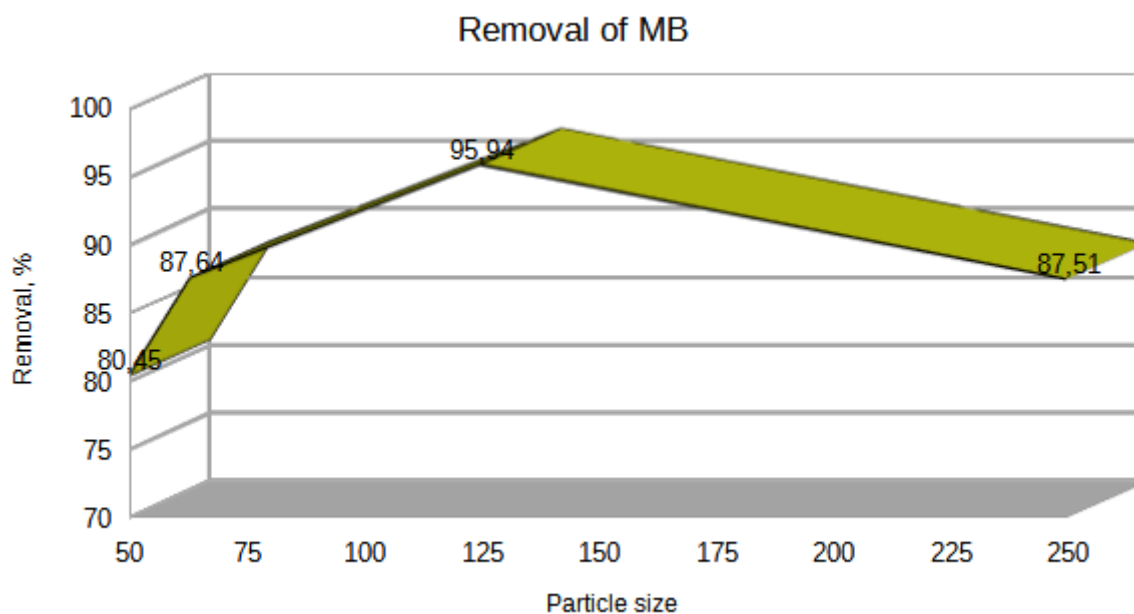


**Figure 4:** Effect of particle size of AC on removal% of MB.



### Adsorption Isotherms

Adsorption isotherm illustrates the variation of  $\theta$  (the fractional coverage of the surface) with an equilibrium concentration of adsorbate ( $C_e$ ; mg/L) at a chosen temperature.  $\theta$  can be expressed as the quantity of adsorbate adsorbed by adsorbent ( $q_e$ ; mg/g). In the literature, the most used and studied isotherm equation is Langmuir equation. Several additional isotherm models are also well explored in the literature, for instance Freundlich isotherm, Sips isotherm, Liu isotherm, and Redlich-Peterson isotherm (46). The adsorption capacity depends on the equilibrium concentration of the adsorbate, the pH, and the solution's temperature. Therefore, the adsorption system's environmental parameters must be carefully monitored at specified values throughout the experiment period (47). The adsorption models' parameters provide valuable information on the adsorbate-adsorbent interactions, surface properties, and adsorption mechanism. However, it is less valuable than kinetics and thermodynamics in clarifying the adsorption mechanism. The  $q_e$  versus  $C_e$  graph of the whole adsorption isotherm plays a significant role in determining the regions where the empirical data for the adsorption equilibrium is actually present (48). Vasanth Kumar and Sivanesan (49) have proposed that using the equilibrium data covering the entire isotherm is the best method to achieve the parameters in isotherm expressions. In this research, the nonlinear form of well-known equilibrium isotherm models (Langmuir (Equation 9) and Freundlich (Equation 11)) was conducted to elucidate the adsorptive behavior of MB dye onto the AC and to calculate the adsorption isotherms parameters to avoid the most common error in analyzing adsorption equilibrium data associated with the use of linear formulas of models. According to Langmuir, adsorption takes place over a homogenous surface through monolayer adsorption, where all the adsorption positions are duplicate and energetically equivalent. The nonlinear form of the Langmuir model is shown in Equation 9. Conversely, the Freundlich model is an experimental equation constructed on a heterogeneous surface. Its nonlinear form is described in Equation 11. Langmuir constant,  $K_L$  (L/mg) is correlated to the association amongst adsorbents and adsorbates whereas Freundlich constants,  $K_F$  ((mg/g)/(mg/L) $n$ ) and  $n$ , (dimensionless;  $0 < n < 1$ ) are correlated to adsorption capacity and adsorption intensity, respectively (31). The Freundlich constant,  $n$ ,

which characterizes the adsorption strength, illustrates the intensity of adsorption's driving force or surface's heterogeneity (adsorption isotherm becomes linear when  $n = 1$ , favorable when  $n < 1$ , and unfavorable when  $n > 1$ ).

When studying the adsorption equilibrium using the Langmuir model, it is appropriate to compute the value of the separation factor  $R_L$  (dimensionless), through which the basic properties of the Langmuir isotherm are expressed. The separation factor is defined in Equation 18 as follows:

$$R_L = \frac{1}{1 + K_L C_0} \quad (18)$$

Where  $R_L$  is a separation factor (dimensionless) of a solid-liquid adsorption system,  $K_L$  is the equilibrium constant of Langmuir, and  $C_0$  is the initial concentration of MB. The separation factor,  $R_L$  was utilized to predict whether the adsorption system was favorable ( $0 < R_L < 1$ ), unfavorable ( $R_L > 1$ ), linear ( $R_L = 1$ ), or irreversible ( $R_L = 0$ ) (31).

The adsorption isotherms (Langmuir and Freundlich) plots for the adsorption of MB onto AC obtained from pomegranate peel at different temperatures are shown in Figure 5 (a) and (b), respectively. It is evident that the experimental data are highly consistent with the adsorption equilibrium in the region expressed with the Langmuir model, which is described via saturation at high concentrations. This assumption is supported by the higher value of adjusted determination coefficients ( $R^2_{adj}=0.97955$ ) and lower chi-square values ( $\chi^2=0.02766$ ) of the Langmuir model compared to those of Freundlich model ( $R^2_{adj}=0.72963$ ;  $\chi^2=0.36572$ ). In addition, the exponent value,  $n = 0.1667$  (a parameter of the Freundlich equation), was less than 1, reflecting favorable conditions for adsorption. Also, the values of separation factor ( $R_L$ ), calculated from Langmuir constant  $K_L$ , for different initial concentrations were lying in the range of ( $0 < R_L < 1$ ), indicates that the adsorption was favorable, as shown in Table 2. Therefore, mathematically, the Langmuir model is better than the Freundlich model to describe the adsorption isotherm of MB dye on AC., i.e., and the observed adsorption behavior was predominantly monolayer chemisorption.

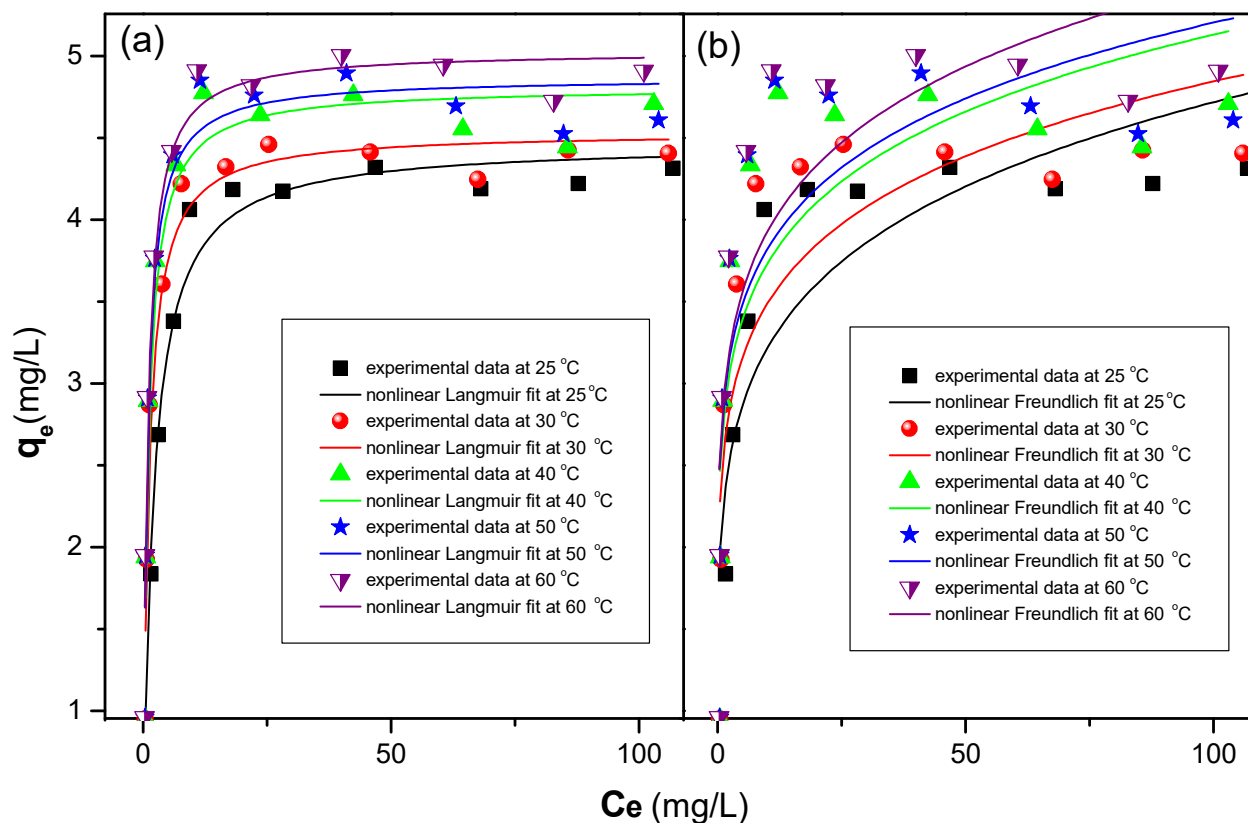


**Figure 5:** Adsorption equilibrium isotherm of MB dye on AC, pH 5.01;  $C_i$  20 mg/L; and contact time 120 min. (a) Langmuir isotherm, (b) Freundlich isotherm.

**Table 2:** Isotherm parameters for adsorption of methylene blue on AC at 25 °C.

T °C	Langmuir parameters					Freundlich parameters			
	$Q_{max}$ (mg/g)	$K_L$ (L/mg)	$x^2$	$R^2$	$R_L$	$K_F$ (mg/g)/(mg/L) <sup>n</sup>	n	$x^2$	$R^2$
25	4.47	0.50	0.027	0.979	0.167 - 0.013	2.189	0.167	0.366	0.729
30	4.54	0.95	0.059	0.959	0.095 - 0.007	2.507	0.143	0.456	0.683
40	4.81	1.07	0.107	0.937	0.085 - 0.000	2.710	0.139	0.610	0.643
50	4.87	1.23	0.095	0.947	0.075 - 0.005	2.800	0.135	0.643	0.639
60	5.03	1.22	0.083	0.958	0.076 - 0.005	2.827	0.142	0.602	0.692

### Kinetics of Adsorption

The study of adsorption kinetic provides precious information about the mechanism of the adsorption process. Numerous kinetic models were developed to obtain essential real values of the adsorption kinetic constants. In the present study, two well-known kinetic models (pseudo-first-order 'PFO' and pseudo-second-order 'PSO') and the general-order kinetic equation, GO, were utilized to discuss the adsorption kinetic of MB onto AC. The kinetic experiments implemented at the optimal conditions (pH ~ 5, initial concentration of dye,  $C_i$  20 mg/L, AC particles with 125  $\mu$ m, and contact time of 2 h) at temperatures of 35 °C and 60 °C. The common mistake in analyzing adsorption kinetics data is the use of linearized forms of kinetic models due to complexities associated with recognizing the error structure in the data when converting a nonlinear equation into a linear equation using various transformations and the extent to which mathematical manipulation of the data influences

the structure of the equation (46). Linearization requires an equal variance for all  $q_t$  values through the data set, which is really not equal in complete range. This might consequence in an incorrect assessment of the best fit as evaluated by the correlation coefficient (R), resulting in an error in the determination coefficient ( $R^2$ ) as well as in the adjusted determination coefficient ( $R^2_{adj}$ ). Therefore, higher  $R^2$  values do not inevitably mean a better match for experimental data. Nonlinear kinetic models were therefore used in this analysis. The fitting results of experimental data and the predicted nonlinear PSO plot of adsorption of MB dye onto AC at pH 5.0 and temperatures of 35 °C and 60 °C were presented in Figure 6 (a). The experimental data and nonlinear PFO, and the GO kinetic plots for the same data and conditions were shown in Figure 6 (b) and Figure 7, respectively. Moreover, the kinetic parameters;  $k_2$ ,  $k_1$ ,  $k_N$ ,  $q_e$ , and n, along with the values of statistical parameters, were enlisted in Table 3. It is evident,

from the results, that the relatively higher  $R^2_{adj}$  and lower  $\chi^2$  values of the nonlinear PSO equation compared to that of the PFO confirm the nonlinear PSO kinetic expression as the best-fit expression to represent the kinetic uptake of MB onto prepared AC. The adjusted determination coefficients ( $R^2_{adj}$ ) for the PSO model (0.9348 and 0.9626 at 208 and 333 K respectively) were much more significant than that for the PFO model (0.6854 and 0.8538), indicating that MB adsorption onto AC can be explained as a pseudo-second-order model. Furthermore, the low values of reduced chi-square ( $\chi^2$ ) for PSO fit (0.0026 and 0.0027) compared with that of PFO (0.0124 and 0.0106) indicate that the adsorption capacities,  $q_{e,cal}$ , calculated by PSO model were similar to the experimental data,  $q_{e,exp}$ . For the plots shown in Figure 7, the general-order

adsorption kinetics model at 333 K showed low  $\chi^2$  values (0.0026), and high  $R^2_{adj}$  value (0.964), the adsorption uptake at equilibrium ( $q_e$ ) is 2.00611 mg/g, the constant rate  $k_N$  is 0.60946 (g/mg)1.8574/min and the order of kinetic model ( $n$ ) is 1.8574. The value of  $n$  (1.86) is closer to 2 than 1, reinforcing the previous observation that the PSO kinetic model presented best-fit than PFO. Thus, the  $n$ -value of 1.857 may as well be due to changes in adsorption kinetics from PSO to PFO during the adsorbate-adsorbent contact period. Therefore, it can be possible to characterize the MB adsorption onto AC as a pseudo-second-order model. It can be inferred that the adsorption process can take place faster at elevated temperatures based on the adsorption rate constant of PSO,  $k_2$ , at 308 K and 333 K.

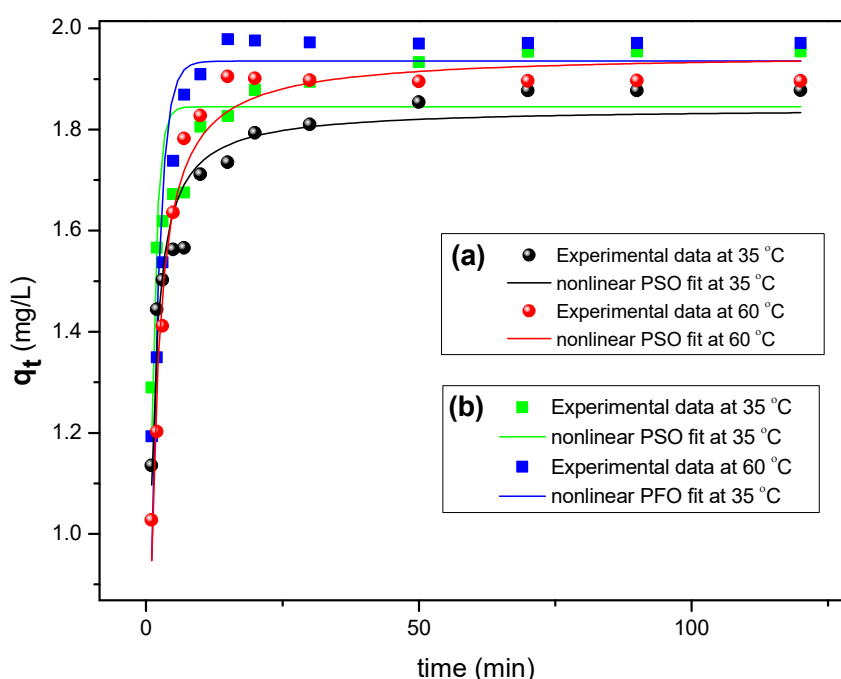


**Figure 6:** Application of kinetic models for adsorption of MB onto AC at 35 and 60 °C. (a) Nonlinear pseudo-second-order fit (b) Nonlinear pseudo-first-order fit.

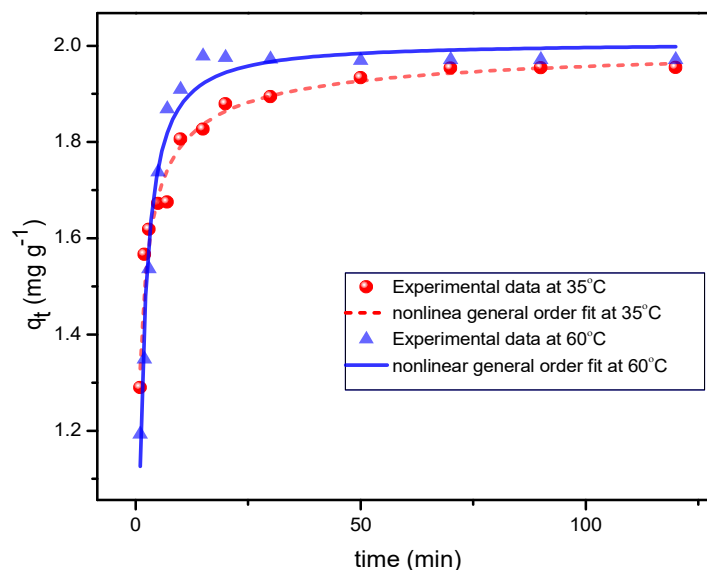


**Figure 7:** Nonlinear general-order fit for sorption of MB onto AC (35 and 60 °C).

**Table 3:** Kinetic parameters for the adsorption of MB onto AC at various conditions from a nonlinear method

Parameter	At 308 K		At 333 K	
	Value	Standard Error	Value	Standard Error
$C_i$ (mg/L)	20.00		20.00	
$q_{e,exp}$ (mg/g)	1.77	0.19	1.80	0.27
<b>Pseudo-second-order</b>				
$q_{e,cal}$ (mg/g)	1.92	0.02	2.02	0.02
$k_2$ (g/mg. min.)	0.6178	0.1032	0.9760	0.0546
$R_{adj}^2$	0.9348		0.9626	
$\chi^2$	0.0026		0.0027	
<b>Pseudo-first-order</b>				
$q_{e,cal}$ (mg/g)	1.85	0.03	1.9355	0.03362
$k_1$ (min <sup>-1</sup> )	1.0325	0.1432	0.6726	0.06926
$R_{adj}^2$	0.6854		0.8538	
$\chi^2$	0.0124		0.0106	
<b>General-order</b>				
$q_{e,cal}$ (mg/g)	2.01846	0.04743	2.00611	0.03052
$k_N$ ((g/mg) <sup>n</sup> /min.)	0.4899	0.13874	0.60946	0.06289
$N$	2.71673	0.38239	1.8574	0.1792
$R_{adj}^2$	0.96922		0.96402	
$\chi^2$	0.00122		0.00261	

### Diffusion Study

The diffusion mechanism of MB adsorption onto the AC was explored using linearized transformation of the intra-particle diffusion model presented in Equation (19).

$$q_t = k_p \sqrt{t} + C \quad (19)$$

Where  $k_p$  (mg/g min<sup>1/2</sup>) is the rate constant of the intra-particle diffusion and  $C$  (mg/g) is a constant associated with the thickness of the boundary layer. The fitting of the kinetic data into the intra-particle diffusion model can be useful for

identifying the adsorption mechanisms and predicting the rate limiting step of the adsorption process. In general there are four steps involved in transport processes during adsorption by porous adsorbents were proposed: (a) bulk transport of adsorbate in the solution phase to the liquid film enclosing the adsorbent, which can occur very fast, therefore it has no effect in kinetic. (b) film diffusion or boundary layer diffusion (occurs slowly) in which the adsorbate transport from the bulk liquid phase across the hydrodynamic boundary film to the external surface of the adsorbent. (d) intra-particle diffusion (occurs

slowly); here the adsorbate molecules transport from exterior surface of the adsorbent into the pores of the adsorbent. (e) adsorptive attachment of adsorbate onto active sites often occurs very quickly; therefore, it is also not significant for kinetic design (16,17).

To determine the rate-controlling step and hence to interpret the mechanism of adsorption process, the intra-particle diffusion model was engaged and the results were showed in Figure 8. The plots of adsorbate uptake ( $q_t$ ) against the square root of time ( $\sqrt{t}$ ) exhibited two different linear portions, and do not pass through the origin. Such a deviation of the straight line from the origin may be considered due to the difference in the rate of diffusion of the dye molecules at the initial stage of the process. The intercepts of the plots (C) (Table 4) are 1.53 and 1.64 mg/g at 35 °C and 60 °C respectively. The multiple linear regions plot revealed that the adsorption process is controlled by a multisteps mechanism not only governed by intra-particle diffusion because the lines do not

pass through the origin. This indicates that the rate controlling steps involve film diffusion step and intra-particle diffusion step. Moreover, the value of C reflects the boundary layer thickness effect. It observed that the boundary layer effect slightly increases with the temperature. The first portion of linear regions in the plot is attributed to the liquid-film diffusion mass transfer; whereas the second linear portion indicates that the intra-particle diffusion of the dye molecules into the pores of the AC controls the adsorption process (41). Intra-particle diffusion rate constants obtained for different temperatures are  $4.99 \times 10^{-2}$  and  $4.20 \times 10^{-2}$  mg/g min<sup>1/2</sup> at 35 °C and 60 °C, respectively (Table 4).

The mechanism of adsorption of MB from aqueous solutions onto AC is controlled by two slow steps of film diffusion and intra-particle diffusion. The first step of bulk transport of MB molecules in the solution phase is considered as fast process, also the last step of adsorption of adsorbate onto internal active sites is occurs very fast.

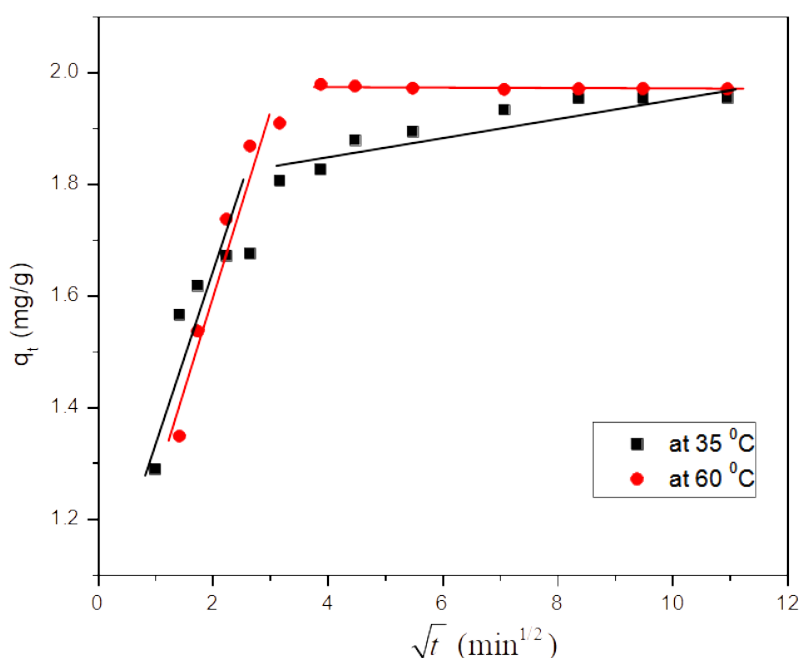


**Figure 8:** Intra-particle diffusion plot for MB adsorption onto AC at 35 °C and 60 °C.

**Table 4:** Intraparticle diffusion model parameters

	<b>K<sub>p</sub> (Slope)</b>	<b>C (Intercept)</b>
At 35 °C	0.04987	1.53348
At 60 °C	0.04199	1.63795

### Thermodynamic Parameters

Thermodynamic studies are a crucial element of predicting adsorption mechanisms (physisorption and chemisorption). The thermodynamic parameters can be determined along with thermodynamics laws using Equations 15, 16, and 17. The precise assessment of thermodynamic

parameters obviously depends directly on the precise calculation of the equilibrium constant among the two phases ( $K_C$ ; dimensionless). The thermodynamic equilibrium constant  $K_C$  values can be obtained from adsorption-isotherm constants or partition coefficient values (50, 51). Accordingly, the  $K_C$  value can be determined from the nonlinear

isotherm equilibrium model constant, which provides best fit for the empirical data (46). Thus,  $K_C$  was calculated from the Langmuir model constant of adsorption equilibrium,  $K_L$  (L/mg) using Equation 20, taking into account the appropriate unit conversion (31, 52):

$$K_C = M_w \times 55.5 \times 1000 \times K_L \quad (20)$$

The factor 55.5 is number of moles of pure water per liter;  $M_w$ , (g/mol.) is adsorbate's molecular weight, methylene blue ( $M_w = 319.85$  g/mol.).

Combining Equation 15 and Equation 20 gives:

$$\Delta G^0 = -RT \ln(M_w \times 55.5 \times 1000 \times K_L) \quad (21)$$

The values of the parameters  $\Delta H^0$  and  $\Delta S^0$  can be computed from the slope and intercept of Van't Hoff equation, Equation 17, respectively. Figure 9 shows the dependence of equilibrium constant on temperature, and Table 5 summarized the information on the thermodynamic parameters of MB adsorption onto the AC process.

The adsorption can be categorized, to a certain point, by the magnitude of enthalpy change. Physisorption, such as van der Waals interaction, characterized by low enthalpy change  $< 20$  kJ/mol, electrostatic interaction ranges from 20 to 80 kJ/mol, and chemisorption bond strengths can be 80 – 450 kJ/mol (53, 54). The positive value of  $\Delta H^0$  (7.53 kJ/mol) suggests the endothermic nature of the process (23), which was further exhibited with an increase in both adsorption capacity (Figure 5 and Table 2) and equilibrium constant (Table 5) as temperature rise. Furthermore, the amount of enthalpy was steady with Van der Waals force (55).

The negative values of  $\Delta G^0$  of MB adsorption onto AC at all investigated temperatures suggest that the adsorption phenomenon occurred favorably and spontaneously with minimal requirements of the adsorption and activation energies. This conclusion was in good agreement with the conclusions drawn from the separation factor analysis ( $0 < R_L < 1$ ). Additionally, the  $\Delta G^0$  and  $K_C$  values dramatically increased as the examination temperatures increased from 30 to 50 °C, demonstrating more energetically favorable adsorption at elevated temperatures.

Furthermore, Nollet, Roels (56) showed that the physisorption process typically had an activation energy of 5 – 40 kJ/mol, whereas chemisorption had relatively higher activation energy (40 – 800 kJ/mol). Hence, the values of  $\Delta H^0$  and  $\Delta G^0$  suggest that a physisorption process drove the adsorption of MB dye onto AC. Simultaneously, the positive value of  $\Delta S^0$  confirmed the increased arbitrariness at the solid-solute interface throughout adsorption and spontaneity of the process. From a thermodynamic point of view, entropy appears to be the driving force for adsorption (57, 58).

#### Determination of Activation Energy

The activation energy for the MB dye adsorption process into AC was estimated from the values of the rate constants at 333 and 308 K using Arrhenius equation as follows (53, 59):

$$k = A e^{-E_a/RT} \quad (22)$$

$$E_a = \frac{R \ln \left( \frac{k_2}{k_1} \right)}{\left( \frac{1}{T_1} + \frac{1}{T_2} \right)} \quad (23)$$

Where  $E_a$  is the activation energy of the adsorption in J/mol;  $k_1$  and  $k_2$  are the rate constant obtained from nonlinear analysis according to the PSO at temperatures of  $T_1$  and  $T_2$  (K) respectively;  $A$  is the Arrhenius constant, temperature-independent factor in (g/mg. min.);  $R$  is the universal gas constant (8.314 J/mol. K). The activation energy value, computed according to the Arrhenius equation, was 15.6 kJ/mol using 20 mg/L initial concentration of MB, where it is of the similar magnitude as the activation energy of activated chemical sorption. The positive value of  $E_a$  suggested that temperature rise assists the adsorption. However, the obedience of the experimental data to PSO kinetic model in addition to the value of  $E_a$  of the process does not necessarily suggest that the adsorption process is chemisorption. It is essential to demonstrate the formation of such chemical bonds using specific analytical techniques (FTIR, Raman spectroscopy, and so on) merged with thermodynamic parameters of enthalpy and entropy changes to decide whether the process is chemisorption or physisorption.



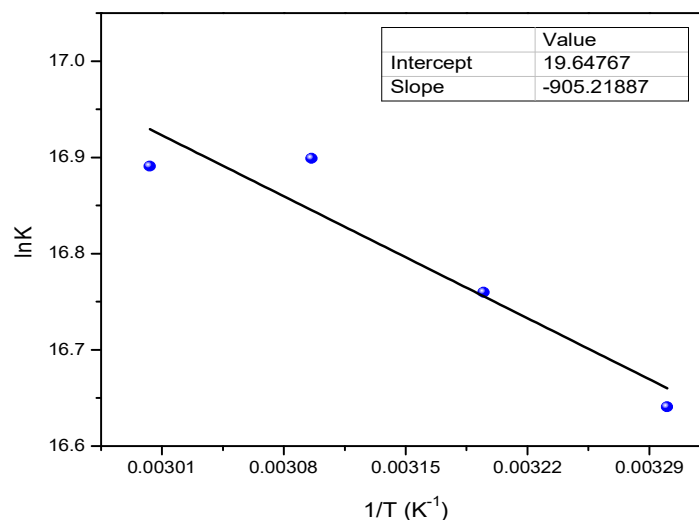


**Figure 9:** Van't Hoff plot for adsorption of MB dye onto AC.

**Table 5:** Thermodynamic parameters for adsorption of MB onto the synthesized AC.

T (K)	K <sub>c</sub>	ΔG° (kJ/mol)	ΔH° (kJ/mol)	ΔS° (J/mol. K)
298	8875838	- 39.64		
303	16864091	- 41.92		
313	18994292	- 43.61	7.53	163.35
323	21834560	- 45.38		
333	21657044	- 46.76		

## CONCLUSION

The adsorption of methylene blue from aqueous solution onto activated carbon prepared from pomegranate peel was investigated. The equilibrium isotherm, kinetics, and thermodynamics parameters of adsorption were determined using nonlinear regression analysis. The system attained equilibrium state after 50 minutes with a removal% of > 96.5%. The maximum uptake of MB at equilibrium ( $q_e = 5.03$  mg/g) was observed at 60 °C using 90 mg/L initial concentration of dye solution and 125 μm particle size of adsorbent. The adsorption equilibrium study revealed that the Langmuir model was best fitted to the equilibrium data of adsorption, Langmuir constant  $K_L = 1.22$  L/mg at 60 °C. The kinetic data has been best explained by pseudo-second-order kinetic model ( $R_{2,adj} = 0.9626$  and  $x^2 = 0.0027$  at 333 K). The mechanism of adsorption process involve both external film diffusion and intra-particle or pore diffusion as limiting steps. The values of the thermodynamic equilibrium constant ( $K_c$ ) were determined from Langmuir adsorption-isotherm constants. The thermodynamics parameters showed that the adsorption of MB onto AC was spontaneous ( $\Delta G^\circ$  between - 39.64 kJ/mol to - 46.76 kJ/mol) and endothermic ( $\Delta H^\circ = +7.53$  kJ/mol) in nature. Moreover, the ( $+\Delta S^\circ$ ) value (163.35 J/mol.K) indicated an increased randomness at the solid-solution interface during the adsorption process.

## ACKNOWLEDGMENTS

The authors express their sincere gratitude to the Department of Applied Chemistry, International University of Africa, in Sudan, for financially supporting this study.

## AUTHORS CONTRIBUTION STATEMENT

Ibrahim Y. Erwa conceptualized and designed this work. Omar A. Alrefaei and Issa M. Hassan conducted the experimental works and prepared the draft of the manuscript. Omer A. Ishag manages literature review and revised manuscripts. All authors discussed the methodology and results and approved the final manuscript.

## CONFLICT OF INTEREST

The authors declare no conflict of interest.

## REFERENCES

1. Kanakaraju D, Yahya MS, Wong S-P. Removal of chemical oxygen demand from agro effluent by ZnO photocatalysis and photo-Fenton. SN Appl Sci. 2019 Jul;1(7):738. <DOI>.
2. Bolisetty S, Peydayesh M, Mezzenga R. Sustainable technologies for water purification from heavy metals: review and analysis. Chem Soc Rev. 2019;48(2):463-87. <DOI>.

3. Haseena M, Malik MF, Javed A, Arshad S, Asif N, Zulfiqar S, et al. Water pollution and human health. *Environmental Risk Assessment and Remediation*. 2017;1(3):16–9. [<DOI>](#).
4. Guivarch E, Trevin S, Lahitte C, Oturan MA. Degradation of azo dyes in water by Electro-Fenton process. *Environmental Chemistry Letters*. 2003 Mar 1;1(1):38–44. [<DOI>](#).
5. Tara N, Siddiqui SI, Rathi G, Chaudhry SA, Inamuddin, Asiri AM. Nano-engineered Adsorbent for the Removal of Dyes from Water: A Review. *CAC*. 2020 Jan 8;16(1):14–40. [<DOI>](#).
6. Dawood S, Sen T. Review on Dye Removal from Its Aqueous Solution into Alternative Cost Effective and Non-Conventional Adsorbents. *Journal of Chemical and Process Engineering*. 2014;1(104):1–11.
7. Rafatullah Mohd, Sulaiman O, Hashim R, Ahmad A. Adsorption of methylene blue on low-cost adsorbents: A review. *Journal of Hazardous Materials*. 2010 May;177(1–3):70–80. [<DOI>](#).
8. Gupta VK, Kumar R, Nayak A, Saleh TA, Barakat MA. Adsorptive removal of dyes from aqueous solution onto carbon nanotubes: A review. *Advances in Colloid and Interface Science*. 2013 Jun;193–194:24–34. [<DOI>](#).
9. Babu BR, Parande A, Raghu S, Kumar TP. Textile technology-an overview of wastes produced during cotton textile processing and effluent treatment methods. *Journal of Cotton Sciences*. 2007;11:110.
10. Kasih TP, Kharisma A, Perdana MK, Murphiyanto RDJ. Development of non-thermal plasma jet and its potential application for color degradation of organic pollutant in wastewater treatment. *IOP Conference Series: Earth and Environmental Science*. 2017 Dec;109:012004. [<DOI>](#).
11. Beluci N de CL, Mateus GAP, Miyashiro CS, Homem NC, Gomes RG, Fagundes-Klen MR, et al. Hybrid treatment of coagulation/flocculation process followed by ultrafiltration in TiO<sub>2</sub>-modified membranes to improve the removal of reactive black 5 dye. *Science of The Total Environment*. 2019 May;664:222–9. [<DOI>](#).
12. Erwa IY, Ibrahim AA. Removal of chromium (VI) ions from aqueous solution using wood sawdust as adsorbent. *Journal of Natural and Medical Sciences*. 2016;17(2):112.
13. Jawad AH, Abdulhameed AS, Mastuli MS. Acid-fractionalized biomass material for methylene blue dye removal: a comprehensive adsorption and mechanism study. *Journal of Taibah University for Science*. 2020 Jan 1;14(1):305–13. [<DOI>](#).
14. Segun Esan O, Nurudeen Abiola O, Owoyomi O, Olumuyiwa Aboluwoye C, Olubunmi Osundiya M. Adsorption of Brilliant Green onto Luffa Cylindrical Sponge: Equilibrium, Kinetics, and Thermodynamic Studies. *ISRN Physical Chemistry*. 2014 Mar 4;2014:1–12. [<DOI>](#).
15. Mahmoud ME, Nabil GM, Khalifa MA, El-Mallah NM, Hassouba HM. Effective removal of crystal violet and methylene blue dyes from water by surface functionalized zirconium silicate nanocomposite. *Journal of Environmental Chemical Engineering*. 2019 Apr;7(2):103009. [<DOI>](#).
16. Yunusa U, Usman B, Ibrahim M. Modeling and Regeneration Studies for the Removal of Crystal Violet Using Balanites aegyptiaca Seed Shell Activated Carbon. *JOTCSA*. 2020 Dec 29;8(1):197–210. [<DOI>](#).
17. Felix N, Ienna N, Ikelle I, Anselm O, Nwabueze E, Emeka I, et al. Activated Plantain Peel Biochar As Adsorbent For Removal of Zinc(II) Ions From Aqueous Solution: Equilibrium and Kinetics Studies. *JOTCSA*. 2018 Oct 30;5(3):1257–70. [<DOI>](#).
18. Gökirmak Söğüt E, Çalışkan Kiliç N. Equilibrium and Kinetic Studies of a Cationic Dye Adsorption Onto Raw Clay. *JOTCSA*. 2020 Jul 13;7(3):713–26. [<DOI>](#).
19. He Y-C, Yang J, Kan W-Q, Zhang H-M, Liu Y-Y, Ma J-F. A new microporous anionic metal-organic framework as a platform for highly selective adsorption and separation of organic dyes. *J Mater Chem A*. 2015;3(4):1675–81. [<DOI>](#).
20. Huber F, Berwanger J, Polesya S, Mankovsky S, Ebert H, Giessibl FJ. Chemical bond formation showing a transition from physisorption to chemisorption. *Science*. 2019 Oct 11;366(6462):235–8. [<DOI>](#).
21. Kosheleva RI, Mitropoulos AC, Kyzas GZ. Synthesis of activated carbon from food waste. *Environ Chem Lett*. 2019 Mar;17(1):429–38. [<DOI>](#).
22. Heidarinejad Z, Dehghani MH, Heidari M, Javedan G, Ali I, Sillanpää M. Methods for preparation and activation of activated carbon: a review. *Environ Chem Lett*. 2020 Mar;18(2):393–415. [<DOI>](#).
23. Ali AF, Kovo AS, Adetunji SA. Methylene Blue and Brilliant Green Dyes Removal from Aqueous Solution Using Agricultural Wastes Activated Carbon. *JEAS*. 2017;07(02):95–107. [<DOI>](#).
24. Ponnusami V, Krithika V, Madhuram R, Srivastava SN. Biosorption of reactive dye using acid-treated rice husk: Factorial design analysis. *Journal of Hazardous Materials*. 2007 Apr;142(1–2):397–403. [<DOI>](#).
25. Bharti V, Vikrant K, Goswami M, Tiwari H, Sonwani RK, Lee J, et al. Biodegradation of methylene blue dye in a batch and continuous mode using biochar as packing media. *Environmental Research*. 2019 Apr;171:356–64. [<DOI>](#).
26. Clifton JI, Leikin JB. Methylene Blue. *American Journal of Therapeutics*. 2003;10(4):289–91. [<URL>](#).
27. Hama Aziz KH, Mahyar A, Miessner H, Mueller S, Kalass D, Moeller D, et al. Application of a planar falling film reactor for decomposition and mineralization of methylene blue in the aqueous media via ozonation, Fenton, photocatalysis and non-thermal plasma: A comparative study. *Process Safety and Environmental Protection*. 2018 Jan;113:319–29. [<DOI>](#).
28. Yagub MT, Sen TK, Ang HM. Equilibrium, Kinetics, and Thermodynamics of Methylene Blue Adsorption by

- Pine Tree Leaves. *Water Air Soil Pollut.* 2012 Oct;223(8):5267-82. [<DOI>](#).
29. Dekhyl A, Mohamed H, Alwan L. Preparation of activated charcoal as a new adsorbent from the natural plant sources. *Tikrit Journal of Pure Science.* 2017;22(10):110-5. [<URL>](#).
30. Sogbochi E. Evaluation of Adsorption Capacity of Methylene Blue in Aqueous Medium by Two Adsorbents: The Raw Hull of *Lophira lanceolata* and Its Activated Carbon. *AJPC.* 2017;6(5):76. [<DOI>](#).
31. Tran HN, You S-J, Chao H-P. Fast and efficient adsorption of methylene green 5 on activated carbon prepared from new chemical activation method. *Journal of Environmental Management.* 2017 Mar;188:322-36. [<DOI>](#).
32. Yuan N, Cai H, Liu T, Huang Q, Zhang X. Adsorptive removal of methylene blue from aqueous solution using coal fly ash-derived mesoporous silica material. *Adsorption Science & Technology.* 2019 May;37(3-4):333-48. [<DOI>](#).
33. Tran HN, You S-J, Chao H-P. Thermodynamic parameters of cadmium adsorption onto orange peel calculated from various methods: A comparison study. *Journal of Environmental Chemical Engineering.* 2016 Sep;4(3):2671-82. [<DOI>](#).
34. Ali MM, Fatthee FE, AbdulkarimThunoon A. Preparation of Activated Carbon from (*Punica granatum*. sp) Wood by Chemical Treatment Using Potassium Hydroxide. *Tikrit Journal of Pure Science.* 2019;24(6):45-50.
35. Moyo M, Chikazaza L, Nyamunda BC, Guyo U. Adsorption Batch Studies on the Removal of Pb(II) Using Maize Tassel Based Activated Carbon. *Journal of Chemistry.* 2013;2013:1-8. [<DOI>](#).
36. Dkheel A-AB. Preparation Of A Charcoal From Pine Wood Via Chemical Treatment. *Tikrit Journal of Pure Science.* 2012;17(3):153-5.
37. Salleh MAM, Mahmoud DK, Karim WAWA, Idris A. Cationic and anionic dye adsorption by agricultural solid wastes: A comprehensive review. *Desalination.* 2011 Oct;280(1-3):1-13. [<DOI>](#).
38. Zhang Y, Liu J, Du X, Shao W. Preparation of reusable glass hollow fiber membranes and methylene blue adsorption. *Journal of the European Ceramic Society.* 2019 Dec;39(15):4891-900. [<DOI>](#).
39. Hai TN. Comments on "Effect of Temperature on the Adsorption of Methylene Blue Dye onto Sulfuric Acid-Treated Orange Peel." *Chemical Engineering Communications.* 2017 Jan 2;204(1):134-9. [<DOI>](#).
40. Eren Z, Acar FN. Adsorption of Reactive Black 5 from an aqueous solution: equilibrium and kinetic studies. *Desalination.* 2006 Jun;194(1-3):1-10. [<DOI>](#).
41. Hamdaoui O, Chiha M. Removal of Methylene Blue from Aqueous Solutions by Wheat Bran. *Acta Chim Slov.* 2007;54(2):407-18.
42. Kuang Y, Zhang X, Zhou S. Adsorption of Methylene Blue in Water onto Activated Carbon by Surfactant Modification. *Water.* 2020 Feb 21;12(2):587. [<DOI>](#).
43. Corda NC, Kini MS. A Review on Adsorption of Cationic Dyes using Activated Carbon. Raghuvir PB, Mathew TM, editors. *MATEC Web Conf.* 2018;144:02022. [<DOI>](#).
44. Rashid RA, Jawad AH, Ishak MAM, Kasim NN. KOH-activated carbon developed from biomass waste: adsorption equilibrium, kinetic and thermodynamic studies for Methylene blue uptake. *Desalination and Water Treatment.* 2016 Dec 1;57(56):27226-36. [<DOI>](#).
45. El Qada EN, Allen SJ, Walker GM. Adsorption of Methylene Blue onto activated carbon produced from steam activated bituminous coal: A study of equilibrium adsorption isotherm. *Chemical Engineering Journal.* 2006 Nov;124(1-3):103-10. [<DOI>](#).
46. Lima ÉC, Adebayo MA, Machado FM. Kinetic and Equilibrium Models of Adsorption. In: Bergmann CP, Machado FM, editors. *Carbon Nanomaterials as Adsorbents for Environmental and Biological Applications* [Internet]. Cham: Springer International Publishing; 2015 [cited 2021 Dec 5]. p. 33-69. (Carbon Nanostructures). [<URL>](#).
47. Milonjić SK. Comments on the authors' response to the comments on "Factors influencing the removal of divalent cations by hydroxyapatite", by Smicklas et al. *Journal of Hazardous Materials.* 2010 Apr 15;176(1-3):1126-7. [<DOI>](#).
48. Kumar KV. Comments on "Adsorption of acid dye onto organobentonite." *Journal of Hazardous Materials.* 2006 Sep;137(1):638-9. [<DOI>](#).
49. Vasanth Kumar K, Sivanesan S. Equilibrium data, isotherm parameters and process design for partial and complete isotherm of methylene blue onto activated carbon. *Journal of Hazardous Materials.* 2006 Jun 30;134(1-3):237-44. [<DOI>](#).
50. Liu Y. Is the Free Energy Change of Adsorption Correctly Calculated? *J Chem Eng Data.* 2009 Jul 9;54(7):1981-5. [<DOI>](#).
51. Doke KM, Khan EM. Adsorption thermodynamics to clean up wastewater; critical review. *Reviews in Environmental Science and Bio/Technology.* 2013;12(1):25-44. [<DOI>](#).
52. Zhou X, Zhou X. The unit problem in the thermodynamic calculation of adsorption using the Langmuir equation. *Chemical Engineering Communications.* 2014 Nov 2;201(11):1459-67. [<DOI>](#).
53. Machado FM, Bergmann CP, Fernandes THM, Lima EC, Royer B, Calvete T, et al. Adsorption of Reactive Red M-2BE dye from water solutions by multi-walled carbon nanotubes and activated carbon. *Journal of Hazardous Materials.* 2011 Sep;192(3):1122-31. [<DOI>](#).
54. Faust SD, Aly OM. *Adsorption Processes for Water Treatment.* [Internet]. Cambridge: Elsevier Science; 2014 [cited 2021 Dec 5]. ISBN: 978-1-4831-6263-8.

55. Kuo C-Y, Wu C-H, Wu J-Y. Adsorption of direct dyes from aqueous solutions by carbon nanotubes: Determination of equilibrium, kinetics and thermodynamics parameters. *Journal of Colloid and Interface Science*. 2008 Nov;327(2):308–15. [<DOI>](#).

56. Nollet H, Roels M, Lutgen P, Van der Meeren P, Verstraete W. Removal of PCBs from wastewater using fly ash. *Chemosphere*. 2003 Nov;53(6):655–65. [<DOI>](#).

57. Fan S, Wang Y, Wang Z, Tang J, Tang J, Li X. Removal of methylene blue from aqueous solution by

sewage sludge-derived biochar: Adsorption kinetics, equilibrium, thermodynamics and mechanism. *Journal of Environmental Chemical Engineering*. 2017 Feb;5(1):601–11. [<DOI>](#).

58. Mouni L, Belkhiri L, Bollinger J-C, Bouzaza A, Assadi A, Tirri A, et al. Removal of Methylene Blue from aqueous solutions by adsorption on Kaolin: Kinetic and equilibrium studies. *Applied Clay Science*. 2018 Mar;153:38–45. [<DOI>](#).

59. Han R, Zhang J, Han P, Wang Y, Zhao Z, Tang M. Study of equilibrium, kinetic and thermodynamic parameters about methylene blue adsorption onto natural zeolite. *Chemical Engineering Journal*. 2009 Jan;145(3):496–504. [<DOI>](#).





## Synthesis and Characterization of Azobenzene Derived from 8-aminoquinoline in Aqueous Media

İdris KARAKAYA<sup>1</sup>  

<sup>1</sup>Department of Chemistry, College of Basic Sciences, Gebze Technical University, 41400 Gebze, Turkey

**Abstract:** A series of novel 8-(aryldiazenyl)quinolones have been synthesized effectively with excellent yields by using 8-aminoquinoline and a variety of aryldiazonium salts containing electron donating and withdrawing moieties in aqueous media. The structure of the synthesized azo dyes has been characterized by NMR, FTIR, mass spectroscopy, and UV-Vis techniques. The compounds' absorption maxima values are in the range of 427 nm and 445 nm due to  $\pi$ - $\pi^*$  charge transfer transition. It can be evaluated that azobenzenes have more absorbance ability in the strong donor systems.

**Keywords:** Azo dye, 8-aminoquinoline, aqueous media, diazonium salt, azobenzene

**Submitted:** October 20, 2021. **Accepted:** December 06 2021.

**Cite this:** Karakaya İ. Synthesis and Characterization of Azobenzene Derived from 8-aminoquinoline in Aqueous Media. JOTCSA. 2022;9(1):85-114.

**DOI:** <https://doi.org/10.18596/jotcsa.1012453>.

**\*Corresponding author. E-mail:** [karakaya@gtu.edu.tr](mailto:karakaya@gtu.edu.tr).

### INTRODUCTION

Azobenzenes are an important class of organic compounds that are widely used as organic dyes (1, 2), protein probes (3, 4), chemosensors (5, 6), cosmetics (7-9), nanotubes (10, 11) and polymers (12-14). Due to the presence of N-N linkages, they have been used for pharmacological applications such as antiviral, anti-inflammatory, antimicrobial, antitumor, antidiabetics, and antituberculous (15-25). Beyond their potential in these application areas, azo-compounds are mostly used as dyes. Until the late 1800s, all dyes were obtained from natural sources. However, limitation of the natural dye sources led scientists to synthesize dyes with a wide variety of new colors. Azo dyes can be easily prepared by using diazo and coupling components that are generally low-cost materials (26). Due to remarkable stability, light resistance and easy diversification of donor and acceptor groups in the organic compounds, azo dyes are one-step ahead of other dyes (27, 28). Currently, the dyes and pigments market are valued for approximately USD \$33 billion (29) and keeping the number and production volume about 70% in mind, azo dyes are

the largest class of organic dye around the world (30). Having such a large market share, as a matter of course increases the tendency towards azo dyes.

Quinoline backbones are considered as one of the main classes of heterocyclic chemistry and are found in many natural products, alkaloids, and synthetic molecules (31-33). Quinoline forms the main framework of drugs used clinically in the treatment of many diseases (34). After first discovering chloroquine as an antimalarial drug in 1934, many other analogues were explored such as mefloquine, piperquine, primaquine and amodiaquine (35-39). Also, they are used as antibiotics such as gatifloxacin, moxifloxacin, ciprofloxacin, sparfloxacin, levofloxacin, and norfloxacin (40-42). In addition, due to the formation of stable complexes with many metals, quinolines are known as the best chelating agents (43-48).

In this regard, herein the author reports the simple, efficient synthesis and characterization of 8-(aryldiazenyl)quinolines (**6a-g**) by using 8-



aminoquinoline (**3a**) and aryldiazonium salts (**5a-g**) in aqueous media.

## EXPERIMENTAL SECTION

### General considerations

All the chemicals used were used as received without further purification. IR spectra were recorded on a PerkinElmer Spectrum 100 FT-IR spectrometer. The UV-Visible absorption spectra were carried out with a Shimadzu UV-3600 UV-Vis NIR spectrophotometer in the wavelength range of 200–800 nm. Melting points were determined by using a Stuart melting point apparatus. NMR spectra were recorded on a 500 MHz Varian or Bruker spectrometer. Mass spectra were recorded on a Bruker microflex LT MALDI spectrometer. The spectra are presented in the Supplementary Section at the end of this article.

### Synthesis of 8-aminoquinoline (**3a**)

Under an ice bath, sulfuric acid (2.0 mL) was added onto quinoline (5 mmol, 1.0 equiv) then 65% nitric acid (3.0 equiv) were added dropwise and stirred for 4h at rt. The mixture was poured into the ice water and neutralized with NaOH; and then extracted with dichloromethane. After dried over Na<sub>2</sub>SO<sub>4</sub> and evaporated in vacuo, used next step without purification(49).

Mixture of nitroquinolines (**2a-b**) and 5% Pd/C was solved in ethanol and suspension was saturated with hydrogen gas under atmospheric pressure at 40 °C until the starting material was consumed. 2 h later, the mixture was filtered and evaporated. The crude product was purified by silica gel column chromatography, eluting with EtOAc in hexanes to yield the desired 8-aminoquinoline **3a** is isolated as a brown solid in a yield of 32% (50).

Obtained as a brown solid (231 mg, 32%); <sup>1</sup>H NMR (500 MHz, CDCl<sub>3</sub>) δ 8.71 – 8.60 (m, 1H), 7.93 (d, *J* = 8.2 Hz, 1H), 7.29 – 7.16 (m, 2H), 7.02 (d, *J* = 8.1 Hz, 1H), 6.80 (d, *J* = 7.4 Hz, 1H), 4.89 (s, 2H).

### General Procedure for Synthesis of Aryl Diazonium Salts (**5a-g**)

The appropriate aniline (2.0 mmol) and 0.68 mL 50% HBF<sub>4</sub> aq. in 2.0 mL distilled water was placed in an ice bath and the temperature was set to 0 °C then sodium nitrite (2.0 mmol) solution in 1.5 mL distilled water was added dropwise. The reaction was stirred 30 min., precipitate was filtered and washed with water (15 mL) and diethyl ether (15 mL). After final filtration, the compound was dried under low pressure and yielded the desired product (51).

*4-tert-butylbenzenediazonium tetrafluoroborate* (**5a**)

Obtained as a white solid (416 mg, 84%); <sup>1</sup>H NMR (500 MHz, DMSO-d<sub>6</sub>) δ 8.58 (d, *J* = 7.3 Hz, 1H), 8.03 (d, *J* = 7.3 Hz, 1H), 1.35 (s, 9H).

*4-Trifluoromethylbenzenediazonium tetrafluoroborate* (**5b**)

Obtained as a white solid (462 mg, 89%); <sup>1</sup>H NMR (500 MHz, DMSO-d<sub>6</sub>) δ 8.90 (d, *J* = 8.0 Hz, 2H), 8.42 (d, *J* = 8.0 Hz, 2H).

*2-Chlorobenzenediazonium tetrafluoroborate* (**5c**)

Obtained as a white solid (294 mg, 65%); <sup>1</sup>H NMR (500 MHz, DMSO-d<sub>6</sub>) δ 8.85 (d, *J* = 8.1 Hz, 1H), 8.28 (d, *J* = 8.2 Hz, 1H), 8.20 (d, *J* = 8.4 Hz, 1H), 7.96 (t, *J* = 6.2 Hz, 1H).

*2-Trifluoromethylbenzenediazonium tetrafluoroborate* (**5d**)

Obtained as a white solid (369 mg, 71%); <sup>1</sup>H NMR (500 MHz, DMSO-d<sub>6</sub>) δ 9.08 (d, *J* = 6.6 Hz, 1H), 8.49 (s, 2H), 8.39 – 8.30 (m, 1H).

*3-Fluorobenzenediazonium tetrafluoroborate* (**5e**)

Obtained as a white solid (231 mg, 55%); <sup>1</sup>H NMR (500 MHz, DMSO-d<sub>6</sub>) δ 8.67 (d, *J* = 6.0 Hz, 1H), 8.59 (d, *J* = 7.8 Hz, 1H), 8.22 (t, *J* = 7.4 Hz, 1H), 8.09 – 8.01 (m, 1H).

*4-Ethynylbenzenediazonium tetrafluoroborate* (**5f**)

Obtained as a pale brown solid (344 mg, 73%); <sup>1</sup>H NMR (500 MHz, DMSO-d<sub>6</sub>) δ 8.67 (d, *J* = 7.9 Hz, 2H), 8.06 (d, *J* = 7.8 Hz, 2H), 5.15 (s, 1H).

*4-Fluorobenzenediazonium tetrafluoroborate* (**5g**)

Obtained as a white solid (243 mg, 58%); <sup>1</sup>H NMR (500 MHz, DMSO-d<sub>6</sub>) δ 8.83 – 8.73 (m, 2H), 7.88 (t, *J* = 8.7 Hz, 2H).

### General Procedure for Synthesis of 8-(aryldiazenyl)quinoline (**6a-g**)

8-aminoquinoline (0.1 mmol, 1.0 equiv) and aryl diazonium salt (0.11 mmol, 1.1 equiv.) was dissolved in 2.0 mL distilled water and stirred 30 min at RT. Extracted with ethyl acetate, dried over Na<sub>2</sub>SO<sub>4</sub> and evaporated in vacuo. The crude product was purified by silica gel column chromatography, eluting with EtOAc in hexanes to yield the desired product.

*(E)-5-((4-(tert-butyl)phenyl)diazenyl) quinolin-8-amine* (**6a**)

Obtained as a reddish-orange solid (28 mg, 92%); mp: 149-151 °C, <sup>1</sup>H NMR (500 MHz, CDCl<sub>3</sub>) δ 9.31 (d, *J* = 8.5 Hz, 1H), 8.85 (s, 1H), 8.01 (d, *J* = 7.5 Hz, 1H), 7.91 (d, *J* = 7.5 Hz, 2H), 7.56 (d, *J* = 7.3 Hz, 3H), 6.97 (d, *J* = 7.5 Hz, 1H), 5.50 (s, 2H), 1.41 (d, *J* = 0.9 Hz, 9H); <sup>13</sup>C NMR (126 MHz, CDCl<sub>3</sub>) δ 153.28, 151.39, 147.82, 147.79, 147.42, 138.43, 137.18, 132.32, 127.98, 125.96, 125.91, 122.22, 122.18, 115.10, 109.02, 34.92, 31.31; IR (neat, cm<sup>-1</sup>) 3478, 3353, 2952, 2919, 2855, 1615, 1587, 1565, 1508, 1473, 1428, 1174, 1126, 846, 785;

MALDI-TOF  $m/z$  calcd for  $C_{19}H_{21}N_4$  ( $[M + H]^+$ ) 305,177, found 305.336.

*(E)-5-((4-(trifluoromethyl)phenyl)diazenyl)quinolin-8-amine (6b)*

Obtained as a maroon solid (31 mg, 98%); mp: 137-139 °C;  $^1H$  NMR (500 MHz,  $CDCl_3$ )  $\delta$  9.28 (d,  $J = 6.5$  Hz, 1H), 8.85 (s, 1H), 8.14 - 7.95 (m, 3H), 7.78 (d,  $J = 7.0$  Hz, 2H), 7.58 (d,  $J = 2.2$  Hz, 1H), 7.02 - 6.84 (m, 1H), 5.69 (s, 2H);  $^{13}C$  NMR (126 MHz,  $CDCl_3$ )  $\delta$  155.33, 148.73, 147.94 (d,  $J = 3.8$  Hz), 138.02, 136.89, 132.14, 130.79 (q,  $J = 32.4$  Hz), 128.37, 126.62 - 125.81 (m), 125.22, 123.05, 122.86 (d,  $J = 5.4$  Hz), 122.54, 116.22, 108.87; IR (neat,  $cm^{-1}$ ) 3433, 3317, 2951, 2918, 2851, 1609, 1553, 1504, 1475, 1440, 1382, 1154, 1104, 1065, 843; MALDI-TOF  $m/z$  calcd for  $C_{16}H_{12}F_3N_4$  ( $[M + H]^+$ ) 317,101, found 317.139.

*(E)-5-((2-chlorophenyl)diazenyl)quinolin-8-amine (6c)*

Obtained as an orange solid (25 mg, 89%); mp: 156-158 °C;  $^1H$  NMR (500 MHz,  $CDCl_3$ ) 9.37 (d,  $J = 8.1$  Hz, 1H), 8.85 (s, 1H), 8.13 (d,  $J = 7.5$  Hz, 1H), 7.83 (d,  $J = 7.0$  Hz, 1H), 7.57 (d,  $J = 4.6$  Hz, 2H), 7.35 (t,  $J = 13.9$  Hz, 2H), 6.98 (d,  $J = 7.0$  Hz, 1H), 5.63 (s, 2H);  $^{13}C$  NMR (126 MHz,  $CDCl_3$ )  $\delta$  149.49, 148.42, 147.88, 138.55, 137.00, 134.40, 132.47, 130.60, 130.27, 127.79, 127.21, 122.95, 118.16, 117.67, 108.96; IR (neat,  $cm^{-1}$ ) 3457, 3301, 2949, 2917, 2845, 1610, 1587, 1508, 1370, 1340, 1244, 1175, 1120, 824, 785, 754; MALDI-TOF  $m/z$  calcd for  $C_{15}H_{12}ClN_4$  ( $[M + H]^+$ ) 283,075, found 282.933.

*(E)-5-((2-(trifluoromethyl)phenyl)diazenyl)quinolin-8-amine (6d)*

Obtained as a rust solid (30 mg, 95%); mp: 145-147 °C;  $^1H$  NMR (500 MHz,  $CDCl_3$ )  $\delta$  9.37 (dd,  $J = 8.6, 1.7$  Hz, 1H), 8.85 (dd,  $J = 4.1, 1.7$  Hz, 1H), 8.12 (d,  $J = 8.5$  Hz, 1H), 7.95 (d,  $J = 8.1$  Hz, 1H), 7.84 (d,  $J = 7.8$  Hz, 1H), 7.67 (t,  $J = 7.5$  Hz, 1H), 7.59 (dd,  $J = 8.6, 4.1$  Hz, 1H), 7.50 (t,  $J = 7.6$  Hz, 1H), 6.98 (d,  $J = 8.5$  Hz, 1H), 5.72 (s, 2H);  $^{13}C$  NMR (126 MHz,  $CDCl_3$ )  $\delta$  175.95, 150.49, 148.69, 147.87, 138.42, 136.85, 132.40 (d,  $J = 4.5$  Hz), 128.90, 128.06, 126.71 - 126.25 (m), 125.40, 122.96, 118.26, 116.35, 109.12; IR (neat,  $cm^{-1}$ ) 3458, 3318, 2952, 2915, 2851, 1621, 1600, 1506, 1424, 1387, 1310, 1238, 1130, 1048, 1032, 815, 791, 751; MALDI-TOF  $m/z$  calcd for  $C_{16}H_{12}F_3N_4$  ( $[M + H]^+$ ) 317,101, found 317.072.

*(E)-5-((3-fluorophenyl)diazenyl)quinolin-8-amine (6e)*

Obtained as a rust solid (24 mg, 91%); mp: 136-138 °C;  $^1H$  NMR (500 MHz,  $CDCl_3$ )  $\delta$  9.19 (dd,  $J = 8.5, 1.7$  Hz, 1H), 8.75 (dd,  $J = 4.1, 1.7$  Hz, 1H), 7.95 (d,  $J = 8.5$  Hz, 1H), 7.69 (dd,  $J = 7.9, 0.6$  Hz, 1H), 7.62 - 7.52 (m, 1H), 7.48 (dd,  $J = 8.5, 4.1$  Hz, 1H), 7.40 (td,  $J = 8.0, 6.1$  Hz, 1H), 7.08 - 6.99 (m, 1H), 6.89 - 6.83 (m, 1H), 5.52 (s, 2H);  $^{13}C$  NMR (126 MHz,  $CDCl_3$ )  $\delta$  164.41, 162.45, 155.06 (d,  $J =$

7.1 Hz), 148.35, 147.95, 137.91, 137.02, 132.22, 130.15 (d,  $J = 8.5$  Hz), 128.28, 122.75, 120.23 (d,  $J = 2.7$  Hz), 116.47, 116.30, 115.87, 108.94, 107.56, 107.38; IR (neat,  $cm^{-1}$ ) 3430, 3309, 3165, 2951, 2920, 2851, 1729, 1619, 1566, 1508, 1475, 1379, 1335, 1246, 1205, 1100, 965, 866, 780, 682; MALDI-TOF  $m/z$  calcd for  $C_{15}H_{12}FN_4$  ( $[M + H]^+$ ) 267,1046, found 266.992.

*(E)-5-((4-ethynylphenyl)diazenyl)quinolin-8-amine (6f)*

Obtained as a rust solid (23 mg, 84%); mp: 186-188 °C;  $^1H$  NMR (500 MHz,  $CDCl_3$ )  $\delta$  9.30 (d,  $J = 8.2$  Hz, 1H), 8.85 (s, 1H), 8.05 (d,  $J = 8.3$  Hz, 1H), 7.92 (d,  $J = 8.2$  Hz, 2H), 7.71 - 7.51 (m, 3H), 6.97 (d,  $J = 8.2$  Hz, 1H), 5.60 (s, 2H), 3.23 (s, 1H);  $^{13}C$  NMR (126 MHz,  $CDCl_3$ )  $\delta$  153.09, 148.23, 147.88, 138.23, 137.02, 132.96, 132.22, 128.23, 123.17, 122.65, 122.41, 115.73, 108.96, 83.62, 78.92; IR (neat,  $cm^{-1}$ ) 3429, 3305, 3177, 2923, 2847, 1719, 1611, 1508, 1378, 1328, 1246, 1192, 839, 790; MALDI-TOF  $m/z$  calcd for  $C_{17}H_{13}N_4$  ( $[M + H]^+$ ) 273,114, found 272.861.

*(E)-5-((4-fluorophenyl)diazenyl)quinolin-8-amine (6g)*

Obtained as an orange solid (26 mg, 96%); mp: 162-164 °C;  $^1H$  NMR (500 MHz,  $CDCl_3$ )  $\delta$  9.28 (d,  $J = 6.7$  Hz, 1H), 8.85 (s, 1H), 8.00 (d,  $J = 21.5$  Hz, 3H), 7.57 (d,  $J = 4.3$  Hz, 1H), 7.22 (s, 2H), 7.03 - 6.92 (m, 1H), 5.55 (s, 2H);  $^{13}C$  NMR (126 MHz,  $CDCl_3$ )  $\delta$  164.61, 162.61, 149.98, 147.86 (d,  $J = 5.0$  Hz), 147.78, 138.04, 137.09, 132.18, 128.03, 125.03 - 123.91 (m), 122.50 (dd,  $J = 7.9, 5.7$  Hz), 115.91 (dd,  $J = 23.3, 6.2$  Hz), 115.38 (d,  $J = 5.0$  Hz), 108.95; IR (neat,  $cm^{-1}$ ) 3446, 3321, 2925, 2851, 1615, 1591, 1567, 1510, 1492, 1385, 1334, 1248, 1223, 1184, 847, 788; MALDI-TOF  $m/z$  calcd for  $C_{15}H_{12}FN_4$  ( $[M + H]^+$ ) 267,105, found 266.961.

## RESULTS AND DISCUSSION

In this work, novel azobenzenes (**6a-g**) have been synthesized with excellent yields. The synthetic route has been illustrated in Scheme 1. At first, quinoline was nitrated in the presence of nitric acid and sulfuric acid, and a mixture of 5-nitroquinoline and 8-nitroquinoline (**2a-b**) was obtained. Without any purification, this mixture was subjected for hydrogenolysis in the presence of  $H_2/Pd$  and amino quinoline forms (**3a-b**) were attained by full conversion. On the other hand, aniline derivatives were converted to the corresponding diazonium salts (**5a-g**) in single step with good and acceptable yields. Finally, azobenzenes as target products were synthesized by reacting with 8-aminoquinoline (**3a**) and aryl diazonium salts (**5a-g**) in aqueous media at room temperature in facile manner. Diazonium salts with electron donating or withdrawing groups substituted at different positions of benzene gave the target product 8-(aryldiazenyl)quinolines (**6a-g**) quite successfully with exceptional yields. Structural

features of the 8-(aryldiazenyl)quinolines (**6a-g**) were fully elucidated using NMR, UV-Visible absorption spectra and mass spectrometry.

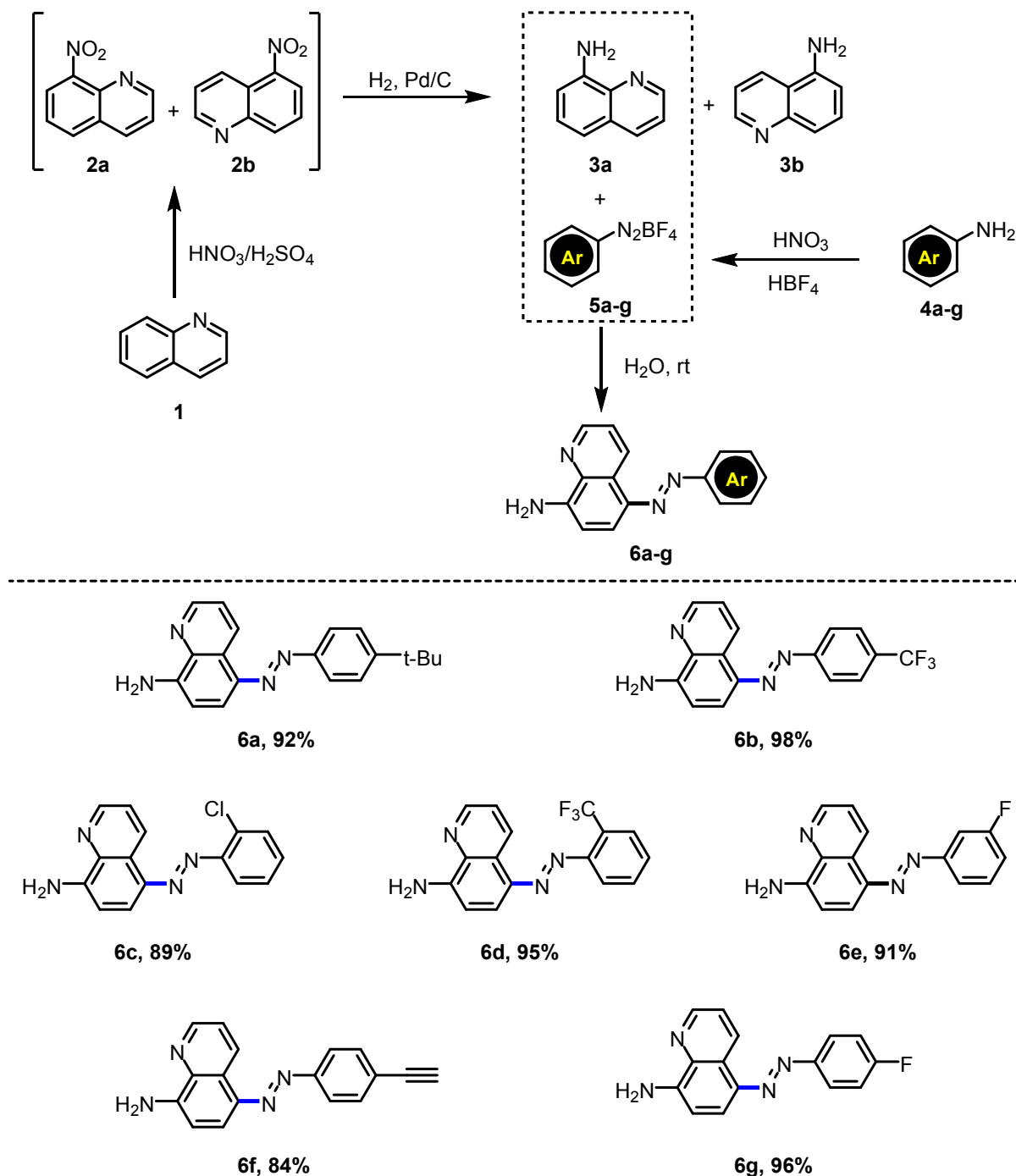


**Figure 1:** Synthetic route for the preparation of azobenzenes.

UV-Vis spectra of the compounds were collected in acetonitrile solvent with Shimadzu UV-3600 UV-Vis NIR spectrophotometer and they were presented in Figure 2. Their maximal values and molar absorption coefficients were also recorded in Table 1. As seen in Table 1, the absorption maximal values of the compounds are between 427 nm and 445 nm due to  $n\text{-}\pi^*$  charge transfer transition (52).

The absorption bands are slightly shifted to longer wavelengths (redshifted) in the order of **6a**, **6g**, **6c**, **6e**, **6b**, **6d**, and **6f**. Generally, as the electron donor strength increases, the absorption band maximum shifts to longer wavelengths (53); however, here the opposite effects were observed, similar to the literature (54). When their molar absorption coefficient was compared, **6a** had the

biggest molar absorption coefficient and **6f** had the lowest molar absorption coefficient among the compounds presented. It can be concluded that the

compounds have more absorbance ability in the strong donor systems.

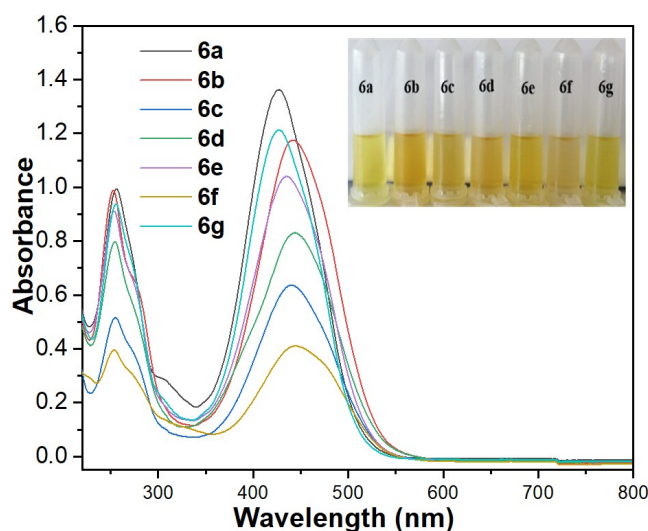


**Figure 2:** UV-Vis spectrum of the compounds (50  $\mu\text{M}$ ) in ACN.

**Table 1:** Absorption maximal values of the compounds.

Compounds	Absorption Maxima	Molar Absorption Coefficient ( $\epsilon$ ) ( $\text{cm}^{-1}\text{M}^{-1}$ )
<b>6a</b>	427	27,180
<b>6b</b>	442	23,500
<b>6c</b>	430	12,640
<b>6d</b>	442	16,560
<b>6e</b>	435	20,740
<b>6f</b>	445	8,260
<b>6g</b>	428	24,220

## CONCLUSION

As a summary, the author hereby discloses the simple, easy and operational synthesis of novel 8-(aryldiazenyl)quinolones and their structural characterization was carried out by varied analytical techniques as NMR, IR, UV-Visible, and mass spectroscopy. The compounds were provided with excellent yields ranging from 89% to 98%. UV-Vis spectrum of the azobenzenes was collected in acetonitrile solvent and maximal values were measured between 427 nm and 445 nm. The molar absorptivity of compounds showed that their electronic transition is by virtue of  $n\text{-}\pi^*$ . It can be assumed that the compounds have greater absorbance ability in strong donor systems. New azobenzenes with potentially dye and pharmaceutical agents due to the aminoquinoline backbone and diazo unit were brought to the literature.

## CONFLICT OF INTEREST

There are no conflicts to declare.

## REFERENCES

- Bafana A, Devi SS, Chakrabarti T. Azo dyes: past, present and the future. *Environmental Reviews*. 2011;19:350-71. [<DOI>](#)
- Hunger K, Schmidt MU. *Industrial Organic Pigments* [Internet]. Wiley; 2018. [<DOI>](#).
- Banghart MR, Mourot A, Fortin D, Yao JZ, Kramer RH, Trauner D. Photochromic Blockers of Voltage-Gated Potassium Channels. *Angewandte Chemie International Edition*. 2009;48(48):9097-101. [<DOI>](#).
- Lim SY, Hong KH, Kim D II, Kwon H, Kim HJ. Tunable Heptamethine-Azo Dye Conjugate as an NIR Fluorescent Probe for the Selective Detection of Mitochondrial Glutathione over Cysteine and Homocysteine. *Journal of the American Chemical Society*. 2014;136(19):7018-25. [<DOI>](#).
- DiCesare N, Lakowicz JR. New Color Chemosensors for Monosaccharides Based on Azo Dyes. *Organic Letters*. 2001;3(24):3891-3. [<DOI>](#).
- Chang KC, Su IH, Wang YY, Chung WS. A Bifunctional Chromogenic Calix[4]arene Chemosensor for Both Cations and Anions: A Potential  $\text{Ca}^{2+}$  and  $\text{F}^-$  Switched

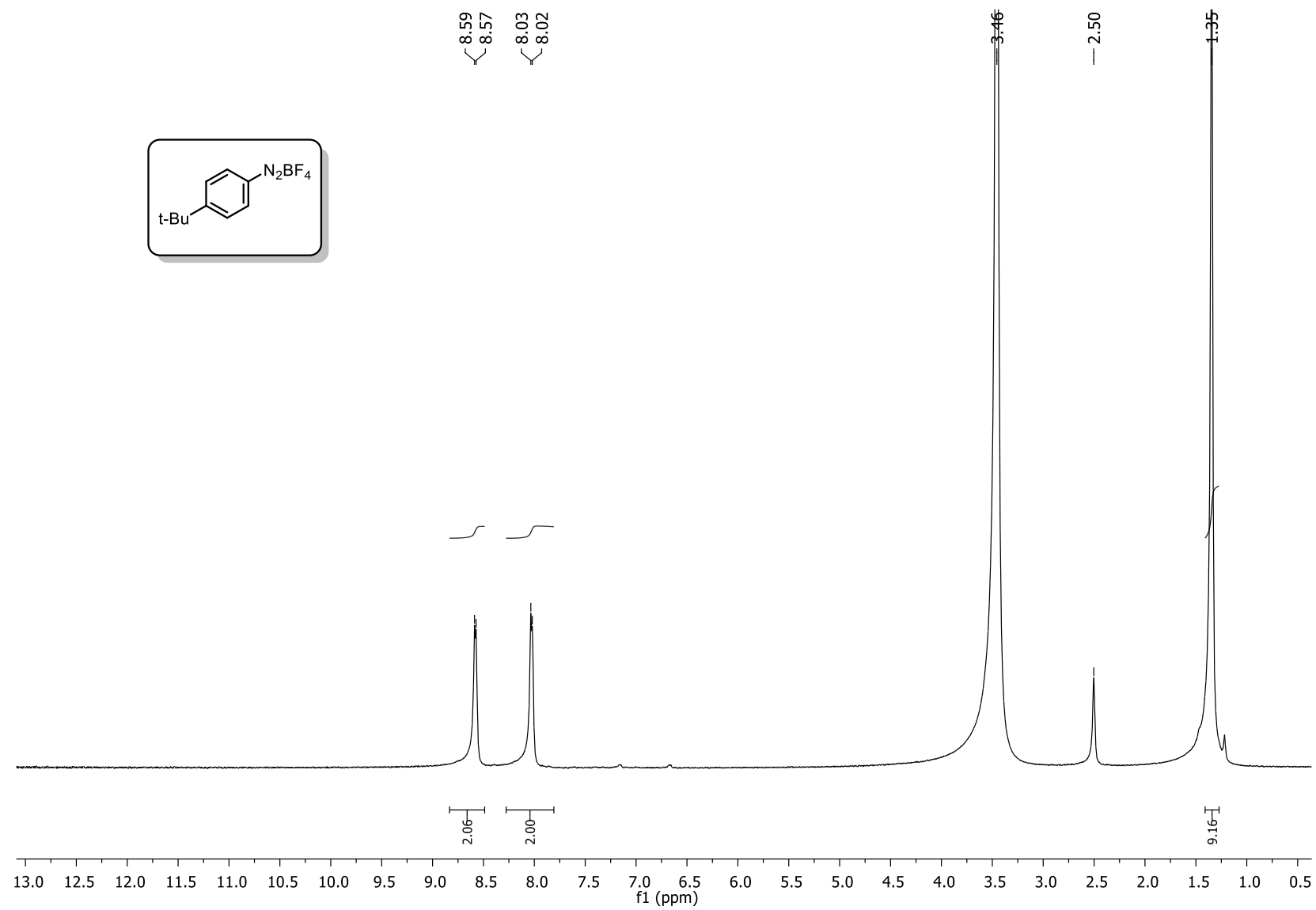
- Inhibit Logic Gate with a YES Logic Function. *European Journal of Organic Chemistry*. 2010;2010(24):4700-4. [<DOI>](#).
7. Leulescu M, Rotaru A, Moanță A, Iacobescu G, Pălărie I, Cioateră N, et. al. Azorubine: physical, thermal and bioactive properties of the widely employed food, pharmaceutical and cosmetic red azo dye material. *Journal of Thermal Analysis and Calorimetry*. 2021;143(6):3945-67. [<DOI>](#).
  8. Wang LH, Shu-Juan H. Studies on the voltammetric behavior of azo dyes and its determination in cosmetic products. *Russian Journal of Electrochemistry*. 2010;46(12):1414-8. [<DOI>](#).
  9. Rawat D, Sharma RS, Karmakar S, Arora LS, Mishra V. Ecotoxic potential of a presumably non-toxic azo dye. *Ecotoxicology and Environmental Safety*. 2018;148:528-37. [<DOI>](#).
  10. Khaligh NG, Hamid SBA, Hazarkhani H. TiO<sub>2</sub> nanotubes and sonication: Synthesis of azo-linked xanthenes. *Inorganic and Nano-Metal Chemistry*. 2017;47(10):1468-74. [<DOI>](#).
  11. Merino E. Synthesis of azobenzenes: the coloured pieces of molecular materials. *Chemical Society Reviews*. 2011;40(7):3835-53. [<DOI>](#).
  12. Qiu F, Cao Y, Xu H, Jiang Y, Zhou Y, Liu J. Synthesis and properties of polymer containing azo-dye chromophores for nonlinear optical applications. *Dyes and Pigments*. 2007;75(2):454-9. [<DOI>](#).
  13. Çanakçı D, Serin S. Synthesis of new azo dye polymers based on naphthol by oxidative polycondensation: antimicrobial activity and fastness studies. *Journal of Polymer Research*. 2020;27(1):11. [<DOI>](#).
  14. Çanakçı D. Synthesis, Spectroscopic, Thermodynamics and Kinetics Analysis Study of Novel Polymers Containing Various Azo Chromophore. *Scientific Reports*. 2020;10(1):477. [<DOI>](#).
  15. Farghaly TA, Abdallah ZA. Synthesis, azo-hydrazone tautomerism and antitumor screening of N-(3-ethoxycarbonyl-4,5,6,7-tetrahydro-benzo[b]thien-2-yl)-2-arylhydrazono-3-oxo butanamide derivatives. *Arkivoc*. 2009;2008(17):295-305. [<DOI>](#).
  16. Ali Y, Hamid SA, Rashid U. Biomedical Applications of Aromatic Azo Compounds. *Mini-Reviews in Medicinal Chemistry*. 2018;18(18):1548-58. [<DOI>](#).
  17. Akram D, Elhaty IA, AlNeyadi SS. Synthesis and Antibacterial Activity of Rhodanine-Based Azo Dyes and Their Use as Spectrophotometric Chemosensor for Fe<sup>3+</sup> Ions. *Chemosensors*. 2020;8(1):16. [<DOI>](#).
  18. Unnisa A, Abouziad AS, Baratam A, Chenchu Lakshmi KNV, Hussain T, Kunduru RD, et. al. Design, synthesis, characterization, computational study and in-vitro antioxidant and anti-inflammatory activities of few novel 6-aryl substituted pyrimidine azo dyes. *Arabian Journal of Chemistry*. 2020;13(12):8638-49. [<DOI>](#).
  19. Kennedy DA, Vembu N, Fronczek FR, Devocelle M. Synthesis of Mutual Azo Prodrugs of Anti-inflammatory Agents and Peptides Facilitated by  $\alpha$ -Aminoisobutyric Acid. *The Journal of Organic Chemistry*. 2011;76(23):9641-7. [<DOI>](#).
  20. Adu JK, Amengor CDK, Mohammed Ibrahim N, Amaning-Danquah C, Owusu Ansah C, Gbadago DD, vd. Synthesis and In Vitro Antimicrobial and Anthelmintic Evaluation of Naphtholic and Phenolic Azo Dyes. *Journal of Tropical Medicine*. 2020;2020:1-8. [<DOI>](#).
  21. Shaki H, Gharanjig K, Khosravi A. Synthesis and investigation of antimicrobial activity and spectrophotometric and dyeing properties of some novel azo disperse dyes based on naphthalimides. *Biotechnology Progress*. 2015;31(4):1086-95. [<DOI>](#).
  22. Saeed AM, AlNeyadi SS, Abdou IM. Anticancer activity of novel Schiff bases and azo dyes derived from 3-amino-4-hydroxy-2H-pyrano[3,2-c]quinoline-2,5(6H)-dione. *Heterocyclic Communications*. 2020;26(1):192-205. [<DOI>](#).
  23. Abd-El-Aziz AS, Alsaggaf A, Assirey E, Naqvi A, Okasha RM, Afifi TH, et. al. A New Family of Benzo[h]Chromene Based Azo Dye: Synthesis, In-Silico and DFT Studies with In Vitro Antimicrobial and Antiproliferative Assessment. *International Journal of Molecular Sciences*. 2021;22(6):2807. [<DOI>](#).
  24. Tahir T, Shahzad MI, Tabassum R, Rafiq M, Ashfaq M, Hassan M, et. al. Diaryl azo derivatives as anti-diabetic and antimicrobial agents: synthesis, in vitro , kinetic and docking studies. *Journal of Enzyme Inhibition and Medicinal Chemistry*. 2021;36(1):1509-20. [<DOI>](#).
  25. Mallikarjuna NM, Keshavayya J. Synthesis, spectroscopic characterization and pharmacological studies on novel sulfamethaxazole based azo dyes. *Journal of King Saud University - Science*. 2020;32(1):251-9. [<DOI>](#).
  26. Dusan M, Biljana BN, Bozic B, Kovrljia I, Ladarevic J, Uscumlic G. Synthesis, solvatochromism, and biological activity of novel azo dyes bearing 2-pyridone and benzimidazole moieties. *Turkish Journal Of Chemistry*. 2018;42(3). [<DOI>](#).
  27. Surucu O, Abaci S, Seferoğlu Z. Electrochemical characterization of azo dye (E)-1-(4-((4-(phenylamino)phenyl)diazenyl)phenyl)ethanone (DPA). *Electrochimica Acta*. 2016;195:175-83. [<DOI>](#).
  28. Harisha S, Keshavayya J, Kumara Swamy BE, Viswanath CC. Synthesis, characterization and electrochemical studies of azo dyes derived from barbituric acid. *Dyes and Pigments*. 2017;136:742-53. [<DOI>](#).
  29. Grand View Research. *Dyes & Pigments Market Size, Share & Trends Analysis Report [Internet]*. 2021.
  30. Carliell CM, Barclay SJ, Shaw C, Wheatley AD,

- Buckley CA. The Effect of Salts Used in Textile Dyeing on Microbial Decolourisation of a Reactive Azo Dye. *Environmental Technology*. 1998;19(11):1133-7. <DOI>.
31. He Y, Zhao N, Qiu L, Zhang X, Fan X. Regio- and Chemoselective Mono- and Bisnitration of 8-Amino quinoline Amides with Fe(NO<sub>3</sub>)<sub>3</sub>·9H<sub>2</sub>O as Promoter and Nitro Source. *Organic Letters*. 2016;18(23):6054-7. <DOI>.
32. Nanayakkara NPD, Ager AL, Bartlett MS, Yardley V, Croft SL, Khan IA, et. al. Antiparasitic Activities and Toxicities of Individual Enantiomers of the 8-Aminoquinoline 8-[(4-Amino-1-Methylbutyl)Amino]-6-Methoxy-4-Methyl-5-[3,4-Dichlorophenoxy]Quinoline Succinate. *Antimicrobial Agents and Chemotherapy*. 2008;52(6):2130-7. <DOI>.
33. Warhurst DC. Understanding resistance to antimalarial 4-aminoquinolines, cinchona alkaloids and the highly hydrophobic arylaminoalcohols. *Current Science*. 2007;92:1556-60.
34. Bray P, Park B, Asadollaly E, Biagini G, Jeyadevan J, Berry N, et. al. A Medicinal Chemistry Perspective on 4-Aminoquinoline Antimalarial Drugs. *Current Topics in Medicinal Chemistry*. 2006;6(5):479-507. <DOI>.
35. Golden EB, Cho H-Y, Hofman FM, Louie SG, Schönthal AH, Chen TC. Quinoline-based antimalarial drugs: a novel class of autophagy inhibitors. *Neurosurgical Focus*. 2015;38(3):E12. <DOI>.
36. Vandekerckhove S, D'hooghe M. Quinoline-based antimalarial hybrid compounds. *Bioorganic & Medicinal Chemistry*. 2015;23(16):5098-119. <DOI>.
37. Foley M, Tilley L. Quinoline antimalarials: Mechanisms of action and resistance. *International Journal for Parasitology*. 1997;27(2):231-40. <DOI>.
38. Egan TJ, Ncokazi KK. Quinoline antimalarials decrease the rate of  $\beta$ -hematin formation. *Journal of Inorganic Biochemistry*. 2005;99(7):1532-9. <DOI>.
39. Kaur K, Jain M, Reddy RP, Jain R. Quinolines and structurally related heterocycles as antimalarials. *European Journal of Medicinal Chemistry*. 2010;45(8):3245-64. <DOI>.
40. Oliphant CM, Green GM. Quinolones: a comprehensive review. *American Family Physician*. 2002;65(3):455-64.
41. Romero AH. Role of Trifluoromethyl Substitution in Design of Antimalarial Quinolones: a Comprehensive Review. *Topics in Current Chemistry*. 2019;377(2):9. <DOI>.
42. King DE, Malone R, Lilley SH. New classification and update on the quinolone antibiotics. *American Family Physician*. 2000;61(9):2741-8.
43. Prachayasittikul V, Prachayasittikul V, Prachayasittikul S, Ruchirawat S. 8-Hydroxyquinolines: a review of their metal chelating properties and medicinal applications. *Drug Design, Development and Therapy*. 2013;1157. <DOI>.
44. Zhu C, Wang Y, Mao Q, Li F, Li Y, Chen C. Two 8-Hydroxyquinolate Based Supramolecular Coordination Compounds: Synthesis, Structures and Spectral Properties. *Materials*. 2017;10(3):313. <DOI>.
45. Kuchárová V, Kuchár J, Zaric M, Canovic P, Arsenijevic N, Volarevic V, et. al. Low-dimensional compounds containing bioactive ligands. Part XI: Synthesis, structures, spectra, in vitro anti-tumor and antimicrobial activities of 3d metal complexes with 8-hydroxyquinoline-5-sulfonic acid. *Inorganica Chimica Acta*. 2019;497:119062. <DOI>.
46. DiMauro EF, Mamai A, Kozłowski MC. Synthesis, Characterization, and Metal Complexes of a Salen Ligand Containing a Quinoline Base. *Organometallics*. 2003;22(4):850-5. <DOI>.
47. Allu S, Swamy KCK. Ruthenium-catalyzed synthesis of isoquinolones with 8-aminoquinoline as a bidentate directing group in C-H functionalization. *The Journal of organic chemistry*. 2014;79 9:3963-72.
48. Reddy BVS, Reddy LR, Corey EJ. Novel acetoxylation and C-C coupling reactions at unactivated positions in alpha-amino acid derivatives. *Organic Letters*. 2006;8(15):3391-4. <DOI>.
49. Pedron J, Boudot C, Hutter S, Bourgeade-Delmas S, Stigliani JL, Sournia-Saquet A, et. al. Novel 8-nitroquinolin-2(1H)-ones as NTR-bioactivated antikinoplastid molecules: Synthesis, electrochemical and SAR study. *European Journal Of Medicinal Chemistry*. 2018;155:135-52.
50. Ferlin MG, Chiarelto G, Castagliuolo I. Synthesis and characterization of some N-mannich bases of [1,2,3]triazoloquinolines. *Journal of Heterocyclic Chemistry*. 2002;39(4):631-8. <DOI>.
51. Hari DP, Schroll P, König B. Metal-free, visible-light-mediated direct C-H arylation of heteroarenes with aryl diazonium salts. *Journal of the American Chemical Society*. 2012;134 6:2958-61.
52. Ouyang X, Zeng H, Xie Y. Synthesis and photoluminescence properties of 8-hydroxyquinoline derivatives and their metallic complexes. *Frontiers of Chemistry in China*. 2007;2(4):407-13. <DOI>.
53. Elangovan A, Yang SW, Lin JH, Kao KM, Ho TI. Synthesis and electrogenerated chemiluminescence of donor-substituted phenylquinolinylethyne and phenylisoquinolinylethyne: effect of positional isomerism. *Organic & Biomolecular Chemistry*. 2004;2(11):1597. <DOI>.

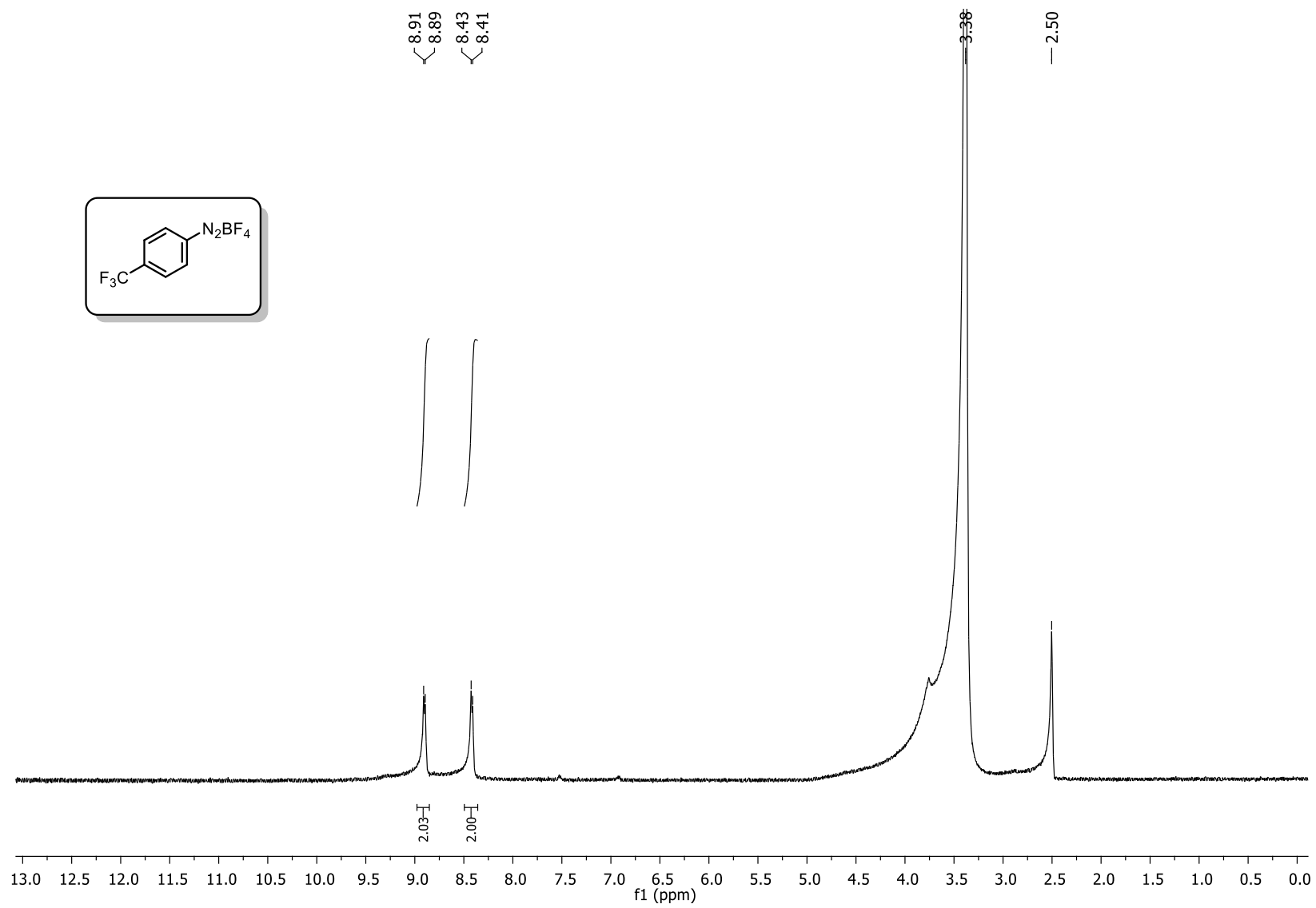
54. Slodek A, Filapek M, Szafraniec G, Grudzka I, Pisarski WA, Malecki JG, et. al. Synthesis, Electrochemistry, Crystal Structures, and Optical Properties of Quinoline Derivatives with a 2,2'-Bithiophene Motif. *European Journal of Organic Chemistry*. 2014;2014(24):5256-64. [<DOI>](#).



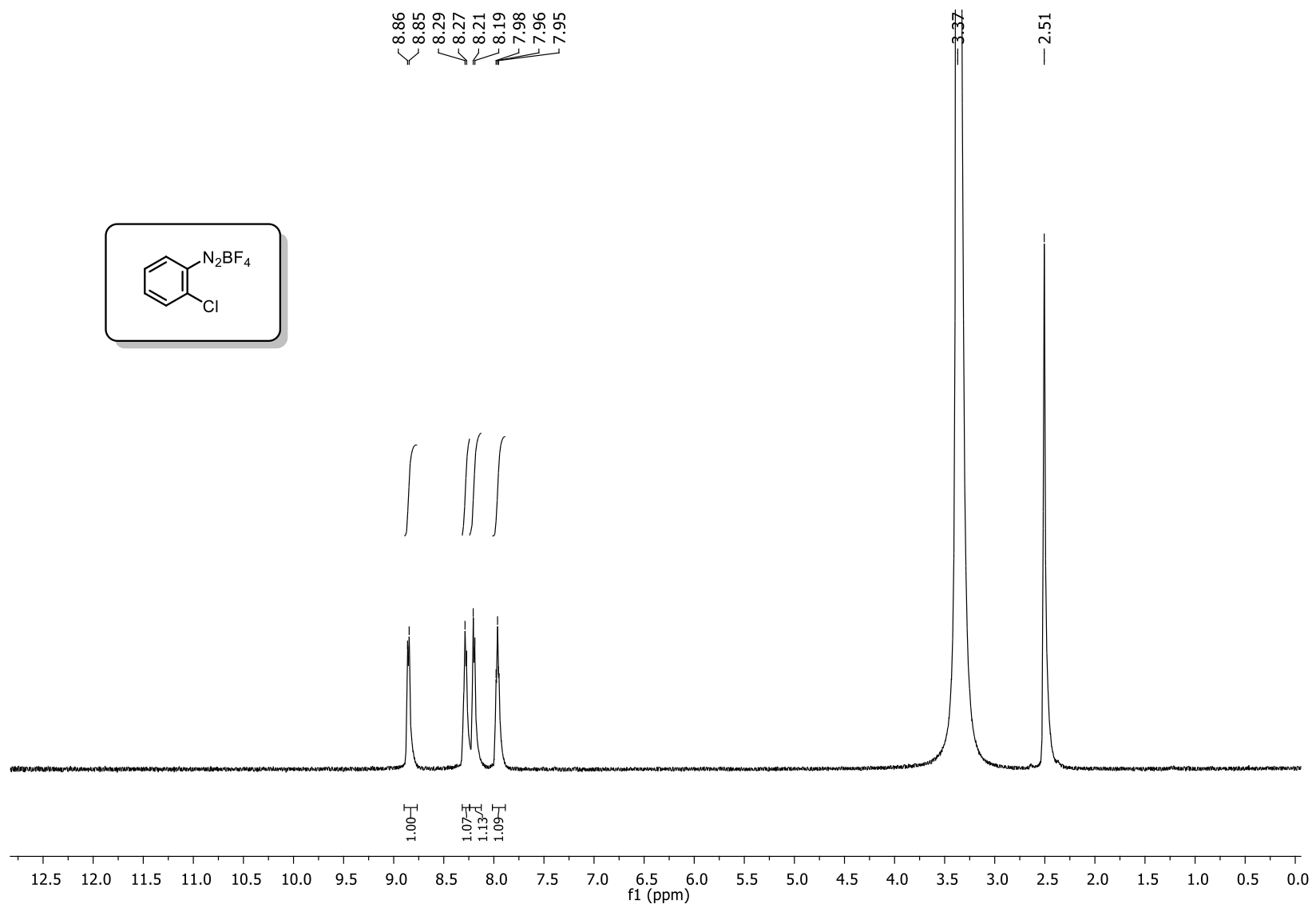
$^1\text{H}$  NMR ( $\text{CDCl}_3$ , 500 MHz) spectrum of 4-tert-butylbenzenediazonium tetrafluoroborate (**5a**)



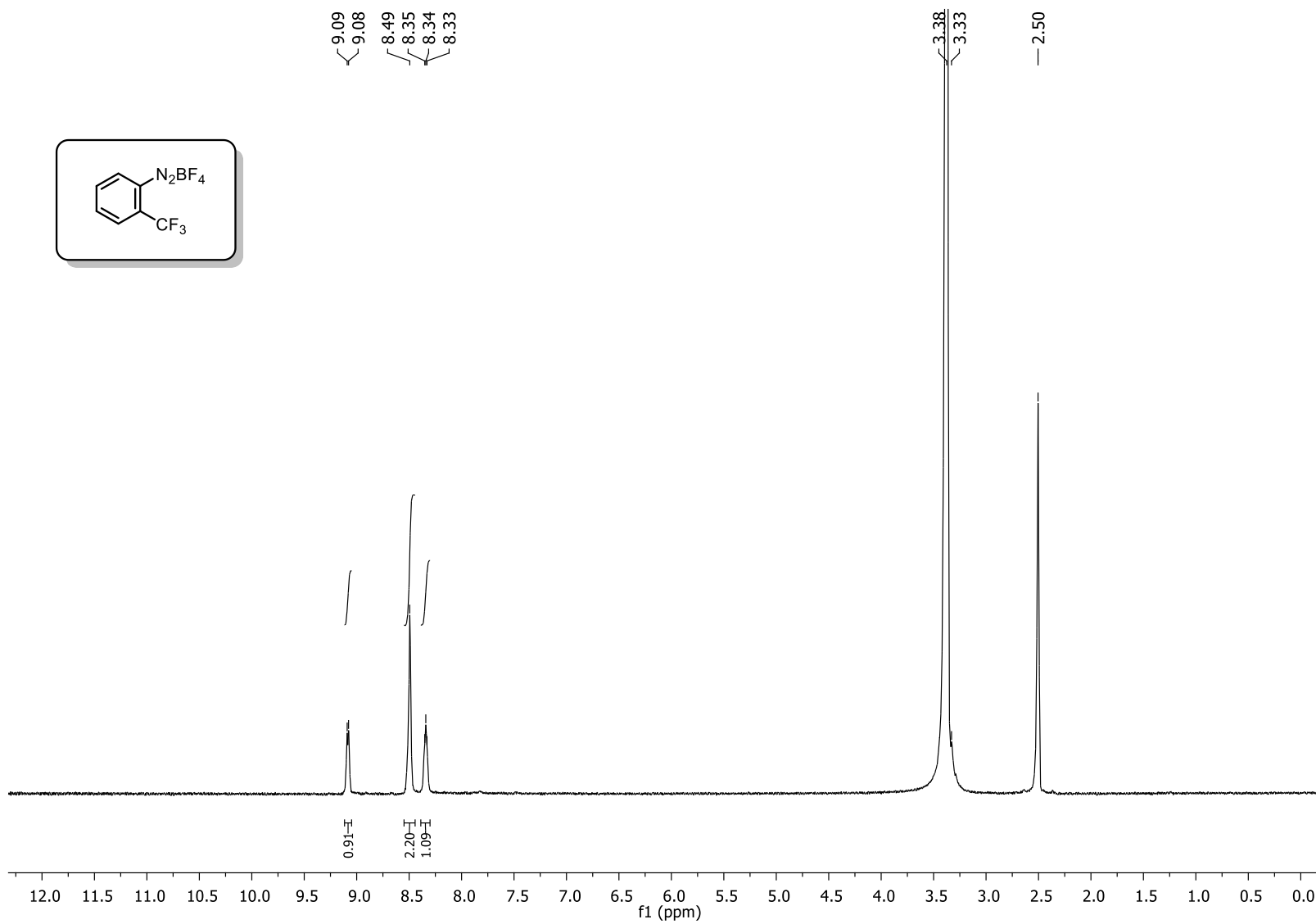
$^1\text{H}$  NMR ( $\text{CDCl}_3$ , 500 MHz) spectrum of 4-trifluoromethylbenzenediazonium tetrafluoroborate (**5b**)



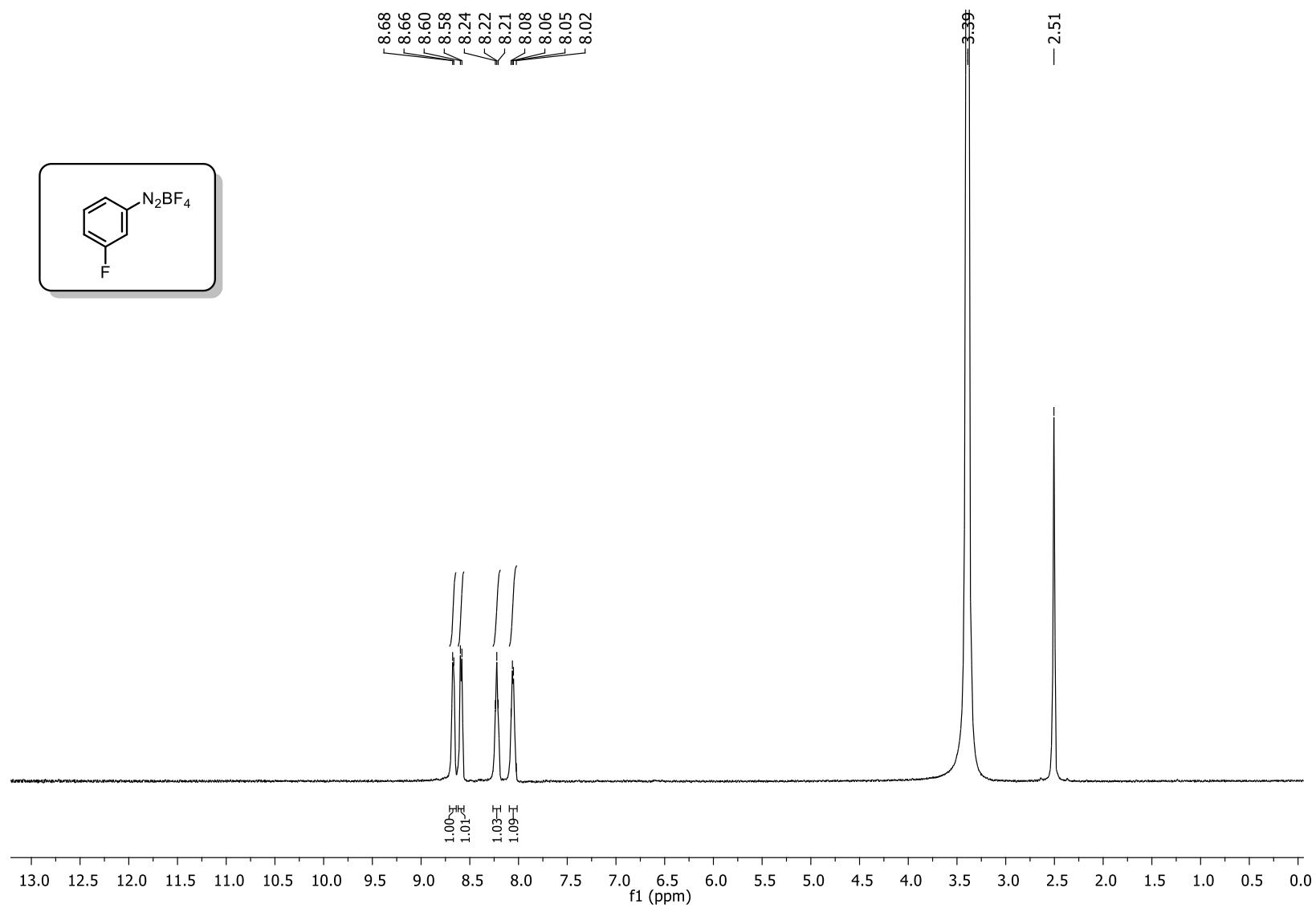
$^1\text{H}$  NMR ( $\text{CDCl}_3$ , 500 MHz) spectrum of 2-chlorobenzenediazonium tetrafluoroborate (**5c**)



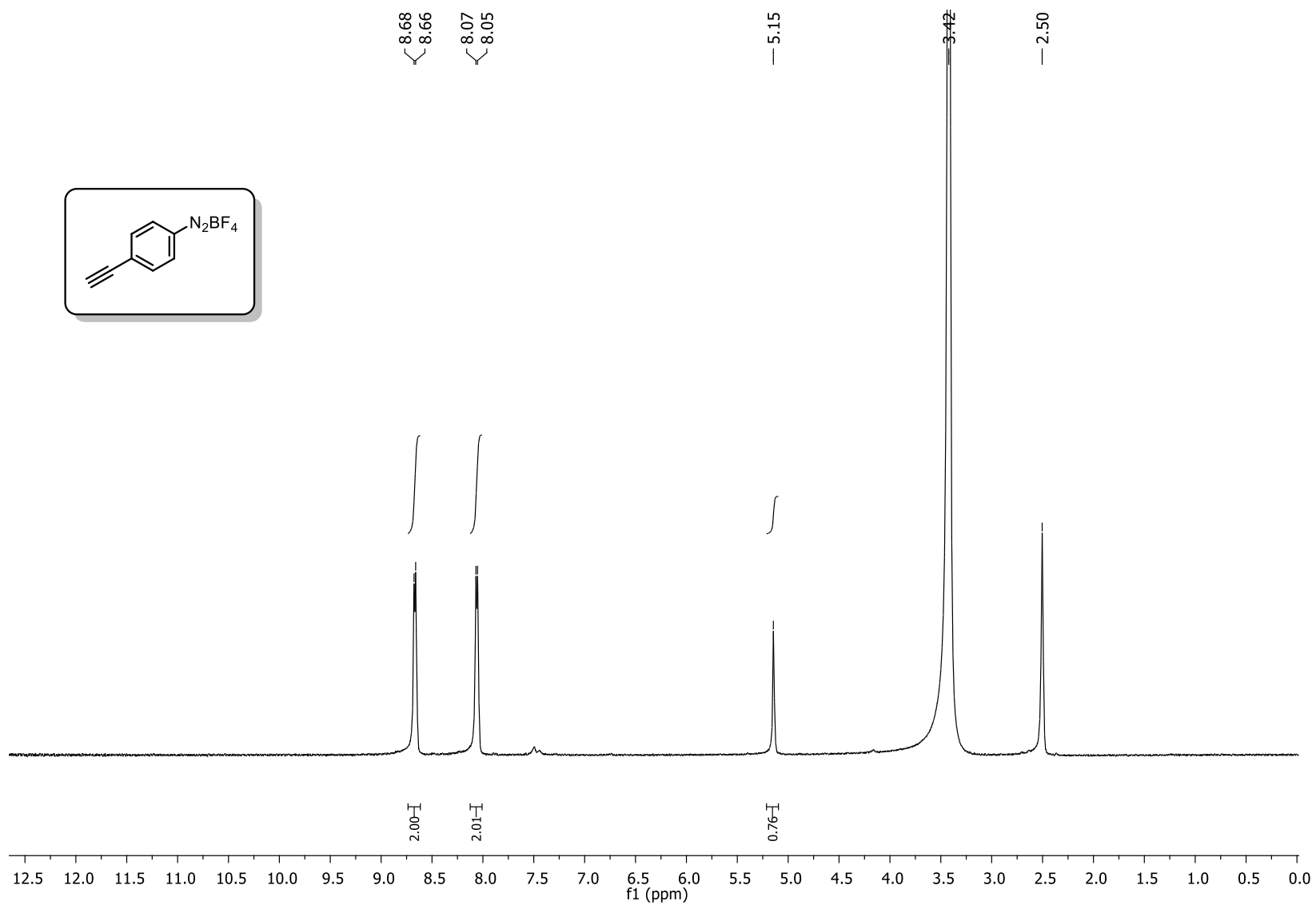
$^1\text{H}$  NMR ( $\text{CDCl}_3$ , 500 MHz) spectrum of 2-trifluoromethylbenzenediazonium tetrafluoroborate (**5d**)



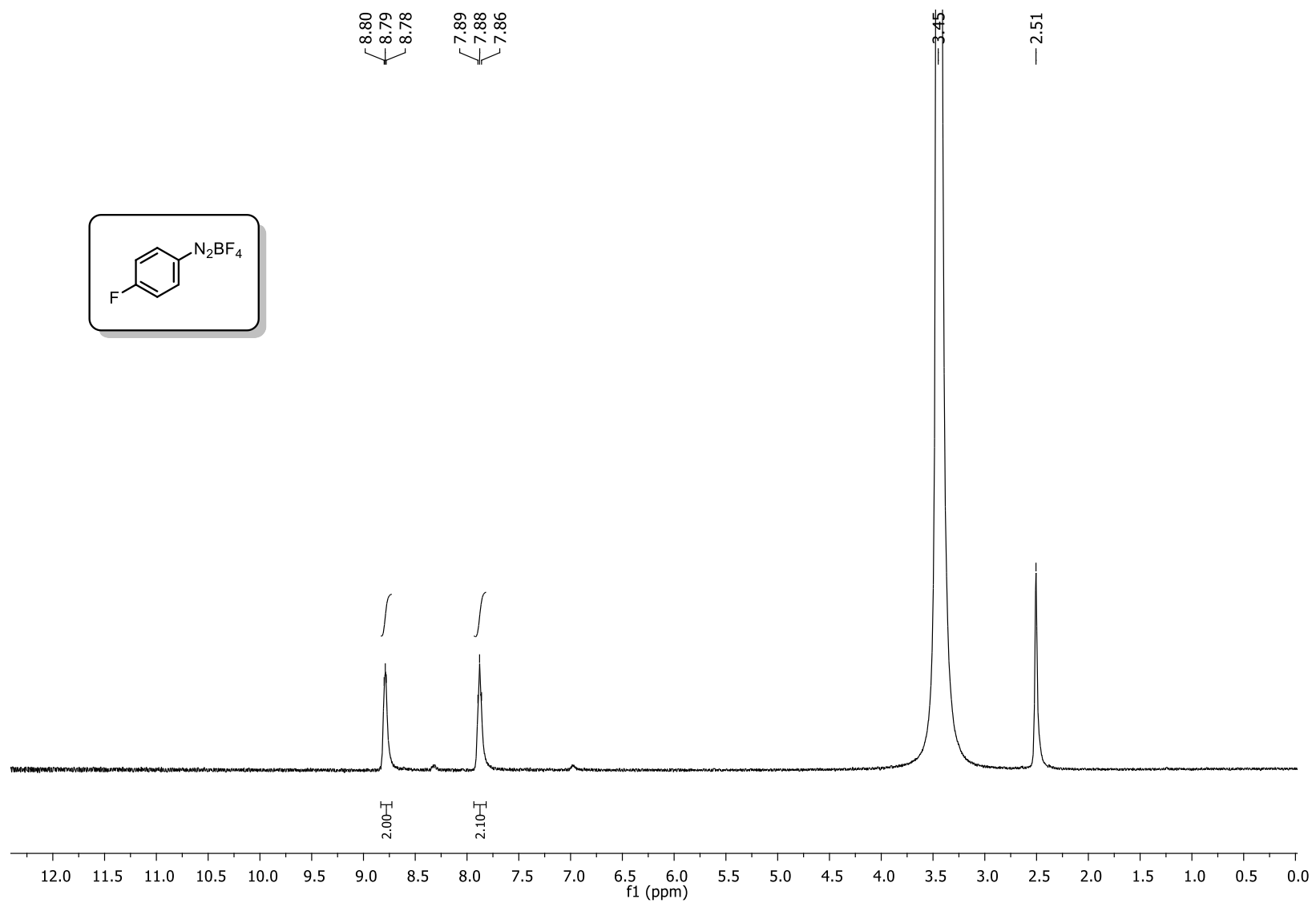
$^1\text{H}$  NMR ( $\text{CDCl}_3$ , 500 MHz) spectrum of 3-fluorobenzenediazonium tetrafluoroborate (**5e**)



$^1\text{H}$  NMR ( $\text{CDCl}_3$ , 500 MHz) spectrum of 4-ethynylbenzenediazonium tetrafluoroborate (**5f**)

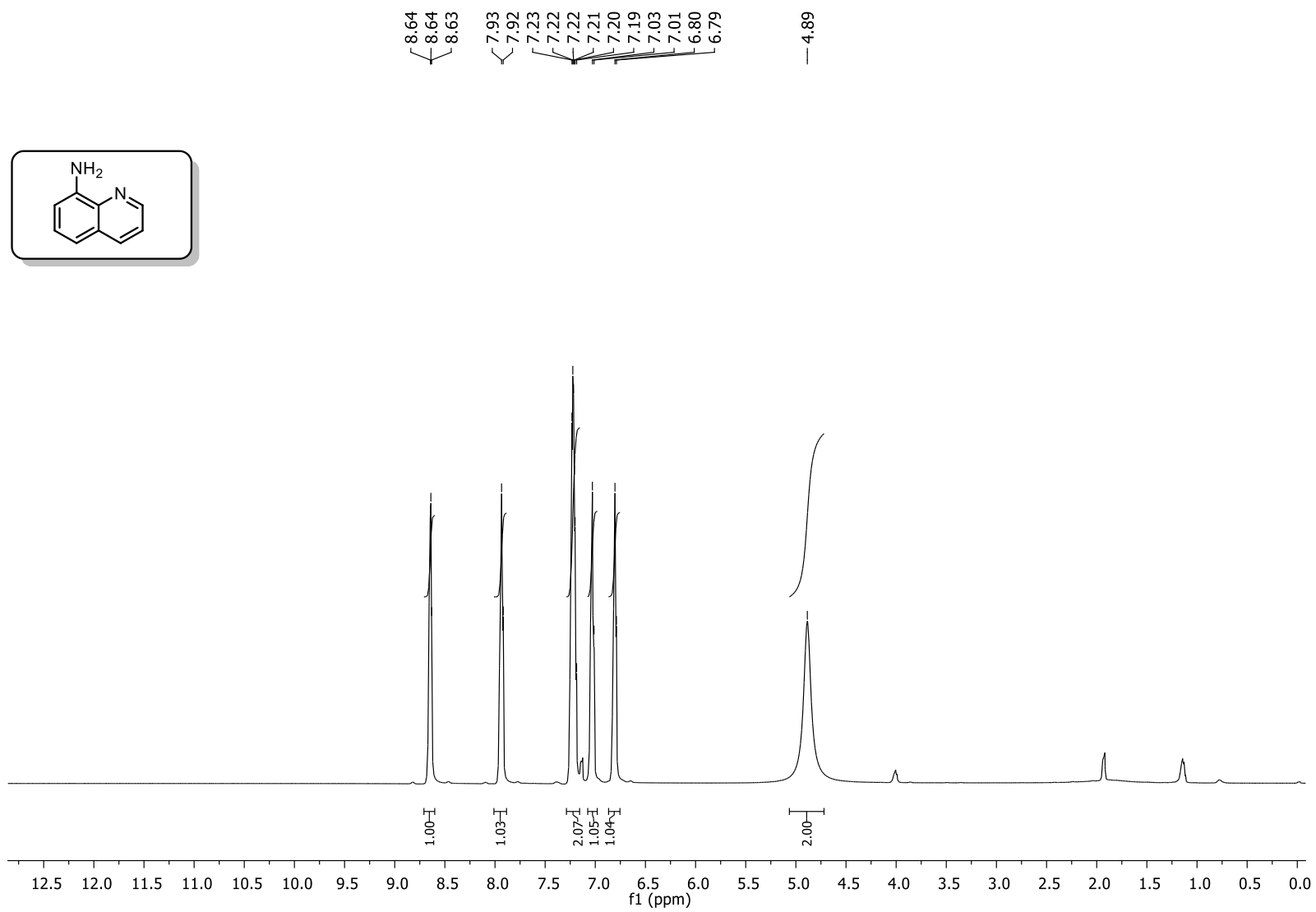


$^1\text{H}$  NMR ( $\text{CDCl}_3$ , 500 MHz) spectrum of 4-fluorobenzenediazonium tetrafluoroborate (**5g**)

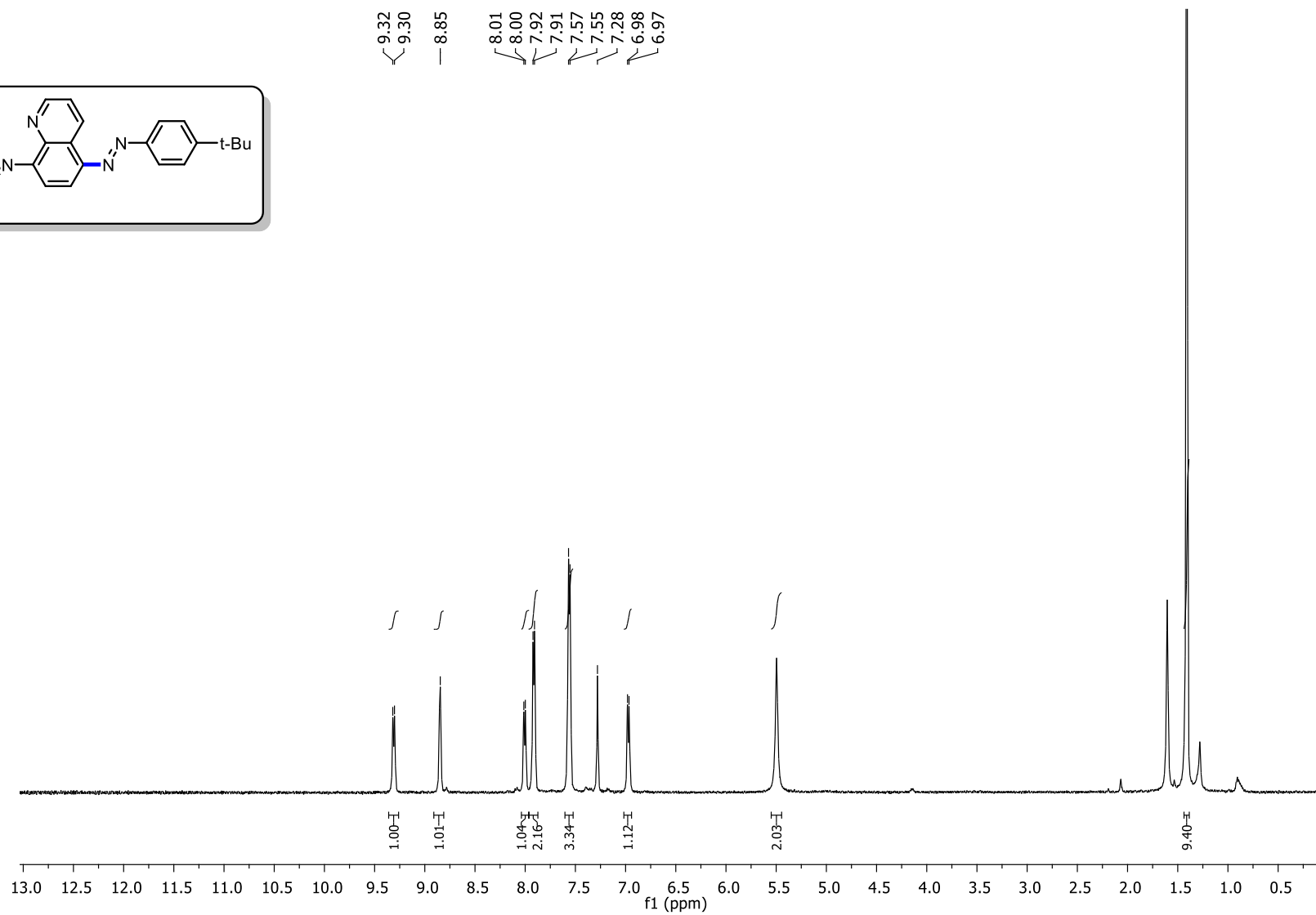
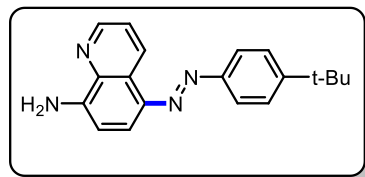




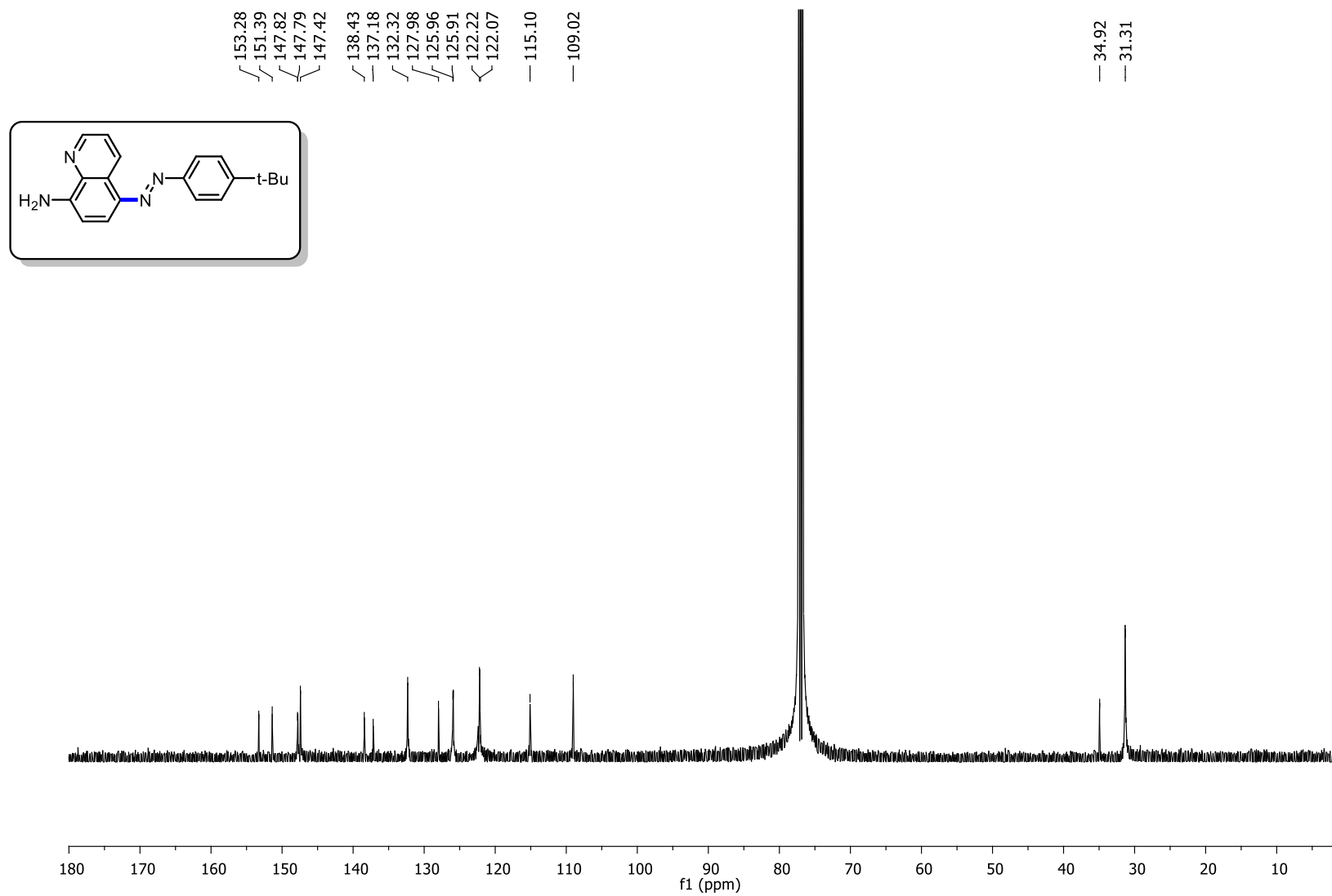
$^1\text{H}$  NMR ( $\text{CDCl}_3$ , 500 MHz) spectrum of 8-aminoquinoline (**3a**)



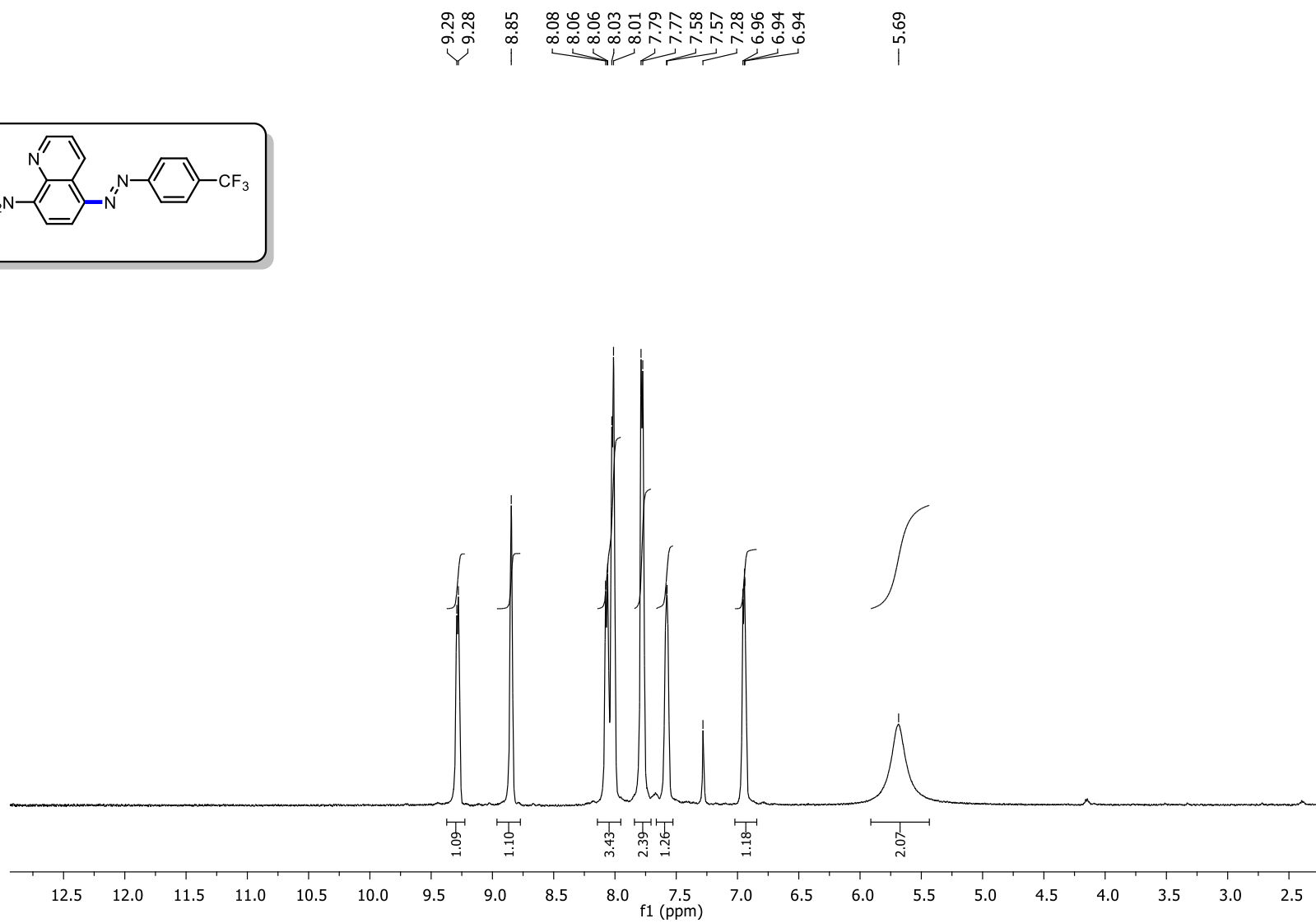
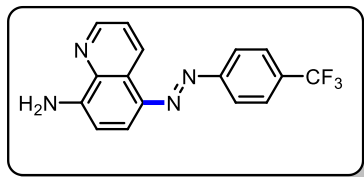
<sup>1</sup>H NMR (CDCl<sub>3</sub>, 500 MHz) spectrum of (E)-5-((4-(tert-butyl)phenyl)diazenyl)quinolin-8-amine (**6a**)



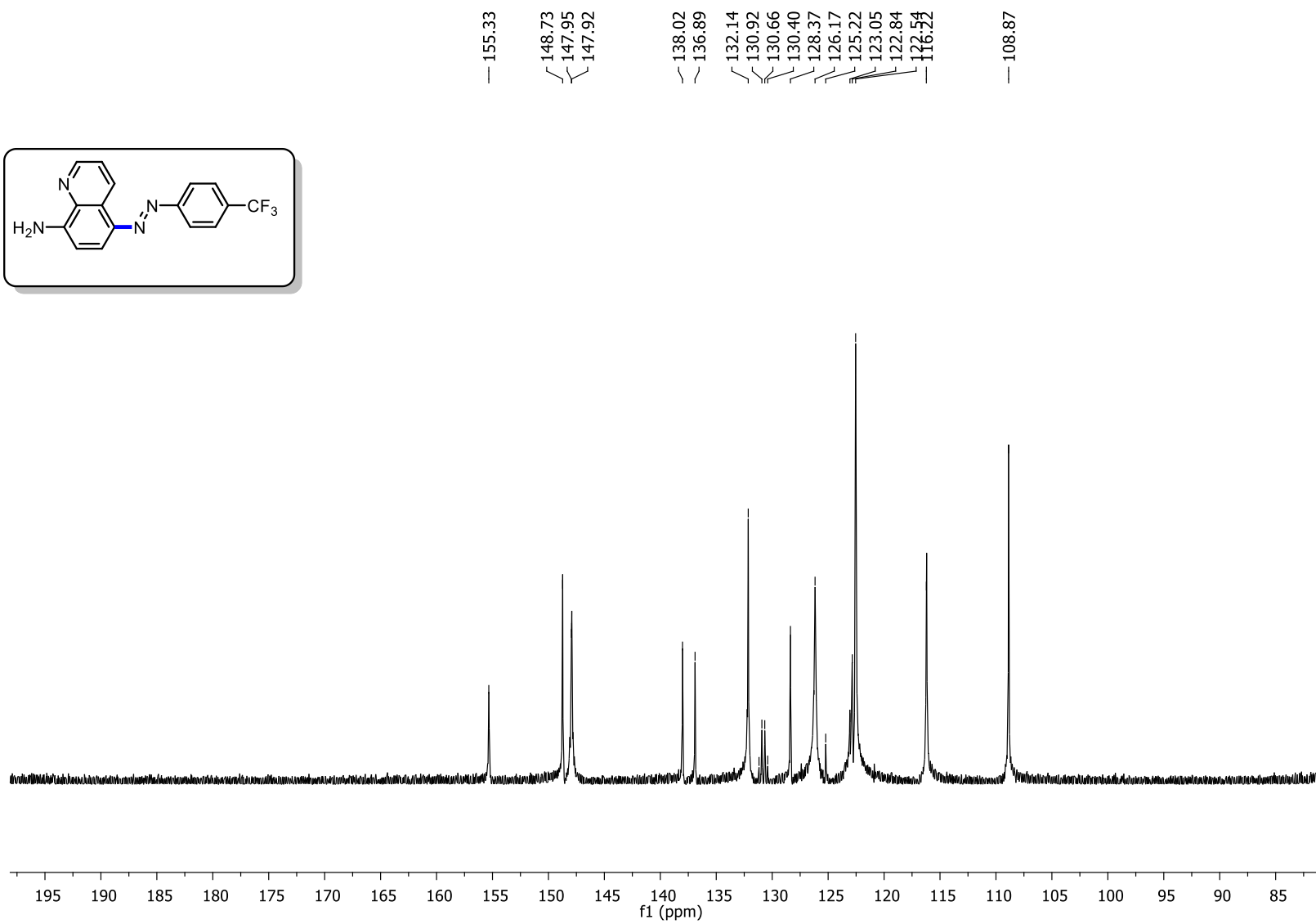
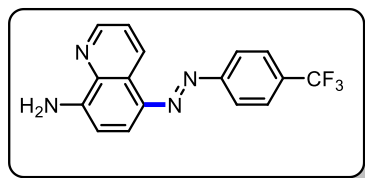
<sup>13</sup>C NMR (CDCl<sub>3</sub>, 126 MHz) spectrum of (E)-5-((4-(tert-butyl)phenyl)diazenyl)quinolin-8-amine (**6a**)



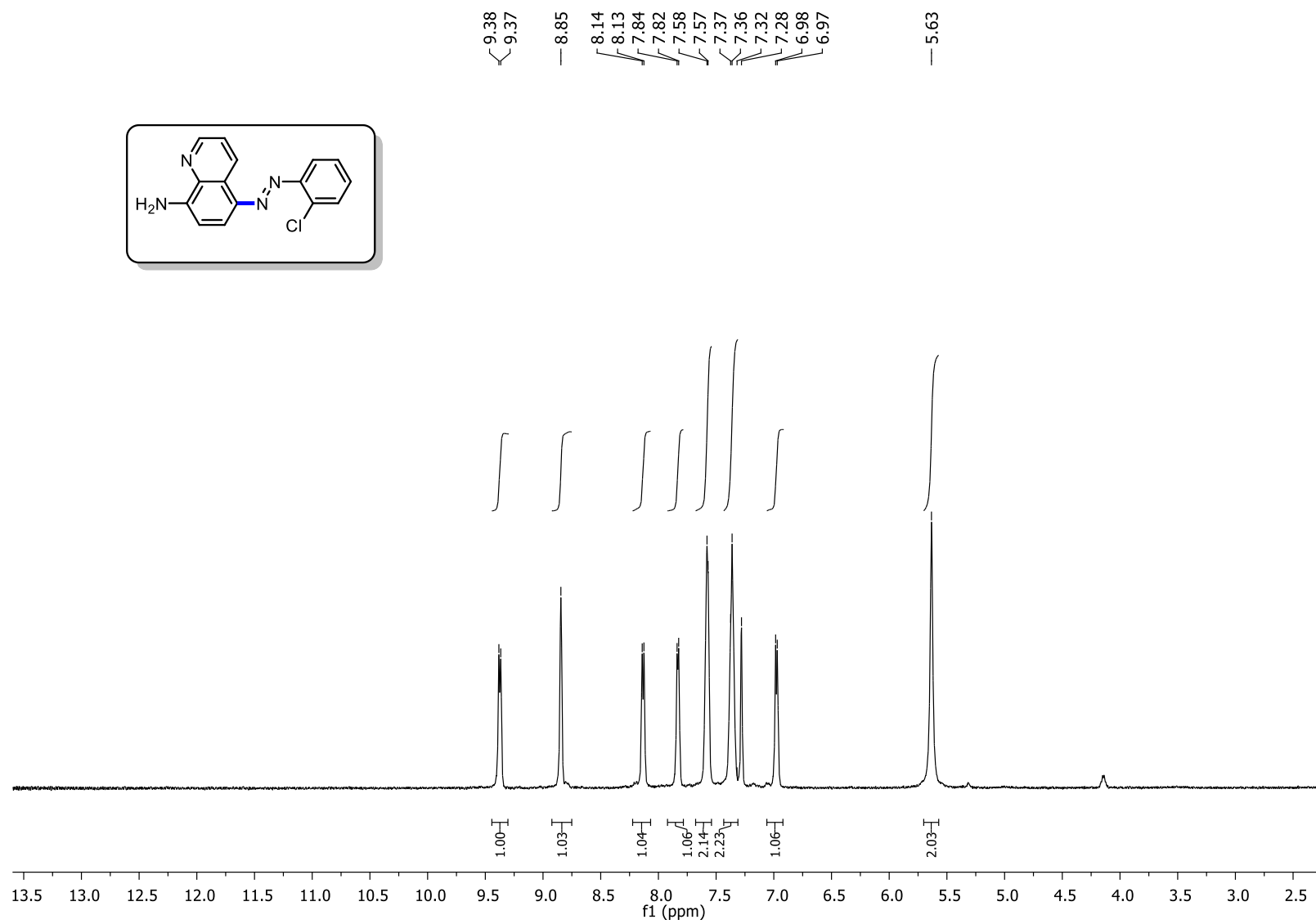
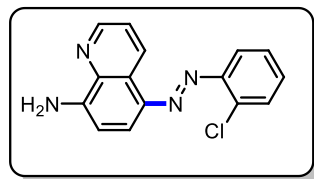
$^1\text{H}$  NMR ( $\text{CDCl}_3$ , 500 MHz) spectrum of (E)-5-((4-(trifluoromethyl)phenyl)diazenyl)quinolin-8-amine (**6b**)



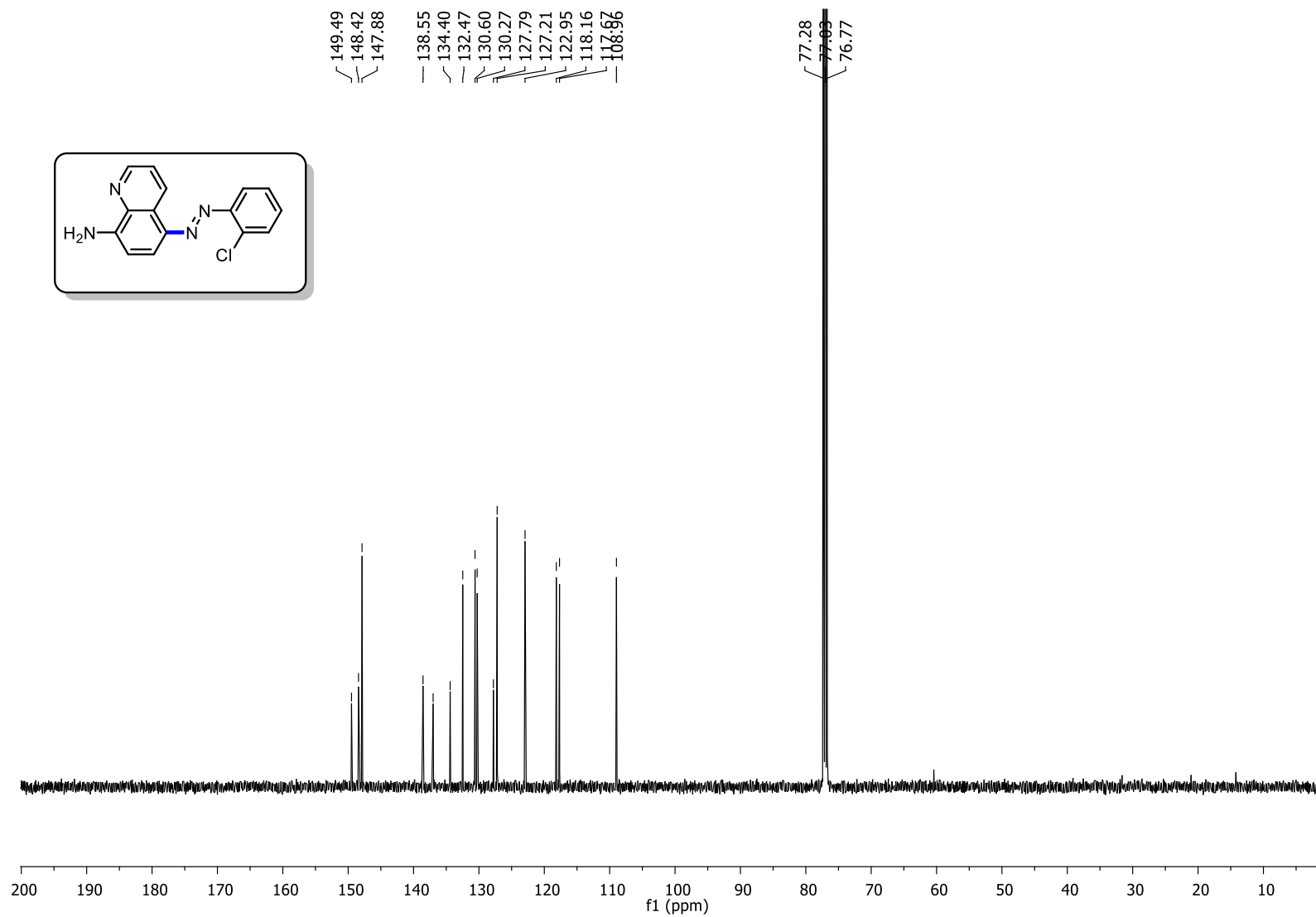
<sup>13</sup>C NMR (CDCl<sub>3</sub>, 126 MHz) spectrum of (E)-5-((4-(trifluoromethyl)phenyl)diazenyl)quinolin-8-amine (**6b**)



$^1\text{H}$  NMR ( $\text{CDCl}_3$ , 500 MHz) spectrum of (E)-5-((2-chlorophenyl)diazenyl)quinolin-8-amine (**6c**)

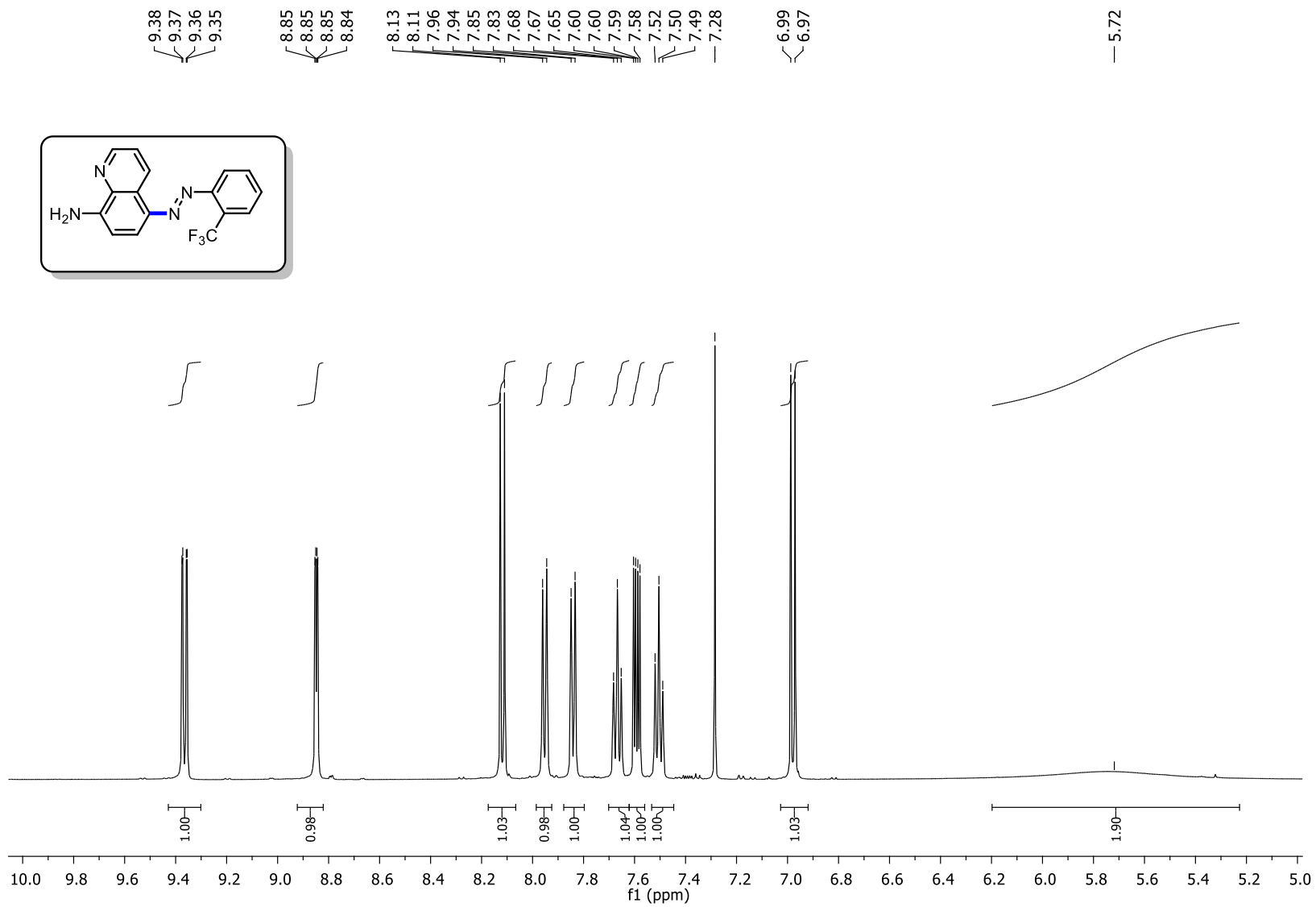


$^{13}\text{C}$  NMR ( $\text{CDCl}_3$ , 126 MHz) spectrum of (E)-5-((2-chlorophenyl)diazenyl)quinolin-8-amine (**6c**)

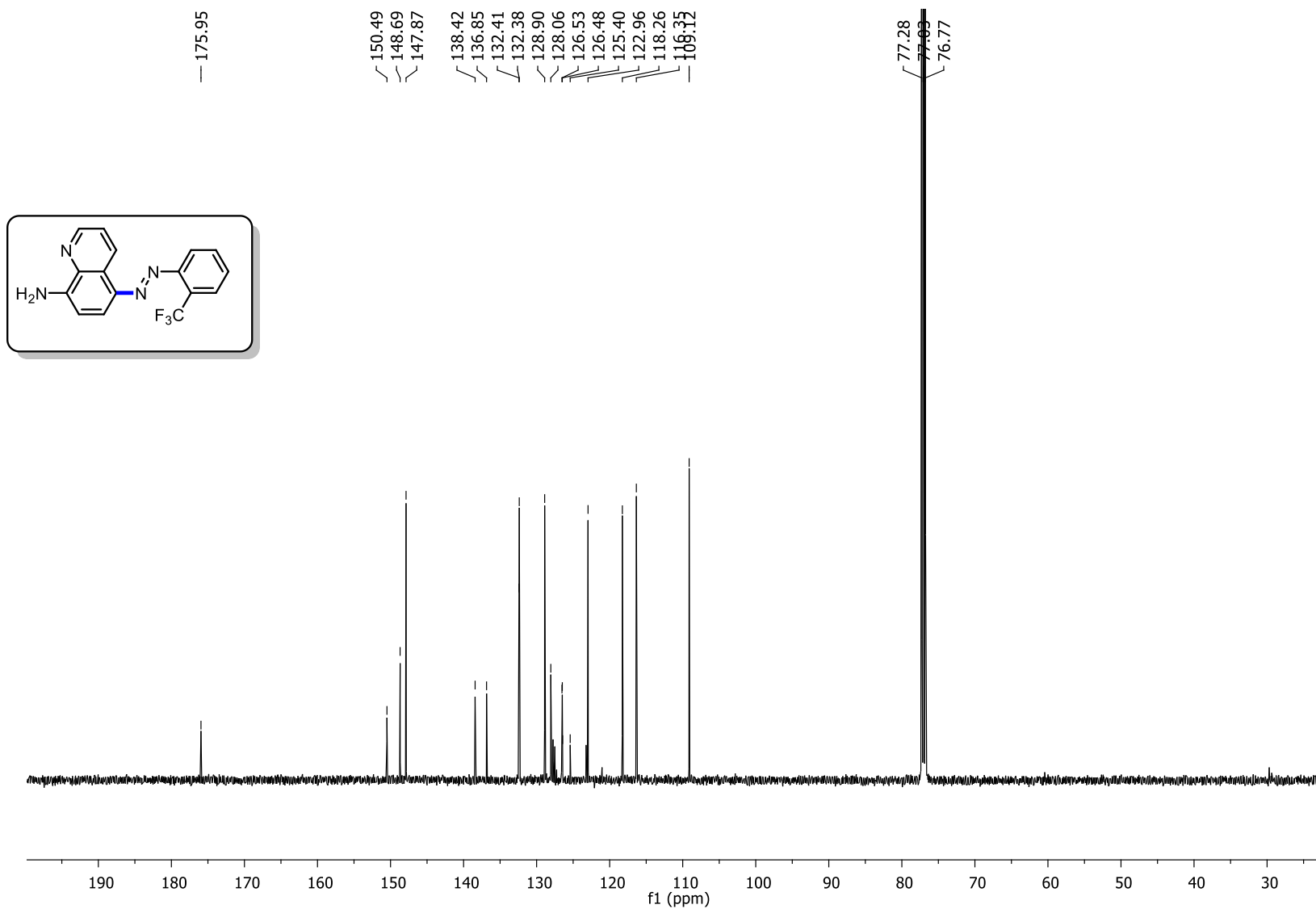




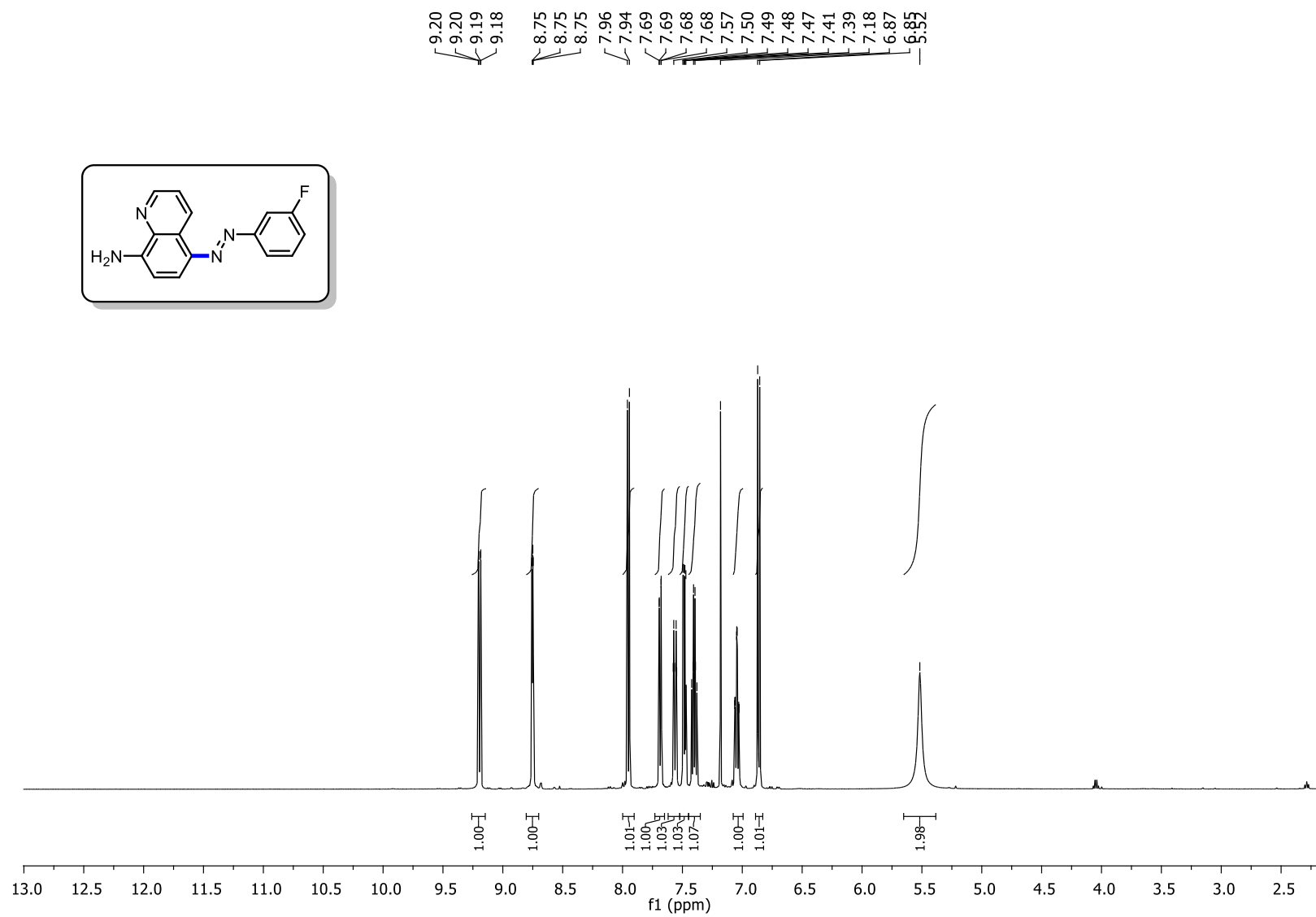
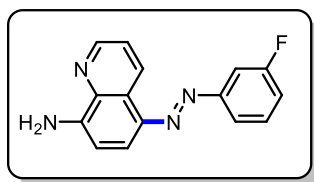
<sup>1</sup>H NMR (CDCl<sub>3</sub>, 500 MHz) spectrum of (E)-5-((2-(trifluoromethyl)phenyl)diazenyl)quinolin-8-amine (**6d**)



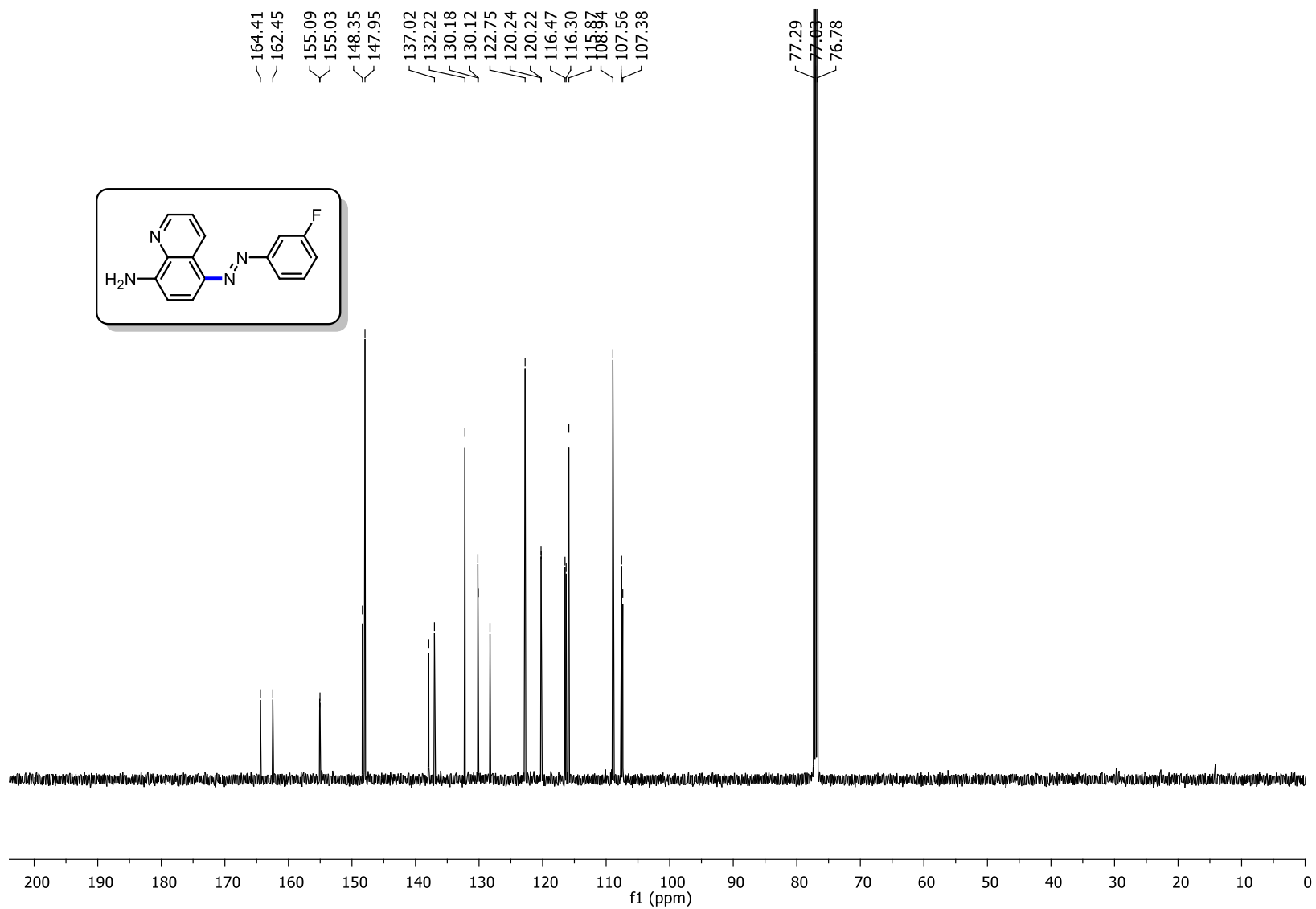
$^{13}\text{C}$  NMR ( $\text{CDCl}_3$ , 126 MHz) spectrum of (E)-5-((2-(trifluoromethyl)phenyl)diazenyl)quinolin-8-amine (**6d**)



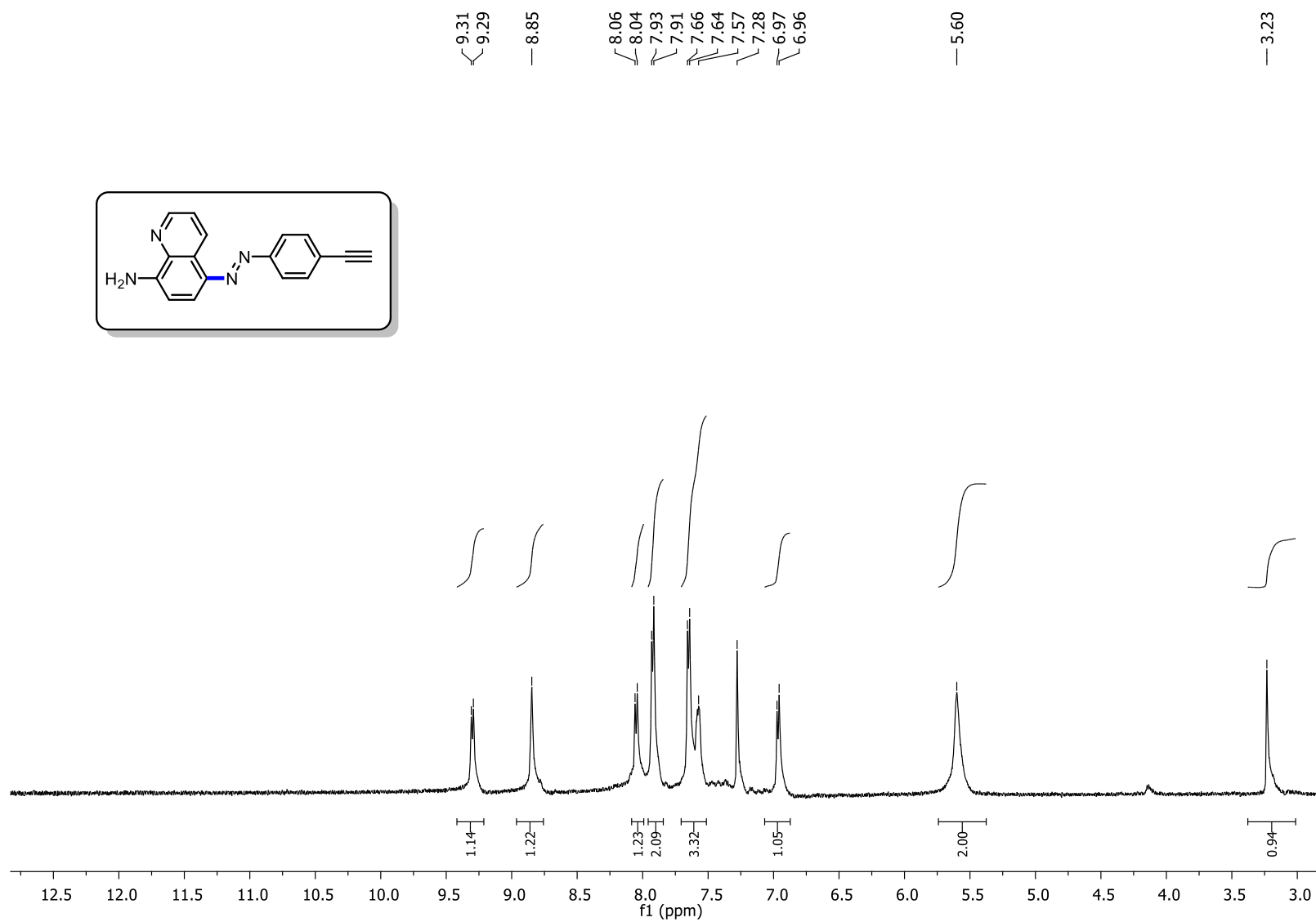
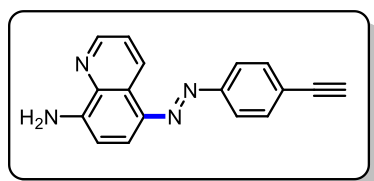
$^1\text{H}$  NMR ( $\text{CDCl}_3$ , 500 MHz) spectrum of (E)-5-((3-fluorophenyl)diazenyl)quinolin-8-amine (**6e**)



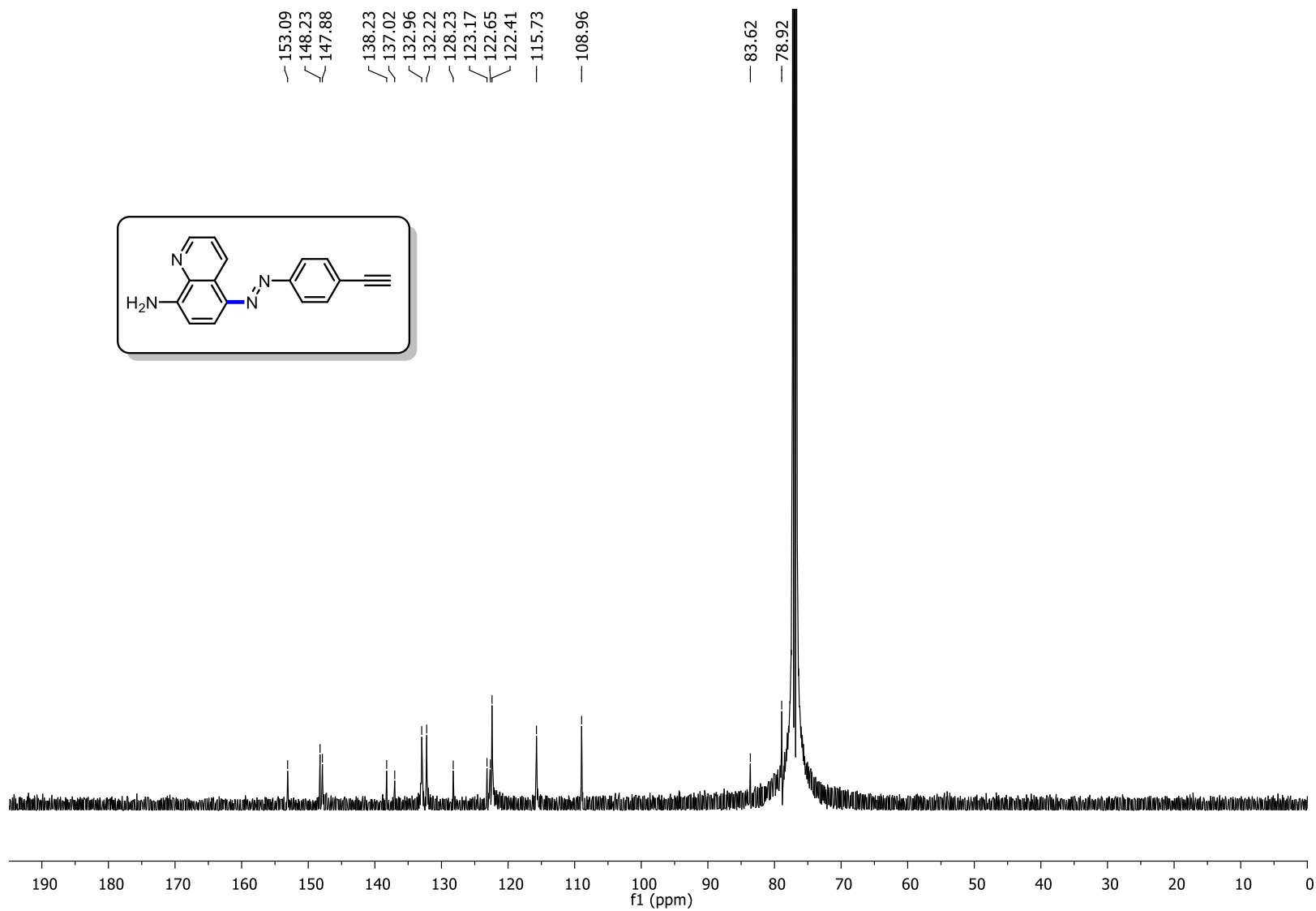
<sup>13</sup>C NMR (CDCl<sub>3</sub>, 126 MHz) spectrum of (E)-5-((3-fluorophenyl)diazenyl)quinolin-8-amine (**6e**)



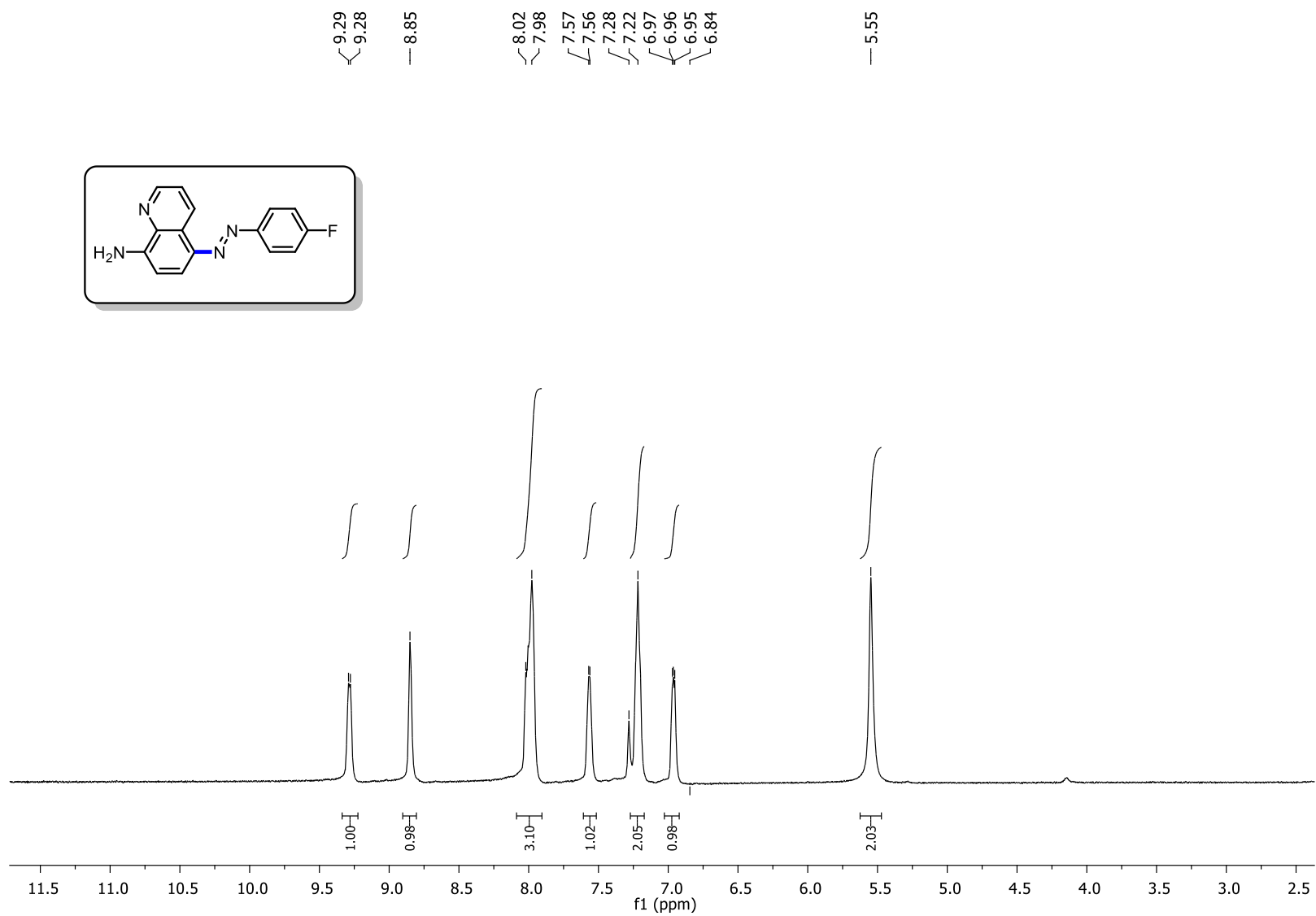
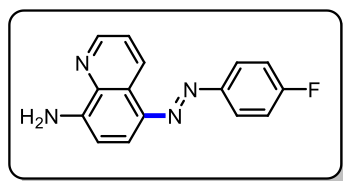
$^1\text{H}$  NMR ( $\text{CDCl}_3$ , 500 MHz) spectrum of (E)-5-((4-ethynylphenyl)diazenyl)quinolin-8-amine (**6f**)



$^{13}\text{C}$  NMR ( $\text{CDCl}_3$ , 126 MHz) spectrum of (E)-5-((4-ethynylphenyl)diazenyl)quinolin-8-amine (**6f**)

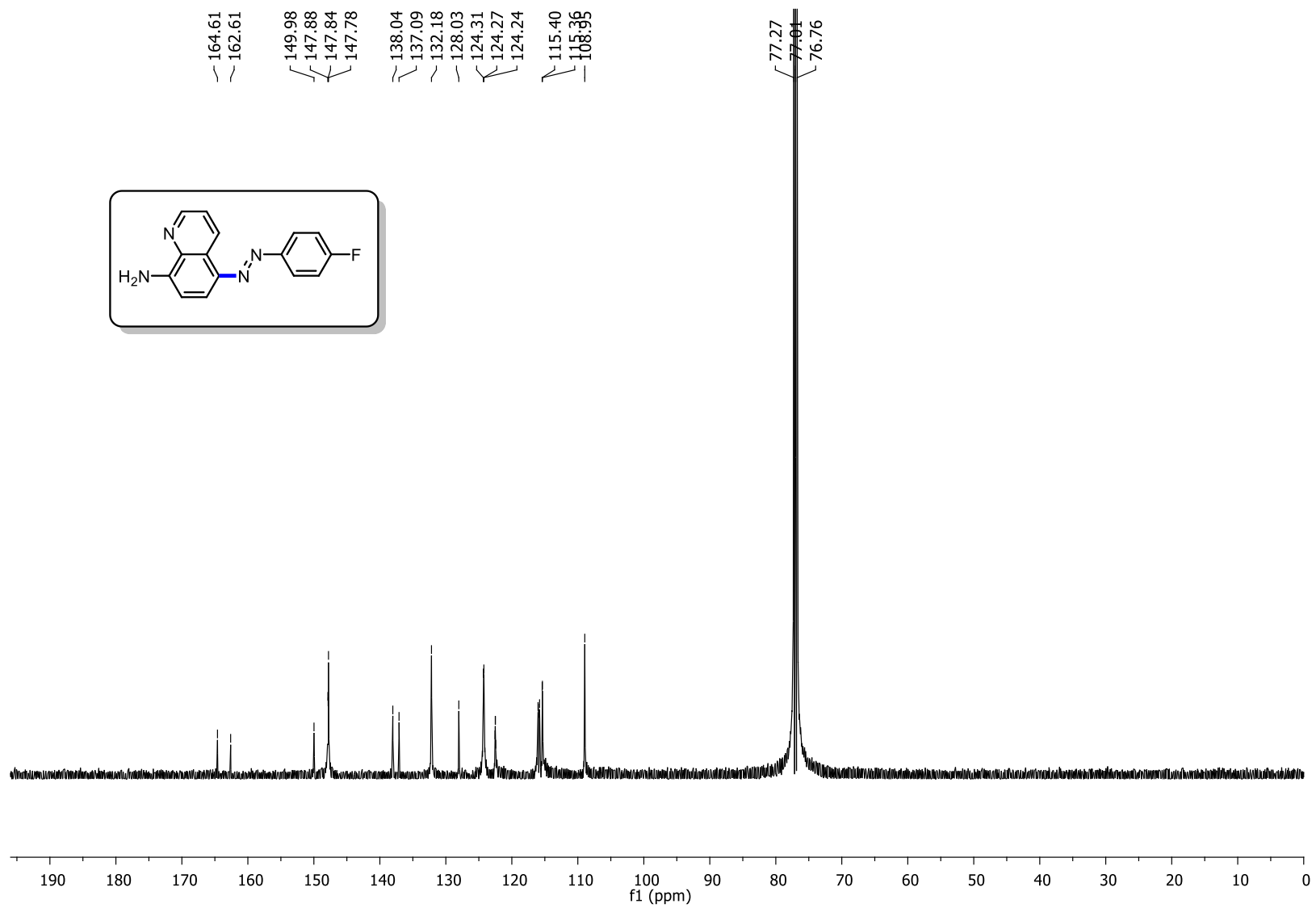


$^1\text{H}$  NMR ( $\text{CDCl}_3$ , 500 MHz) spectrum of (E)-5-((4-fluorophenyl)diazenyl)quinolin-8-amine (**6g**)





$^{13}\text{C}$  NMR ( $\text{CDCl}_3$ , 126 MHz) spectrum of (E)-5-((4-fluorophenyl)diazenyl)quinolin-8-amine (**6g**)





## Determination of the Molecular Mass of Hydrolyzed Fibroin Obtained from Natural Silk Fibroin by Spectrophotometry

Khushnadbek Odilbekovich ESHCHANOV<sup>1</sup> , Mukhabbat Matnazarovna BALTAEVA<sup>1</sup> 

<sup>1</sup>Urgench State University, Department of Chemistry, Urgench, 220100, Uzbekistan

**Abstract:** In our previous scientific publications, we have recommended spectrophotometry as a method for determining the molecular mass of silk fibroin. As a result of our research, we were able to obtain hydrolyzed fibroin ("HF") with high polyfunctional high sorption properties from natural silk fibroin by thermal methods under acidic conditions and the influence of UHF rays. We used spectrophotometry to determine the molecular mass of "HF" obtained by two different methods. It was observed that there are differences between the molecular masses of "HF" obtained by thermal methods and under the influence of ultra-high frequency (UHF) rays. It was found that the molecular mass of "HF" obtained thermally under acidic conditions was 246,6 kDa, and the molecular mass of "HF" obtained under the influence of UHF rays was 307 kDa. The main reason for the different molecular masses of "HF" was considered to be the fact that the process duration of "HF" production methods varies.

**Keywords:** Spectrophotometry, hydrolyzed fibroin ("HF"), ultra-high frequency (UHF) rays, UV spectrum, molecular mass.

**Submitted:** July 10, 2021. **Accepted:** December 07, 2021.

**Cite this:** Eshchanov KO, Baltaeva M. Determination of the Molecular Mass of Hydrolyzed Fibroin Obtained from Natural Silk Fibroin by Spectrophotometry. JOTCSA. 2022;9(1):115-20.

\*DOI: <https://doi.org/10.18596/jotcsa.969482>.

\*Corresponding author. E-mail: [olmos\\_77@mail.ru](mailto:olmos_77@mail.ru)

### INTRODUCTION

Silkworm fiber is a thin, hard, and shiny fiber, a natural textile raw material made from the fluid that comes out of the silkworm's two silk glands. Silk is made up of two strands wrapped around a silkworm cocoon that are not glued together, coated with sericin (silk glue), and glued together. This fiber contains 70-75% fibroin (protein), 20-25% sericin, 2-3% various minerals, 1-1,5% wax and oils.

Silk is used for silk weaving, baked yarn and in engineering, aviation, aerospace and electrical engineering (1). In production technologies, fibers and films are made on the basis of natural cocoons.

The fibroin in silk is insoluble in water. In hot water, the sericin protein dissolves, which covers the top of the fiber. Silk fiber can withstand temperatures up to 140 °C. When the temperature rises to 140-170 °C, the protein in the fiber undergoes a structural change. The density of the fiber depends on the type of silk. For example, the densities of Mulberry and Tussah silks are 1.33 and 1.32 g/cm<sup>3</sup>, respectively. Other types of silk have an average density of 1.6 g/cm<sup>3</sup> (2, 3).

Fibroin is a fibrillar protein that forms the polymer basis of natural silk. The primary structure of these proteins depends on the nature of the natural cocoon, the silkworm's diet, time, and other biological factors. The largest mass fraction (90%) in the fibroin macromolecule corresponds to the amino acid residues Gly, Ala, Tyr, Ser. There is also a very small amount ( $\omega < 1\%$ ) of Cys in the

fibroin macromolecule. The polypeptide chain of fibroin contains hydrophilic and hydrophobic amino acid groups in a 6.3:1 ratio. The fibroin molecule consists of crystalline ( $\beta$ -structure) and amorphous ( $\alpha$ -spiral) parts in which the polymer chain is sequentially arranged (4, 5).

Fibroin is insoluble in alcohol, ether, benzene, acetone, carbon disulfide, and other organic solvents. Salts of calcium, strontium, barium, which form a solution in a neutral medium, and hydrogen halide acids, and Schweizer's reagent form colloidal systems in alkaline solutions. Soluble in concentrated phosphate, sulfate, hydrochloric acid, and liquid ammonia at low temperatures (between 9 and 11 °C) (6).

Silk fibroin is also soluble in concentrated  $ZnCl_2$  solution and ammoniacal solutions of nickel(II) hydroxide. Fibroin is well soluble in copper(II) glycerate and ethylenediamine copper(II) in solutions of dichloroacetic and formic acids. Solutions of 0.7% to 1% concentrates of fibroin can be prepared in solution. It is possible to form a fibroin solution in N-methylmorpholine-N-oxide at 74-76 °C. Fibroin is well soluble in hydrotron solvents, such as iodides and rhodanides of  $Li^+$ ,  $K^+$ ,  $Na^+$ ; halides and rhodanides of  $Ca^{2+}$ ,  $Zn^{2+}$ ; di and trichlor (or fluorine) are soluble in acetic acids. With 56% of NaSCN with 10% DMSO, the viscosity of silk fibroin at 25 °C in aqueous solution is well studied, and the following expressions apply to this solution (6, 7):

$$[\eta] = 0.4 \times 10^{-4} M_w^{0.58} \quad (\text{Eq.1})$$

Silk fibroin is well soluble in a solvent mixed with  $CaCl_2:C_2H_5OH:H_2O$  (8). Examination of the solution by UV spectrophotometry revealed that the maximum absorption wavelength is close to 280 nm.

The silk fibroin molecule consists of 3 chains, the heavy chain (which can range from 390 kDa to 500 kDa), the light chain (26 kDa), and the P-25 glycoprotein (25 kDa) (9). The literature indicates that the molecular weight of fibroin is 60-150 kDa (average 84 kDa) as determined by ultracentrifugation and diffusion methods (10). By measuring the osmotic pressure, it was determined that the molecular mass of silk fibroin is 30 kDa (11).

Silk fibroin was found to be up to 250 kDa in 9.3 M LiBr solution by SDS-PAGE (8). Silk fibroin was found to be 300 kDa in  $CaCl_2$ -ethanol solution using the SDS-PAGE method (12).

To determine the molecular mass of silk fibroin, it is necessary to convert it into a solution. We have

shown in our previous work that we used spectrophotometry to determine the molecular mass of silk fibroin (13).

As a result of our research, we studied the methods of production of hydrolyzed fibroin with high sorption properties from silk fibroin and determined the optimal conditions. "HF" from silk fibroin fiber was obtained by the thermal method under acidic conditions and the influence of UHF rays (2450 MHz). The result is a powdery white "HF". It was studied that the time of obtaining "HF" from silk fibroin under the influence of UHF rays ends 5-6 times faster than the thermal method (14). "HF"s multifunctional high sorbent properties have the potential to be used in pharmaceuticals, cosmetics, food, and other industries.

## EXPERIMENTAL SECTION

### Materials

Fibrous waste of silk (cleaned of additives, Khorezmipagi LLC, Urgench, Uzbekistan), Sodium carbonate (purity 99,9%), HCl (chemically pure) was purchased from Chimreaktivinvest (Uzbekistan). Calcium chloride and ethyl alcohol (98%) were purchased from Fortek company (Uzbekistan).

### Instrumentation

Bidistilled water is obtained from the "GFL 2104 Double distillation water still" device (Germany). The experiments used UV-1800 Shimadzu spectrometer, Thermostat spare parts (Assistant cat. № 3180) (Hamburg, Germany).

### Procedure

*Obtaining "HF" thermally in an acidic environment*  
The cocoon is placed in a 500 mL heat-resistant beaker and a 0.5%  $Na_2CO_3$  solution (1:50  $\omega/v$ ) is poured over it. Boil a glass of water in a bath for 30 minutes. The fiber is then removed from the beaker and boiled for 10 min with distilled water. The boiled fiber is washed with a mixture of distilled water until salts are removed from the mixture. The fiber is dried in an oven at 70 °C for 4 hours. Transfer the obtained fiber to a 500 mL heat-resistant beaker and top with a 3% HCl solution (1:50  $\omega/v$ ). Heat in a glass container at a temperature of 90-95 °C for 80-90 min. The result is a white powdery "HF".

*Obtaining "HF" from silk fibroin under the influence of UHF rays*

Put cocoon fiber and 0.5%  $Na_2CO_3$  solution (1:50  $\omega/v$ ) in a 500 mL beaker. Boil the solution in a glass for 30 minutes. At the end of the allotted time, remove the fiber from the container and rinse with distilled water (until no  $Na_2CO_3$  remains). Transfer the washed fiber to a 500 mL beaker and top with a 3% HCl (1:50  $\omega/v$ ) solution.

The glass is placed in the microwave. Hydrolysis of fibroin fibers is carried out under the influence of 510 W UHF rays (2450 MHz). The result is a white powdery "HF".

*Determination of molecular masses of "HF" samples obtained by thermal and UHF rays by spectrophotometry*

The measured "HF" powder mass was dissolved in a solution of  $\text{CaCl}_2:\text{C}_2\text{H}_5\text{OH}:\text{H}_2\text{O}$  (1:2:8 mol) at a temperature of 65 °C. In order to determine the molecular mass of "HF" obtained thermally in an acidic environment, solutions with a concentration of 0.04, 0.06, 0.0833, 0.1, 0.125, 0.25, and 0.5 g/L were prepared. The UV-1800 Shimadzu spectrophotometer indicated that the maximum absorption wavelength of the prepared solutions of "HF" was 280 nm. The light absorption was determined in a 1 cm thick ( $l$ ) cuvette.

The above operations were also performed for "HF" obtained under the influence of UHF rays. To

determine the molecular mass of "HF", solutions with concentrations of 0.508, 0.14, 0.07, 0.035, and 0.0175 g/L were prepared. The light absorption of "HF" solutions obtained under the influence of UHF rays was determined.

## RESULTS AND DISCUSSION

The UV spectra of "HF" obtained thermally in an acidic environment were studied (Figure 1). The light absorption values of "HF" solutions at 280 nm were determined and the  $A/l$  and  $C$  correlation graphs were plotted (Figure 2). To determine the molecular mass of "HF", it is necessary to determine the angular length ( $\alpha$ ) of the graph line  $A/l-C$  concerning the  $C$  axis. Molecular mass is determined by the following formula.

$$M = \frac{\epsilon}{\text{tg } \alpha} \quad (\text{Eq. 2})$$

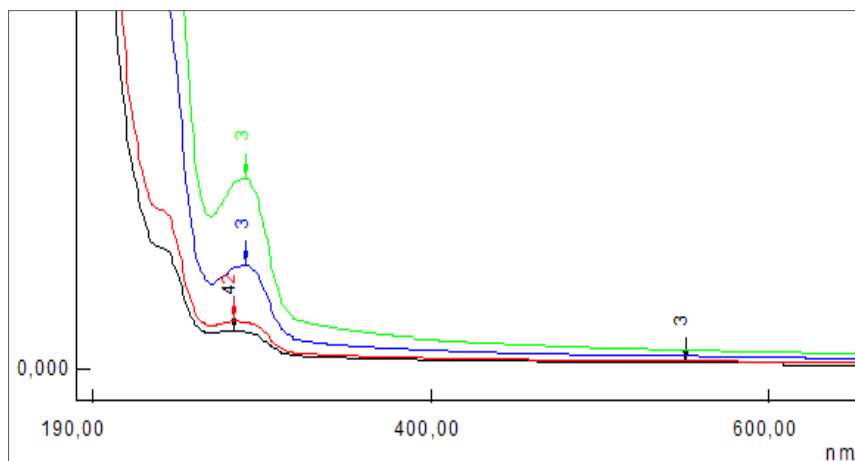


**Figure 1:** UV spectra of thermally obtained "HF" solutions.

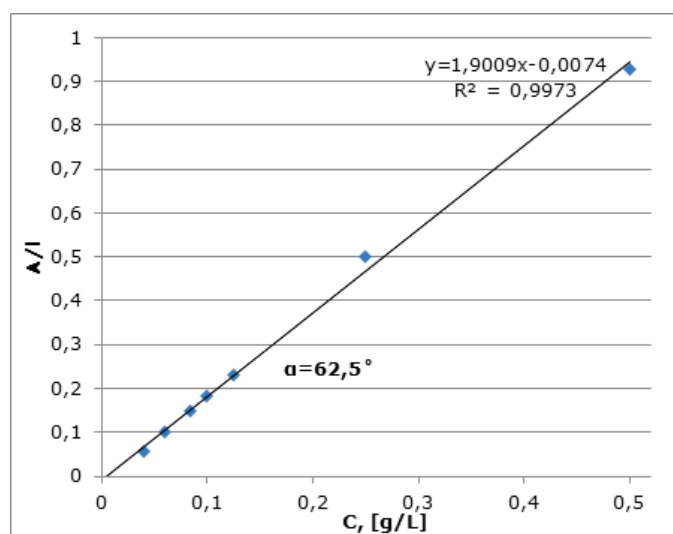


**Figure 2:** Graph of  $A/l$  and  $C$  dependence of "HF" solution obtained by thermal method.

Based on the results obtained by the spectrophotometric method, it was determined that the molecular mass of "HF" obtained by the thermal method using formula (Eq. 2) is 246.6 kDa. The molecular mass of "HF" obtained from silk fibroin under the influence of UHF rays in an

acidic medium was also determined by spectrophotometry. The light absorption of "HF" solutions obtained under the influence of UHF rays was determined and the A/I-C correlation graph was plotted (Figure 4).

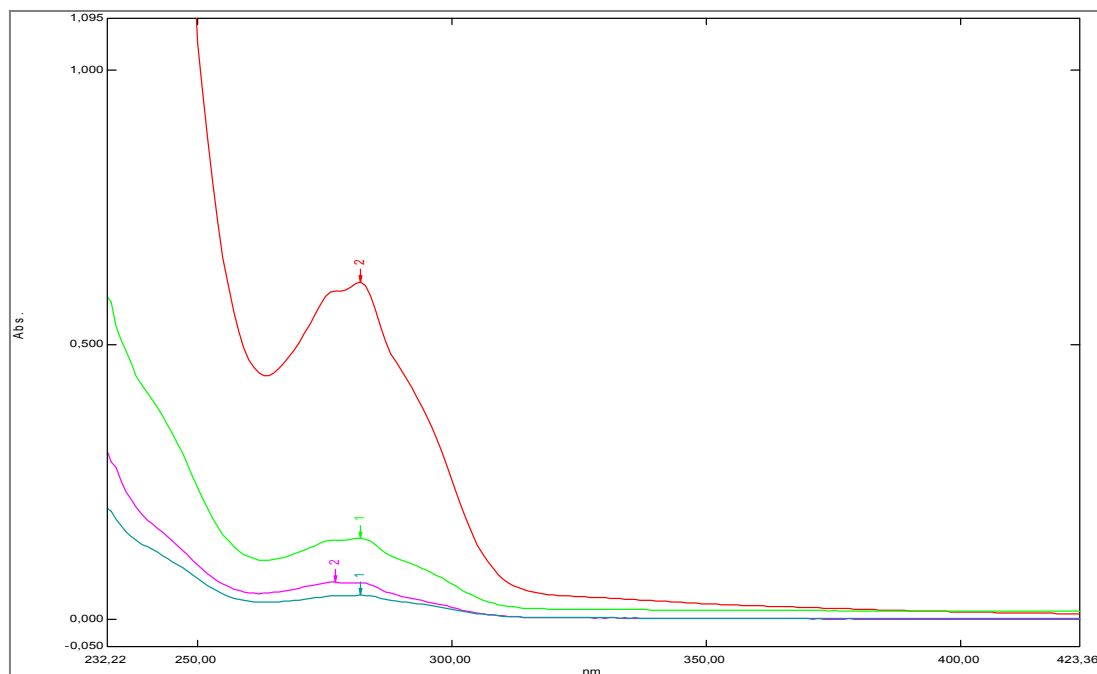


**Figure 3:** UV spectra of "HF" solutions obtained under the influence of UHF rays.

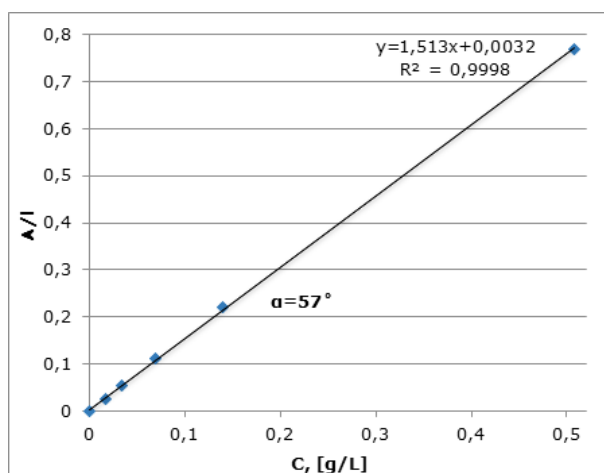


**Figure 4:** Graph of A/I and C dependence of "HF" solution obtained under the influence of UHF rays.

The angular length of the graph line relative to the concentration (C) axis was found to be  $57^\circ$ . The molecular mass of "HF" obtained under the influence of UHF rays was found to be 307 kDa using formula (Eq. 2).

## CONCLUSION

We hypothesized that the reason for the differences between the molecular masses of "HF"s

obtained by thermal methods and under the influence of UHF rays is that the process of obtaining "HF" takes place at different times. Because it takes more time to obtain "HF" from silk fibroin by thermal methods, fibroin molecules are hydrolyzed into smaller pieces. Therefore, it can be observed that the masses of "HF" molecules obtained by thermal methods are smaller.

Determining the molecular mass of fibroin-containing proteins using the method of spectrophotometry is superior to other methods of determining the molecular mass with speed and low cost, accuracy. In this method, the determination of molecular mass is almost unaffected by various external factors. In determining the molecular mass, coagulation, and sedimentation of the protein in solution may adversely affect the results. Therefore, special attention should be paid to the state of the solution of the protein, the molecular weight of which is determined.

## REFERENCES

1. Wang YJ, Zhag YQ. Three-Layered Sericins around the Silk Fibroin Fiber from *Bombyx mori* Cocoon and their Amino Acid Composition. *AMR*. 2011 Jan;175-176:158-63. [<DOI>](#).
2. Liu X, Zhang K-Q. Silk Fiber — Molecular Formation Mechanism, Structure- Property Relationship and Advanced Applications. In: Lesieur C, editor. *Oligomerization of Chemical and Biological Compounds* [Internet]. InTech; 2014 [cited 2021 Dec 11]. ISBN: 978-953-51-1617-2. [<URL>](#)
3. Sashina E, Heinemann K, Horst B, Novoselov N, Frank M. Method for dissolving natural silk. Russian Federation Patent, no: 2385649, 2007.
4. Kunz RI, Brancalhão RMC, Ribeiro L de FC, Natali MRM. Silkworm Sericin: Properties and Biomedical Applications. *BioMed Research International*. 2016;2016:1-19. [<DOI>](#).
5. Brestkin YuV. Dynamic coil-extended chain phase transition in the longitudinal field. *Acta Polym*. 1987 Aug;38(8):470-7. [<DOI>](#).
6. Geller B, Geller A, Chirtulov V. Practical Guide to Physical Chemistry of Fiber-Forming Polymers. Vol. 432. 1996. 432 p.
7. David V. Introduction to Biophysics. Mir Publishers; 1982. 210 p.
8. Zhang H, Li L, Dai F, Zhang H, Ni B, Zhou W, et al. Preparation and characterization of silk fibroin as a biomaterial with potential for drug delivery. *J Transl Med*. 2012 Dec;10(1):117. [<DOI>](#).
9. Tanaka K, Inoue S, Mizuno S. Hydrophobic interaction of P25, containing Asn-linked oligosaccharide chains, with the H-L complex of silk fibroin produced by *Bombyx mori*. *Insect Biochemistry and Molecular Biology*. 1999 Mar;29(3):269-76. [<DOI>](#)H.
10. Holmes F, Smith D. Sedimentation and Diffusion of Soluble Fibroin. *Nature*. 169:193. [<URL>](#).
11. Coleman D, Howitt F. Studies on silk proteins I. The properties and constitution of fibroin. The conversion of fibroin into a water-soluble form and its bearing on the phenomenon of denaturation. *Proc R Soc Lond A*. 1947 Jul 8;190(1021):145-69. [<DOI>](#).
12. Feng Y, Lin J, Niu L, Wang Y, Cheng Z, Sun X, et al. High Molecular Weight Silk Fibroin Prepared by Papain Degumming. *Polymers*. 2020 Sep 16;12(9):2105. [<DOI>](#).
13. Eshchanov KO, Baltayeva M, Sarimsakov A. Determination of the Molecular Mass of Silk Fibroin Using the Method of Spectrophotometry. *Annals of RSCB*. 2021;25(2):4083-90. [<URL>](#).
14. Eshchanov KO, Baltayeva M, Sarimsakov A. Purification of Cottonseed Oil Using A Sorbent Obtained from the Fibrous Waste of Natural Silk. *Annals of RSCB*. 2021;25(1):692-8. [<URL>](#).







## Chitosan-Graft-Polyacrylamide Based Release Systems: Effect of pH and Crosslinking

Ahmet KÜÇÜKÇALIK , Cüneyt H. ÜNLÜ\*  

Istanbul Technical University Science & Letters Faculty, Chemistry Department Maslak TR34469 Istanbul TURKEY

**Abstract:** This study covers the synthesis and release behavior of chitosan-graft-polyacrylamide copolymers in aqueous media at different pH values. The copolymers were synthesized using redox polymerization with ceric ammonium nitrate (CAN) in 1% aqueous acetic acid solution as the initiator. Optimum condition for the graft copolymer synthesis was determined as 3.85 g/L chitosan, 0.27 M acrylamide (AAm) monomer at 40 °C with a CAN per gram chitosan as 6 mmol using 0.05 M stock solution in 0.1 N HNO<sub>3</sub>. Then the crosslinked copolymers were synthesized using methylenebisacrylamide (MBA) as a crosslinker varying mass proportions of AAm:MBA as 15:1, 20:1, and 30:1. Obtained material amount (polymer yield) and molecular weight of crosslinked copolymers were lower than the graft copolymer as expected. Acetylsalicylic acid (ASA) release behaviors of all copolymers were monitored with UV-visible spectroscopy at different pH values (2, 6, and 8.5) corresponding to different media in the body (stomach, skin, and intestine, respectively). According to the results, the release behavior changed the least among the samples with respect to medium pH and of was the most affected.

**Keywords:** Drug delivery systems; chitosan; emulsion polymerization; graft copolymers.

**Submitted:** July 09, 2021. **Accepted:** December 08, 2021.

**Cite this:** Küçükçalık A, Ünlü CH. Chitosan-graft-Polyacrylamide Based Release Systems: Effect of pH and Crosslinking. JOTCSA. 2022;9(1):121-30.

**DOI:** <https://doi.org/10.18596/jotcsa.968037>.

**\*Corresponding author. E-mail:** [unlucu@itu.edu.tr](mailto:unlucu@itu.edu.tr).

### INTRODUCTION

Chitosan is the second most abundant macromolecule in nature after cellulose. It has many aspects being biocompatible, biodegradable, non-toxic, convenient to modification, etc (1,2). It has a linear structure which is composed of 1,4-β-2-amino-2-deoxy-D-glucose (deacetylated D-glucosamine) and N-acetyl-D-glucosamine units. Chitosan is obtained by deacetylation of chitin; in fact, chitin and chitosan are only different in degree of deacetylation (DDA); when DDA is higher than 50% the biopolymer is called as chitosan, otherwise as chitin. The structural features such as crystallinity and solubility are also very closely related with DDA, i.e. chitin and chitosan portions of the 50% DDA biopolymer form an amorphous block copolymer while 99% DDA is a linear, random

semicrystalline copolymer (3). Solubility also increases with increasing DDA; amine groups of the chitosan has a pK value of approximately 6.5 indicating that if the medium pH < 4 chitosan is soluble forming a polycationic structure (3-5).

Ceric ion initiated polymerizations are widely used for aqueous grafting vinyl polymers onto reducing agents which has one or more O-H groups (6), i.e. PEG (7), cellulose (8,9), and xylan (10). Initiation step involves oxidation of O-H groups through a radical pathway. First, ceric ion and reducing agent (i.e. cellulose) form a 5-membered chelate complex; then in acidic medium this complex decomposes, creating a radical on either carbon or oxygen, reducing Ce(IV) to Ce(III) (9). The creation of radicals is a set of complex equilibria including the concentrations of components, temperature and

duration of the reaction. If these factors are not set properly reaction may lead to oxidation of reducing compound terminating the radical created (i.e. low polymer yield). Another problem may be self-creation of radical from air oxygen or from solvent (water) leading to homopolymers. In order to prevent the mentioned side effects an optimum condition has to be found. Having active sites chitosan also can react with ceric ion like cellulose and other polysaccharides (11,12).

Controlled release systems or controlled drug delivery systems are used for delivering some therapeutic agent at a certain site or releasing it slowly in the body; thus the agent is needed to incorporate to a polymeric network structure (13). Chitosan is widely preferred for controlled release systems especially due to unique properties which are mentioned above including biocompatibility and swelling behavior at low pH (1,13). After modification with polyacrylamide swelling property of chitosan enhances and this copolymer may be used as a matrix which become very popular component for controlled release systems. There are many parameters affecting swelling, and in turn release behavior, of the copolymer; some of these parameters are pH, temperature, concentration, and salinity (2,14,15). Chitosan-polyacrylamide release matrix is used in earlier studies with several differences, for example Bulut has used chitosan-graft-polyacrylamide matrix supporting with carboxymethylcellulose to encapsulate and release ibuprofen (12), and Wang et al. has grafted polyacrylamide and poly(N-isopropylacrylamide) to chitosan to use obtain a gel structure both sensitive to pH and temperature (16). Presence or number of crosslinks among the copolymer which is grafted onto chitosan chains may affect the release rate in media with different pH values.

In this study, chitosan functionalization via redox polymerization using ceric ammonium nitrate as initiator to graft linear or crosslinked polyacrylamide moieties onto chitosan has aimed in order to obtain controlled release systems. First, optimization of the reaction conditions was achieved. Then spectral and physical characterizations of the samples was done. Finally, controlled release experiments were done at different pH values which were corresponding to different environmental values as acidic (pH 2, stomach), nearly neutral (pH 6, skin), and basic (pH 8.5, intestine).

## MATERIALS AND METHODS

### Chemicals and solutions

Chitosan 99% DDA (Sigma Aldrich), nitric acid (65%, d=1.40 g/mL, Merck), acrylamide (AAm) (Merck), methylenebisacrylamide (MBA) (Fluka), sodium hydroxide (Merck), acetylsalicylic acid (ASA) (Sigma-Aldrich), glacial acetic acid (Merck), isopropyl alcohol (technical grade, distilled prior to

every use), acetone (Merck). Rest of the chemicals were all of Merck brand and used as received.

Ceric ammonium nitrate (CAN) was Sigma-Aldrich brand and it was used as a stock solution of 0.05 M in 0.1 M nitric acid.

Acidic buffer solution (pH 2) was prepared dissolving KCl (7.45 g) in water; then HCl (37%, 1.75 mL) was added to the mixture and completed to 1.0 L with distilled water.

Slightly acidic buffer solution (pH 6) was prepared dissolving Na<sub>2</sub>HPO<sub>4</sub>·7 H<sub>2</sub>O (1.307 g) and NaH<sub>2</sub>PO<sub>4</sub>·H<sub>2</sub>O (13.127 g) in water; then the mixture completed up to 1.0 L with distilled water.

Basic buffer solution (pH 8.5) was prepared dissolving H<sub>3</sub>BO<sub>3</sub> (61.83 g) and NaOH (10.00 g) in water; then the mixture completed to 1.0 L with distilled water.

### Instruments

FTIR measurements were carried out on Thermo Scientific Nicolet 380 equipped with a diamond crystal ATR module in a range of 4000–400 cm<sup>-1</sup> in percent transmission mode.

NMR measurements were carried out on an Agilent instrument (500 MHz for <sup>1</sup>H, 11.7 T) using D<sub>2</sub>O as solvent.

UV-visible spectra were taken on Perkin Elmer Lambda 25 model instrument in 200-400 nm wavelength range.

### Molecular weight determination

Molecular weight determinations were carried out using viscometric method with Ubbelohde viscometer. Mark-Houwink constants for polyacrylamide was K = 6.31×10<sup>-3</sup> mL/g and α = 0.80 in water at 30 °C. (17) Intrinsic viscosity ( $[\eta]$ ) was determined using Solomon-Ciuta equation (1). (18,19)

$$[\eta] = \frac{\sqrt{2 - (\eta_{sp} - \ln \eta_{rel})}}{C} \quad (1)$$

### Thermogravimetric analyses

Thermogravimetric analyses (TGA) were carried out on a Perkin Elmer Pyris 1 TGA with a heating rate of 20 °C/min in 30-1000 °C range.

### Statistical analysis

Principal component analysis (PCA) was performed on first derivative FTIR data using R software (version 4.0.0) running on 64-bit MS Windows 10 platform. First order derivatives of the spectra in range between 1800 and 850 cm<sup>-1</sup>, which were calculated via the Savitzky-Golay algorithm averaging 4 points left and right side using a third

order polynomial, were used in order to eliminate the errors that could arise from overlapping.

### Synthesis of Chitosan-graft-Poly(Acrylamide) (ChAAm)

Chitosan (0.1 g) and AAm (0.5 g) were dissolved in 10 mL 1% acetic acid separately in 15 minutes at 40 °C; then both solutions were mixed to have a chitosan:AAm mass proportion of 1:5. After stirring at 40 °C for another 15 minutes 6 mL of CAN solution was slowly added to the mixture in 15 minutes. Polymerization was allowed to continue for 3 hours at the same temperature. Then the mixture was poured into 5 volumes of isopropanol to precipitate grafted copolymer. The medium pH was adjusted with to approximately 9 with 1 M NaOH; then the alcoholic mixture was left to precipitate the small chains overnight at -35 °C. The graft copolymer was separated centrifuging at 200-G for 5 minutes, then left to dry first in air, then in the vacuum.

The percentage (G%) and efficiency (E%) of grafting was calculated as following equations (2) and (3). (11)

$$G\% = \frac{W_{cop} - W_{chitosan}}{W_{chitosan}} \times 100 \quad (2)$$

$$E\% = \frac{W_{cop} - W_{chitosan}}{W_{monomer}} \times 100 \quad (3)$$

### Synthesis of Crosslinked Grafted Copolymer (ChAAx)

Polymerization procedure for crosslinked copolymers was similar, but after addition of CAN solution methylenebisacrylamide (MBA) was added to the mixture as crosslinking agent in different proportions relative to AAm. The proportions of AAm:MBA were 15:1, 20:1, 30:1, by mass. The

termination and precipitation parts of the procedure was followed likewise.

### Loading and Releasing Acetyl Salicylic Acid

Loading of ASA was carried out using polyelectrolyte complex (PEC) method. The copolymer (108 mg) was dissolved in 10 mL of 1% acetic acid; in another container acetylsalicylic acid (ASA) was dissolved in 10 mL of water, then it was made alkaline with addition of 1 M NaOH. The alkaline ASA solution was dripped slowly into acidic copolymer solution in 10 minutes. Afterwards, the ASA-copolymer mixture was poured into acetone solution to precipitate. In order to accelerate and promote precipitation the final solution was cooled in deep freeze (-25 °C). The loaded copolymers were collected centrifuging the cold mixture. The loaded samples were washed with acetone, dried first in air, then in vacuum. Then the loaded copolymer was pressed to convert into a pellet.

Release of ASA from the copolymer matrix was monitored using UV-visible spectroscopy using the intensity of the signal located at 300 nm. First calibration curves were obtained for ASA at 3 different pH using proper buffer solutions. Then the loaded copolymer was placed in a container with 10 mL appropriate buffer solution and UV measurements were done periodically.

## RESULTS AND DISCUSSIONS

Chitosan is a naturally occurring polymer and is mainly composed of  $\beta$ -2-amino-anhydroglucose units linked through 1 to 4 positions. Having active OH sites chitosan reduces ceric ion, creating radicals with a redox reaction leading to initiation of a vinyl polymerization (6). Radical generation from cellulose is related with a chelate complex formation (8,9). Thus a similar path is expected for chitosan; the formed radical may be on nitrogen, oxygen, or carbon (Figure 1).

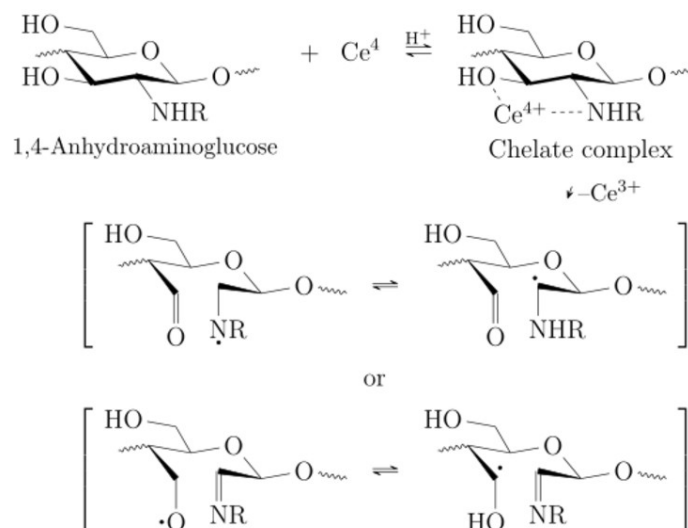
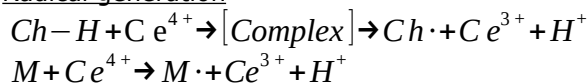


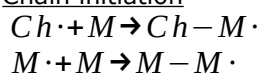
**Figure 1:** Plausible mechanism of radical generation with ceric ion and chitosan.

Although a reducing agent is needed to create radicals, sometimes ceric ion and aerial oxygen (or water) can also react to produce radicals, leading to homopolymers. The possible reactions were given in the scheme below. This unfavorable situation can be prevented adjusting reaction conditions. Other unwanted side reactions involving reducing agent, chitosan, were degradation in acidic medium or oxidation by ceric ion.

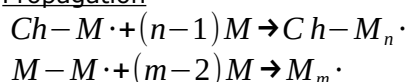
#### Radical generation



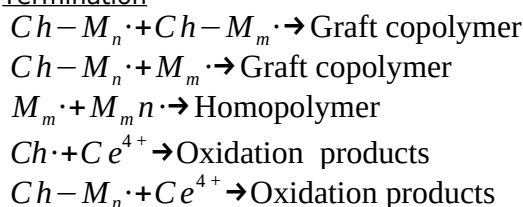
#### Chain initiation



#### Propagation



#### Termination



**Scheme 1:** Possible reactions in the medium containing chitosan (Ch), CAN ( $\text{Ce}^{4+}$ ), and monomer (AAM, MBA).

Ceric ion initiated polymerization reactions were affected by several factors including total acid concentration, reducing agent type, concentrations, reaction temperature, and duration (7,20,21). These

factors were interfering among each other; thus an optimization run was necessary for different monomer and/or reducing agent couples to have a maximum yield of desired product, i.e. graft copolymer. As previous studies implied each factor had an individual apex interfering with each other starting with a predetermined condition obtained from earlier works was favorable (7,8,10).

Releasing experiments were carried out in 1% acetic acid in order to carry out the reaction in a homogeneous solution as chitosan was soluble in acidic solutions. As the results indicated that using inert atmosphere was not needed. Changes in temperature and/or reaction period caused a decrease in G% and E%. Optimum conditions were determined as 40 °C, 3.85 g/L chitosan, 0.27 M AAm; CAN proportions were used as 6 mmol CAN per gram chitosan, and 43 mmol CAN per mol AAm. Under these conditions a G% of 350% was observed (E% was 70%) and copolymer labelled as ChAAm.

Blank experiment (using the same conditions without chitosan) resulted in a reaction yield of 8%. This result indicated that chitosan was needed to produce radicals to start the polymerization.

After determining optimum conditions crosslinked copolymers were synthesized using same parameters with addition of MBA as crosslinking agent at different amounts. AAm:MBA proportions were set as 15:1, 20:1, and 30:1 by mass; these proportions were corresponding to 33:1, 43:1, and 65:1 AAm:MBA by mole. The crosslinked copolymers were labelled as ChAAx-15, ChAAx-20, and ChAAx-30 after their AAm:MBA proportions. Introduction of MBA resulted in a decrease in obtained product amount in the first place. When a detailed examination was made it was seen that G% was decreasing with an increase in AAm:MBA proportion. As the proportion was adjusted as 15:1,

20:1, and 30:1 the G% values were observed as 317, 206, and 157%, respectively. Also, E% was affected in a similar manner; it was observed as 60, 40, and 31% for ChAAx-15, ChAAx-20, and ChAAx-30 while it was 70% for ChAAM. This occurrence was probably due to crosslinks of MBA were both amongst acrylamide chains and chitosan chains at the same time.

### Characterizations of Graft Copolymers

Molecular weight determinations were done utilizing the viscometric method. Intrinsic viscosity, and in turn molecular weight of the copolymers, was determined by Solomon-Ciuta and Mark-Houwink equations, respectively. Mark-Houwink constants ( $6.31 \times 10^{-3}$  mL/g and  $\alpha = 0.80$ ) belong to polyacrylamide in aqueous solution at 30 °C (17). Although this method could not give the absolute molecular weight, it might give useful information about the samples for comparative purposes. The molecular weight of ChAAM was determined as 55 kDa while increasing MBA component caused a decrease; molecular weight of ChAAx-15 was 17

kDa, it was measured as 12 kDa for ChAAx-20 and as 10 kDa for ChAAx-30.

Characteristic FTIR signals that were related to chitosan were summarized as O-H and N-H stretching vibrations (overlapped) as a broad signal with peak positions at  $3357$  and  $3282$   $\text{cm}^{-1}$ , various C-H stretching vibrations with a peak at  $2870$   $\text{cm}^{-1}$ . Amide I and/or adsorbed water vibrations were observed at  $1644$   $\text{cm}^{-1}$ , amide II vibration at  $1566$   $\text{cm}^{-1}$ , various C-C-H, C-O-C, C-C-O bending, and C-C, C-O stretching vibrations between  $1500$ – $800$   $\text{cm}^{-1}$ . The signal at ca.  $899$   $\text{cm}^{-1}$  belonged to the anomeric ( $C_1$ ) region of the chitosan indicating  $\beta$  conformation (5).

The FTIR spectrum of obtained copolymer (ChAAM) displayed characteristic signals of polyacrylamide besides chitosan; stretching vibrations at  $3341$  and  $3206$   $\text{cm}^{-1}$ , amide C=O stretching (amide I) at  $1660$   $\text{cm}^{-1}$ , bending (amide II) at  $1621$   $\text{cm}^{-1}$ , stretching (amide III) at  $1422$   $\text{cm}^{-1}$  (22) (Figure 2).

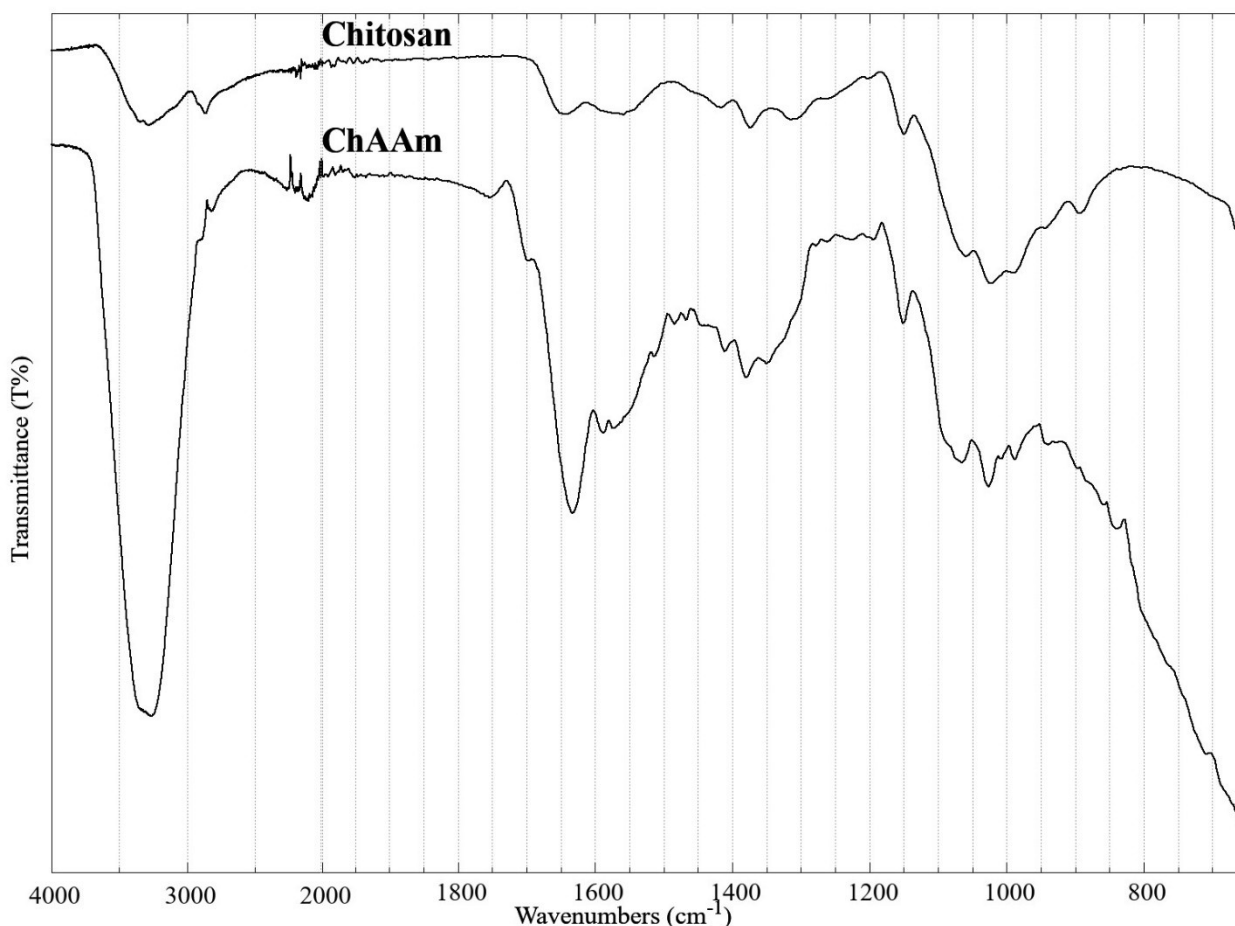


**Figure 2:** FTIR spectra of chitosan and ChAAM copolymer.

Comparison of FTIR spectra belonging to chitosan and ChAAM indicated that grafting of polyacrylamide onto chitosan was achieved. Crosslinking agent, MBA, caused a broadening in

amide I, and II signals, also an additional signal at amide III region was observed. As these signals appeared with introduction of MBA it was thought that crosslinked copolymers were obtained.

Additionally,  $C_1$  related signal was observed around  $895\text{ cm}^{-1}$  for crosslinked copolymer indicating a slight conformational relaxation on chitosan backbone.

FTIR spectra of chitosan and acrylamide copolymers were quite similar in many aspects. Moreover,  $C=O$  stretching vibrations of acrylamide moieties overlapped with chitosan signals. In order to identify and characterize copolymers a statistical method, PCA, was applied to the FTIR data. Sampling a typical FTIR spectrum several hundreds of points in correlation to each other stored. Applying PCA this correlation was removed creating uncorrelated variates known as principal component (PC) scores. The PCs could be defined as new, orthogonal axes where variances were maximized. Thus, the projection of PCs against one another could reveal the clustering or structural information regarding

the major components that are responsible for the change in certain region of the spectrum.

The scores plot of the first three PCs, which together account for 99% of total variance, was shown in Figure 3. In the plot PC1 and PC3 were used as x- and y- axes, respectively, same colors indicating near-by groups in PC2. Chitosan appeared nearly at the center of the plot while ChAAm was observed at the right-hand side of PC1. As this occurrence was related with grating a detailed analysis on loadings plot of the PCs indicated that positions on the plot were mainly related with amide  $C=O$  stretching vibration (from AAm) around  $1670\text{ cm}^{-1}$  and C-O (of chitosan backbone) related signals in  $1300\text{-}900\text{ cm}^{-1}$  range. Introduction of crosslinking agent resulted in shifts on PC3 while slight changes were observed on PC1. This result also supported that the presence of MBA leads to more crosslinked structures than grafting onto chitosan backbone.

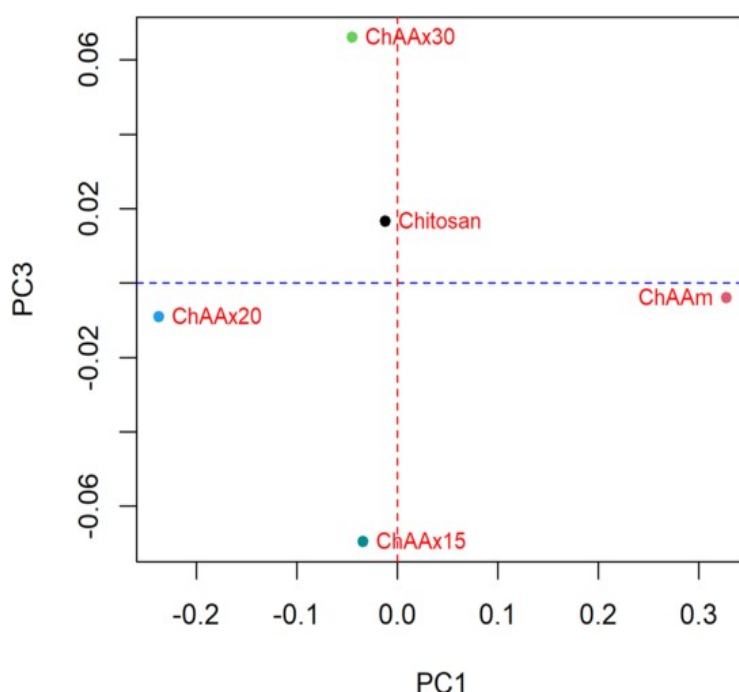


**Figure 3:** Resulting scores plot of PCA for copolymer samples.

Thermal characterizations of copolymers were carried out using TGA. First loss was due to adsorbed water, and was observed as a broad signal starting around  $40\text{ }^{\circ}\text{C}$  and ended around  $150\text{ }^{\circ}\text{C}$  with a proportion of 10 to 15%. This loss had a maximum weight loss temperature,  $T_{H_2O}$ , observed at  $101\text{ }^{\circ}\text{C}$  for chitosan. Then another degradation was observed between  $250$  and  $430\text{ }^{\circ}\text{C}$ ; the maximum degradation temperature,  $T_{max}$ , for this event was also determined from derivative TGA (DTGA) plot as  $334\text{ }^{\circ}\text{C}$ .

Introduction of polyacrylamide moiety onto chitosan backbone resulted in an increase in  $T_{H_2O}$ ; it was observed as  $125\text{ }^{\circ}\text{C}$  for ChAAm. In addition, an increase in the intensity of derivative peak indicated

that introduction of polyacrylamide moieties increased the water uptake of the copolymer as expected. The second decomposition, which was related, with mainly decomposition of polyacrylamide portion observed between  $250$  and  $400\text{ }^{\circ}\text{C}$  with a peak position at  $300\text{ }^{\circ}\text{C}$  in DTGA. There was also an additional signal maximum in DTGA located at  $487\text{ }^{\circ}\text{C}$  that was related with the second stage decomposition of polyacrylamide.

Crosslinked copolymers displayed slightly higher values for each thermal event. Water loss signal was observed as  $112\text{ }^{\circ}\text{C}$  for ChAAx-15,  $130\text{ }^{\circ}\text{C}$  for ChAAx-20, and  $93\text{ }^{\circ}\text{C}$  for ChAAx-30. Polyacrylamide decomposition pattern was observed in the same range with ChAAm; however, maximum degradation



temperatures were changing according to AAm:MBA ratio. ChAAx-15 and ChAAx-30 had a small signal around 280 °C and a stronger signal peaked around 310 °C which was very close to the peak signal for ChAAm. However, ChAAx-20 displayed two distinct signals in this range one was located around 330 °C and another at 386 °C. The shape pattern was also different for this decomposition. This occurrence was probably due to different amounts of crosslinking in the structure.

### Release Experiments

Controlled release experiments were done using 4 different copolymer matrices (ChAAm, ChAAx-15, ChAAx-20, ChAAx-30) at 3 different pHs (2, 6, and 8.5). Releasing material was acetylsalicylic acid (ASA). The experiments were carried out at ambient temperature; ASA:copolymer proportion were kept

constant at 1:3 by mass. ASA was loaded to the copolymer matrix using polyelectrolyte complex (PEC) method. In this method, ASA was encapsulated by copolymer matrix.

After preparation the pellets were placed in corresponding buffer solutions for pH 2, 6, or 8.5. The pH selection of the buffers was done for imitating the medium of stomach (strongly acidic), skin (weakly acidic or nearly neutral), and intestine (basic) for in vitro studies, respectively. In order to monitor the release of ASA calibration measurements were done separately in corresponding buffer solutions. The collected data was evaluated in two ways: the effect of the crosslinking at the same pH (Figure 4), and the effect of the pH for same matrix (Figure 5).

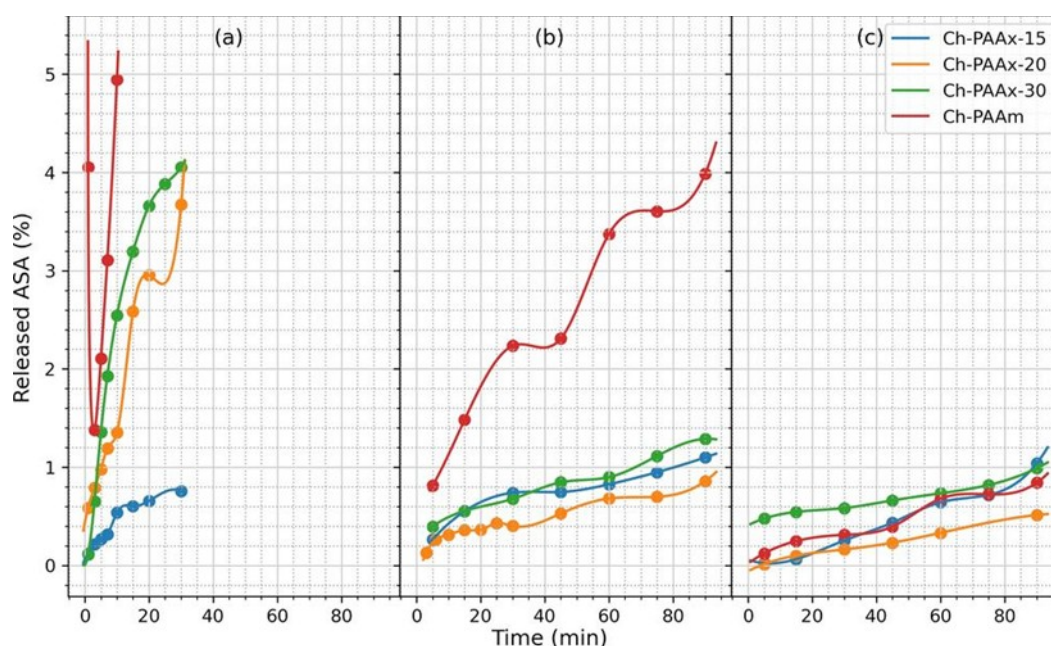


**Figure 4:** ASA release from the ASA:copolymer matrix at pH a) 2, b) 6, c) 8.5.

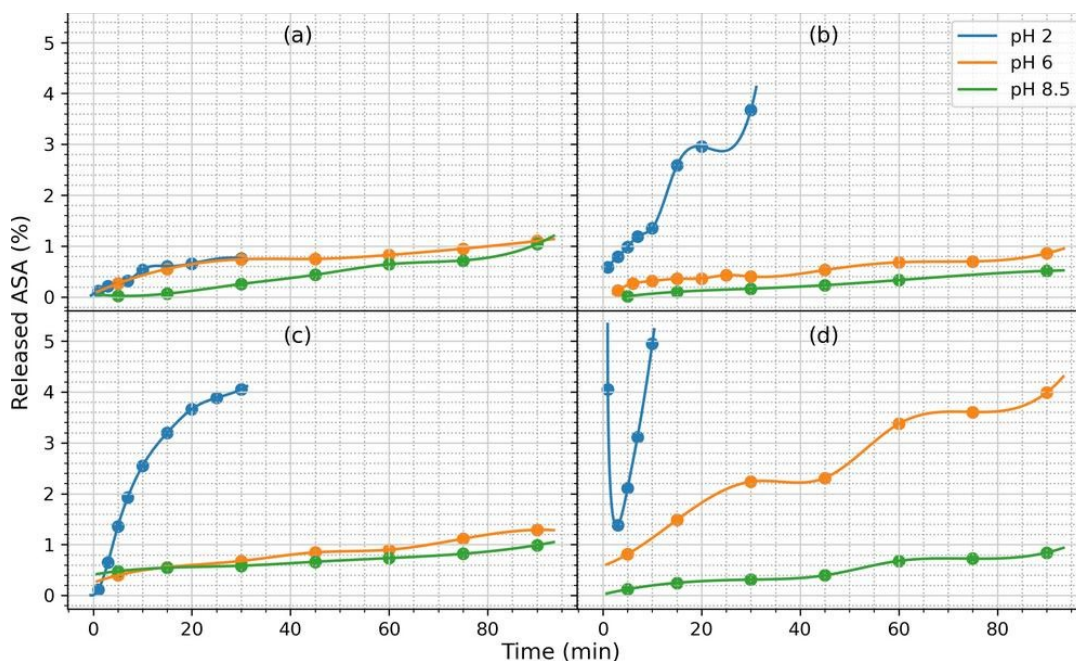


**Figure 5:** ASA release from the ASA:copolymer matrix based on a) ChAAx-15, b) ChAAx-20, c) ChAAx-30, d) ChAAm.

The UV-visible spectrum of ASA displayed several absorption bands within the wavelength range of 200-450 nm. The strongest signals were located around 200 nm with two peak positions one was located around 215 nm, and the other was at 225 nm. This distinction was clear for pH 2, but for other pH values 225 nm signal lost intensity and became a shoulder to 215 nm. Another strong signal was located at 300 nm. All signals were shifted insignificantly as a result of changing medium pH. Chitosan displayed a signal only around 200 nm due to amide carbonyl transitions especially for pH 2, in the other two spectra this signal was observed slightly lower than 200 nm, so only tailing part of the signal was seen. Thus, quantitative ASA measurements were taken using the signal at 300 nm in order to prevent interferences.

The release rate was influenced by medium acidity as the matrix was very sensitive to pH (Figure 4a-c). Having N-H groups with an approximate pK value of 6.5 (4,5) chitosan backbone was expected to dissolve in acidic media. However, grafted polyacrylamide moieties retarded or prevented complete dissolution possibly due to extensive hydrogen bonding and/or crosslinking resulting in swelled structures. Increasing amount of MBA resulted in a structure with a higher number of crosslinks; thus, swelling behavior was influenced by composition.

For ChAAm, release behavior was extremely different from the rest of the samples at strongly acidic pH. First, a high and rapid UV response was observed when the matrix was placed in release medium; then the response decreased until 1.4% and then increased again. A possible explanation for

this event was fast expansion of the matrix in acidic medium. In this case, hydrogen bonds were the only interaction holding the matrix together; when dissolution occurred in the buffer, the loaded ASA was released at once in an uncontrolled fashion. However, later the dissolved polymer chains reabsorbed ASA leading to a decrease in the UV absorption and then release of ASA was started again at a lower rate.

Unlike ChAAm, crosslinked copolymers displayed a more stable release behavior as expected. All crosslinked copolymers displayed a linear model for release, except ChAAm-20 that released ASA displaying a logarithmic model. Among the crosslinked copolymers, the slowest release was observed for ChAAx-15, which had the highest MBA proportion thus the highest number of crosslinks. This was expected, as intensive number of crosslinks caused the smallest pore size of the matrix; thus, ASA was released slower via these pores of the swelled matrix at a small rate. At this pH ChAAx-30 was also displayed a similar behavior indicating even a small number of covalently bonded crosslinks was affecting the swelled structure and its pore size as the matrix did not disperse easily in the medium and standing together forming up a swelled structure. Then ASA should permeate through the pores of this swelled structure. ChAAx-20 and ChAAx-30 displayed similar results with an exception in release model. When compared the release based on the component ChAAx-20 matrix was nearly linear while ChAAx-30 matrix was more a fit to logarithmic model.

When pH was changed to 6.0 release rate slowed down for all copolymers. Still being in a medium



more acidic than pK value of chitosan, ChAAM based matrix displayed the highest release rate among them. The rest of the matrices displayed very close results. All matrices displayed an almost linear release model.

A similar result was also observed for pH 8.5; this time even release from the matrix based on ChAAM was very close to the crosslinked copolymers.

At the same pH the difference in release behavior was due to swelling characteristics; as expected the smaller the pore size or the higher the number of crosslinks the slower the release rate.

In Figure 5a-d release behavior was shown as a function of copolymer composition; the release differences for the same copolymer at different pH values.

When the plots were evaluated, it was seen that pH clearly affected the release rate as well as composition of the copolymer. Amongst the copolymers, the slowest release was observed for ChAAx-15 regardless the medium acidic properties. It was the least affected matrix material due to extensive crosslinks of MBA.

Because of a decrease in MBA amount of the copolymer, corresponding to a decrease in crosslink intensity matrices became more sensitive to the medium pH. ChAAx-20 and ChAAx-30 gave very similar results; they released ASA rapidly in acidic medium while release was slowed down to similar values at higher pH values for both. The most sensitive matrix was ChAAM based; it was affected by medium pH dramatically. As mentioned above it released ASA at once re-adsorbing and re-releasing it again at a slower rate in acidic medium. At pH 6 release rate decreased and became more stable than acidic medium. In basic medium, the release rate decreased down to the lowest rate, which was very close to the rest of the copolymers.

## CONCLUSION

ChAAM was synthesized with an efficiency of 68% corresponding to 340% grafting. Using determined condition crosslinked copolymers were synthesized with 15:1, 20:1, 30:1 mass proportions of AAm:MBA (ChAAx-15, ChAAx-20, ChAAx-30, respectively). The expectation was as the AAm:MBA proportion went higher MBA amount went lower resulting in a decrease in crosslinking. The results indicated that change in AAm:MBA proportion lead to different efficiency and grafting percentages. Thus, optimizing studies could be done for higher efficiency values for different proportions and/or a kinetic model would be determined.

The release behaviors of the prepared copolymers were monitored at 3 different pH values as 2, 6, and

8.5 for model media for stomach, skin, and intestine media, respectively. Loading ASA and monitoring release at different pH media indicated that the least pH sensitive matrix among these was ChAAx-15 as it was stable and similar release behavior at all pH values, and the most pH sensitive was ChAAM as it had nothing but hydrogen bonds to hold the matrix together. According to the results, ChAAM based release matrices were suitable for skin-care applications while ChAAx-15 based ones were suitable for all pH values to release at a steady rate. Further studies could be done with different therapeutic agents, at different temperatures, and in vivo tests could be run.

## CONFLICT OF INTEREST

The authors declare no conflict of interest.

## ACKNOWLEDGMENTS

Authors thank to Istanbul Technical University Scientific Research Foundation for financial support.

## REFERENCES

1. Shariatnia Z. Pharmaceutical applications of chitosan. *Advances in Colloid and Interface Science*. 2019 Jan;263:131–94. [<DOI>](#).
2. Sahoo D, Sahoo S, Mohanty P, Sasmal S, Nayak PL. Chitosan: a New Versatile Bio-polymer for Various Applications. *Designed Monomers and Polymers*. 2009 Jan;12(5):377–404. [<DOI>](#).
3. Barbosa MA, Gonçalves IC, Moreno PMD, Gonçalves RM, Santos SG, Pêgo AP, et al. 2.13 Chitosan. In: *Comprehensive Biomaterials II* [Internet]. Elsevier; 2017 [cited 2021 Dec 11]. p. 279–305. ISBN: 978-0-08-100692-4. [<URL>](#).
4. Oyervides-Muñoz E, Pollet E, Ulrich G, de Jesús Sosa-Santillán G, Avérous L. Original method for synthesis of chitosan-based antimicrobial agent by quaternary ammonium grafting. *Carbohydrate Polymers*. 2017 Feb;157:1922–32. [<DOI>](#).
5. Ünlü C, Pollet E, Avérous L. Original Macromolecular Architectures Based on poly( $\epsilon$ -caprolactone) and poly( $\epsilon$ -thiocaprolactone) Grafted onto Chitosan Backbone. *IJMS*. 2018 Nov 29;19(12):3799. [<DOI>](#).
6. Mino G, Kaizerman S. A new method for the preparation of graft copolymers. Polymerization initiated by ceric ion redox systems. *J Polym Sci*. 1958 Aug;31(122):242–3. [<DOI>](#).
7. Atici OG, Akar A, Ayar Y, Mecit O. Synthesis of block copolymers via redox polymerization. *J Appl Polym Sci*. 1999 Feb 28;71(9):1385–95. [<DOI>](#).

8. Kalaoğlu Öİ, Ünlü CH, Galioğlu Atıcı O. Synthesis, characterization and electrospinning of corn cob cellulose-graft-polyacrylonitrile and their clay nanocomposites. *Carbohydrate Polymers*. 2016 Aug;147:37–44. [<DOI>](#).
9. Pottenger CR, Johnson DC. Mechanism of cerium (IV) oxidation of glucose and cellulose. *J Polym Sci A-1 Polym Chem*. 1970 Feb;8(2):301–18. [<DOI>](#).
10. Ünlü CH, Öztekin NS, Atıcı OG. Synthesis and thermal characterization of xylan-graft-polyacrylonitrile. *Carbohydrate Polymers*. 2012 Oct;90(2):1120–6. [<DOI>](#).
11. Zohuriaan-Mehr M. Advances in Chitin and Chitosan Modification through Graft Copolymerization: A Comprehensive Review. *Iranian Polymer Journal*. 2005;14(3):235–65. [<URL>](#).
12. Bulut E. Ibuprofen microencapsulation within acrylamide-grafted chitosan and methylcellulose interpenetrating polymer network microspheres: Synthesis, characterization, and release studies. *Artificial Cells, Nanomedicine, and Biotechnology*. 2015 Mar 6;1–11. [<DOI>](#).
13. Bhattarai N, Gunn J, Zhang M. Chitosan-based hydrogels for controlled, localized drug delivery. *Advanced Drug Delivery Reviews*. 2010 Jan;62(1):83–99. [<DOI>](#).
14. Martinez-Ruvalcaba A, Sanchez-Diaz JC, Becerra F, Cruz-Barba LE, Gonzalez-Alvarez A. Swelling characterization and drug delivery kinetics of polyacrylamide-co-itaconic acid/chitosan hydrogels. *Express Polym Lett*. 2009;3(1):25–32. [<DOI>](#).
15. Prabakaran M. Review Paper: Chitosan Derivatives as Promising Materials for Controlled Drug Delivery. *J Biomater Appl*. 2008 Jul;23(1):5–36. [<DOI>](#).
16. Wang L, Jian Y, Le X, Lu W, Ma C, Zhang J, et al. Actuating and memorizing bilayer hydrogels for a self-deformed shape memory function. *Chem Commun*. 2018;54(10):1229–32. [<DOI>](#).
17. Scholtan von W. Molekulargewichtsbestimmung von Polyacrylamid mittels der Ultrazentrifuge. *Makromol Chem*. 1954;14(1):169–78. [<DOI>](#).
18. Pamies R, Hernández Cifre JG, del Carmen López Martínez M, García de la Torre J. Determination of intrinsic viscosities of macromolecules and nanoparticles. Comparison of single-point and dilution procedures. *Colloid Polym Sci*. 2008 Sep;286(11):1223–31. [<DOI>](#).
19. Solomon OF, Ciuta IZ. Détermination de la viscosité intrinsèque de solutions de polymères par une simple détermination de la viscosité. *J Appl Polym Sci*. 1962 Nov;6(24):683–6. [<DOI>](#).
20. Akar A, Galioğlu O, Göçmen A, Sarac AS. Copolymer of ketonic resin-polyacrylonitrile. *J Appl Polym Sci*. 1990 Apr 20;39(8):1657–63. [<DOI>](#).
21. Galioğlu O, Soydan AB, Akar A, Saraç AS. Block/graft copolymer synthesis via ceric salt. *Angew Makromol Chemie*. 1994 Jan;214(1):19–28. [<DOI>](#).
22. Murugan R, Mohan S, Bigotto A. FTIR and polarised Raman spectra of acrylamide and polyacrylamide. *Journal of the Korean Physical Society*. 1998;32(4):505–12.



## Optimization and Characterization of Cellulose Nanocrystal Production from Aseptic Tetra Pak Food Packaging Waste

Damla Akgün<sup>1</sup> , Duygu Ova Özcan<sup>2\*</sup>  , Bikem Övez<sup>2</sup> 

<sup>1</sup>Selkasan Kagit ve Paketleme Malzemeleri İmalat San ve Tic. A. Ş., Manisa, Turkey

<sup>2</sup>Ege University, Faculty of Engineering, Department of Chemical Engineering, Izmir, Turkey

**Abstract:** Cellulose fibers were extracted from the recycled Tetra Pak aseptic food package wastes, and high value-added cellulose nanocrystals (CNC) were produced by the acidic hydrolysis. At the optimum H<sub>2</sub>SO<sub>4</sub> concentration of 25% w, the whiteness index of CNC obtained at 30 °C for 30 min CNC was 84.42%, while it was 56.00% for 50 °C for 60 min CNC. The effects of temperature and time on the hydrolysis yield were optimized by the Central Composite Design and the maximum yield was determined at the condition where the temperature was high and the time was the lowest. The physical and structural properties of different CNCs were investigated using several characterization techniques. The FTIR and TGA analyses of the CNCs obtained at different temperatures and times showed similar spectra and degradation temperatures with each other, respectively. The crystallinity index of alkaline-treated cellulose calculated from the XRD patterns was much lower than those of all of the CNCs. According to AFM measurements and SEM micrographs, it was confirmed that as the temperature and time increased, the diameters of the CNCs were reduced. The lowest diameter value was measured as 175 nm at 50 °C for 60 min CNC, whereas, on the other hand, the highest diameter value was measured as 403 nm at 30 °C for 30 min CNC.

**Keywords:** Cellulose nanocrystals, extraction, waste recovery, Tetra Pak, Central Composite Design.

**Submitted:** September 16, 2021. **Accepted:** December 17, 2021.

**Cite this:** Akgün D, Ova Özcan D, Övez B. Optimization and Characterization of Cellulose Nanocrystal Production from Aseptic Tetra Pak Food Packaging Waste. JOTCSA. 2022;9(1):131–48.

**DOI:** <https://doi.org/10.18596/jotcsa.996450>.

**\*Corresponding author. E-mail:** [duygu.ova@ege.edu.tr](mailto:duygu.ova@ege.edu.tr).

### INTRODUCTION

Today, in the European Union, nearly 100 million liters of liquids and beverages such as milk and fruit juice are packaged in cartons which means 977,000 tons of packaging material and waste (1). More than 179 million Tetra Pak packages were being sold worldwide in 2014 (2, 3). After the consumption of food or the liquid product, most of packages end up as household and/ or municipal solid waste. At this stage, treatment of the waste arises as an important problem for sustainable processes. The recycling of Tetra Pak packaging has the benefit of minimizing the need for virgin material, decreases the air pollution, also contributes to energy savings and provides a reduction in CO<sub>2</sub> emissions (2). Some parts of these packages are systematically

recuperated, sorted, and then recycled. According to declared data by Tetra Pak (2021), number of recycled Tetra Pak packages increased from 32 billion in 2010 to 50 billion in 2020 which is approximately 27% of the total number of packages produced (4).

In the recycling of Tetra Pak packages, one of the most important parts is the recycling of the paperboard layer, which contains mostly cellulose, hemicellulose, and lignin, because of its natural biodegradable content (5). As a chemical raw material, cellulose has been mostly used in the form of fibers or derivatives for a wide range of products and materials such as plastics, composites textiles, a food structuring agent, photographic films, and rayon (6). It exists in the cell walls of various

plants, for maintaining their structure and also in a wide variety of living species, such as bacteria, algae, fungi, and tunicates (7). Furthermore, cellulose is renewable, biodegradable and biocompatible, so it is considered as an alternative to nondegradable fossil fuel-based polymers (8). Different cellulose sources have different cellulose content such as banana peel, nut shell, and corn stover having 13.2, 25-30 and 38% cellulose content, respectively. The properties like crystallinity or thermal degradation might be varied depending on the cellulose content of the starting material and treatment method/condition (9).

Increased demand for high-performance materials with tailored mechanical and physical properties has resulted in searching for different materials like nanocellulose which is recently the most attractive renewable material for advanced applications. Nanocellulose can be divided to three types which are cellulose nanocrystal, cellulose nano fiber, and bacterial cellulose (10). Cellulose nanocrystals are mainly produced from cellulose fibers involving selective hydrolysis of amorphous cellulose parts, resulting in high crystallinity of particles. Rod-like shaped cellulose nanocrystals are renewable, biodegradable, biocompatible, and nontoxic eco-friendly materials.

The cellulose in the Tetra Pak waste sources always contains substantial lignin and hemicellulose fractions. These materials should be removed to obtain pure cellulosic fibers prior to the production of cellulose nanocrystals (11). The alkali treatment is good for removing the impurities such as lignin, hemicellulose, pectin, and waxes in the fibers. Besides, it can expose the larger area of cellulose (12). The following bleaching procedure contributes to the removal the residual phenolic molecules like lignin that was refractive to alkali treatments and part of the hemicellulose yielding a white cellulose material suitable for a more effective production of cellulose nanocrystals (3). The purpose of this bleaching treatment is to break down phenolic compounds or molecules with chromophoric groups present in lignin, and to remove the by-products, and thus whitening the material. Bleaching might be performed by chlorine based agents such as NaOCl or NaClO<sub>2</sub> and oxygen-based agents such as H<sub>2</sub>O<sub>2</sub> or

ozone. NaOCl or NaClO<sub>2</sub> are cheap oxidizing agents which make it possible to render the removal of lignin efficiently. H<sub>2</sub>O<sub>2</sub>, used as a precursor in sodium chlorite treatments, can break alkaline-resistant linkage which is formed between lignin and hemicellulose after alkaline treatment, and also act as an oxidizing agent to delignify lignocellulosic fiber. If oxygen-based agents are used, the bleaching process takes more time (13).

In this study, the necessity of purifying the recycled cellulose fibers from the Tetra Pak packages used as starting material and the variation of the processing conditions on the reaction efficiency were investigated. In order to investigate the success of the valorization of Tetra Pak packages, the physical and structural properties of the cellulose nanocrystals obtained from hydrolysis, at various processing conditions such as H<sub>2</sub>SO<sub>4</sub> concentration, temperature, and time were examined using some characterization techniques and the yield was optimized.

## EXPERIMENTAL SECTION

### Chemicals and Methods

The recycled Tetra Pak which is used as a cellulose source was supplied from the waste management company Selkasan Kagit ve Paketleme Malzemeleri İmalat San ve Tic. A. Ş. (Manisa, Turkey). Sodium hydroxide (NaOH) in the form of granules for alkali treatment, sodium hypochlorite (NaOCl) used as a bleaching agent, and for hydrolysis, 97% pure sulfuric acid (H<sub>2</sub>SO<sub>4</sub>) were purchased from Merck (Darmstadt, Germany). All the chemicals were reagent grade and distilled water was utilized as the diluent solvent. Commercial microcrystalline cellulose powder was purchased from Sigma Aldrich (Ireland) with dimension of 20 µm used as the reference standard.

The product material, nanocellulose was extracted from paperboard based recycled liquid food packages, which were selected milk and juice packages. The purification and isolation steps of the whole process involve cellulose extraction, alkali treatment, bleaching, and the production of cellulose nanocrystals (CNC) as shown in Figure 1.

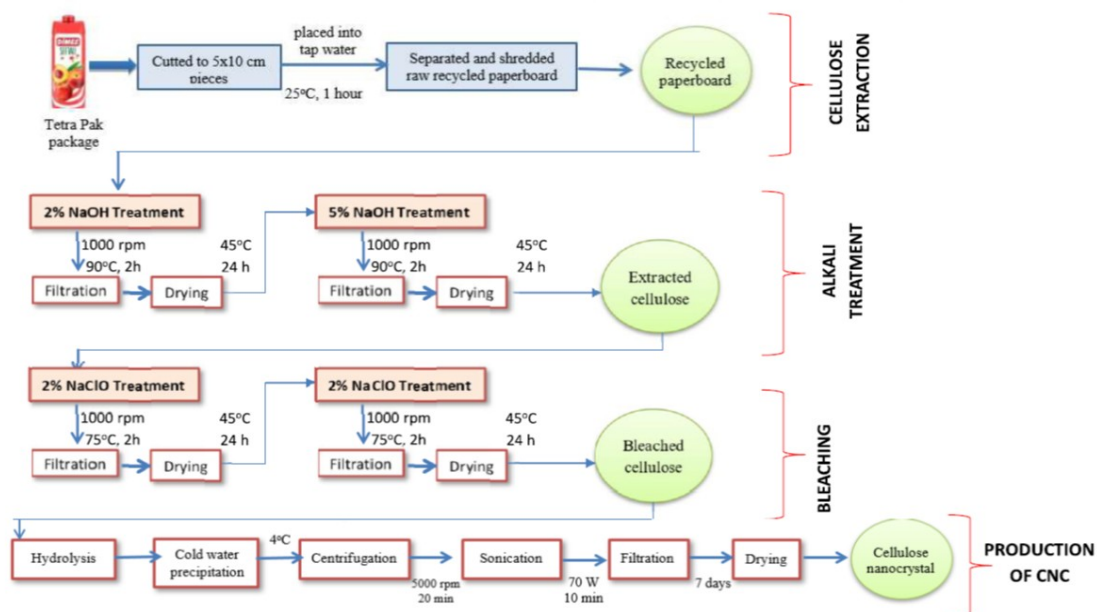


**Figure 1:** Flow diagram of production of nanocrystal cellulose from Tetra Pak waste packages.

**Cellulose Extraction from Tetra Pak Waste Packages**

For easier separation of the paper layer from the other two layers, Tetra Pak packages were cut into 5x10 cm pieces which are shown as Figure 2 (a). Then they were placed into a bowl which was full of water at room temperature for 1 hour. After 1 hour in water, the paperboard layer was peeled off as

shown in the Figure 2 (b), not completely separated from polyethylene and labeled as raw recycled cellulose. To increase the surface area, the raw recycled cellulose was shredded into pieces about 1x1 cm as shown in the Figure 2 (c). At the end of this step, the raw recycled paperboard was ready for the alkaline treatment.

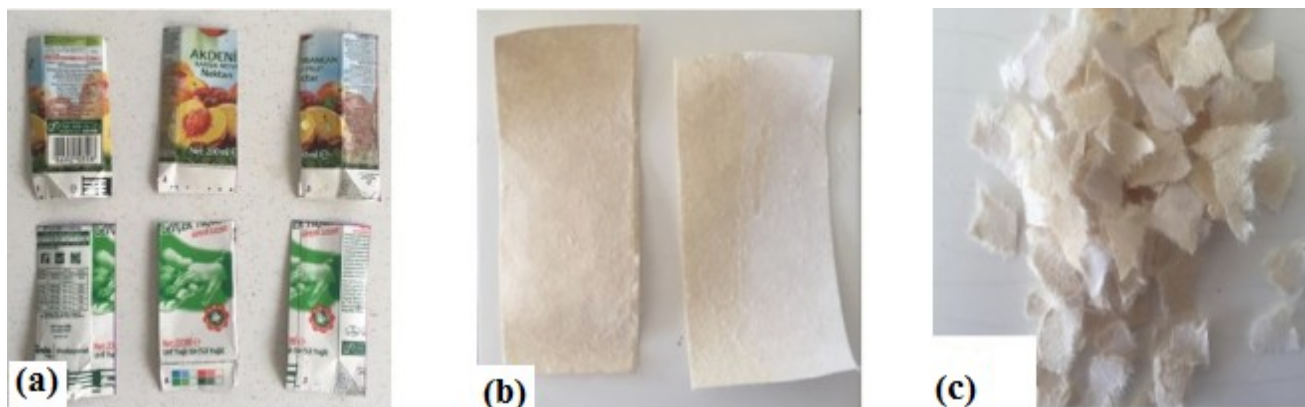


**Figure 2:** (a) Tetra Pak packages of 5x10 cm, (b) raw recycled cellulose separated from Tetra Pak package, and (c) shredded raw recycled cellulose.

**Alkaline Treatment**

The extracted raw cellulose was treated with a 2% w aqueous NaOH solution with a pH of 12 at a solid to liquid ratio of 1:100. The purpose of a 2% w aqueous NaOH treatment is to remove the different impurities such as waxes, pectin, proteins, soluble mineral salts, and silica ash etc., present in the raw material. Then the mixture was placed onto a multi hotplate WiseStir type SMHS-6 magnetic stirrer at

90 °C at 1000 rpm for 2 hours (3). The cellulose fibers obtained were filtered and washed with distilled water until a neutral pH was reached in order to avoid any reactions in the following steps. The filtered cellulose fibers were dried at 50 °C for 24 hours in a closed air-circulating oven with normal room air (14). Figure 3 (a) and (b) show filtered and dried alkaline-treated cellulose after alkaline treatment with a 2% w NaOH.



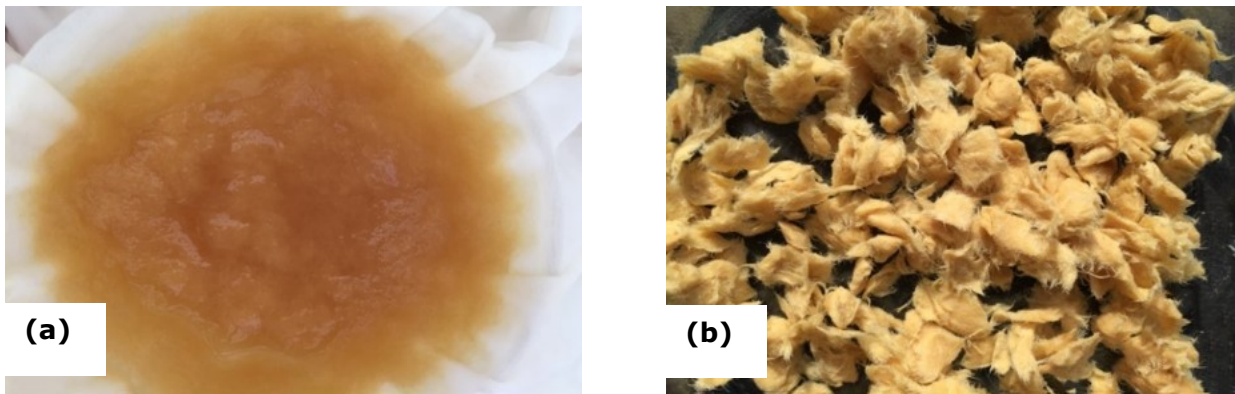


**Figure 3:** (a) Filtered and (b) dried alkaline-treated cellulose after a 2% w NaOH treatment.

The dried cellulose fibers were submitted to a second alkali treatment using a 5% w aqueous NaOH solution with a pH of 13.5 at a solid to liquid ratio of 1:100. The purpose of the subsequent alkali treatment using a 5% w aqueous NaOH solution specifically targeted a reduction of the lignin content in the recycled fibers without inducing swelling.

Then the mixture was again stirred at 90° C at 1000 rpm for 2 hours and then the filtered and washed cellulose fibers were dried at 40 °C for 24 hours as described above. At the end of the cellulose extraction process, the obtained cellulose fibers are named as alkaline-treated cellulose as shown in Figure 4 (a) and (b).

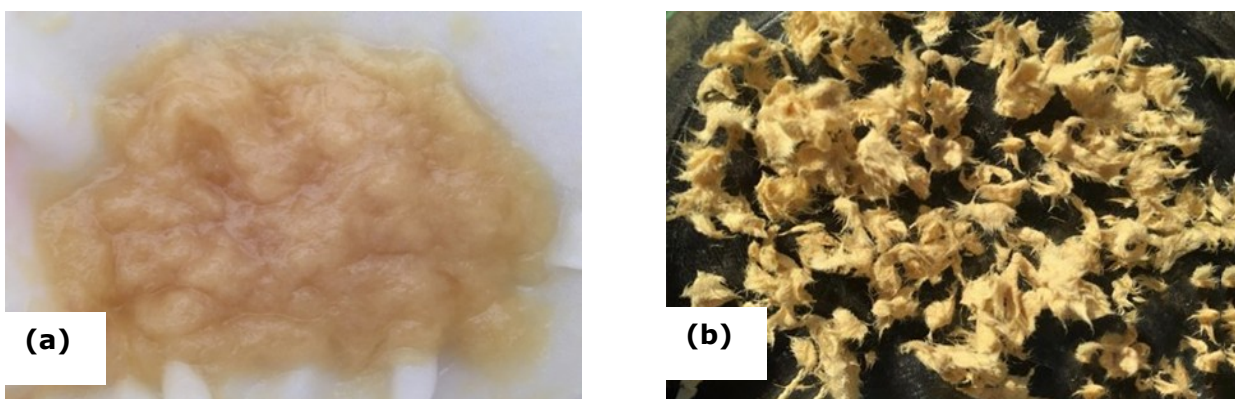


**Figure 4:** (a) Filtered and (b) dried alkaline-treated cellulose after a 5% w NaOH treatment.

### Bleaching

Alkaline-treated cellulose bleached twice with a 5% w aqueous NaOCl solution. The cellulose biomass was treated with a 5% w aqueous NaOCl solution at a solid to liquid ratio of 1:100 (15). The mixture was placed onto a magnetic stirrer at 75 °C at 1000 rpm for 2 hours. For the second bleaching, the same

procedure was repeated. Similar to the alkali treatment, the filtered and washed bleached cellulose was dried at 50 °C for 24 hours. The filtered and dried bleached cellulose after the first and second bleachings are illustrated in Figures 5 and 6, respectively.

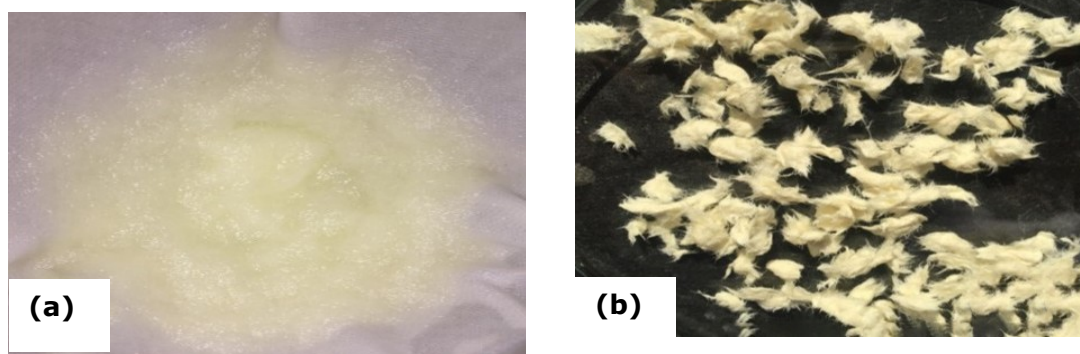


**Figure 5:** (a) Filtered and (b) dried alkaline-treated cellulose after the first 5% w NaOCl treatment.

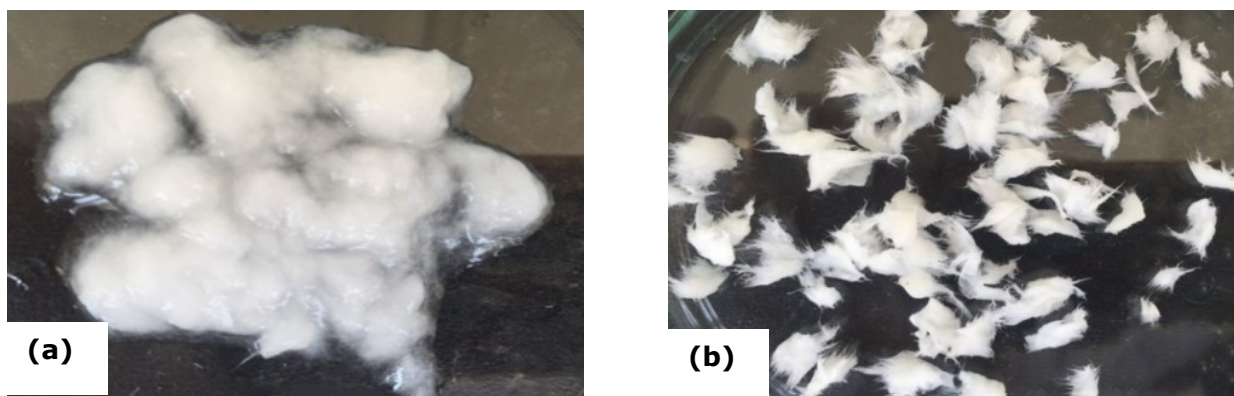


**Figure 6:** (a) Filtered and (b) dried alkaline-treated cellulose after the second 5% w NaOCl treatment.

The improved whiteness of the alkaline-treated, first and second bleached cellulose samples under mechanical stirring are shown in Figure 7 (a), (b), and (c), respectively.

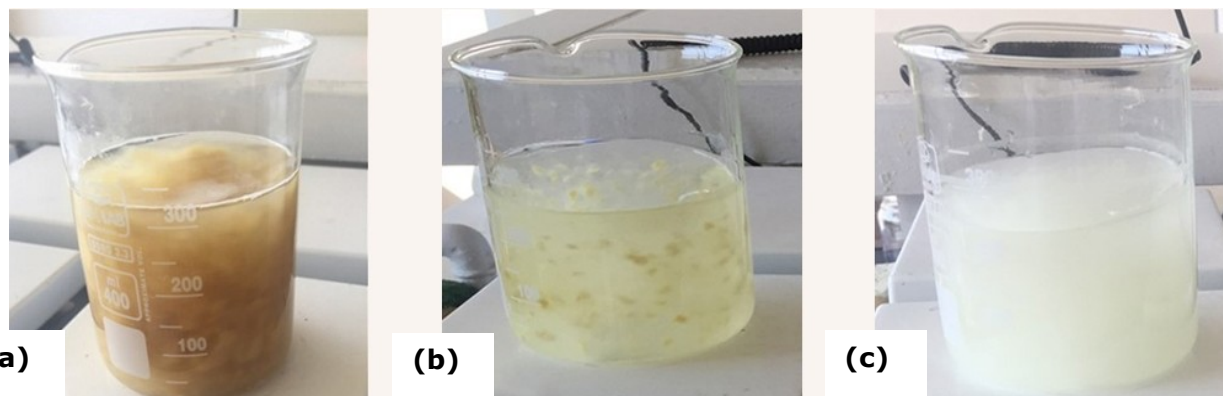


**Figure 7:** (a) Alkaline-treated (b) bleached cellulose for the first time, and (c) bleached cellulose for the second time.

### Production of Cellulose Nanocrystals

The bleached cellulose was hydrolyzed with  $H_2SO_4$ , where, cellulose nanogel was obtained. Cellulose nanocrystals are produced from cellulose nanogel via the steps of cold-water precipitation, centrifugation, filtration, sonication, and drying.

#### Hydrolysis

The effect of three main parameters that affect the hydrolysis efficiency such as concentration of  $H_2SO_4$ , temperature, and hydrolysis time were examined. The ratio of the bleached cellulose and aqueous  $H_2SO_4$  solution was kept constant at 1:100 where the concentration of  $H_2SO_4$  was changed to 10, 20, 25, 30, and 40% w.  $H_2SO_4$  was added to the cellulose-water mixture drop by drop on the magnetic stirrer at 1000 rpm placed in a cold-water bath (at 4 °C) in order to eliminate the burning of the cellulose because of the exothermic reaction between  $H_2SO_4$  and  $H_2O$ . In order to achieve the highest hydrolysis efficiency, three different temperatures of 30, 40, and 50 °C and three different hydrolysis times of 30, 45, and 60 minutes were investigated at constant  $H_2SO_4$  concentration.

#### Cold water precipitation and centrifugation

At the end of the hydrolysis process, in order to finish the hydrolysis reaction, the hydrolyzed cellulose must be quenched with 100 mL of cold distilled water at 4 °C. For removing any colloidal impurities from hydrolyzed cellulose, a centrifugation step was carried out twice at 5000 rpm for 15 min.

#### Filtration

In order to remove remaining acids and salts from the hydrolyzed cellulose, a filtration step was carried out. The centrifuged cellulose was filtered and washed with distilled water until a neutral pH was reached after 7 days. 100 mL of distilled water was added to the filtered and dried cellulose.

#### Sonication

A Bandelin Sonopuls ultrasonic homogenizer equipped with 3 mm probe at a power of 70 W and amplitude of 30% for 10 minutes was used in the ice bath for avoiding agglomeration (3). The cellulose nanocrystal suspension resulting from this process was stored at 4 °C for further analysis. After sonication, the samples were dried in a closed

air-circulating oven at 40 °C and the resulting products are shown in Figure 8.

### Characterization Methods

Color determination values for the calculation of the whiteness indices of the samples were determined using a Hunterlab ColorFlex CFLX-45-2 (Reston, USA). After adjusting the H<sub>2</sub>SO<sub>4</sub> concentration to an optimum value depending on the color measurement values, the effects of temperature and time on hydrolysis efficiency were investigated by further characterization methods. The functional groups of the samples were obtained by Fourier Transform Infrared spectra (FTIR) using KBr pellets with a Perkin Elmer Spectrum 100 Model in 650-4000 cm<sup>-1</sup> spectral range with a resolution of 4 cm<sup>-1</sup> at room temperature. X-ray Diffraction (XRD) analysis was conducted to identify the crystallographic structures of samples by Rigaku Smartlab Diffractometer. Thermal stability behavior (TGA) was investigated at atmospheric pressure using a TA Instrument SDT Q600. The morphology and dimension analyses of the different cellulose nanocrystals were investigated with an AFM method using a BRUKER Dimension Edge with Scan Asyst atomic force microscope at peak force tapping mod on an area of 20 x 20 µm. A detailed morphological characterization was carried out by a Thermo Fischer Scientific Apreo scanning electron microscope (SEM). Prior to analysis, samples which were sonicated and coated on glass lamella were sputter-coated with gold/platinum using a vacuum plasma spray under argon atmosphere.

#### Whiteness index calculation

One of the several numerical indices was used to indicate the whiteness index (WI), which is an important output to proceed with the most effective H<sub>2</sub>SO<sub>4</sub> concentration, as in Eq. (1) (16):

$$WI = 100 - \left[ (100 - L)^2 + (a^2 + b^2) \right]^{1/2} \quad (1)$$

where L, a, and b refer to coordinates in Hunter's L, a, and b Color Difference Equation.

#### Yield calculation

Before hydrolysis, the bleached celluloses was firstly weighed and recorded. Then the resulting cellulose nanocrystal product obtained after sonication and drying were weighed and recorded. The yield, which is an important output to determine the optimum temperature and time, was calculated as in Eq. (2) (17):

$$\text{Yield} = \frac{m_1}{m_2} \times 100\% \quad (2)$$

where m<sub>1</sub> is the mass of the cellulose nanocrystals obtained after sonication and drying and m<sub>2</sub> is the mass of the bleached cellulose before hydrolysis.

#### Crystallinity index calculation

The crystallinity index was calculated from the X-Ray diffraction patterns obtained over the range of 2θ=5-70°. From the XRD patterns, the crystallinity index (CrI) of samples was calculated based on the intensity between (200) and (101) lattice diffraction peaks by using following Eq. (3) (18):

$$CrI = \left[ \frac{(I_{200} - I_{am})}{I_{200}} \right] \times 100\% \quad (3)$$

where I<sub>200</sub> represents both crystalline and amorphous region of cellulose (maximum intensity at 2θ=22.5°) and I<sub>am</sub> represents only amorphous phase (intensity of diffraction at 2θ=16°).

#### Data Analysis

In terms of experimental design, the effects of two important factors, temperature within the limits of 30 to 50 (°C, X<sub>1</sub>), and time within the limits of 30 to 60 (min, X<sub>2</sub>) on the hydrolysis yield were performed with the help of the face centered (α=1) Central Composite Design (CCD) of the Response Surface Methodology (RSM) using Design Expert® 12.0.1.0 software (Stat-Ease, Inc., Minnesota, USA, 2019). The central condition was defined as 40 °C, and 45 min, then a unit scale was set as 10 °C for temperature, and 15 min for time. Consequently, there were 13 base runs consisting of 4 cube points, 5 center points in cube, and 4 axial points. The yield was correlated with the independent operating variables and defined in terms of a second-order polynomial equation (Eq. (4)):

$$Y = a_0 + \sum a_i X_i + \sum a_{ii} X_i^2 + \sum a_{ij} X_i X_j \quad (4)$$

where, a<sub>0</sub>, a<sub>i</sub>, a<sub>ii</sub>, and a<sub>ij</sub> are constant, linear, quadratic, and interaction coefficients, whereas X<sub>i</sub>, X<sub>i</sub><sup>2</sup>, and X<sub>j</sub> represent the linear, quadratic, and interaction effects of factors, respectively. At a 95% confidence interval, the model significance and suitability were determined using the analysis of variance (ANOVA).



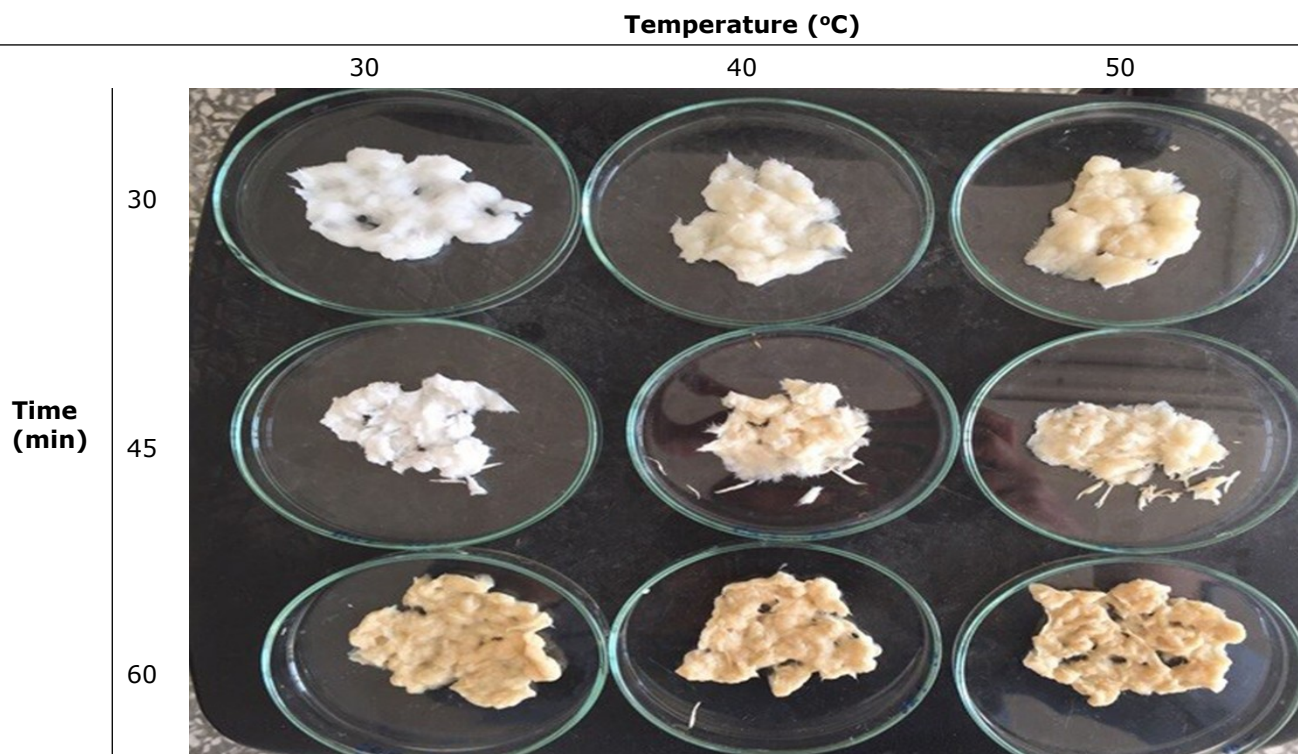


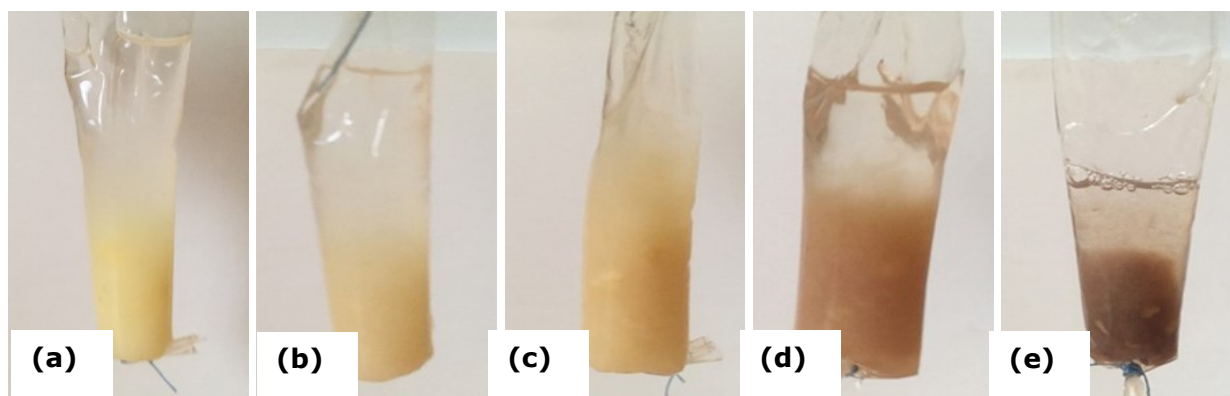
**Figure 8:** Resulting dried products after sonication at different temperatures and hydrolysis times.

## RESULTS AND DISCUSSION

### Effect of H<sub>2</sub>SO<sub>4</sub> Concentration on Hydrolysis Efficiency

Paper fibers, still containing polyethylene and aluminum, must be treated with acetic acid solution for 100% separation (19). Thus, if an extra chemical treatment was performed via acetic acid solution, then it would cause additional cost during production. However, the main purpose of this study is to achieve suitable reaction conditions and to improve efficiency with lower cost. The amount of acid is the key factor for determining the costs and environmental impacts. The first stage of this investigation is the possibility of using a lower acid

amount to produce cellulose nanocrystals. In order to determine the effect of acid concentration and identify a suitable concentration, five different concentrations of aqueous H<sub>2</sub>SO<sub>4</sub> solutions were prepared such as 10, 20, 25, 30, and 40% w at a constant temperature of 40 °C and time of 45 min. Figure 9 (a)-(e) shows the effect of acid concentration on the color with the increasing amount of H<sub>2</sub>SO<sub>4</sub>. With the increasing amount of H<sub>2</sub>SO<sub>4</sub> from Figure 9 (a) to (e), the decomposition of cellulose increases. On the other hand, excessive amount of H<sub>2</sub>SO<sub>4</sub> causes the cellulose to become a dark color of cellulose as seen in Figure 9 (e) which is an undesired situation for cellulose nanocrystal quality.



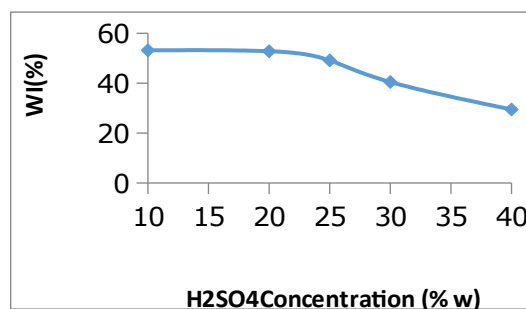
**Figure 9:** Cellulose samples after H<sub>2</sub>SO<sub>4</sub> treatment with concentrations of (a) 10%, (b) 20%, (c) 25%, (d) 30%, and (e) 40% by weight at 40 °C and 45 min.

Figure 10 shows the effect of acid concentration on the whiteness index (WI%). The color of the hydrolyzed cellulose became darker with the increasing  $H_2SO_4$  concentration as was proven previously in Figure 9. Until the 30% w of  $H_2SO_4$ , the darkening occurred slowly and the cellulose nanocrystals had a relatively lighter color. At 30% w of  $H_2SO_4$ , the color of cellulose nanocrystal turned into brown and after this concentration, i.e. at 40% w of  $H_2SO_4$ , the cellulose nanocrystal showed the darkest color. 25 wt% of  $H_2SO_4$  appeared to be the most acceptable concentration in terms of level of whiteness.

Compared to the studies in literature,  $H_2SO_4$  concentration range appears to be in-between 50-72% w (20) and the optimum concentration is determined to be 64% w in most of the studies (21, 22). However, this value depends on the cellulose source. When the resource changes, the hydrolysis conditions also alter accordingly, where, in this study, the concentration of  $H_2SO_4$  that was necessary for an effective hydrolysis reaction was found to be 25% w.

#### Effect of Temperature and Time on Hydrolysis Efficiency

The effect of temperature and time on hydrolysis efficiency was investigated at constant  $H_2SO_4$  concentration of 25% w. The hydrolysis reaction performed at three different temperatures which were 30, 40, and 50 °C and for three different times which are 30, 45, and 60 min.



**Figure 10:** The effect of acid concentration on the whiteness index (WI%).

#### Whiteness index output

After the color determination test, whiteness indexes of cellulose nanocrystals were calculated using L, a, and b values which are given in Table 1. The lightness values (L) decrease with increasing temperature and time, whereas, the redness values (a) of the cellulose nanocrystals increase with increasing temperature and time. The yellowness values (b) increases slightly with increasing temperature and time. The change of color was evident for the darkening of cellulose nanocrystals at higher temperature and time. According to Table 1, the whiteness index values decrease with the increasing amount of temperature and time, so, the color of the cellulose nanocrystals became darker. As expected, the highest white color was observed for the cellulose nanocrystal obtained at 30 °C for 30 min as 84.42% and the darkest color was observed for cellulose nanocrystal obtained at 50 °C for 60 min as 56.00%.

**Table 1:** The whiteness index (%) values due to varying temperature and time.

	Temperature (°C)			
	30	40	50	
Time (min)	30	84.42	64.08	57.96
	45	73.55	67.68	67.23
	60	69.84	62.45	56.00

#### Yield optimization

The yield of cellulose nanocrystals was calculated based on the samples after sonication and filtration in order to avoid the effect of the oversized particles from agglomeration and incomplete reaction. The yield results of the experimental base runs of uncoded values for the selected temperature, and time are tabulated in Table 2.

As it can be deduced from Table 2, that the highest and lowest yields were observed for cellulose nanocrystal obtained at 30 °C for 30 min as 61.20% and 50 °C for 60 min as 46.32%, respectively. The binary effects of the two factors on the yield are depicted by the three-dimensional response surface, together with the contour plot in Figure 11 (a-b).

**Table 2:** The yield (%) values under different temperature, and time factors and their levels.

Std order	Run order	Temperature (°C)	Time (min)	Yield (%)
1	1	30	30	61.20
13	2	40	45	57.22
2	3	50	30	56.09
9	4	40	45	57.98
6	5	50	45	50.75
7	6	40	30	59.62
12	7	40	45	57.45
4	8	50	60	46.32
5	9	30	45	59.10
8	10	40	60	52.11
10	11	40	45	56.93
11	12	40	45	57.13
3	13	30	60	58.20

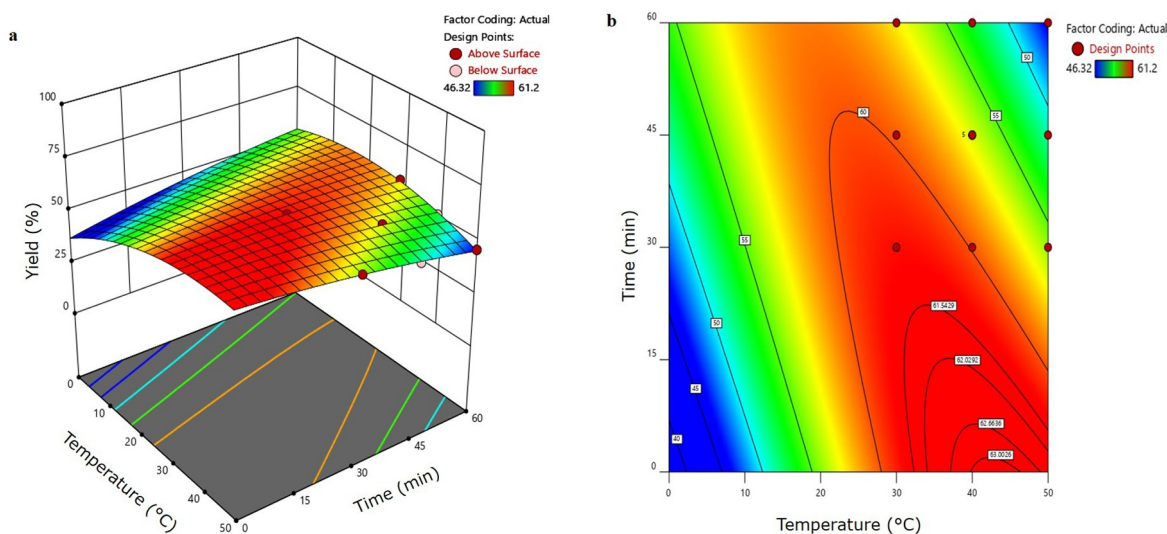


**Figure 11:** (a) The surface and (b) the counter plot of the yield with respect to the changes in the temperature (°C), and time (min).

As seen in Figure 11 (a), by decreasing or increasing the temperature and time simultaneously, the yield of cellulose nanocrystals deteriorated as Lu and Hsieh (2010) have found (23). These conditions form the endpoints of the curvature. The counter plot in Figure 11 (b) proves that the lowest yield values shown by the blue color were achieved at low-low and high-high temperature and time. The maximum yield was obtained at the condition where the temperature was high, and the time was the lowest. As referred

in Diop and Lavoie (2017)’s study, the phenomenon about higher yield at lower time is related to the irregularity of the crystalline region (3).

As a result of the modelling studies, the second-order polynomial equation of the yield (%) as a function of temperature, and time was expressed as in Eq. (5):

$$Y = 36.01609 + 1.24486 \times T + 0.429726 \times t - 0.014493 \times T^2 - 0.002264 \times t^2 - 0.011283 \times T \times t \quad (5)$$

**Table 3:** ANOVA of the yield data for temperature, and time effects.

Source	DF	Adj SS	Adj MS	F-value	P-value
<b>Model</b>	5	196.47	39.29	71.48	0
$T (X_1)$	1	107.02	107.02	194.67	0
$t (X_2)$	1	68.55	68.55	124.69	0
$T^2 (X_1^2)$	1	5.80	5.80	10.55	0.0141
$t^2 (X_2^2)$	1	0.72	0.72	1.30	0.2912
$Txt (X_1 X_2)$	1	11.46	11.46	20.84	0.0026
<b>Residual</b>	7	3.85	0.55		
Lack of Fit	3	3.20	1.07	6.58	0.0501
Pure Error	4	0.6483	0.16		
<b>Total</b>	12	200.31			
<b>Fit Statistics</b>	<b>Std. Dev.</b>	<b>R<sup>2</sup> (%)</b>	<b>R<sup>2</sup>-adj (%)</b>	<b>R<sup>2</sup>-pred (%)</b>	
	0.7414	98.08	96.71	87.92	

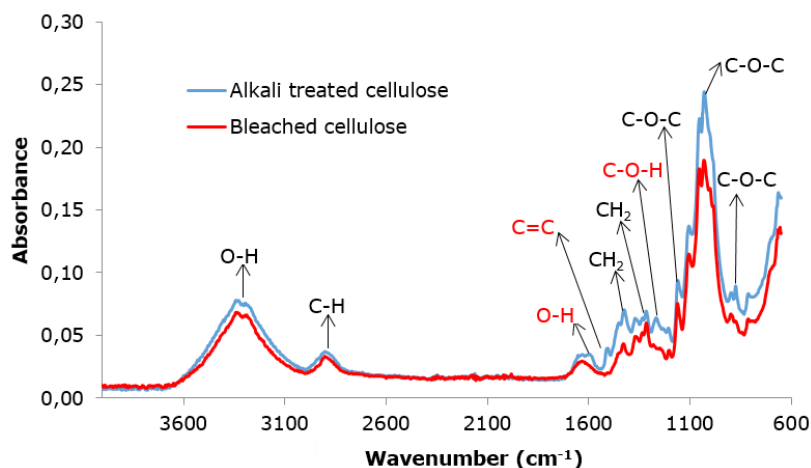
In equation 5,  $T$  stands for temperature ( $^{\circ}\text{C}$ ), and  $t$  for time (min). The analysis of variance for the proposed quadratic model is tabulated in Table 3. The model F-value of 71.48 and the lack of fit of the p-value of 0.05 presented in Table 3 implied that the model was significant and exhibited a good fit. All the terms of the model were significant due to P-values being smaller than 0.05, except the quadratic term of time. Both from the F-value being the highest and p value being the lowest, it is clear that the temperature is more effective factor on the yield compared to the time. The correlation coefficients,  $R^2$ ,  $R^2$ -adj, and  $R^2$ -pred being 98.08%, 96.71%, and 87.92%, respectively could be attributed to the observed and the predicted value agreement (Table 3).

#### FTIR analysis

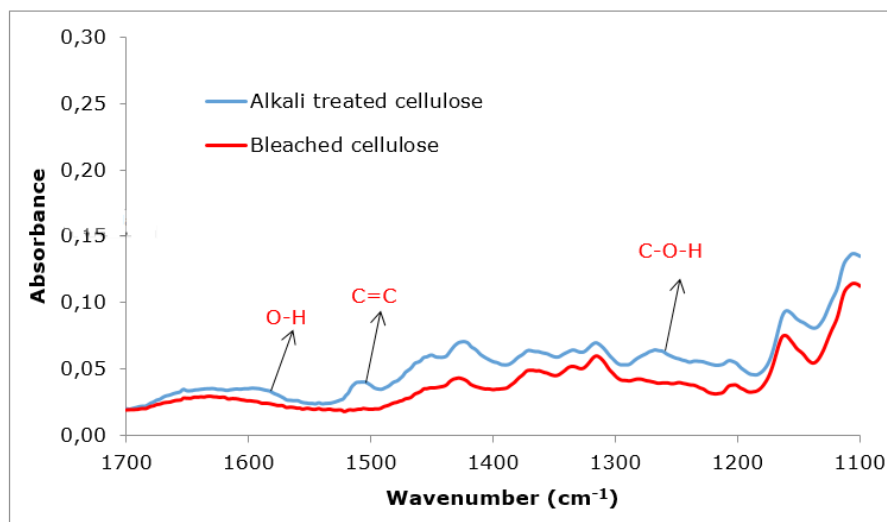
After the paper and polyethylene layers were separated appropriately from the Tetra Pak package, functional groups of alkaline-treated and bleached cellulose have been analyzed using FTIR spectroscopy (Figure 12).

From Figure 12, it can be observed that both alkaline-treated, and bleached cellulose showed peaks at 3345 and 2921  $\text{cm}^{-1}$  which were attributed to aromatic and aliphatic O-H stretching

intramolecular hydrogen bonds for cellulose and to the C-H stretching vibrations of the methyl group respectively (24). For the alkaline-treated cellulose two peaks were encountered at 1516 and 1590  $\text{cm}^{-1}$ , but not observed for bleached cellulose because these peaks were related to the O-H bending in water and C=C stretching vibration of the aromatic ring in the residual lignin (25) which can be clearly seen in the magnified FTIR spectra in Figure 13. The peaks which were observed at wave numbers of 1436 and 1321  $\text{cm}^{-1}$  were related to respectively the  $\text{CH}_2$  bending vibration in cellulose and the  $\text{CH}_2$  rocking vibration. These two peaks were attributed to cellulose, hence they both existed in the alkaline-treated and bleached cellulose. However, the peak at 1280  $\text{cm}^{-1}$  was not observed in the bleached cellulose since this peak was related to the C-O-H stretching at  $\text{C}_6$  which was attributed to lignin and xylan content (26, 27). The peaks appeared at the wave numbers of 1197, 1035, and 903  $\text{cm}^{-1}$  were related to C-O-C symmetric stretching and OH plane deformation, C-O-C pyranose ring stretching vibration, and the cellulosic  $\beta$ -glycosidic linkages, respectively (26, 27). When the alkaline-treated and bleached cellulose were compared, this observation could corroborate that the alkaline treatment and bleaching process had successfully reduced most of the impurities, especially its lignin content.

**Figure 12:** FTIR spectra of alkaline-treated and bleached cellulose.





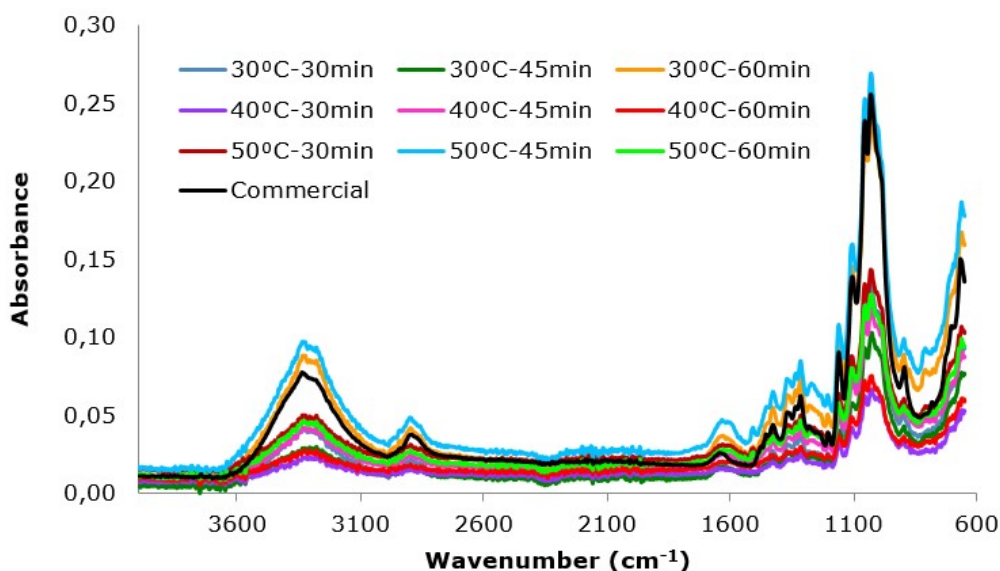
**Figure 13:** Magnified FTIR spectra of alkaline-treated and bleached cellulose revealing the vibration between 1700 and 1100  $\text{cm}^{-1}$ .

Figure 14 represents FTIR spectra of CNCs produced at different temperatures and times in comparison with commercial microcrystalline cellulose. According to Figure 14, at 3345, 2921, 1516, 1590, 1436, 1321, 1197, 1035, and 903  $\text{cm}^{-1}$ , the same peaks appeared for all samples. All characteristic peaks of cellulose were observed similarly for the CNCs obtained at nine conditions. Comparing Figure 12 and 14, it is seen that the CNCs have the same peaks like bleached cellulose. Unlike alkaline-treated

cellulose, the peaks were not observed at the wave numbers of 1590, 1516, and 1280  $\text{cm}^{-1}$ . So, with the acid hydrolysis process, any kind of change does not occur in the structure of the bleached cellulose.

#### XRD analysis

XRD analyses of the cellulose nanocrystal samples produced at different temperature and time in comparison with the alkaline-treated cellulose were performed (28) as seen in Figure 15.



**Figure 14:** FTIR spectra of cellulose nanocrystals produced at different temperatures and times.

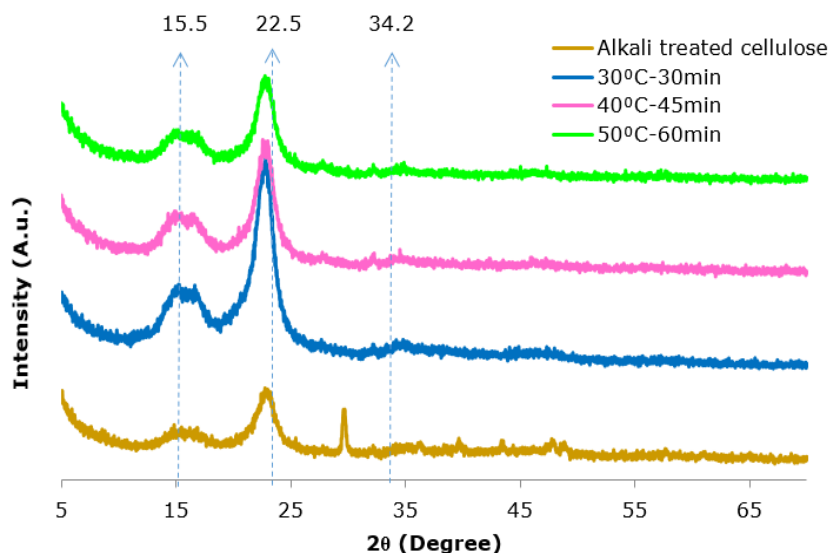


**Figure 15:** XRD patterns of the alkaline-treated cellulose and cellulose nanocrystals produced at different temperatures and times.

According to Figure 15, the XRD patterns of alkaline-treated cellulose and cellulose nanocrystals showed similar peaks at three different planes which are  $2\theta=15.5$  (plane 110),  $2\theta=22.5$  (plane 200), and  $2\theta=34.2$  (plane 004) which are the characteristic peaks of the cellulose I crystalline structure (29, 30). This observation was suggested that the crystalline structure of cellulose I remained even after alkali and acid hydrolysis treatments (31, 32). At two peak points, the alkaline-treated cellulose slightly differed from the cellulose nanocrystals. At the first point, around  $15.5^\circ$ , two peaks were observed for the cellulose nanocrystals and only one peak was observed for the alkaline-treated cellulose which was attributed to higher crystallinity (33). At the second point, peaks at  $15.5^\circ$ ,  $22.5^\circ$ , and  $34.2^\circ$ , were more intensified for the cellulose nanocrystals according to the alkaline-treated cellulose. During acidic hydrolysis, hemicellulose and lignin were dissolved and the remaining crystalline cellulose part was isolated. These particles caused intense and sharp peaks because of efficiently removing the amorphous parts (33) meaning that with acidic hydrolysis, most of amorphous parts were removed and crystallinity was increased.

The variation of the crystallinity index values calculated by Eq. (3) for the alkaline-treated

cellulose and cellulose nanocrystals is shown in Figure 16. The crystallinity index values of all the cellulose nanocrystals were greater than that of the alkaline-treated cellulose. The reason for this is the residual lignin and hemicellulose content after the alkali treatment and bleaching procedure, the crystallinity index slightly increased because of removing most of the impurities (33). According to Figure 16, the crystallinity index values of cellulose nanocrystals were found as 72, 71, and 69% for  $30^\circ\text{C}$  for 30 min,  $40^\circ\text{C}$  for 45 min, and  $50^\circ\text{C}$  for 60 min, respectively which are very close to each other. Similar behavior was observed by dos Santos et al. (2013) and Nascimento et al. (2018) (21, 34). Another parameter affecting the crystallinity index is particle size. Shorter particles foster a better surface contact with the hydrolytic solution and result in a more efficient access to the inter-crystalline regions. So, the crystallinity index tends to extent. Hence, the reason for the lower crystallinity index could be attributed to the larger particle size.

#### TGA analysis

The thermal stability behaviors of the cellulose nanocrystal samples produced at different temperature and time in comparison with the alkaline-treated cellulose are shown in Figure 17.

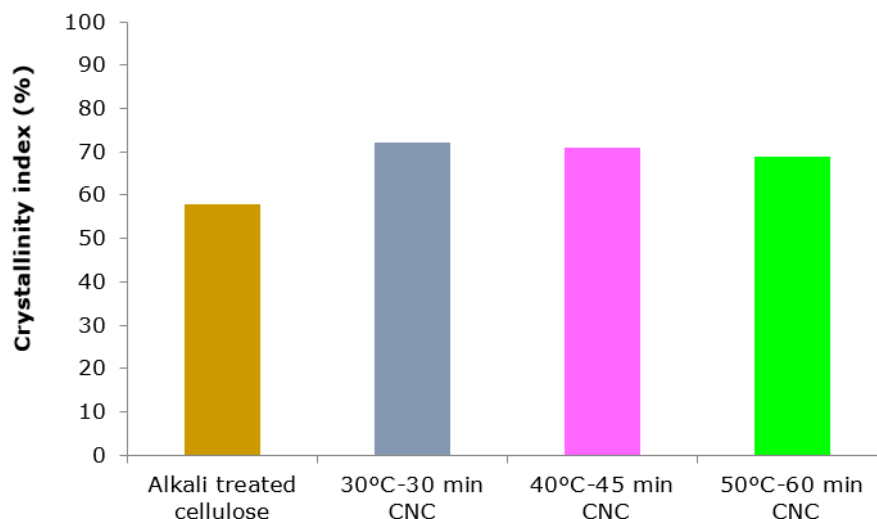


**Figure 16:** The crystallinity index values of the alkaline-treated cellulose and cellulose nanocrystals produced at different temperatures and times.

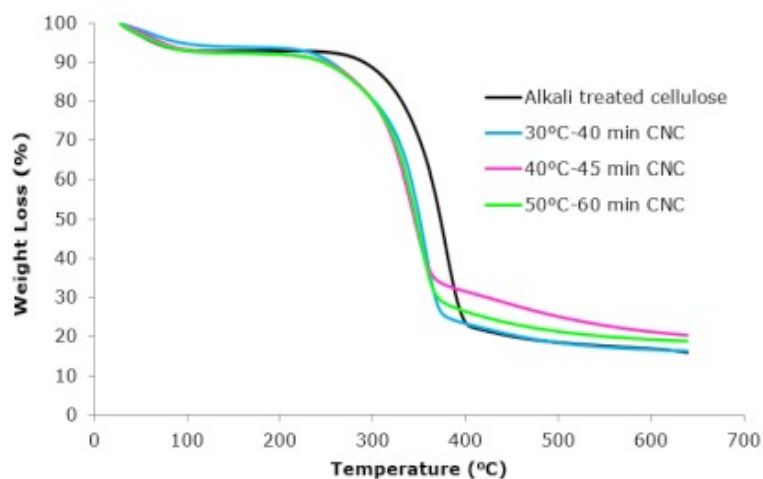


**Figure 17:** TGA curves of alkaline-treated cellulose and cellulose nanocrystals produced at different temperatures and times.

In Figure 17, two degradation phases and small mass losses (<10%) were detected for all samples, which corresponded to the evaporation of water from the surface of the samples (21, 35, 36). The first degradation was observed around 100 °C and the temperature range between 100 and 200 °C is a signal of the depolymerization of non-cellulosic components such as hemicellulose revealing the breakage of the glycosidic bonds. The second degradation peaks were observed at 354, 345 and 352 °C for CNCs produced at 30 °C for 30 min, 40 °C for 45 min, and 50 °C for 60 min, respectively showing the degradation of the  $\alpha$ -cellulose (37, 38). The degradation temperature for all of the cellulose nanocrystals were nearly the same. Besides, mass losses for the cellulose nanocrystals were also almost identical (65%). So, the degradation temperature of CNCs did not vary significantly with respect to the hydrolysis temperature and time. Also the thermogram of 30 °C for 30 min CNC has a

small peak at 279 °C corresponding to hemicellulose decomposition (27). This shows that the hemicellulose was not exactly removed from 30 °C for 30 min CNC, however exactly removed from 40 °C for 45 min, and 50 °C for 60 min CNC.

The thermal degradation for three of CNCs started at nearly 220 °C, while for the alkaline-treated cellulose degradation began at nearly 290 °C. The replacement of hydroxyl groups by acid sulfate ( $\text{O-SO}_3\text{H}$ ) groups in the hydrolysis step decreased the activation energy for the degradation of CNCs, making the sample less resistant to the pyrolysis. Therefore, the dehydration reactions occurred leading to the release of water and catalyzed nanocrystal decomposition (33).

#### *AFM analysis and dimension measurement*

The 3D AFM images of the cellulose nanocrystals obtained at various temperature and time are

shown in Figure 18, where, the bright and dark regions represented the crystalline areas and the amorphous portions in the direction of the fiber axis in the cellulose structure, respectively (39). As the temperature increased from 30 °C to 50 °C and time increased from 30 min to 60 min, the brighter regions occupied larger area than the darker regions meaning that the cellulose consisted both amorphous and crystalline parts and with the increment in temperature and time, the crystalline regions were enhanced while amorphous regions were reduced as expected. Moreover, rod-shaped

nanoparticles with individual nanocrystals and some aggregates of the cellulose fibers could be observed from Figure 18. During the process of acidic hydrolysis, the amorphous parts of cellulosic fibers were transversely cleaved, while the straight crystalline parts intact remained. Consequently, the sizes of the fibers were reduced. The aggregates were probably corresponded to the high specific area and strong hydrogen bonds existing in cellulose. Therefore, the bundles of cellulose nanocrystals fabricated larger dimensions (40).

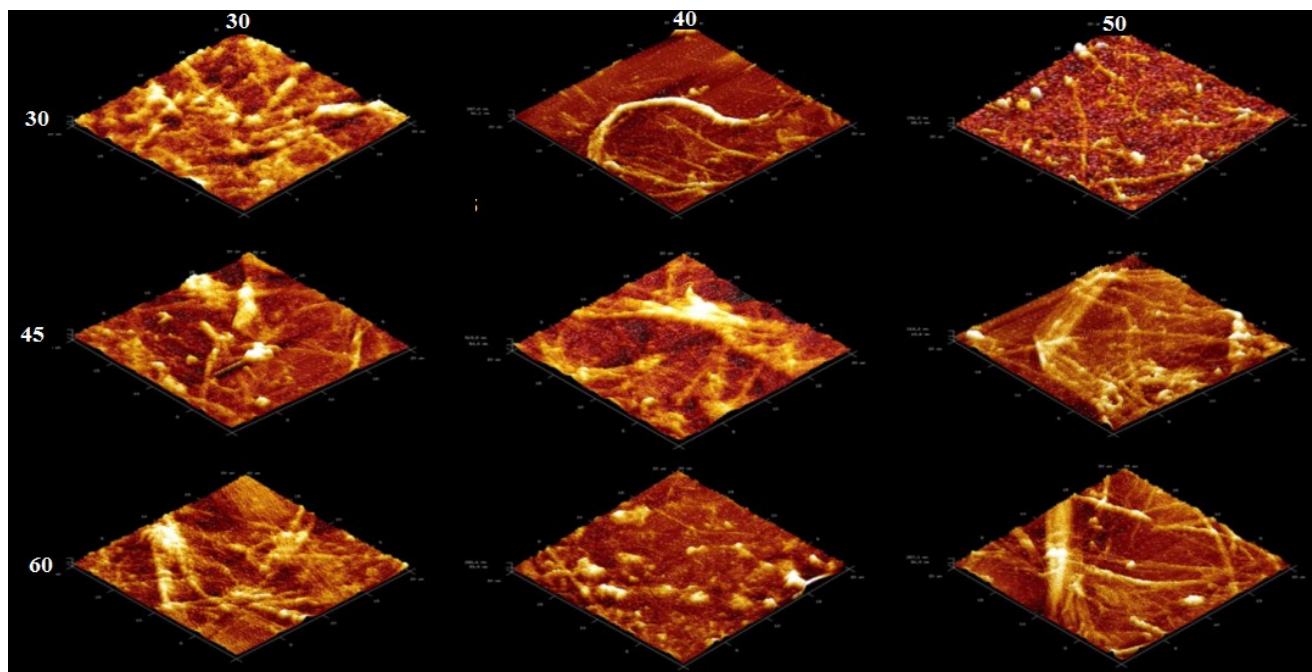


**Figure 18:** The 3D AFM images of CNCs produced at various temperatures (°C, x axis) and times (minutes, y axis).

The diameters of the cellulose nanocrystals produced at different temperature and time were tabulated in Table 4. The diameters of the cellulose nanocrystals were reduced with the increasing temperature and time as expected (22, 34). The

highest diameter value was measured as 403 nm at 30 °C for 30 min CNC, and conversely, the lowest diameter value was measured as 175 nm at 50 °C for 60 min CNC.

**Table 4:** The diameters (nm) of CNCs due to varying temperature and time.

		Temperature ( °C)		
		30	40	50
Time (min)	30	403	314	205
	45	319	314	189
	60	306	306-314	175



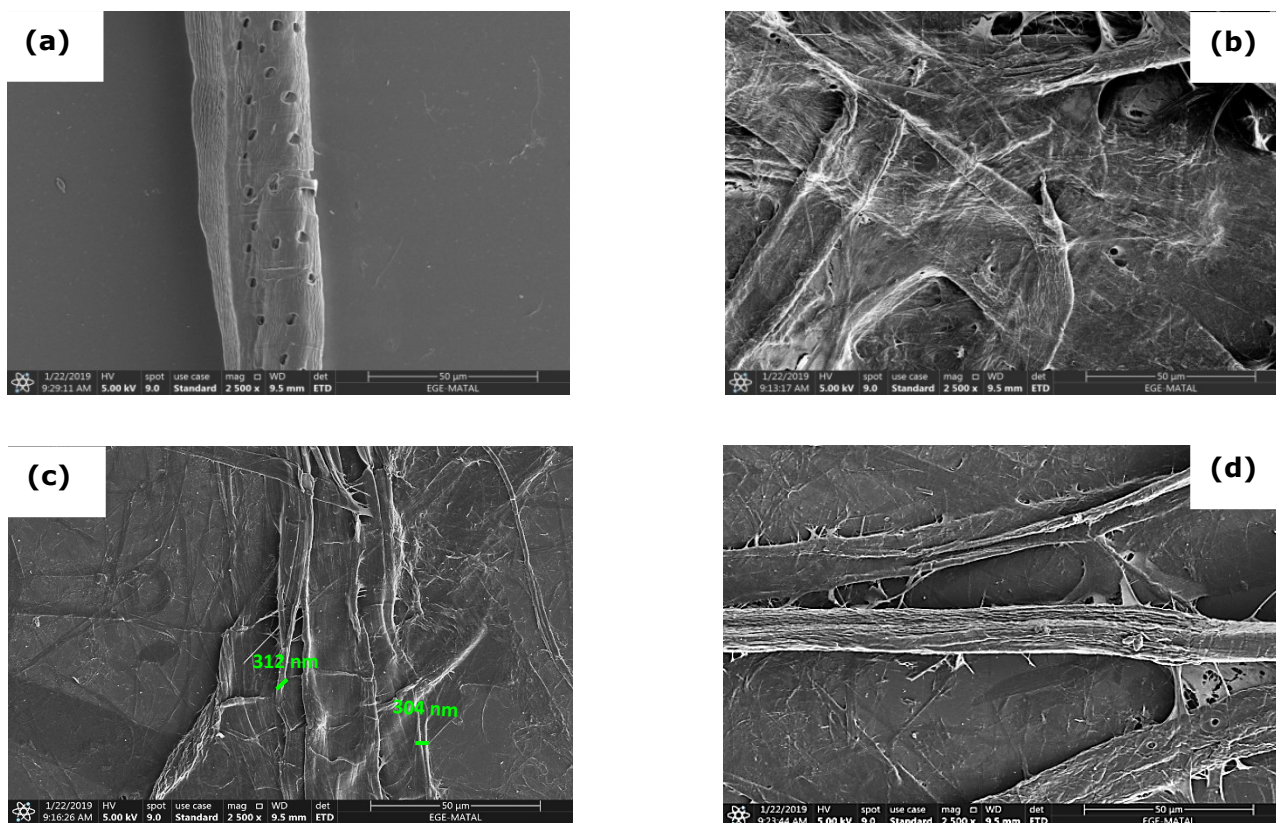


**Figure 19:** SEM images of (a) alkaline-treated cellulose, and the cellulose nanocrystals produced at (b) 30 °C-30 min, (c) 40 °C-45 min, and (d) 50 °C-60 min.

The dimensions of nanocellulose depend strongly on the processing techniques.  $H_2SO_4$  hydrolysis usually could cleave the amorphous parts of cellulose fibers transversely, resulting in the diameter reduction of fibers (41). Another factor that affects the diameter of cellulose nanocrystal is the starting source of the cellulose. In the literature, the approximate diameters for most of the cellulose nanocrystals obtained from different sources like arecanut husk, bamboo, beer residue and elephant grass were found to be in the range of 1-10, 50-100, 146-173, and 8-5 nm respectively (42, 43, 34). The measured diameters from the AFM images of the cellulose nanocrystals were larger than the actual values due to the severe tip broadening effect in AFM measurements. Aggregation and overlapping of the individual fibers made it difficult to determine the accurate size and aspect ratios of the CNCs.

#### SEM Analysis

The detailed morphological structures of the alkaline-treated and cellulose nanocrystals produced at different temperature and time (30 °C-30 min, 40 °C-45 min, and 50 °C-60 min) were investigated by SEM images taken at 50  $\mu$ m in Figure 19 (a-d), respectively. The rod-shaped cellulose nanocrystals were examined in all of the images (33, 44). In Figure 19 (a), it is seen that the alkaline-treated cellulose had a smoother surface without flakes, but there existed still small dots on fibers that might be

because of the hemicellulose and lignin content. According to Figure 19 (b), the cellulose nanocrystal obtained at 30 °C for 30 min had aggregation and its fibers were long and tortuous. With the increment in temperature and time based on Figure 19 (c) and (d), the surface of cellulose nanocrystals became smoother, the complexity of the structure and aggregation on the surface decreased. Besides that, the diameters of the cellulose nanocrystals reduced and the fibers were much more individually distributed and aligned.

#### CONCLUSION

In this study, a potentially viable recycling route was followed to produce cellulose nanocrystals, which have wide application areas and an ecofriendly nature, from multilayered recycled aseptic Tetra Pak waste food packages by the acid hydrolysis method with  $H_2SO_4$  after a series of alkali treatment and bleaching processes. The effects of temperature of 30, 40, and 50 °C and time of 30, 45, and 60 min on the hydrolysis efficiency were investigated. At the optimum  $H_2SO_4$  concentration of 25% w, the whiteness index was measured as 49.13%, after this point, this value rapidly decreases. The whiteness index of the cellulose nanocrystals at 30 °C for 30 min was 84.42%, while it was 56.00% at 50 °C for 60 min showing that the whiteness index decreased with respect to an

increase in temperature and time. Optimization studies using the experimental design carried out for the yield showed that the maximum yield was obtained at the condition where the temperature was high and the time was the lowest.

The FTIR spectra of the cellulose nanocrystal obtained at different temperatures and times were nearly the same with each other and showed similarity with the bleached cellulose. The XRD patterns of cellulose nanocrystals showed that with the acidic hydrolysis, the amorphous parts were removed and crystallinity was increased. The crystallinity index of alkaline-treated cellulose was much lower than those of the cellulose nanocrystals. From TGA graph, it was seen that the degradation temperatures of all cellulose nanocrystals were nearly the same and lower than the alkaline-treated cellulose. With respect to AFM results, it was concluded that as the temperature and time increased, the diameters of the cellulose nanocrystals were reduced. The lowest diameter value was measured as 175 nm at 50 °C for 60 min CNC, whereas, on the other hand, the highest diameter value was measured as 403 nm at 30 °C for 30 min CNC. SEM micrographs also confirmed that the surface of cellulose nanocrystals became smoother, the diameters of the cellulose nanocrystals reduced and the fibers were much more individually distributed with the increment in temperature and time.

### CONFLICT OF INTEREST

The authors declare that they have no known competing financial interests or personal relationships that could have appeared to influence the work reported in this paper.

### ACKNOWLEDGMENTS

The authors would like to express their heartiest gratitude and sincere thanks to Prof. Dr. Serap CESUR (Ege University) for her support and guidance.

### REFERENCES

1. Szabó AM, Koltai L, Fodor L. Comparative analysis of aluminium and aluminium free recycled multilayered beverage carton packaging. *J Graph Eng Des.* 2013;42:13-9.
2. Baskoro Lokahita, Muhammad Aziz, Yoshikawa K, Takahashi F. Energy and resource recovery from Tetra Pak waste using hydrothermal treatment. *Applied Energy.* 2017 Dec;207:107-13. <DOI>.
3. Diop CIK, Lavoie J-M. Isolation of Nanocrystalline Cellulose: A Technological Route for Valorizing Recycled Tetra Pak Aseptic Multilayered Food Packaging Wastes. *Waste Biomass Valor.* 2017 Jan;8(1):41-56. <DOI>.

4. Anonymous. Tetra Pak. Sustainability Report 2021 [Internet]. Tetra Pak; 2021. Available from: [https://www.tetrapak.com/content/dam/tetrapak/publicweb/gb/en/sustainability/TetraPak\\_Sustainability\\_Report\\_2021](https://www.tetrapak.com/content/dam/tetrapak/publicweb/gb/en/sustainability/TetraPak_Sustainability_Report_2021)
5. Yilgor N, Köse C, Terzi E, Figen AK, Ibach R, Kartal SN, et al. Degradation Behavior and Accelerated Weathering of Composite Boards Produced from Waste Tetra Pak® Packaging Materials. *BioResources.* 2014 Jun 25;9(3):4784-807. <DOI>.
6. Eyley S, Thielemans W. Surface modification of cellulose nanocrystals. *Nanoscale.* 2014;6(14):7764-79. <DOI>.
7. Habibi Y, Lucia LA, Rojas OJ. Cellulose Nanocrystals: Chemistry, Self-Assembly, and Applications. *Chem Rev.* 2010 Jun 9;110(6):3479-500. <DOI>.
8. George J, S N S. Cellulose nanocrystals: synthesis, functional properties, and applications. *NSA.* 2015 Nov;45. <DOI>.
9. Anwar Z, Gulfraz M, Irshad M. Agro-industrial lignocellulosic biomass a key to unlock the future bio-energy: A brief review. *Journal of Radiation Research and Applied Sciences.* 2014 Apr;7(2):163-73. <DOI>.
10. Abitbol T, Rivkin A, Cao Y, Nevo Y, Abraham E, Ben-Shalom T, et al. Nanocellulose, a tiny fiber with huge applications. *Current Opinion in Biotechnology.* 2016 Jun;39:76-88. <DOI>.
11. Yang J. Manufacturing of Nanocrystalline Cellulose [Internet] [Master of Science Thesis]. [Finland]: Aalto University School of Chemical Engineering; 2017. <URL>.
12. Faruk O, Bledzki AK, Fink H-P, Sain M. Biocomposites reinforced with natural fibers: 2000-2010. *Progress in Polymer Science.* 2012 Nov;37(11):1552-96. <DOI>.
13. Ng H-M, Sin LT, Tee T-T, Bee S-T, Hui D, Low C-Y, et al. Extraction of cellulose nanocrystals from plant sources for application as reinforcing agent in polymers. *Composites Part B: Engineering.* 2015 Jun;75:176-200. <DOI>.
14. Rosa MF, Medeiros ES, Malmonge JA, Gregorski KS, Wood DF, Mattoso LHC, et al. Cellulose nanowhiskers from coconut husk fibers: Effect of preparation conditions on their thermal and morphological behavior. *Carbohydrate Polymers.* 2010 May;81(1):83-92. <DOI>.
15. Manzato L, Rabelo LCA, de Souza SM, da Silva CG, Sanches EA, Rabelo D, et al. New approach for extraction of cellulose from tucumã's endocarp and its structural characterization. *Journal of Molecular Structure.* 2017 Sep;1143:229-34. <DOI>.
16. Gooch JW, editor. *Encyclopedic dictionary of polymers.* 2nd ed. New York: Springer; 2011. 1 p. ISBN: 978-1-4419-6246-1.
17. Rodsamran P, Sothornvit R. Renewable cellulose source: isolation and characterisation of cellulose from rice stubble residues. *Int J Food Sci Technol.* 2015 Sep;50(9):1953-9. <DOI>.
18. Segal L, Creely JJ, Martin AE, Conrad CM. An Empirical Method for Estimating the Degree of Crystallinity of Native

Cellulose Using the X-Ray Diffractometer. *Textile Research Journal*. 1959 Oct;29(10):786-94. [<DOI>](#).

19. Şahin GG, Karaboyacı M. Process and machinery design for the recycling of tetra pak components. *Journal of Cleaner Production*. 2021 Nov;323:129186. [<DOI>](#).

20. Lee HV, Hamid SBA, Zain SK. Conversion of Lignocellulosic Biomass to Nanocellulose: Structure and Chemical Process. *The Scientific World Journal*. 2014;2014:1-20. [<DOI>](#).

21. Santos RM dos, Flauzino Neto WP, Silvério HA, Martins DF, Dantas NO, Pasquini D. Cellulose nanocrystals from pineapple leaf, a new approach for the reuse of this agro-waste. *Industrial Crops and Products*. 2013 Oct;50:707-14. [<DOI>](#).

22. Fahma F, Iwamoto S, Hori N, Iwata T, Takemura A. Isolation, preparation, and characterization of nanofibers from oil palm empty-fruit-bunch (OPEFB). *Cellulose*. 2010 Oct;17(5):977-85. [<DOI>](#).

23. Lu P, Hsieh Y-L. Preparation and characterization of cellulose nanocrystals from rice straw. *Carbohydrate Polymers*. 2012 Jan;87(1):564-73. [<DOI>](#).

24. Ciolacu D, Ciolacu F, Popa V. Amorphous cellulose-Structure and characterization. *Cellul Chem Technol*. 2011;45(1-2):13-21. [<URL>](#).

25. Alemdar A, Sain M. Isolation and characterization of nanofibers from agricultural residues–Wheat straw and soy hulls. *Bioresource Technology*. 2008 Apr;99(6):1664-71. [<DOI>](#).

26. Fan M, Dai D, Huang B. Fourier Transform Infrared Spectroscopy for Natural Fibres. In: Salih Mohammed Salih, editor. *Fourier Transform-Materials Analysis* [Internet]. 2012 [cited 2021 Dec 18]. ISBN: 978-953-51-4293-5. [<URL>](#).

27. Chieng B, Lee S, Ibrahim N, Then Y, Loo Y. Isolation and Characterization of Cellulose Nanocrystals from Oil Palm Mesocarp Fiber. *Polymers*. 2017 Aug 11;9(12):355. [<DOI>](#).

28. Mazlita Y, Lee HV, Hamid SBA. Preparation of Cellulose Nanocrystals Bio-Polymer from Agro-Industrial Wastes: Separation and Characterization. *Polymers and Polymer Composites*. 2016 Nov;24(9):719-28. [<DOI>](#).

29. Kumar A, Singh Negi Y, Choudhary V, Kant Bhardwaj N. Characterization of Cellulose Nanocrystals Produced by Acid-Hydrolysis from Sugarcane Bagasse as Agro-Waste. *JMPC*. 2020 Oct 29;2(1):1-8. [<DOI>](#).

30. Feng X, Meng X, Zhao J, Miao M, Shi L, Zhang S, et al. Extraction and preparation of cellulose nanocrystals from dealginated kelp residue: structures and morphological characterization. *Cellulose*. 2015 Jun;22(3):1763-72. [<DOI>](#).

31. Dai H, Ou S, Huang Y, Huang H. Utilization of pineapple peel for production of nanocellulose and film application. *Cellulose*. 2018 Mar;25(3):1743-56. [<DOI>](#).

32. Oushabi A, Sair S, Oudrhiri Hassani F, Abboud Y, Tanane O, El Bouari A. The effect of alkali treatment on mechanical, morphological and thermal properties of date

palm fibers (DPFs): Study of the interface of DPF–Polyurethane composite. *South African Journal of Chemical Engineering*. 2017 Jun;23:116-23. [<DOI>](#).

33. Rosli NA, Ahmad I, Abdullah I. Isolation and Characterization of Cellulose Nanocrystals from Agave angustifolia Fibre. *BioResources*. 2013 Feb 21;8(2):1893-908. [<DOI>](#).

34. Nascimento SA, Rezende CA. Combined approaches to obtain cellulose nanocrystals, nanofibrils and fermentable sugars from elephant grass. *Carbohydrate Polymers*. 2018 Jan;180:38-45. [<DOI>](#).

35. Khawas P, Deka SC. Isolation and characterization of cellulose nanofibers from culinary banana peel using high-intensity ultrasonication combined with chemical treatment. *Carbohydrate Polymers*. 2016 Feb;137:608-16. [<DOI>](#).

36. Lamaming J, Hashim R, Leh CP, Sulaiman O, Sugimoto T, Nasir M. Isolation and characterization of cellulose nanocrystals from parenchyma and vascular bundle of oil palm trunk (*Elaeis guineensis*). *Carbohydrate Polymers*. 2015 Dec;134:534-40. [<DOI>](#).

37. Sonia A, Priya Dasan K. Chemical, morphology and thermal evaluation of cellulose microfibrils obtained from Hibiscus sabdariffa. *Carbohydrate Polymers*. 2013 Jan;92(1):668-74. [<DOI>](#).

38. Rhim J-W, Reddy JP, Luo X. Isolation of cellulose nanocrystals from onion skin and their utilization for the preparation of agar-based bio-nanocomposites films. *Cellulose*. 2015 Feb;22(1):407-20. [<DOI>](#).

39. Mandal A, Chakrabarty D. Isolation of nanocellulose from waste sugarcane bagasse (SCB) and its characterization. *Carbohydrate Polymers*. 2011 Aug;86(3):1291-9. [<DOI>](#).

40. Meng F, Wang G, Du X, Wang Z, Xu S, Zhang Y. Extraction and characterization of cellulose nanofibers and nanocrystals from liquefied banana pseudo-stem residue. *Composites Part B: Engineering*. 2019 Mar;160:341-7. [<DOI>](#).

41. Naduparambath S, T.V. J, V. S, M.P. S, Balan AK, E. P. Isolation and characterisation of cellulose nanocrystals from sago seed shells. *Carbohydrate Polymers*. 2018 Jan;180:13-20. [<DOI>](#).

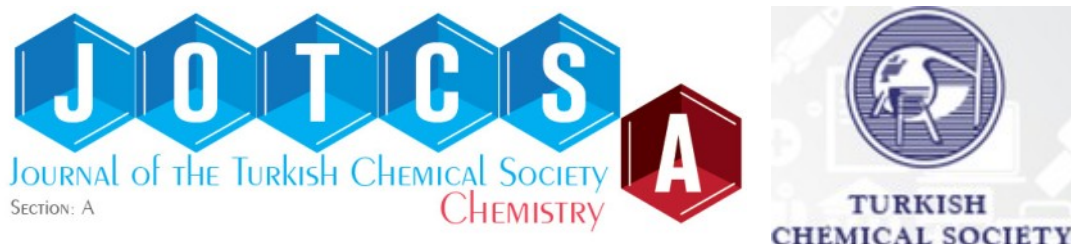
42. Liu D, Zhong T, Chang PR, Li K, Wu Q. Starch composites reinforced by bamboo cellulosic crystals. *Bioresource Technology*. 2010 Apr;101(7):2529-36. [<DOI>](#).

43. C.S. JC, George N, Narayanankutty SK. Isolation and characterization of cellulose nanofibrils from arecanut husk fibre. *Carbohydrate Polymers*. 2016 May;142:158-66. [<DOI>](#).

44. Prado KS, Spinacé MAS. Isolation and characterization of cellulose nanocrystals from pineapple crown waste and their potential uses. *International Journal of Biological Macromolecules*. 2019 Feb;122:410-6. [<DOI>](#).







## Role of Initiator Structure on Thiol-Ene Polymerization: A Comprehensive Theoretical Study

Isa Degirmenci<sup>1</sup>  

<sup>1</sup>Ondokuz Mayıs University, Chemical Engineering Department, Samsun, 55139, Turkey

**Abstract:** The effect of initiator nature on thiol-ene polymerization was elaborated in this work with two initiators, four thiols, and eight monomers by utilizing the M06-2X/6-31++G(d,p) level of theory. For this purpose, a comparative investigation was carried out by modeling hydrogen abstraction from thiols ( $k_{HA}$ ) and addition reaction to monomers ( $k_i$ ), which is considered a side reaction. It was confirmed that the 2,2-dimethoxy-2-phenylacetophenone (DMPA) initiator is a suitable thiol-ene initiator except for the polymerization of electron-deficient or conjugated monomers. It was determined that the azobis(isobutyronitrile) (AIBN) initiator could not give a homogeneous thiol-ene product regardless of the monomer structure. However, it has been found that aromatic thiols should be used to obtain relatively better results with this initiator.

**Keywords:** Thiol-ene polymerization; density functional theory; reaction kinetics; structure-reactivity relationships.

**Submitted:** October 01, 2021. **Accepted:** December 28, 2021.

**Cite this:** Degirmenci I. Role of Initiator Structure on Thiol-Ene Polymerization: A Comprehensive Theoretical Study. JOTCSA. 2022;9(1):149-62.

**DOI:** <https://doi.org/10.18596/jotcsa.1003469>.

**\*Corresponding author. E-mail:** [isa.degirmenci@omu.edu.tr](mailto:isa.degirmenci@omu.edu.tr)

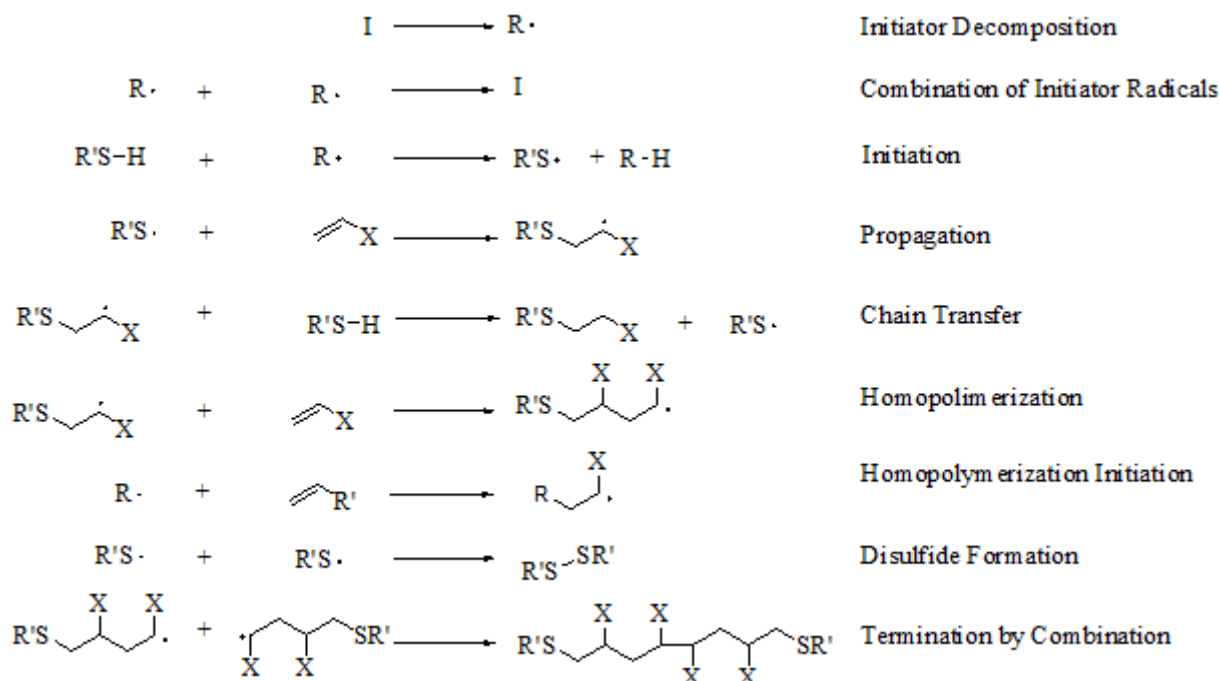
### INTRODUCTION

Thiol-ene reaction has attracted attention in the polymer field due to its unique mechanism, which combines the advantages of classical radical and step-growth polymerizations as a radical step-growth procedure (1-3). It also has a "click chemistry" feature (3) as it exhibits properties such as being fast, solvent-free, insensitive to oxygen, showing late gel points, with a high yield (4), not forming by-products, forming a uniform polymer structure, and giving products with a narrow glassy transition temperature (3). Thiol-ene polymerization was first used on surface coatings and films by photo-curable polymers and resins (5). Today, there are many applications from electro-optical materials (6) to dendrimers (7) and from drug carriers (8) to microfluidic devices (9-11).

Many experimental and theoretical studies have focused on the elaboration of steps of thiol-ene polymerization and factors affecting the process (12), such as the effect of solvent medium (13-15), the influence of substrate (12,16), or thiol reactivity (17-19). It was demonstrated that the main driving force for the thiol-ene polymerization is the rate ratios for propagation and chain transfer reactions ( $k_p/k_{ct}$ ) (12). However, the literature studies have shown that one of the factors affecting the polymerization processes is the electronic structure of the initiator. Experimental and theoretical studies on this subject are limited (20,21). As depicted in Scheme 1, one of the side reactions is radical initiator addition to alkene functionality, leading to classical free radical initiation of homopolymerization. Recombination of initiator radicals, disulfide formations, and

termination by the combination of carbon-centered radicals are other possible side reactions. This study basically focused on the initiation of homopolymerization since this side reaction can consume one of the thiol-ene polymerization reactants. Our previous study has given clues

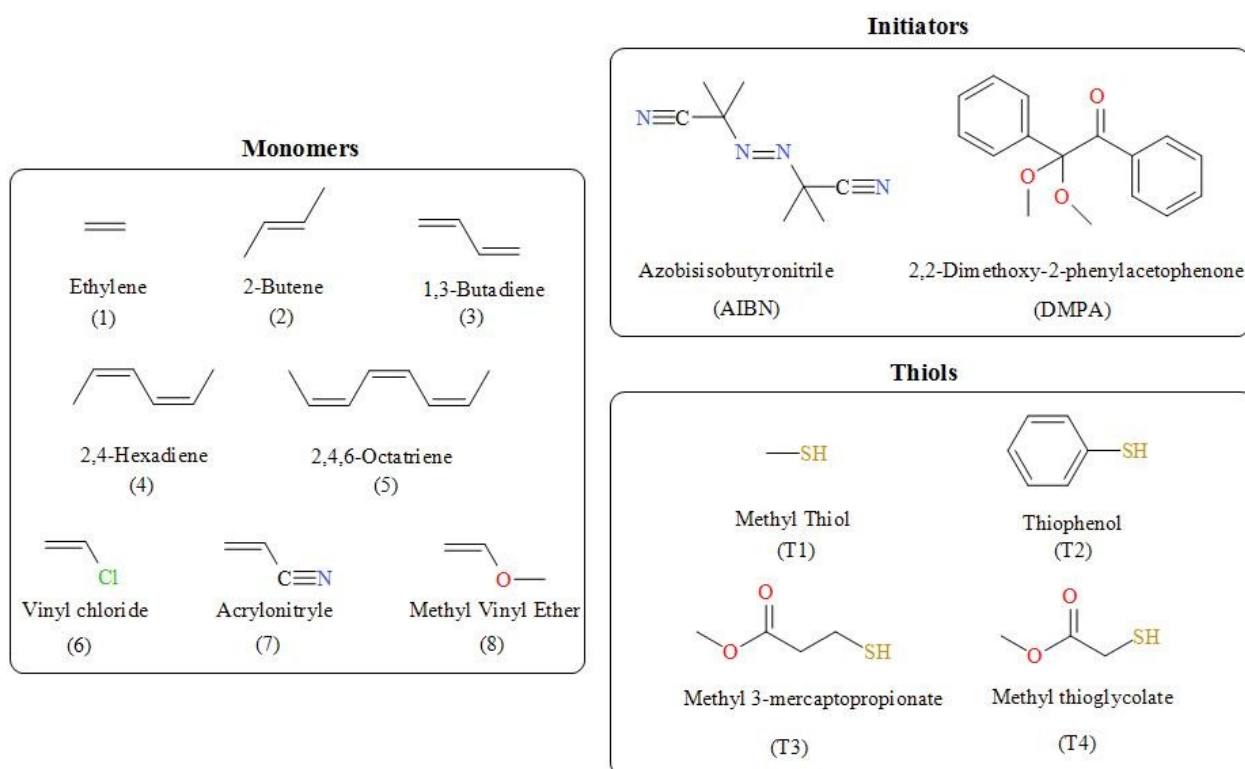
about this point by investigating a limited number of thiol and alkene functionality (21). In this study, elaboration of initiator performance was extended a larger reaction sets with eight alkenes, four thiols, and two different initiators.



**Scheme 1:** List of possible reactions during thiol-ene polymerization (22).

Hydrogen abstraction from thiols by initiator radicals is the critical step for initiating thiol-ene polymerization. However, initiator radicals can also attack alkene C=C double bond, which initiates classical radical polymerization and is considered a side reaction. Therefore, the reactivity analysis of

radicals generated from azobis(isobutyronitrile) (AIBN) as a classical radical polymerization initiator and 2,2-dimethoxy-2-phenylacetophenone (DMPA) as a thiol-ene polymerization initiator has a crucial role in investigating the efficiency of an initiator for an effective thiol-ene polymerization.



**Scheme 2:** Chemical structures of monomers, thiols, and initiators investigated in this study.

Methyl thiol (T1), thiophenol (T2), methyl 3-mercaptopropionate (T3), and methyl thioglycolate (T4) were used to analyze the effect of thiol functionality. Moreover, eight alkenes were tested due to their different electronic natures, from electron-deficient to electron-rich or conjugated structures, to investigate thiol radical attacks to monomers, which gives by-products.

## METHODOLOGY

Quantum chemical calculations were carried out by using the Gaussian 16 program package (23). All geometry optimizations, frequencies, and energies were calculated by using M06-2X functional (24). M06-2X/6-31++G(d,p) level of theory has been performed successfully to model thiol-ene polymerization (15,17). Therefore, this level of theory is preferred to model the performance of initiators. The rate constants were predicted using the transition state theory mentioned in the literature (25). The tunneling ( $\kappa$ ) coefficient was calculated based on the Wigner approximation, given in the following equation (26,27).

$$\kappa(T) = 1 + \frac{1}{24} \left| \frac{h\omega^\ddagger}{k_B T} \right|^2$$

Where,  $h$  is Planck's constant ( $6.6260755 \times 10^{-34}$  J.s),  $\omega^\ddagger$  is the imaginary frequency,  $k_B$  is the

Boltzmann's constant ( $1.380658 \times 10^{-23}$  J.K<sup>-1</sup>), and  $T$  is the temperature (298.15 K). Moreover, the stability of concerned radicals was expressed by the standard radical stabilization energies (RSE) (28, 29).

## RESULTS AND DISCUSSION

Thiol-ene reaction has appeared in literature since 1905 (30). Many experimental (12,31-36) or theoretical (15-17,19,21) studies have been carried out to elucidate the mechanism of thiol-ene polymerization. However, limited studies have focused on the role of the initiator on polymerization involving thiol-ene reactions (20-22,37,38). For the first time, a comprehensive investigation was carried out by application of quantum chemical tools in this study.

It was elaborated that whether azobis(isobutyronitrile) (AIBN) and 2,2-dimethoxy-2-phenylacetophenone (DMPA) give side reactions in thiol-ene polymerization. Exposure to light or heat leads to the decomposition of these initiators to form radicalic species. Since the polymerization reactions are performed as based on the reactivity of the radicals formed, the decomposition step of the initiators was not modeled by quantum chemical methods. What is expected from the radicals formed is that they initiate thiol-ene polymerization by abstracting the hydrogen atom

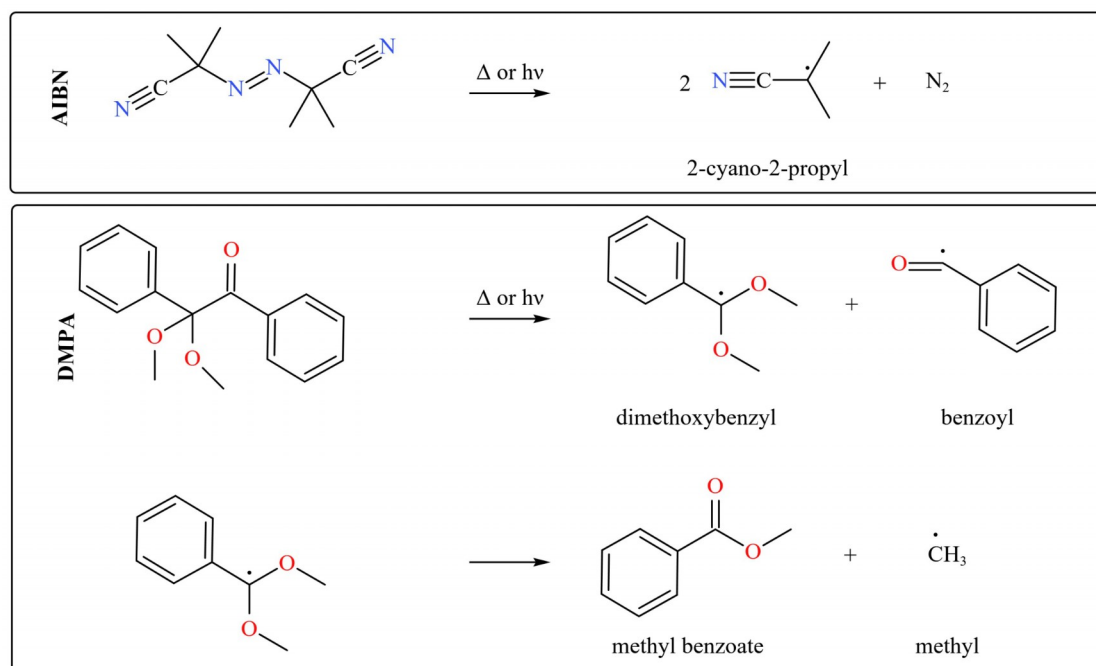


from thiols. Otherwise, the initiator radical can give a side reaction by attacking the monomer effectively. This possibility reduces the efficiency of the thiol-ene polymerization.

### Hydrogen Abstraction from Thiols

Application of AIBN as the initiator produces 2-cyano-2-propyl radical ( $\text{NC}(\text{CH}_3)_2\text{C}\cdot$ ). On the other hand, when DMPA is used as the initiator, two

different radicals are formed in the first place, the benzoyl and dimethoxy radicals. While the benzoyl radical ( $\text{C}_6\text{H}_5\text{CO}\cdot$ ) is stable, the other radical is unstable and undergoes further decomposition to yield methyl radical ( $\text{CH}_3\cdot$ ) and methyl benzoate (39). For this reason, when examining the reactivity of DMPA, the reactions of  $\text{CH}_3\cdot$  and  $\text{C}_6\text{H}_5\text{CO}\cdot$  radicals have to be taken into account.



**Scheme 3:** Radicals formed from the initiators.

Hydrogen abstraction reactions of the  $\text{NC}(\text{CH}_3)_2\text{C}\cdot$  radical are significantly less exothermic than the reaction of the other radicals (Table S1). This is because  $\text{NC}(\text{CH}_3)_2\text{C}\cdot$  radical is much more stable than the others (21). For example, while the enthalpy of the reaction with thiophenol is  $-45.90$  kJ/mol, it is  $-110.84$  kJ/mol when the  $\text{CH}_3\cdot$  radical reacts with the same thiol,  $-54.13$  kJ/mol when the  $\text{C}_6\text{H}_5\text{CO}\cdot$  radical reacts. Reactions with other thiols have a similar tendency. The fact that the enthalpies of the reactions carried out with T3 and T4 thiols are similar is due to almost the same stability of the sulfur-centered radicals (Table S1). The order of stability for considered thiyl radicals is  $\text{T2-r} > \text{T1-r} > \text{T3-r} \approx \text{T4-r}$  (Figure S2), causing the reaction enthalpies to have the same order in terms of exothermicity (Table S1). All exothermic reactions can be interpreted as breaking the weak H-S sigma bond and forming a relatively stronger C-H sigma bond instead.

The stability of the attacking radical has a critical role in both the reaction enthalpies and the size of the activation energies. For example, when the

most stable  $\text{NC}(\text{CH}_3)_2\text{C}\cdot$  radical reacts with the T4 thiol, the reaction enthalpy is  $-15.56$  kJ/mol, and the reaction barrier in Gibbs free energy is  $67.72$  kJ/mol. When the most unstable  $\text{CH}_3\cdot$  radical attacks the same thiol, the reaction enthalpy is  $-80.49$  kJ/mol, and the reaction barrier in Gibbs free energy is  $38.84$  kJ/mol. It is a fact that when the thiol structure changes, the reaction barriers and enthalpies change accordingly. However, it is seen that the barriers of the reactions with the  $\text{NC}(\text{CH}_3)_2\text{C}\cdot$  radical are larger than  $55.00$  kJ/mol, while the barriers in the reactions of other radicals are smaller than  $45.00$  kJ/mol. These results show that the radical formed from AIBN performs a much slower hydrogen abstraction reaction than the radicals formed from DMPA. Another remarkable point is that the reaction barrier is significantly reduced when the hydrogen scavenging reaction is carried out with thiophenol. It means that the reaction with the thiol takes place faster than the others.

### Addition Reactions

The radicals generated from AIBN and DMPA initiators have the potential to react with monomers as a side reaction. The conformational analysis for this reaction of radicals is given in Figure S4. The located activated complex geometries found out from this study are shown in Figures S5-S7, and all reaction energetics and kinetics are given in Tables S2-S4.

Based on the quantum chemically calculated results, the exothermicity of the reactions with the AIBN radical is less than the reactions of the other radicals. Even, it is endergonic for 2-butene and vinyl ether (1.25 kJ/mol and 5.13 kJ/mol, respectively). All reactions of other radicals ( $\text{CH}_3\bullet$  and  $\text{C}_6\text{H}_5\text{CO}\bullet$ ) are relatively exothermic. For example, when the  $\text{CH}_3\bullet$  radical is added to vinyl ether, the reaction enthalpy is -106.42 kJ/mol, and when  $\text{C}_6\text{H}_5\text{CO}\bullet$  is added to the same monomer, it is -80.44 kJ/mol.

It was observed that there was a direct relationship between the stability of the attacking radicals to the monomers and the activation Gibbs energies. The more stable  $\text{NC}(\text{CH}_3)_2\text{C}\bullet$  radical has higher reaction barriers, while the less stable  $\text{CH}_3\bullet$  and  $\text{C}_6\text{H}_5\text{CO}\bullet$  radicals have lower activation energies (Table S2). If the reactivity of  $\text{CH}_3\bullet$  and  $\text{C}_6\text{H}_5\text{CO}\bullet$  radicals are compared among themselves, interestingly, it is seen that the barriers to the reactions of the more unstable  $\text{CH}_3\bullet$  radical are relatively higher. The SOMO energies of the radicals can explain this. It was calculated -0.28407 Hartree for  $\text{CH}_3\bullet$ , while SOMO energy is relatively higher (-0.26103 Hartree) for  $\text{C}_6\text{H}_5\text{CO}\bullet$ . Therefore, SOMO of  $\text{C}_6\text{H}_5\text{CO}\bullet$  has the potential to more stabilizing the transition state structure by effective interaction with  $\pi^*$  orbital of the substrate. In addition, the interaction of the monomer with the  $\pi$  orbitals in the pi bond system of the  $\text{C}_6\text{H}_5\text{CO}\bullet$  radical leads to more stable transition state geometries (Figure S7).

### Reaction Kinetics

In this study, what is expected from a good initiator candidate is that the generated radical should prefer to react with thiol instead of monomer. This preference is presented by a large difference between the rate constants ( $k_{\text{HA}} \gg k_i$ ). More favored hydrogen abstraction from thiol can result in more homogeneous thiol-ene polymerization. If there is a competition between these two reactions, the initiator radical reduces the monomer concentration, increasing the heterogeneity of polymerization product. The mentioned rate constants are given in Table 1, and the logarithms of the ratios of these calculated rate constants,  $\log(k_{\text{HA}}/k_i)$ , are given in Table 2.

The addition reaction of alkyl thiyl radicals to electron-deficient monomers occur relatively faster (1,3-butadiene, 2,4-hexadiene, 2,4,6-octatriene, and acrylonitrile) than the electron-rich monomers (2-butene, vinyl chloride, and methyl vinyl ether). If the rate constants of the hydrogen abstraction reactions from thiols are evaluated, it is seen that they are greater than  $10^7 \text{ M}^{-1}\cdot\text{s}^{-1}$  for the radicals  $\text{CH}_3\bullet$  and  $\text{C}_6\text{H}_5\text{CO}\bullet$ . When the radical formed from AIBN is used in the hydrogen abstraction reaction, this value is lowered below  $10^5 \text{ M}^{-1}\cdot\text{s}^{-1}$ .

When the hydrogen abstraction reaction rate is closer to the addition reaction rate for the AIBN, the initiator enhances the side reaction. However, it was calculated that the hydrogen abstraction ( $1.82\text{E}+04 \text{ M}^{-1}\cdot\text{s}^{-1}$ ) from  $\text{C}_6\text{H}_5\text{-SH}$  by the formed radicals from AIBN occurred faster than other thiols. It means that using the AIBN initiator, the best thiol-ene polymerization is possible with the preference of aromatic thiols. In the case of using the DMPA initiator, better results are obtained as a general tendency of initiators. However, by-product formation is possible for electron-deficient monomers (1,3-butadiene, 2,4-hexadiene, 2,4,6-octatriene, and acrylonitrile) since they have relatively fast addition reactions. Especially for acrylonitrile, the rate constant in the addition reaction with  $\text{C}_6\text{H}_5\text{CO}\bullet$  is very large ( $1.03\text{E}+06 \text{ M}^{-1}\cdot\text{s}^{-1}$ ).

**Table 1:** Addition ( $k_i$ ) and hydrogen abstraction reaction ( $k_{HA}$ ) kinetics ( $M^{-1}.s^{-1}$ ) for  $NC(CH_3)_2C\bullet$ ,  $CH_3\bullet$ , and  $C_6H_5CO\bullet$  radicals.

	$NC(CH_3)_2C\bullet$	$CH_3\bullet$	$C_6H_5CO\bullet$
Addition to monomers ( $k_i$ )			
ethylene (1)	2.57E-01	1.24E+02	4.04E+02
2-butene (2)	5.69E-02	3.92E+00	3.76E+02
1,3-butadiene (3)	1.78E+02	3.49E+04	2.86E+04
2,4-hexadiene (4)	6.46E+00	2.99E+02	2.44E+04
2,4,6-octatriene (5)	2.20E+02	2.16E+03	8.22E+04
vinyl chloride (6)	2.78E+00	7.17E+02	1.55E+03
acrylonitrile (7)	6.04E+01	4.59E+04	1.03E+06
methyl vinyl ether (8)	1.27E+00	9.13E+00	3.63E+02
Hydrogen abstraction from thiols ( $k_{HA}$ )*			
T1**	1.50E+02	4.66E+07	3.01E+08
T2	1.82E+04	1.36E+08	3.62E+08
T3**	2.18E+03	2.32E+07	5.25E+07
T4	4.73E+02	4.41E+07	2.37E+08

\* Wigner's tunneling correction was performed. \*\* Reference (21)

The hydrogen abstraction rate constants of  $NC(CH_3)_2C\bullet$  radical vary between  $1.50E+02 M^{-1}.s^{-1}$  and  $1.82E+04 M^{-1}.s^{-1}$  (Table 1). Moreover, rate constants of its addition to alkenes vary between  $5.69E-02 M^{-1}.s^{-1}$  (2-butene (2)) and  $2.20E+02 M^{-1}.s^{-1}$  (2,4,6-octatriene (A5)). These results show that the rates of the specific reactions are very close to each other when the AIBN initiator is used. Especially in conjugated monomers, such as 1,3-butadiene or 2,4,6-octatriene, the addition reaction rate constants are in the order of  $10^2 M^{-1}.s^{-1}$ . Therefore, the possibility of desired thiol-ene polymer product cannot be obtained due to this side reaction. Furthermore, an increase in the initiator concentration also leads to an increase in the probability of side reaction. These findings explain why AIBN is not a good initiator for the polymerization. When DMPA is used as the initiator, kinetic data for the hydrogen abstraction rate constants of the radical  $CH_3\bullet$  vary between  $2.32E+07 M^{-1}.s^{-1}$  and  $1.36E+08 M^{-1}.s^{-1}$  (Table 1). For the addition reaction of the same radical, kinetic data changes from  $3.92E+00 M^{-1}.s^{-1}$  (2-butene (2)) to  $4.59E+04 M^{-1}.s^{-1}$  (acrylonitrile (7)). The kinetic data addition reaction for the commercial monomers, especially 1,3-butadiene and acrylonitrile, are in the order of  $10^4 M^{-1}.s^{-1}$ . Compared to the AIBN radical ( $NC(CH_3)_2C\bullet$ ), a larger difference is obtained between the rate constants. The hydrogen abstraction by the benzoyl ( $C_6H_5CO\bullet$ ) radical, another radical formed from DMPA, is significantly fast and its rate coefficient changes from  $5.25E+07 M^{-1}.s^{-1}$  to  $3.62E+08 M^{-1}.s^{-1}$ . As a side reaction, attacking the same radical to the alkenes is relatively slow, and rate coefficients of this reaction change from  $3.63E+02 M^{-1}.s^{-1}$  (methyl vinyl ether) to  $1.03E+06 M^{-1}.s^{-1}$  (acrylonitrile). Again, the difference between

the rate constants is better compared to the AIBN radical ( $NC(CH_3)_2C\bullet$ ). Nevertheless, the rate constant of the addition to commercial monomers, especially acrylonitrile, is above the order of  $10^5 M^{-1}.s^{-1}$ . As a result, electron-poor monomers have a great possibility to give heterogeneous thiol-ene polymerization products with both radicals formed from DMPA. This probability decreases as the initiator concentration decreases, or better results can be obtained without using an initiator.

Table 2 makes kinetic evaluation more understandable and straightforward. The data in the table were obtained by taking the logarithm of the  $k_{HA}/k_i$  ratio for the reactions. In this way, it is made visible to what extent the rates of both reactions compete with each other. The  $\log(k_{HA}/k_i)$  data colors were determined according to the following definition; red for values less than two, yellow for values between two and three, and blue for values greater than three. The red color symbolizes that the presence of side reactions is significant, the yellow color symbolizes that the by-product may show itself, albeit partially, and the blue color symbolizes that the presence of the by-product is negligible. As a result, it was demonstrated that the AIBN initiator is not a good option for the polymerization since it has a high probability of forming by-products. The applicability of the DMPA initiator for thiol-ene polymerization is well known and has also been proven by quantum chemical calculations. It was predicted that the heterogeneity of the polymerization product resulting from side reactions would increase when initiator concentration is kept high. These findings are also well correlated with a kinetic modeling investigation in the previous literature study (38).

**Table 2:** Ratios for the reaction rate constants of hydrogen abstraction from thiols and addition reactions of  $\text{NC}(\text{CH}_3)_2\text{C}\cdot$ ,  $\text{CH}_3\cdot$ , and  $\text{C}_6\text{H}_5\text{CO}\cdot$  radicals to monomers on a logarithmic scale,  $\log(k_{\text{HA}}/k_i)$ .

Monomers	$\text{NC}(\text{CH}_3)_2\text{C}\cdot$				$\text{CH}_3\cdot$				$\text{C}_6\text{H}_5\text{CO}\cdot$			
	T1	T2	T3	T4	T1	T2	T3	T4	T1	T2	T3	T4
ethylene (1)	2.8	4.9	3.9	3.3	5.6	6.0	5.3	5.6	5.9	6.0	5.1	5.8
2-butene (2)	3.4	5.5	4.6	3.9	7.1	7.5	6.8	7.1	5.9	6.0	5.1	5.8
1,3-butadiene (3)	-0.1	2.0	1.1	0.4	3.1	3.6	2.8	3.1	4.0	4.1	3.3	3.9
2,4-hexadiene (4)	1.4	3.4	2.5	1.9	5.2	5.7	4.9	5.2	4.1	4.2	3.3	4.0
2,4,6-octatriene (5)	-0.2	1.9	1.0	0.3	4.3	4.8	4.0	4.3	3.6	3.6	2.8	3.5
vinyl chloride (6)	1.7	3.8	2.9	2.2	4.8	5.3	4.5	4.8	5.3	5.4	4.5	5.2
acrylonitrile (7)	0.4	2.5	1.6	0.9	3.0	3.5	2.7	3.0	2.5	2.5	1.7	2.4
methyl vinyl ether (8)	2.1	4.2	3.2	2.6	6.7	7.2	6.4	6.7	5.9	6.0	5.2	5.8

The colored values defined as red is  $x < 2$ , yellow is  $2 < x < 3$ , and blue is  $x > 3$  ( $x = k_{\text{HA}}/k_i$ ).

## CONCLUSION

This comprehensive quantum chemical study demonstrates the importance of initiator selection for thiol-ene polymerization. It was found out that aromatic thiols (such as thiophenol) were more prone to thiol-ene polymerization when AIBN is preferred as the initiator. Best results with this combination were obtained with 2-butene and methyl vinyl ether. Regardless of the type of initiator, 2-butene has a high affinity for the thiol-ene reaction. It is worth noting that initiators have a high tendency to initiate classical radical polymerization as a side polymerization with electron-deficient or conjugated monomers. As a general assessment, the performance of AIBN is not satisfactory compared to the application of DMPA.

Radicals formed from DMPA have been found to initiate the thiol-ene reaction without any problems, regardless of the thiol structure, except for electron-poor or conjugated monomers. Especially 2-butene, vinyl chloride, methyl vinyl ether have a low tendency to give by-products with this initiator. Even conjugated 2,4-hexadiene monomer can effectively initiate thiol-ene reaction instead of classical radical polymerization initiation. Another finding is that the  $\text{C}_6\text{H}_5\text{CO}\cdot$  radical is more likely to form by-products than the  $\text{CH}_3\cdot$  radical for the DMPA initiator. In any case, it was calculated that radicals formed from DMPA had a lower tendency to side-reactions than radicals formed from AIBN.

It is worth noting that these results only provide some information about the initiation step of the thiol-ene polymerization. A good initiation does not always mean that it results in a good

polymerization; other reactions in the thiol-ene polymerization mechanism, such as propagation and chain transfer, strongly depend on the chemical structures of monomers and thiols, as mentioned in the introduction. On the other hand, a poor initiation performance always results in a heterogeneous product.

## ACKNOWLEDGMENTS

I am thankful for CPU usage and funding to the Scientific and Technological Research Council of Turkey (TUBITAK, Project Number: 217Z073). TUBITAK ULAKBIM, High Performance and Grid Computing Center (TRUBA resources) partially provided computing resources used in this work.

## REFERENCES

- Griesbaum K. Problems and Possibilities of the Free-Radical Addition of Thiols to Unsaturated Compounds. *Angew Chem Int Ed Engl.* 1970 Apr;9(4):273-87. [<DOI>](#).
- Dondoni A. The Emergence of Thiol-Ene Coupling as a Click Process for Materials and Bioorganic Chemistry. *Angew Chem Int Ed.* 2008 Nov 10;47(47):8995-7. [<DOI>](#).
- Hoyle CE, Bowman CN. Thiol-Ene Click Chemistry. *Angewandte Chemie International Edition.* 2010 Feb 22;49(9):1540-73. [<DOI>](#).
- Hoyle CE, Lowe AB, Bowman CN. Thiol-click chemistry: a multifaceted toolbox for small molecule and polymer synthesis. *Chem Soc Rev.* 2010;39(4):1355-87. [<DOI>](#).
- Jacobine A, Fouassier J, Rabek J. Radiation curing in polymer science and technology. vol III, Elsevier (London). 1993;

6. Sun Y, Gao Y, Zhou L, Huang J, Fang H, Ma H, et al. A Study on the Electro-Optical Properties of Thiol-Ene Polymer Dispersed Cholesteric Liquid Crystal (PDChLC) Films. *Molecules*. 2017 Feb 22;22(2):317. [<DOI>](#).
7. Heidecke CD, Lindhorst TK. Iterative Synthesis of Spaced Glycodendrons as Oligomannoside Mimetics and Evaluation of Their Antiadhesive Properties. *Chem Eur J*. 2007 Nov 5;13(32):9056–67. [<DOI>](#).
8. Chen G, Amajjahe S, Stenzel MH. Synthesis of thiol-linked neoglycopolymers and thermo-responsive glycomicelles as potential drug carrier. *Chem Commun*. 2009;(10):1198-200. [<DOI>](#).
9. Natali M, Begolo S, Carofiglio T, Mistura G. Rapid prototyping of multilayer thiolene microfluidic chips by photopolymerization and transfer lamination. *Lab Chip*. 2008;8(3):492-4. [<DOI>](#).
10. Cabral JT, Hudson SD, Harrison C, Douglas JF. Frontal Photopolymerization for Microfluidic Applications. *Langmuir*. 2004 Nov 1;20(23):10020–9. [<DOI>](#).
11. Cygan ZT, Cabral JT, Beers KL, Amis EJ. Microfluidic Platform for the Generation of Organic-Phase Microreactors. *Langmuir*. 2005 Apr 1;21(8):3629–34. [<DOI>](#).
12. Cramer NB, Reddy SK, O'Brien AK, Bowman CN. Thiol-Ene Photopolymerization Mechanism and Rate Limiting Step Changes for Various Vinyl Functional Group Chemistries. *Macromolecules*. 2003 Oct 1;36(21):7964–9. [<DOI>](#).
13. Zgrzeba A, Andrzejewska E, Marcinkowska A. Ionic liquid – containing ionogels by thiol-ene photopolymerization. Kinetics and solvent effect. *RSC Adv*. 2015;5(121):100354–61. [<DOI>](#).
14. Marcinkowska A, Zgrzeba A, Lota G, Kopczyński K, Andrzejewska E. Ionogels by thiol-ene photopolymerization in ionic liquids: Formation, morphology and properties. *Polymer*. 2019 Jan;160:272–81. [<DOI>](#).
15. Munar I, Findik V, Degirmenci I, Aviyente V. Solvent Effects on Thiol-Ene Kinetics and Reactivity of Carbon and Sulfur Radicals. *J Phys Chem A*. 2020 Apr 2;124(13):2580–90. [<DOI>](#).
16. Northrop BH, Coffey RN. Thiol-Ene Click Chemistry: Computational and Kinetic Analysis of the Influence of Alkene Functionality. *J Am Chem Soc*. 2012 Aug 22;134(33):13804–17. [<DOI>](#).
17. Findik V, Degirmenci I, Çatak Ş, Aviyente V. Theoretical investigation of thiol-ene click reactions: A DFT perspective. *European Polymer Journal*. 2019 Jan;110:211–20. [<DOI>](#).
18. Long KF, Bongiardina NJ, Mayordomo P, Olin MJ, Ortega AD, Bowman CN. Effects of 1°, 2°, and 3° Thiols on Thiol-Ene Reactions: Polymerization Kinetics and Mechanical Behavior. *Macromolecules*. 2020 Jul 28;53(14):5805–15. [<DOI>](#).
19. Coote ML, Degirmenci I. Theory and Applications of Thiyl Radicals in Polymer Chemistry. In: *Computational Quantum Chemistry* [Internet]. Elsevier; 2019 [cited 2021 Dec 29]. p. 195–218. ISBN: 978-0-12-815983-5. [<URL>](#).
20. Hafeez S, Khatri V, Kashyap HK, Nebhani L. Computational and experimental approach to evaluate the effect of initiator concentration, solvents, and enes on the TEMPO driven thiol-ene reaction. *New J Chem*. 2020;44(43):18625–32. [<DOI>](#).
21. Degirmenci I. Effect of Initiator Structure on Thiol-Ene Polymerization: A DFT Study. *Macromol Theory Simul*. 2021 Sep;2100040. [<DOI>](#).
22. Koo SPS, Stamenović MM, Prasath RA, Inglis AJ, Du Prez FE, Barner-Kowollik C, et al. Limitations of radical thiol-ene reactions for polymer-polymer conjugation. *J Polym Sci A Polym Chem*. 2010 Apr 15;48(8):1699–713. [<DOI>](#).
23. Frisch M, Trucks G, Schlegel H, Scuseria G, Robb M, Cheeseman J et al. *Gaussian 16 Rev. B. 01*. Gaussian, Inc., Wallingford, CT; 2016.
24. Zhao Y, Truhlar DG. The M06 suite of density functionals for main group thermochemistry, thermochemical kinetics, noncovalent interactions, excited states, and transition elements: two new functionals and systematic testing of four M06-class functionals and 12 other functionals. *Theor Chem Account*. 2008 May;120(1–3):215–41. [<DOI>](#).
25. Furuncuoğlu T, Uğur İ, Değirmenci İ, Aviyente V. Role of Chain Transfer Agents in Free Radical Polymerization Kinetics. *Macromolecules*. 2010 Feb 23;43(4):1823–35. [<DOI>](#).
26. Truong TN, Truhlar DG. Ab initio transition state theory calculations of the reaction rate for OH+CH<sub>4</sub> →H<sub>2</sub>O+CH<sub>3</sub>. *The Journal of Chemical Physics*. 1990 Aug;93(3):1761–9. [<DOI>](#).
27. Duan X, Scheiner S. Energetics, proton transfer rates, and kinetic isotope effects in bent hydrogen bonds. *Journal of the American Chemical Society*. 1992;114(14):5849–56. ISSN: 0002-7863.
28. Griller D, Ingold KU. Persistent carbon-centered radicals. *Accounts of Chemical Research*. 1976;9(1):13–9. ISSN: 0001-4842.
29. Coote ML, Lin CY, Beckwith ALJ, Zavitsas AA. A comparison of methods for measuring relative radical stabilities of carbon-centred radicals. *Phys Chem Chem Phys*. 2010;12(33):9597. [<DOI>](#).
30. Posner T. Beiträge zur Kenntniss der ungesättigten Verbindungen. II. Ueber die Addition von Mercaptanen an ungesättigte Kohlenwasserstoffe. *Ber Dtsch Chem Ges*. 1905;38(1):646–57.
31. Hoyle CE, Lee TY, Roper T. Thiol-enes: Chemistry of the past with promise for the future. *J Polym Sci A Polym Chem*. 2004 Nov 1;42(21):5301–38. [<DOI>](#).

32. Chiou B-S, English RJ, Khan SA. Rheology and Photo-Cross-Linking of Thiol–Ene Polymers. *Macromolecules*. 1996 Jan 1;29(16):5368–74. [<DOI>](#).
33. Hoyle CE, Hensel RD, Grubb MB. Temperature dependence of the laser-initiated polymerization of a thiol-ene system. *J Polym Sci Polym Chem Ed*. 1984 Aug;22(8):1865–73. [<DOI>](#).
34. Cramer NB, Bowman CN. Kinetics of thiol-ene and thiol-acrylate photopolymerizations with real-time fourier transform infrared. *J Polym Sci A Polym Chem*. 2001 Oct 1;39(19):3311–9. [<DOI>](#).
35. Cramer NB, Scott JP, Bowman CN. Photopolymerizations of Thiol–Ene Polymers without Photoinitiators. *Macromolecules*. 2002 Jul 1;35(14):5361–5. [<DOI>](#).
36. Cramer NB, Davies T, O'Brien AK, Bowman CN. Mechanism and Modeling of a Thiol–Ene Photopolymerization. *Macromolecules*. 2003 Jun 1;36(12):4631–6. [<DOI>](#).
37. Uygun M, Tasdelen MA, Yagci Y. Influence of Type of Initiation on Thiol-Ene “Click” Chemistry: Influence of Type of Initiation on Thiol-Ene “Click” Chemistry. *Macromol Chem Phys*. 2010 Jan 5;211(1):103–10. [<DOI>](#).
38. Derboven P, D’hooge DR, Stamenovic MM, Espeel P, Marin GB, Du Prez FE, et al. Kinetic Modeling of Radical Thiol–Ene Chemistry for Macromolecular Design: Importance of Side Reactions and Diffusional Limitations. *Macromolecules*. 2013 Mar 12;46(5):1732–42. [<DOI>](#).
39. Mucci V, Vallo C. Efficiency of 2,2-dimethoxy-2-phenylacetophenone for the photopolymerization of methacrylate monomers in thick sections. *J Appl Polym Sci*. 2012 Jan 5;123(1):418–25. [<DOI>](#).

## **Role of Initiator Structure on Thiol-Ene Polymerization: A Comprehensive Theoretical Study**

Isa Degirmenci

Chemical Engineering Department, Ondokuz Mayıs University, 55139 Samsun, Turkey

E-mail: [isa.degirmenci@omu.edu.tr](mailto:isa.degirmenci@omu.edu.tr)



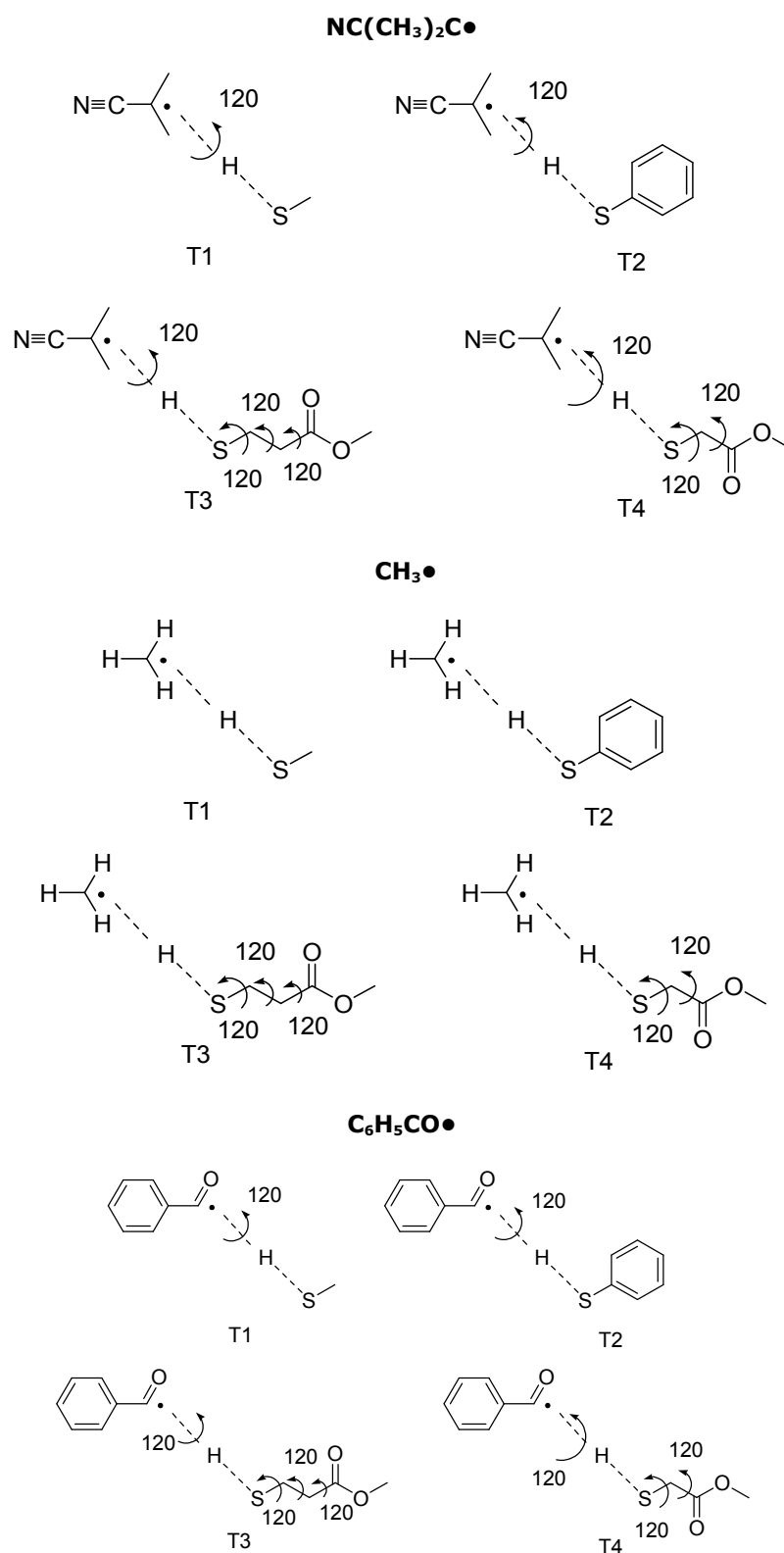


**Figure S1:** Schematic representation of conformational analysis at the transition states for hydrogen abstraction reaction of  $\text{NC}(\text{CH}_3)_2\text{C}\bullet$ ,  $\text{CH}_3\bullet$ , and  $\text{C}_6\text{H}_5\text{CO}\bullet$  radicals from T1, T2, T3, and T4 thiols.

**Table S1:** Energetics (kJ/mol) and kinetics ( $\text{L}\cdot\text{mol}^{-1}\cdot\text{s}^{-1}$ ) for the hydrogen abstraction reaction from T1, T2, T3, and T4 thiols by  $\text{NC}(\text{CH}_3)_2\text{C}\cdot$ ,  $\text{CH}_3\cdot$ , and  $\text{C}_6\text{H}_5\text{CO}\cdot$  radicals.

	Thiol	$\Delta H_{\text{rxn}}$	$\Delta G_{\text{rxn}}$	$\Delta H^\ddagger$	$\text{DG}^\ddagger$
$\text{NC}(\text{CH}_3)_2\text{C}\cdot$	T1	-21.72	-13.57	21.66	70.67
	T2	-45.90	-35.92	3.87	58.61
	T3	-15.57	-9.88	8.25	64.11
	T4	-15.56	-8.20	11.10	67.72
$\text{CH}_3\cdot$	T1	-86.66	-81.28	2.84	38.77
	T2	-110.84	-103.63	-2.29	35.85
	T3	-80.51	-77.59	1.18	40.41
	T4	-80.49	-75.91	-2.50	38.84
$\text{C}_6\text{H}_5\text{CO}\cdot$	T1	-29.95	-27.20	-2.42	33.96
	T2	-54.13	-49.55	-14.41	33.29
	T3	-23.80	-23.51	-15.02	38.14
	T4	-23.78	-21.83	-16.59	34.55

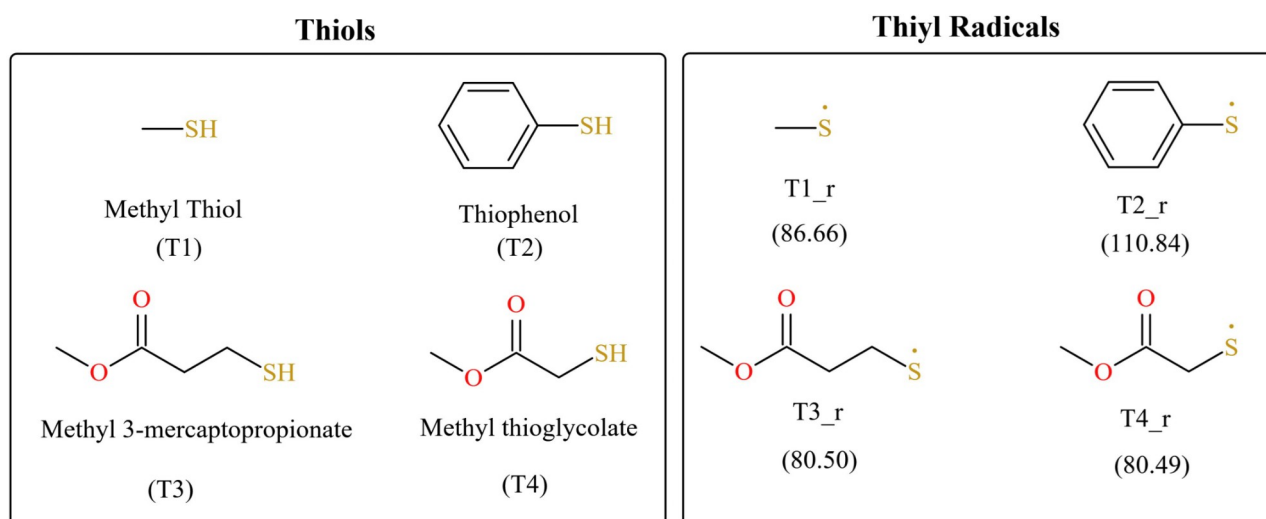


**Figure S2:** Chemical structures of thiols, formed thiyl radicals from the considered thiols and their radical stabilisation energies (RSE) in kJ/mol.

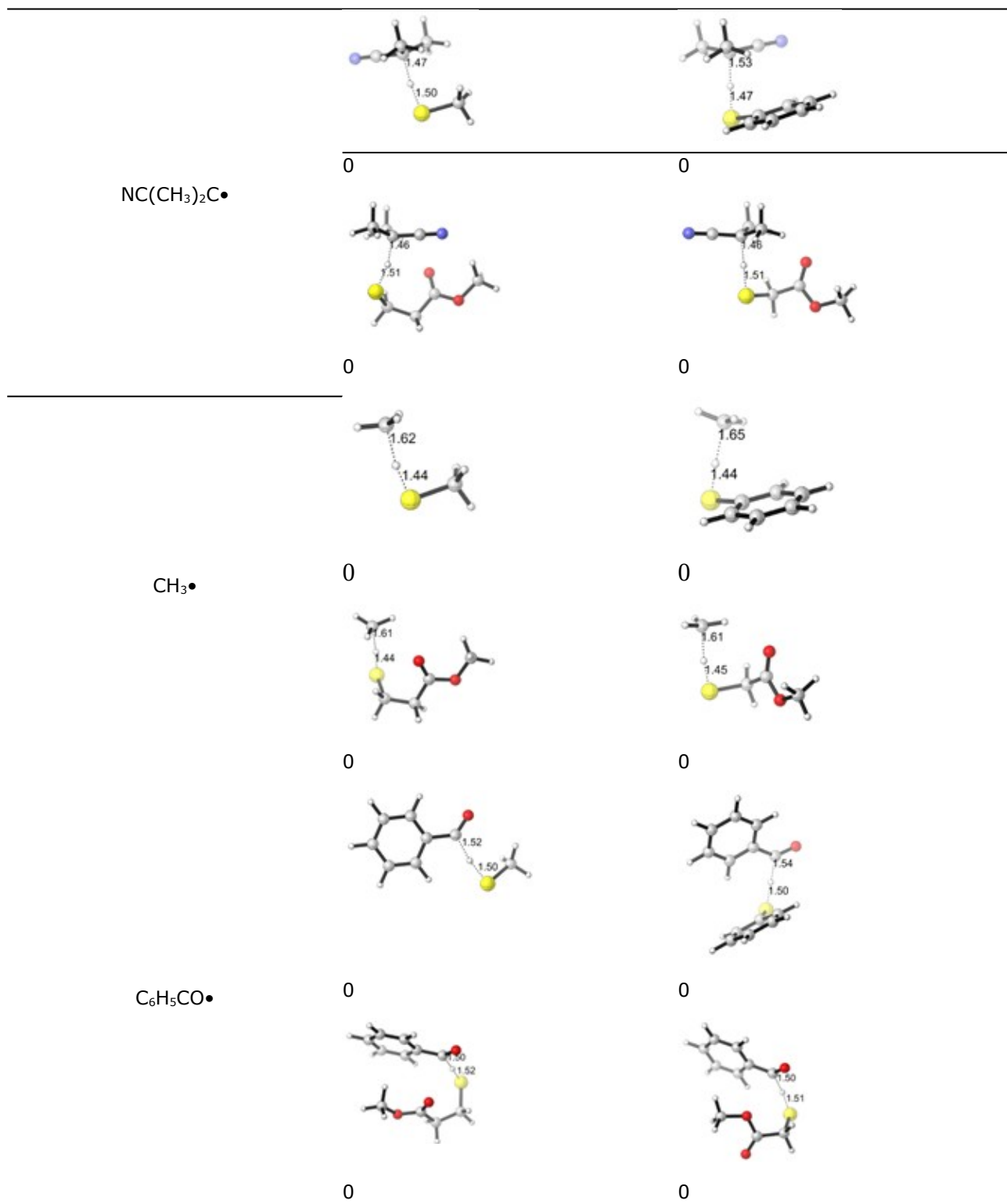


**Figure S3:** Hydrogen abstraction transition state geometries of NC(CH<sub>3</sub>)<sub>2</sub>C•, CH<sub>3</sub>•, and C<sub>6</sub>H<sub>5</sub>CO• radicals from T1, T2, T3, and T4 thiols.



## Synthesis, Characterization, DFT Calculations, and Catalytic Epoxidation of Two Oxovanadium(IV) Schiff Base Complexes

Asha Fadalla Wady<sup>1</sup> , Mohammed Awad Ali Khalid<sup>2,\*</sup>  , Mohammed Traheeb Alotaibi<sup>2</sup>   
and Yusuf Sulfab Ahmed<sup>3</sup> 

<sup>1</sup> University of Kordofan, Department of Chemistry, Alobaid, 11111, Sudan

<sup>2</sup> University of Taif, Department of Chemistry, Turabah, 21995, Saudi Arabia

<sup>3</sup> University of Khartoum, Department of Chemistry, Khartoum, 11115, Sudan

**Abstract:** The present paper reports the synthesis, characterization, and DFT calculations of two oxovanadium (IV) Schiff base complexes symbolized as VOL<sub>1</sub> and VOL<sub>2</sub>, which prepared by the reaction of bivalent tridentate Schiff base ligands (*E*)-2-((5-chloro-2-hydroxybenzylidene)amino)acetic acid and (*E*)-2-((2-hydroxy-5-nitrobenzylidene)amino)acetic acid and VO(acac)<sub>2</sub> as vanadium source. The Schiff base ligands and its oxovanadium (IV) complexes were characterized by the elemental analysis (C, H, N), FTIR, <sup>1</sup>H NMR and <sup>13</sup>C NMR, DFT calculations were performed to derive some of their molecular properties. Schiff base ligands coordinated to vanadium center via nitrogen from the azomethine group and one oxygen from the hydroxyl attached to the benzene ring and one oxygen from hydroxyl of carboxyl group. The catalytic activity of the two complexes were tested against cyclooctene and found that both complexes were highly effective and selective in optimized conditions when used as cyclooctene epoxidation catalysts with the conversion percentage of 91.85% (with VOL<sub>1</sub>) and 87.40% (with VOL<sub>2</sub>) at 78 °C within a period of ten hours. To understand the structural properties of the two complexes, the two complexes were well optimized at B3LYP/6-31G(d,p) level of theory, structural parameters such as electron affinity, global electrophilicity, global hardness, electronegativity, ionization potential, and electron chemical potential based on HOMO and LUMO energy values were calculated.

**Keywords:** Schiff base, DFT calculations, epoxidation catalysis, geometry optimizations, oxovanadium complexes, global chemical reactivity.

**Submitted:** October 15, 2021. **Accepted:** December 29, 2021.

**Cite this:** Wady AF, Khalid MAA, Alotaibi MT, Ahmed YS. Synthesis, Characterization, DFT Calculations, and Catalytic Epoxidation of Two Oxovanadium(IV) Schiff Base Complexes. JOTCSA. 2022;9(1):163-208.

**DOI:** <https://doi.org/10.18596/jotcsa.1008578>.

**\*Corresponding author. E-mail:** [m.khalid@tu.edu.sa](mailto:m.khalid@tu.edu.sa) , [mkhalid@uofk.edu](mailto:mkhalid@uofk.edu), Telephone: +966534173719.

### INTRODUCTION

Transition metal complexes synthesized from Schiff bases have shown high potential to be versatile catalysts in organic synthesis and have remarkable developments in recent decades, and engage in some types of chemical transformations such as hydrogenation, hydration (1), decarbonylation (2), olefin metathesis (3), Diels-Alder reaction (4), nitro aldol reaction (5), isomerization (6), cyclopropanation (7), enol-ester synthesis (8),

oxidation of hydrocarbon (9,10), epoxidation (11,12), and other related catalytic process (1). Metal complexes synthesized from Schiff bases have also showed high activity in asymmetric catalysis (13), and those complexes derived from aromatic carbonyl compounds have found to be very active in metalloprotein modeling as well as asymmetric catalysis (14-16). Epoxidation reaction catalysis as a special field has received great attention in last few years and many reports have raised on several methods of synthesis of catalytic complexes from

many Schiff bases along with their catalytic activity evaluation (17-20).

One of the most important petrochemical industrial reactions is conversion of alkenes to alkene epoxides (21), a process that considers as a primary source for many fine chemicals, hence in organic synthesis researchers from over the globe have engaged in such catalytic epoxidation of alkenes and investigation is directed to olefin epoxidation catalysis (22,23), many transition metal complexes of titanium (24), manganese (25), molybdenum (26), and rhenium (27) have been synthesized and their activities were tested in the alkene epoxidation. Remarkably, styrene oxide as industrial precursor has been synthesized in good yield using transition metal catalysts, since then this epoxide has been used in many industries, among them is soap, pharmaceuticals, cosmetic essences, perfumes, and food flavoring agents (28,29). After establishing of many industrial epoxide's synthesis methods, researchers have directed their efforts to understand the catalytic pathways, many reports agreed with the pathways through generation of some transition metal ions as reaction intermediates with higher oxidation states (21), one interesting example is the asymmetric epoxides that synthesized from cis-disubstituted and cis-trisubstituted olefins, in this regard manganese(III) complexes of specific chiral salen are found to be enantioselective with very high yields (30), in some other cases, pathways have been found to pass through synthesis of heterogeneous complexes which were found to be of great advantage over homogeneous catalysts because of their higher stability under wide range of temperatures, and easy products separation (31,32), following this Janssen et al. have synthesized manganese(III) salen dimeric complex (33), which is retained in cross-linked polymer membrane have shown high activity in epoxidation synthesis. Special interests have been forwarded to pharmaceutical and agrochemical fields to use asymmetric epoxidation of alkenes for synthesis of desired drugs through chiral intermediates mechanisms, in this regard Jacobsen-Katsuki Salen (Mn)-catalyzed reaction is widely used for the asymmetric epoxidation of non-functionalized olefins (34,35).

Vanadium complexes have been commonly utilized and widely used in epoxidation catalysis, oxovanadium complexes prepared from Schiff-based ligands are the most useful, for example, oxovanadium (IV) complexes when combined with oxygen or other peroxide were found to be very effective in sulfide and olefin epoxidation (36,37). Mukaiyama aldol additions have been unraveled by the catalytic activity of vanadyl complexes based on 2,2'-biphenol core ligands, hence diastereoselectivity (up to 90/10 (anti/syn)) was achieved, the other worthy mentioned finding is that

revealed by Uang (38), he used  $V(O)(acac)_2$  in the aerobic oxidative coupling of 2-naphthols.

In this paper, we focused on developing a new type of active vanadyl complexes specifically for the epoxidation process by study the synthesis and characterization of two new oxidovanadium (IV) complexes obtained from the reaction of  $VO(acac)_2$  and  $H_2L_1$  (5-chlorosalicylaldehyde-glycine) and  $H_2L_2$  (5-nitrosalicylaldehyde-glycine) ligands (Scheme 1) and to carry out catalytic activity and a detailed DFT investigation of these complexes. The structures of the two complexes are shown in Figure 1.

## EXPERIMENTAL SECTION

### Materials

For synthesis and analysis processes all reagents and solvents were purchased from Merck and were used as received without further purification. Deuterium oxide, 99.9%, was obtained from Aldrich chemical company USA. Cis-cyclooctene, 95%, Substituted salicylaldehyde (5-chloro, 5-nitro), amino acids (glycine), sodium hydroxide, tris(acetylacetonato)vanadium (IV) and  $VO(acac)_2$  were purchased from (Sigma Aldrich). Ethanol, acetonitrile, n-hexane, methanol, p-xylene, acetophenone, and isopropanol were used as solvents for purification, recrystallization, epoxidation, and solution making.

### Instrumentation

Infrared spectra of the ligands and their corresponding catalysts were recorded on FTIR spectrometer 10.5.1, frontier (FTIR)-Perkin Elmer-ZnSe/Diamond-ATR. NMR spectra of the ligands and catalysts were recorded on Bruker AVIII 40,  $^1H$  NMR 500 MHz,  $^{13}C$  NMR 126 MHz, US. For complexes and ligands, elemental analyses were recorded on HEKA tech EURO EA (CHSN). an Agilent GC Model 7890B was used for determining the epoxidation of cyclooctene to cyclooctane epoxide, GC column used as Agilent HP-5 with dimensions 0.25  $\mu m$ , the oven temperature was set at 70  $^{\circ}C$ .

### Synthesis of the ligands ( $H_2L_1$ and $H_2L_2$ )

The preparation of the ligands  $H_2L_1$  and  $H_2L_2$  were carried out by mixing of 1:1 molar ratio solution of nitro-salicylaldehyde or chloro-salicylaldehyde in methanol with a solution of glycine dissolved in methanolic solution under reflux condition for several hours.

The reaction is carried in a 250 mL round-bottomed flask containing 150 mL of absolute ethanol, to the flask's content 10 mmol (1.565 g) of 5-chlorosalicylaldehyde or 10 mmol (1.671 g) 5-nitrosalicylaldehyde, 10 mmol (0.75 g) of glycine, and 10 mmol (0.40 g) of NaOH, the mixture was refluxed with stirring for 5 hrs. After cooling to room

temperature, the mixture was poured into a 100 mL ice-water in a beaker and left overnight in a refrigerator, yellow crystals were precipitated, filtered off, washed with slightly cold water, and dried in an oven (39), and finally recrystallized from ethanol until a pure product was obtained, the synthesized ligand from substituted chloro-salicylaldehyde ( $H_2L_1$ ) is 2- $\{[(E)-(5\text{-chloro-2-hydroxyphenyl})\text{methylidene})\text{amino}\}$  acetic acid and from substituted nitro-salicylaldehyde ( $H_2L_2$ ) is 2- $\{[(E)-(2\text{-hydroxy-5-nitrophenyl})\text{methylidene})\text{amino}\}$  acetic acid.

### $H_2L_1$ [(E)-2-((5-chloro-2-hydroxybenzylidene)amino)acetic acid]

Color: Shiny yellow. Yield: 92%. FT-IR (KBr,  $\nu$ ,  $\text{cm}^{-1}$ ): 3100 (OH) (Ar-OH), 3050 (OH) (Carboxyl-OH), 1910 (C=O) (Carboxyl), 1680 (C=N).  $^1\text{H}$  NMR (500 MHz,  $\text{D}_2\text{O}$ ,  $\delta$ , ppm): 9.90 (s, 1H, COOH), 8.15 (s, 1H, CH=N), 7.37 (s, 1H, C-H ring), 6.59 (d, 2H, CH-CH ring), 3.37 (s, 2H,  $\text{CH}_2\text{COOH}$ ).  $^{13}\text{C}$ NMR (126 MHz,  $\text{CDCl}_3$ ,  $\delta$ , ppm): 118.32 (1C, Ar-CH-Cl), 167.07 (1C, Ar-Cl), 125.30 (1C, Ar-CH-C), 115.93 (1C, Ar-C-CH<sub>2</sub>), 129.79 (1C, Ar-C-O), 124.74 (1C, Ar-CH-CH), 172.66 (1C, C=N), 42.15 (1C,  $\text{CH}_2\text{-N}$ ), 193.30 (1C, COOH). Anal. Calcd. for  $\text{C}_9\text{H}_8\text{ClNO}_3$ : C, 50.55; H, 3.77; N, 6.56. Found: C, 50.30; H, 3.40; N, 6.53.

### $H_2L_2$ [(E)-2-((2-hydroxy-5-nitrobenzylidene)amino)acetic acid]

Color: Faint Yellow. Yield: 86%. FT-IR (KBr,  $\nu$ ,  $\text{cm}^{-1}$ ): 2890 (OH) (Ar-OH), 2605 (OH) (Carboxyl-OH), 1725 (C=O) (Carboxyl), 1650 (C=N).  $^1\text{H}$  NMR (500 MHz,  $\text{D}_2\text{O}$ ,  $\delta$ , ppm): 9.92 (s, 1H, COOH), 8.3 (s, 1H, CH=N), 8.05 (s, 1H, C-H ring), 6.52 (d, 2H, CH-CH ring), 3.45 (s, 2H,  $\text{CH}_2\text{COOH}$ ).  $^{13}\text{C}$ NMR (126 MHz,  $\text{CDCl}_3$ ,  $\delta$ , ppm): 128.53 (1C, Ar-CH-C  $\text{NO}_2$ ), 172.49 (1C, Ar-Cl), 124.00 (1C, Ar-CH-C), 123.25 (1C, Ar-C-CH<sub>2</sub>), 131.18 (1C, Ar-C-O), 135.10 (1C, Ar-CH-CH), 179.68 (1C, C=N), 41.43 (1C,  $\text{CH}_2\text{-N}$ ), 193.57 (1C, COOH). Anal. Calcd. for  $\text{C}_9\text{H}_8\text{N}_2\text{O}_5$ : C, 48.17; H, 3.60; N, 12.50. Found: C, 48.08; H, 3.14; N, 12.30.

### Synthesis of $\text{VOL}_1$ and $\text{VOL}_2$ complexes

Subsequently, after successful preparation of the two ligands, the prepared ligands  $H_2L_1$  or  $H_2L_2$  and  $\text{VO}(\text{acac})_2$  in a molar ratio of 1:1 in methanol were refluxed for 10 hours, then the vanadyl Schiff base complexes were separated.

In a 100 mL round-bottomed flask, 5 mmol of each ligand (1.138 g of  $H_2L_1$  or 1.190 g of  $H_2L_2$ ) were dissolved in 45 mL of methanol and to this solution 5 mmol of  $\text{VO}(\text{acac})_2$  (1.280 g) dissolved in 10 mL of MeOH was added, the content was refluxed with stirring for 4 hours. After reducing the solvent to one-fifth volume, the content was left to cool to room temperature and kept in a refrigerator for seven days, greenish crystals were separated,

filtered off, washed with *n*-hexane, and dried in an oven (39).

### $\text{VOL}_1$

Color: Faint green. Yield: 67%. FT-IR (KBr,  $\nu$ ,  $\text{cm}^{-1}$ ): 940 (V=O), 1740 (C=O), 1620 (C=N).  $^{13}\text{C}$ NMR (126 MHz,  $\text{CDCl}_3$ ,  $\delta$ , ppm): 121.6 (1C, Ar-CH-Cl), 166.1 (1C, Ar-Cl), 134.9 (1C, Ar-CH-C), 122.4 (1C, Ar-C-CH<sub>2</sub>), 164.5 (1C, Ar-C-O), 132.4 (1C, Ar-CH-CH), 174.8 (1C, C=N), 62.1 (1C,  $\text{CH}_2\text{-N}$ ), 204.0 (1C, COO). Anal. Calcd. for  $\text{C}_9\text{H}_6\text{ClNO}_4\text{V}$ : C, 41.01; H, 2.73; N, 4.78. Found: C, 41.09; H, 2.83; N, 4.38.

### $\text{VOL}_2$

Color: Faint greenish blue. Yield: 64 %. FT-IR (KBr,  $\nu$ ,  $\text{cm}^{-1}$ ): 995 (V=O), 1645 (C=O), 1593 (C=N).  $^{13}\text{C}$ NMR (126 MHz,  $\text{CDCl}_3$ ,  $\delta$ , ppm): 121.7 (1C, Ar-CH-C $\text{NO}_2$ ), 137.0 (1C, Ar-C  $\text{NO}_2$ ), 129.8 (1C, Ar-CH-C), 119.7 (1C, Ar-C-CH<sub>2</sub>), 131.4 (1C, Ar-C-O), 135.0 (1C, Ar-CH-CH), 191.29 (1C, C=N), 62.92 (1C,  $\text{CH}_2\text{-N}$ ), 204.1 (1C, COO). Anal. Calcd. for  $\text{C}_9\text{H}_6\text{N}_2\text{O}_6\text{V}$ : C, 39.58; H, 2.63; N, 9.23. Found: C, 39.55; H, 2.82; N, 9.03.

### General procedure of the epoxidation reaction

Batch reactions were conducted in 4 mL of GC-grade acetonitrile as solvent. The reactions were started by the addition of a solution of the catalyst ( $\text{VOL}_1$  or  $\text{VOL}_2$ ) dissolved in acetonitrile to a solution of *cis*-cyclooctene (0.2015 mmol) and  $\text{H}_2\text{O}_2$  (50% (*w*:*v*) in water) (0.403 mmol) according to the stoichiometry of (1 *cis*-cyclooctene:2  $\text{H}_2\text{O}_2$  : 1 catalyst) in acetonitrile to give a total reaction volume of 4 mL. The progress of the reaction was monitored by periodic sampling for GC determination, therefore aliquots of the reaction mixture were withdrawn and added to activated  $\text{MnO}_2$  as a  $\text{H}_2\text{O}_2$  decomposition agent to quench the reactions (39). To remove solid materials, quenched reaction mixture was filtered off over activated neutral alumina oxide, then two GC samples were prepared for each experiment using 200  $\mu\text{L}$  of filtrate, 500  $\mu\text{L}$  of external standard solution (*p*-xylene and acetophenone 4 mg/mL in *i*PrOH) and 800  $\mu\text{L}$  of *n*-hexane. Time-dependent yield experiments were conducted in a total volume of 12 mL using the same stoichiometry and concentrations. Control experiments were performed as a reference without the use of a catalyst.

### Computational method

Electronic structure calculations were performed using the Gaussian 16W software (40) mainly to reveal the vibrational properties and structural characteristics of the ligands and their corresponding complexes. Geometry optimizations for the target complexes  $\text{VOL}_1$  and  $\text{VOL}_2$  were fulfilled using Density Functional Theory (DFT) based on Beck's three parameter exchange functional and Lee-Yang-Parr nonlocal correlation



functional (B3LYP) (41,42) and the 6-31+G(d,p) orbital basis sets for all atoms to describe their molecular properties including their stability and reactivity. Characterization of the located stationary points as minimal or transitional states is carried out by vibrational frequency calculations at the same level of theory. Unrestricted DFT at the B3LYP/6-31+G(d,p) level of theory is used to fully optimize the two complexes with no constraints and extract the geometries in gas phase and some selected solvents, in this regard all calculations were performed in the presence of the selected solvent by placing the molecules in a cavity within the solvent field. The integral equation formalism variant along with the Polarizable Continuum Model (IEFPCM) is used for the calculations (43).

With the help of the ChemCraft program (44) the vibrational modes were examined. To correlate between experimental and calculated frequencies a factor of 0.96 is used to account for the inharmonicity of the calculated frequencies. For both complexes the natural population analysis (NPA) is used for assigning the partial charge distributions. GaussView version 6.0.16 (45) is used to visualize the final optimized structures. Then the relationship between the molecular, the electronic structure, and the stability of the molecules were investigated. Therefore, some molecular descriptors such as the calculation of the highest occupied molecular orbitals (HOMOs) and the lowest unoccupied molecular orbitals (LUMOs), frontier orbital energy gap, molecular dipole moment ( $\mu$ ), electron affinity (EA), ionization potential (IP), electronegativity ( $\chi$ ) that determines the tendency of the electrophile to acquire an additional electronic charge, global hardness ( $\eta$ ), softness ( $\sigma$ ), and electrophilicity index ( $\omega$ ), were calculated using the DFT method along with Koopman's theorem and have been used to understand the properties and activity of the newly prepared complexes, reference 46 accounts for more theoretical equations. Furthermore, VOL<sub>2</sub> as a representative, its optimization is confirmed by a higher basal set using Orca Program Version 4.2.1 (47), and Gamess US Program Version 30 JUN 2019-R1-Patch-1-mkl (48), for both programs, Avogadro software version 1.2.0 (49) is used to draw molecular structures and generate input files, as well as GaussSum version 3.0 (50) which is used for NBO and frontier molecular orbital analysis, finally the catalytic cycle mechanistic aspects are followed with the DFT at the B3LYP/6-31+G(d,p) and UPBEPBE (unrestricted Perdew, Burke, and Enzerhof exchange and correlation functional)/LanL2DZ (Los Alamos National Laboratory Double Zeta) level (51-54).

## RESULTS AND DISCUSSION

In this work, the two isomers of the ligands and their complexes were characterized by spectroscopic techniques (FT-IR, <sup>1</sup>H and <sup>13</sup>C NMR) and theoretical DFT is carried to confirm their molecular structures. The preparation procedure of the ligands H<sub>2</sub>L<sub>1</sub> and H<sub>2</sub>L<sub>2</sub> and their corresponding VOL<sub>1</sub> and VOL<sub>2</sub> complexes was presented in Scheme 1 (detailed method of preparation can be found above). After ligands preparation, the ligands H<sub>2</sub>L<sub>1</sub> or H<sub>2</sub>L<sub>2</sub> and VO(acac)<sub>2</sub> in a molar ratio of 1:1 in methanol were refluxed for 10 hours, then the vanadyl Schiff base complexes were separated.

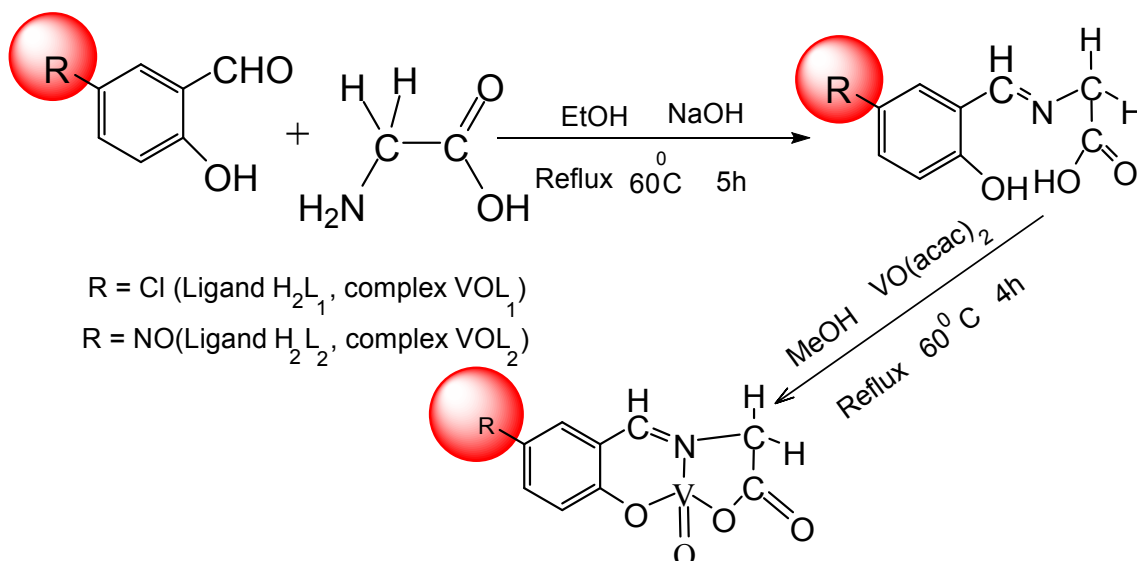
The complexation reaction of metal:ligand was proceeded as 1:1 molar ratio, this pattern was indicated from the analytical data and suggested a coordination through azomethine nitrogen and two oxygen atoms from the deprotonated phenolic groups and the carboxyl group, also the analytical data revealed that four of the V(IV) equatorial coordination sites are bound to the ligand molecule leaving fifth site empty which will be filled later to maintain the epoxidation reaction. Figure 1 shows the optimized structure diagram of complexes VOL<sub>1</sub> and VOL<sub>2</sub>.

### Elemental analysis

The elemental analysis of C, H, and N of the compounds considered are given under each compound experimental data, the results of C, H and N percentages agreed with the structural composition suggested for the ligand and the vanadyl complexes and confirmed a 1:1 (metal: ligand) stoichiometry.

### Infrared spectral studies

The FTIR spectra of the ligands and their complexes were compared to determine any changes during complexation and to confirm their structures. The assignment of infrared bands of the Schiff bases and their vanadyl complexes agreed with the expected values. The ligands (H<sub>2</sub>L<sub>1</sub> and H<sub>2</sub>L<sub>2</sub>) showed a medium broad band in the range of 3000-3080 cm<sup>-1</sup> which attributed to the phenolic and carboxylic OH groups, an intense band at 1680 cm<sup>-1</sup> for H<sub>2</sub>L<sub>1</sub> and 1650 cm<sup>-1</sup> for H<sub>2</sub>L<sub>2</sub> that are due to  $\nu$ (C=N) stretching vibration mode, medium band at 1739 cm<sup>-1</sup> for H<sub>2</sub>L<sub>1</sub> and 1736 cm<sup>-1</sup> for H<sub>2</sub>L<sub>2</sub> are assigned to  $\nu$ (C=O) stretching frequency, and phenolic C-O stretching absorption is seen at 1273 cm<sup>-1</sup> for H<sub>2</sub>L<sub>1</sub> and 1288 cm<sup>-1</sup> for H<sub>2</sub>L<sub>2</sub>.



**Scheme 1:** Preparation pattern of the new tridentate (O, N) Schiff base ligands  $H_2L_1$  and  $H_2L_2$  and its  $VOL_1$  and  $VOL_2$  complexes.

The FTIR spectra of the complexes compared with those of the ligands indicated that the  $\nu(C=N)$  band appeared at  $1620\text{ cm}^{-1}$  for  $VOL_1$  and  $1592\text{ cm}^{-1}$  for  $VOL_2$  complexes which are shifted on complexation indicating complexation through the nitrogen atom of azomethine (55,56), the band showed at  $1300\text{ cm}^{-1}$  for  $VOL_1$  and  $1290\text{ cm}^{-1}$  for  $VOL_2$  attributed to

$\nu(\text{PhC-O})$  stretching, the OH stretching bands found in the ligands' spectra appeared on the region of  $3000\text{-}3080\text{ cm}^{-1}$  are absent in the complexes' spectra, indicative of complexation of vanadium by OH group of phenolato and carboxyl after deprotonation.

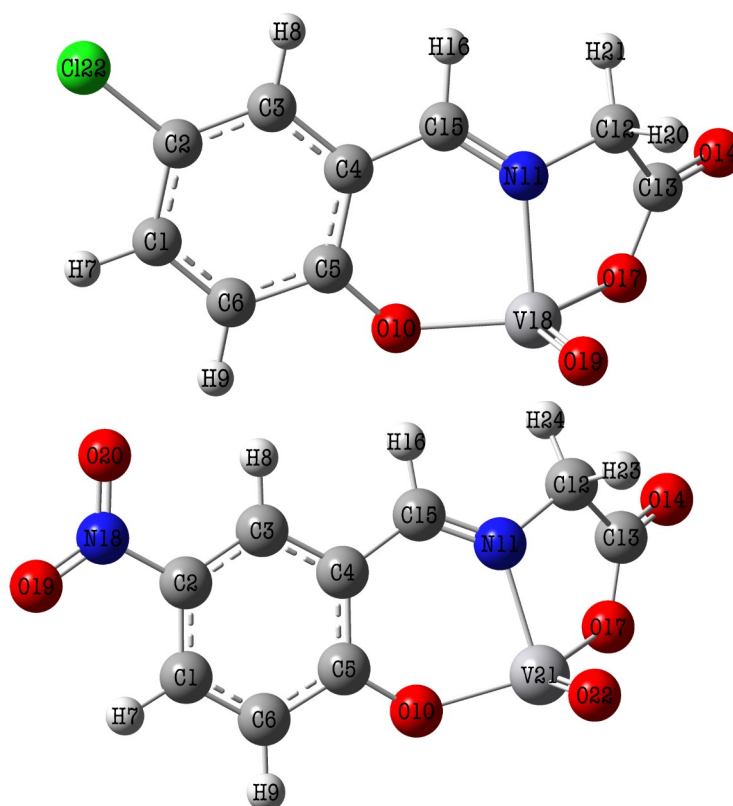


**Figure 1:** The optimized structure and atom numbering scheme for complex  $VOL_1$  (top) and  $VOL_2$  (bottom), structure optimization is carried out using B3LYP/6-31+G(d,p) level of theory.

The  $\nu(\text{C}=\text{O})$  stretching absorptions emerged at the region (1740 and 1730  $\text{cm}^{-1}$  for complexes  $\text{VOL}_1$  and  $\text{VOL}_2$  respectively). Conclusive evidence of bonding is also shown by the observation of new bands in the spectra of the complexes appearing at (870 and 840  $\text{cm}^{-1}$  for complex  $\text{VOL}_1$ ) and (840 and 800  $\text{cm}^{-1}$  for complex  $\text{VOL}_2$ ) where these are assigned to  $\nu(\text{V}-\text{O}-\text{carboxyl})$  and  $\nu(\text{V}-\text{O}-\text{phenol})$  stretching respectively, these two bands are not observed in the ligand's spectrum. Oxovanadium complexes generally showed  $\nu(\text{V}=\text{O})$  of polynuclear linear chain structures ( $\text{V}=\text{O}\cdots\text{V}=\text{O}\cdots$ ) at around 860  $\text{cm}^{-1}$  with orange color, and monomeric structure at around 950  $\text{cm}^{-1}$  with a green color in the solid state and solution (57,58). Sharp FTIR bands at 941  $\text{cm}^{-1}$  and 937  $\text{cm}^{-1}$  for complexes  $\text{VOL}_1$  and  $\text{VOL}_2$  respectively are noticed and attributed to the monomeric form of VOL complexes in the solid state (59). Vergopoulos et.al (60) used crystallographic means to establish similar monomeric nature of related complexes. Beside that the  $\pi$ -bond located in the  $\text{C}=\text{C}$  benzene ring of the ligand does not show a significant shift of the stretching mode that noticed around 1600  $\text{cm}^{-1}$  upon complexation. Hence the FTIR data indicated a pattern of complexation through the azomethine nitrogen, phenolic and carboxylic oxygens, similar structure of vanadium complex is suggested by Jamaluddin et. al. (61), for more details please refer to Figures S-1 to S-6 in the appendices.

### NMR spectra

The  $^1\text{H}$  NMR and  $^{13}\text{C}$  NMR spectra of Schiff bases ligands  $\text{H}_2\text{L}_1$  and  $\text{H}_2\text{L}_2$  and their complexes  $\text{VOL}_1$  and  $\text{VOL}_2$  have been studied using  $\text{D}_2\text{O}$  as a solvent. All expected region of protons calculated from the integration curves and those obtained from the values of the expected (CHN) analysis agreed with each other. In the  $^1\text{H}$  NMR spectral data of the two ligands as shown in Table 1, both ligands show a broad signal at 9.90 ppm (13.00-DFT) ( $\text{H}_2\text{L}_1$ ) and 9.92 ppm (13.00-DFT) ( $\text{H}_2\text{L}_2$ ) due to the carboxylic OH resonance.

The absence of this signal in the complexes (as the whole NMR spectrum of the complexes are not found due to the paramagnetic nature of the vanadium (IV)), suggested that this is in conformity with the coordination of the phenolate oxygen to the vanadium center. Phenolic proton does not usually appear in proton NMR because they are rapidly exchanged with  $\text{D}_2\text{O}$  and or (in this case) hid due to the chloro group's orientation in benzene ring.

The proton observed as a signal at around 8.15 ppm (8.70-DFT) ( $\text{H}_2\text{L}_1$ ) and 8.30 ppm (8.74-DFT) ( $\text{H}_2\text{L}_2$ ) corresponding to azomethine proton resonance ( $\text{CH}=\text{N}$ ), which have been showed a slight calculated downfield shift ( $\Delta\delta$ -DFT 0.02-0.12 ppm) of the proton signal in the ligands with respect to the corresponding complexes suggested the

coordination of the azomethine nitrogen atom to the vanadium center.

Aromatic and  $\text{CH}_2$  protons of the ligands, as well as in the complexes, appeared well within their expected ranges. The  $^1\text{H}$  NMR of oxovanadium (IV) complexes  $\text{VOL}_1$  and  $\text{VOL}_2$  were recorded in  $\text{DMSO}-d_6$  at 500 and 126 MHz. In all cases, no signal was observed. This is due to the paramagnetic nature of the vanadium (IV) center.

It has been found from  $^{13}\text{C}$  analysis, Table 1, that large  $\Delta\delta$  ( $=\delta$ -complex- $\delta$ -ligand) values (not shown in the Table) for the carbon atoms attached to the phenolic oxygen ( $\text{C}_5$ ), azomethine nitrogen ( $\text{C}_{16}$  in case of  $\text{H}_2\text{L}_1$  and  $\text{C}_{15}$  in case of  $\text{H}_2\text{L}_2$  and both complexes), and carboxylic carbon atom ( $\text{C}_{14}$  in case of  $\text{H}_2\text{L}_1$  and  $\text{C}_{13}$  in case of  $\text{H}_2\text{L}_2$  and both complexes) suggest coordination of these atoms to the vanadium center (62).

DFT calculations is also carried out with the  $^{17}\text{O}$  NMR, which revealed that a large downfield shift occurred for phenolic oxygen, giving rise for  $\Delta\delta$  values to be 153.6, and for carboxylic OH oxygen to be 144.5, also  $^{15}\text{N}$  NMR of azomethine nitrogen reveals upfield shift, and giving rise for  $\Delta\delta$  to be 31.0. All these findings suggest the coordination of these atoms. Good correlation between the calculated and experimental  $^1\text{H}$  and  $^{13}\text{C}$  chemical shifts in  $\text{D}_2\text{O}$ , and  $\text{DMSO}-d_6$  results is confirmed in Figure S-7 in the appendices with good correlation factor  $R^2$  ranged from 0.80-0.98 values, for more details please refer to Figures S-8 to S-15 in the appendices.

### UV-Vis spectral analysis

TD-DFT calculations were carried out to obtain information on the nature of the excited state, UV-Vis absorption spectra of  $\text{VOL}_1$  and  $\text{VOL}_2$  in gas phase and some selected polar and nonpolar solvents were simulated by using Time-Dependent density functional theory (TD-DFT) and the polarizable continuum model (PCM) method with the unrestricted 6-31+G(d,p) basis set. The electric charges were obtained using natural bond orbital (NBO) calculations.

Due to the presence of many  $n$  electrons allocated in the aromatic ring and many nonbonding electrons allocated in oxygen and nitrogen atoms in the two complexes  $\text{VOL}_1$  and  $\text{VOL}_2$ , the  $n \rightarrow \pi^*$  and  $n \rightarrow \pi^*$  electronic transitions are the main contributors to UV-Vis absorption. These electronic transitions emerge from electron motions between the frontier molecular orbitals (FMOs), which are the higher occupied molecular orbitals (HOMOs) and the lower unoccupied molecular orbitals (LUMOs). PCM/TD-B3LYP/6-31+G(d,p) method is used to calculate the theoretical UV-Visible electronic transitions in some solvents, results are shown in Figures 2 and 3. The

absorption wavelengths maxima are obtained by applying the above method of theory from single point calculations on the ground state, optimized geometries in gas phase and selected solvents (vertical transitions). One interesting observation that can be derived from Figures 2 and 3 (internal graphs) is that the slight but continuous change in excitation wavelength with the change in solvent polarity, in the case of VOL<sub>1</sub> the excitation wavelength (excitation energy) is decreased with increasing solvent polarity, while in the case of VOL<sub>2</sub> the excitation wavelengths is decreased with decreasing solvent polarity.

This contradictory effect is observed due to the difference in electronic density around the molecule which in turn comes from the difference in the functional group presence in the benzene ring, the chloro group in VOL<sub>1</sub> is classified as a donor group,

hence increasing electron density in the whole molecule specially around vanadium center, and more energy needed to excite the vanadium individual electron upon increasing solvent polarity, inversely nitro group in VOL<sub>2</sub> is classified as withdrawing group, hence the electron density from the whole molecule is withdrawn, and the electron density around vanadium center is became less intense and electron is excited easily, this lead to notice that the excited state in both complexes is affected by solvent polarity, and indicates that beside  $\pi \rightarrow \pi^*$  and  $n \rightarrow \pi^*$  electronic transitions the excited state has a dominant ligand to metal charge transfer character (LMCT).

### Geometry optimization

The structures of VOL<sub>1</sub> and VOL<sub>2</sub> were optimized using DFT at the unrestricted B3LYP/6-31+G(d,p) level of theory.

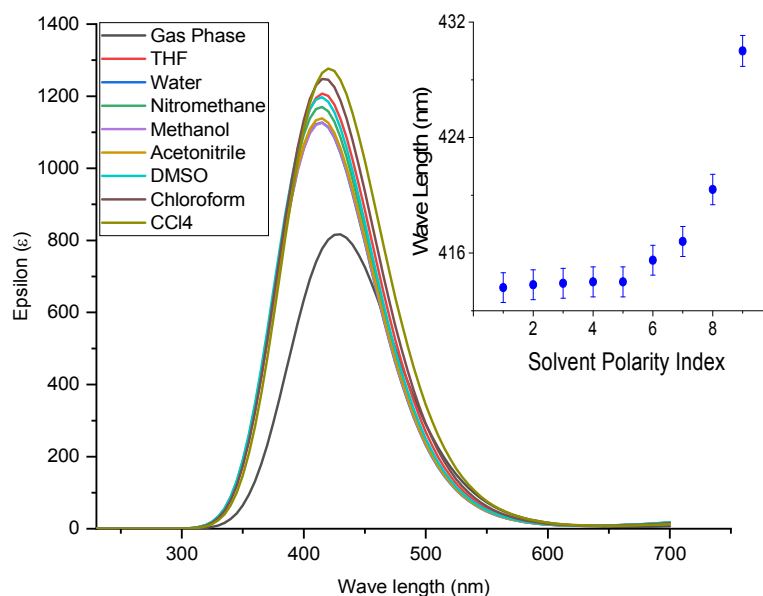


**Figure 2:** VOL<sub>1</sub> complex absorbance wavelengths for solvents: Gas phase = 430.0 nm, THF = 415.5 nm, Water = 413.6 nm, Nitromethane = 414.0 nm, Methanol = 413.9 nm, Acetonitrile = 413.9 nm, DMSO = 414.0 nm, Chloroform = 416.8 nm, CCl<sub>4</sub> = 420.4 nm, calculated UV-Vis is simulated by using the Time-Dependent density functional theory (TD-DFT) and the polarizable continuum model (PCM) method with the unrestricted B3LYP/6-31+G(d,p) level of theory.

**Table 1:** Comparison of the calculated chemical shifts (GIAO B3LYP/6-31+G(d,p)) with experimental ones in D<sub>2</sub>O.

<b>Comp.</b>	<b>Atom numbering and NMR values</b>									
<b>H<sub>2</sub>L<sub>1</sub></b>		<b>H-7</b>	<b>H-8</b>	<b>H-9</b>	<b>H-17</b>	<b>H-19</b>	<b>H-21</b>	<b>H-22</b>		
	<b>Exp.</b>	7.40	7.25	6.70	8.15	3.35	9.90	3.35		
	<b>DFT-1</b>	7.77	7.71	7.40	8.70	5.00	13.00	4.43		
		<b>C-1</b>	<b>C-2</b>	<b>C-3</b>	<b>C-4</b>	<b>C-5</b>	<b>C-6</b>	<b>C-13</b>	<b>C-14</b>	<b>C-16</b>
	<b>Exp.</b>	129.79	124.74	125.30	118.32	167.07	115.93	42.15	193.30	172.66
	<b>DFT-1</b>	119.80	118.70	119.50	107.60	147.20	105.40	53.45	158.30	155.40
<b>H<sub>2</sub>L<sub>2</sub></b>		<b>H-7</b>	<b>H-8</b>	<b>H-9</b>	<b>H-16</b>	<b>H-18</b>	<b>H-20</b>	<b>H-21</b>		
	<b>Exp.</b>	8.30	7.90	6.55	8.30	3.40	9.92	3.40		
	<b>DFT-1</b>	8.70	8.73	7.34	8.74	5.13	13.92	4.18		
		<b>C-1</b>	<b>C-2</b>	<b>C-3</b>	<b>C-4</b>	<b>C-5</b>	<b>C-6</b>	<b>C-12</b>	<b>C-13</b>	<b>C-15</b>
	<b>Exp.</b>	131.18	135.10	124.00	128.53	172.49	123.25	41.43	193.57	172.49
	<b>DFT-1</b>	115.80	128.70	117.60	105.90	153.2	104.60	52.31	155.3	152.00
<b>VOL<sub>1</sub></b>		<b>H-7</b>	<b>H-8</b>	<b>H-9</b>	<b>H-16</b>	<b>H-20</b>	<b>H-21</b>			
	<b>DFT-1</b>	7.91	7.86	7.21	8.72	5.16	4.69			
	<b>DFT-2</b>	7.91	7.85	7.21	8.70	5.16	4.68			
	<b>DFT-3</b>	7.91	7.85	7.21	8.71	5.16	4.69			
		<b>C-1</b>	<b>C-2</b>	<b>C-3</b>	<b>C-4</b>	<b>C-5</b>	<b>C-6</b>	<b>C-12</b>	<b>C-13</b>	<b>C-15</b>
	<b>Exp.</b>	164.50	132.40	134.90	121.60	166.10	122.40	62.10	204.00	174.80
	<b>DFT-1</b>	124.86	119.85	122.43	111.01	152.19	106.63	58.25	161.38	156.57
	<b>DFT-2</b>	124.87	119.90	122.36	110.98	152.18	106.67	58.26	161.16	156.46
	<b>DFT-3</b>	124.87	119.88	122.39	111.00	152.18	106.65	58.25	161.27	156.51
	<b>VOL<sub>2</sub></b>		<b>H-7</b>	<b>H-8</b>	<b>H-9</b>	<b>H-16</b>	<b>H-23</b>	<b>H-24</b>		
<b>DFT-1</b>		8.92	9.09	7.26	8.87	5.22	4.77			
<b>DFT-2</b>		8.92	9.08	7.26	8.86	5.21	4.76			
<b>DFT-3</b>		8.92	9.08	7.26	8.87	5.22	4.76			
		<b>C-1</b>	<b>C-2</b>	<b>C-3</b>	<b>C-4</b>	<b>C-5</b>	<b>C-6</b>	<b>C-12</b>	<b>C-13</b>	<b>C-15</b>
<b>Exp.</b>		131.40	135.00	129.80	121.70	137.00	119.70	62.92	204.10	191.29
<b>DFT-1</b>		119.68	130.42	121.36	110.78	158.04	107.44	58.56	160.70	153.03
<b>DFT-2</b>		119.71	130.40	121.27	110.73	157.99	107.45	58.57	160.48	153.93
<b>DFT-3</b>		119.70	130.41	121.31	110.76	158.01	107.45	58.57	160.59	153.98

Solvents: (DFT-1 = D<sub>2</sub>O, DFT-2 = Ethanol, DFT-3 = Nitromethane). For atom labeling, see structure diagram Figure 1.

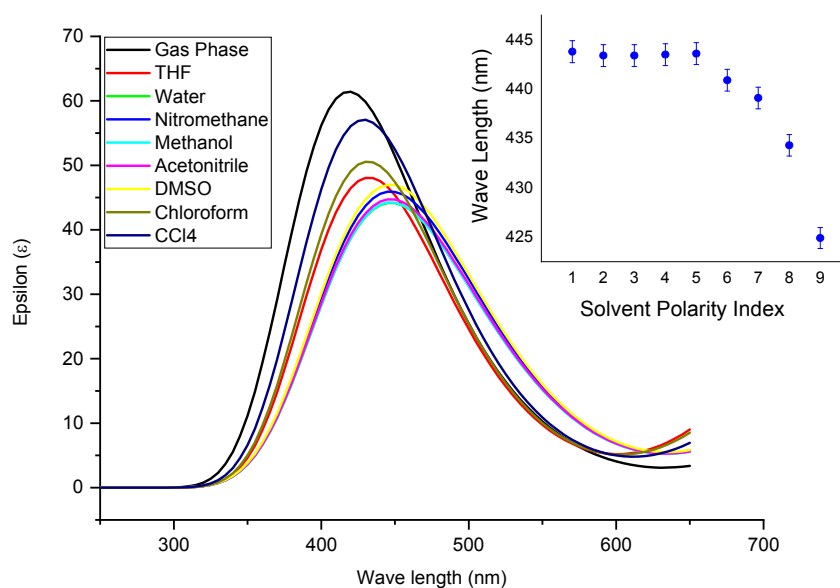


**Figure 3:** VOL<sub>2</sub> complex absorbance wavelengths for solvents: Gas phase = 424.9 nm, THF = 440.9 nm, Water = 443.8 nm, Nitromethane = 443.5 nm, Methanol = 443.4 nm, Acetonitrile = 443.4 nm, DMSO = 443.6 nm, Chloroform = 439.1 nm, CCl<sub>4</sub> = 449.7 nm, calculated UV-Vis is simulated by using the Time-Dependent density functional theory (TD-DFT) and the polarizable continuum model (PCM) method with the unrestricted B3LYP/6-31+G(d,p) level of theory.

**Table 2:** Selected bond distances (Å) and angles (°) for VOL<sub>2</sub> optimized complex using three different calculation methods.

Characters	G16W DFT B3LYP/6- 31+G(d,p)	Orca M06L def2- TZVP def2- TZVP/C	Gamess- US UHF- M06 -SPK- DZP	Experimental	Reference
<i>Optimized bonds (Å)</i>					
V <sub>21</sub> -O <sub>22</sub>	1.5610	1.5827	1.567	1.581 1.599	(63) (64)
V <sub>21</sub> -O <sub>10</sub>	1.8837	1.9147	1.886	1.869	(63)
V <sub>21</sub> -O <sub>17</sub>	1.8900	1.9070	1.893	1.891	(63)
V <sub>21</sub> -N <sub>11</sub>	2.0175	2.0071	2.006	2.076	(63)
O <sub>10</sub> -C <sub>5</sub>	1.3100	1.3046	1.306	1.355	(64)
O <sub>17</sub> -C <sub>13</sub>	1.3237	1.3260	1.327		
<i>Optimized angles (°)</i>					
O <sub>22</sub> -V <sub>21</sub> -O <sub>17</sub>	115.6	118.9	115.6		
O <sub>22</sub> -V <sub>21</sub> -O <sub>10</sub>	115.7	120.5	115.6		
O <sub>22</sub> -V <sub>21</sub> -N <sub>11</sub>	106.8	107.1	106.0		
V <sub>21</sub> -O <sub>10</sub> -C <sub>5</sub>	130.8	129.7	128.5		
V <sub>21</sub> -O <sub>17</sub> -C <sub>13</sub>	120.0	119.6	119.7		
V <sub>21</sub> -N <sub>11</sub> -C <sub>12</sub>	109.9	110.0	110.1		
V <sub>21</sub> -N <sub>11</sub> -C <sub>15</sub>	126.4	125.8	125.9	121.7	(64)
<i>Elect. Energy (Hartree)</i>	-1851.44	-1860.59	-1850.93		

The HF energies were found to be -2106.52 and -1851.44 Hartree, respectively. To confirm the optimized structures, VOL<sub>2</sub> is further optimized with two more different methods, first the structure were inserted in Avogadro software and input files were generated, one input file is called by Orca Program

Version 4.2.1 and M06L def2-TZVP def2-TZVP/C bases set is applied which took 127 hrs. to converge, the other input file is called by Gamess US Program Version 2019-R1-Patch-1-mkl, and UHF M06 SPK-DZP bases set is applied which took 168 hrs. to converge. The bond lengths and angles are

listed in Table 2. The bond distances in optimized structures are shown in Figure 1. Generally, there are no significant differences in the angles and bond distances between the three optimized structures, and this in agreement with some bond distances found in literature for some known bond distances, for example, (V=O).

### Frontier Molecular Orbitals (FMO)

To get some insights in to the chemical stability of a molecule and in the interactions between atoms, frontier molecular orbitals (FMOs) are performed. FMOs effectively can determines some interesting characteristics of the molecules, including optical properties and biological activities, and mostly can be used in the HOMO (highest occupied molecular orbital) and the LUMO (lowest unoccupied molecular orbital) determination. Determining the HOMO and LUMO can, in turn, represents what parts on the molecule that can play as the donor or acceptor.

Figures S-16 and S-17 (in the appendices) show the electron density in HOMO and LUMO molecular orbitals for VOL<sub>1</sub> and VOL<sub>2</sub> complexes, respectively. The HOMO and LUMO orbitals were found to be

delocalized over the complex molecule. The high electron density is concentrated on nitrogen atoms in HOMO and reduced in LUMO suggesting a transition pattern of  $n \rightarrow \pi^*$ . In LUMO of the two complexes, part of the electron density was found to be localized on the benzene rings. The TD-DFT calculations indicate that the absorption spectra of complex VOL<sub>1</sub> have three dominant bands at 404.5 nm, 423.5 nm, and 430.0 nm, and for complex VOL<sub>2</sub> there are four dominant absorption bands at 400.7 nm, 424.9 nm, 457.6 nm, and 498.3 nm in the region studied theoretically, more details can be found in Tables 4 and 5.

The essential band for VOL<sub>1</sub> complex is 430 nm ( $R_{rel} = 14.15$ ) corresponding to  $\alpha$ -spin HOMO( $\alpha$ ) to LUMO( $\alpha$ ) transition (34% and  $\Delta E = 0.98$  eV) and H-1( $\alpha$ ) to L+4( $\alpha$ ) transition (13% and  $\Delta E = 0.37$  eV), together with a  $\beta$ -spin HOMO( $\beta$ ) to LUMO( $\beta$ ) transition (41% and  $\Delta E = 1.18$  eV), while the essential band for complex VOL<sub>2</sub> is 424.9 nm ( $R_{rel} = 10.71$ ) corresponds to  $\alpha$ -spin HOMO( $\alpha$ ) to L+4( $\alpha$ ) transition (48% and  $\Delta E = 1.40$  eV) and HOMO( $\alpha$ ) to L+5( $\alpha$ ) transition (17% and  $\Delta E = 0.50$  eV).

**Table 3:** The calculated vertical excitation energies (eV), wavelengths (nm), oscillatory strength, and main orbital contributions to the excited states (only contributions >10% are given) for the VOL<sub>1</sub> complex calculated with TD-DFT/6-31+G(d,p) method in the gas phase.

Energy (eV)	Wavelength (nm)	Oscillatory strength	Major orbital contribution
2.40	517.3	0.0001	HOMO( $\alpha$ ) $\rightarrow$ LUMO( $\alpha$ ) (53%), HOMO( $\beta$ ) $\rightarrow$ LUMO( $\beta$ ) (38%)
2.49	498.0	0.0002	H-1( $\alpha$ ) $\rightarrow$ L+2( $\alpha$ ) (56%), H-1( $\alpha$ ) $\rightarrow$ L+3( $\alpha$ ) (16%)
2.89	430.0	0.0161	HOMO( $\alpha$ ) $\rightarrow$ LUMO( $\alpha$ ) (34%), HOMO( $\beta$ ) $\rightarrow$ LUMO( $\beta$ ) (41%), H-1( $\alpha$ ) $\rightarrow$ L+4( $\alpha$ ) (13%)
2.93	423.5	0.0032	H-1( $\alpha$ ) $\rightarrow$ L+4( $\alpha$ ) (53%)
3.07	404.5	0.001	H-2( $\alpha$ ) $\rightarrow$ LUMO( $\alpha$ ) (18%), H-3( $\alpha$ ) $\rightarrow$ LUMO( $\alpha$ ) (11%), H-1( $\beta$ ) $\rightarrow$ LUMO( $\beta$ ) (17%), H-2( $\beta$ ) $\rightarrow$ LUMO( $\beta$ ) (13%)

When investigating the electronic density distribution in the orbitals involved in these transitions Figures S-16 and S-17 (in the appendices) for VOL<sub>1</sub> and VOL<sub>2</sub> complexes respectively, both indicated that these excitations have dominant ligand to metal charge transfer characters (LMCT), this is supported by the observation held in the inner graphs Figures 2 and 3 which involves the change in the excitation wavelengths with change in solvent polarity, and accordingly both excited states are sensitive to any change in the surrounding environment that involve charging species or polar solvents. Simulated spectrum for complex VOL<sub>1</sub> Figure S-16 (in the appendices) holds other electronic transitions, the band at 423.5 nm involves the contribution from H-

1( $\alpha$ ) to L+4( $\alpha$ ) (53% and  $\Delta E = 1.55$  eV) and is seen as ligand-based transitions with a dominant  $n \rightarrow \pi^*$  character. The band at 404.5 nm includes more transitions, which involves contributions from H-2( $\alpha$ ) (18% and  $\Delta E = 0.55$  eV), and H-3( $\alpha$ ) (11% and  $\Delta E = 0.34$  eV) to LUMO( $\alpha$ ), and H-1( $\beta$ ) (17% and  $\Delta E = 0.52$  eV), and H-2( $\beta$ ) (13% and  $\Delta E = 0.40$  eV) to LUMO( $\beta$ ), and are ligand-based transitions with dominant  $n \rightarrow \pi^*$ , and to less extent transition from  $n \rightarrow \pi^*$  and  $n$ (nitrogen)  $\rightarrow$   $d$ (one of vanadium  $d$  orbital) characters, the effect of chlorine atom on the electron density of excited state is significantly observed in the transition at 430 nm which involve HOMO( $\alpha$ ) to LUMO( $\alpha$ ), HOMO( $\beta$ ) to LUMO( $\beta$ ) and H-1( $\alpha$ ) to L+4( $\alpha$ ).



**Table 4:** The calculated vertical excitation energies (eV), wavelengths (nm), oscillatory strength, and main orbital contributions to the excited states (only contributions >10% are given) for the VOL<sub>2</sub> complex calculated with TD-DFT/6-31+G(d,p) method in the gas phase.

Energy (eV)	Wavelength (nm)	Oscillatory strength	Major orbital contribution
2.49	498.3	0.0002	HOMO(a) → L+3(a) (55%)
2.71	457.6	0.0002	H-1(a) → LUMO(a) (38%), HOMO(β) → LUMO(β) (33%)
2.89	430.1	0.000045	H-7(a) → L+1(a) (42%), H-6(β) → L+1(β) (40%)
2.92	424.9	0.0006	HOMO(a) → L+4(a) (48%), HOMO(a) → L+5(a) (17%)
3.10	400.7	0.0008	H-1(a) → LUMO(a) (17%), H-1(a) → L+1(a) (25%), HOMO(β) → L+1(β) (24%)

Ligand to metal charge transfer character (LMCT) can be observed in the simulated spectrum for complex VOL<sub>2</sub>, Figure S-17 (in the appendices) at 498.3 nm band, which involves the transition HOMO(a) to L+3(a) (55% and  $\Delta E = 1.37$  eV), beside that the band at 400.7 nm involves the transitions H-1(a) to LUMO(a) (17% and  $\Delta E = 0.53$  eV), H-1(a) to L+1(a) (25% and  $\Delta E = 0.78$  eV), and HOMO(β) to L+1(β) (24% and  $\Delta E = 0.74$  eV) and is ligand based transitions with dominant  $n \rightarrow \pi^*$ , the band at 457.6 nm involves contributions from H-1(a) to LUMO(a) (38% and  $\Delta E = 1.03$  eV) and HOMO(β) to LUMO(β) (33% and  $\Delta E = 0.89$  eV), and is seen as ligand based transitions with dominant  $n \rightarrow \pi^*$ , and to less extent transition from  $n \rightarrow \pi^*$ , also the effect of nitro group on the electron density of excited state is significantly observed in the transition at 424.9 nm which involves transition from HOMO(a) to L+5(a).

#### Molecular electrostatic potential surface

To investigate the molecular structure of both oxovanadium complexes more deeply, molecular electrostatic potential surface (MEP) calculations were performed using the results from TD-DFT calculations. MEP calculation is performed to illustrate the distribution of charges (positive, negative, and neutral) regions in the complex and that help in understanding the interactions between the molecules, also to determine the nature of the chemical bond (65). For both complex molecules

VOL<sub>1</sub> and VOL<sub>2</sub> the MEP surface of as calculated on the ground state optimized geometry in the gas phase at B3LYP/6-31+G(d,p) level of theory are presented in Figure 4. The MEP maps revealed according to color code values between -0.122 (deepest red) to +0.122 a.u. (deepest blue) for VOL<sub>1</sub> complex, and from -0.135 (deepest red) to +0.135 a.u. (deepest blue) for VOL<sub>2</sub> complex. Different colors are used to represent different values of the electrostatic potential at the complex molecule surface, and the potential decreases in the order blue < green < yellow < orange < red. Analysis of the MEP map suggests that in VOL<sub>1</sub> complex, the negative region (yellow coded region) is localized around carboxylate oxygen, and the positive region (bluish coded region) is localized around the vanadium atom, for VOL<sub>2</sub> complex the negative region is localized around carboxylate oxygens and nitro group oxygen, and the positive region is localized around the vanadium center, and finally the greater regions of faint-blue color in both complexes represent intermediary potential. Since the green color is towards the increasing range of potential (towards the blue color), the complexes possess smaller electronegativity, with electron-deficient regions preferring an approach by nucleophiles (65). The MEP maps are in accordance with the calculated atomic charges of both complex molecules and indicated that an asymmetrical charge distribution in the complexes may have implications on their physicochemical properties.

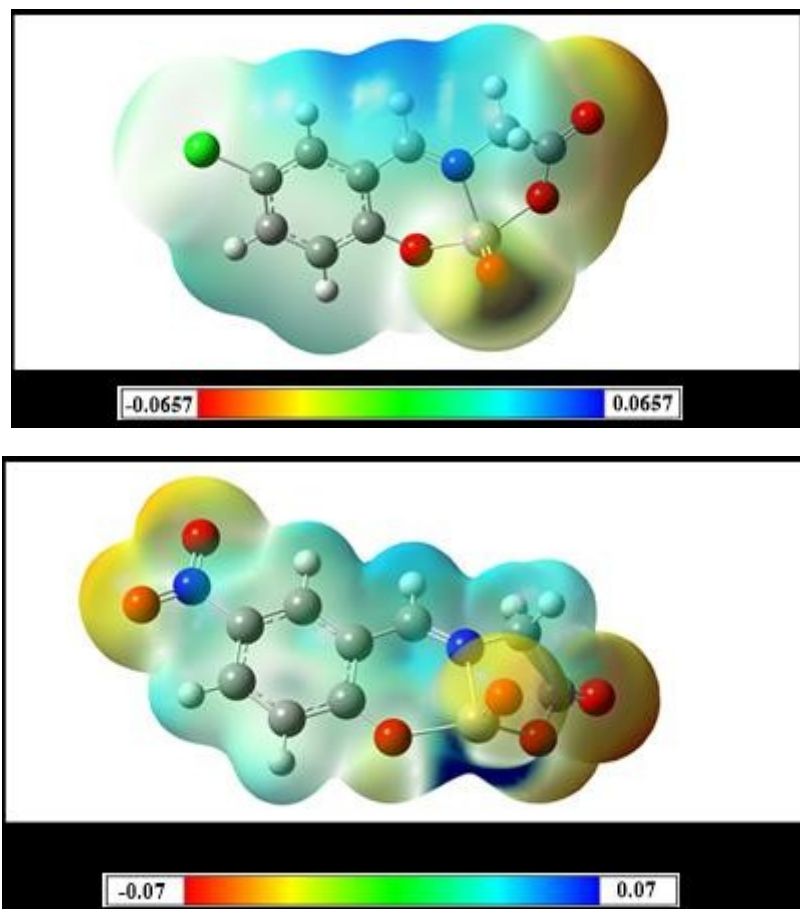


**Figure 4:** Molecular electrostatic potential (MEP) map for the ground state optimized geometry of VOL<sub>1</sub> (upper panel) and VOL<sub>2</sub> (lower panel) complexes calculated at gas phase using B3LYP/6-31+G(d,p) level of theory.

### Global chemical reactivity

Density functional theory (DFT) (66) in this type of calculation is to provide theoretical insights into the chemical reactivity and selectivity of the two complexes, this includes the electronegativity ( $\chi$ ), hardness ( $\eta$ ), softness ( $S$ ), electrophilicity index ( $\omega$ ). The first who made links between chemical reactivity and density functional theory is Parr *et al.* (67), in this regards the chemical potential (DFT) links the first derivative of the energy with respect to the  $n$  number of electrons, and therefore with the negative of the electronegativity  $\chi$ . Via the application of Koopmans' theorem (68), the ionization potential ( $I$ ) is defined as the amount of energy required to remove an electron from a molecule. Electron affinity ( $A$ ) is defined as the energy released when a proton is added to a system. It is related to the energy of the  $E_{\text{HOMO}}$  and  $E_{\text{LUMO}}$  through the equation of:

$$I = -E_{\text{HOMO}} \quad (\text{Eq. 1})$$

$$A = -E_{\text{LUMO}} \quad (\text{Eq. 2})$$

By knowing the values of  $A$  and  $I$ , values of global hardness ( $\eta$ ) and electronegativity  $\chi$  can be determined. The electronegativity is defined as the measure of the power of an atom or a group of atoms to attract electrons towards itself, Hardness ( $\eta$ ) (69) can be defined within the DFT as the second derivative of the  $E$  with respect to  $N$  as the  $v(r)$  property which measures both the stability and reactivity. It can be estimated by using the equation:

$$\chi = \frac{1}{2}(I + A) \quad (\text{Eq. 3})$$

$$\eta = \frac{1}{2}(I - A) \quad (\text{Eq. 4})$$

Chemical softness ( $S$ ) is the measure of the capacity of an atom or a group of atoms to receive electrons, it is estimated by using the equation:

$$S = \frac{1}{\eta} \quad (\text{Eq. 5})$$

$$\omega = \frac{\mu^2}{2\eta} \quad (\text{Eq. 6})$$

It is further anticipated that electrophilicity index as a measure of energy lowering due to maximal electron flow between donor and acceptor (70). They defined the electrophilicity index ( $\omega$ ) as follows.

According to the definition, this index measures the propensity of chemical species to accept electrons. A good reactive nucleophile is characterized by a lower value of  $\mu$ ,  $\omega$ ; and conversely, a good electrophile is characterized by a high value of  $\mu$ ,  $\omega$ . All the global quantities of SLG were calculated.

**Table 5:** Quantum chemical parameters for VOL<sub>1</sub> and VOL<sub>2</sub> complexes obtained with the DFT at B3LYP/6-31+G(d,p) method in gas phase.

Quantum chemical parameters	VOL <sub>1</sub>	VOL <sub>2</sub>
E <sub>LUMO</sub> (eV)	-3.396	-3.710
E <sub>HOMO</sub> (eV)	-6.934	-7.453
ΔE (eV)	3.538	3.743
Ionization Potential, IP (eV)	6.934	7.453
Electron Affinity, EA (eV)	3.396	3.710
Electronegativity, $\chi$ (eV)	5.165	5.582
Global Hardness, $\eta$ (eV)	1.769	1.872
Molecular Dipole Moment, $\mu$ (debye)	5.157	1.215
Global Softness, $\sigma$ (eV) <sup>-1</sup>	0.565	0.534
Electrophilicity Index, $\omega$ (eV)	13.297	0.738
Electronic Energy (Hartree)	-2106.52	-1851.44

It has been common that the molecule with high energy gap is the one with higher hardness, from the data showed in Table 5 that VOL<sub>2</sub> complex is the one with the high energy gap, higher global hardness, and less global softness than the values of VOL<sub>1</sub> complex.

#### Application in epoxidation catalysis

Epoxidation reactions were investigated under optimized conditions using VOL<sub>1</sub> or VOL<sub>2</sub> complexes as catalysts, cis-cyclooctene as substrate, and H<sub>2</sub>O<sub>2</sub> as oxidant. The time course of the epoxidation reaction have been followed for at least ten hours at a specific temperature, Figure 5 shows the increasing of converted amount of cyclooctene in mmol at three different temperatures, at low temperature (20 °C) VOL<sub>2</sub> gives a higher conversion percent, while at high temperature (78 °C) VOL<sub>1</sub> is better and gives a higher conversion, this is confirmed by study of the total conversion at different temperatures as it can be shown in Table 6, the highest conversion is observed at 60 and 78 °C. Blank reactions show that no significant amounts of epoxide are formed in the absence of catalysts.

In the case of using VOL<sub>1</sub>, the conversion percent at 78 °C reached a maximum of 68% after the first two hours, when the reaction time was increased to ten hours the conversion was a little changed and finally reached 91.85%, in the case of using VOL<sub>2</sub> it took four hours to reach a maximum of 71.27% and then increasing by 16.13% to reach 87.40% after another six hours.

Making a comparison between withdrawing and donating substituted groups allocated in the benzene ring toward enhancing catalytic efficacy of the two complexes, VOL<sub>1</sub> is designated with a donating chloro substituted group at C<sub>2</sub> and VOL<sub>2</sub> with a nitro withdrawing group at C<sub>2</sub>, for atom numbering see structure diagram Figure 1, the conversion of cyclooctene in the presence of catalyst VOL<sub>1</sub> (91.85% at 78°C) is higher than that of VOL<sub>2</sub> (88.42% at 78°C), it seems from this finding that the catalytic efficacy is increased with increasing the whole molecule electron density, this is agreed with the finding of *Vergopoulos et al.* (60).

Throughout the course of the reaction, at higher temperatures the color of the reaction contents is gradually changed in the presence of both catalysts from the original green to brownish red, the color change occurs much faster in presence of VOL<sub>1</sub> than that of VOL<sub>2</sub> catalyst, indicating the conversion of V(IV) oxidation state to V(V). Catalytic activities of some V(IV) Schiff base complexes were investigated by Rayati et al (71), they used tertiary butyl hydrogen peroxide (TBHP) as an oxidant for cyclooctene epoxidation reaction, the conversion found is high as (94–95%).

Another epoxidation reaction is studied by Martins and his co-workers (72), they used tertiary butyl hydrogen peroxide (TBHP) and H<sub>2</sub>O<sub>2</sub> as an oxidant, and diamine bis(phenolate) vanadium complex as catalyst for the epoxidation of cyclooctene, they found that the catalyst activity for the epoxidation reaction in the presence of H<sub>2</sub>O<sub>2</sub> is much lower than that in the presence TBHP in acetonitrile as solvent.

From the two studies and others, a higher epoxidation conversion is observed if the reaction is carried out in aprotic solvents, such as carbon tetrachloride, and chloroform, than in protic solvents such as water and alcohol, and the reason

for such decrease is attributed to the higher ability of protic solvents to coordinate with metallic center in the catalyst complex in the vacant position that should be accommodated by the substrate molecule to maintain the catalyst reaction.

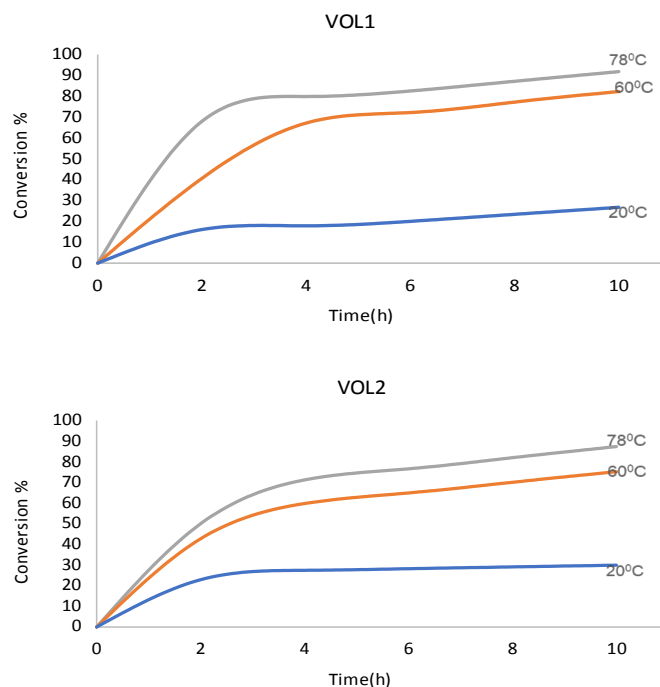


**Figure 5:** Conversion percent of cyclooctene in amount percent at three different temperatures, for VOL<sub>1</sub> (top) and VOL<sub>2</sub> (bottom), for more details please refer to Figures (S-18 to S-26) in the appendices.

**Table 6:** Conversion percent at different reaction temperatures for cyclooctene epoxidation by VOL<sub>1</sub>, VOL<sub>2</sub> complexes.

Run	Time (h)	Conversion (%)					
		20 °C		60 °C		78 °C	
		VOL <sub>1</sub>	VOL <sub>2</sub>	VOL <sub>1</sub>	VOL <sub>2</sub>	VOL <sub>1</sub>	VOL <sub>2</sub>
1	2	16.11	22.92	40.63	42.77	68.00	50.05
2	4	17.90	27.46	67.19	59.81	79.91	71.27
3	6	20.05	28.23	72.22	64.96	82.56	76.65
4	8	23.41	29.12	77.23	70.11	87.21	82.03
5	10	26.78	29.96	82.29	75.25	91.85	87.40

Recently the mechanistic aspects of the catalytic epoxidation of alkenes by vanadium(IV) complexes were reviewed by Conte *et al.* (73). The formation of peroxovanadium(V) species in the epoxidation route for alkenes has been established. This can be examined by titration of a solution of the vanadium(IV) Schiff base complex with TBHP, and confirmed by the reduction of the intensity of the bands at 375 and 285 nm, along with the gradual appearance of two new bands at 330 and 265 nm, this agreed with the same findings in references, the disappearance of spectral peaks and the presence of two peaks at 355 and 310 nm suggest the oxidation of vanadium(IV) and the interaction of the formed

vanadium(V) complex with TBHP to give oxoperoxovanadium(V) species, which is believed to be the active center in the epoxidation of cyclooctene by the vanadium(IV) Schiff base, this is further confirmed by the addition of the highly coordinating molecule imidazole during the epoxidation under optimized conditions, where upon the addition of the imidazole to the reaction mixture the epoxide yield was lowered, another interesting evidence of changing oxidation state from vanadium(IV) to vanadium(V) upon addition of oxidant is came from the work of Correia *et al.* (74) as they used <sup>51</sup>V NMR spectroscopy to monitor the oxidation state change, upon the addition of an

aqueous 30% solution of  $\text{H}_2\text{O}_2$  to the methanolic solutions of their complexes the resonance at ca.  $-485$  ppm progressively disappears and a new

resonance appears between ca.  $-525$  and  $-580$  ppm, and tentatively they assigned this species to be a peroxidovanadate complex.

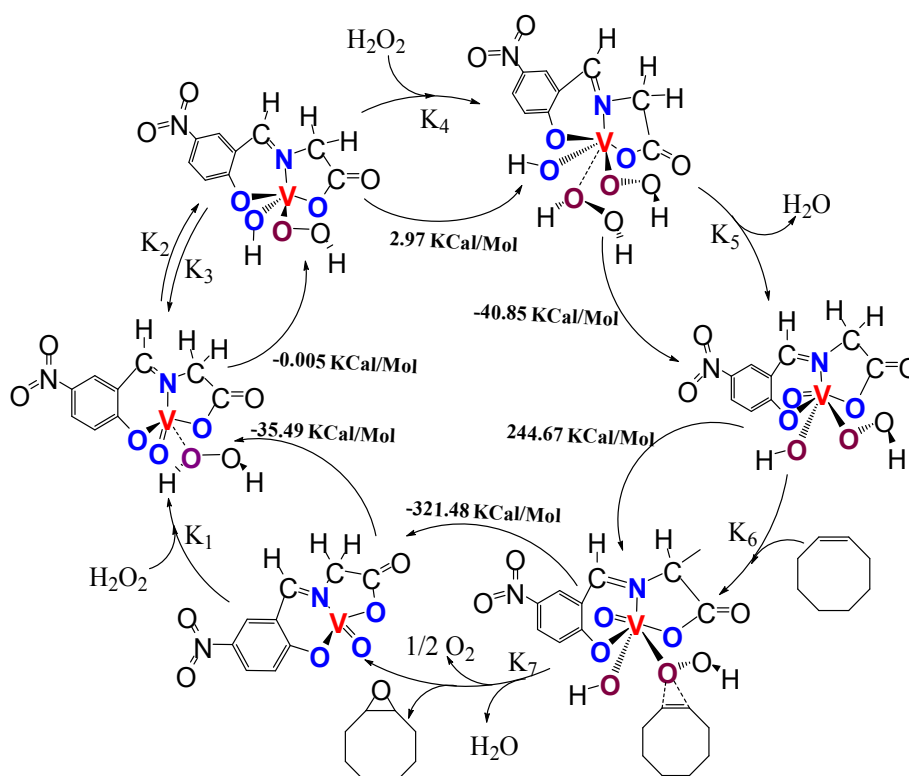


**Figure 6:** Illustration of a six-step mechanism for account of our and previous findings on the epoxidation of cyclooctene.

Figure 6 illustrates the proposed six step mechanism to account for the findings of ours and others on the epoxidation of cyclooctene under optimized conditions using  $\text{H}_2\text{O}_2$  as oxidant, the first step is include binding of the  $\text{VOL}_2$  ( $\text{VOL}_2$  took as a representative) catalyst to the oxidant, this step is evolving of heat as from gaussian calculations the free energy difference is equal to  $-35.49$  Kcal/mol, the second step is believed to be reversible as the free energy difference is very small,  $-0.005$  kcal/mol, this step is involved a hydrogen transfer from peroxo group to convert the  $\text{V}=\text{O}$  to  $\text{V}-\text{OH}$ , product of step two is subject to binding with the next oxidant molecule in step three, leading to unstable product with the free energy difference of  $+2.97$  kcal/mol, stabilization of this molecule is occurred after evolving of one water molecule with the following internal rearrangement in step four.

Now the product of step four is bind to the cyclooctene molecule to give far unstable molecule with a free energy difference of  $+244.67$  kcal/mol, cyclooctane peroxide is evolved in the last step along with the other water and oxygen molecules, and the catalyst molecule is being free to start another catalytic cycle, the free energy difference of last step is  $-321.48$  kcal/mol, all steps are one

direction except step two which believed is reversible. Having this mechanism established, another confirmation of this mechanism to be logic is needed.

Therefore further confirmation of this mechanism is performed with computer simulation using the commercially available program Berkeley Madonna 10.1.2 (75), via the variable step-size Rosenbrock integration method for stiff systems of a differential equation, differential equation of the six steps reaction rates is generated and three modules are suggested, one for each temperature ( $20$ ,  $60$  and  $78$  °C), the simulations yield values quite close to the experimental results, the root mean square values, as a sign of goodness of the simulation, is found to be  $0.00117$ ,  $0.00402$ , and  $0.00475$  for simulation carried out at each temperature respectively, which indicate very nice correlation between simulated and experimental results. Values of partial reaction rate constants are calculated and tabulated in Table 7, from Table 7 one can assumes that the mechanism is involved two rate determining steps, step one when the first  $\text{H}_2\text{O}_2$  molecule is bound to the catalyst molecule and the other one is step five when the cyclooctene molecule is bound to the cycle, the observed rate

constants (the sum of all rate constant values) are calculated and related to Arrhenius equation, and subsequently theoretical activation energy of the

reaction is calculated and found to be around 24.2 kJ/mol with a frequency factor (Arrhenius constant) of around  $0.2E+6$  mmol/sec.

**Table 7:** Values of partial reaction rate constants of the suggested model used for simulations (Dot Lines) are shown in Figure 7.

Parameter	k values (20 °C)	k values (60 °C)	k values (78 °C)
$k_1$ (mmol/s)	4.96E-03	1.3E-03	1.82E-03
$k_2$ (1/s)	3.89	98.8	105.1
$k_3$ (1/s)	4.0E-03	1.1E-06	140.1
$k_4$ (mmol/s)	4.0E-04	43.27	34.4
$k_5$ (1/s)	45.05	0.57	2.97
$k_6$ (mmol/s)	0.86	8.6E-04	5.8E-04
$k_7$ (1/s)	12.32	2.65	7.30
$k_{obs}$	8.87	37.18	41.40
T k	293.15	333.15	351.15
1/T	3.41E-03	3.00E-03	2.85E-03
Ln $k_{obs}$	2.18	3.62	3.72
Observed Activation Energy (J/mol)	24173.0		
Frequency factor	0.2E+6		

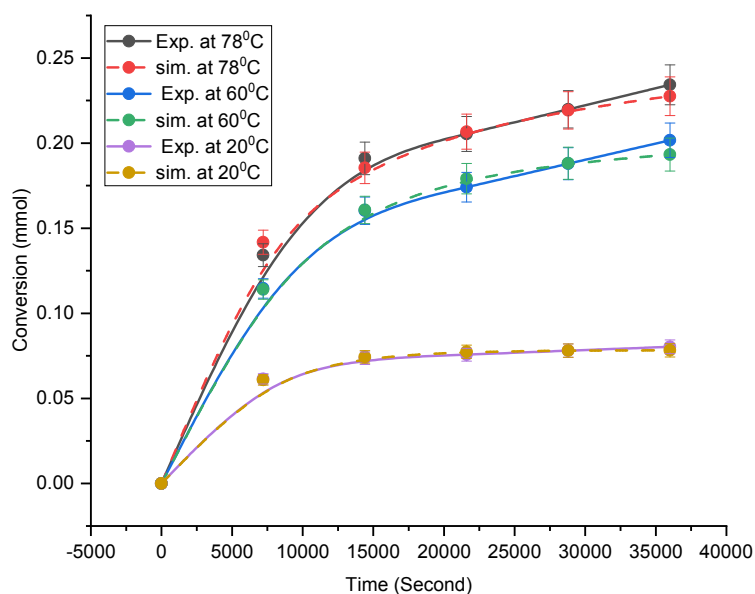


**Figure 7:** Computer simulation of cyclooctene epoxidation conversion with  $VOL_1$  as catalyst, Berkeley Madonna 8.0 program (commercial) from the University of California, Berkeley is used for the simulation, the variable used is step-size Rosenbrock integration method for stiff systems of differential equations. (Solid lines represent the trend of the measured points, dot lines represent the fit to the solid lines).

Figure 7 shows the correlation between experimental and simulated results, both lines are almost typical, indicating the validity of the model used. This mechanism is quite similar to that suggested by Mathavan (76), the critical step in Mathavan mechanism is the change in the oxidation state of the vanadium catalyst from oxidation state IV to V, then followed by the subsequent binding of the substrate compound (phenol in this case), and the final product.

## CONCLUSION

In summary, we have synthesized and characterized two Schiff-base vanadium (IV) complexes and have used them as catalysts in olefin epoxidation. Both are found to be catalytically active in industrially important epoxidation reactions in acetonitrile solvent media under homogeneous conditions. Hydrogen peroxide was used as the oxidant and cyclooctene as a representative of olefins. The

catalytic efficacy is increased with increasing reaction temperatures. With the aid of computer softwares, some interesting findings have been derived, after optimizing the molecular structures of both catalysts, molecular structures are confirmed in terms of correlation between FTIR,  $^1\text{H}$  NMR, and  $^{13}\text{C}$  NMR, the energy gap between ground and excited states is calculated, some other properties in term of HOMO and LUMO is defined, finally hypothetical mechanism of reaction involved six reaction steps are suggested, and found to be logic and pretty similar to other published ones.

### CONFLICT OF INTEREST

The authors have no conflicts of interest to declare that are relevant to the content of this article.

### ACKNOWLEDGMENTS

The Author would like to thank The German Academic Exchange Services for funding this research, and the author like to thank the Gamess Us Company and Orca company for providing free academic softwares.

### REFERENCES

- Drozdak R, Allaert B, Ledoux N, Dragutan I, Dragutan V, Verpoort F. Ruthenium complexes bearing bidentate Schiff base ligands as efficient catalysts for organic and polymer syntheses. *Coordination Chemistry Reviews*. 2005 Dec;249(24):3055–74. [<DOI>](#).
- Pariya C, Jayaprakash KN, Sarkar A. Alkene metathesis: new developments in catalyst design and application. *Coordination Chemistry Reviews*. 1998 Jan;168:1–48. [<DOI>](#).
- Gan C, Lai G, Zhang Z, Wang Z, Zhou M-M. Efficient and enantioselective nitroaldol reaction catalyzed by copper Schiff-base complexes. *Tetrahedron: Asymmetry*. 2006 Mar;17(5):725–8. [<DOI>](#).
- Liu D-F, Lü X-Q, Lu R. Homogeneous and heterogeneous styrene epoxidation catalyzed by copper(II) and nickel(II) Schiff base complexes. *Transition Met Chem*. 2014 Sep;39(6):705–12. [<DOI>](#).
- Ray A, Rosair GM, Pilet G, Dede B, Gómez-García CJ, Signorella S, et al. Preferential azido bridging regulating the structural aspects in cobalt(III) and copper(II)-Schiff base complexes: Syntheses, magnetostructural correlations and catalytic studies. *Inorganica Chimica Acta*. 2011 Sep;375(1):20–30. [<DOI>](#).
- de Vries JG, Roelfes G, Green R. Ruthenium catalysed redox transformation of cinnamaldehyde to 3-phenylpropionic acid and methyl ester. *Tetrahedron Letters*. 1998 Nov;39(45):8329–32. [<DOI>](#).
- Odenkirk W, Rheingold AL, Bosnich B. Homogeneous catalysis: a ruthenium-based Lewis-acid catalyst for the Diels-Alder reaction. *J Am Chem Soc*. 1992 Jul;114(16):6392–8. [<DOI>](#).
- Kardanpour R, Tangestaninejad S, Mirkhani V, Moghadam M, Mohammadpoor-Baltork I, Zadehahmadi F. Efficient alkene epoxidation catalyzed by molybdenyl acetylacetonate supported on aminated UiO-66 metal-organic framework. *Journal of Solid State Chemistry*. 2015 Mar;226:262–72. [<DOI>](#).
- Sabater MJ, Corma A, Domenech A, Fornés V, García H. Chiral salen manganese complex encapsulated within zeolite Y: a heterogeneous enantioselective catalyst for the epoxidation of alkenes. *Chem Commun*. 1997;(14):1285–6. [<DOI>](#).
- Srikanth A, Nagendrappa G, Chandrasekaran S. Catalytic epoxidation of cyclic vinylsilanes by ruthenium(II) complexes under aerobic conditions. *Tetrahedron*. 2003 Sep;59(39):7761–5. [<DOI>](#).
- de Clercq B, Verpoort F. Assessing the Scope of the Introduction of Schiff Bases as Co-Ligands for Monometallic and Homobimetallic Ruthenium Ring-Opening Metathesis Polymerisation and Ring-Closing Metathesis Initiators. *Adv Synth Catal*. 2002 Aug;344(6–7):639–48. [<URL>](#).
- Xi Z, Wang H, Sun Y, Zhou N, Cao G, Li M. Direct epoxidation of olefins catalyzed by heteropolyoxometalates with molecular oxygen and recyclable reductant. *Journal of Molecular Catalysis A: Chemical*. 2001 Mar;168(1–2):299–301. [<DOI>](#).
- Canali L, Sherrington DC. Utilisation of homogeneous and supported chiral metal(salen) complexes in asymmetric catalysis. *Chem Soc Rev*. 1999;28(2):85–93. [<DOI>](#).
- Berkessel A, Frauenkron M, Schwenkreis T, Steinmetz A. Pentacoordinated manganese complexes as biomimetic catalysts for asymmetric epoxidations with hydrogen peroxide. *Journal of Molecular Catalysis A: Chemical*. 1997 Mar;117(1–3):339–46. [<DOI>](#).
- Ho C-W, Cheng W-C, Cheng M-C, Peng S-M, Cheng K-F, Che C-M. Preparation and reactivities of chiral manganese(III) and copper(II) complexes of binaphthyl Schiff bases. *J Chem Soc, Dalton Trans*. 1996;(4):405. [<DOI>](#).
- Solomon EI, Sundaram UM, Machonkin TE. Multicopper Oxidases and Oxygenases. *Chem Rev*. 1996 Jan 1;96(7):2563–606. [<DOI>](#).
- Judmaier ME, Holzer C, Volpe M, Mösch-Zanetti NC. Molybdenum(VI) Dioxo Complexes Employing Schiff Base Ligands with an Intramolecular Donor for Highly Selective Olefin Epoxidation. *Inorg Chem*. 2012 Sep 17;51(18):9956–66. [<DOI>](#).
- Lu X-H, Lei J, Wei X-L, Ma X-T, Zhang T-J, Hu W, et al. Selectively catalytic epoxidation of  $\alpha$ -pinene with dry air over the composite catalysts of Co-MOR(L) with Schiff-base ligands. *Journal of Molecular Catalysis A: Chemical*. 2015 May;400:71–80. [<DOI>](#).
- Pasayat S, Böhme M, Dhaka S, Dash SP, Majumder S, Maurya MR, et al. Synthesis, Theoretical Study and Catalytic Application of Oxidometal (Mo or V) Complexes: Unexpected Coordination Due to Ligand Rearrangement



- through Metal-Mediated C–C Bond Formation. *Eur J Inorg Chem.* 2016 Apr;2016(10):1604–18. <DOI>.
20. Wei FY. A mononuclear nickel(II) complex and a dinuclear manganese(III) complex derived from N,N'-bis(5-methoxysalicylidene)-1,2-ethanediamine: Synthesis, crystal structures and catalytic epoxidation property. *Russ J Coord Chem.* 2016 Jan;42(1):44–9. <DOI>.
21. Adhikary C, Bera R, Dutta B, Jana S, Bocelli G, Cantoni A, et al. Catalytic efficacy of Schiff-base copper(II) complexes: Synthesis, X-ray structure and olefin oxidation. *Polyhedron.* 2008 Apr;27(6):1556–62. <DOI>.
22. Koola JD, Kochi JK. Nickel catalysis of olefin epoxidation. *Inorg Chem.* 1987 Mar;26(6):908–16. <DOI>.
23. Groves JT, Watanabe Yoshihito. The mechanism of olefin epoxidation by oxo-iron porphyrins. Direct observation of an intermediate. *J Am Chem Soc.* 1986 Feb;108(3):507–8. <DOI>.
24. Maschmeyer T, Rey F, Sankar G, Thomas JM. Heterogeneous catalysts obtained by grafting metallocene complexes onto mesoporous silica. *Nature.* 1995 Nov;378(6553):159–62. <DOI>.
25. Mohajer D, Tangestaninejad S. Efficient catalytic epoxidation of alkenes by a manganese porphyrin and periodate in the presence of imidazole. *J Chem Soc, Chem Commun.* 1993;(3):240. <DOI>.
26. Martos-Calvente R, de la Peña O'Shea VA, Campos-Martin JM, Fierro JLG, Gutiérrez-Puebla E. Synthesis of bis[N,O-{2'-pyridyl-methanolate}]dioxomolybdenum(VI) epoxidation catalyst and novel crystal structure derived from X-ray diffraction and DFT calculations. *Journal of Molecular Catalysis A: Chemical.* 2004 Jun;214(2):269–72. <DOI>.
27. Herrmann WA, Fischer RW, Marz DW. Methyltrioxorhenium as Catalyst for Olefin Oxidation. *Angew Chem Int Ed Engl.* 1991 Dec;30(12):1638–41. <DOI>.
28. Copéret C, Adolffson H, Sharpless KB. A simple and efficient method for epoxidation of terminal alkenes. *Chem Commun.* 1997;(16):1565–6. <DOI>.
29. De Vos DE, Sels BF, Reynaers M, Subba Rao YV, Jacobs PA. Epoxidation of terminal or electron-deficient olefins with H<sub>2</sub>O<sub>2</sub>, catalysed by Mn-trimethyltriazacyclonane complexes in the presence of an oxalate buffer. *Tetrahedron Letters.* 1998 May;39(20):3221–4. <DOI>.
30. Palucki M, Pospisil PJ, Zhang W, Jacobsen EN. Highly Enantioselective, Low-Temperature Epoxidation of Styrene. *J Am Chem Soc.* 1994 Oct;116(20):9333–4. <DOI>.
31. Jiang J, Ma K, Zheng Y, Cai S, Li R, Ma J. Cobalt salophen complex immobilized into montmorillonite as catalyst for the epoxidation of cyclohexene by air. *Applied Clay Science.* 2009 Jul;45(3):117–22. <DOI>.
32. Yang Y, Zhang Y, Hao S, Guan J, Ding H, Shang F, et al. Heterogenization of functionalized Cu(II) and VO(IV) Schiff base complexes by direct immobilization onto amino-modified SBA-15: Styrene oxidation catalysts with enhanced reactivity. *Applied Catalysis A: General.* 2010 Jun;381(1–2):274–81. <DOI>.
33. Janssen KBM, Laquiere I, Dehaen W, Parton RF, Vankelecom IFJ, Jacobs PA. A dimeric form of Jacobsen's catalyst for improved retention in a polydimethylsiloxane membrane. *Tetrahedron: Asymmetry.* 1997 Oct;8(20):3481–7. <DOI>.
34. Feng H-X, Wang R-M, He Y-F, Lei Z-Q, Wang Y-P, Xia C-G, et al. Preparation and catalysis of porous silica supported metal Schiff-base complex. *Journal of Molecular Catalysis A: Chemical.* 2000 Sep;159(1):25–9. <DOI>.
35. Katsuki T. Catalytic asymmetric oxidations using optically active (salen)manganese(III) complexes as catalysts. *Coordination Chemistry Reviews.* 1995 Mar;140:189–214. <DOI>.
36. Bolm C, Bienewald F. Asymmetric Sulfide Oxidation with Vanadium Catalysts and H<sub>2</sub>O<sub>2</sub>. *Angew Chem Int Ed Engl.* 1996 Jan 5;34(2324):2640–2. <DOI>.
37. Dichmann K, Hamer G, Nyburg SC, Reynolds WF. The 2:1 vanadyl acetylacetonate:1,4-dioxane complex. A nuclear magnetic resonance and X-ray crystal structure study. *J Chem Soc D.* 1970;(20):1295. <DOI>.
38. Hwang D-R, Chen C-P, Uang B-J. Aerobic catalytic oxidative coupling of 2-naphthols and phenols by VO(acac)<sub>2</sub>. *Chem Commun.* 1999;(13):1207–8. <DOI>.
39. Grivani G, Bruno G, Rudbari HA, Khalaji AD, Pourteimouri P. Synthesis, characterization and crystal structure determination of a new oxovanadium(IV) Schiff base complex: The catalytic activity in the epoxidation of cyclooctene. *Inorganic Chemistry Communications.* 2012 Apr;18:15–20. <DOI>.
40. Frisch M, Trucks G, Schlegel H, Scuseria G, Robb M, Cheeseman J. Gaussian 16 Rev. C. 01. Gaussian, Inc., Wallingford, CT; 2016.
41. Becke AD. A new mixing of Hartree–Fock and local density-functional theories. *The Journal of Chemical Physics.* 1993 Jan 15;98(2):1372–7. <DOI>.
42. Lee C, Yang W, Parr RG. Development of the Colle-Salvetti correlation-energy formula into a functional of the electron density. *Phys Rev B.* 1988 Jan 15;37(2):785–9. <DOI>.
43. Tomasi J, Mennucci B, Cammi R. Quantum Mechanical Continuum Solvation Models. *Chem Rev.* 2005 Aug 1;105(8):2999–3094. <DOI>.
44. Anonymous. Chemcraft - graphical software for visualization of quantum chemistry computations. [Internet]. ChemCraft. <URL>.
45. Dennington R, Keith T. Gaussview, version 6.1 [Internet]. Gaussview software. 2019 [cited 2022 Jan 1]. <URL>.
46. Hait D, Head-Gordon M. How Accurate Is Density Functional Theory at Predicting Dipole Moments? An

- Assessment Using a New Database of 200 Benchmark Values. *J Chem Theory Comput.* 2018 Apr 10;14(4):1969–81. [<DOI>](#).
47. Neese F. Software update: the ORCA program system, version 4.0. *WIREs Comput Mol Sci* [Internet]. 2018 Jan [cited 2022 Jan 1];8(1). [<DOI>](#).
48. Schmidt MW, Baldrige KK, Boatz JA, Elbert ST, Gordon MS, Jensen JH, et al. General atomic and molecular electronic structure system. *J Comput Chem.* 1993 Nov;14(11):1347–63. [<DOI>](#).
49. Hanwell MD, Curtis DE, Lonie DC, Vandermeersch T, Zurek E, Hutchison GR. Avogadro: an advanced semantic chemical editor, visualization, and analysis platform. *J Cheminform.* 2012 Dec;4(1):17. [<DOI>](#).
50. O'Boyle NM, Tenderholt AL, Langner KM. cclib: A library for package-independent computational chemistry algorithms. *J Comput Chem.* 2008 Apr 15;29(5):839–45. [<DOI>](#).
51. Hay PJ, Wadt WR. Ab initio effective core potentials for molecular calculations. Potentials for the transition metal atoms Sc to Hg. *The Journal of Chemical Physics.* 1985 Jan;82(1):270–83. [<DOI>](#).
52. Wadt WR, Hay PJ. Ab initio effective core potentials for molecular calculations. Potentials for main group elements Na to Bi. *The Journal of Chemical Physics.* 1985 Jan;82(1):284–98. [<DOI>](#).
53. Hay PJ, Wadt WR. Ab initio effective core potentials for molecular calculations. Potentials for K to Au including the outermost core orbitals. *The Journal of Chemical Physics.* 1985 Jan;82(1):299–310. [<DOI>](#).
54. Perdew JP, Burke K, Ernzerhof M. Generalized Gradient Approximation Made Simple. *Phys Rev Lett.* 1996 Oct 28;77(18):3865–8. [<DOI>](#).
55. Goodgame M, Hayward PJ. Infrared spectra (1650–400 cm. <sup>-1</sup>) of  $\gamma$ -picoline metal co-ordination complexes. *J Chem Soc A.* 1966;0(0):632–4. [<DOI>](#).
56. Syamal A, Kale KS. Magnetic and spectral properties of oxovanadium(IV) complexes of ONO donor tridentate, dibasic Schiff bases derived from salicylaldehyde or substituted salicylaldehyde and o-hydroxybenzylamine. *Inorg Chem.* 1979 Apr;18(4):992–5. [<DOI>](#).
57. Selbin J. The Chemistry of Oxovanadium(IV). *Chem Rev.* 1965 Apr 1;65(2):153–75. [<DOI>](#).
58. Selbin J. Oxovanadium(IV) complexes. *Coordination Chemistry Reviews.* 1966 Aug;1(3):293–314. [<DOI>](#).
59. Dinda R, Sengupta P, Ghosh S, Mak TCW. Valence Delocalization in a Mixed-Oxidation Divanadium (IV, V) Complex Electrogenerated from Its Structurally Characterized Divanadium (V) Analogue with a Tridentate (ONO) Ligand. *Inorg Chem.* 2002 Mar 1;41(6):1684–8. [<DOI>](#).
60. Vergopoulos V, Prietsch W, Fritzsche M, Rehder D. Binding of L-histidine to vanadium. Structure of exo-[VO<sub>2</sub>{N-(2-oxidonaphthal)-His}]. *Inorg Chem.* 1993 Apr;32(9):1844–9. [<DOI>](#).
61. Abrarin S, Ahmed MJ. A highly sensitive and selective spectrophotometric method for the determination of vanadium at nanotrace levels in some environmental, biological, soil, food, and pharmaceutical samples using salicylaldehyde-benzoylhydrazone. *Eur J Chem.* 2020 Dec 31;11(4):385–95. [<DOI>](#).
62. Keramidas AD, Papaioannou AB, Vlahos A, Kabanos TA, Bonas G, Makriyannis A, et al. Model Investigations for Vanadium–Protein Interactions. Synthetic, Structural, and Physical Studies of Vanadium(III) and Oxovanadium(IV/V) Complexes with Amidate Ligands. *Inorg Chem.* 1996 Jan 1;35(2):357–67. [<DOI>](#).
63. Schmidt A-C, Hermsen M, Rominger F, Dehn R, Teles JH, Schäfer A, et al. Synthesis of Mono- and Dinuclear Vanadium Complexes and Their Reactivity toward Dehydroperoxidation of Alkyl Hydroperoxides. *Inorg Chem.* 2017 Feb 6;56(3):1319–32. [<DOI>](#).
64. Maurya RC, Chourasia J, Rajak D, Malik BA, Mir JM, Jain N, et al. Oxovanadium(IV) complexes of bioinorganic and medicinal relevance: Synthesis, characterization and 3D molecular modeling of some oxovanadium(IV) complexes involving O, N-donor environment of salicylaldehyde-based sulfa drug Schiff bases. *Arabian Journal of Chemistry.* 2016 Nov;9:S1084–100. [<DOI>](#).
65. Politzer P, Laurence PR, Jayasuriya K. Molecular electrostatic potentials: an effective tool for the elucidation of biochemical phenomena. *Environmental Health Perspectives.* 1985 Sep;61:191–202. [<DOI>](#).
66. Frenking G, Shaik S, editors. The chemical bond. 1: Fundamental aspects of chemical bonding. Weinheim: Wiley-VCH; 2014. 411 p. ISBN: 978-3-527-33314-1.
67. Parr RG, Szentpály L v., Liu S. Electrophilicity Index. *J Am Chem Soc.* 1999 Mar 1;121(9):1922–4. [<DOI>](#).
68. Koopmans T. Über die Zuordnung von Wellenfunktionen und Eigenwerten zu den Einzelnen Elektronen Eines Atoms. *Physica.* 1934 Jan;1(1–6):104–13. [<DOI>](#).
69. Ayers PW. The physical basis of the hard/soft acid/base principle. *Faraday Discuss.* 2007;135:161–90. [<DOI>](#).
70. Chattaraj PK, Sarkar U, Roy DR. Electrophilicity Index. *Chem Rev.* 2006 Jun 1;106(6):2065–91. [<DOI>](#).
71. Rayati S, Koliaei M, Ashouri F, Mohebbi S, Wojtczak A, Kozakiewicz A. Oxovanadium(IV) Schiff base complexes derived from 2,2'-dimethylpropanediamine: A homogeneous catalyst for cyclooctene and styrene oxidation. *Applied Catalysis A: General.* 2008 Aug;346(1–2):65–71. [<DOI>](#).
72. Madeira F, Barroso S, Namorado S, Reis PM, Royo B, Martins AM. Epoxidation of cis-cyclooctene using diamine bis(phenolate) vanadium, molybdenum and tungsten complexes as catalysts. *Inorganica Chimica Acta.* 2012 Mar;383:152–6. [<DOI>](#).

73. Conte V, Coletti A, Floris B, Licini G, Zonta C. Mechanistic aspects of vanadium catalysed oxidations with peroxides. *Coordination Chemistry Reviews*. 2011 Oct;255(19–20):2165–77. [<DOI>](#).

74. Maurya MR, Sarkar B, Avecilla F, Correia I. Vanadium( iv and v ) complexes of pyrazolone based ligands: Synthesis, structural characterization and catalytic applications. *Dalton Trans*. 2016;45(43):17343–64. [<DOI>](#).

75. Marcoline F, Grabe M, Nayak S, Zahnley T, Oster G, Robert M. Berkeley Madonna version 10.1.2 [Internet]. Berkeley Madonna version 10.1.2. 2017. Available from: [<URL>](#).

76. Mathavan A, Ramdass A, Rajagopal S. Kinetic study of the oxovanadium(IV)–salen-catalyzed H<sub>2</sub>O<sub>2</sub> oxidation of phenols. *Transition Met Chem*. 2015 May;40(4):355–62. [<DOI>](#).

## Supplementary Information

### Synthesis, Characterization, DFT Calculations, and Catalytic Epoxidation of Two Oxovanadium(IV) Schiff Base Complexes

Asha Fadalla Wady<sup>1</sup>, Mohammed Awad Ali Khalid<sup>2,\*</sup>, Mohammed Traheeb Alotaibi<sup>2</sup> and Yusuf Sulfab Ahmed<sup>3</sup>

<sup>1</sup> University of Kordofan, Department of Chemistry, Alobaid, 11111, Sudan

<sup>2</sup> University of Taif, Department of Chemistry, Turabah, 21995, Saudi Arabia

<sup>3</sup> University of Khartoum, Department of Chemistry, Khartoum, 11115, Sudan

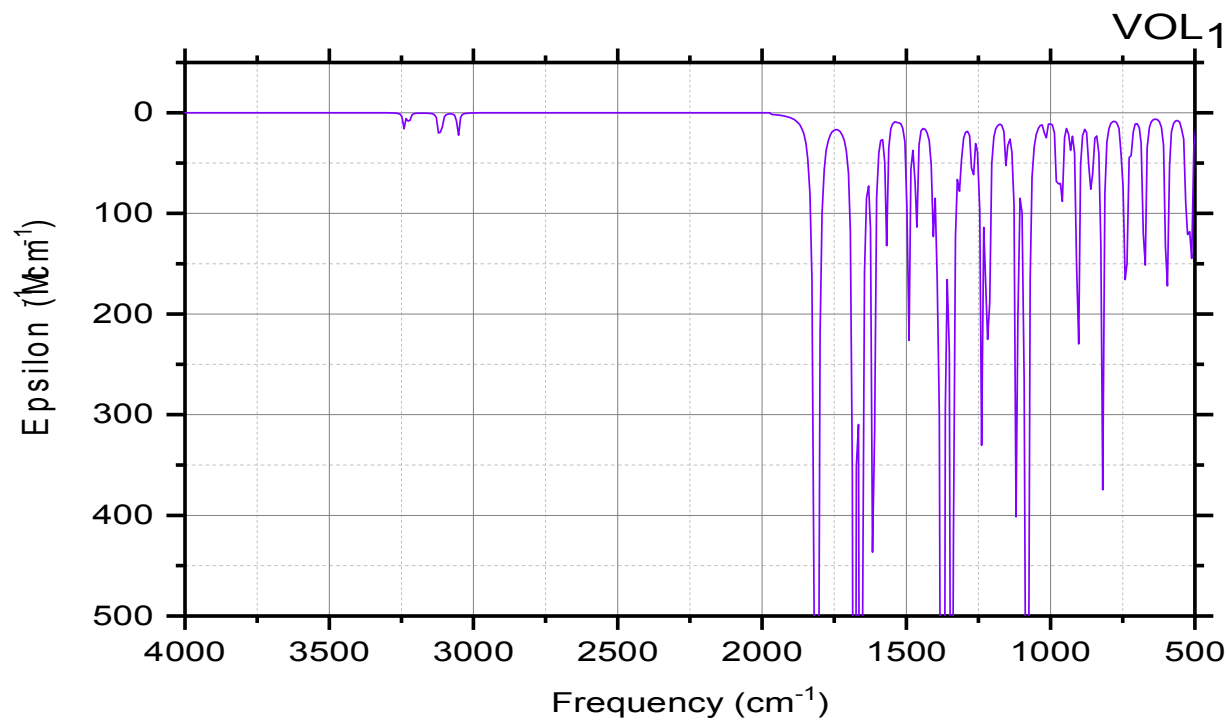


**Figure S-1.** Calculated FTIR for VOL<sub>1</sub> Complex Using B3LYP/ 6-31+G(d,p) level of theory.

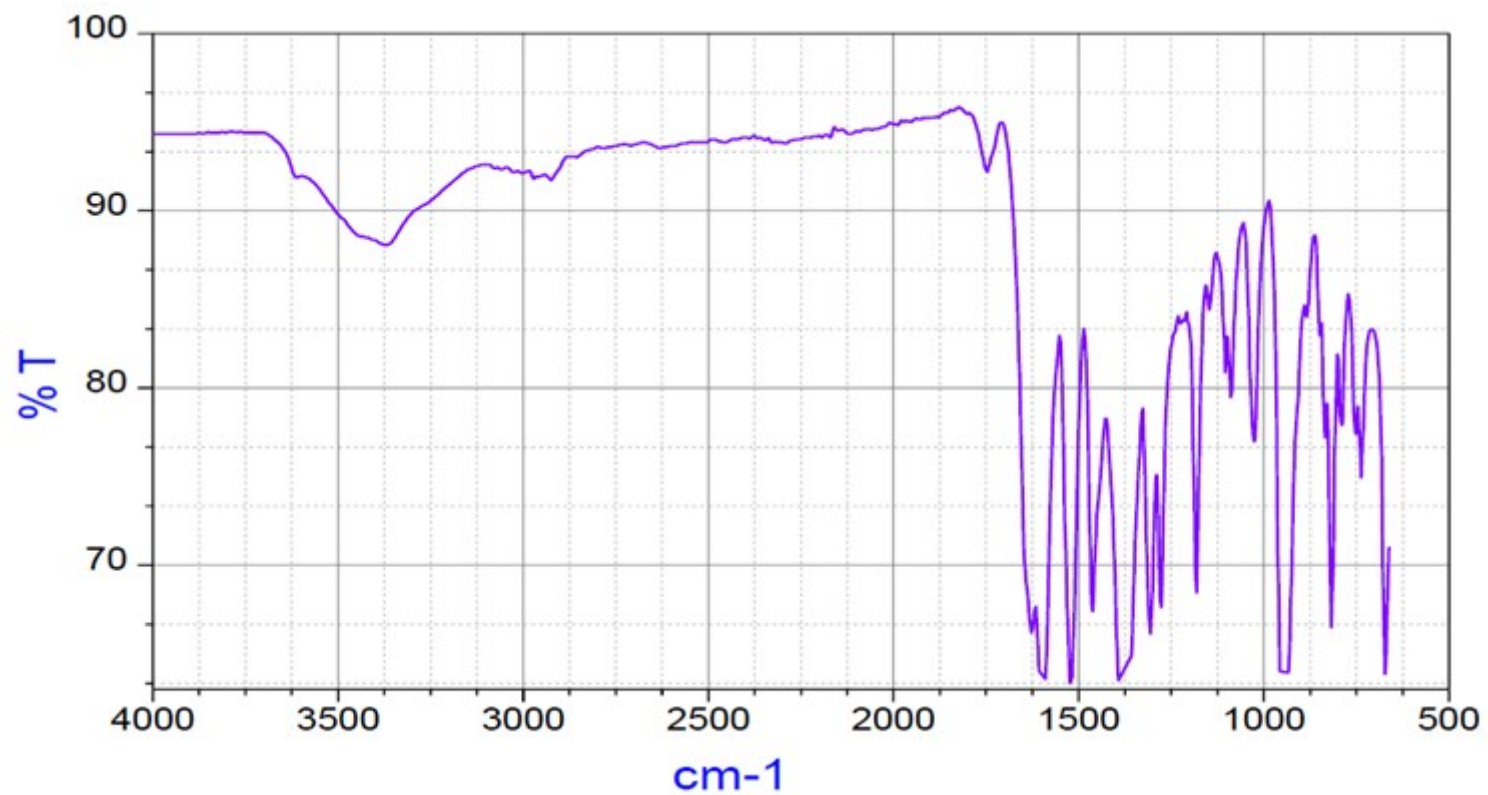


**Figure S-2.** Experimental FTIR for VOL<sub>1</sub> Complex.

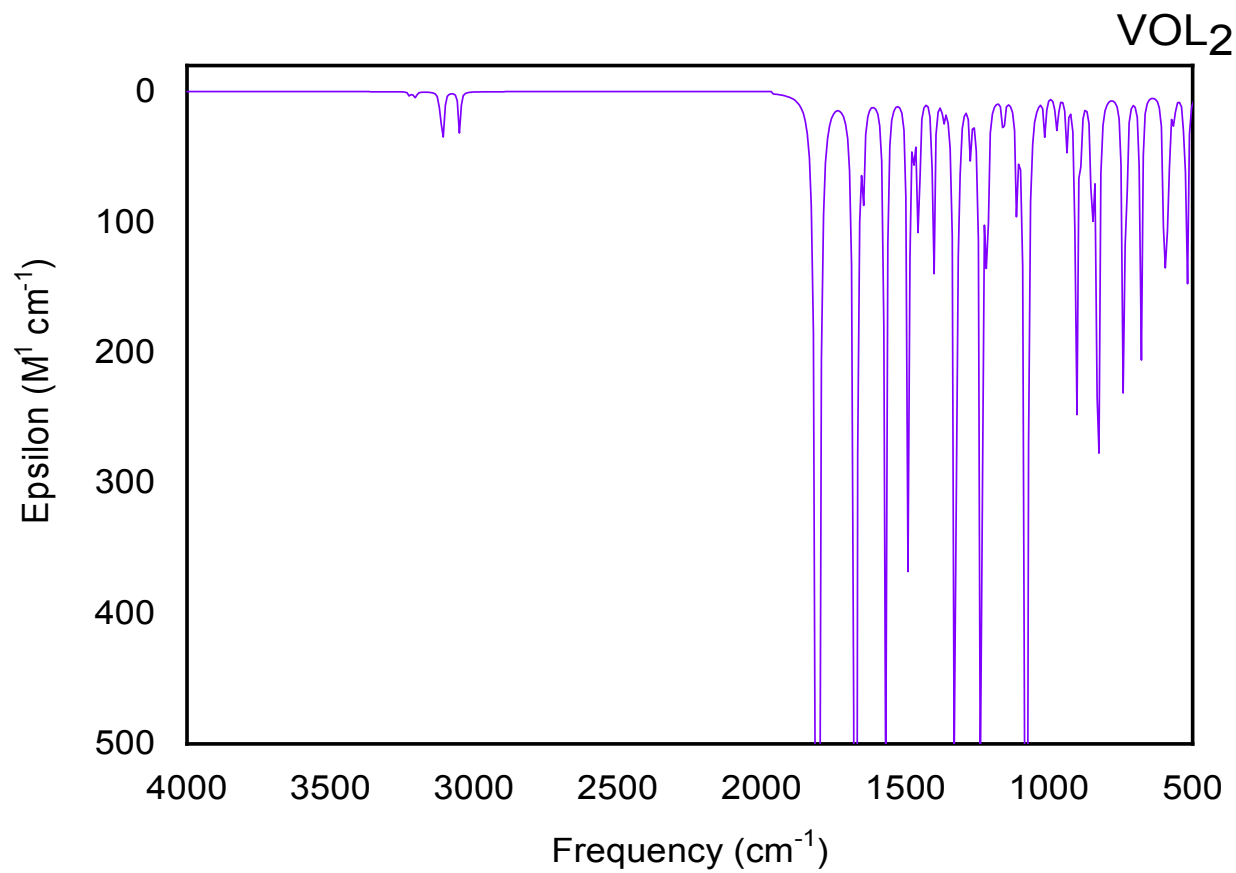


**Figure S-3.** Calculated FTIR for VOL<sub>2</sub> Complex Using B3LYP/ 6-31+G(d,p) level of theory.

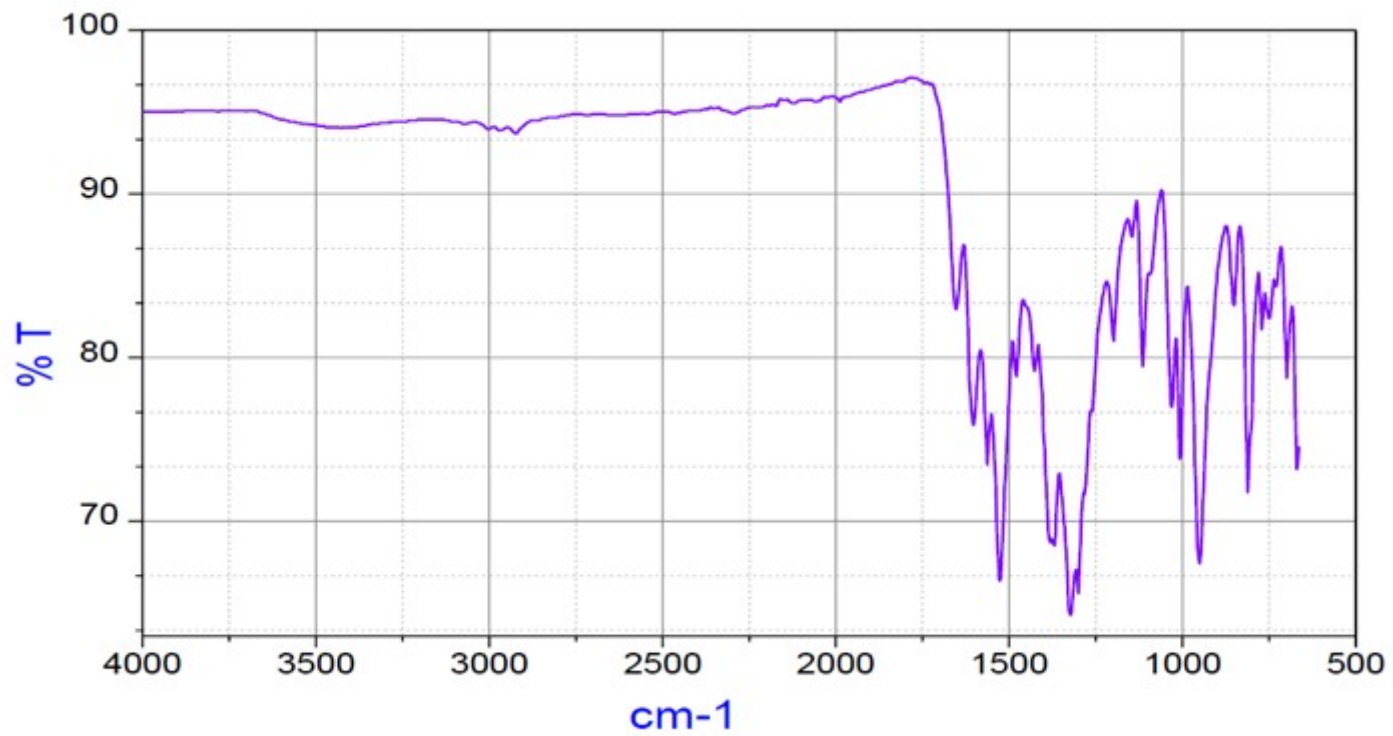


**Figure S-4.** Experimental FTIR for VOL<sub>2</sub> Complex.



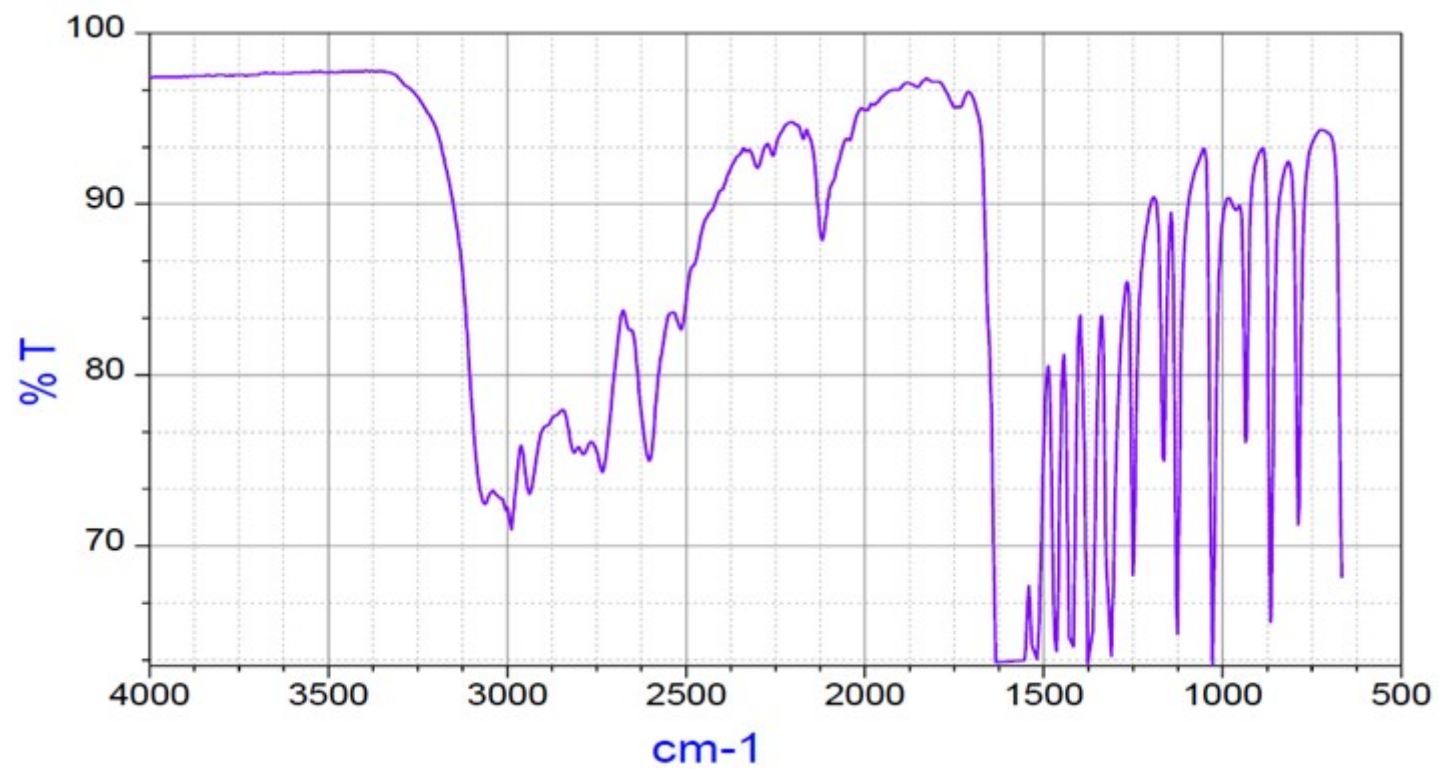


**Figure S-5.** Experimental FTIR for H<sub>2</sub>L<sub>1</sub> ligand.

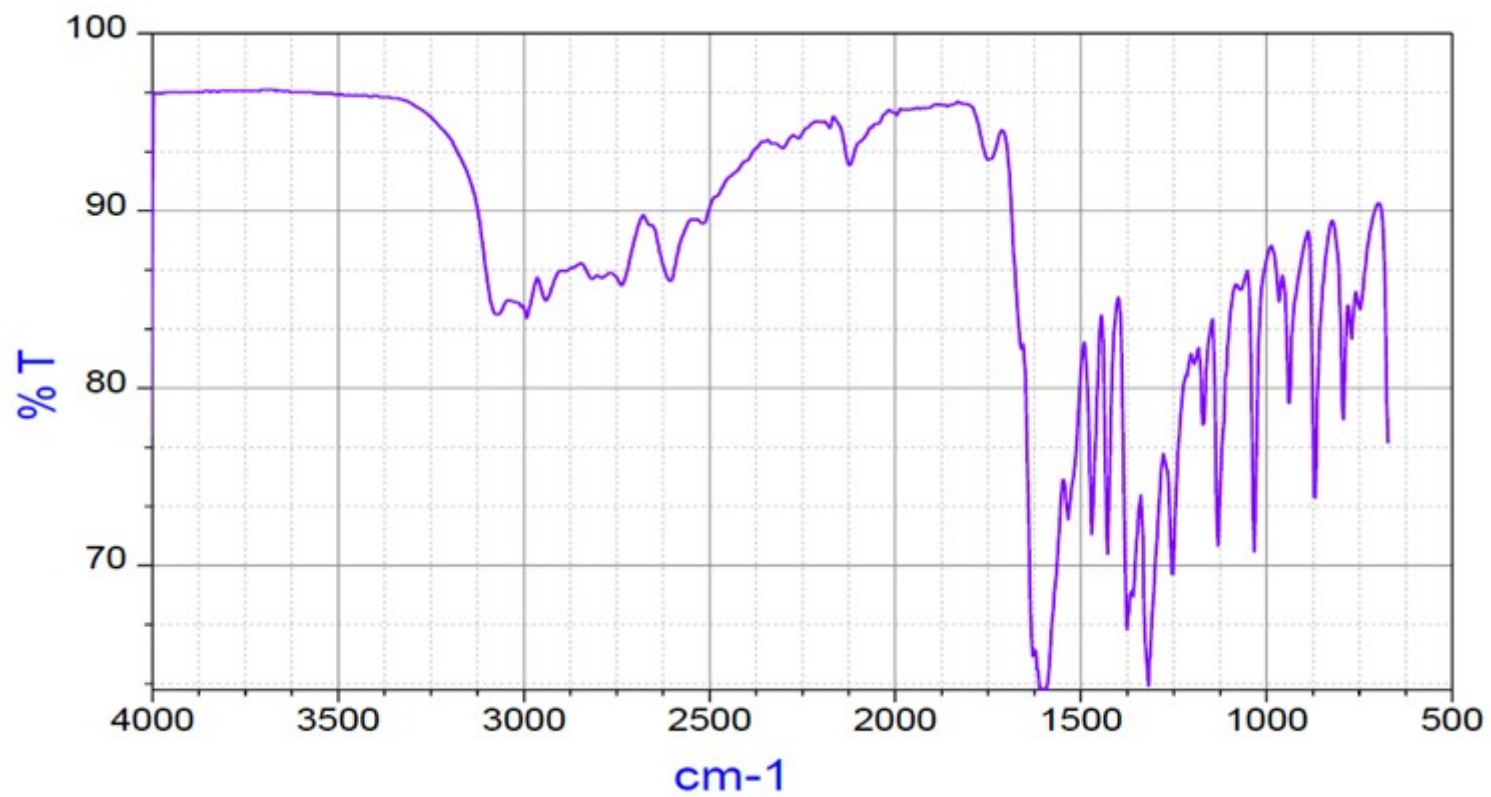


**Figure S-6.** Experimental FTIR for H<sub>2</sub>L<sub>2</sub> ligand.

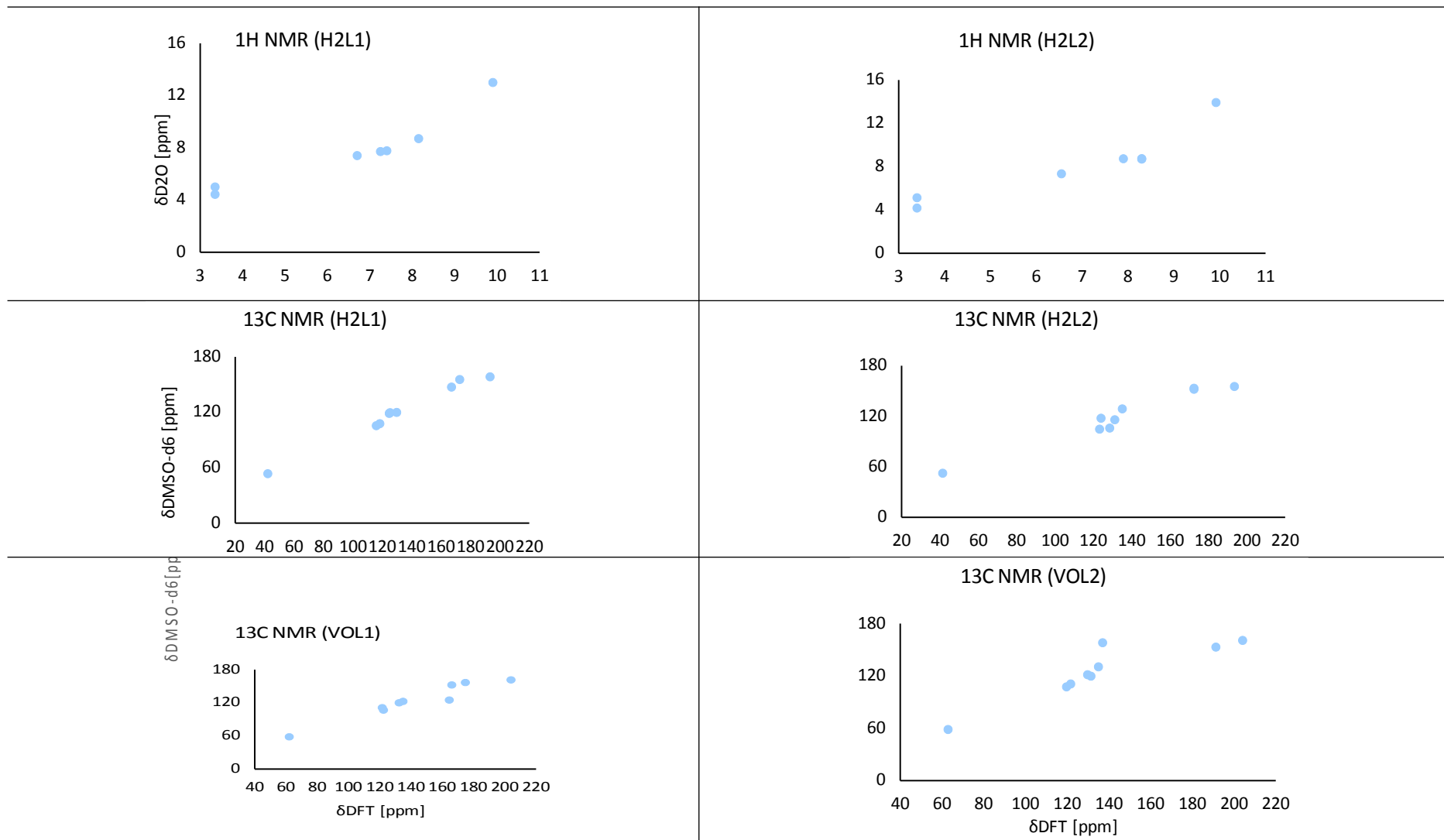


**Figure S-7.** Correlation between experimental and calculated  $^1\text{H}$  and  $^{13}\text{C}$  chemical shifts in  $\text{D}_2\text{O}$ , and  $\text{DMSO}-d_6$  solvents.

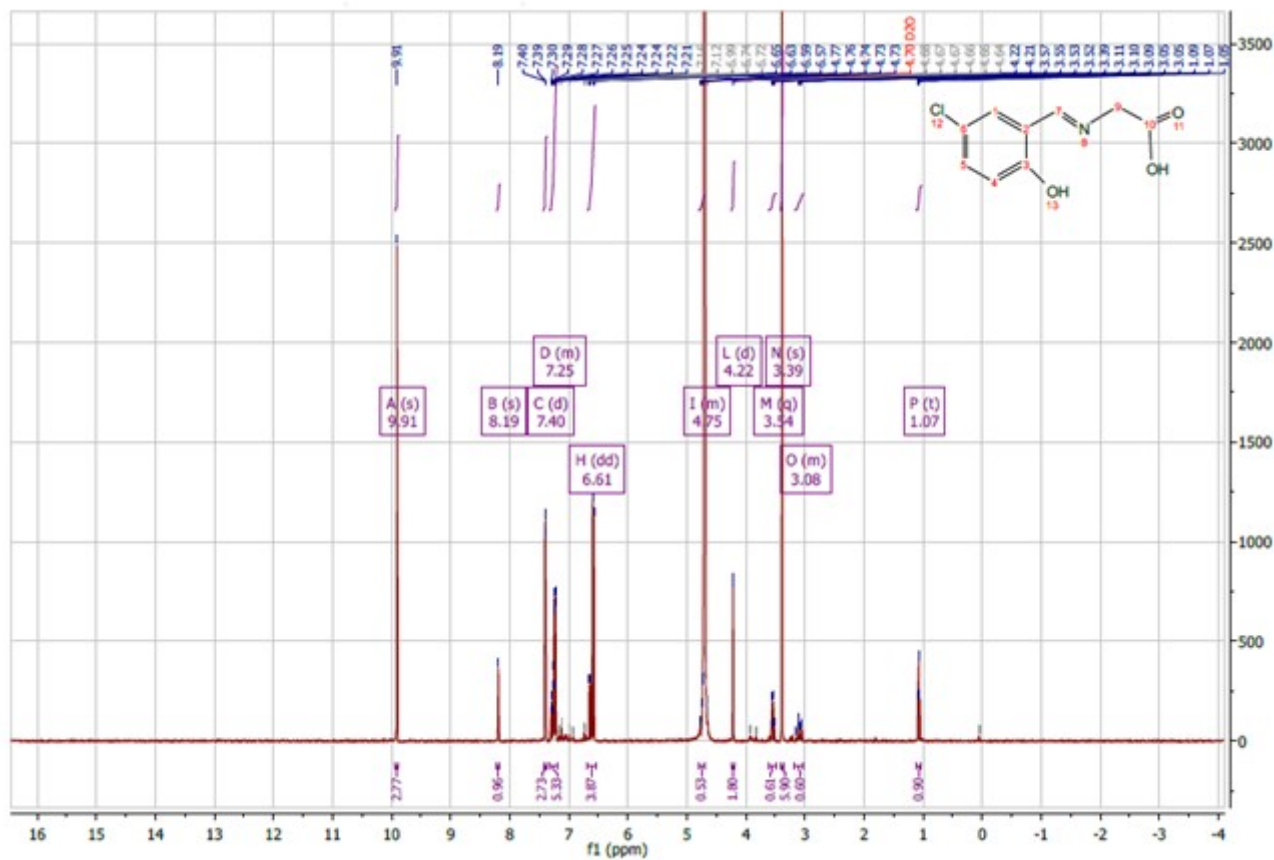


**Figure S-8.** Experimental  $^1\text{H}$  NMR for the  $\text{H}_2\text{L}_1$ ,  $^1\text{H}$  NMR spectra is recorded on Bruker AVIII 40, 500 MHz, US.

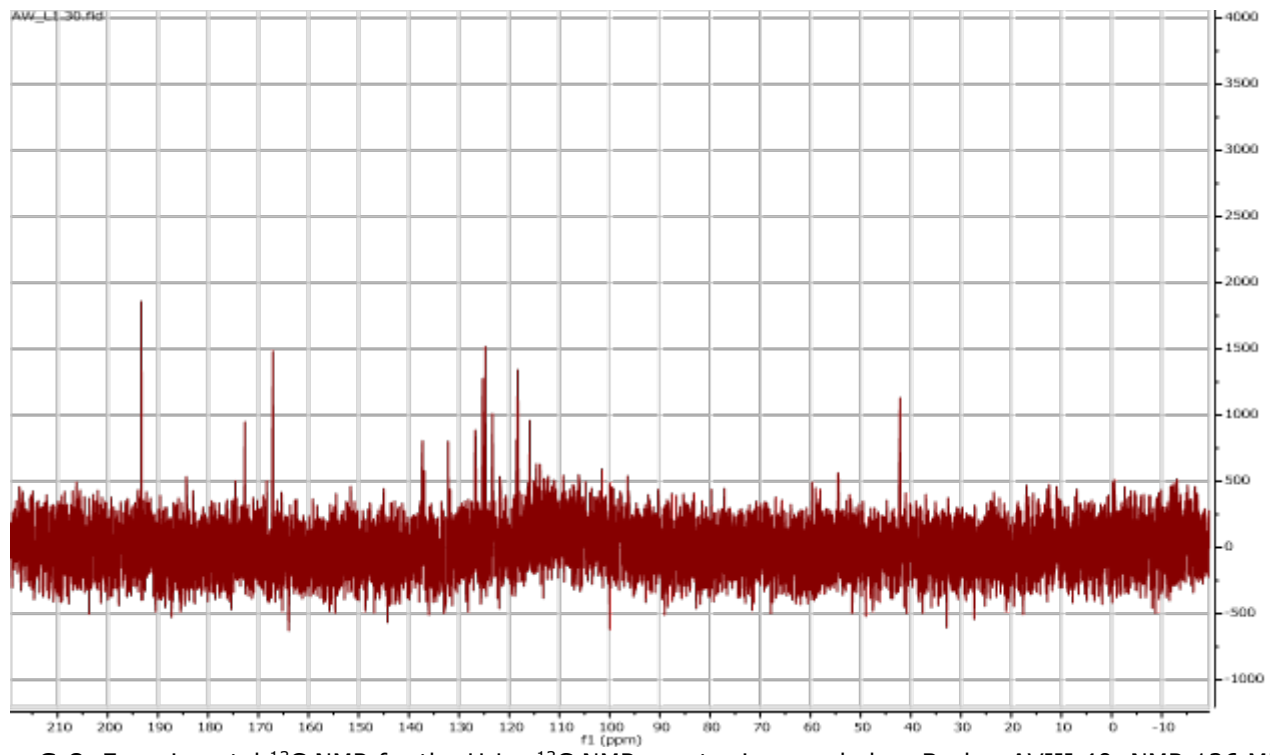


**Figure S-9.** Experimental  $^{13}\text{C}$  NMR for the  $\text{H}_2\text{L}_1$ .  $^{13}\text{C}$  NMR spectra is recorded on Bruker AVIII 40, NMR 126 MHz, US.

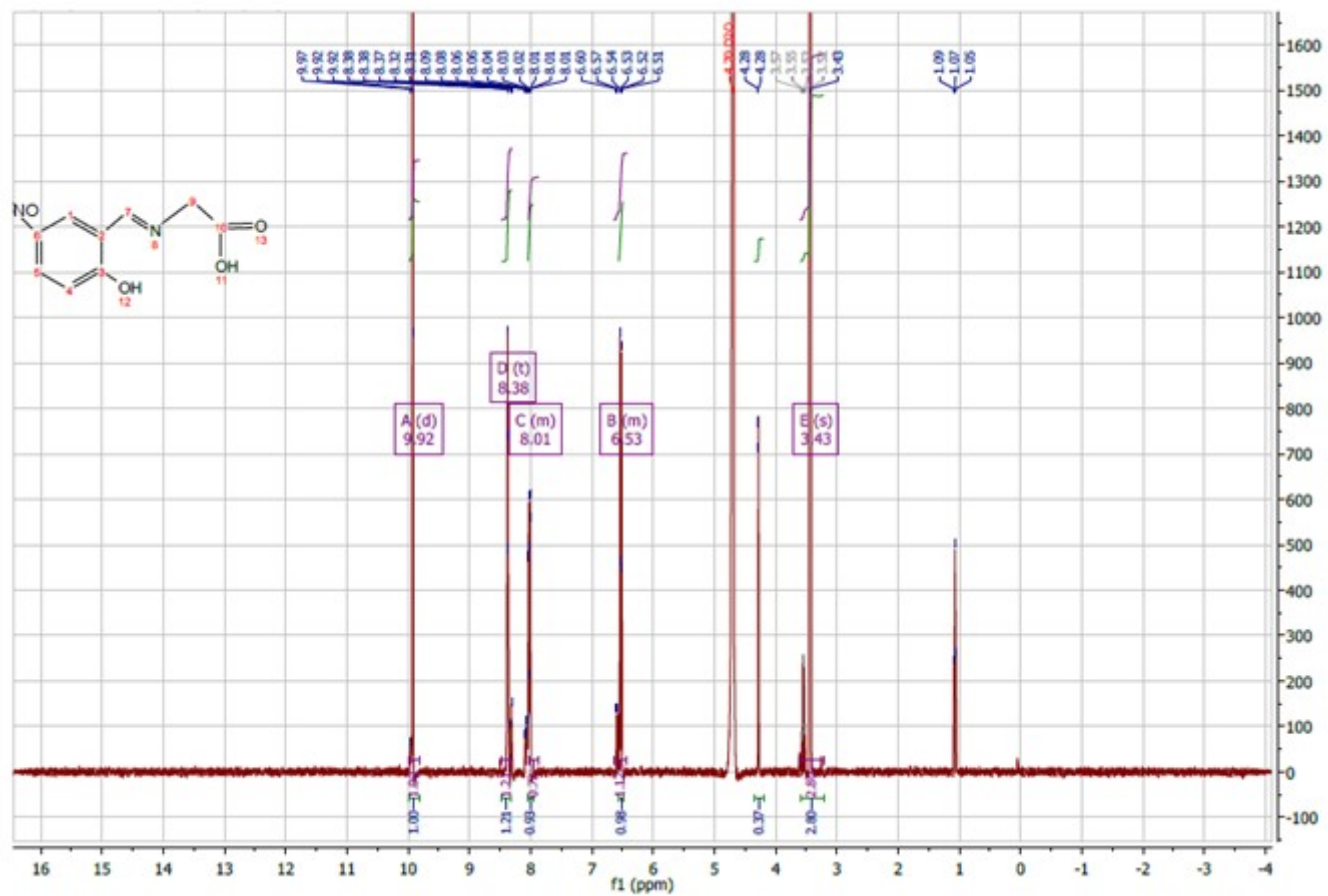


**Figure S-10.** Experimental  $^1H$  NMR for the  $H_2L_2$ .  $^1H$  NMR spectra is recorded on Bruker AVIII 40, 500 MHz, US.

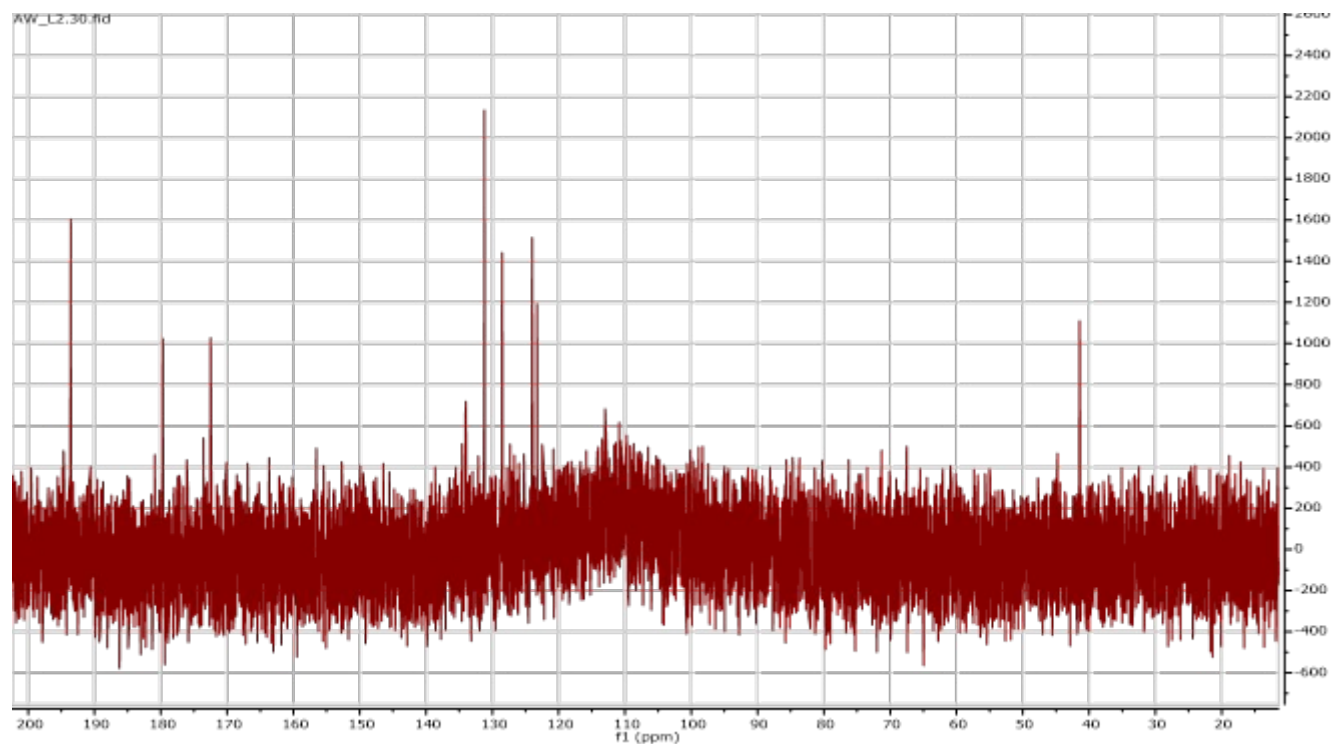


**Figure S-11.** Experimental  $^{13}\text{C}$  NMR for the  $\text{H}_2\text{L}_2$ .  $^{13}\text{C}$  NMR spectra is recorded on Bruker AVIII 40, NMR 126 MHz, US.



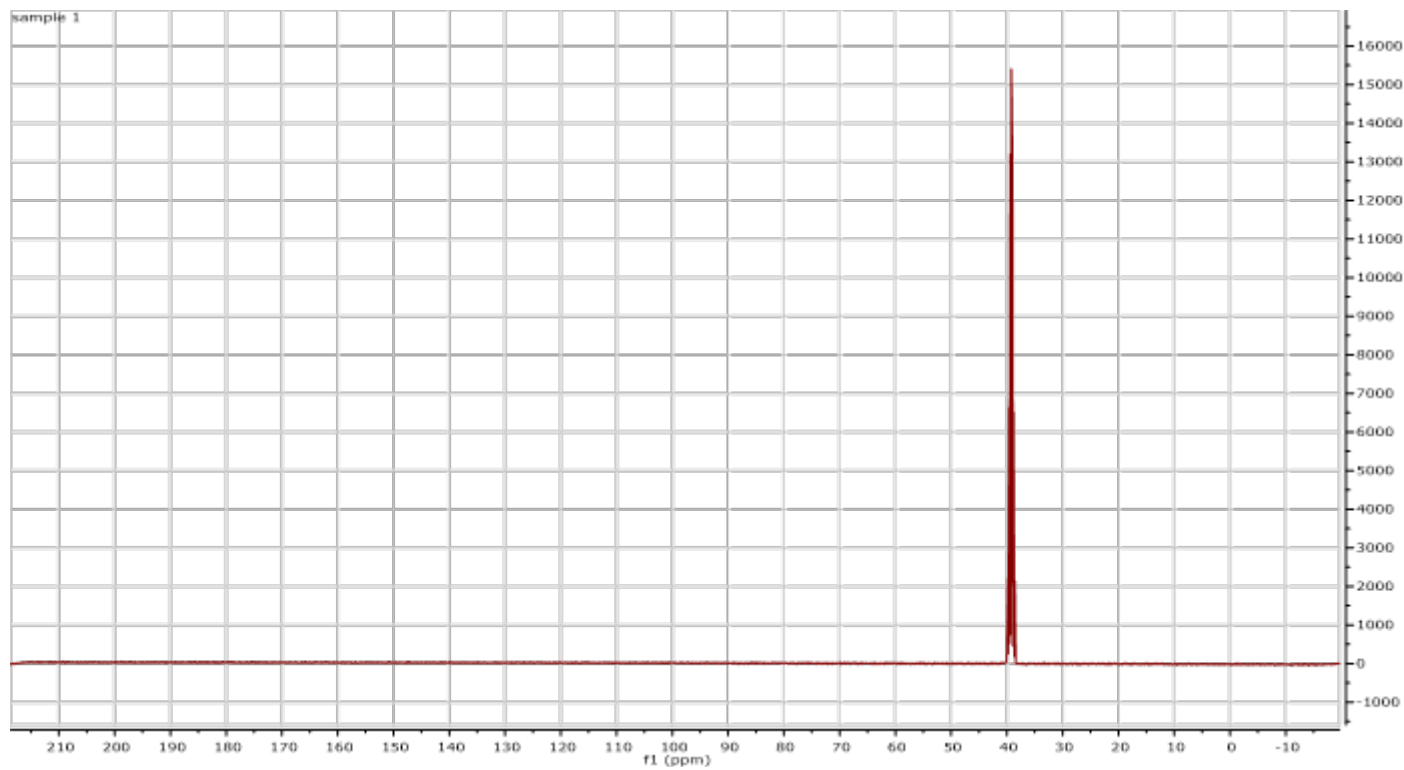


**Figure S-12.** Experimental  $^1\text{H}$  NMR for the VOL<sub>1</sub>.  $^1\text{H}$  NMR spectra is recorded on Bruker AVIII 40, 500 MHz, US.

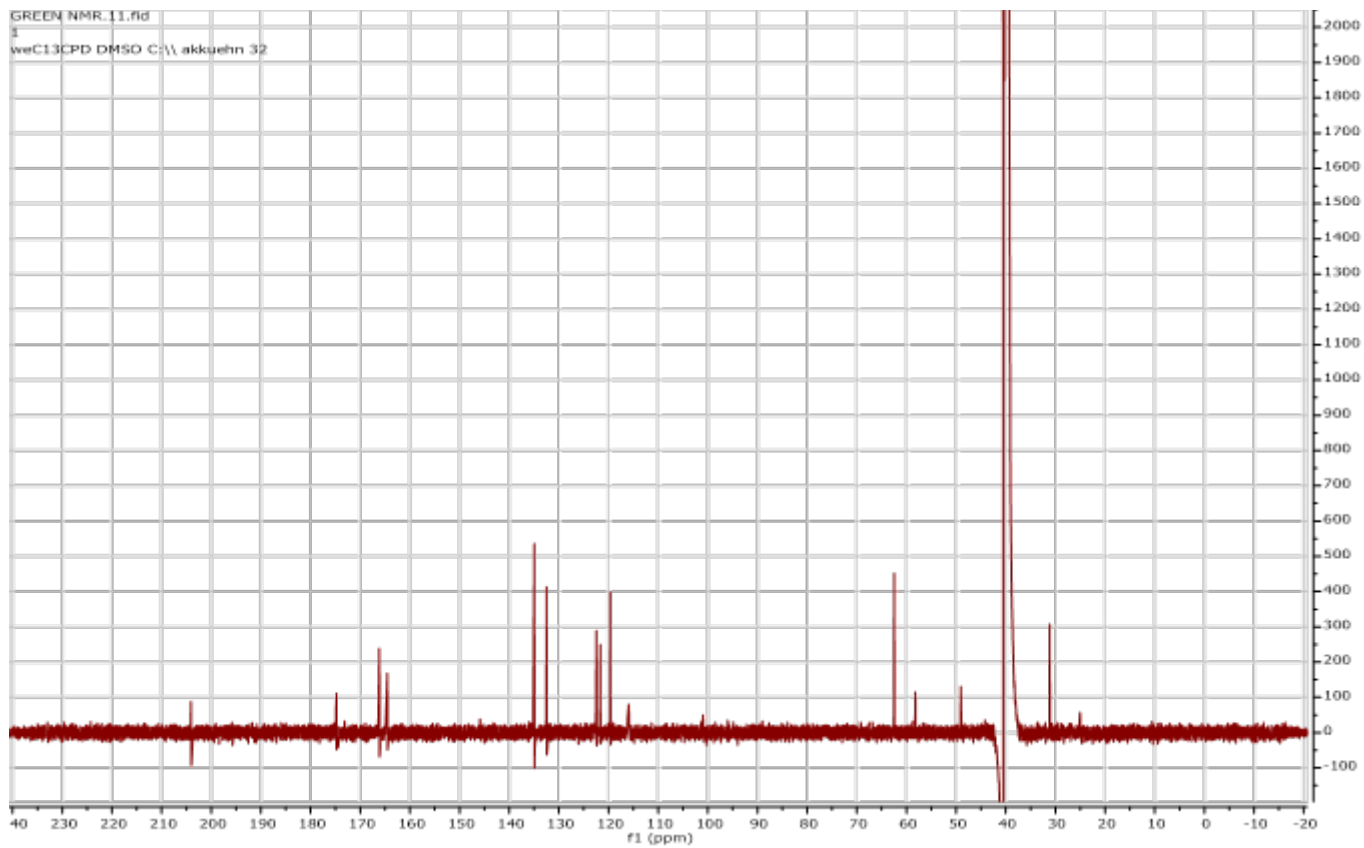


**Figure S-13.** Experimental <sup>13</sup>C NMR for the VOL<sub>1</sub>. <sup>13</sup>C NMR spectra is recorded on Bruker AVIII 40, NMR 126 MHz, US.

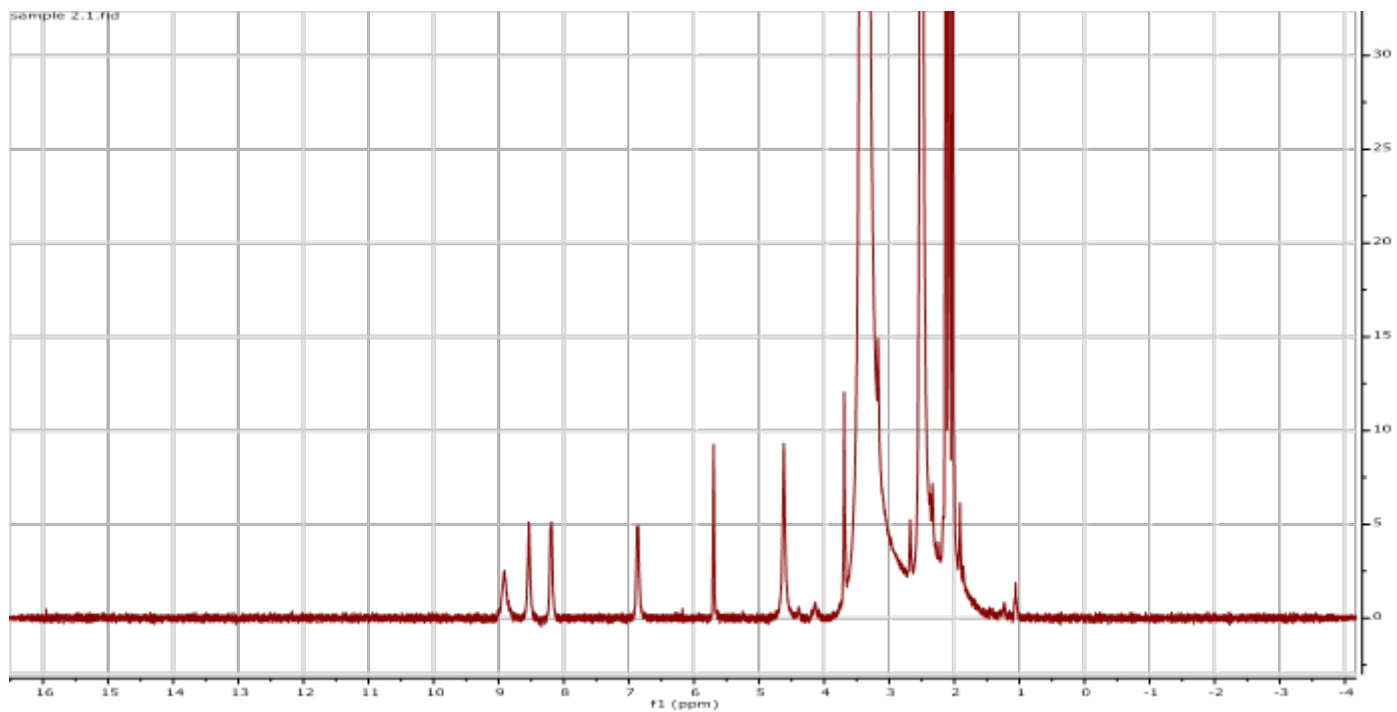


**Figure S-14.** Experimental  $^1\text{H}$  NMR for the VOL<sub>2</sub>.  $^1\text{H}$  NMR spectra is recorded on Bruker AVIII 40, 500 MHz, US.

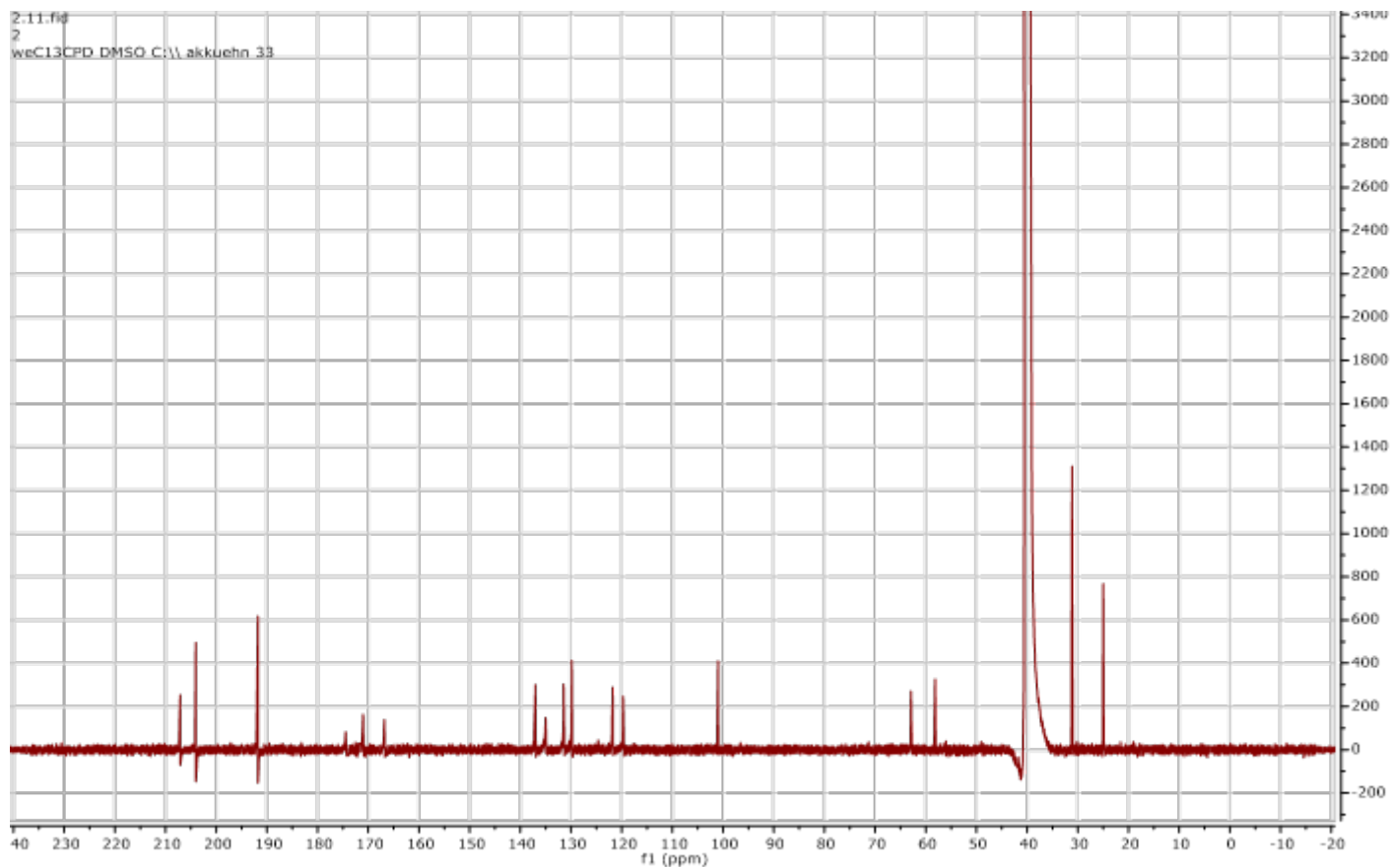


**Figure S-15.** Experimental  $^{13}\text{C}$  NMR for the VOL<sub>2</sub>.  $^{13}\text{C}$  NMR spectra is recorded on Bruker AVIII 40, NMR 126 MHz, US.

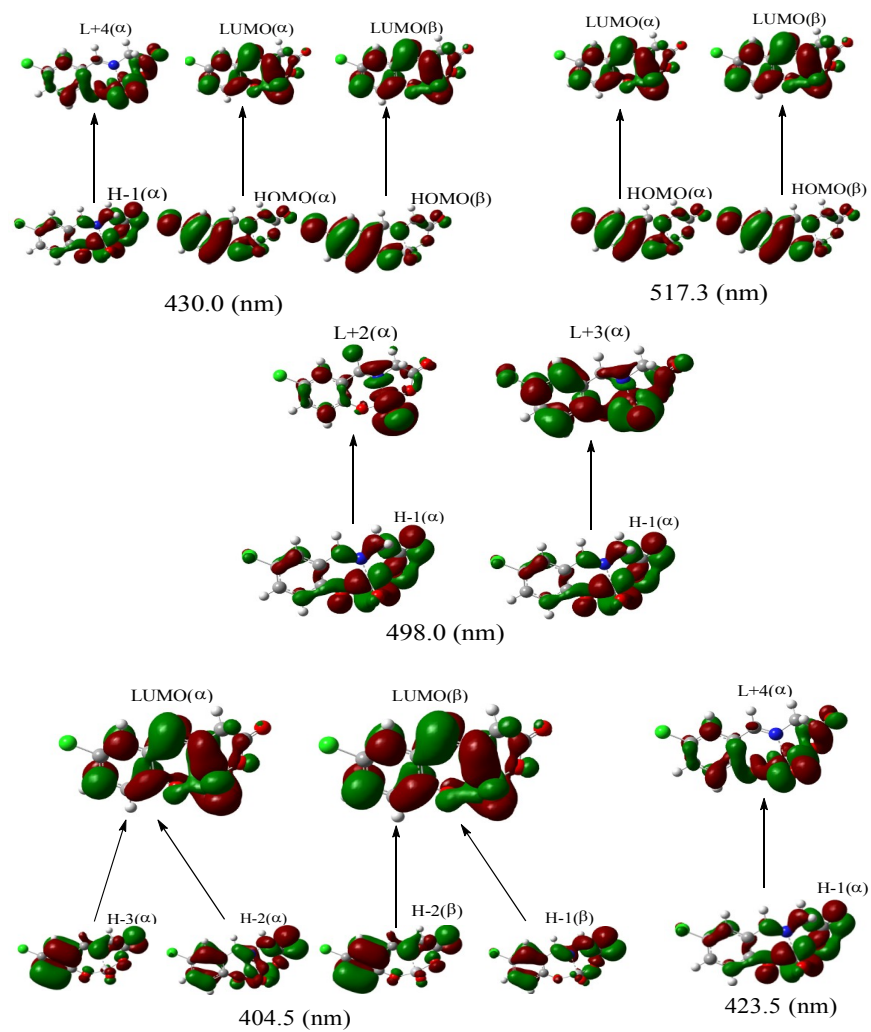


**Figure S-16.** Schematic representation of the main orbital contributions to the TD-DFT/6-31+G(d,p) calculated excitations for the VOL<sub>1</sub> complex.

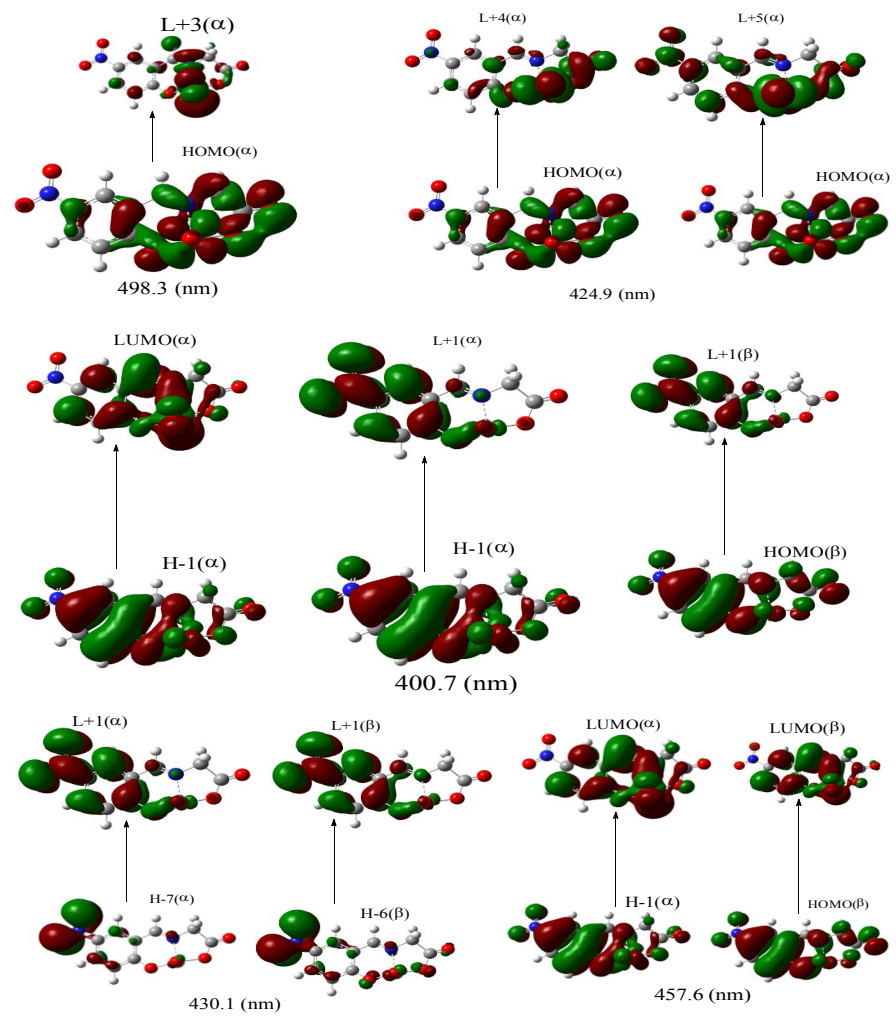


**Figure S-17.** Schematic representation of the main orbital contributions to the TD-DFT/6-31+G(d,p) calculated excitations for the VOL<sub>2</sub> complex.

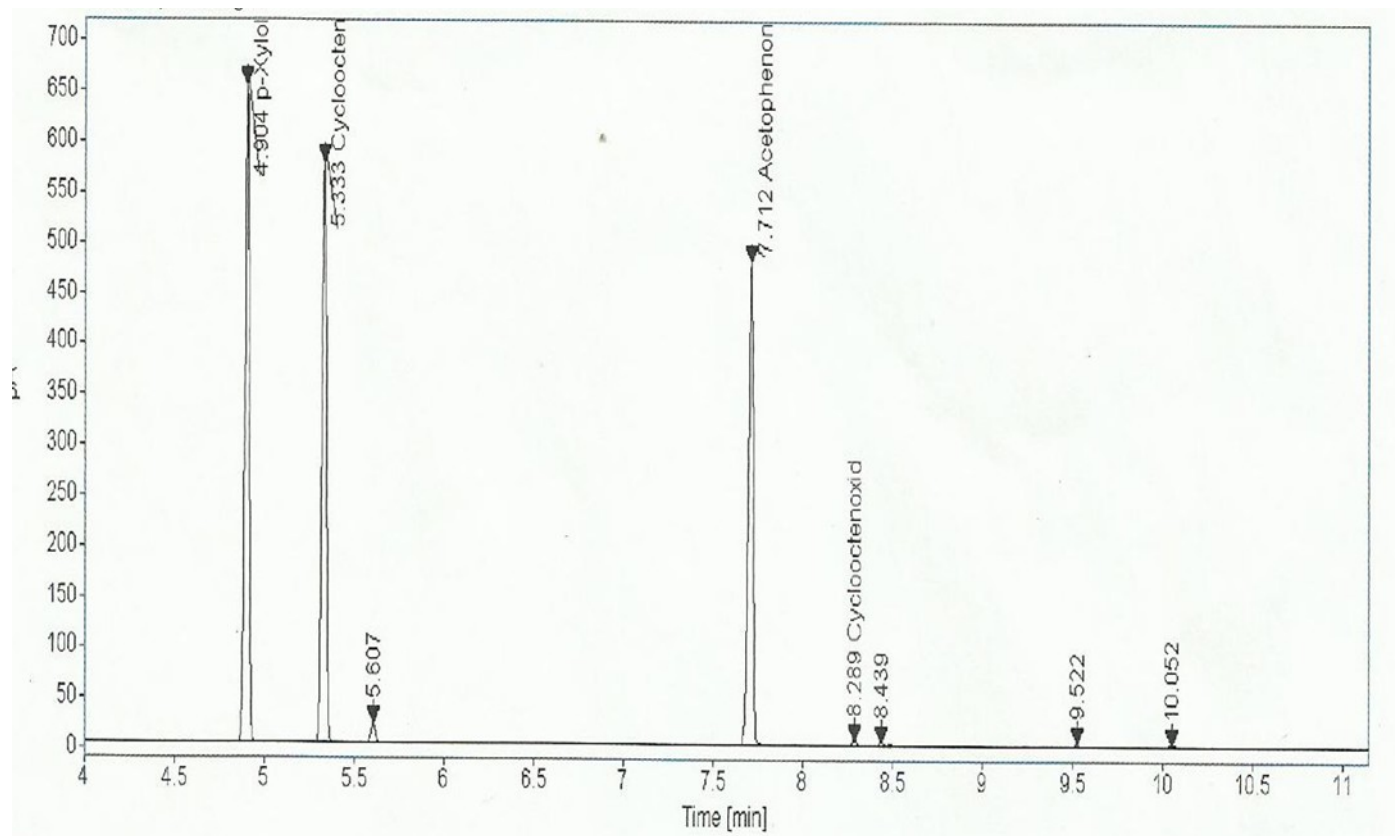


**Figure S-18.** Epoxidation of cyclooctene at 20°C after 2h – complex (VOL<sub>1</sub>). Measured using an Agilent GC Model 7890B and GC column used is Agilent HP-5 with dimensions 0.25 µm.

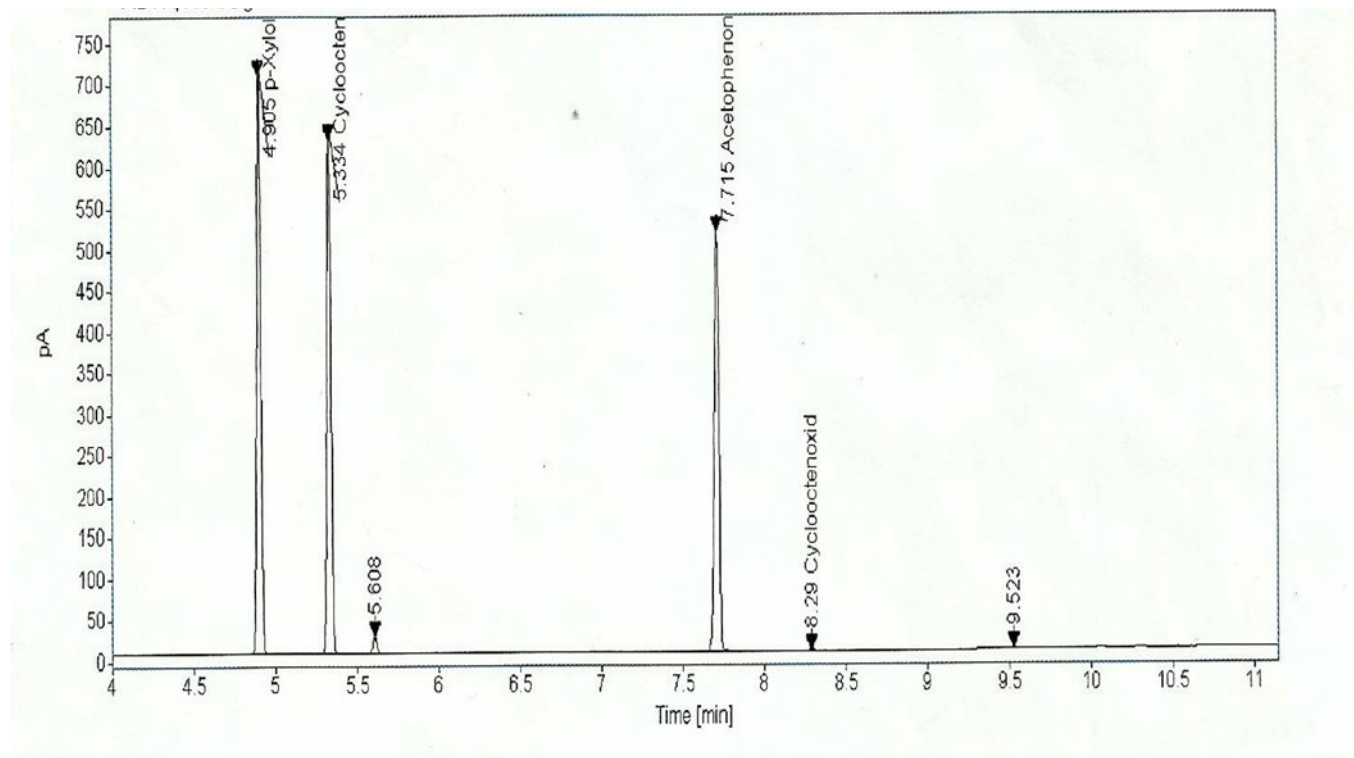


**Figure S-19.** Epoxidation of cyclooctene at 20°C after 4h – complex (VOL<sub>1</sub>). Measured using an Agilent GC Model 7890B and GC column used is Agilent HP-5 with dimensions 0.25 µm.



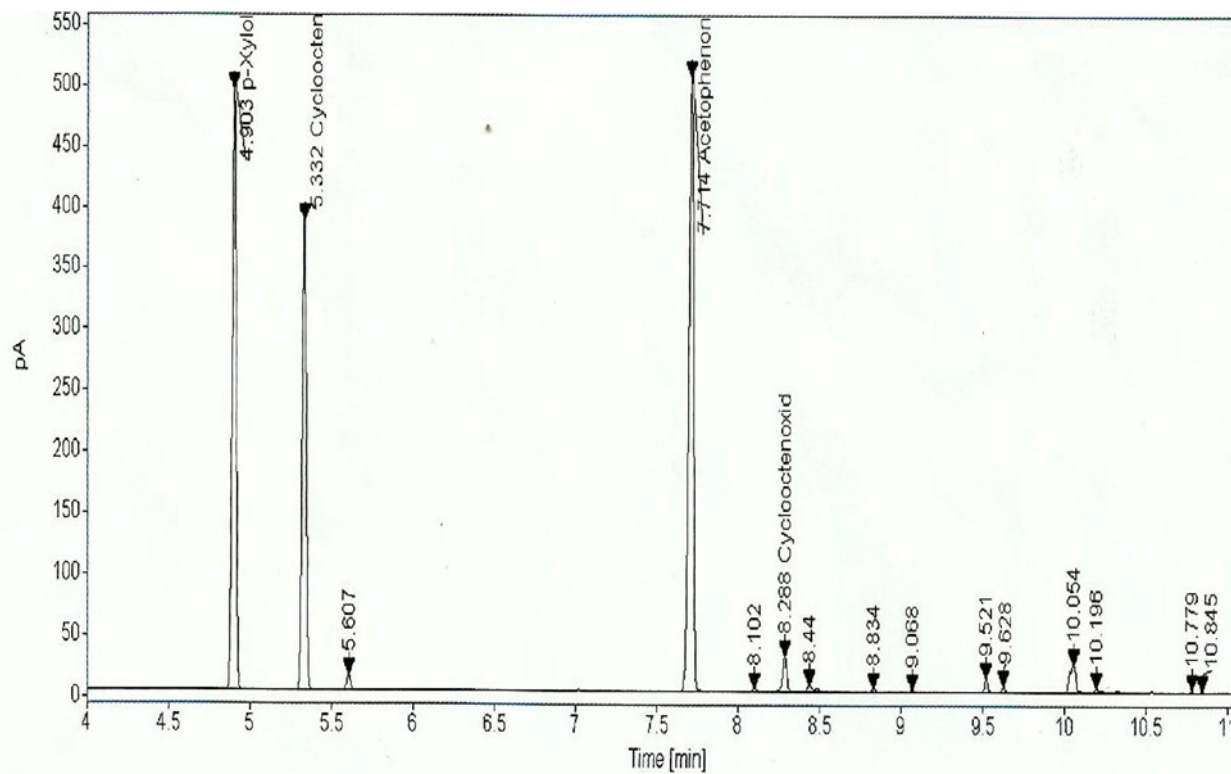


**Figure S-20.** Epoxidation of cyclooctene at 20°C after 10h- complex (VOL<sub>1</sub>). Measured using an Agilent GC Model 7890B and GC column used is Agilent HP-5 with dimensions 0.25 µm.

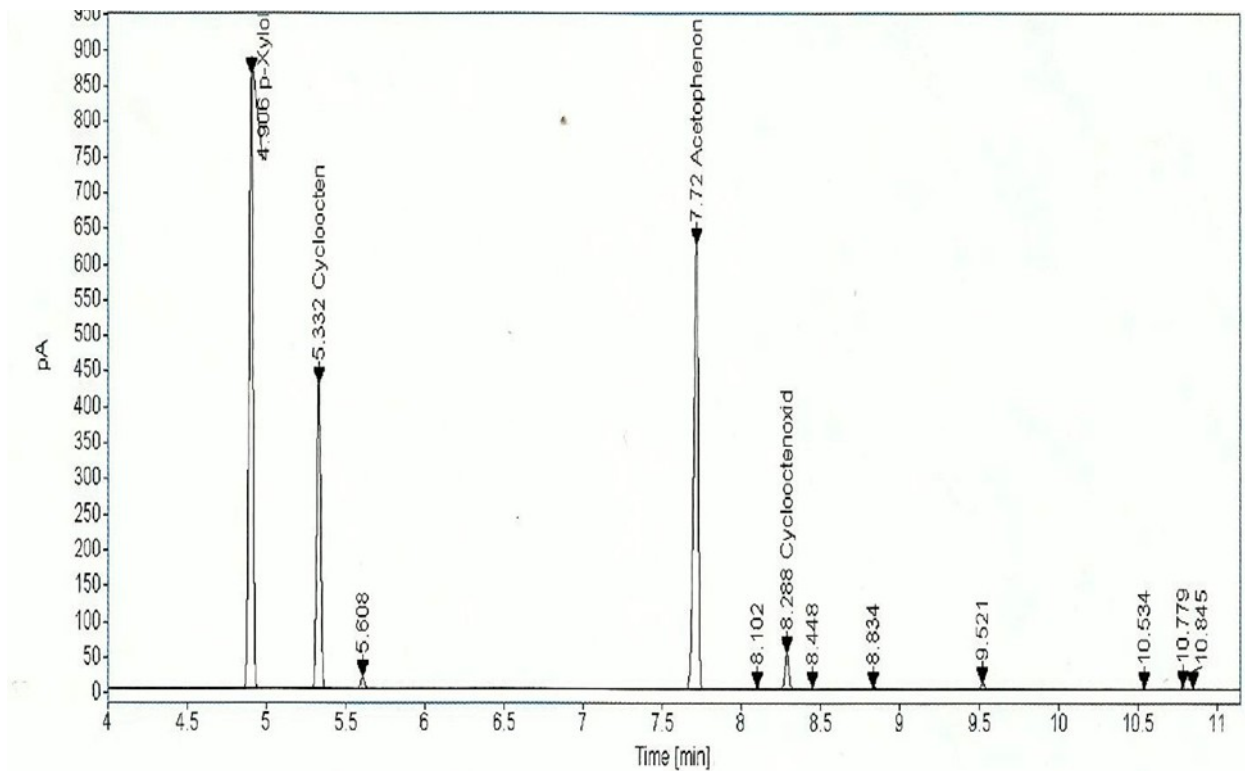


**Figure S-21.** Epoxidation of cyclooctene at 60°C after 2h – complex (VOL<sub>1</sub>). Measured using an Agilent GC Model 7890B and GC column used is Agilent HP-5 with dimensions 0.25 µm.

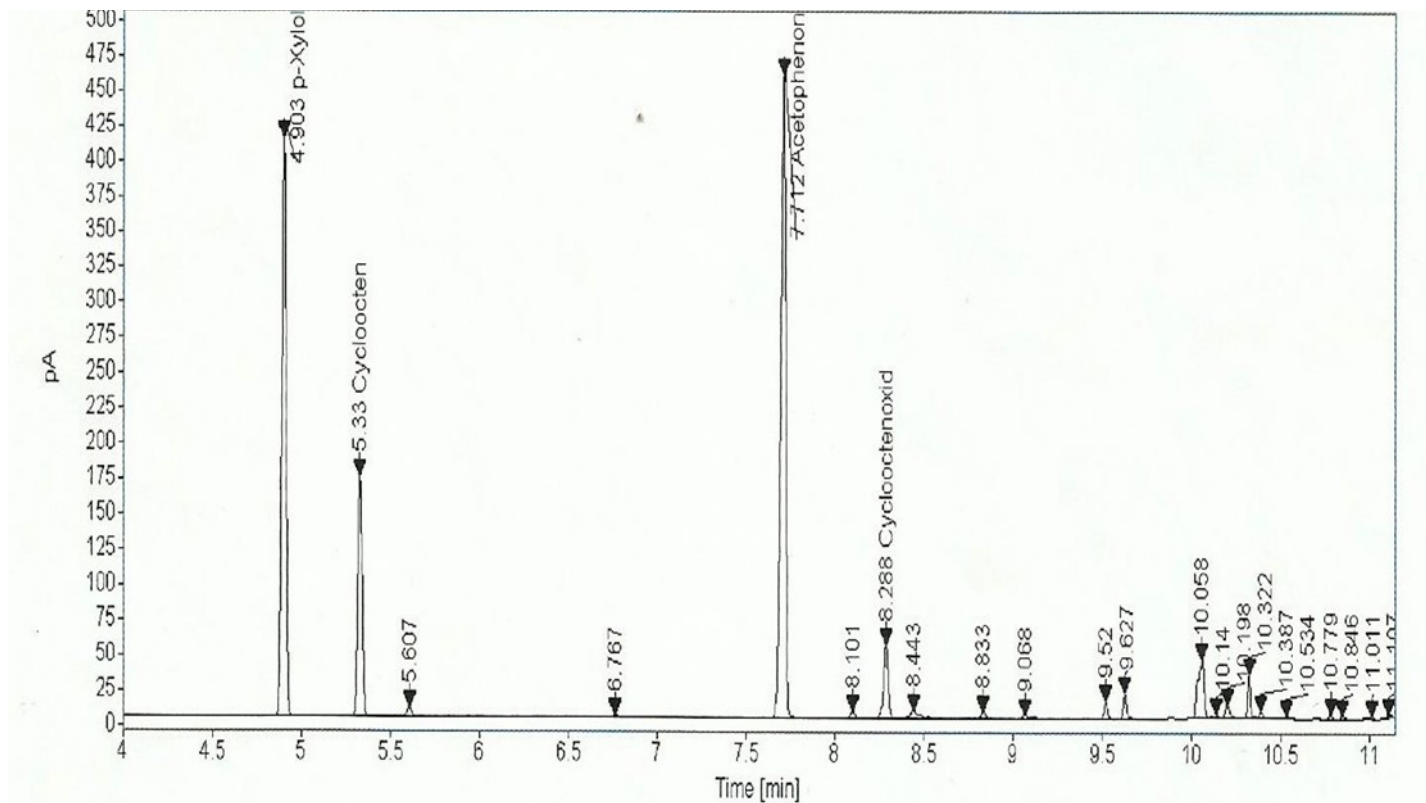


**Figure S-22.** Epoxidation of cyclooctene at 60°C after 4h - complex (VOL<sub>1</sub>). Measured using an Agilent GC Model 7890B and GC column used is Agilent HP-5 with dimensions 0.25 µm.

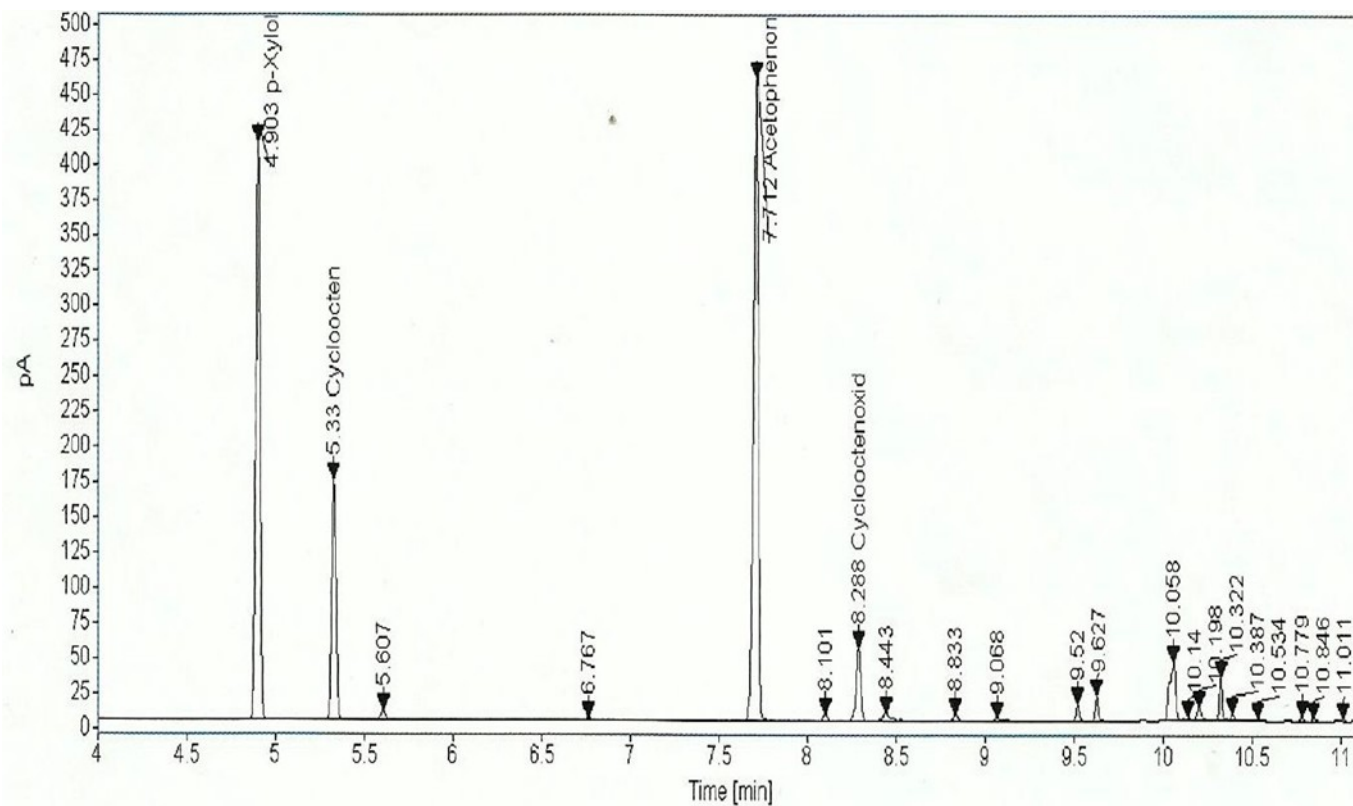


**Figure S-23.** Epoxidation of cyclooctene at 60°C after 10h – complex (VOL<sub>1</sub>). Measured using an Agilent GC Model 7890B and GC column used is Agilent HP-5 with dimensions 0.25 µm.

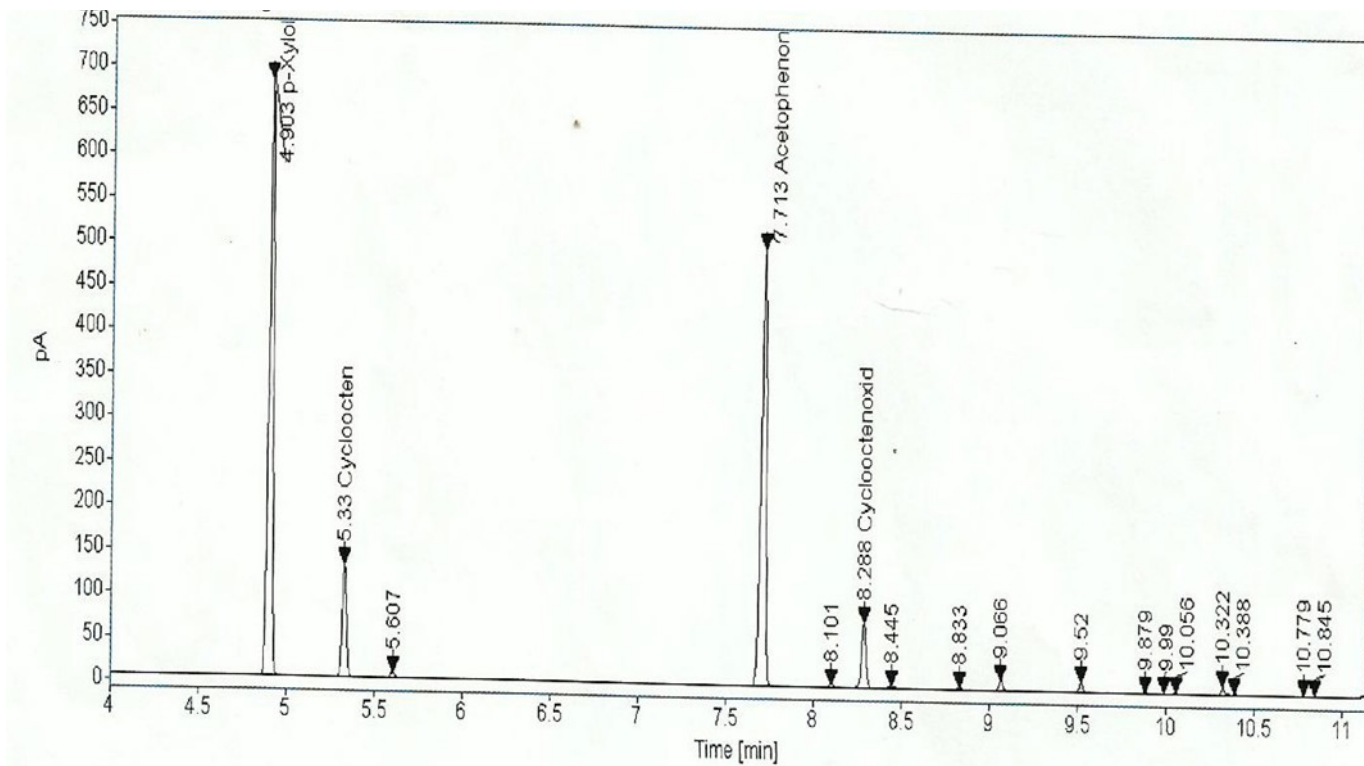


**Figure S-24.** Epoxidation of cyclooctene at 78°C after 2h – complex (VOL<sub>1</sub>). Measured using an Agilent GC Model 7890B and GC column used is Agilent HP-5 with dimensions 0.25 µm.

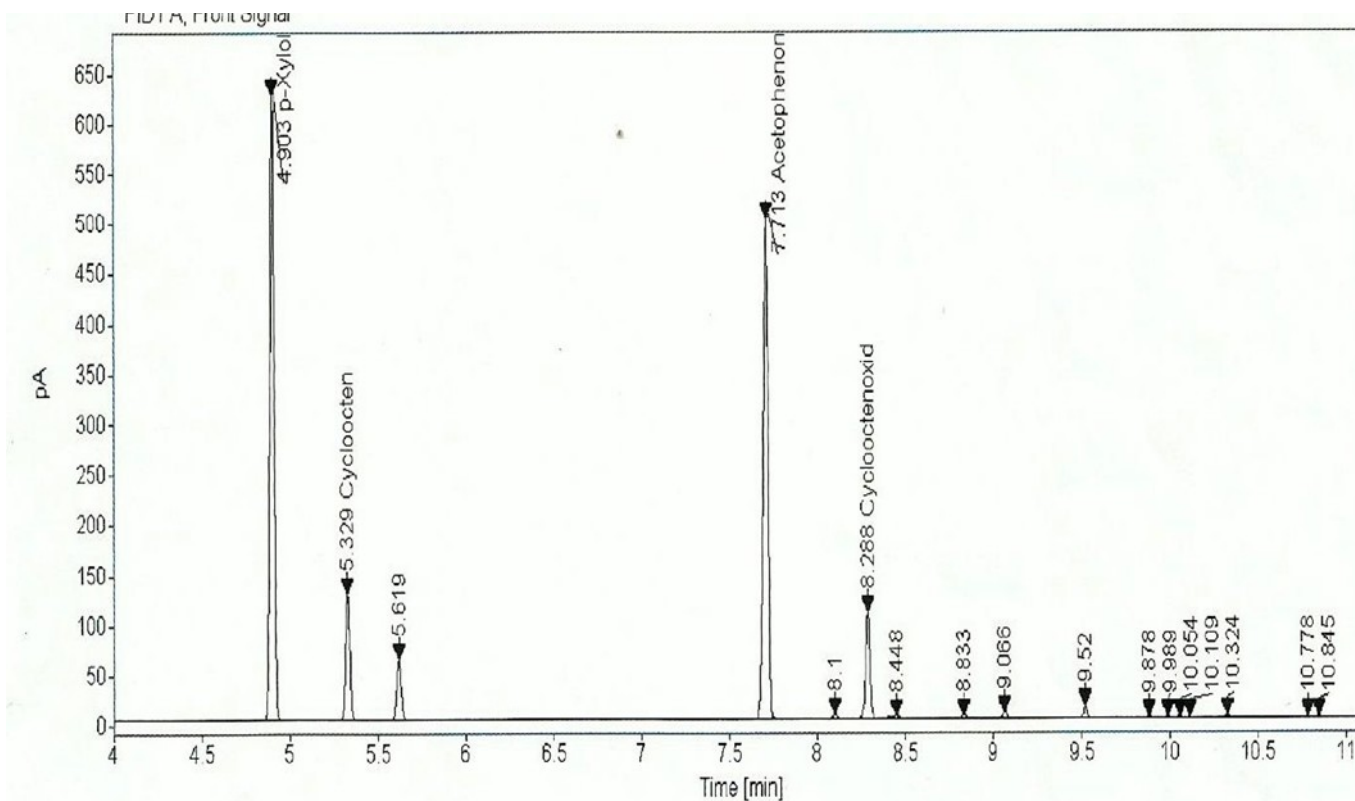


**Figure S-25.** Epoxidation of cyclooctene at 78°C after 4h – complex (VOL<sub>1</sub>). Measured using an Agilent GC Model 7890B and GC column used is Agilent HP-5 with dimensions 0.25 µm.

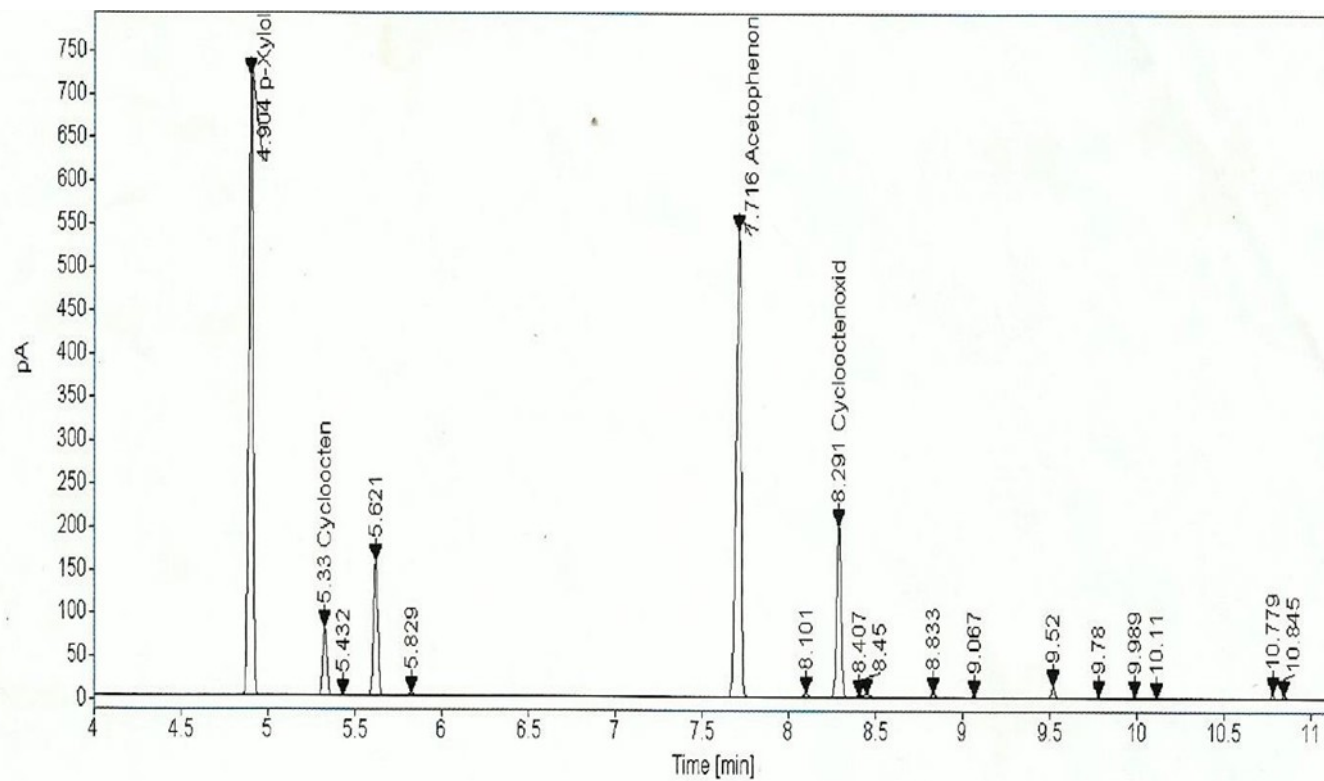


**Figure S-26.** Epoxidation of cyclooctene at 78°C after 10h - complex (VOL<sub>1</sub>). Measured using an Agilent GC Model 7890B and GC column used is Agilent HP-5 with dimensions 0.25 µm.





## Box Behnken Design in the Optimization of Rhodamine B Adsorption onto Activated Carbon Prepared from *Delonix regia* Seeds and Pods

Samsudeen Olanrewaju Azeez<sup>1\*</sup> , Ismaila Olalekan Saheed<sup>1</sup> ,  
Folahan Amoo Adekola<sup>2</sup> , Akeem Adebayo Jimoh<sup>1</sup> , David Morakinyo Aransiola<sup>1</sup>   
and Zuliah A. Abdulsalam<sup>1</sup> 

<sup>1</sup>Kwara State University, Faculty of Pure and Applied Sciences, Department of Chemistry and Industrial Chemistry, 241103, Malete, Nigeria.

<sup>2</sup>University of Ilorin, Faculty of Physical Sciences, Department of Industrial Chemistry, 240003, Ilorin, Nigeria

**Abstract:** The uptake of Rhodamine B (RhB) dye onto chemically prepared activated carbon from *Delonix regia* pods (DPAC) and seeds (DSAC) by response surface methodology was investigated. The activated carbons were prepared with 1 M nitric acid and characterized by BET FTIR, SEM and EDX. The results obtained revealed that the prepared activated carbons DPAC and DSAC with pore diameter 4.04 nm and 3.48 nm respectively possess mesoporous structures. Optimization of the four operating variables viz; concentration, adsorbent dosage, contact time, and pH on RhB adsorption were examined using Box Behnken design (BBD). The maximum removal efficiency of RhB from aqueous solution was achieved at 99.16% and 98.36% for DSAC and DPAC respectively with an initial RhB concentration of 55 mg/L, 0.1 g dosage, pH 12, and 725 min for both adsorbents. The actual values of 99.16% (DSAC) and 98.36% (DPAC) compared with predicted values 101.7% (DSAC) and 99.40% (DPAC) have a good agreement and this confirms the suitability of the proposed model. The adsorption process fitted best into the Freundlich isotherm model. The adsorption process was adequately described by the pseudo-second-order kinetics model. Intra-particle diffusion appears to control the adsorption process but is not the only rate-limiting step.

**Keywords:** *Delonix regia*, Activated carbon, Box Behnken Design, Adsorption isotherm, Rhodamine B

**Submitted:** March 15, 2021. **Accepted:** January 07, 2022.

**Cite this:** Azeez SO, Saheed IO, Adekola FA, Jimoh AA, Aransiola DM, Abdulsalam ZA. Box Behnken Design in the Optimization of Rhodamine B Adsorption onto Activated Carbon Prepared from *Delonix regia* Seeds and Pods. JOTCSA. 2022;9(1):209–26.

**DOI:** <https://doi.org/10.18596/jotcsa.893472>.

**\*Corresponding author. E-mail:** [samsudeen.azeez@kwasu.edu.ng](mailto:samsudeen.azeez@kwasu.edu.ng).

### INTRODUCTION

Out of several synthetic dyes, rhodamine B remains one of the prominent, unavoidably dangerous, and more functional organic dyes used largely in textile and paper industries. It is applied in the cell membrane and water tracing studies (1). This is as a result of its high water solubility and photo-stability. However, it creates a severe environmental problem due to its toxicity to human

and aquatic lives when discharged into the environment. The presence of this dye in water bodies decreases light penetration and thus disrupts the photosynthetic processes (2,3). In extreme cases, it causes cancer (4,5). Consequently, it is imperative to treat wastewater containing this dye before its release into the environment for human and aquatic safety. Many treatment methods had been put into consideration for the removal of dyestuff from



wastewater such as oxidation (6), photochemical degradation (7), electrochemical degradation (8), and membrane separation (9). Though most of the aforementioned treatment methods for separating dyes from dye-containing wastewater have great limitations which include exorbitant, less effectiveness, production of toxic materials, and high energy demands (10). However, adsorption as a treatment technique employing activated carbon is immensely gaining worldwide acceptance for removing dyes and other organic pollutants from aqueous solutions owing to its ease of operation, low cost, simple design, and regeneration (11,12). Furthermore, there has been much interest in the creation of new and more effective materials for organic pollutants removal knowing that commercial activated carbon which is the most extensively used adsorbent is expensive (13). Hence there is a need for the evolution of natural, more accessible, and low-priced activated carbon adsorbents from agricultural wastes such as *Delonix regia* pods and seeds for dye removal.

*Delonix regia*, a flame tree also known as flamboyant tree aboriginal to Madagascar but commonly planted in the tropics. It is a flowering plant belonging to the Fabaceae family and subfamily Caesalpinioideae. It is grown as an ornamental tree in parks, gardens, school compounds, and residential for shades and shelter. In English, it is regarded as Royal Poinciana or Flamboyant also called Pansheke in the Yoruba language which is one of the major tribes in Nigeria. The pods and seeds of *Delonix regia* are non-edible and as such regarded as agricultural wastes except for the aesthetic purposes of the tree (14).

The optimization parameters were designed based on the factorial design of experiments and analyzed statistically. The experimental design technique is a useful tool to study biodegradation and adsorption because it provides statistical models that help in elucidating the interactions among the parameters that have been optimized (15,16). Furthermore, they are important for systematic investigations which require a few experiments and also help to interpret results meaningfully. Response surface methodology (RSM) is a factorial design based on the statistical analyzing method. It is used for designing experiments, studying the effective factors, and searching for the optimum conditions (17,18). The most commonly used designs in RSM are Box Behnken design (BBD) and Central Composite Design (CCD). However, BBD is agreed to be an effective and efficient design in RSM to CCD (19). This model was widely accepted in industries such as the food and drug industry, biological and chemical processes, enhancing the production of quality products and reduction in the cost of the

operation (16,20). This technique has been usefully employed in many operating processes for achieving its optimization. The basis of this investigation is to prepare and characterize a low-cost activated carbon from *Delonix regia* pods and seeds via acid treatment and its employment in the adsorption of Rhodamine B in aqueous media using Box Behnken Design (BBD) in response surface methodology (RSM) to optimize the operating parameters such as concentration, pH, adsorbent dosage and contact time.

## EXPERIMENTAL SECTION

### Chemicals and Apparatus

The reagents and chemicals for this experiment were of analytical grade and used directly with no further purifications. Rhodamine B was purchased from BDH (Prolabo, Leuven Belgium), sodium hydroxide (NaOH), nitric acid (HNO<sub>3</sub>, ≥90.0%), hydrochloric acid (HCl, 37%) were all supplied by Sigma Aldrich, USA. The apparatus used are BET surface area analyzer (Micromeritics ASAP 2020 V3.02H model, Norcross, GA, U.S.A), UV/Visible spectrophotometer (Bechman Coulter DU 730 Pasadena, CA, USA), Perkin-Elmer Spectrum GX-FTIR Spectrometer (version 10.6 0, TU, Dublin), SEM/EDX ASPEX 3020 model (Delmont, PA 15626-1723-USA).

### Sample collection and preparation of Adsorbent

The *Delonix regia* pods and seeds were obtained from Kwara State University, Malete, Nigeria. The seeds were separated from the pods, handpicked to remove sands, and washed thoroughly to remove dust particles. Then sundried, and the pods crushed into smaller sizes. The seeds and pods of *Delonix regia* were carbonized separately at the temperature of 500 °C and 400 °C respectively for 180 min. Activation of the carbonized products was done after pulverizing using nitric acid: which involves impregnating 100 g of both the carbonized seeds and pods into 500 mL of 1 M HNO<sub>3</sub> in a separate beaker and stirring for 24 h. The resulting activated carbon was filtered and washed with deionized water to neutrality and dried in the oven at 110 °C to remove all moisture components. Thereafter, the *Delonix regia* seeds activated carbon (DSAC) and *Delonix regia* pods activated carbon (DPAC) were ground and sieved into < 63 μm mesh size (21).

### Characterization of the adsorbents

The surface area of the adsorbents (DSAC and DPAC) was determined by Brunauer, Emmett and Teller (BET) analysis of N<sub>2</sub> adsorption at 77 K by the use of Micromeritics ASAP 2020 V3.02H model. The functional groups present on the adsorbents were investigated by Fourier Transform Infrared Spectrometer (Perkin-Elmer Spectrum GX). The

morphologies and elemental composition of DSAC and DPAC were analyzed using SEM, ASPEX 3020 model for SEM and EDX respectively.

### Preparation of adsorbate

A 1000 mg/L of rhodamine B dye (RhB) stock solution was prepared by dissolving 1 g of the dye in 1 L of deionized water in a standard volumetric flask. The working solutions were then prepared from the stock via serial dilution (11).

### Adsorption experiments

The batch adsorption method was used to investigate the initial RhB dye concentration, effects of pH, contact time, and adsorbent dosage. The experiment entails the addition of 0.1 g of DSAC and DPAC to 20 mL of RhB solution of desired concentrations in a 100 mL conical flask and placed in a temperature-controlled water bath shaker. The solutions were agitated for 2 h at a temperature of  $28 \pm 2$  °C and a speed of 180 rpm. 0.1 M HCl and 0.1 M NaOH solutions were used to control the pH of the solution. The resultant mixture was then centrifuged and filtered. Thereafter, the change in concentration of the RhB solution was monitored using a UV/Visible spectrophotometer (Bechman Coulter DU 730 Pasadena, CA, USA) operated at a maximum wavelength ( $\lambda_{max}$ ) of 554 nm. The influence of operational parameters such as contact time, pH, and adsorbent dosage was studied. The % of RhB removed was measured by Equation 1 (11,21).

$$\%adsorbed = \frac{(C_0 - C_e)}{C_0} \times 100 \quad (\text{Eq. 1})$$

where,  $C_0$  = initial RhB dye concentration (mg/L) and  $C_e$  = equilibrium RhB dye concentration (mg/L).

### Optimization of operating parameters of the adsorption process

The optimization experimental parameters of the adsorption process of RhB by activated carbon prepared from DSAC and DPAC were ascertained by Box Behnken Design (BBD) under response surface methodology (RSM). The design was employed to generate sets of designed experiments using Design Expert 11.1.2.0 with four factors; concentration (A), adsorbent dosage (B), pH (C), and contact time (D) based on a four-level full or fractional factorial design with an incomplete block design of experiments and were analyzed statistically. Comprehensively, specific numbers of factors are fixed in between all combinations in each design block, but other factors are kept at the central values (16,17). The BBD has four variables which were varied at two levels that is, low (-1) and high (+1) with 29 experimental runs. The responses were presented as the adsorption efficiency (%). Table 1 and 2 shows the experimental runs and variables. The experimental data were analyzed and fit the quadratic model which describes the nature of the process as expressed by the empirical equation in Equation 2.

$$H = \beta_0 + \sum_{i=1}^k \beta_i x_i + \sum_{i=1}^k \beta_{ii} x_i^2 + \sum_{1 \leq i < j \leq k} \beta_{ij} x_i x_j + \epsilon \quad (\text{Eq. 2})$$

Where,  $H$  is the response;  $x_i$  = variables;  $k$  = number of variables;  $\beta_0$  = constant term;  $\beta_i$  = coefficients of linear parameters,  $\beta_{ij}$  = coefficient of the interaction parameters;  $\beta_{ii}$  = coefficient of the quadratic parameter;  $\epsilon$  = residual associated to the experiments.

**Table 1:** Box Behnken Design and its Actual and Predicted Values for DSAC.

Experimental run	Independent variables				Response (%)	
	(A) Concentration (mg/L)	(B) Dose (g)	(C) Time (min)	(D) pH	Actual removal	Predicted removal
1	100	0.4	725	12	98.70	98.96
2	55	0.4	1440	12	98.50	97.16
3	55	0.4	10	2	89.51	90.64
4	55	0.4	725	7	97.85	98.05
5	55	0.7	725	2	94.40	92.47
6	100	0.4	1440	7	98.50	97.23
7	10	0.4	725	12	87.91	87.80
8	55	0.4	725	7	98.00	98.05
9	55	0.7	725	12	95.85	95.25
10	10	0.4	10	7	79.63	81.51
11	55	0.4	1440	2	97.85	98.40
12	100	0.7	725	7	94.30	95.23

13	55	0.1	1440	7	99.05	99.42
14	55	0.4	10	12	97.12	96.36
15	55	0.1	10	7	99.12	96.71
16	10	0.7	725	7	79.83	80.18
17	10	0.4	725	2	85.93	85.27
18	100	0.4	10	7	92.25	93.18
19	100	0.1	725	7	99.18	98.61
20	55	0.1	725	12	99.16	101.70
21	55	0.7	10	7	88.93	88.16
22	55	0.4	725	7	97.97	98.05
23	10	0.1	725	7	91.90	90.76
24	55	0.4	725	7	98.65	98.05
25	55	0.7	1440	7	92.00	94.01
26	55	0.1	725	2	98.78	99.99
27	10	0.4	1440	7	86.33	86.01
28	100	0.4	725	2	97.30	97.01
29	55	0.4	725	7	97.77	98.05

**Table 2:** Box Behnken Design and its Actual and Predicted Values for DPAC.

Experimental runs	Independent variables				Response (%)	
	(A) Concentration (mg/L)	(B) Dose (g)	(C) Time (min)	(D) pH	Actual removal	Predicted removal
1	100	0.4	725	12	97.25	95.99
2	55	0.4	1440	12	97.57	96.75
3	55	0.4	10	2	92.42	91.40
4	55	0.4	725	7	97.08	97.14
5	55	0.7	725	2	90.23	89.30
6	100	0.4	1440	7	97.77	97.91
7	10	0.4	725	12	88.80	89.16
8	55	0.4	725	7	97.93	97.14
9	55	0.7	725	12	88.97	90.51
10	10	0.4	10	7	82.33	82.30
11	55	0.4	1440	2	97.60	96.61
12	100	0.7	725	7	96.08	95.59
13	55	0.1	1440	7	98.02	99.54
14	55	0.4	10	12	95.85	94.99
15	55	0.1	10	7	95.88	96.72
16	10	0.7	725	7	78.85	77.61
17	10	0.4	725	2	79.00	82.00
18	100	0.4	10	7	96.62	97.47
19	100	0.1	725	7	98.58	97.97
20	55	0.1	725	12	98.36	99.40
21	55	0.7	10	7	87.60	87.82
22	55	0.4	725	7	96.95	97.14
23	10	0.1	725	7	93.05	91.70
24	55	0.4	725	7	96.90	97.14
25	55	0.7	1440	7	91.07	91.97
26	55	0.1	725	2	98.32	96.89
27	10	0.4	1440	7	89.58	88.84
28	100	0.4	725	2	98.05	99.42
29	55	0.4	725	7	96.85	97.14

## RESULTS AND DISCUSSION

### Characterization of Adsorbents

#### Surface area determination and elemental analysis

The surface area characteristics of DSAC and DPAC were discovered using Brunauer, Emmett and

Teller (BET) analysis, and their results are depicted in Table 3. The values of the BET surface area for both adsorbents are considerably high, which suggests that DSAC and DPAC possess surface properties that are suitable as adsorbent materials for the uptake of RhB. The result obtained also

showed that the surface area and pore volume of DSAC is higher than that of DPAC with both adsorbents having pore diameter considered to be mesoporous (in the range of 2-50 nm) (22). It is expected that both adsorbents would be good

materials in the sorption of dye. The EDX analysis showed a higher percentage of carbon and a lower oxygen percentage (see Table 3) for both DSAC and DPAC which is a result of the acid treatment.

**Table 3:** Characteristics of DSAC and DPAC.

Adsorbents	DSAC	DPAC
BET Surface area ( $\text{m}^2\text{g}^{-1}$ )	305.00	301.77
Average pore volume ( $\text{cm}^3\text{g}^{-1}$ )	0.18	0.16
Average pore diameter (nm)	3.48	4.04
% C	74.08	79.36
% O	25.79	20.46

### FTIR spectroscopic analysis of DSAC and DPAC

FTIR spectroscopy was used to monitor the adsorption of RhB onto DSAC and DPAC. Figures 1a and 1b show the FTIR spectra of both adsorbent materials before and after adsorption. DSAC spectra before adsorption show a strong absorption peak at  $3436.39\text{ cm}^{-1}$  due to O-H stretching of alcohol (10,23),  $1573.00\text{ cm}^{-1}$  corresponding to C=C of aromatic (23-25),  $1376.56\text{ cm}^{-1}$  attributed to C-O stretching vibration (24). After adsorption, there was a decrease in intensity and shift in adsorption bands to O-H

( $3430.27\text{ cm}^{-1}$ ) and C=C ( $1566.88\text{ cm}^{-1}$ ). In addition, there was a disappearance of C-O stretching vibration, which indicates that the functional group partakes in the adsorption process (11). For DPAC, there were reductions in the intensities and shift of bands from  $3433.92\text{--}3415.87\text{ cm}^{-1}$  (O-H of alcohol),  $1603.56\text{--}1588.46\text{ cm}^{-1}$  (C=C of aromatic),  $1701.62\text{--}1693.10\text{ cm}^{-1}$  (C=O) (23,26,27) and  $1231.74\text{--}1221.39\text{ cm}^{-1}$  (C-O stretching). However a new peak appeared at  $753.76\text{ cm}^{-1}$  (aromatic vibrations), revealing the uptake of RhB by DPAC (11).

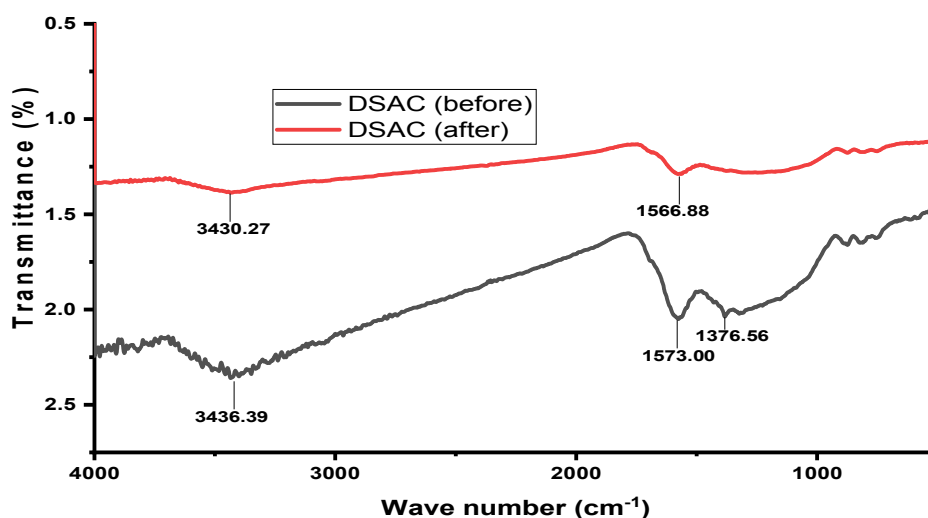


**Figure 1a:** FTIR spectra of DSAC (before and after adsorption).

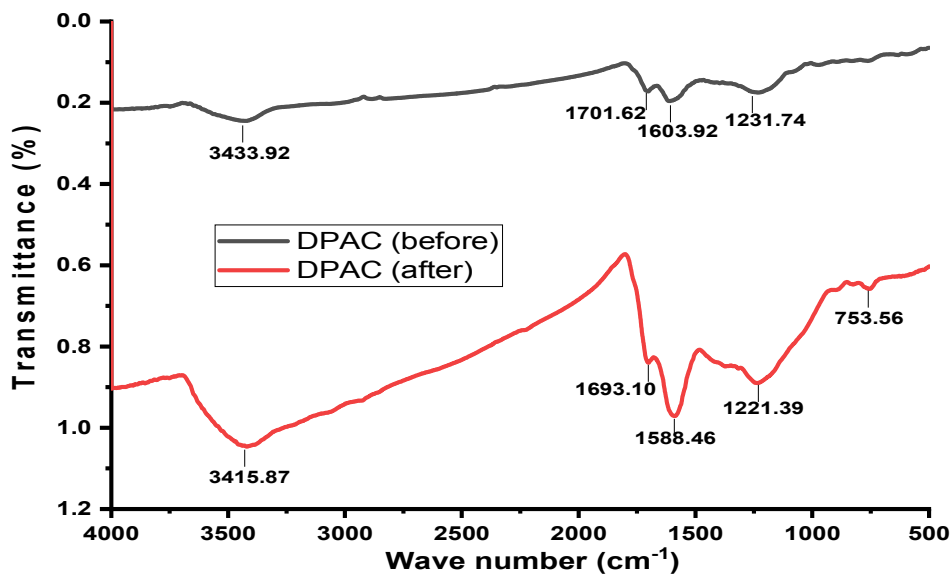
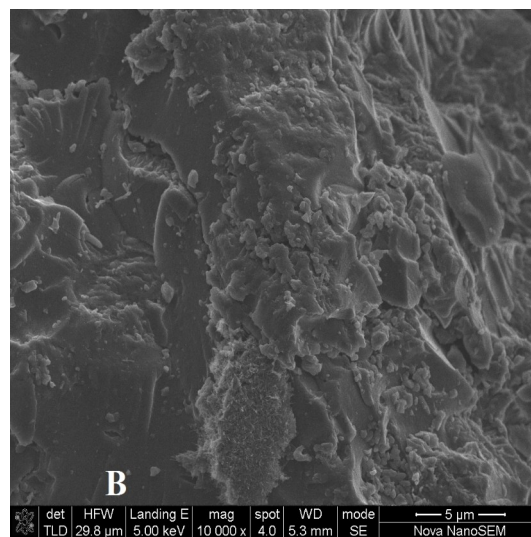
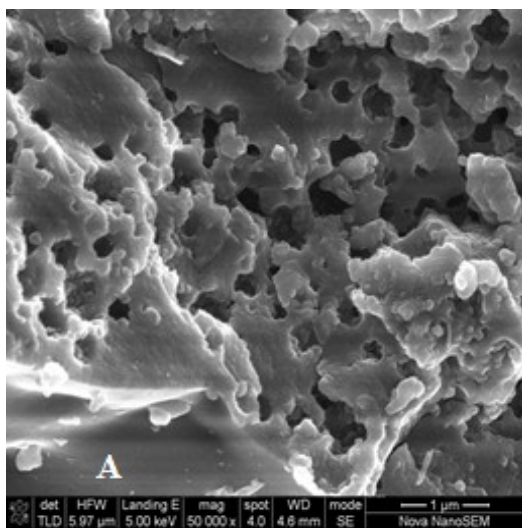


Figure 1b: FTIR spectra of DPAC (before and after adsorption).

**Scanning electron microscopy (SEM)**

SEM analysis was conducted to examine the surface morphologies of DSAC and DPAC before and after adsorption of RhB as shown in Figure 2. The SEM micrograph of DSAC before adsorption (Figure 2a) showed that there are many pores

available for adsorption of RhB compared to DPAC (Figure 2c) with uneven like stone rough surfaces due to activation by acid treatment (10,28). The SEM micrographs of the loaded DSAC and DPAC (Figure 2b & 2d) indicated that the surfaces have been covered by RhB dye molecules.



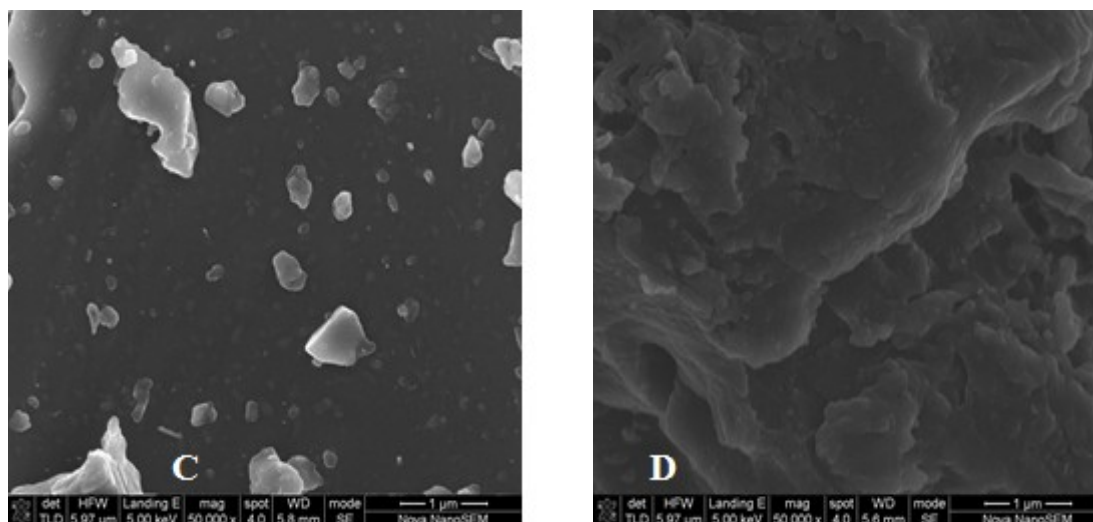


**Figure 2:** SEM micrograph of the adsorbents: (a) DSAC before RhB adsorption, (b) DSAC after RhB adsorption; (c) DPAC before RhB adsorption, and (d) DPAC after RhB adsorption.

### Formulation of Model and optimization of adsorption of RhB onto DSAC and DPAC by BBD

BBD as a modeling technique was employed to analyze the relationship between the experimental variables to the sorption of RhB onto DSAC and DPAC and their corresponding responses of RhB removal efficiency from aqueous solution as presented in Table 1 and 2. The removal efficiency

of RhB by DSAC and DPAC was found to be greater than 99% and 98% respectively. The quadratic model equation between the adsorption responses depict RhB removal efficiency ( $H$ ) and the operating variables; initial concentrations ( $A$ ), adsorbent dosage ( $B$ ), time ( $C$ ), and pH ( $D$ ) achieved by Design expert 11.1.2.0 is given in Equations (3) and (4).

$$H_{DSAC} = +98.05 + 5.72A - 3.49B + 2.14C + 1.12D + 1.80AB + 0.1125AC - 0.1450AD + 0.7850BC + 0.2675BD - 1.74C^2 - 5.97A^2 - 0.8794B^2 - 2.59C^2 + 0.1843D^2 \quad (\text{Eq. 3})$$

$$H_{DPAC} = +97.14 + 6.06A - 4.12B + 1.74C + 0.9317D + 2.93AB - 1.53AC - 2.65AD + 0.3325BC - 0.3250BD - 0.8650CD - 4.407A^2 - 2.02B^2 - 1.11C^2 + 1.10D^2 \quad (\text{Eq. 4})$$

$H_{DSAC}$  and  $H_{DPAC}$  are the removal efficiency (response variables) and  $A$ ,  $B$ ,  $C$ , and  $D$  are the coded operating variables. To establish the regression model, which is significant statistically,

the insignificant terms in Equations 3 and 4 with  $p$  values  $>0.05$  were removed. Consequently, Equations 5 and 6 were obtained;

$$H_{DSAC} = +98.05 + 5.72A - 3.49B + 2.14C + 1.12D + 1.80AB - 1.74CD - 5.97A^2 - 2.59C^2 \quad (\text{Eq. 5})$$

$$H_{DPAC} = +97.14 + 6.06A - 4.12B + 1.74C + 0.9317D + 2.93AB - 2.65AD + 0.3325BC - 4.407A^2 - 2.02B^2 \quad (\text{Eq. 6})$$

The suitability of the proposed models was evaluated by the Design expert 11.1.2.0 as shown in Tables 4 and 5. The  $F$ -values 24.82 and 27.86 for DSAC and DPAC respectively of the quadratic model and their low  $p$  values ( $<0.0001$ ) suggested that the models are significant. The regression coefficient ( $R^2$ ) values 0.9613 and 0.9653 were high. The adjusted ( $R^2$ ) values of 0.9225 (DSAC) and 0.9307 (DPAC) compared with the predicted  $R^2$  (0.7791) and 0.8040 for both adsorbents were

in reasonable agreement. A model is considered significant if its  $p$ -value  $< 0.05$ . As presented in Tables 4 and 5, it can be seen that the linear terms  $A$ ,  $B$ ,  $C$ ,  $D$ , the interaction terms  $AB$  and  $CD$ , and the quadratic terms  $A^2$  and  $C^2$  are the significant terms for RhB onto DSAC. While linear terms ( $A$ ,  $B$ , and  $C$ ), interaction terms ( $AB$  and  $AD$ ), and the quadratic terms ( $A^2$  and  $B^2$ ) are significant for RhB onto DPAC (17,29).



**Table 4:** Anova for quadratic model on the removal RhB onto DSAC.

Source	Sum of Squares	df	Mean Square	F-value	p-value	Comments
Model	900.19	14	64.30	24.82	< 0.0001	Significant
A-Concentration	393.31	1	393.31	151.82	< 0.0001	Significant
B-Dose	146.16	1	146.16	56.42	< 0.0001	Significant
C-Time	54.91	1	54.91	21.20	0.0004	Significant
D-pH	15.12	1	15.12	5.84	0.0299	Significant
AB	12.92	1	12.92	4.99	0.0423	Significant
AC	0.0506	1	0.0506	0.0195	0.8908	
AD	0.0841	1	0.0841	0.0325	0.8596	
BC	2.46	1	2.46	0.9515	0.3459	
BD	0.2862	1	0.2862	0.1105	0.7445	
CD	12.11	1	12.11	4.67	0.0484	Significant
A <sup>2</sup>	231.33	1	231.33	89.30	< 0.0001	Significant
B <sup>2</sup>	5.02	1	5.02	1.94	0.1858	
C <sup>2</sup>	43.62	1	43.62	16.84	0.0011	Significant
D <sup>2</sup>	0.2204	1	0.2204	0.0851	0.7748	
Residual	36.27	14	2.59			
Pure Error	0.4873	4	0.1218			
Cor Total	936.46	28				
Cor Total	936.46	28				
Std. Dev.	1.61					

Mean = 94.22; C.V.% = 1.71; R<sup>2</sup> = 0.9613; Adjusted. R<sup>2</sup> = 0.9225; Predicted. R<sup>2</sup> = 0.7791; Adeq. Precision = 18.5854

**Table 5:** Anova for quadratic model on the removal of RhB onto DPAC.

Source	Sum of Squares	df	Mean Square	F-value	p-value	Comments
Model	902.04	14	64.43	27.86	< 0.0001	Significant
A-Concentration	440.93	1	440.93	190.65	< 0.0001	Significant
B-Dose	203.45	1	203.45	87.97	< 0.0001	Significant
C-Time	36.44	1	36.44	15.75	0.0014	Significant
D-pH	10.42	1	10.42	4.50	0.0521	
AB	34.22	1	34.22	14.80	0.0018	Significant
AC	9.30	1	9.30	4.02	0.0646	
AD	28.09	1	28.09	12.15	0.0036	Significant
BC	0.4422	1	0.4422	0.1912	0.6686	
BD	0.4225	1	0.4225	0.1827	0.6756	
CD	2.99	1	2.99	1.29	0.2744	
A <sup>2</sup>	125.75	1	125.75	54.38	< 0.0001	Significant
B <sup>2</sup>	26.52	1	26.52	11.47	0.0044	Significant
C <sup>2</sup>	7.98	1	7.98	3.45	0.0843	
D <sup>2</sup>	7.79	1	7.79	3.37	0.0879	
Residual	32.38	14	2.31			
Pure Error	0.8055	4	0.2014			
Cor Total	934.41	28				
Std. Dev.	1.52					

Mean = 93.57; C.V.% = 1.63; R<sup>2</sup> = 0.9653; Adjusted. R<sup>2</sup> = 0.9307; Predicted. R<sup>2</sup> = 0.8040; Adeq. Precision = 20.0466

Figure 3 (a and b) are the actual versus predicted plots for both adsorbents. It is apparent that the data points on the plots were distributed close to the straight line; thus, implying a good relationship between the actual and predicted values of the

responses. This is following the report of (17,29). These results clearly showed that the quadratic model tested was sufficient in predicting the response variables for the experimental data.

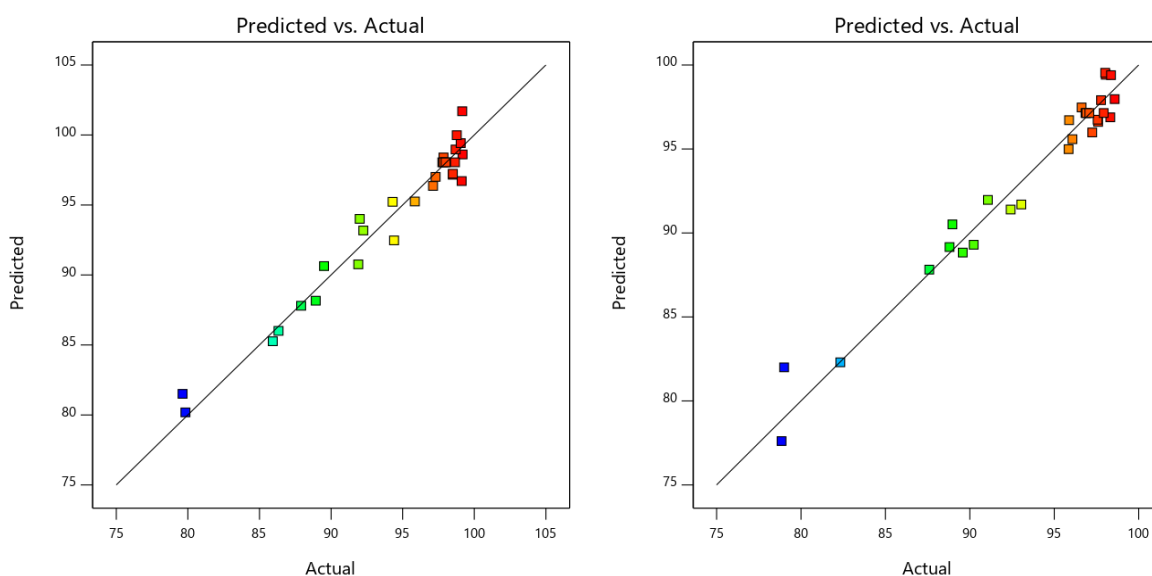


**Figure 3:** Actual vs predicted plots of RhB on DSAC (left), DPAC (right).

The 3-D response surface plots (Figures 4-9) were developed to determine the effect of the combinations of operating variables on the removal efficiency of RhB onto DSAC and DPAC. In Figures 4 (a and b), it is apparent that the adsorption process is greatly affected by the pH of a solution. The charge on the adsorbent's surface and the nature of adsorbate in solution depends on pH. The figures show the effects of pH and initial concentration on the sorption of RhB onto DSAC and DPAC. The percentage of RhB sorbed was noticed to increase as the pH and concentration increased for both adsorbents at fixed adsorbent dosage (0.1 g) and time (725 min). This is because, at higher pH, there are more hydroxyl ions in the solution resulting in electrostatic attraction between RhB dye and the adsorbents. However, at lower pH, there are more protons in the solution and the surface of the RhB dye is cationic thereby leading to electrostatic repulsion between the adsorbents and adsorbate in solution. Hence a decrease in the removal efficiency of RhB dyes. This is in line with the observations made by (21,26,30). The interaction between initial concentration and contact time is presented in Figure 5 (a and b). The percentage removal of RhB with time increases until equilibrium was attained at 60 mg/L and 725 min for both adsorbents. Figure 6 (a and b) depicted that there was better interaction between the adsorbent dose and concentration of RhB. The removal efficiency of RhB was low at a higher dosage and lower concentration. Although, the removal efficiency increases as the concentration increased at a lower dose. This may be attributed to the overcrowding

of the adsorbent particle at the adsorption site at a higher dosage. Figure 7 (a and b) gives the reliance of removal efficiency of RhB on adsorption time and pH for both adsorbents. The percentage removal of RhB is low at a lower time and pH as a result of more positive ions in the solution. While at high adsorption time and pH the rate of sorption was higher and this is due to the electrostatic attraction between RhB dye and the adsorbents as well as more interactions between the dye molecule and the adsorbents. Figure 8 (a and b) depicts the effect of the dual interaction between dose and pH on the response for complete RhB adsorbed from aqueous solution at a fixed initial RhB concentration and contact time. This dual interaction has no significant impact ( $p > 0.05$ ) on the adsorption of RhB for both adsorbents. The highest percentage removal of RhB was recorded at a lower dose and high pH. At a lower dose, there are several vacant sites ready for adsorption and at higher pH, there are more negative ions in the solution resulting in electrostatic interaction between RhB dye and the adsorbents. Thus, the enhanced removal efficiency of RhB dyes. These observations align with the reports of (26,30). The interactive effect between dose and time on the response surface for the percentage removal of RhB by DSAC and DPAC at constant pH and initial RhB concentration is presented in Figure 9 (a and b). The adsorption efficiency of RhB was at the highest at a low dosage for both adsorbents and increases as the time of contact increases revealing an antagonistic effect between the two variables (26).



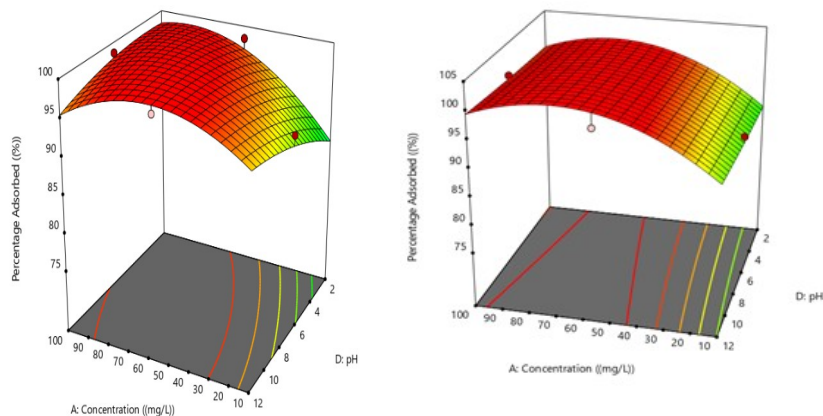


**Figure 4:** 3D plots on the effect of concentration and pH on adsorption of RhB on DSAC (left); DPAC (right) at 0.1 g dose and 725 min.

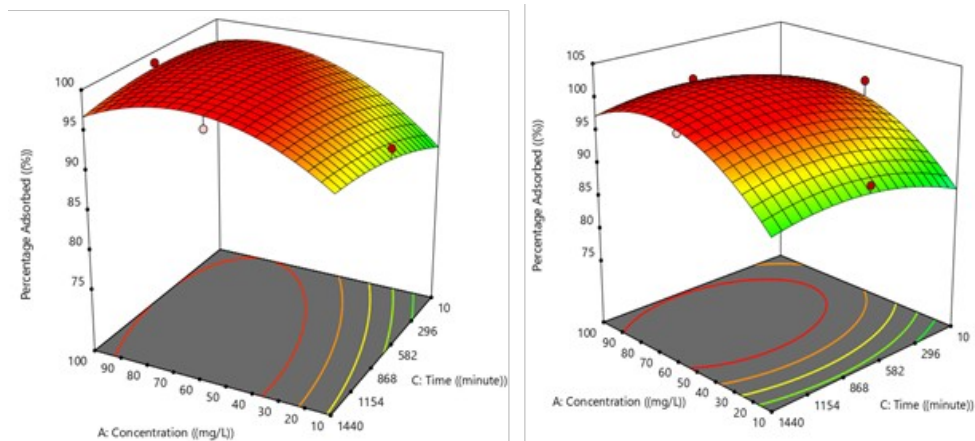


**Figure 5:** 3D plots on the effect of concentration and time on adsorption of RhB on DSAC (left); (b) DPAC (right) at 0.1 g dose and pH 12.

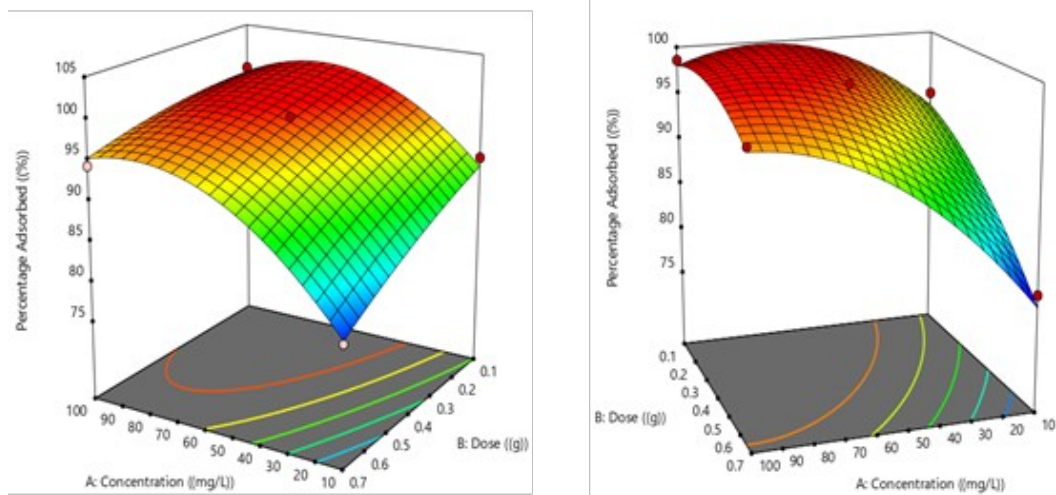


**Figure 6:** 3D plots on the effect of concentration and dose on adsorption of RhB on (left) DSAC; (right) DPAC at pH 12 and 725 min.

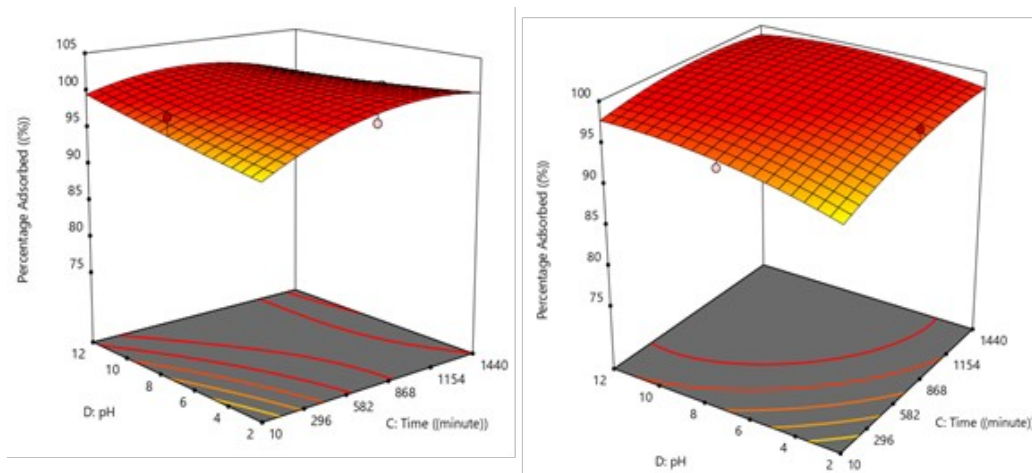


**Figure 7:** 3D plots on the effect of time and pH on adsorption of RhB on DSAC (left); DPAC (right) at 55 mg/L and 0.1 g.

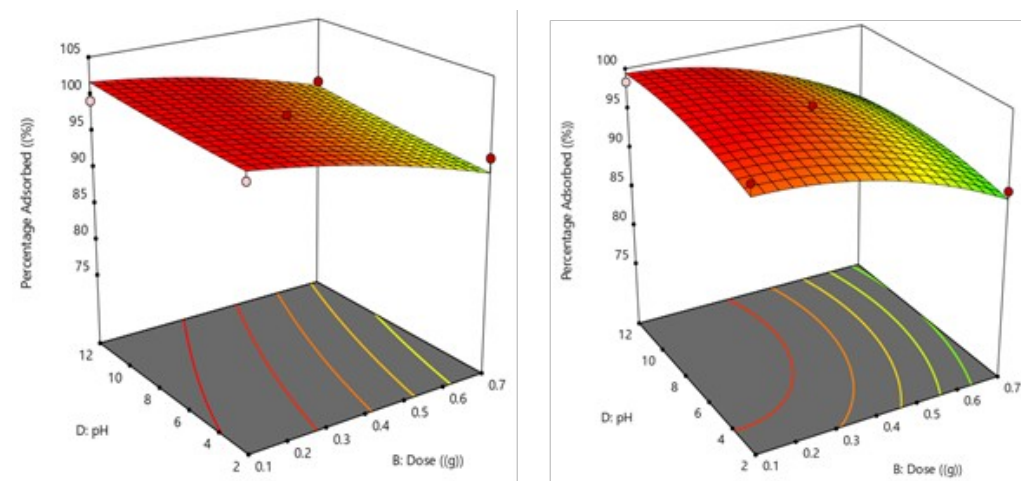


**Figure 8:** 3D plots on the effect of Dose and pH on adsorption of RhB on (a) DSAC; (b) DPAC at 55 mg/L and 725 min.

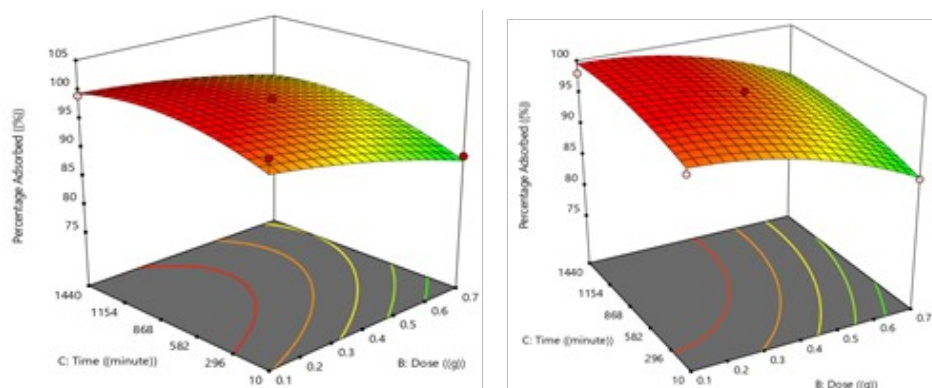


**Figure 9:** 3D plots on the effect of Dose and Time on adsorption of RhB on (left) DSAC; (right) DPAC at 55 mg/L and pH 12.

**Interactive effects of the parameters on RhB removal onto DSAC and DPAC**

The perturbation plot is usually employed to study the interactions among all operating variables simultaneously (31). Figure 10 (a and b) shows the percentage removal of RhB as a function of

each operating parameter from the lowest coded value with other parameters at a constant level in the center point of the design. In Figure 10, it is obvious that initial concentration, adsorbent dose, contact time, and pH have an observable impact on RhB removal for both adsorbents.

**Adsorption isotherm**

Isotherms are primarily used to illustrate the adsorption process. It explains how the adsorbate relates with the adsorbent and explains the nature and mechanism of the adsorption procedure (32). The adsorption isotherm data of RhB onto DSAC and DPAC were studied by Freundlich, Langmuir, and Temkin isotherms. The nearness of the value of the correlation coefficient ( $R^2$ ) to one, the better is the agreement of the experimental data with the model. The Langmuir isotherm validates the adsorption process as a monolayer on a surface having a finite number of similar sites. A linear form of the Langmuir isotherm is expressed in Equation 7a. The dimensionless equilibrium parameter ( $R_L$ ) represented in Equation 7b confirms the favorability of the process. The adsorption process is favorable if  $R_L$  value falls between 0 and 1 ( $0 < R_L < 1$ ), linear when  $R_L=1$ , irreversible when  $R_L = 0$  and unfavorable when  $R_L > 1$ . Where  $C_e$  is the equilibrium concentration of the RhB in solution (mg/L),  $q_e$  is the amount of RhB adsorbed per unit mass of adsorbate (mg/g),  $Q_0$ , and  $K_L$  is the adsorption capacity and the Langmuir equilibrium constant of adsorption, respectively. Freundlich isotherm described the heterogeneity of the adsorption process i.e. a multilayer adsorption mechanism as presented in Equation 8.  $K_f$  and  $n$  are the Freundlich constants calculated from the slopes and intercepts of the linear graphs of  $\log q_e$

versus  $\log C_e$ .  $C_e$  is the equilibrium concentration of the RhB in solution (mg/L).  $q_e$  the amount of RhB adsorbed per unit mass of adsorbate (mg/g),  $n$  indicates how favorable is the adsorption process and  $K_f$  reflects the adsorption strength. The Temkin model believes that heat of adsorption decreases linearly with coverage as represented in Equation 9. It considers the adsorbent-adsorbate relationship.  $A_T$  is the Temkin equilibrium constant (L/g),  $b_T$  is the Temkin constant related to the heat of sorption (J/mol) which can be calculated from the plot of  $q_e$  against  $\ln C_e$ .  $R$  is the molar gas constant (8.314 J/mol/K), and  $T$  is the absolute temperature (10,26).

$$\frac{C_e}{q_e} = \frac{1}{Q_0 K_L} + \frac{1}{Q_0} C_e \quad (\text{Eq. 7a})$$

$$R_L = \frac{1}{(1 + K_L C_o)} \quad (\text{Eq. 7b})$$

$$\log q_e = \frac{1}{n} \log C_e + \log K_f \quad (\text{Eq. 8})$$

$$q_e = \frac{RT}{b_T} \ln A_T + \frac{RT}{b_T} \ln C_e \quad (\text{Eq. 9})$$

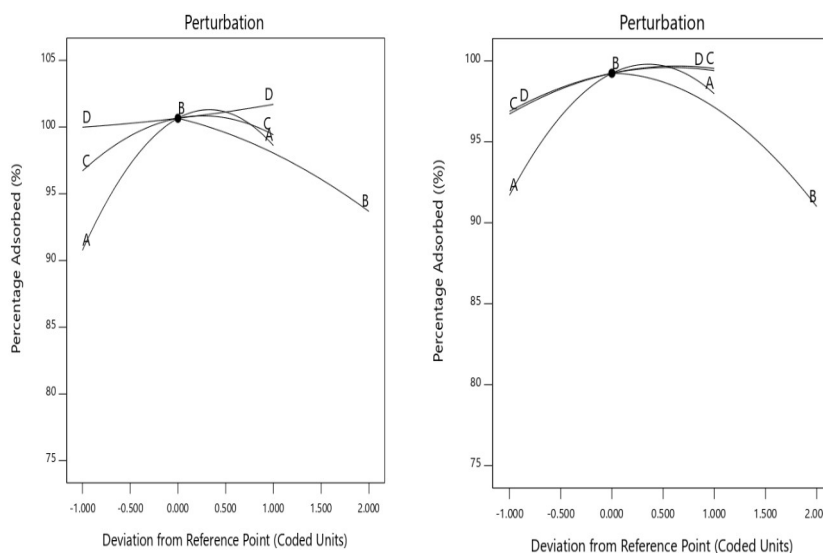


**Figure 10:** Perturbation plots for the percentage of RhB removal onto DSAC (left); DPAC (right).

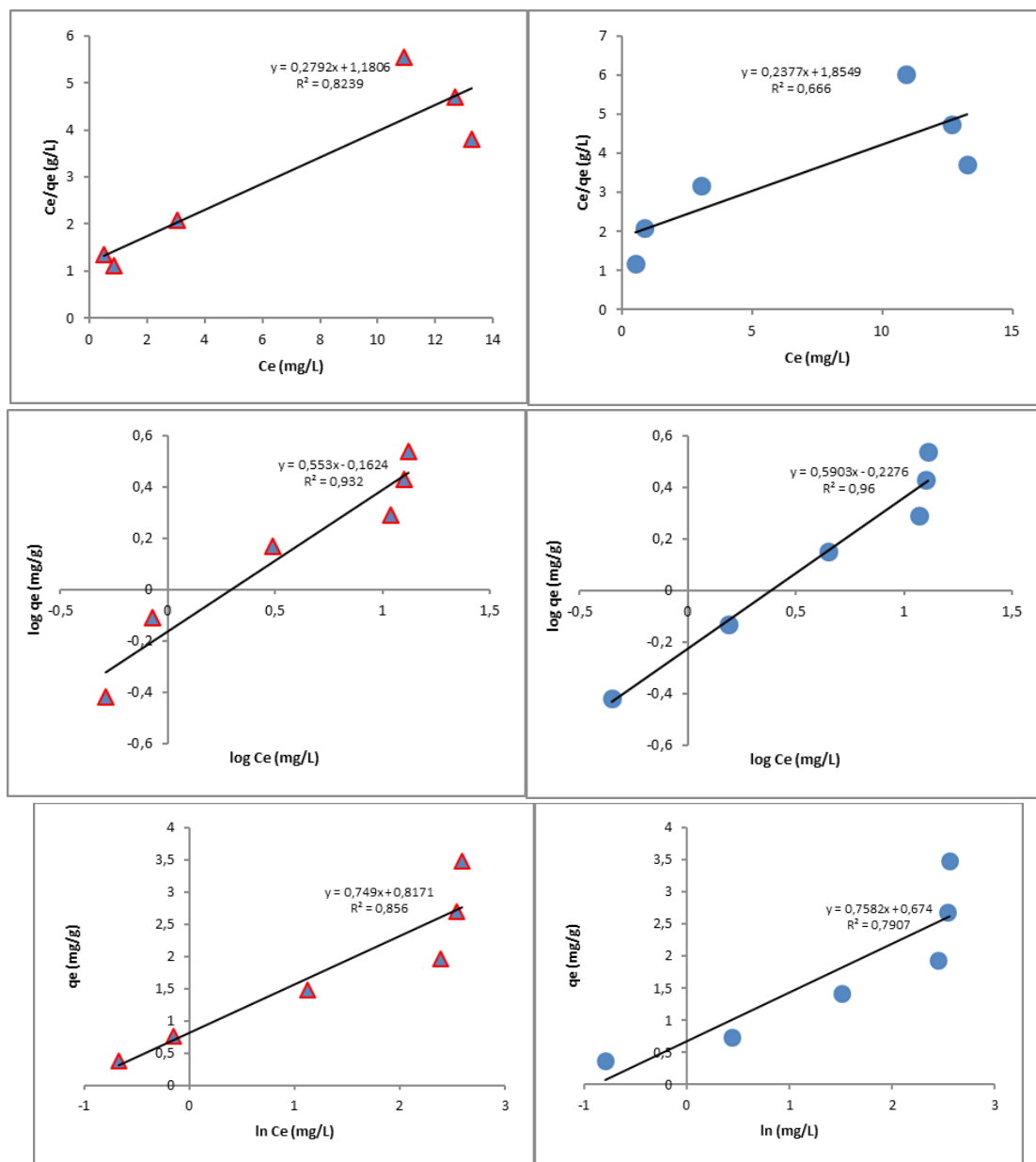


**Figure 11:** (Top row) Langmuir Isotherm plots for the sorption of RhB onto DSAC and DPAC; (middle row) Freundlich Isotherm plots for the sorption of RhB onto DSAC and DPAC; (bottom row) Temkin Isotherm plots for the sorption of RhB onto DSAC and DPAC.

The results of the isotherm studies and their related parameters obtained are shown in Figure 11 and Table 6. The correlation coefficient values (R<sup>2</sup>) of Freundlich isotherm (0.932 and 0.960) for RhB onto DSAC and DPAC respectively were found to be higher compared to that of the Langmuir model (0.825 and 0.740) and Temkin isotherm (0.857 and 0.791) which implies that the adsorption process fitted best into Freundlich isotherm model. This means that the sorption of RhB onto the surfaces of DSAC and DPAC was

heterogeneous. The values of n calculated for both adsorbents were greater than one indicating the favorability of the adsorption process while the constant K<sub>f</sub> with values of 0.689 and 0.593 (mg/g) for both DSAC and DPAC respectively, revealed that there was greater adsorption affinity between RhB and DSAC than DPAC. This is in concordance with the observation of (11). However, the process could not be described by both Langmuir and Temkin isotherm due to low R<sup>2</sup> values (R<sup>2</sup><0.9). Their constants are presented in Table 6.

**Table 6:** Isotherm parameters for the uptake of RhB onto DSAC and DPAC.

Isotherm model	Parameters/constants	DSAC	DPAC
Freundlich	R <sup>2</sup>	0.932	0.960
	K <sub>f</sub>	0.689	0.593
	n	1.808	1.695
Langmuir	R <sup>2</sup>	0.825	0.740
	q <sub>o</sub> (mg/g)	3.584	4.219
	K <sub>L</sub> (L/mg)	0.236	0.128
	R <sub>L</sub>	0.078	0.135
Temkin	R <sup>2</sup>	0.857	0.791
	A <sub>T</sub> (L/g)	2.115	2.134
	B <sub>T</sub> (J/mol)	3341.13	3301.47

**Kinetic models**

Four kinetic models viz pseudo-first-order, pseudo-second-order, Elovich, and Intraparticle diffusion were considered for the sorption of RhB onto DSAC and DPAC to establish the kinetics and mechanism of the adsorption process.

The Pseudo-first-order rate equation as given by (33,34), expressed as:

$$\ln(q_e - q_t) = \ln q_{e,cal} - k_1 t \quad (\text{Eq. 10})$$

The pseudo-second-order kinetic model equation was given as:

$$\frac{t}{q_t} = \frac{1}{k_2 q_{e,cal}^2} + \frac{1}{q_{e,cal}} \times t \quad (\text{Eq. 11})$$

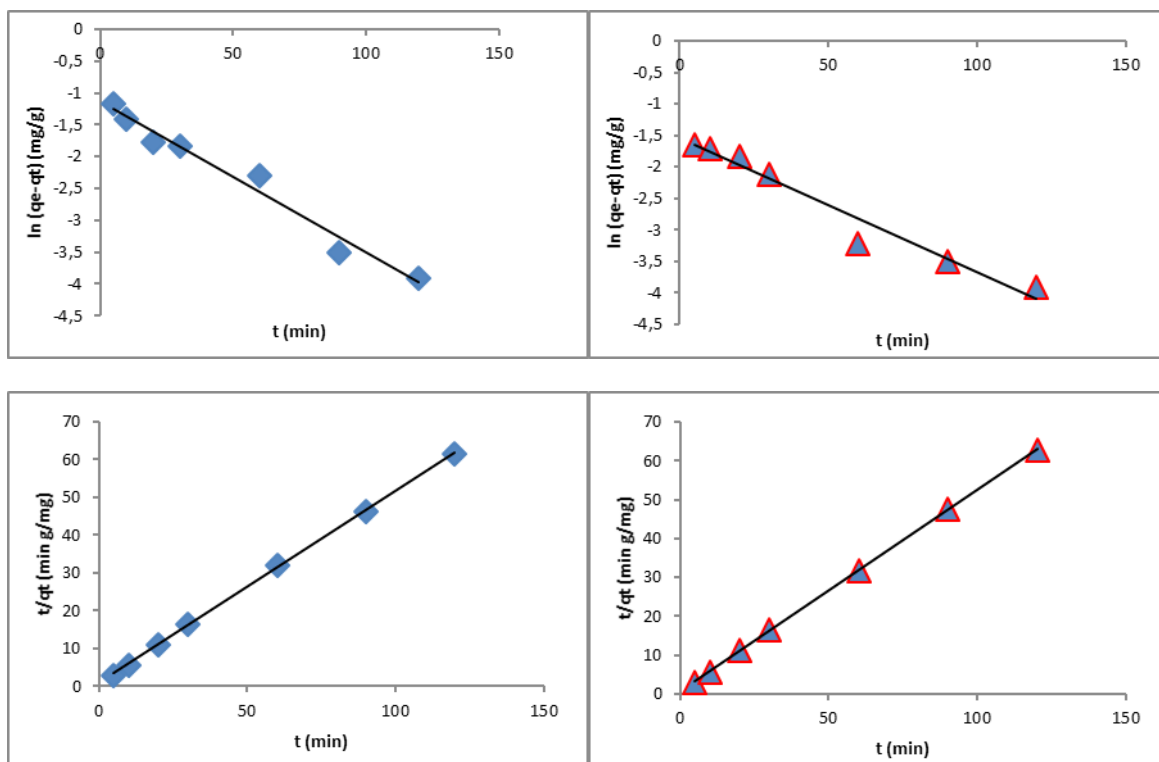
The Elovich equation is expressed as:

$$q_t = \frac{1}{\alpha} \ln(\alpha\beta) + \frac{1}{\alpha} \ln t \quad (\text{Eq. 12})$$

The intra-particle diffusion equation is expressed as:

$$q_t = k_d t^{1/2} + C \quad (\text{Eq. 13})$$

where q<sub>e</sub> and q<sub>t</sub> both in mg/g are the amounts of RhB dye sorbed at equilibrium and at any time t (min). k<sub>1</sub> (min<sup>-1</sup>), k<sub>2</sub> (g/mg min), and k<sub>d</sub> (mg/g min<sup>1/2</sup>) are the rate constants of the pseudo-first-order, pseudo-second-order, and intra-particle diffusion models respectively. α is the initial adsorption rate (mg/g min) and β is the desorption constant (g/mg) while C is a constant which gives an idea about the thickness of the boundary layer (11,35).



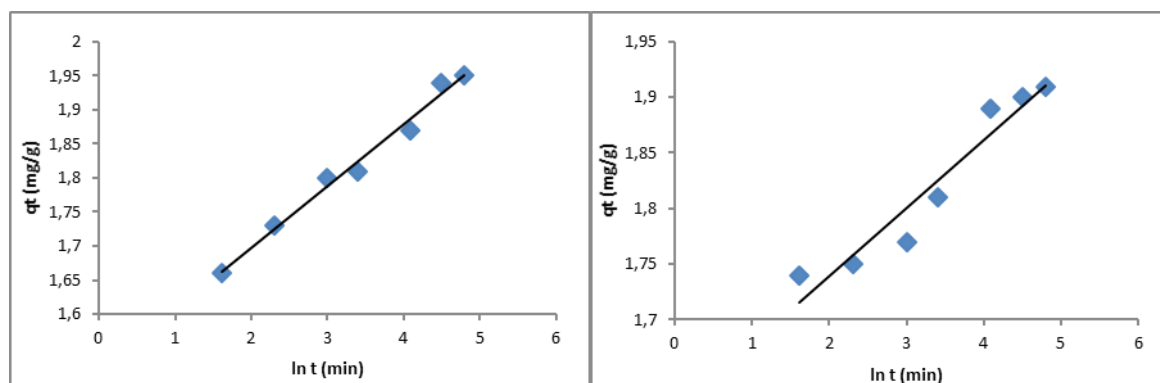


**Figure 12:** (Top row) Pseudo-first-order kinetics plots for the sorption of RhB onto DSAC and DPAC; (middle row) Pseudo second order kinetics plots for the sorption of RhB onto DSAC and DPAC; (bottom row) Elovich plots for the sorption of RhB onto DSAC and DPAC.

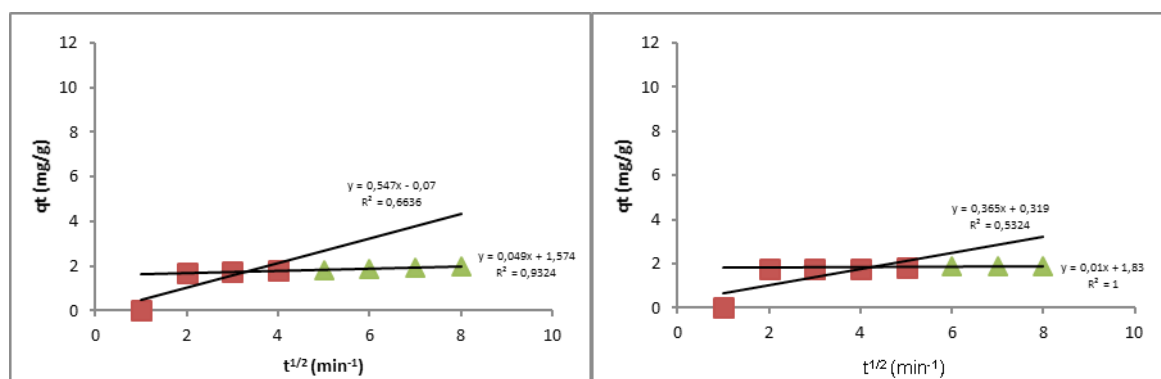


**Figure 13:** Intra-particle diffusion plots for the sorption of RhB onto (left) DSAC and (right) DPAC.

The graphs of all the kinetic models were presented in Figure 12 and their parameters were calculated as shown in Table 7. The plots of  $q_t$  versus  $t$  (Fig. 12c and 12d) have the highest correlation coefficient values ( $R^2 = 0.999$ ) for both adsorbents compared to other kinetic model plots. The calculated  $q_e$  values of the pseudo-second-order kinetic model with the experimental  $q_e$  values for both DSAC and DPAC were in close agreement (Table 7). The values of the pseudo-second-order rate constants ( $k_2$ ) 0.282 and 0.414  $\text{g mg}^{-1} \text{min}^{-1}$  for DSAC and DPAC respectively indicated that the adsorption is fast. Impliedly, the adsorption followed the pseudo-second-order kinetics model which adequately described the process. Indicating that the chemical process appeared to control the adsorption of RhB onto

DSAC and DPAC. This conforms to the results of (11,29).

The intra-particle diffusion plots of RhB onto DSAC and DPAC were given in Figure 13 and their constant parameters were calculated (Table 8). The figures revealed that the adsorption process is in two stages. The first segment is the exterior surface adsorption of RhB while the second linear part is the progressive adsorption of the RhB stage where intra-particle or pore diffusion was rate-limiting. The higher correlation coefficient ( $R^2$ ) values and high boundary layer ( $C$ ) of the second stage is an indication that intra-particle diffusion appears to control the adsorption of RhB onto both adsorbents but is not the only rate-limiting step. These observations follow the reports of (26,29).



**Table 7:** Kinetic parameters for the sorption of RhB onto DSAC and DPAC.

Kinetic models	Parameters	DSAC	DPAC
Pseudo first order	$K_1$ ( $\text{min}^{-1}$ )	0.023	0.021
	$Q_{e, \text{cal}}$ (mg/g)	0.32	0.21
	$R^2$	0.975	0.958
Pseudo second order	$K_2$ (g/mg/min)	0.282	0.414
	$Q_{e, \text{cal}}$ (mg/g)	1.97	1.93
	$Q_{e, \text{exp}}$ (mg/g)	1.96	1.92
	$R^2$	0.999	0.999
Elovich	$\alpha$	11.11	16.39
	$\beta$	$1.85 \times 10^6$	$1.95 \times 10^{10}$
	$R^2$	0.986	0.927

**Table 8:** Intra-particle diffusion parameters for the sorption of RhB onto DSAC and DPAC.

Parameters	DSAC		DPAC	
	Line 1	Line 2	Line 1	Line 2
$K_d$ (mg/ g $\text{min}^{-1/2}$ )	0.547	0.049	0.356	0.01
C	-0.07	1.574	0.319	1.83
$R^2$	0.663	0.932	0.532	1

## CONCLUSION

Based on this study and the results obtained, it can be established that both DSAC and DPAC are promising and potential materials for removing organic hazardous pollutants such as dyes from aqueous media. Adsorption operating variables such as initial RhB concentration, adsorbent dosage, time, and pH were successfully optimized and significant for the removal of RhB by DSAC and DPAC. The actual and predicted values having a good agreement confirms the suitability of the proposed model. The optimum removal efficiency of RhB by DSAC and DPAC occurs at 55 mg/L initial RhB concentration, 0.1 g dosage, 725 min, and pH 12 with removal percentage greater than 99% and 98% for DSAC and DPAC respectively. Freundlich Isotherm models adequately described the adsorption process. Comparatively, DSAC appears to exhibit a better performance for the uptake of RhB than DPAC. The adsorption followed the pseudo-second-order kinetics model and adequately described the process among the kinetic models tested. Thus, the adsorption appears to be controlled by the chemical process.

## ACKNOWLEDGMENTS

The authors are most grateful to Chemistry and Industrial Chemistry Unit, Kwara State University, Malete, Nigeria for providing the laboratory facilities necessary to carry out the proposed study.

## AUTHORS' CONTRIBUTIONS

The authors SO Azeez, IO Saheed, FA Adekola, AA Jimoh, DM Aransiola, and ZA Abdulsalam designed and performed the experiment and as well analyzed experimental data. All the authors worked on characterization analysis and the

drafting of the manuscript. All authors read and approved the final manuscript.

## COMPETING INTERESTS

Authors declare that there were no competing interests.

## REFERENCES

- Aldegs Y, Elbarghouthi M, Elsheikh A, Walker G. Effect of solution pH, ionic strength, and temperature on adsorption behavior of reactive dyes on activated carbon. *Dyes and Pigments*. 2008;77(1):16–23. <DOI>.
- Royer B, Cardoso NF, Lima EC, Macedo TR, Airoidi C. A useful organofunctionalized layered silicate for textile dye removal. *Journal of Hazardous Materials*. 2010 Sep;181(1–3):366–74. <DOI>.
- Memon FN, Memon S. Sorption and Desorption of Basic Dyes from Industrial Wastewater Using Calix[4]arene Based Impregnated Material. *Separation Science and Technology*. 2015 May 24;50(8):1135–46. <DOI>.
- Rangabhashiyam S, Anu N, Selvaraju N. Sequestration of dye from textile industry wastewater using agricultural waste products as adsorbents. *Journal of Environmental Chemical Engineering*. 2013 Dec;1(4):629–41. <DOI>.
- Bello O, Bello I, Adegoke K. Adsorption of dyes using different types of sand: A review. *South Afr J Chem*. 2013;66:117–29. <URL>.
- Malik PK, Saha SK. Oxidation of direct dyes with hydrogen peroxide using ferrous ion as catalyst. *Separation and Purification Technology*. 2003 Jun;31(3):241–50. <DOI>.
- Gupta VK, Jain R, Mittal A, Mathur M, Sikarwar S. Photochemical degradation of the hazardous dye Safranin-T using TiO<sub>2</sub> catalyst. *Journal of Colloid and Interface Science*. 2007 May;309(2):464–9. <DOI>.

8. Fan L, Zhou Y, Yang W, Chen G, Yang F. Electrochemical degradation of aqueous solution of Amaranth azo dye on ACF under potentiostatic model. *Dyes and Pigments*. 2008;76(2):440–6. [<DOI>](#).
9. Sachdeva S, Kumar A. Preparation of nanoporous composite carbon membrane for separation of rhodamine B dye. *Journal of Membrane Science*. 2009 Mar 5;329(1–2):2–10. [<DOI>](#).
10. Saheed IO, Adekola FA, Olatunji GA. Sorption study of methylene blue on activated carbon prepared from *Jatropha curcas* and *Terminalia catappa* seed coats. *Journal of the Turkish Chemical Society, Section A: Chemistry*. 2016 Dec 7;4(1):375–375. [<DOI>](#).
11. Inyinbor AA, Adekola FA, Olatunji GA. Adsorption of Rhodamine B dye from aqueous solution on *Irvingia gabonensis* biomass: Kinetics and thermodynamics studies. *SAfr.j.chem [Internet]*. 2015 [cited 2022 Jan 11];68. [<DOI>](#).
12. Azeez S, Adekola F. Sorption of 4-Nitroaniline on Activated Kaolinitic Clay and *Jatropha curcas* Activated Carbon in Aqueous Solution. *Jordan J Chem*. 2021;11(2):130–49. [<URL>](#).
13. Malik PK. Dye removal from wastewater using activated carbon developed from sawdust: adsorption equilibrium and kinetics. *Journal of Hazardous Materials*. 2004 Sep;113(1–3):81–8. [<DOI>](#).
14. Webb DB, editor. *A Guide to species selection for tropical and sub-tropical plantations*. 2nd ed., rev. Oxford: Unit of Tropical Silviculture, Commonwealth Forestry Institute, University of Oxford; 1984. 256 p. (Tropical forestry papers). ISBN: 978-0-85074-068-4.
15. Alam Z, Muyibi SA, Toramae J. Statistical optimization of adsorption processes for removal of 2,4-dichlorophenol by activated carbon derived from oil palm empty fruit bunches. *Journal of Environmental Sciences*. 2007 Jan;19(6):674–7. [<DOI>](#).
16. Sudamalla P, Saravanan P, Matheswaran M. Optimization of operating parameters using response surface methodology for adsorption of crystal violet by activated carbon prepared from mango kernel. *Environ Res*. 2012;22(1):1–7.
17. Ani JU, Okoro UC, Aneke LE, Onukwuli OD, Obi IO, Akpomie KG, et al. Application of response surface methodology for optimization of dissolved solids adsorption by activated coal. *Appl Water Sci*. 2019 Apr;9(3):60. [<DOI>](#).
18. Nwabanne J, Igbokwe P. Application of response surface methodology for preparation of activated carbon from palmyra palm nut. *New York Sci J*. 2012;5(9):18–25.
19. Fu JF, Zhao YQ, Xue XD, Li WC, Babatunde AO. Multivariate-parameter optimization of acid blue-7 wastewater treatment by Ti/TiO<sub>2</sub> photoelectrocatalysis via the Box–Behnken design. *Desalination*. 2009 Jul;243(1–3):42–51. [<DOI>](#).
20. Meilgaard M, Civille GV, Carr BT. *Sensory evaluation techniques*. 3rd ed. Boca Raton, Fla: CRC Press; 1999. 387 p. ISBN: 978-0-8493-0276-3.
21. Amuda OS, Olayiwola AO, Alade AO, Farombi AG, Adebisi SA. Adsorption of Methylene Blue from Aqueous Solution Using Steam-Activated Carbon Produced from *Lantana camara* Stem. *JEP*. 2014;05(13):1352–63. [<DOI>](#).
22. Tangjuank S, Insuk N, Tontrakoon J, Udeye V. Adsorption of lead (II) and cadmium (II) ions from aqueous solutions by adsorption on activated carbon prepared from cashew nut shells. *World Academy of Science, Engineering and Technology*. 2009;52:110–6.
23. Oyekanmi AA, Ahmad A, Hossain K, Rafatullah M. Adsorption of Rhodamine B dye from aqueous solution onto acid treated banana peel: Response surface methodology, kinetics and isotherm studies. *Rittschof D, editor. PLoS ONE*. 2019 May 15;14(5):e0216878. [<DOI>](#).
24. Azeez S, Adekola F. Kinetics and Thermodynamics of Sorption of 4-Nitrophenol on Activated Kaolinitic Clay and *Jatropha Curcas* Activated Carbon from Aqueous Solution. *Pak J Anal Environ Chem*. 2016;17(1):93–105. [<URL>](#).
25. Abdolrahimi N, Tadjarodi A. Adsorption of Rhodamine-B from Aqueous Solution by Activated Carbon from Almond Shell. *Proceedings*. 2019 Nov 14;41(1):51. [<DOI>](#).
26. Adekola F, Inyinbor A, Olatunji G. EDTA Modified *Irvingia gabonensis*: An Efficient Bioresource Material for the Removal of Rhodamine B. *Pakistan Journal of Analytical & Environmental Chemistry*. 2015;16(2):10. [<URL>](#).
27. Postai DL, Demarchi CA, Zanatta F, Melo DCC, Rodrigues CA. Adsorption of rhodamine B and methylene blue dyes using waste of seeds of *Aleurites Moluccana*, a low cost adsorbent. *Alexandria Engineering Journal*. 2016 Jun;55(2):1713–23. [<DOI>](#).
28. Prasad AL, Santhi T. Adsorption of hazardous cationic dyes from aqueous solution onto *Acacia nilotica* leaves as an eco friendly adsorbent. *Sustainable Environment Research*. 2012;22(2):113–22.
29. Mehrizad A. Adsorption studies of some phenol derivatives onto Ag-cuttlebone nanobiocomposite: modeling of process by response surface methodology. *Res Chem Intermed*. 2017 Jul;43(7):4295–310. [<DOI>](#).
30. Hameed BH, Mahmoud DK, Ahmad AL. Equilibrium modeling and kinetic studies on the adsorption of basic dye by a low-cost adsorbent: Coconut (*Cocos nucifera*) bunch waste. *Journal of Hazardous Materials*. 2008 Oct;158(1):65–72. [<DOI>](#).
31. Rahman N, Nasir M. Application of Box–Behnken design and desirability function in the optimization of Cd(II) removal from aqueous solution using poly(o-phenylenediamine)/hydrous zirconium oxide composite: equilibrium modeling, kinetic and thermodynamic studies. *Environ Sci Pollut Res*. 2018 Sep;25(26):26114–34. [<DOI>](#).
32. Etim UJ, Umoren SA, Eduok UM. Coconut coir dust as



a low cost adsorbent for the removal of cationic dye from aqueous solution. Journal of Saudi Chemical Society. 2016 Sep;20:S67–76. [<DOI>](#).

33. Yuh-Shan H. Citation review of Lagergren kinetic rate equation on adsorption reactions. Scientometrics. 2004;59(1):171–7. [<DOI>](#).

34. Idris MN, Ahmad ZA, Ahmad MA. Adsorption

equilibrium of malachite green dye onto rubber seed coat based activated carbon. International Journal of Basic & Applied Sciences. 2011;11(3):38–43.

35. Rathour R, Das P, Aikat K. Microwave-assisted synthesis of graphene and its application for adsorptive removal of malachite green: thermodynamics, kinetics and isotherm study. Desalination and Water Treatment. 2016 Apr 2;57(16):7312–21. [<DOI>](#).



## Chemical Synthesis, Kinetics, and Characterization of Nano-Lead Oxide Powder

Damilola Tope OGUNDELE <sup>1\*</sup> , Samsudeen Olanrewaju AZEEZ<sup>1</sup> ,  
and Akeem Adebayo JIMOH<sup>1</sup> 

<sup>1</sup>Kwara State University, Department of Chemistry and Industrial Chemistry (241103), Malete, Nigeria.

**Abstract:** Systematic chemical decomposition, leaching, desulfurization, reducing and precipitation of spent lead-acid batteries to extract lead in oxide form as a valuable product using organic acid, salt of the acid, and hydrogen peroxide were studied in this present work. Citric acid was found a suitable leachant to dissolve lead. With 1 M citric acid, 2 M sodium citrate, and hydrogen peroxide, 180 min reaction time, solid/liquid ratio of 100 g/L, 30 °C temperature, and 500 rpm speed, > 97% extraction of lead in citrate form was achieved. Leaching kinetics followed  $1 - 3(1 - X)^{2/3} + 2(1 - X) = Kct$  ash diffusion controls dense constant-sized-spherical particles model with an activation energy of 8.3 kJ/mol. The precipitate was calcined at 400 °C to produce  $\alpha$ - and  $\beta$ -PbO with a particle size of 19 nm which can be used as a raw material in the production of a new lead-acid battery.

**Keywords:** Leaching, kinetic study, leaching models, nanoparticle.

**Submitted:** May 06, 2021. **Accepted:** January 17, 2022.

**Cite this:** Ogundele DT, Azeez SO, Jimoh AA. Chemical Synthesis, Kinetics, and Characterization of Nano-Lead Oxide Powder. JOTCSA. 2022;9(1):227-36.

**DOI:** <https://doi.org/10.18596/jotcsa.928341>.

**\*Corresponding author.** E-mail: ([oludeledamilola@gmail.com](mailto:oludeledamilola@gmail.com)), Tel: (08034396529).

### INTRODUCTION

Lead(II) oxide (PbO) nanoparticles show unique optical, electronic, magnetic, luminescent, gas sensing, ultraviolet-blocker, and catalytic properties due to their dimensions, shapes, and surrounding chemical elements (1,2). One of the diverse approaches of synthesizing PbO at nano-dimensions is simultaneous chemical leaching and precipitation of metal sulfide and metal oxides from spent lead battery paste which proved to be a profound process of reducing emission. Chemical conversion is a very simple and convenient method for particle size control at nano dimensions (3).

Nanometer dimensions of nanoparticles are reported factors that enhance the aggregation of the particles thereby influencing the size, shape, chemical, physical and biological properties. It is therefore necessary to minimize aggregation and keep the particles at desirable sizes by the use of suitable organic/inorganic reagents usually referred to as

capping agents (1). These reagents also play an important role in controlling the size and shape of nanoparticles. The metal nanoparticles contain some carboxylate groups (functional groups) which serve as capping agents in the formation of nanoparticles and bind to the metal surface of the nanoparticles. It prevents degradation and preserves the properties of the nanoparticles (16).

Wet chemical treatment of spent lead-acid battery does not involve smelting and roasting as the usual practices of recovering Pb from Spent Lead Acid Battery (SLABs) thereby, it eliminates environmental impact associated with the smelting process. The smelting process requires an enormous temperature of > 1000 °C and the emission of SO<sub>2</sub> gas in addition to lead fume generation (4,5). Some researchers have investigated the chemical conversion of metal components of spent batteries such as PbSO<sub>4</sub>, PbO<sub>2</sub>, PbO, and metallic Pb (6), but they did not carry out the kinetic study using

shrinking core model to obtain rate-controlling steps as intended by this study.

Therefore, this work aimed to synthesis PbO nanoparticles via wet chemical conversion, studied the effect of leaching temperature on leaching rate by testing all equations of shrinking core model, and obtained the activation energy for this process by Arrhenius plots.

## EXPERIMENTAL

Spent lead-acid battery paste that was locally sourced, randomly homogenized, and composited

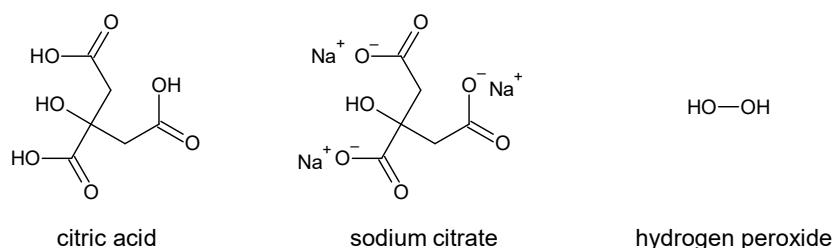


**Figure 1:** Structural and anchoring groups of organic acids.

The leaching of SLAB paste was done in a temperature-controlled, closed three-necked Pyrex flask glass reactor. The sample was introduced into the leachants of pre-determined pH of 3.94 for optimum leaching and precipitation in ratio 2:1:2 in different conditions determined: 1 M citric acid, 2 M sodium citrate, and 2 M hydrogen peroxide, 100 g/L (S/L), 30 °C, 500 rpm, and 3 h.

Mechanical agitation of the sample was achieved using a magnetic stirrer which was adequate to ignore the mass transfer effect during leaching. The samples were taken at an interval of time and analyzed using Atomic Absorption Spectroscopy (AAS). On completion of each experiment, the precipitate/residues were vacuum-filtered and dried at 70 °C in a temperature-controlled oven. The percentage extractions by each acid were calculated and the precipitate of best recovery was subjected to characterization. Extraction and leaching kinetics were performed to probe the mechanism of dissolution of the battery paste in organic acid. The kinetic study helps understand solid-fluid reactions of dense particles and to affirm the certainty of leaching temperature, energy consumption, and to validate the morphology obtained from the SEM spectra. All the standard equations of shrinking core models were investigated for the reaction from the data obtained during leaching experiments. This is the most widespread model elucidating on the fluid-solid reaction of dense particles. The standard equations of the model are:

$$X = K_c t \quad (\text{Eq. 1})$$

was used as a precursor for the production of PbO nanoparticles. The paste was characterized to examine the phases, morphology, and elemental composition before wet chemical conversion. The binding characteristic sites of the organic acid and its salt, and reductant used as leaching, desulfurizing, reducing, and precipitating agents are provided in Figure 1. The organic acid tested was fruit acid with polycarboxylic groups as binding sites. All the chemicals employed in the study were from Merck chemicals, AnalaR grade with high purity without further purification. Deionized water was used for all experimental works.

Film diffusion control dense constant size small particles– all Geometrics

$$1 - (1 - X)^{\frac{2}{3}} = K_c t \quad (\text{Eq. 2})$$

Film diffusion control dense shrinking spheres

$$1 - (1 - X)^{\frac{1}{2}} = K_c t \quad (\text{Eq. 3})$$

Chemical reaction control dense constant size cylindrical particles

$$1 - (1 - X)^{\frac{1}{3}} = K_c t \quad (\text{Eq. 4})$$

Chemical reaction control dense constant size or shrinking spheres

$$1 - 3(1 - X)^{\frac{2}{3}} + 2(1 - X) = K_c t \quad (\text{Eq. 5})$$

Ash diffusion control dense constant size-spherical particles

where  $K_c$  = reaction rate constant ( $\text{min}^{-1}$ );  $t$  = time (min);  $X$  = fraction reacted of Pb (% extraction/100)(7).

## Material Characterization

The precipitate was calcined at 400 °C pre-determined calcination temperature by Thermo Gravimetric Differential Thermal Analysis (TG-DTA) and instrumental characterizations were carried out to substantiate the lead oxide nanoparticle/ powder. X-ray diffraction patterns of powdered samples were

collected using Bruker X-ray diffractometer (XRD, D8 Discovery, US) with Cu-K $\alpha$  radiation and  $\lambda=1.5406 \text{ \AA}$ . The morphology of the samples was examined using a Field emission gun-scanning electron microscope (Model FEI 430) fitted with an energy dispersive X-ray spectrometer (FEG-SEM/EDAX) and operated at 15.0 kV after coating the sample with silver. EDX spectra were collected on SEM/EDX SDD Apollo 40 Resolution 131.44 Model FEI 430. Thermal analyses were conducted on lead citrate precursors using a platinum crucible and alumina reference recorded on HITACHI STA 7300. FTIR spectra were recorded

on a Nicolet 5700 spectrometer using the KBr pellet method.

**RESULTS AND DISCUSSION**

**XRD Analysis of SLAB Paste**

The X-ray diffraction pattern of the paste is shown in Figure 2. Chemical phases in the paste revealed PbSO<sub>4</sub>, PbO<sub>2</sub>, PbO, Pb<sub>3</sub>O<sub>2</sub>SO<sub>4</sub> and metallic Pb. These phases are in line with chemical phases identified by literatures except for Pb<sub>3</sub>O<sub>2</sub>SO<sub>4</sub> identified in this research (6,8).

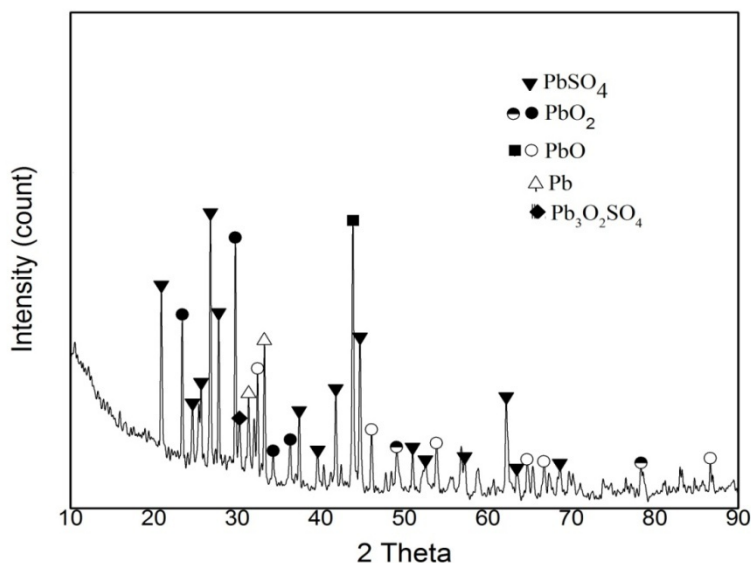


**Figure 2:** XRD pattern of used lead-acid battery paste.

**FE-SEM, EDS Analysis of SLAB Paste**

Figure 3 shows the typical morphology of the spent paste from automobile car batteries. Bulk and area scanning of the paste revealed a greater percentage of the micrograph as lead sulfate as compared to the image of PbSO<sub>4</sub> by (9). The energy dispersive spectra of point analysis obtained confirmed the

presence of Pb, O, S, Fe, as dominant elements in the paste and trace amount of carbon as the sample was coated on carbon tape. The percentages of Pb 63%, sulfur 11%, oxygen 18%, and iron 5% showed that the material is predominantly lead sulfate with traces of iron.

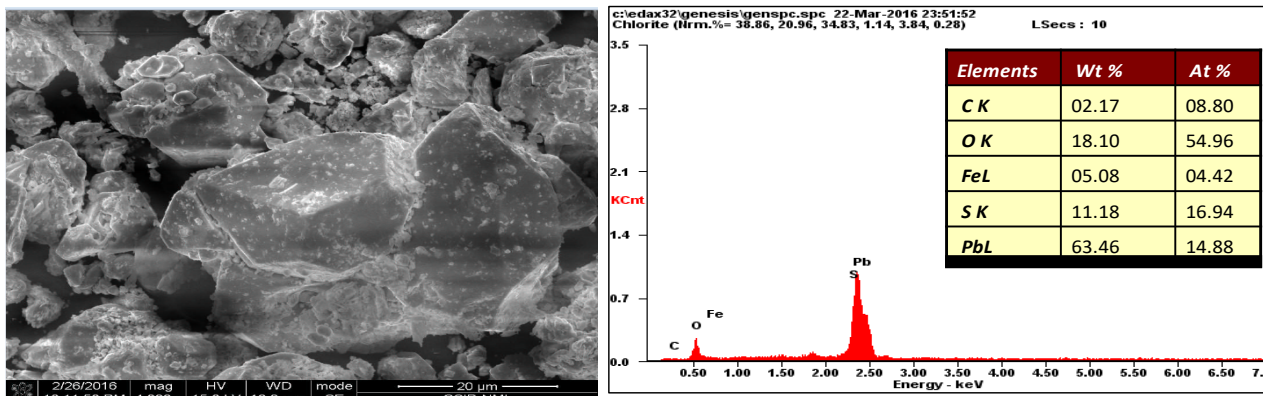


**Figure 3:** FE-SEM, EDS spectra of spent lead-acid battery paste.

**XRD Analysis of Lead Citrate**

The XRD phase of the synthesized lead citrate is shown in Figure 4. None of the phases identified in the paste were observed in the resulting precipitate indicating complete reaction between the paste and the leaching agents.

**FE-SEM, EDS Analysis of Lead Citrate**

The morphology of the lead citrate is revealed in Figure 5. The citrate is sheet-shaped which filtered out of the leaching solution with ease. The morphology changed from the block material to a sheet-like shape after the reaction. Energy dispersive spectra of the synthesized lead citrate

gave the percentages of elements present in the precursor as lead 81%, sulfur 1%, oxygen 7%, and carbon 9% (Figure 4) against the percentages of these elements in the paste lead 63%, sulfur 11%, iron 5%, oxygen 18%, and carbon 2% (Figure 3). Deducing from these results, sulfur in the paste has been reduced drastically from 11% to 1% which was the major process (desulfurization). It was also observed that iron was present in the paste but has been eliminated in the precipitate probably as iron sulfate. This observation affirms the purity of the lead citrate synthesized. The lead citrate was used to synthesize the desired PbO nano-sized particles.

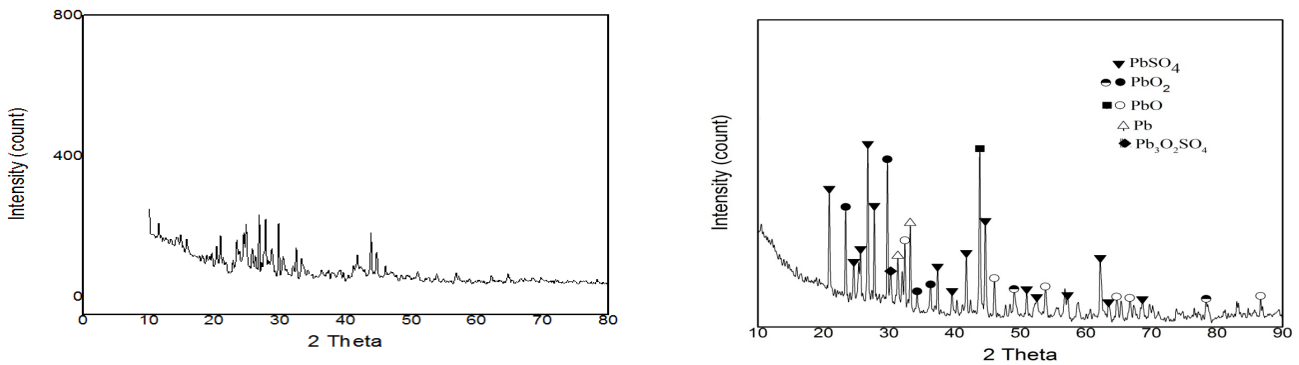


Figure 4: XRD patterns of citric acid synthesized precipitate (left) and spent paste (right).

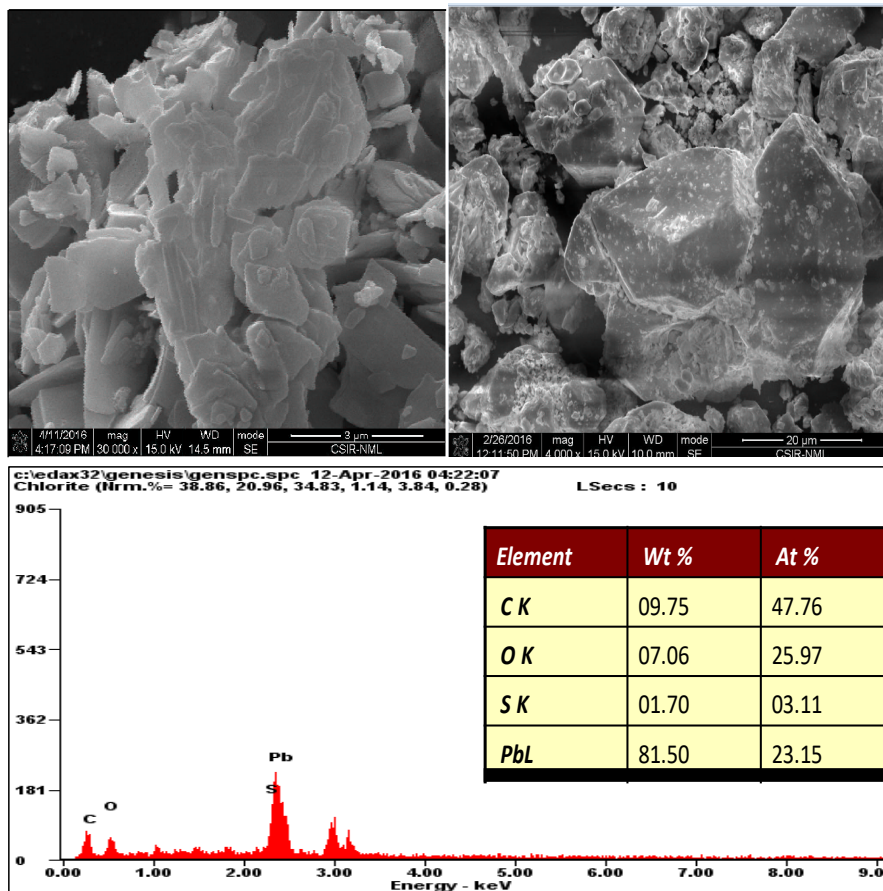
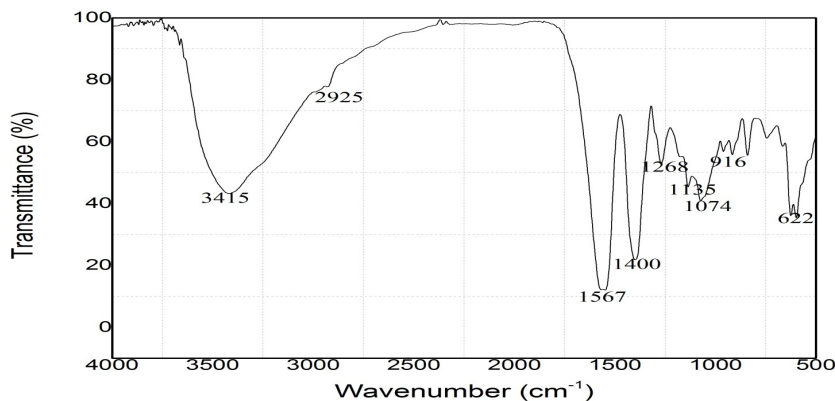


Figure 5: FE-SEM, EDS spectra of lead citrate precipitate and spent paste.

**FT-IR Analysis of Lead Citrate**

The FT-IR spectrum in Figure 6 was obtained to analyze the vibrations of the groups present in the lead citrate synthesized. FT-IR analysis showed strong absorption of carboxylate structure. The band 3415 cm<sup>-1</sup> revealed O-H strong stretching, while 2925 cm<sup>-1</sup> showed C-H stretching. Symmetric vibration of the range 1567 cm<sup>-1</sup> to 1400 cm<sup>-1</sup>

belonged to the carboxylate group. The weak bands of 1268 cm<sup>-1</sup> to 1074 cm<sup>-1</sup> are the C=O stretching which is a characteristic of citric acid. The band at 916 cm<sup>-1</sup> in the fingerprint region showed C-H stretching and the band 622 cm<sup>-1</sup> denotes the Pb-O-Pb bond. The strong intense peak of 1400 cm<sup>-1</sup> is a result of O-H bending vibration in adsorbed water (1).



**Figure 6:** FT-IR spectrum of lead citrate precipitate.

**XRD Analysis of Nano-PbO**

The XRD pattern of the nano lead oxide powder obtained after thermal treatment of the lead citrate

matched well with the tetragonal and orthorhombic PbO of JCPDS,1986 with intense peaks as shown in Figure 7.

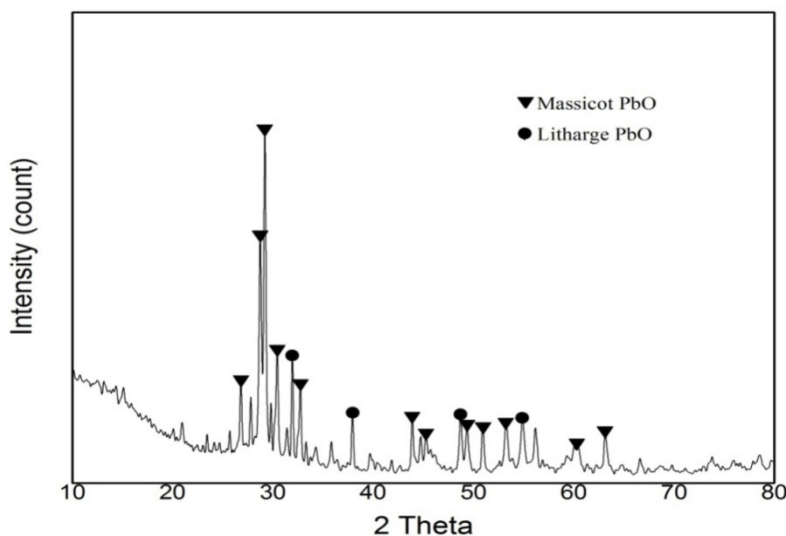


**Figure 7:** XRD spectra of nano-PbO.

**XRD-Particle Size**

An XRD analysis of the prepared sample PbO was carried out using X'pert PRO PANalytical diffractometer, Cu-Kα X-rays of wavelength (λ) 1.5406 Å. XRD pattern of Lead Oxide nanoparticle prepared is shown in Figure 7. The average size of the product was calculated using the Debye-Scherrer formula (1).

where D is the mean particle size; λ is the wavelength of CuKα -1.5406Å; β is the full width at half maximum (FWHM); and θ is Bragg's diffraction angle. The particle size calculated by the above formula was 19 nm. This result is in line with (17).

$$D = 0.9 \frac{\lambda}{\beta} \cos \theta \quad (\text{Eq. 6})$$

**FE-SEM and EDS of Nano-PbO**

The SEM and EDS spectra of nano-PbO obtained show a high agglomeration of the particles. The nano-PbO is spherical. The SEM morphology of the products as shown in Figure 8 revealed the particle size of the products at a range of 19 nm (16). This



is similar to what was reported in (13). The morphology of the lead citrate was observed to have changed from a sheet-like structure with the calcination temperature. The particles were agglomerated at the 400 °C pre-determined temperature from our previous publication. EDS spectra showed significant peaks identified to be

characteristic peaks of Pb and O proving that the products were mainly lead oxide.

The color of the products changed from the dark SLAB paste to whitish color of the lead citrate before calcination to yellow products of nano lead oxide Figure. 9(10)

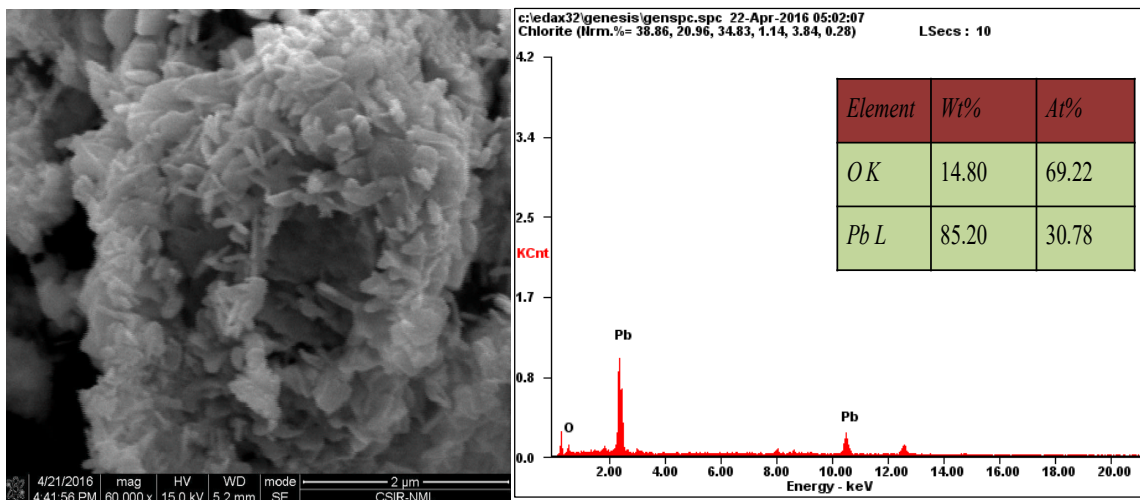


Figure 8: SEM, EDS images of nano PbO.

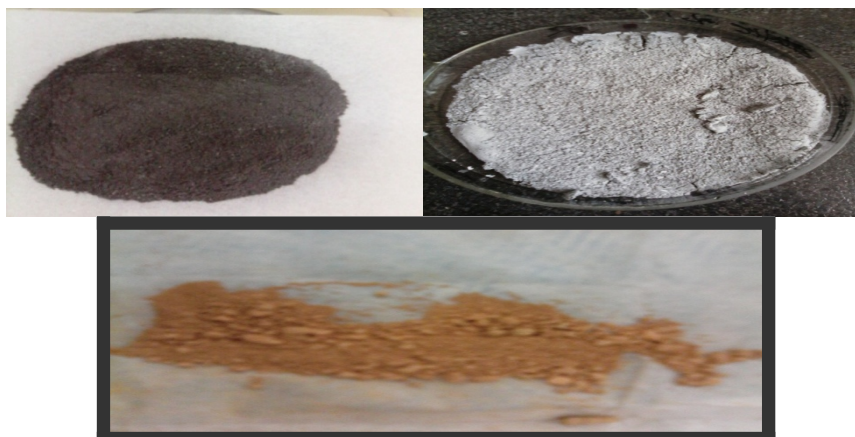


Figure 9: Color changes of the samples.

**Specific Surface Area (SSA)**

This is one of the properties of solids which is the total surface area of a material per unit mass. It is scientifically derived and is applied to ascertain the type and properties of materials. It has several applications in adsorption, heterogeneous catalysis, and reaction on surfaces. It can be determined by the formula:

$$SSA = \frac{SA_{part}}{V_{part} \times \text{Density}} \quad (\text{Eq. 7})$$

where SSA is the specific surface area; SA part is the surface area of the particle; V part is particle volume; and Density is the theoretical density of lead oxide. SSA can also be calculated using Equation 8:

$$S = 6 \times \frac{10^3}{D\rho} \quad (\text{Eq. 8})$$

where S is the specific surface area; D is the mean particle size; ρ is the density of lead oxide. Mathematically, both relations give the same value. SSA calculated by the formula was 33 m<sup>2</sup>/g (11,17).

**Crystallinity Index (I<sub>cry</sub>)**

The crystallinity of a solid defines the degree of structural order in the solid. It is determined by comparing particle size measured from XRD data with particle size from SEM/TEM measurement. It can be calculated using the relation:

$$I_{cry} = \frac{D_p}{D} \quad (\text{Eq. 9})$$

where  $D_p$  is the particle size from SEM/TEM; and  $D$  is the particle size from the Scherrer formula (11).

If the  $I_{cry}$  value is close to 1, it is assumed the particle size is monocrystalline; and where it is greater than or much larger, it is assumed to be polycrystalline. The calculated crystallinity index was 3, which implied that the product was polycrystalline (15).

### Leaching Kinetic Studies

The leaching kinetics studies of the paste were done by experimenting at different reaction times and different acid concentrations with pulp density (S/L) ratio of 100 g/L. The result is presented in Figure 10; an increase in acid concentrations increased the lead in solution at a varied time. All standard equations of shrinking core models were analyzed for reaction kinetics of lead dissolution.

Examination of the experimental results in all the models using the above equations, the kinetics followed Ash diffusion control model, i.e  $1-3(1-X)^{2/3}+2(1-X) = K_c t$  as exemplified in Figure 10 and Table 1 for 1 M and 3 M citric acid concentration

while at 2 M concentration, chemical reaction control model was best fitted. The ash diffusion model was affirmed by the SEM/EDX studies. The spongy structure of the leached residue indicated that elemental Pb was deposited during the early period of leaching. The deposited Pb acted as a permeable layer permitting ash diffusion-control reaction kinetics, the SEM image is shown in Figure 11. The model fitted at 2M citric acid with  $1-(1-X)^{1/2} = K_c t$  chemical reaction control dense cylindrical particles. This is depicted in the SEM photograph in Figure 10 which confirmed the model of the reaction. The equations were selected based on the highest values of  $R^2$  the regression coefficient in each study Figure 12. The Activation energy of the ash diffusion control model was calculated using Arrhenius' equation  $K_c = Ae^{-E_a/RT}$  to be 8.3 kJ/mol and the chemical control model was 33.3 kJ/mol. Michael (12) reported that aqueous diffusion control reactions often have low activation energies of less than 15,000 J/mol. and chemical control has larger activation energies. The reactions in this study are not strongly influenced by temperature as room temperature was found suitable for the experiments which confirmed kinetic reaction processes. Lead(II) oxides ( $\alpha, \beta$ ) at a nano dimension of 19 nm and a specific surface area of 33 m<sup>2</sup>/g polycrystalline were produced.

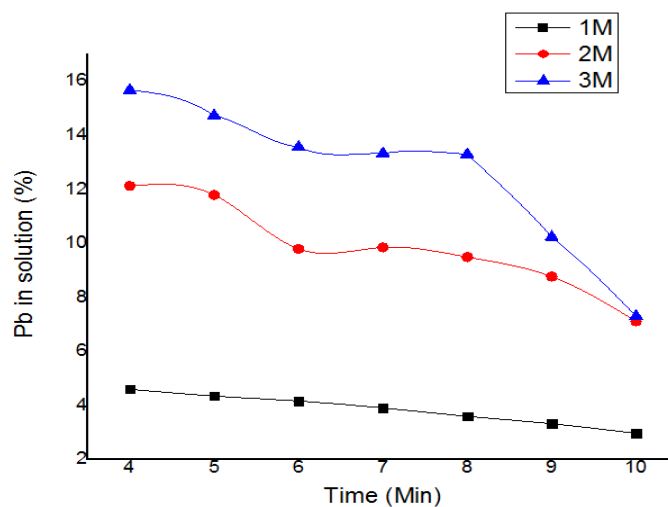


**Figure 10:** Kinetics of Pb leaching at 100 g/L with citric acid.



**Table 1:** Regression Coefficient Values for different shrinking core models for the kinetics of leaching of lead-acid battery paste.

S/N	Citric Acid conc. (M)	X	$1-(1-X)^{2/3}$	$1-(1-X)^{1/2}$	$1-(1-X)^{1/3}$	$1-3(1-X)^{2/3}+2(1-X)$	Model selected
A	1	0.9927	0.9928	0.9929	0.9929	0.9979	$1-3(1-X)^{2/3}+2(1-X)$
B	2	0.9207	0.9209	0.921	0.921	0.9199	$1-(1-X)^{1/2}$
C	3	0.8409	0.8533	0.8546	0.8287	0.8983	$1-3(1-X)^{2/3}+2(1-X)$

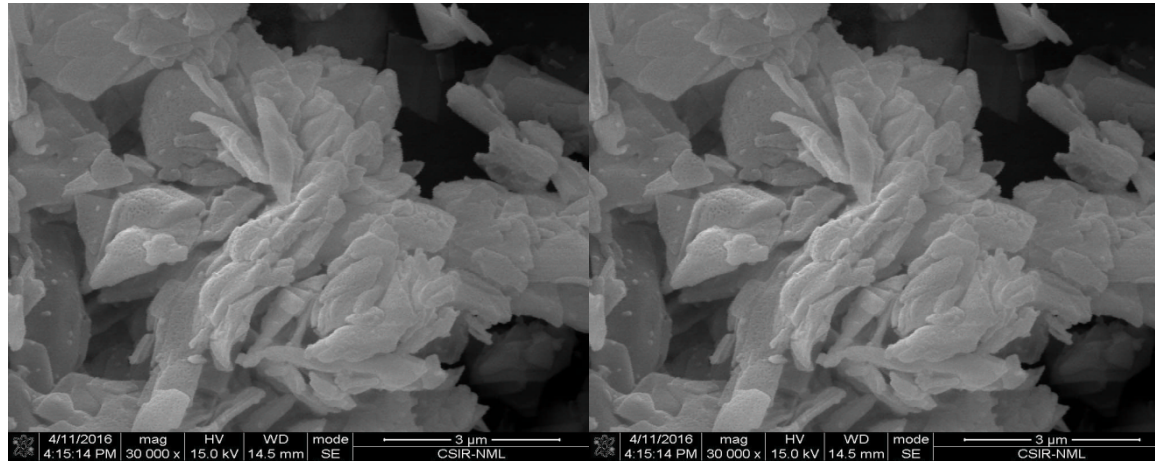


**Figure 11:** SEM images of leached residue for kinetics studies.

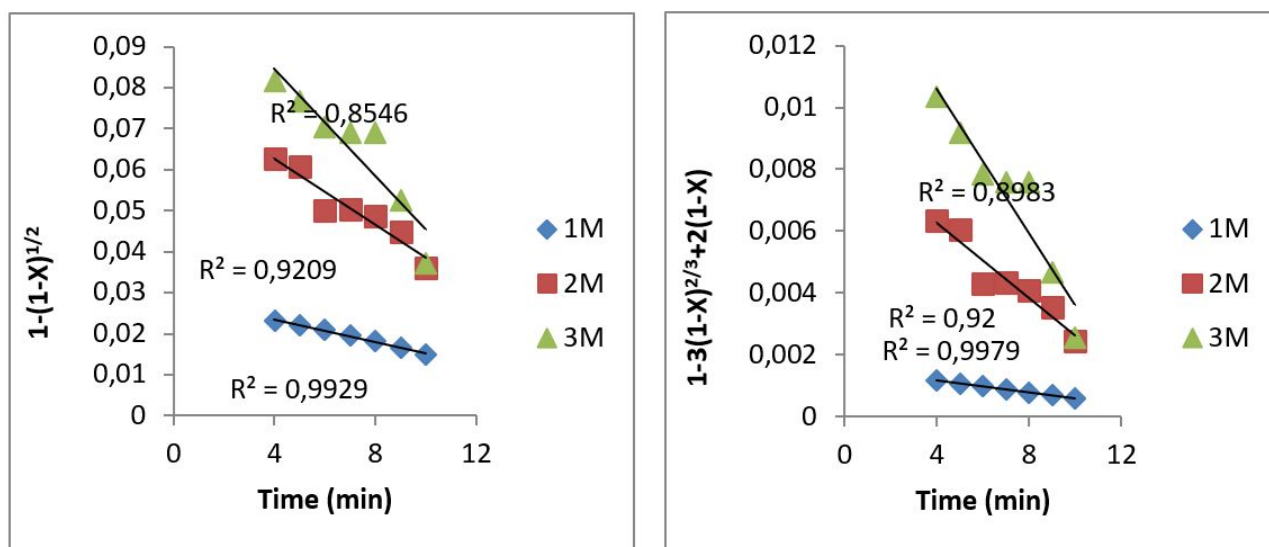


**Figure 12:** Fittings of lead conversion into equations of shrinking core model for lead-acid battery paste. Chemical reaction control dense constant size cylindrical particles (left), Ash diffusion control dense constant size- spherical particles (right).

## CONCLUSION

Wet chemical synthesis of nano-PbO from spent SLABs via citric acid system was demonstrated in this study. Characterization of the nano powder revealed spherically shaped PbO at nano dimension. Citric acid showed good adhesive properties to the Pb component of the spent paste. A combination of pure  $\alpha$ - $\beta$  PbO was synthesized as final product without impurities. The product is suitable as raw material in the fabrication of new lead acid battery as the combination is most desired industrially. The reaction kinetics of the paste follows ash diffusion control model leaching with citric acid system. The activation energies of the overall reactions are 8.3 kJ/mol and 33.3 kJ/mol for 1 & 3 M acid system ash diffusion and 2 M chemical control acid system respectively.

## ACKNOWLEDGMENTS

The researchers express their profound gratitude to *i-PSG* of CSIR- National Metallurgical Laboratory Jamshedpur, India for providing analytical facilities to fulfilling the experimental data collection.

## AUTHORS' CONTRIBUTIONS

The authors designed and carried out the experiment and analyzed the experimental data. All the authors worked on characterization analysis and the drafting of the manuscript. All authors read and approved the final manuscript.

## FUNDING

This work was supported by the Tertiary Education Trust fund of the Federal Republic of Nigeria and the Centre for Science & Technology of the Non-aligned and Other Developing Countries (NAM S& T) for the RTF-DCS fellowship (NAM - 05/74/2015).

## COMPETING INTERESTS

The authors declare that there were no competing interests.

## REFERENCES

1. Arulmozhi KT, Mythili N. Studies on the chemical synthesis and characterization of lead oxide nanoparticles with different organic capping agents. *AIP Advances*. 2013 Dec;3(12):122122. <DOI>.
2. Alagar M, Theivasant T, Raja AK. Chemical Synthesis of Nano-sized Particles of Lead Oxide and their Characterization Studies. *J of Applied Sciences*. 2012 Feb 1;12(4):398-401. <DOI>.
3. Liu N, Senthil RA, Zhang X, Pan J, Sun Y, Liu X. A green and cost-effective process for recovery of high purity  $\alpha$ -PbO from spent lead acid batteries. *Journal of Cleaner Production*. 2020 Sep;267:122107. <DOI>.
4. Sonmez MS, Kumar RV. Leaching of waste battery paste components. Part 1: Lead citrate synthesis from PbO and PbO<sub>2</sub>. *Hydrometallurgy*. 2009 Jan;95(1-2):53-60. <DOI>.
5. Sonmez MS, Kumar RV. Leaching of waste battery paste components. Part 2: Leaching and desulphurisation of PbSO<sub>4</sub> by citric acid and sodium citrate solution. *Hydrometallurgy*. 2009 Jan;95(1-2):82-6. <DOI>.
6. Li L, Zhu X, Yang D, Gao L, Liu J, Kumar RV, et al.

Preparation and characterization of nano-structured lead oxide from spent lead acid battery paste. *Journal of Hazardous Materials*. 2012 Feb;203–204:274–82. [<DOI>](#).

7. Li X, Xing P, Du X, Gao S, Chen C. Influencing factors and kinetics analysis on the leaching of iron from boron carbide waste-scrap with ultrasound-assisted method. *Ultrasonics Sonochemistry*. 2017 Sep;38:84–91. [<DOI>](#).

8. Zhu X, Li L, Sun X, Yang D, Gao L, Liu J, et al. Preparation of basic lead oxide from spent lead acid battery paste via chemical conversion. *Hydrometallurgy*. 2012 Apr;117–118:24–31. [<DOI>](#).

9. Sajadi SAA. A Comparative Investigation of Lead Sulfate and Lead Oxide Sulfate Study of Morphology and Thermal Decomposition. *AJAC*. 2011;02(02):206–11. [<DOI>](#).

10. Mahmoudabad MK, Kashani-Motlagh MM. Synthesis and characterization of PbO nanostructure and NiO doped with PbO through combustion of citrate/nitrate gel. *Int J Phys Sci*. 2011;6(24):5720–5. [<DOI>](#).

11. Nowsath Rifaya M, Theivasanthi T, Alagar M. Chemical Capping Synthesis of Nickel Oxide Nanoparticles and their Characterizations Studies. *NN*. 2012 Dec 1;2(5):134–8. [<DOI>](#).

12. Free M. *Hydrometallurgy: fundamentals and*

*applications* [Internet]. 2013 [cited 2022 Jan 17]. Available from: <http://site.ebrary.com/id/1075340018>. ISBN: 978-1-118-23077-0.

13. Jenkins R, Fawcett TG, Smith DK, Visser JW, Morris MC, Frevel LK. JCPDS — International Centre for Diffraction Data Sample Preparation Methods in X-Ray Powder Diffraction. *Powder Diffr*. 1986 Jun;1(2):51–63. [<DOI>](#).

14. Bratovcic A. Synthesis, Characterization, Applications, and Toxicity of Lead Oxide Nanoparticles. In: Chooto P, editor. *Lead Chemistry* [Internet]. IntechOpen; 2020 [cited 2022 Jan 17]. ISBN: 978-1-83962-568-8. [<URL>](#).

15. Spek AL. Structure validation in chemical crystallography. *Acta Crystallogr D Biol Crystallogr*. 2009 Feb 1;65(2):148–55. [<DOI>](#).

16. Fard MJS, Hayati P, Naraghi HS, Tabeie SA. Synthesis and characterization of a new nano lead(II) 0-D coordination supramolecular compound: A precursor to produce pure phase nano-sized lead(II) oxide. *Ultrasonics Sonochemistry*. 2017 Nov;39:129–36. [<DOI>](#).

17. Anonymous. *Lead Oxide Nanoparticles / Nanopowder* [Internet]. *Lead Oxide Nanoparticles / Nanopowder*. 2022. [<URL>](#).



## Adsorption of Methylene Blue and Methyl Orange from Aqueous Solution using Orange Peel and CTAB-Modified Orange Peel

Aulia Dewi Rosanti<sup>1\*</sup>   ID, Yuly Kusumawati<sup>2</sup> ID, Fahmi Hidayat<sup>1</sup> ID, Arif Fadlan<sup>2</sup> ID, Anggita R. K. Wardani<sup>1</sup> ID, Herlina Agusyanti Anggraeni<sup>1</sup> ID

<sup>1</sup>Universitas Islam Kadiri, Department of Chemistry, Kediri, 64128, Indonesia

<sup>2</sup>Institut Teknologi Sepuluh Nopember, Department of Chemistry, Surabaya, 60111, Indonesia

**Abstract :** Cationic and anionic dyes are frequently used in industrial sectors and cause many environmental and health problems. Orange peel has the potential to absorb dye as an adsorbent. This study aimed to explore the adsorption of methylene blue (MB) as a cationic dye and methyl orange (MO) as an anionic dye using orange peel (OP) and its modification using cetyltrimethylammonium bromide (CTAB). OP and OP-CTAB biomass materials were characterized using FT-IR (Fourier transform infrared), surface area analysis using BET (Brunauer-Emmett-Teller) and SEM EDX (Scanning Electron Microscopy-Energy Dispersive X-Ray Spectroscopy). Based on the study results, OP has a microporous skin structure and OP-CTAB mesopores. Based on the effect of contact time, it is known that the best adsorption process on MB was to use OP adsorbent with the optimum amount of dye adsorbed produced at 50th minute that was 5.881 ppm, while the best adsorption process on MO was using OP-CTAB adsorbent with the optimum amount of dye was at 50th that was equal to 13.34 ppm. Based on the adsorption kinetics data, the adsorption of MO and MB dyes by OP and OP-CTAB followed the pseudo second order reaction kinetics model. The adsorption of MO and MB by both OP and OP-CTAB followed Langmuir's adsorption isotherm, meaning that the adsorption process in both MO and MB using OP and OP-CTAB appeared on homogeneous surface sites, while there was no interaction between adsorbate molecules and adjacent locations that means the adsorption process only occurred physically.

**Keywords:** CTAB-modified Orange Peel, Orange Peel, Methylene Blue, Methyl Orange.

**Submitted:** October 01, 2021. **Accepted:** January 18, 2022.

**Cite this:** Rosanti AD, Kusumawati Y, Hidayat F, Fadlan A, Wardani ARK, Agusyanti HA. Adsorption of Methylene Blue and Methyl Orange from Aqueous Solution using Orange Peel and CTAB-Modified Orange Peel. JOTCSA. 2022;9(1):237-46.

**DOI:** <https://doi.org/10.18596/jotcsa.1003132>.

**\*Corresponding author. E-mail:** [aulia.dewi.r@uniska-kediri.ac.id](mailto:aulia.dewi.r@uniska-kediri.ac.id).

### INTRODUCTION

Dyes have been used in various industrial sectors, especially in the textile, rubber, plastic, leather, cosmetics, food, and medicine industries. Dye waste from these industries can cause dangerous environmental problems. This is because some dyes have toxic, carcinogenic, and mutagenic properties (1,

2). Dyes used in the industrial sector, especially textiles, include methyl orange and methylene blue (1-3). Methyl orange and methylene blue are azo dyes that are nonbiodegradable, making them very difficult to degrade (3-5).

Several methods have been used to remove dye waste, including coagulation, complexation, ion

exchange, and adsorption (6). Adsorption is not only used to remove toxic metal ions from water but also can be used to remove dyes from water (7,8). Adsorption is the most commonly used method to remove azo dyes because it is relatively easy, efficient, inexpensive, and environmentally friendly. The use of biomass as a cheap and environmentally friendly adsorbent has begun to be considered as a replacement for commercially activated carbon (9). One of the potential biomass adsorbents is orange peel, and currently, the total area of citrus plantations in Indonesia is more than 57,000 hectares with a production of 2.5 million tons (10). Orange peel (OP) contains pectin, hemicellulose, lignin, chlorophyll, and other low molecular weight hydrocarbons. Thus,

orange peel has the potential to absorb color from diluted solutions as an adsorbent (11).

Some studies have shown the use of orange peel as an adsorbent, including Krisnan and George (2), who found that the higher the adsorbent dose of orange peel is, the greater the amount of methylene blue that can be removed. This study showed that 2.2 grams of orange peel can remove 96% of methylene blue in 60 minutes. Nascimento et al. in 2014 (12) also reported that orange peel successfully removed Remazol Golden Yellow RNL-150%, Reactive Gray BF-2R and Reactive Turquoise Q-G125 from diluted solution. The other previous studies about the use of orange peel for dye adsorption can be seen in Table 1.

**Table 1:** Previous studies about the use of orange peel for dye adsorption.

Dye name	Max adsorption (mg/g)	References
Congo red	22.44	(13)
Procion orange	1.33	(13)
Rhodamine B	3.23	(13)
Acid violet 17	19.88	(14)
DR 23	10.72	(15)
DR 80	21.05	(15)

Some studies have also suggested that modifying orange peel adsorbents can maximize the adsorption process, including Ahmed et al. in 2012 (1), who successfully removed Reactive Blue 19 using orange peel and NaOH- and cetyltrimethylammonium bromide (CTAB)-modified orange peel. Based on previous studies, modified orange peel is better able to cause desorption of the reactive blue 19 color than the pristine orange peel. This study aimed to remove methylene blue as a cationic dye and methyl orange as an anionic dye using orange peel and CTAB-modified orange peel.

## EXPERIMENTAL METHODS

### Materials

The materials used in this study included orange peel (orange peel was obtained from a local fruit field in northern Sumatra, Indonesia), CTAB (synthesis grade, Merck), methylene blue (Merck), methyl orange (Merck) and Aqua DM (Bratachem).

### Adsorbent Preparation

Orange peels were obtained from a local fruit field in North Sumatra, Indonesia. The preparation of the adsorbent was adapted from the method of Arami et al. (2005) (15) with modification. The OP were washed several times with water and sun-dried for 2 days. The dried materials were mashed and sieved through a 60-mesh sieve. The dried powder from the orange peels was stored in a plastic container before use.

### CTAB Modification of Adsorbent

CTAB modification of the adsorbent was adapted from the method of Taghried and Mayasa (2019), (16) with modification. The orange peel powder (5 grams) was soaked in 1% (w/v) CTAB solution (100 mL) for 24 hours and filtered through a vacuum (17, 18). The obtained precipitate was dried in an oven at 75 °C for 8 hours. The CTAB-modified dried powder was ground and sieved using a 60-mesh sieve.

### Characterization of the Adsorbents

Fourier transform infrared spectroscopy (FTIR, Nicolet Avatar 360 IR) in the range of 400–4000  $\text{cm}^{-1}$  was utilized for surface chemical analysis. The surface morphology of the adsorbents was analyzed by using scanning electron microscopy-energy dispersive X-ray spectroscopy (SEM EDX) (Phenom Desktop ProXL). The specific surface area of the adsorbents was measured by a BET  $\text{N}_2$  surface area analyzer (Quantachrome Quadrasorb Evo QDS-MP 30).

### MB and MO Adsorption Batch Study

In each adsorption experiment, 25 mL of dye solution was added to 20 mg of adsorbent at room temperature, and the mixture was stirred at 400 rpm for 1 hour. The mixture was centrifuged at 3000 rpm for 10 minutes to separate the adsorbents, and then, it was observed at wavelengths of 664.5 nm for MB and 465 nm for MO using a UV-Vis spectrophotometer (T70 UV-Vis Spectrophotometer, PG Instrument Ltd). The amount of MB/MO adsorbed by OP and OP-CTAB at time  $t$ ,  $q_t$  (mg/g), was calculated by Equation (1) (1):

$$q_t = \frac{(C_0 - C_t)V}{w} \quad (\text{Eq. 1})$$

The MB/MO percentage of adsorption was calculated by Equation (2) (1):

$$\% \text{ Removal} = \frac{(C_0 - C_t)}{C_0} \times 100 \quad (\text{Eq. 2})$$

## RESULTS AND DISCUSSION

### FTIR Analysis

FTIR spectroscopy is a useful analytical instrument for the identification of the functional groups in the adsorbents and the interaction of orange peels with CTAB. The FTIR spectra of CTAB, OP and OP-CTAB were in the range of 400-4000  $\text{cm}^{-1}$ , as shown in Figure 1. The FTIR spectra of CTAB showed sharp peaks in the absorption bands at approximately 2918.41 and 2848.08  $\text{cm}^{-1}$  due to the symmetrical and asymmetrical stretching vibrations of the  $\text{CH}_2$  group on CTAB (19-23). In addition, there was a peak at 1479.87  $\text{cm}^{-1}$  for the buckling vibration of the N-C group on CTAB (24).

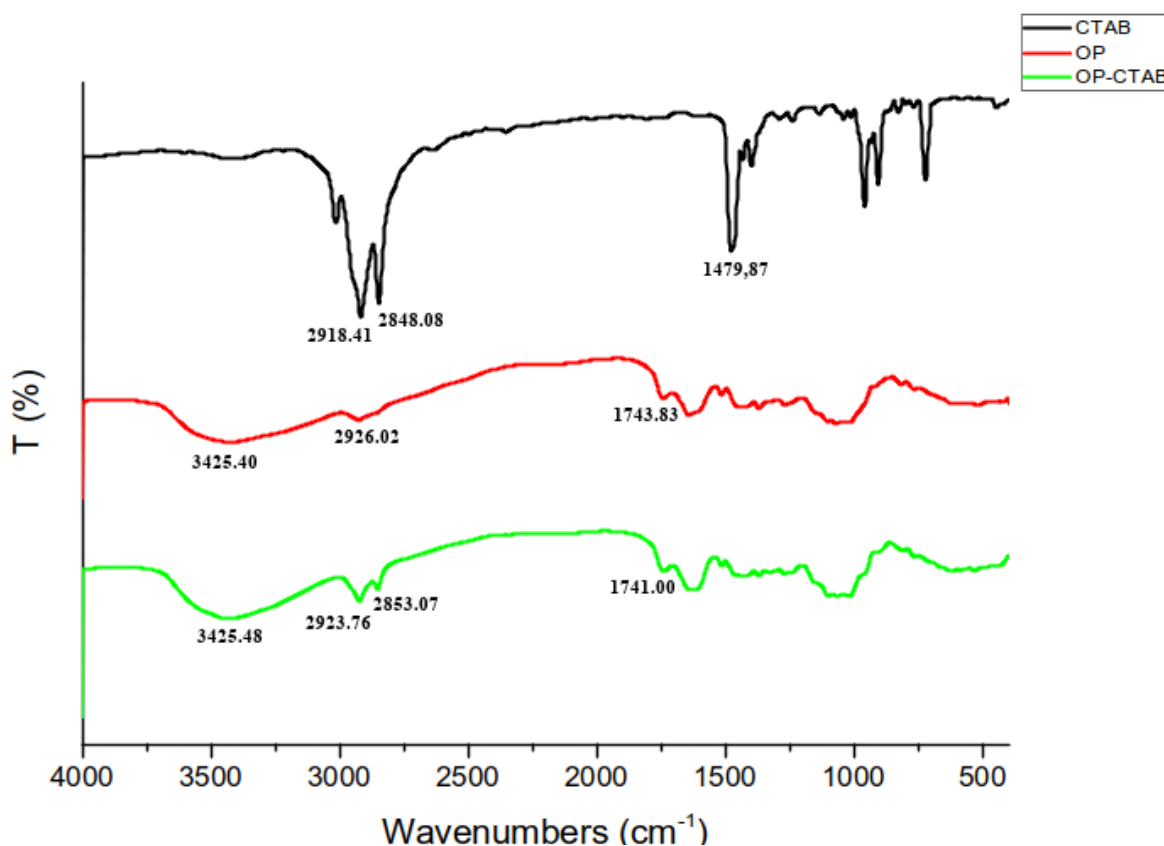


**Figure 1:** IR spectra of CTAB, OP, and OP-CTAB.

In the OP's spectra, the absorption widened at 3425.40  $\text{cm}^{-1}$ , indicating the presence of stretching vibrations from the -OH groups of cellulose, pectin, hemicellulose, and lignin. The peak at 2926.02  $\text{cm}^{-1}$  was due to the C-H stretching vibrations. The 1743.83  $\text{cm}^{-1}$  peak in the OP's spectra indicated the stretching vibrations of the carbonyl groups ( $\text{C}=\text{O}$ ) of pectin, hemicellulose, and lignin. The absorption band was in the wavenumber range of 1300-1000  $\text{cm}^{-1}$  for the C-O

stretching vibration of the carboxylic acid and alcohol groups (25, 26).

The FTIR spectra of OP-CTAB showed similarities with the FTIR spectra of OP, indicating that both have similar functional groups and almost the same compounds. The peak intensity in the FTIR spectra of OP at 2926  $\text{cm}^{-1}$  increased from 26.12 to 38.48 (34.22%) after modification with CTAB. This indicates

that CTAB modification in orange peel increases the number of  $-CH_2-$  groups (1). In addition, the modification of the orange peel by CTAB is also shown by two peaks at wavenumbers of approximately 2923.76 and 2853.07  $cm^{-1}$  in the FTIR spectra of OP-CTAB as the peak from the symmetrical and asymmetrical stretching vibration of the C-H group of CTAB (19, 23).

#### Characterization of OP Powder and OP-CTAB using BET

BET analysis determines the surface area and pore size, while the BJH (Barrett-Joiner-Halenda) method is used to determine the pore volume. In Table 2, the surface area of OP is larger than OP-CTAB. OP has a surface area of 204  $m^2/g$ , and OP-CTAB has a surface area of 27.210  $m^2/g$ . Based on these results, the CTAB modification of OP resulted in a smaller surface area than OP. Although the surface area in OP is larger, OP has a smaller pore size of 1.780 nm, while OP-CTAB has a smaller pore size of 2.045 nm.

**Table 2:** BET Analysis Results for OP and OP-CTAB.

Biomass	Surface Area ( $m^2/g$ )	Pore Volume	Pore size (nm)
OP	204.000	0.181	1.780
OP-CTAB	27.210	0.028	2.045

Based on the pore size, a porous material can be classified into three classes, namely, microporous material (pore size < 2 nm), mesopores (pore size 2-50 nm) and macropores (pore size > 50 nm) (27). OP has a pore size of 1.780 nm, so it can be categorized as a microporous material, while OP-CTAB has a pore size of 2.045 nm, and it can be classified as a mesoporous material. The presence of CTAB induced the formation of mesopores that can be used for polymers and other large compounds that resulted in better particle dispersion (27). Based on the data, it can be concluded that OP has a large surface area but a microporous pore structure, while OP-CTAB has a small surface area but a mesoporous structure whereby mesopores can produce better particle dispersion than other porous structures. In contrast to the results of research from Taghried and Mayasa (2019) (16) which resulted in a larger surface area of OP-CTAB than OP. This is because in this research the

character of orange peel is more porous and it can be seen from the high surface area before the addition of CTAB, so that the CTAB enters the pores, whereas in the previous research it may be less porous, as can be seen from the very low BET result.

#### Characterization of OP Powder and OP-CTAB using SEM EDX

SEM EDX analysis is necessary to determine the morphology and content of elements present on the surface of OP and OP-CTAB. Figure 2 shows that the surface of OP is rougher and more irregular compared to the surface of OP-CTAB. In addition, the addition of CTAB made OP smaller and more separate compared to that without the addition of CTAB. This is supported by the results of BET analysis showing the pores from OP-CTAB compared to OP. According to the BET results, the OP surface area is larger than OP-CTAB, but based on pore size, OP has a microporous structure, while OP-CTAB has a mesoporous structure.

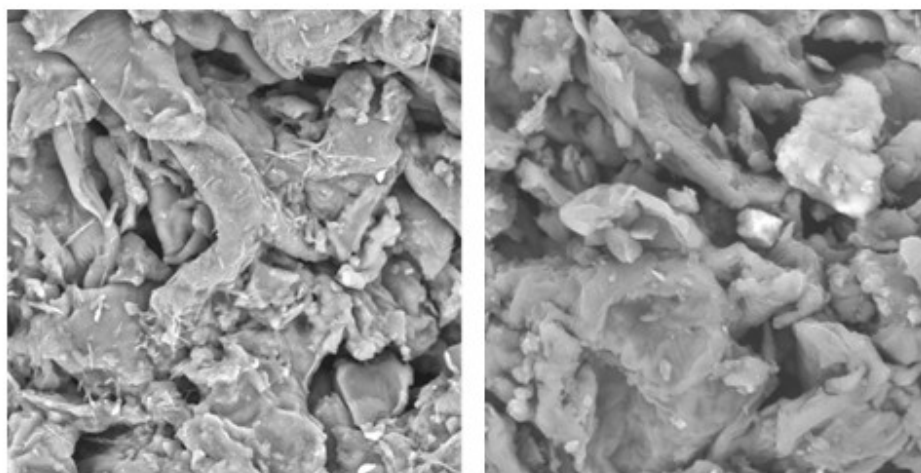


**Figure 2:** Surface morphologies of OP (left) OP-CTAB (right).



In addition to showing the surface morphological results of a material, SEM EDX can be used to determine the elements present on a material surface. Based on Table 3, the surface of OP contains the elements of carbon (C), oxygen (O), calcium (Ca) and potassium (K). In comparison, OP-CTAB contains the elements of carbon (C), oxygen (O), nitrogen (N), and aluminum (Al). Additionally, the EDX results in

Table 3 show the presence of N at 8.410% in OP-CTAB, indicating that CTAB successfully entered or attached to the surface of OP. The presence of the N element from the ammonium group of CTAB with a positive partial charge causes OP-CTAB to have cationic properties, so it is easier to attract anionic dyes than OP.

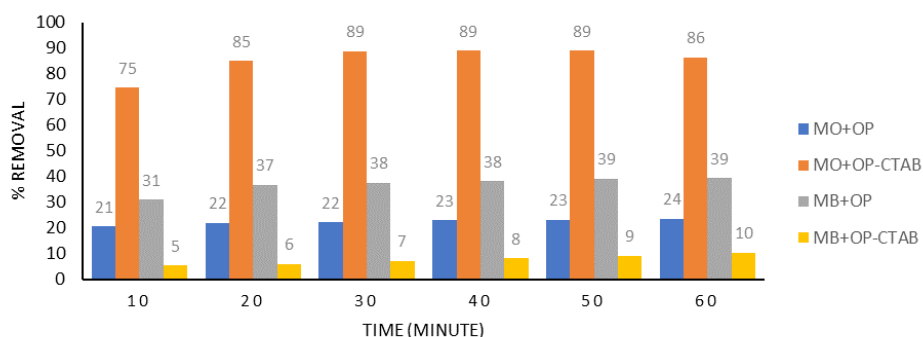
**Table 3:** Total (%) components on OP and OP-CTAB surfaces.

Sample	Element	Mass (%)	Atom (%)
OP	C	62.100	69.460
	O	35.340	29.680
	Ca	1.640	0.550
	K	0.920	0.320
OP-CTAB	C	67.810	73.640
	O	21.200	17.280
	N	8.410	7.830
	Al	2.590	1.250

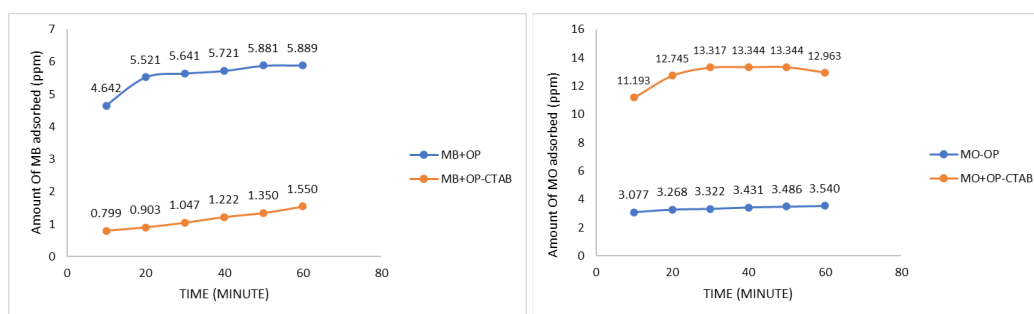
### Contact Time Effect

Figure 3 shows the percentage of MO and MB adsorbed by OP and OP-CTAB at room temperature at 25 °C as a function of contact time. The variation in contact time was 10, 20, 30, 40, 50 and 60 minutes at 15 mg/L MO and MB.

Based on Figure 3, the best color removal rate was for the OP-CTAB adsorbent on MO and for OP on MB. Thus, OP-CTAB was more effectively used to remove MO dyes than MB dyes, while OP was more effectively used to remove MB dyes than MO dyes. The amount of MB and MO that can be adsorbed using OP and OP-CTAB in ppm can be see Figure 4.



**Figure 3:** Relationship between Adsorption Capacity and Contact Time.



**Figure 4:** Amount of adsorbed dye vs. Contact Time MB 15 ppm (left); MO 15 ppm (right).

Based on Figure 4, it is known that the amount of MB that was successfully adsorbed using the OP adsorbent for 60 minutes was 5.889 ppm (39%), while MO was only able to adsorb 3.540 ppm (24%). Different with OP-CTAB adsorbent, the amount of MB that was successfully adsorbed at 60<sup>th</sup> minute on MB was 1.550 ppm (10%) while in MO it was 12.963 ppm (86%). Based on the results can be concluded that OP is better used to adsorb MB dye than MO and OP-CTAB is a better adsorption agent for MO than for MB. OP contains cellulose, pectin, hemicellulose, lignin and other compounds. The pectin compound in OP has a carboxylic acid group that causes OP to be negatively charged so that it is easier to absorb cationic dyes. OP-CTAB was more effective at absorbing anionic dyes due to N<sup>+</sup> derived from the ammonium group, causing OP-CTAB to have more cationic properties than OP. This is supported by the SEM EDX data showing the N content in OP-CTAB; thus, CTAB has successfully entered the OP surface. Cellulosic hydroxyl groups from OP combined with the cationic surfactant (CTAB) will form an ester linkage and present -CH<sub>2</sub>- groups to the fiber, leading to a columbic attraction between the cationic cellulose and the anionic dyes (MO) (1).

Based on Figure 4, it can be seen that the optimum condition of MB adsorption was by using OP that occurs at 50<sup>th</sup> minute was 5.881 ppm. Meanwhile, the optimum condition for MO occurred using OP-CTAB adsorbent at 50<sup>th</sup> minute that was 13.344 ppm. The use of OP-CTAB on MB and OP on MO had not reached optimal adsorption, it can be seen from the trend of the linear line tends to be gentle on MB-OP adsorption and tends to decrease for MO-OP-CTAB at 50<sup>th</sup> and 60<sup>th</sup> minute. It is due to the fact that at the minute the adsorption process had reached the equilibrium between the adsorbent and the adsorbate and reached the saturation limit, so that the adsorption reached the optimum. In contrast with MB-OP-CTAB and MO-OP adsorption processes, the adsorption

process can be seen in the graph that the trend line tends to rise that indicates the adsorption process had not yet reached the optimum. Based on the description above, it can be seen that the best adsorption process on MB was using OP adsorbent with the optimum amount of dye adsorbed produced at 50<sup>th</sup> minute that was 5.881 ppm, while the best adsorption process on MO was using OP-CTAB adsorbent with the optimum amount of dye was at 50<sup>th</sup> minute that was equal to 13.34 ppm.

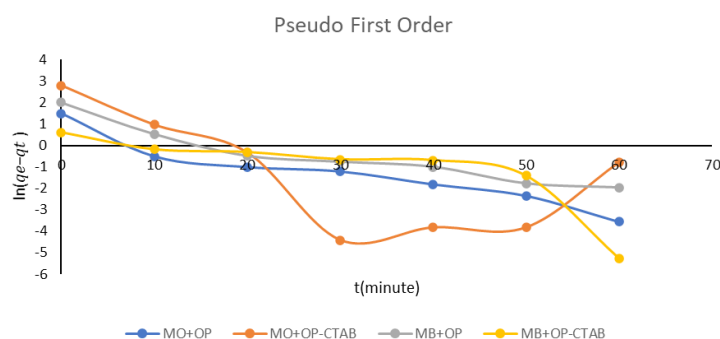
### Adsorption Kinetics

The determination of the reaction order from the adsorption process and reaction rate constants can be analyzed using pseudo first order or pseudo second order reaction kinetics equations. The kinetics of pseudo first order adsorption is based on mass equilibrium assuming that the rate between successful absorption and the time is proportional to the compensation of the dye adsorbed at various times ( $q_e - q_t$ ). Thus, it can be formulated using the following equation:

$$\ln(q_e - q_t) = \ln q_e - k_1 t \quad (\text{Eq. 3})$$

where  $q_e$  is the concentration of adsorbate at equilibrium,  $q_t$  is the concentration of adsorbate at time  $t$ ,  $t$  is the contact time (minutes) and  $k_1$  is the constant rate it adsorbs. At time  $t=0$ , then  $q_t=0$ , and at time  $t=t$ , then  $q_t=q_t$ . The value can be obtained by plotting  $\ln(q_e - q_t)$  versus  $t$  (Figure 5(a)). Meanwhile, the pseudo second order, which can also be referred to as pseudo chemical reactions, is described in Equation 4. The  $k_2$  or pseudo second order reaction rate constant is obtained by plotting a graph of  $t/q_t$  vs.  $t$  (Figure 5(b)). The results of  $R^2$  regression values and reaction rate constants on each reaction kinetics model are shown in Table 4.

$$\frac{t}{q_t} = \frac{1}{k_2 q_e^2} + \frac{1}{q_e} t \quad (\text{Eq. 4})$$



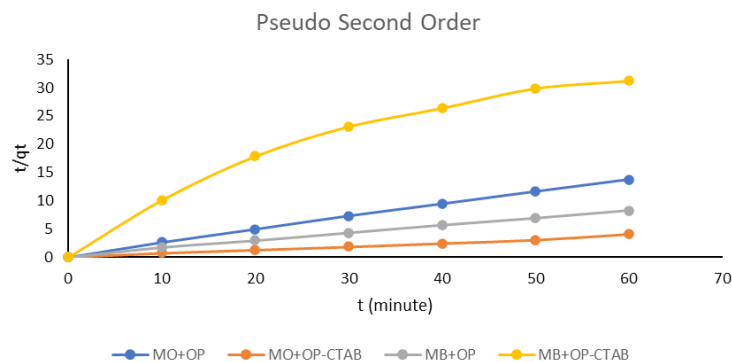


**Figure 5:** Adsorption Kinetics Pseudo first order (top) and Pseudo second order (bottom) from MO+OP; MO+OP-CTAB; MB+OP and MB+OP-CTAB.

Based on Table 4, the linear regression value ( $R^2$ ) of the pseudo second order model was greater than the  $R^2$  value of the pseudo first order model. This proves

that the adsorption of MO and MB dyes by OP and OP-CTAB followed the pseudo second order reaction kinetics model.

**Table 4:** Constants of the reaction rate and linear regression for pseudo first order and pseudo second order kinetics.

Sample	$k_1$	$R^2$	$k_2$	$R^2$
MO+OP	0.069	0.919	0.184	0.999
MO+OP-CTAB	0.030	0.209	0.388	0.996
MB+OP	0.050	0.869	0.085	0.998
MB+OP-CTAB	0.073	0.673	0.055	0.924

Table 4 shows that the reaction rate constant of MO+OP-CTAB was greater than that of MO+OP, indicating that adsorption reactions using OP-CTAB in anionic dyes were faster than those using OP. In cationic dyes, the adsorption reaction rate constant of OP was greater than that of OP-CTAB, confirming that in cationic dyes, OP is more effective than OP-CTAB.

### Adsorption Isotherm

The adsorption isotherm expresses the relationship between the adsorbate concentration and adsorption capacity at equilibrium and a fixed temperature (15). Adsorption isotherms are often used to characterize heavy metal adsorption, dyes, volatile organic compounds, and gases (28). Adsorption isotherm models can also provide information on the maximum adsorption capacity, which is significant in the evaluation of adsorbent performance (29). According to Langmuir's assumption, there are five adsorption processes where the chemisorption mechanism dominates while the shape of the adsorbate molecule

is a single layer or monolayer. In addition, there is no interaction between the adsorbed molecules, and the affinity of the adsorbate molecule is the same for each place on the surface of a homogeneous solid with the adsorbent molecule at a specific location. It does not transfer to the concrete surface and is always irreversible (30). Langmuir's equation can be written as follows (15, 29):

$$\frac{C_e}{q_e} = \frac{1}{k_L} q_{max} + \frac{1}{q_{max}} C_e \quad (\text{Eq. 5})$$

$C_e$  is the concentration of dissolved substances at the time of equilibrium (mg/L),  $q_e$  is the quantity of dyes adsorbed at the time of equilibrium (mg/g),  $q_{max}$  is the maximum adsorption capacity, and  $k_L$  is the ratio of the adsorption rate and desorption rate.  $Q_{max}$  and  $k_L$  values can be determined from the intercept and slope on the linear curve of the relationship of  $C_e/q_e$  vs.  $C_e$  (Figure. 6).

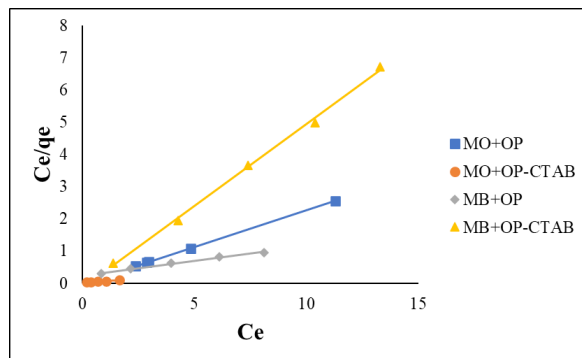


**Figure 6:** Langmuir Isotherm Plot.

Freundlich's model shows that the equilibrium relationship in adsorption can be explained by the absence of molecular separation on the surface after adsorption and the lack of chemical adsorption events. The Freundlich equation occurs only in fissile adsorption events due to the absence of molecular configuration exchanges in the adsorption process. The molecular form of the adsorbate in this process of the adsorption isotherm is a multilayer (30). The Freundlich equation can be written as follows:

$$\log q_e = \log k_f + \frac{1}{n} \log C_e \quad (\text{Eq. 6})$$

$k_f$  is the Freundlich constant that represents the adsorption capacity at the time of equilibrium, and  $1/n$  is the intensity of the adsorption. The values of  $k_f$  and  $1/n$  can be determined through the intercept and slope of the linear curve of the relationship of  $\log q_e$  vs.  $\log C_e$  (Figure. 7).

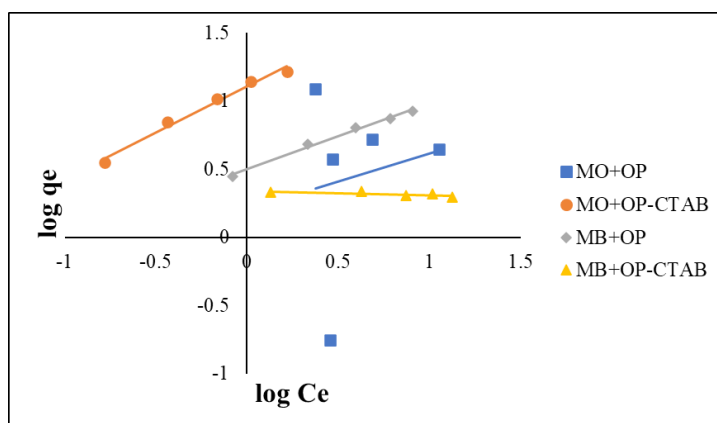


**Figure 7:** Freundlich Isotherm Plot.

In Figure 7, it is shown that both OP and OP-CTAB adsorption isotherms on MO and MB followed Langmuir's adsorption isotherm. This is evidenced by the linearity value ( $R^2$ ) of Langmuir's adsorption isotherm being greater than that of the Freundlich adsorption isotherms (Table 5). Based on these results, it can be concluded that the adsorption process in MO and MB using OP and OP-CTAB occurred on homogeneous surfaces, while there was no interaction between adsorbate molecules and adjacent areas that means the adsorption process

only occurs physically. Table 5 indicates that the highest maximum adsorption capacity ( $q_{\max}$ ) was 27.780, i.e., in the MO adsorption process by OP-CTAB. This suggests that the addition of CTAB can help the adsorption process more maximally with the adsorption of anionic dyes. For the removal of cationic dyes, the use of orange peel without CTAB was better than orange peel with CTAB. This result is proven by the adsorption capacity, in which the MB adsorption process by OP was more significant than the adsorption capacity for removing MB by OP-CTAB.

**Table 5:** Constants and R<sup>2</sup> values of the Langmuir and Freundlich isotherm models.

Sample	Langmuir Isotherm			Freundlich Isotherm		
	k <sub>L</sub>	q <sub>max</sub>	R <sup>2</sup>	k <sub>F</sub>	1/n	R <sup>2</sup>
MO+OP	5.50x10 <sup>15</sup>	4.405	1.000	1.609	0.409	0.025
MO+OP-CTAB	696.180	27.778	0.995	12.840	0.680	0.984
MB+OP	44.800	10.960	0.993	3.160	0.480	0.992
MB+OP-CTAB	-14.780	1.970	0.998	2.190	-0.030	0.498

## CONCLUSION

Based on previous studies, based on the pore size, OP has a microporous structure, while OP-CTAB has a mesoporous structure. The best adsorption process on MB was using OP adsorbent with the optimum amount of dye adsorbed produced at 50<sup>th</sup> minute that was 5.881 ppm, while the best adsorption process on MO was to use adsorbent OP-CTAB with the optimum amount of the best dye was at 50<sup>th</sup> minute that was equal to 13.34 ppm. So, the use of OP-CTAB biomass is better for removing anionic dyes, while OP is better used to remove cationic dyes due to the N element from the ammonium group of CTAB because this group has a positive partial charge causing OP-CTAB to have cationic properties so it is easier to attract anionic dyes than OP. Based on the kinetics adsorption, the adsorption of MO and MB dyes by OP and OP-CTAB followed the pseudo second order kinetic reaction model. The adsorption of MO and MB by OP and OP-CTAB followed the Langmuir adsorption isotherm, meaning that the adsorption process in MO and MB using OP and OP-CTAB appeared on homogeneous surface sites, while there was no interaction between adsorbate molecules and adjacent sites that means the adsorption process only occurs physically.

## ACKNOWLEDGEMENTS

The authors gratefully acknowledge the Indonesian Ministry Education, Culture, Research and Technology for financial support for this research and Universitas Islam Kadiri for the facilities.

## CONFLICT OF INTEREST STATEMENT

The authors declare no conflicts of interest for this article.

## REFERENCES

1. Sayed Ahmed SA, Khalil LB, El-Nabarawy T. Removal of Reactive Blue 19 dye from Aqueous Solution Using Natural and Modified Orange Peel. Carbon letters. 2012 Ekim;13(4):212-20. <DOI>.

2. Krishnan A, George D. Methylene blue removal using orange peel. International Journal of Scientific & Engineering Research. 2016;7(4):250-2.

3. Yuningrat NW, Retug N, Gunamantha IM. Fotodegradasi Methyl Orange Dalam Reaktor Fixed Bed Batu Apung-Semen. J Sains Teknologi [Internet]. 2016 Aug 5;5(1): 692-701. <DOI>.

4. Cristina PM, Mu'nisatun S, Saptaji R. Studi Pendahuluan Mengenai Degradasi Zat Warna Azo (Metil Orange) Dalam Pelarut Air Menggunakan Mesin Berkas Elektron 350 keV/10 mA. Jurnal Forum Nuklir. 2007 May 1;1(1):31.

5. Huda T, Yulitaningtyas TK. Kajian Adsorpsi Methylene Blue Menggunakan Selulosa dari Alang-Alang. Ind J Chem Anal [Internet]. 2018 Sep 20 [cited 2022 Jan 21];1(01): 9-19. <DOI>.

6. Yulianti Z, Munasir. Nanopartikel Fe<sub>3</sub>O<sub>4</sub>/SiO<sub>2</sub> Berbasis Bahan Alam Sebagai Material Pengadsorpsi Pewarna dalam Air. J Inov Fis Indones. 2020;9(1):1-4.

7. Nandi R, Laskar S, Saha B. Surfactant-promoted enhancement in bioremediation of hexavalent chromium to trivalent chromium by naturally occurring wall algae. Res Chem Intermed. 2017 Mar;43(3):1619-34. <DOI>.

8. Mukherjee K, Saha R, Ghosh A, Ghosh SK, Maji PK, Saha B. Surfactant-assisted bioremediation of hexavalent chromium by use of an aqueous extract of sugarcane bagasse. Res Chem Intermed. 2014 Apr;40(4):1727-34. <DOI>.

9. Rahadi B, Robbaniyah A, Pertanian T, Brawijaya U, Veteran J. Analysis of Methyl Orange Concentration Reduction Using Musa Acuminata Cv. Cavendish Banana Peel as Biosorbent. J Sumberd Alam dan Lingkungan. 2019;6(2):29-35.

10. Hanif Z. Pengembangan Agribisnis Jeruk Nusantara. Iptek Hortikultura. 2020;16-N(Gambar 2):27-30.

11. Munagapati VS, Kim D-S. Adsorption of anionic azo dye Congo Red from aqueous solution by Cationic

Modified Orange Peel Powder. *Journal of Molecular Liquids*. 2016 Aug;220:540–8. [<DOI>](#).

12. do Nascimento GE, Duarte MMB, Campos NF, Rocha ORS da, Silva VL da. Adsorption of azo dyes using peanut hull and orange peel: a comparative study. *Environmental Technology*. 2014 Jun 3;35(11):1436–53. [<DOI>](#).

13. Namasivayam C, Muniasamy N, Gayatri K, Rani M, Ranganathan K. Removal of dyes from aqueous solutions by cellulosic waste orange peel. *Bioresource Technology*. 1996 Jul;57(1):37–43. [<DOI>](#).

14. Sivaraj R, Namasivayam C, Kadirvelu K. Orange peel as an adsorbent in the removal of Acid violet 17 (acid dye) from aqueous solutions. *Waste Management*. 2001;21(1):105–10. [<DOI>](#).

15. Arami M, Limaee NY, Mahmoodi NM, Tabrizi NS. Removal of dyes from colored textile wastewater by orange peel adsorbent: Equilibrium and kinetic studies. *Journal of Colloid and Interface Science*. 2005 Aug;288(2):371–6. [<DOI>](#).

16. Salman T, Ali M. Eriochrome Black T dye adsorption onto natural and modified orange peel. *Res J Chem Environ*. 2019;23(1):155–69.

17. Ansari R, Seyghali B, Mohammad-khah A, Zanjanchi MA. Highly Efficient Adsorption of Anionic Dyes from Aqueous Solutions Using Sawdust Modified by Cationic Surfactant of Cetyltrimethylammonium Bromide. *J Surfact Deterg*. 2012 Sep;15(5):557–65. [<DOI>](#).

18. Mohamed Pauzan AS, Ahad N. Biomass Modification Using Cationic Surfactant Cetyltrimethylammonium Bromide (CTAB) to Remove Palm-Based Cooking Oil. *Journal of Chemistry*. 2018 Dec 24;2018:1–7. [<DOI>](#).

19. Ai F, Zhao G, Lv W, Lin J. Facile synthesis of cetyltrimethylammonium bromide-loaded mesoporous silica nanoparticles for efficient inhibition of hepatocellular carcinoma cell proliferation. *Materials Research Express*. 2020 Aug;7(8):085008. [<DOI>](#).

20. del Caño R, Gisbert-González JM, González-Rodríguez J, Sánchez-Obrero G, Madueño R, Blázquez M, et al. Effective replacement of cetyltrimethylammonium bromide (CTAB) by mercaptoalkanoic acids on gold nanorod (AuNR) surfaces in aqueous solutions. *Nanoscale*. 2020;12(2):658–68. [<DOI>](#).

21. Che Ismail NH, Ahmad Bakhtiar NSA, Md. Akil H. Effects of cetyltrimethylammonium bromide (CTAB) on the structural characteristic of non-expandable muscovite. *Materials Chemistry and Physics*. 2017 Aug;196:324–32. [<DOI>](#).

22. Campbell RA, Parker SRW, Day JPR, Bain CD. External Reflection FTIR Spectroscopy of the Cationic Surfactant Hexadecyltrimethylammonium Bromide (CTAB) on an Overflowing Cylinder. *Langmuir*. 2004 Sep 1;20(20):8740–53. [<DOI>](#).

23. Azmiyawati C, Sawitri E, Siahaan P, Darmawan A, Suyati L. Preparation of magnetite-silica-cetyltrimethylammonium for phenol removal based on adsolubilization. *Open Chemistry*. 2020 Apr 21;18(1):369–76. [<DOI>](#).

24. Febiyanti IA, Suseno A, Priyono P. Pengaruh Konsentrasi Surfaktan CTAB (Cetyltrimethylammonium bromide) pada Modifikasi Lempung dengan Oksida Besi sebagai Pemilar. *J Kim Sains Apl*. 2013 Dec 1;16(3):79–83. [<DOI>](#).

25. Feng N, Guo X, Liang S. Adsorption study of copper (II) by chemically modified orange peel. *Journal of Hazardous Materials*. 2009 May 30;164(2–3):1286–92. [<DOI>](#).

26. Anas NAA, Fen YW, Yusof NA, Omar NAS, Ramdzan NSM, Daniyal WMEMM. Investigating the Properties of Cetyltrimethylammonium Bromide/Hydroxylated Graphene Quantum Dots Thin Film for Potential Optical Detection of Heavy Metal Ions. *Materials*. 2020 Jun 6;13(11):2591. [<DOI>](#).

27. Purbaningtias TE, Kurniawati P, Wiyantoko B, Prasetyoko D, Suprpto S. Pengaruh Waktu Aging Pada Modifikasi Pori Zeolit Alam Dengan Ctabr. *J Sains Teknologi*. 2017 Nov 27;6(2):321. [<DOI>](#).

28. Badriyah L, Putri M. Kinetika Adsorpsi Cangkang Telur pada Zat Warna Metilen Biru. *Alchemy*. 2017;5(3):85–91.

29. Wang J, Guo X. Adsorption isotherm models: Classification, physical meaning, application and solving method. *Chemosphere*. 2020 Nov;258:127279. [<DOI>](#).

30. Fadli A, Komalasari M, Amir D, Sari, Siburian R. Model Kesetimbangan Adsorpsi Zn<sup>+2</sup> dengan Kaolin. *Reaktor*. 2004;8(2):59–62.





## Removal of Arsenate in Drinking Water Sources by Combined Coagulation Process

Kadir Özdemir\* 

Zonguldak Bülent Ecevit University, Department of Environmental Engineering, Zonguldak, 67100, Turkey

**Abstract:** The objective of this study is to examine arsenate (As(V)) removal from drinking water sources with combined coagulation processes using Single-Walled Carbon Nanotubes (SWCNTs) and Multiwalled Carbon Nanotubes (MWCNTs). Ulutan Lake Water (ULW) in Zonguldak-Turkey, was used as drinking water source. Conventional coagulation experiments were conducted using aluminum sulfate (Alum) and ferric chloride (FeCl<sub>3</sub>). Water samples were synthesized by spiking 300 µg/L As(V) into ULW samples and also all arsenic removal tests were performed with As(V). The maximum removal percentages of As(V) (97%) was observed with combined SWCNTs and FeCl<sub>3</sub> in ULW. Similar to that of SWCNTs, the removal of As(V) (92%) during the coagulation processes occurred at MWCNT with the addition of FeCl<sub>3</sub>. Compared to SWCNTs, the removal percentage of As(V) was slightly lower when using only MWCNTs (76%). This result demonstrated that SWCNTs were generally more powerful than MWCNTs for removing the As(V). The presence of humic acid (HA) increased As(V) removal with related the solution pH. On the other hand, the changing of As(V) residual concentrations in ULW was observed as a function of pH and the removal of As(V) increases in the acidic pH levels whereas decreases alkaline pH levels. While As(V) removal efficiency was remained constant at acidic pH values, it decreased about 10% at pH 6, 7 and 8 as a result of the competitive adsorption between As(V) and HA. It was observed that the As(V) removal efficiency increased both low and high pH with monovalent electrolyte (NaCl) whereas di-valent ions (Ca<sup>+2</sup> and Mg<sup>+2</sup>) improved As(V) removal only at pH 9 and 10 during the coagulation processes in ULW samples. The results of this study display that combined coagulation process is more effective than conventional coagulation alone for the As(V) removal.

**Keywords:** Arsenate removal, carbon nanotubes, water treatment, combined coagulation.

**Submitted:** August 07, 2021. **Accepted:** January 19, 2022.

**Cite this:** Özdemir K. Removal of Arsenate in Drinking Water Sources by Combined Coagulation Process. JOTCSA. 2022;9(1):247-54.

**DOI:** <https://doi.org/10.18596/jotcsa.980203>.

**\*Corresponding author. E-mail:** [kadirozdemir73@yahoo.com](mailto:kadirozdemir73@yahoo.com).

### INTRODUCTION

The shortage in freshwater resources due to the increased human population and industrial activities is one of the most challenging issue existing in the world in the field of water supply (1,2). According to many studies about toxicity of arsenic, which is a well-known poison, it is carcinogenic for humans (3-5). In other words, arsenic creates a risk of pulmonary, dermal, bladder, and hepatic cancer in humans (6-8). Due to its negative effects on human health, the WHO has set the maximum contaminant

level for arsenic in drinking water as 10 µg L<sup>-1</sup> (9, 10).

Arsenic exists in aqueous systems in both inorganic and organic forms. Major treatment techniques have included chemical coagulation-flocculation, ion exchange and adsorption, and membrane processes (11-14). Coagulation and filtration known as conventional treatment technology is widely used for removing arsenic in surface water sources because of its economy and simplicity.



In water treatment processes, adsorption processes are generally applied due to the simple design and operation as well as the small space requirement. In the literature, it has been reported that many adsorbents such as iron oxide, aluminum oxide, and activated carbon are effective for arsenic removal (15). CNTs have some distinctive features such as high reactivity, small size, easy separation, catalytic potential, large surface area, and large number of active sites that facilitate better arsenic removal efficiency compared to other available adsorbents (16). Though nano adsorbents give better results compared to other adsorbents for arsenic removal, there are two main challenges in using nanomaterials for water purification; one is the non-availability of CNTs at economically affordable prices and the other is the toxicity and the environmental fate of nanomaterials. Additionally, research has shown that CNTs can enter the body through the skin, respiratory tract, or gastrointestinal tract. The objective of the present study is to investigate the removal of arsenic as As(V) in drinking water sources through a combination of coagulation with CNTs. SWCNTs and MWCNTs were used as CNTs for determining to the removal efficiency of arsenic in the coagulation process at the presence of Alum and  $\text{FeCl}_3$ . ULW, an important drinking water source that provides nearly 35,000 m<sup>3</sup> of raw water to the drinking-water treatment plant of Zonguldak city, Turkey. SWCNTs and MWCNTs are also used as coagulant materials to remove arsenic in ULW by a new water treatment technique involving a novel

combined coagulation process. On the other hand, very few studies on the use of combined coagulation process with CNTs have been reported for arsenic removal at the range of world. In addition, the novelty of study is the first attempt in Turkey to examine the removal of arsenic from drinking water sources by a combined coagulation process using CNTs.

## EXPERIMENTAL

### Source water and sampling

The water samples used in this study were collected from raw water entering ULW, Zonguldak- Turkey at four different times. ULW is the water reservoir that contributes significantly to Zonguldak's drinking water treatment plant. The some important chemical properties of ULW are presented in Table 1. Collected samples were quickly sent to the laboratory. Raw water samples were passed through 0.45  $\mu\text{m}$  membrane filter papers within 24 h and stored in a refrigerator at 4 °C. Water samples were synthesized by spiking a required amount of As(V) (300  $\mu\text{g/L}$ ) into ULW prior to the coagulation experiments. The common form of arsenic found in surface waters is As(V). Therefore, arsenic removal tests were performed with As(V). Stock As(V) solutions was prepared with  $\text{Na}_2\text{HAsO}_4 \cdot 7\text{H}_2\text{O}$ . The chemical coagulant stocks, 1 g/L ferric chloride ( $\text{FeCl}_3 \cdot 6\text{H}_2\text{O}$ ) and alum ( $\text{Al}_2(\text{SO}_4)_3 \cdot 18\text{H}_2\text{O}$ ) were prepared with deionized (DI) water, respectively.

**Table 1:** Physicochemical characteristics of ULW samples.

Parameters	Unit	Range	Average
pH	-	7.21-7.85	7.53
Turbidity	NTU	4.41-7.55	5.98
Conductivity	$\mu\text{S/cm}$	432-513	473
Total hardness	mg $\text{CaCO}_3/\text{L}$	126-166	146
Alkalinity	mg $\text{CaCO}_3/\text{L}$	105-123	114
Temperature	°C	10-17	14
As(V)	$\mu\text{g/L}$	<10	<10
TOC	mg/L	4.05-4.81	4.43
$\text{SO}_4^{2-}$	mg/L	22.1-30.2	26.15
$\text{Na}^+$	mg/L	12.3-15.2	13.25
$\text{K}^+$	mg/L	1.83-2.1	1.97
$\text{Mg}^{2+}$	mg/L	6.61-7.89	7.25
$\text{Ca}^{2+}$	mg/L	38.7-42.6	40.66
Iron	mg/L	0.05-0.08	0.07

### Coagulation procedure

Stock solutions containing 5,000 mg/L of the SWCNTs and MWCNTs were prepared by adding 1 g of the CNTs to 200 mL of DI water and stirring with a magnetic stirrer at 600 rpm. The ferric chloride and alum were consistently used for As(V) removal at similar dosages as coagulant. ULW was treated with coagulants in the ranges of 0–100 mg/L and 0–50 mg/L, respectively. However, based on economic

and engineering considerations, 80 mg/L was selected as the optimum coagulant dosage. As the combined coagulation was analyzed, and preliminary testing was applied to determine the optimal coagulant dose for raw water samples. The optimum combined coagulant dosage for ULW was determined as 40 mg/L. Additionally, after conventional and combined coagulation experiments, the treated water was taken with a

syringe and filtered through 0.45- $\mu\text{m}$  membrane filter. For determining As(V), samples were preserved in dilute  $\text{HNO}_3$  (final conc. 0.1%,  $\text{pH} < 2$ ). Additionally, after conventional and combined coagulation experiments, the treated water was taken with filtered through 0.45- $\mu\text{m}$  membrane filter.

### Purified CNTs

One gram of raw CNTs was dispersed into a 100-mL flask containing 40 mL of mixed acid solutions (30 mL of  $\text{HNO}_3$  + 10 mL of  $\text{H}_2\text{SO}_4$ ) for 24 h to remove metal catalysts (Ni nanoparticles). After cleaning, the CNTs were again dispersed in a 100-mL flask containing 40 mL of the mixed acid solutions, which were then shaken in an ultrasonic cleaning bath (Branson 3510 Ultrasonic Cleaner, Connecticut, USA) and heated at 80  $^\circ\text{C}$  in a water bath for 2 h to remove amorphous carbon. After cooling to room temperature, the mixture was filtered with a 0.45- $\mu\text{m}$  glass-fiber filter, and the solid was washed with deionized water until the pH of the filtrate was 7. The filtered solid was then dried at 80  $^\circ\text{C}$  for 2 h to obtain the purified CNTs. This procedure for purifying CNTs has been used by other researchers in previous CNT studies (17). After purifying the CNTs, a simple coagulation process with application of alum was used for precipitating CNTs from the solution and thus, CNTs particles were recollected. Then, the residual CNT waste was sealed carefully using double layers of polyethylene bags and transported to solid waste incineration plants.

### Analytical methods

The experimental analysis such as TOC and UV and As(V) measurements were performed according to in Standard Methods (18). TOC analyses were performed with a Shimadzu TOC-5000 analyzer equipped with an auto sampler77 according to the combustion-infrared method described in Standard Methods 3510-B (18). The sample was injected into a heated reaction chamber packed with a platinum-oxide catalyst oxidizer to oxidize organic carbon into carbon dioxide gas.  $\text{UV}_{254}$  absorbance

measurements were performed in accordance with Standard Methods 5910-B (18) using a Shimadzu 1608 UV-vis spectrophotometer at a wavelength of 254 nm with a 1-cm quartz cell. The samples were first passed through a 0.45- $\mu\text{m}$  membrane filter to remove turbidity, which can interfere with the measurement. Distilled ultrafiltered water was used as the background correction in the spectrophotometer. As (V) analyses were performed with ICP-OES equipped with a manual hydride generator at 188.9 nm wavelength (PerkinElmer SIMAA 6000 AAS ) according to the hydride atomic absorption method described in Standard Methods 3114-B (18). Analyses of  $\text{Ca}^{+2}$ ,  $\text{Mg}^{+2}$  and the other ions in water samples were carried out using the Dionex IC 3000 system (USA) equipped with an AS-19 analytical column and an AG-19 guard column as per USEPA method 300.1 and also its analytical detection limit is  $0.001 \pm 0.0001$  mg/L.

## RESULTS AND DISCUSSION

### As(V) removal by with coagulation using CNTs

Figure 1 (a) shows the removal of As(V) by combined coagulation processes. Using SWCNTs as a coagulant without the addition of a conventional coagulant (Alum or  $\text{FeCl}_3$ ), the highest As(V) removal was recorded as 77%. On the other hand, with the application of alum, the removal of As(V) increased nearly 10%. The higher arsenate removal (>80%) was observed with combined coagulation process (SWCNTs + Alum). In other words, the removal percentages of arsenate was not determined after the optimum SWCNT doses (40 mg/L) with addition of alum (Figure 1). This result can be explained that the electrostatic attraction plays a very important role in facilitating the coprecipitation and also the colloidal properties of the metal salt precipitation is more effective on As(V) removal by coagulation or combined coagulation processes with  $\text{Al}^{3+}$  and  $\text{Fe}^{3+}$  coagulants. Similar observations have been reported by some authors (19, 20).

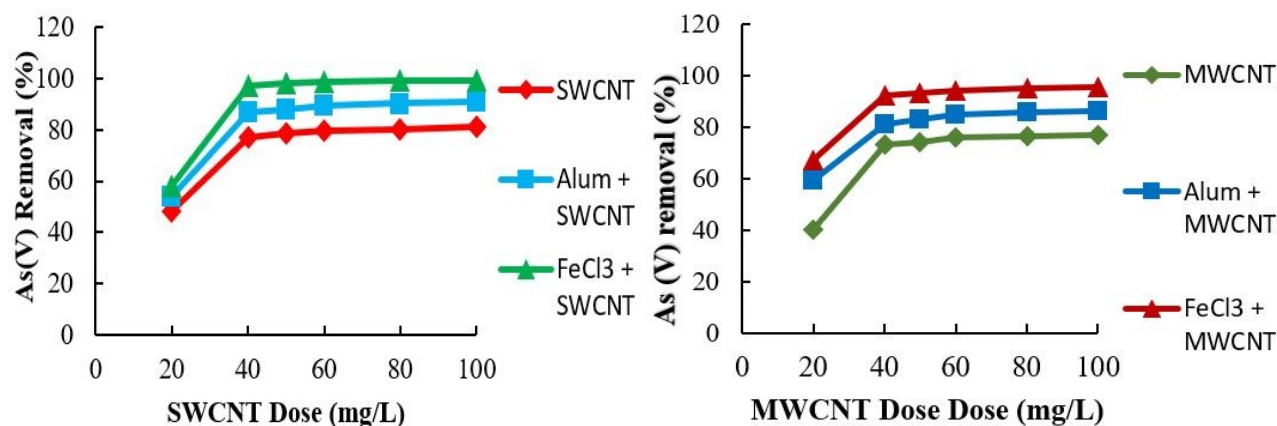


**Figure 1:** Removal of As(V) by SWCNTs and combined coagulation (left). Optimum coagulant dose=40 mg/L. Removal of As(V) by MWCNTs and combined coagulation (right), Optimum coagulant dose=40 mg/L.

The highest removal of arsenate (97%) is recorded with the application of  $\text{FeCl}_3$  (SWCNTs +  $\text{FeCl}_3$ ). Figure 1 (b) demonstrates the removal of As(V) as a result of the application of MWCNTs and conventional coagulants during the coagulation. Arsenate removal obtained using only MWCNT was determined as 76%. On the other hand, with the application of using only SWCNTs, removal percentage of As(V) was measured as 82%. This observation indicates that SWCNTs has larger surface area in adsorption processes, as compared to MWCNTs, resulting in more adsorption sites for chemicals. As shown in Figure 2, the addition of alum increases As(V) levels in combined coagulation process. Figure 2 compares the removal percentage of As(V) using conventional coagulation only and combined coagulation processes for ULW. The removal of As(V) also remained constant at MWCNT doses of 40 mg/L or greater (82%). As the

combined coagulation process is done, high As(V) removal percentages (>95%) was observed in ULW. Although the As(V) removal was 51% with only alum, higher As(V) removal was determined when using only  $\text{FeCl}_3$  (63%) than that with alum. A significant increase was seen when  $\text{FeCl}_3$  was combined with SWCNTs compared to the use of  $\text{FeCl}_3$  only. The highest arsenate removal rate was achieved in coagulation with carbon nanotube types and  $\text{FeCl}_3$  in ULW water samples. Another trend was observed for As(V) removal using alum, which produced the highest As(V) removal alone and combined with SWCNTs (81% and 88%) in ULW samples. Overall, compared to the As(V) removal achieved by employing only conventional coagulation, the combined coagulation is more effective treatment method for drinking water sources including arsenic.

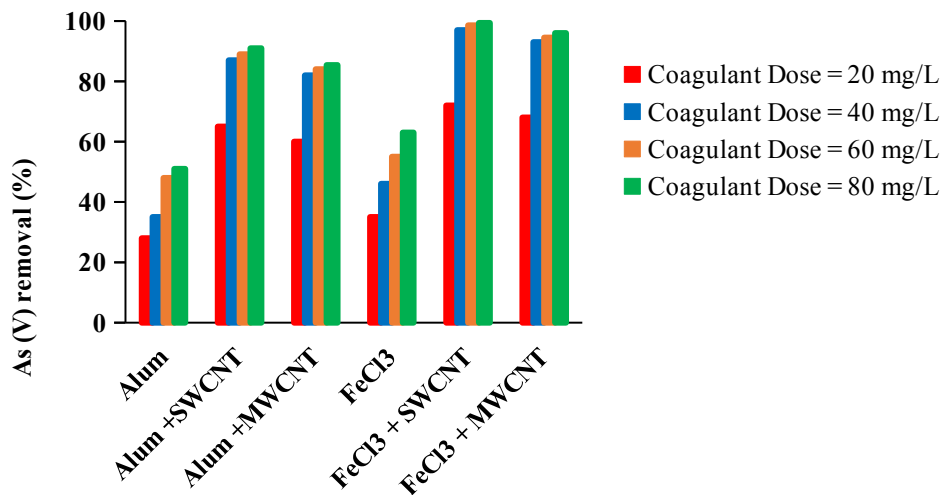


**Figure 2:** Comparison of As(V) removal using conventional combined coagulation processes.

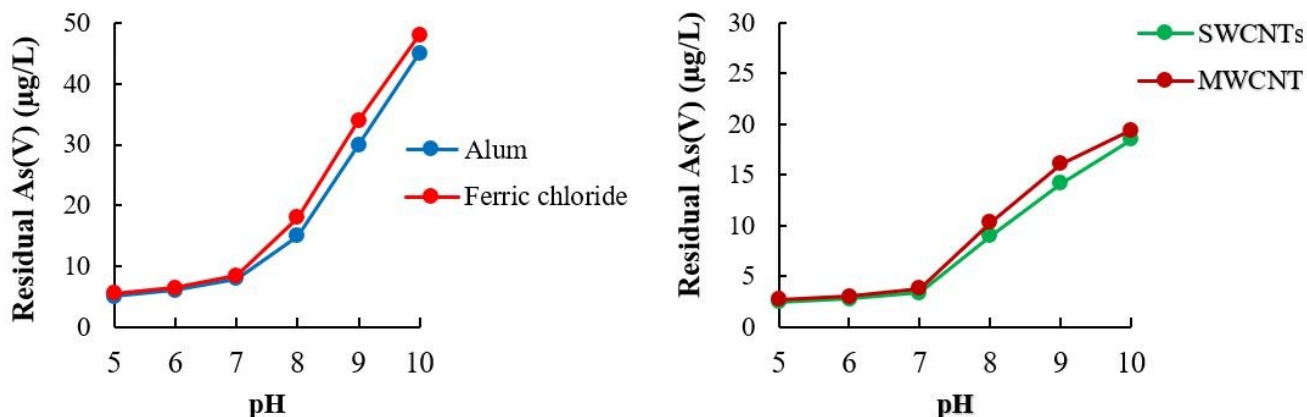


**Figure 3:** The effect of pH on As(V) removal by conventional coagulants (left), CNTs (right).

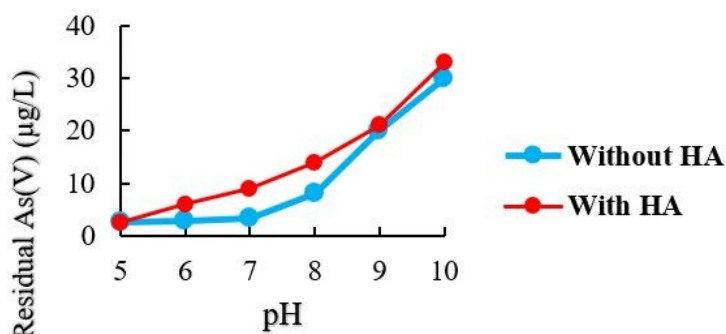


**Figure 4:** The influence of humic acid (HA).

#### Factors affecting the As(V) removal

The arsenate residual concentrations in ULW during coagulation processes as a function of coagulant dose and pH are shown in Figure 3.

The As(V) residual concentrations in ULW due to aluminum and iron oxides/hydroxides generated in coagulation illustrated variable reductions between pH 7 and 10, while at pH 5 and pH 6 the concentrations were more consistent (Figure 3a). The As(V) residual concentrations at pH 5 and 6 were similar, and comparison of removal efficiencies at pH 8 and 10. It was shown that the As(V) removal decreased with increasing pH during the coagulation process. It was reported as based on some literature researches (21, 22). This result also can be revealed that during the coagulation,  $Al^{3+}$  and  $Fe^{3+}$  hydrolyzed and formed different cationic complexes at acidic pH. On the other hand, the changes of As(V) residual concentrations demonstrate a similar trend for SWCNTs and MWCNTs (Figure 3b).

The presence of HA in solution strongly influences As(V) removal by coagulation with CNTs (23). A concentration of 4.25 mg C /L HA was used to examine its effects on the As(V) removal as a function of pH. The results are presented in Figure 4.

As can be seen in Figure 4, the increasing pH value changed the influence of HA on arsenate removal

both conventional and combined coagulation. Similar studies were reported by many researches previously (24). At pH 5, with the addition of HA, As(V) removal efficiency about remained constant at the original maximum removal. Nevertheless, As(V) removal reduced by 5%, 10%, and 15% at pH 6, 7, 8 and 9, respectively. HA has high affinity for the surface of alum and iron oxides, which could modify their properties and block the adsorption sites for As (V). Further, HA was found to readily form both aqueous and surface inner-sphere complexes with cationic metals, which would in turn associate strongly with other anions like those of As (V) by metal-bridging mechanisms.

This trend results in to reduce the competitive adsorption between As(V) and HA on the coagulated iron and aluminum hydroxide and also increases to the As(V) removal. The findings of experimental study confirmed that the removal efficiency of As(V) were increased as the pH increased at the presence of HA and the combined coagulation treatment mechanism was very effective on As(V) and HA removal for studied pH levels in ULW samples.

$Ca^{2+}$  and  $Mg^{2+}$  ions are widely available in surface waters. In this part of study, 0.58 mM  $Ca(OH)_2$  and  $MgCl_2$  were used combined coagulation experiments with SWCNTs+ $FeCl_3$  in order to observe the effect of divalent ions ( $Ca^{2+}$  and  $Mg^{2+}$ ) on As(V) removal due to the different pH values. The results are presented in Figure 5. The addition  $Ca(OH)_2$  and  $MgCl_2$  in ULW

samples including As(V) caused some changes on coagulation process. Both  $\text{Ca}^{2+}$  and  $\text{Mg}^{2+}$  enhanced As(V) removal efficiency, especially at pH 9 and 10.

It has been reported that the presence of  $\text{Ca}^{2+}$  increased the adsorption of As(V) on hydrous alum and ferric oxide and SWCNTs at high pH.

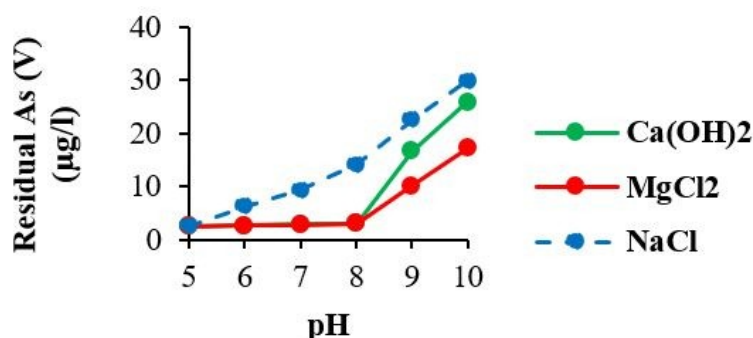


**Figure 5:** The influence of divalent ions ( $\text{Ca}^{+2}$  and  $\text{Mg}^{+2}$ ) and monovalent electrolyte (NaCl) on the removal of As(V).

However,  $\text{Ca}^{2+}$  and  $\text{Mg}^{2+}$  did not affect As(V) removal between pH 5 and 8. These findings coincide with the results of similar studies conducted by Qiao et al. (25) and Meng et al. (26) on arsenic removal. On the other hand, to investigate the change of mono-valent ions on the As(V) at this study, the level of 10 mmol/L NaCl was used in the combined coagulation with SWCNTs+ $\text{FeCl}_3$ .

The results also show in Figure 5 that at the high NaCl concentration of the coagulated suspension was significantly increased the As(V) removal both low and high pH values. Furthermore, monovalent electrolyte (NaCl) have very much stronger effects on As(V) removal than on As(V) removal effects of divalent ions.

### Mechanisms of As(V) removal

SWCNTs and MWCNTs provide sufficient adsorption sites as well act as a good supporting material for other coagulants. Coprecipitation and adsorption are both active As(V) removal mechanisms. Large specific surface area, light mass density, purity, and strong interaction between CNTs and pollutant molecules made the CNTs extensively studied not only adsorbent but also coagulant coagulation data CNTs and conventional with for ULW samples at pH 6 are shown together in Figure 2. As seen in Figure 2, As(V) removal by combined coagulation was more efficient than with only conventional coagulants. In other words, higher As(V) removal percentages (>90%) were observed when using the combined coagulation whereas As(V) removal was recorded as 51% and 63% with only alum and  $\text{FeCl}_3$ , respectively. On the other hand, the differences in As(V) removal efficiency between combined and conventional coagulation were high. Moreover, especially for Alum and  $\text{FeCl}_3$ , the differences were more pronounced at low dosages than that at high dosage. The results from these experiments demonstrate that adsorption onto precipitated Al and Fe hydroxides are the main mechanism for As(V) removal by conventional

coagulants but precipitation/coprecipitation also plays specific roles at low dosages for CNTs. During coagulation process, As(V) removal depended on the coagulant dose and consequently on the number of active sites on the hydroxide surface. For instance; as As(V) removal was observed as 28% and 35% with the only alum and  $\text{FeCl}_3$  dose of 20 mg/L, higher As(V) removals (65-72%) was determined with SWCNTs+Alum and SWCNTs+ $\text{FeCl}_3$ , respectively, at the same dose (Figure 2). Similar trends were determined for MWCNTs+Alum and MWCNTs+ $\text{FeCl}_3$ . This result shows that surface complexation and electrostatic attraction govern the coagulation behavior of As(V) on SWCNTs and MWCNTs and presence of functional groups on the surface are the other significant factors for higher As(V) removal during the combined coagulation compared to conventional coagulation. Also, the extraordinary properties of CNTs such as large surface area, uniformly distributed pores and presence of functional groups on the surface are the other significant factors for higher As(V) removal. Similar results were reported by some researchers (27, 28).

### CONCLUSION

The combined coagulation process using carbon nanomaterials to determine the removal efficiency As(V) for different pH levels and the presence of HA was investigated in this study. Experiments demonstrated that SWCNTs were more effective than MWCNTs in removing As(V) in ULW. This is probably because of the smaller diameter and the larger surface area of the SWCNTs as compared to MWCNTs. The highest removal percentage of arsenate (97%) was observed with the SWCNTs+ $\text{FeCl}_3$ . Also, the As(V) removal was lower when using only conventional coagulants in ULW. Compared to the As(V) removal achieved by employing only conventional coagulation, the combined coagulation treatment generally resulted in higher removal of As(V) in this study. The As(V) removal increased with decreasing pH whereas the



decreasing of the As(V) removal for alkaline pH levels. The maximum As(V) removal was determined at pH 5. Additionally, the influence of HA on arsenate removal increased with solution pH. On the other hand, the highest As(V) removal efficiency was recorded at pH 5, with the addition of HA. During to increasing the concentration of the monovalent electrolyte, As(V) removal increases at low (5, 6) and high (8, 9, 10) pH with coagulation processes. As the divalent ions ( $\text{Ca}^{+2}$  and  $\text{Mg}^{+2}$ ) were added, the removal efficiencies of As(V) were greatly improved at pH 9 and 10. Results from this investigation show that coagulation using CNTs can be effective in the removal of As(V) from various drinking water sources. Therefore, water treatment plant operators can use the CNTs as coagulants or aid-coagulant matter instead of conventional coagulants, such as those described in this paper, to effectively remove As(V).

### CONFLICT OF INTEREST

The author declares that there is no conflict of interest.

### ACKNOWLEDGMENTS

The author would like to thank TUBITAK (Project No. 114Y030) for their financial support.

### REFERENCES

- Mohan D, Pittman CU. Arsenic removal from water/wastewater using adsorbents—a critical review. *J. Hazard. Mater.* 2007;142:1–53. [<DOI>](#).
- Chen Z, Ngo HH, Guo W, Wang X. Analysis of Sidney's water schemes. *Front. Environ. Sci. Eng.* 2013;7:608–615. [<DOI>](#).
- Viraraghavan T, Subramanian KS, Aruldoss JA. Arsenic in drinking water problems and solutions. *Water Sci. Technol.* 1999;40:69–76. [<DOI>](#).
- Smedley PL, Kinniburgh DG. A review of the source, behaviour and distribution of arsenic in natural waters. *Appl. Geochem.* 2002;17:517–568. [<DOI>](#).
- Choong TSY, Chuah TG, Robih Y, Koay FLG, Azni I. Arsenic toxicity, health hazards and removal techniques from water: an overview. *Desalination.* 2007;217:139–166. [<DOI>](#).
- Chen SL, Dzung SR, Yang MH, Chiu KH, Shieh GM, Wai CM. Arsenic species in groundwaters of the blackfoot disease area, Taiwan. *Environ. Sci. Technol.* 1994;28:877. [<DOI>](#).
- Smith AH, Marshall G, Yuan Y. Increased mortality from lung cancer and bronchiectasis in young adults after exposure to arsenic in utero and in early childhood. *Environ. Health Perspect.* 2006;114:1293. [<DOI>](#).
- Hughes MF, Beck BD, Chen Y, Lewis AS, Thomas DJ. Arsenic exposure and toxicology: a historical perspective. *Toxicol. Sci.* 2011;123:305–332. [<DOI>](#).
- WHO. Guidelines for Drinking-water Quality, Recommendations. 4th ed. Geneva; 2011. 564 p. ISBN: 978 92 4 154815 1
- Sullivan C, Tyrer M, Cheeseman CR, Graham NJD. Disposal of water treatment wastes containing arsenic—a review. *Sci. Total Environ.* 2010;408:1770–1778. [<DOI>](#).
- Pal P, Ahammad SK, Pattanayak A, Bhattacharya P. Removal of arsenic from drinking water by chemical precipitation—a modelling and simulation study of the physical chemical processes. *Water Environ. Res.* 2007;79:357–366. [<DOI>](#).
- Anirudhan TS, Jalajamony S. Cellulose-based anion exchanger with tertiary amine functionality for the extraction of arsenic(V) from aqueous media. *J. Environ. Manage.* 2010;91(11):2201–2207. [<DOI>](#).
- Manna AK, Sen M, Martin AR, Pal P. Removal of arsenic from contaminated ground water by solar-driven membrane distillation. *Environ. Pollut.* 2010;158:805–811 [<DOI>](#).
- Medina A, Gamero P, Robles JMA, Izquierdo M. Fly ash from a Mexican mineral coal. II. Source of W zeolite and its effectiveness in arsenic (V) adsorption. *J. Hazard. Mater.* 2010;181:91–104. [<DOI>](#).
- APHA. Standard methods for the examination of water and waste water. Washington, 21st ed. DC: American Public Health Assoc. 2005.
- Samadder SR, Sneha L. Removal of arsenic from water using nano adsorbents and challenges: A review. *J. Environ. Manag.* 2010;166:387–406. [<DOI>](#).
- Özdemir K. The use of carbon nanomaterials for removing natural organic matter in drinking water sources by a combined coagulation process. *Nanomater. Nanotechnol.* 2016;6:1–12. [<DOI>](#).
- Cathalifaud FG, Pallier V, Serpaud B, Bollinger JC. Effect of organic matter on arsenic removal during coagulation/flocculation treatment. *J. Colloid Interface. Sci.* 2010;342:26–32. [<DOI>](#).
- Duan J, Wang Y, Liu S, Li W, Leeuwen VJ, Mulcahy D. Removal of As(III) and As(V) by ferric salts coagulation—Implications of particle size and zeta potential of precipitates. *Sep. Purif. Tech.* 2014;135:64–71. [<DOI>](#).
- Balasubramanian N, Madhavan K. Arsenic Removal from industrial effluent through electrocoagulation. *Chem. Eng. Tech.* 2001;24(5):519–521. [<DOI>](#).
- Rao P, Mak MSH, Liu T, Lai KCK, Lo IMC. Effects of humic acid on arsenic(V) removal by zero-valent iron from groundwater with special references to corrosion products analyses. *Chemosphere* 2009;75:156–162. [<DOI>](#).
- Guan XH, Dong HR, Ma J, Jiang L. Removal of arsenic from water: effects of competing anions on As(III) removal in  $\text{KMnO}_4$ -Fe(II) process. *Water Res.* 2009;43:3891–3899. [<DOI>](#).
- Pallier V, Feuillade-Cathalifaud G, Serpaud B, Bollinger J-G. Effect of organic matter on arsenic removal

during coagulation/flocculation treatment. J. Colloid Interface. Sci. 2010;342:26-32. [<DOI>](#).

24. Qiao JL, Jiang Z, Sun B, Sun YK, Wang Q, Guan XH. Arsenate and arsenite removal by FeCl<sub>3</sub>: effects of pH, As/Fe ratio, initial As concentration and coexisting solutes. Sep. Purif. Technol. 2012;92:106-114. [<DOI>](#).

25. Meng XG, Bang S, Korfiatis GP. Water Res. 2000;34:1255-1261. [<DOI>](#).

26. Zhu H, Jia Y, Wua X, Wang H. Removal of arsenic from water by supported nano zero-valent iron on activated carbon. J. Hazard. Mater. 2009;172:1591-1596. [<DOI>](#).

27. Kong S, Wang Y, Zhan H, Yuan S, Yu M, Liu M. Adsorption/oxidation of arsenic in groundwater by nanoscale Fe-Mn binary oxides loaded on zeolite. Water Environ. Res. 2014;86(2):147-155. [<DOI>](#).





## The Role of the Presence of Aliphatic Alcohols on the Formation of Wormlike Micelle of Anionic-Cationic Surfactants Mixture

Rabah A. Khalil \*<sup>1</sup> , Liqaa H. Alsamarrai <sup>2</sup> 

<sup>1</sup> Department of Chemistry, College of Science, University of Mosul, Mosul, Iraq.

<sup>2</sup> Department of Chemistry, College of Education, University of Samarra, Samarra, Iraq.

**Abstract:** Thermodynamically controlled supramolecular gel or aggregate is commonly resulted from the formation of one-dimensional micelles through specific self-assembling of amphiphilic molecules. This phenomenon is commonly referred to as the formation of worm- or thread-like micelle which is still considered as quite complicated and obscure. This, in spite of the recent physical insight for interpreting this phenomenon, is referred to as the critical intermolecular forces (CIF) of which still needs further support. Therefore, attention by scientists in this field should be given in order to make this transition phenomenon clear. In this work, investigations concerning the effect of addition of aliphatic alcohols with different chain lengths of even carbon numbers (ethanol, 1-butanol, 1-hexanol, 1-octanol and 1-decanol), at different concentrations (0.002-0.040 M), and temperatures on the formation of wormlike micelle for the mixture of anionic sodium dodecylsulfate (SDS) and cationic cetyltrimethylammonium bromide (CTAB) surfactants were carried out. The formation of these one dimensional micelles were practically detected by following the sharp change of physical properties through the presence of a remarkable high viscosity peak. The results indicate there is no linear or systematic relationship between the effects of the presence of these alcohols with their chain lengths. It has been found that the presence of aliphatic alcohols causes a positive effect on the formation of one dimensional micelles. The ability of the transition from spherical to wormlike micelles increases with increasing their concentrations of alcohols except for that of 1-octanol. The obtained achievements were explained in terms of CIF theory which then offered a reasonable support to this theory. It was concluded that alcohols particularly ethanol and 1-octanol can be employed as adjustment reagents for controlling required viscosity of threadlike micelles.

**Keywords:** Wormlike micelles, sodium dodecylsulfate; cetyltrimethylammonium bromide; supramolecular chemistry; soft matter; aliphatic alcohols.

**Submitted:** July 02, 2021. **Accepted:** January 19, 2022.

**Cite this:** Khalil RA, Alsamarrai LH. The Role of the Presence of Aliphatic Alcohols on the Formation of Wormlike Micelle of Anionic-Cationic Surfactants Mixture. JOTCSA. 2022;9(1):275-82.

**DOI:** <https://doi.org/10.18596/jotcsa.961212>.

**\*Corresponding author. E-mail:** [rakhil64@yahoo.com](mailto:rakhil64@yahoo.com).

### INTRODUCTION

There is no doubt concerning with the essential and important applications of surfactants in multi aspects of life. The benefits of use of surface active agents with their traditional spherical micelles are not limited which are increasing day by day (1-4). In special conditions, new version of micelles of one dimensional shape of aggregates which referred as worm- or thread-like micelles are found. The specific characteristics of the rheological behaviors

exhibited by the aqueous solution of wormlike micelles promise their employment in very important applications of various aspects (5-15). These properties are released from the thermodynamically controlled supramolecular structure of the self-assembled amphiphilic molecules which are referred to as the living polymers. On the other side, there are only poor efforts concerning the theoretical background of the formation of these one dimensional supramolecular aggregates. Recently, we have developed a new

physical insight that is called as the Critical Intermolecular Forces (CIF) for interpreting the formation of wormlike micelle (5). This theory was achieved through the investigations of some binary and ternary systems of mixed amphiphilic molecules. The mixture of anionic sodium dodecyl sulfate (SDS) and cationic cetyltrimethylammonium bromide (CTAB) surfactants show a sharp viscosity peak at a weight ratio 80/20 of 3 wt.% CTAB/SDS. No such remarkable high viscosity peak was found for anionic- and cationic-nonionic (Triton-x 100) nor for ternary mixtures of these surfactants (5,14). The suggested CIF theory proposed that the transition phenomenon from spherical micelle structure to one dimensional is resulted from the combination of three main intermolecular forces. These including electrostatic interactions of polar head groups, dispersion forces between hydrophobic or tail groups and the hydrophobic effect that produced from the excess of formed hydrogen bonds between water molecules (icebergs). The theory (CIF) surprisingly stated that the last effect plays the major role in the formation of one dimensional shape of aggregate as never mentioned in the previous studies. The proposal of CIF interprets the transition process from 3D to 1D as at particular concentrations of molecules, a critical state is created by disturbing the balance of intermolecular interactions which makes the transformation towards 1D energetically more favorable. This theory (CIF) is considered as a helpful tool for interpreting and understanding the transformation to 1D shape of aggregate in addition to the accompanied state of gel is and helpful for predicting a new wormlike systems (5,14,15). Two studies were followed for verification CIF theory (14,15). The first was done through exploring the effect of the presence of benzene ring in the non polar chain of surfactant on the transformation process towards 1D. The results show that the existence of benzene ring in sodium dodecylbenzenesulfonate (SDBS) as a mixture with CTAB comparatively decreases the tendency of forming wormlike micelle which parallel to CIF theory (14). The second study also gives support to CIF through studying the role of surfactant head group in the transition process towards 1D shape of aggregate (15). According to literature, there are several publications concerning the formation of wormlike micelles for gaining more information about the factors affecting the transmission phenomenon towards such type of micelle. No study concerning with effect of alcohol chain length on this phenomenon was mentioned (16-22).

However, as a continuation of our previous investigations, a study of the effect of addition of aliphatic alcohols on the transition process towards 1D seems interesting to us. Indeed, the presence of both of hydrophilic hydroxyl and hydrophobic hydrocarbon groups in these substances may disturb the critical intermolecular forces and even could change the transition mechanism. Therefore,

this study could be considered as essential for testing of CIF theory. Therefore, investigations concerning the effect of addition of alcohols with different chain lengths of even carbon numbers (ethanol, 1-butanol, 1-hexanol, 1-octanol and 1-decanol), at different concentrations (0.002-0.040 M) and temperatures on the formation of wormlike micelle for the mixture of anionic SDS and cationic CTAB. Indeed, this study was limited to use only even carbon number of alcohol in order to avoid the effect of zigzag mode which exist in hydrocarbon chains (23).

## EXPERIMENTAL SECTION

The surfactants CTAB ( $\text{CH}_3(\text{CH}_2)_{14}\text{CH}_2\text{N}^+(\text{CH}_3)_3\text{Br}^-$ ) and SDS ( $\text{CH}_3(\text{CH}_2)_{10}\text{CH}_2\text{OSO}_3^- \text{Na}^+$ ) in addition to all aliphatic alcohols (ethanol, 1-butanol, 1-hexanol, 1-octanol and 1-decanol) were used in highly purified form were obtained from VWR Chemicals BDH, Sigma-Aldrich, and Alfa Aesar companies. 3 wt% aqueous solutions of each surfactant was prepared using freshly distilled water at concentrations of 0.1072 and 0.08486 M for CTAB and SDS, respectively. The stock solutions of alcohols were prepared according to their solubility as aqueous surfactants solution of 3 wt% was used as a solvent for non-water soluble alcohols.

Measurements of dynamic viscosity ( $\eta$ ) were carried out using modified Ostwald apparatus as elaborated in Ref. 5. The temperature was controlled within  $\pm 0.1$  °C using water thermostated Hakke NK22. In order to check the reproducibility of the data, all measurements were repeated for at least three times.

## RESULTS AND DISCUSSION

An investigation that deals with the effect of aliphatic alcohols of different chain lengths on the transformation from 3D to 1D shape of aggregate may afford good information about interesting transition. This is due to the fact that the behavior of alcohols differ significantly from each other from molecular interactions point of view. For example, the water solubility of ethanol is very high, while 1-butanol is slightly soluble (7.9 g/100 mL), and 1-hexanol is very slightly soluble (0.6 g/100 mL), while 1-octanol and 1-decanol are immiscible. As far as the previous study indicates the sharp viscosity peak for the mixture of SDS and CTAB due to presence of worm-like micelle which is lying at weight ratio 80/20 of 3 wt.% CTAB/SDS (5). Therefore, the first exploration should be about the effect of the presence of alcohols on the position of this peak. The results as illustrated in Figure 1 show there is no effect on the position of this characteristic peak due to presence of these additives. Indeed, such achievement could provide support to the CIF theory as the long length chain of hydrophobic group plays a major role in the formation of wormlike micelles, as that for CTAB is

exceeding by four CH<sub>2</sub> groups in contrast to that of SDS (5).

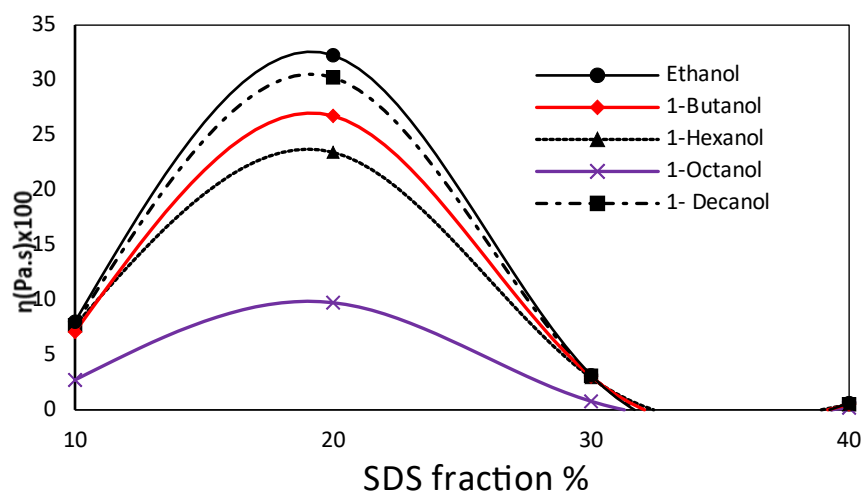


**Figure 1:** It exhibits that there is no effect due to presence of aliphatic alcohols (0.01 M) on the position of the sharp viscosity peak at a weight ratio 80/20 of 3 wt.% CTAB/SDS at 25 °C.

The effect of presence of alcohols at different concentrations of 0.002, 0.010, 0.020, 0.030, and 0.040 on the sharp viscosity peak were investigated at different temperatures as illustrated in Figures 2-6, respectively. In general, these figures show clear enhancement in the ability of the formation of threadlike micelles due to presence of alcohols at different ratios except 1-octanol according to the following sequence:

ethanol > 1-decanol > 1-butanol > 1-hexanol > 1-octanol

Interestingly, such non-systematic consequence is quite parallel with the principle of CIF theory. However, the significant effect of ethanol may be related to the intermolecular interaction of its hydroxyl group with the head groups of spherical micelle which then reduces the attraction between the two oppositely charged molecules, that is, CTAB and SDS. Then the stability of micelle will be reduced which lead to the transformation phenomenon towards one dimensional micelle. On the other side, the relatively remarkable effect of 1-decanol may be accepted for its long hydrophobic chain of the similar length to that of SDS which may cannot be covered by the hydrophobic core of 3D

micelle. Then, 1-decanol may behave as a surfactant through an increase of the hydrophobic effect that is responsible for the transformation towards one dimensional micelle according to CIF theory (5). Another probability of 1-decanol may be released when behaves as a surfactant due to its relatively long hydrophobic chain as involved within the structure of spherical micelle with both CTAB and SDS which then reduces the attraction between head groups leading to the phenomenon of transformation. On the other side, 1-octanol shows a very slight effect towards the transformation phenomenon in comparison with others, even there is a negative effect at relatively high concentration as clearly displayed in Figure 6. The reason for this comparatively unusual behavior of 1-octanol can be related to the considerable stabilization of the structure of 3D micelle through entering its hydrophobic core. Meanwhile, the behaviors of both 1-butanol and 1-hexanol may be correlated to the hydrophobic effect due to excess in number of CH<sub>2</sub> group in contrast to that of both ethanol and 1-octanol. In other words, the activity of 1-butanol and 1-hexanol towards the formation of one dimensional micelles can be considered as the mediator between those of ethanol and 1-octanol.

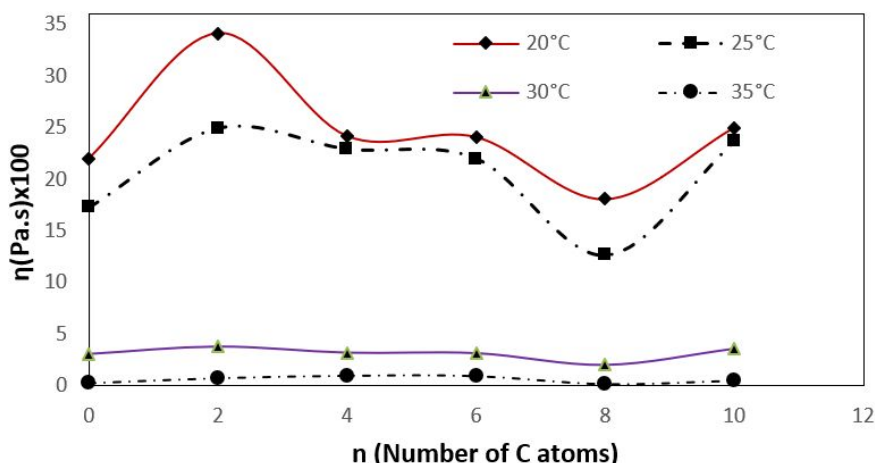


**Figure 2:** Effect of the presence of aliphatic alcohols (ethanol, 1-butanol, 1-hexanol, 1-octanol and 1-decanol) in concentration of 0.002 M on the top viscosity ( $\eta$ ) of the wormlike micelle for the mixture of 3% w/w CTAB/SDS surfactants in water of 80:20 ratio at different temperatures.

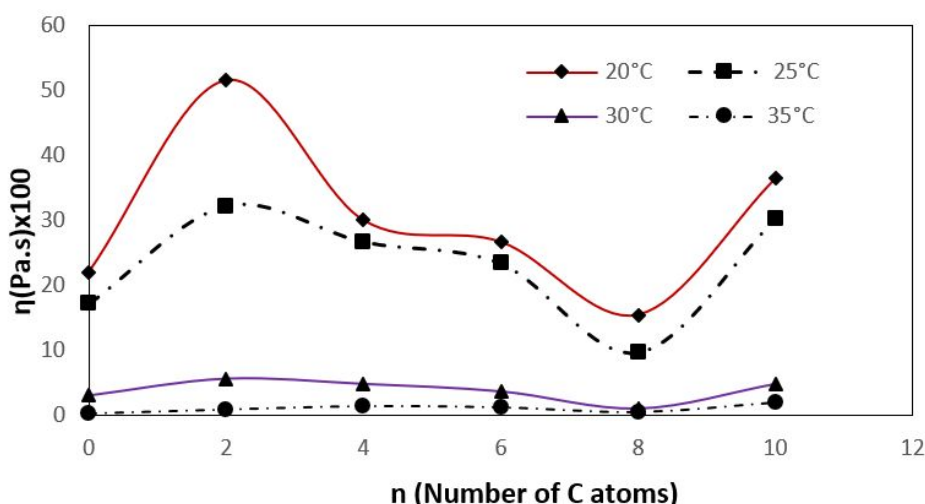


**Figure 3:** Effect of the presence of aliphatic alcohols (ethanol, 1-butanol, 1-hexanol, 1-octanol, and 1-decanol) in concentration of 0.01 M on the top viscosity ( $\eta$ ) of the wormlike micelle for the mixture of 3% w/w CTAB/ SDS surfactants in water of 80:20 ratio at different temperatures.

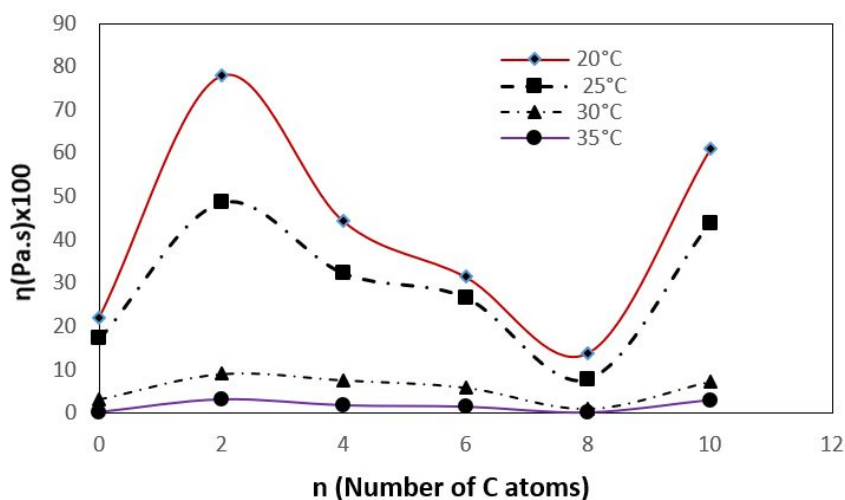


**Figure 4:** Effect of the presence of aliphatic alcohols (ethanol, 1-butanol, 1-hexanol, 1-octanol, and 1-decanol) at a concentration of 0.02 M on the top viscosity ( $\eta$ ) of the wormlike micelle for the mixture of 3% w/w CTAB/ SDS surfactants in water of 80:20 ratio at different temperatures.

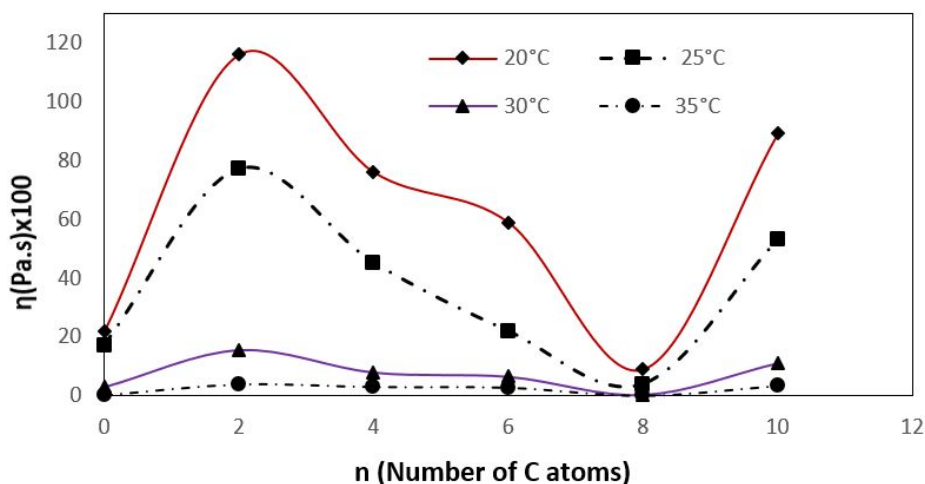


**Figure 5:** Effect of the presence of aliphatic alcohols (ethanol, 1-butanol, 1-hexanol, 1-octanol, and 1-decanol) at a concentration of 0.03 M on the top viscosity ( $\eta$ ) of the wormlike micelle for the mixture of 3% w/w CTAB/ SDS surfactants in water of 80:20 ratio at different temperatures.

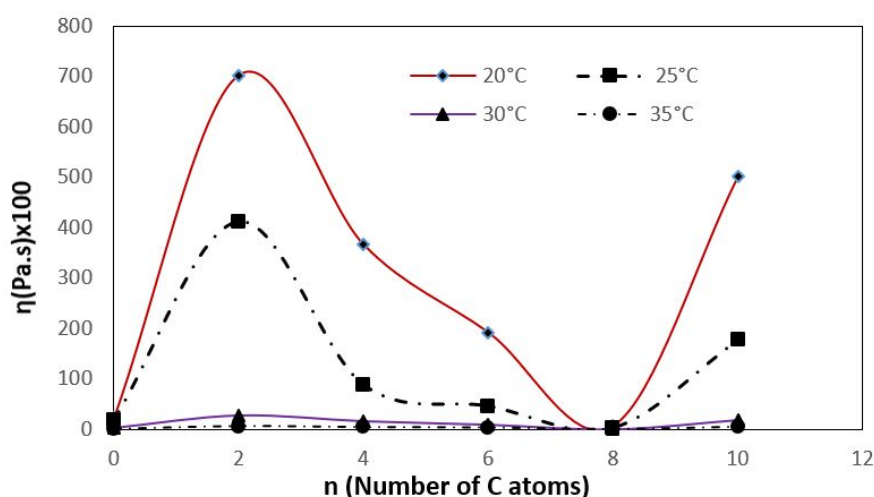


**Figure 6:** Effect of the presence of aliphatic alcohols (ethanol, 1-butanol, 1-hexanol, 1-octanol, and 1-decanol) at a concentration of 0.04 M on the top viscosity ( $\eta$ ) of the wormlike micelle for the mixture of 3% w/w CTAB/ SDS surfactants in water of 80:20 ratio at different temperatures.

Figures 7 and 8 interpret the effect of changing the concentration of aliphatic alcohols on the sharp peak viscosity of 3% w/w CTAB/ SDS surfactants in water of 80:20 ratio at 20 and 25 °C, respectively. Indeed, the relationships of those figures indicating that the ability of the formation of wormlike micelles

increases with increasing the concentration of alcohols except for that of 1-octanol. The reason for this can also be related to the same of above discussion for the relationships of Figures 2-6 in terms of CIF theory.

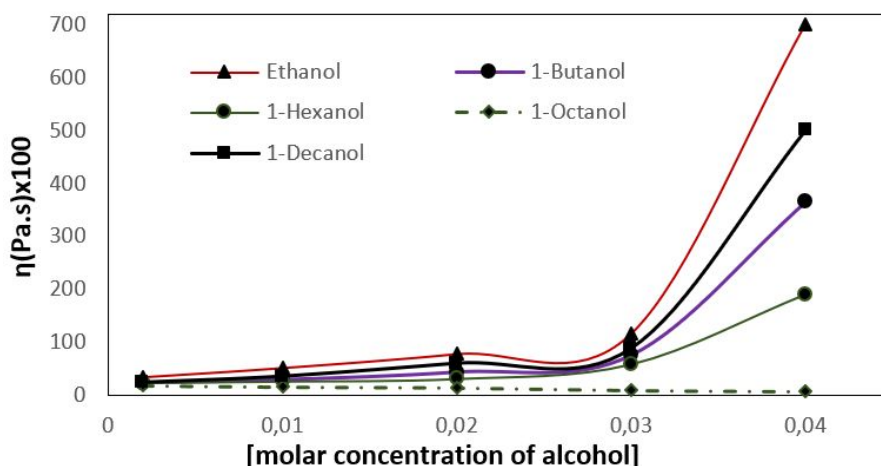


**Figure 7:** Effect of the presence of aliphatic alcohols (ethanol, 1-butanol, 1-hexanol, 1-octanol and 1-decanol) in different concentrations on the top viscosity ( $\eta$ ) of the wormlike micelle for the mixture of 3% w/w CTAB/ SDS surfactants in water of 80:20 ratio at 20 °C temperature.

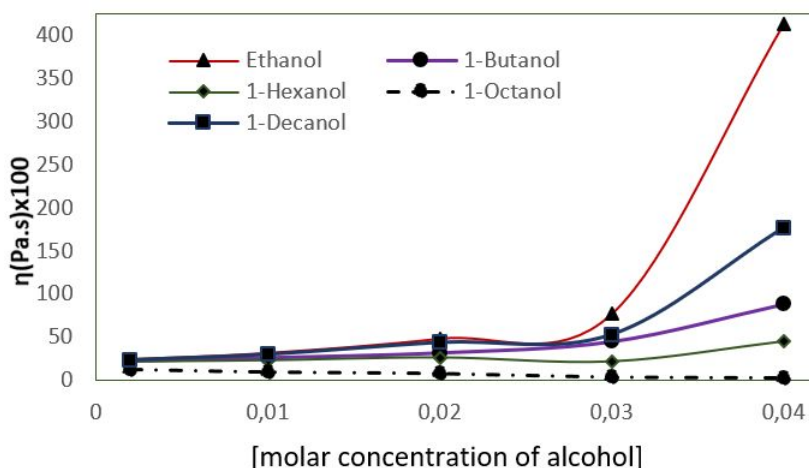


**Figure 8:** Effect of the presence of aliphatic alcohols (ethanol, 1-butanol, 1-hexanol, 1-octanol, and 1-decanol) in different concentrations on the top viscosity ( $\eta$ ) of the wormlike micelle for the mixture of 3% w/w CTAB/ SDS surfactants in water of 80:20 ratio at 25 °C temperature.

## CONCLUSION

On the basis of the above results, one could conclude that the theory of CIF that coping the transformation occurrence from 3D to 1D shape of aggregate is still the right physical insight of this phenomenon. Hence, the presence of aliphatic alcohols helps for reaching the critical state of intermolecular forces of the formed spherical micelle towards the formation of 1D micelle. While, for 1-octanol the matter is quite different as the presence of 1-octanol satisfies the 3D shape of aggregate which then it may work as inhibitor for reaching the critical state, particularly when exists at relatively high concentration. Finally, the results recommended that alcohols particularly ethanol and 1-octanol can be employed as adjustment reagents for controlling required viscosity of threadlike micelles.

## CONFLICT OF INTEREST

The authors declare that they have no conflict of interest.

## ACKNOWLEDGMENTS

Thanks should go to the University of Mosul for supporting the presented work.

## REFERENCES

- Mondal MH, Roy A, Malik S, Ghosh A, Saha B. Review on chemically bonded geminis with cationic heads: second-generation interfactants. *Res Chem Intermed.* 2016 Mar;42(3):1913–28. <DOI>.
- Sar P, Ghosh A, Scarso A, Saha B. Surfactant for better tomorrow: applied aspect of surfactant aggregates from laboratory to industry. *Res Chem Intermed.* 2019 Dec;45(12):6021–41. <DOI>.



3. Chowdhury S, Rakshit A, Acharjee A, Mahali K, Saha B. Surface phenomenon in micellar media: An excellent controlling factor for oxidation of fatty aldehyde in aqueous medium. *Journal of Molecular Liquids*. 2020 Jul;310:113224. [<DOI>](#).
4. Acharjee A, Rakshit A, Chowdhury S, Saha B. Micelle catalysed conversion of 'on water' reactions into 'in water' one. *Journal of Molecular Liquids*. 2021 Jan;321:114897. [<DOI>](#).
5. Khalil RA, Hammad FJ. Critical Intermolecular Forces: A New Physical Insight for the Formation of Wormlike Micelles. *Journal of the Chemical Society of Pakistan*. 2014;36(2):211-20.
6. Rodriguez-Abreu C, Shrestha RG, Shrestha LK, Harush E, Regev O. Worm-Like Soft Nanostructures in Nonionic Systems: Principles, Properties and Application as Templates. *J Nanosci Nanotech*. 2013 Jul 1;13(7):4497-520. [<DOI>](#).
7. Parker A, Fieber W. Viscoelasticity of anionic wormlike micelles: effects of ionic strength and small hydrophobic molecules. *Soft Matter*. 2013;9(4):1203-13. [<DOI>](#).
8. Wang Z, Li Y, Dong X-H, Yu X, Guo K, Su H, et al. Giant gemini surfactants based on polystyrene-hydrophilic polyhedral oligomeric silsesquioxane shape amphiphiles: sequential "click" chemistry and solution self-assembly. *Chem Sci*. 2013;4(3):1345. [<DOI>](#).
9. Dreiss CA. Wormlike micelles: where do we stand? Recent developments, linear rheology and scattering techniques. *Soft Matter*. 2007;3(8):956. [<DOI>](#).
10. Ziserman L, Abezgauz L, Ramon O, Raghavan SR, Danino D. Origins of the Viscosity Peak in Wormlike Micellar Solutions. 1. Mixed Catanionic Surfactants. A Cryo-Transmission Electron Microscopy Study. *Langmuir*. 2009 Sep 15;25(18):10483-9. [<DOI>](#).
11. Li J, Zhao M, Zheng L. Salt-induced wormlike micelles formed by N-alkyl-N-methylpyrrolidinium bromide in aqueous solution. *Colloids and Surfaces A: Physicochemical and Engineering Aspects*. 2012 Feb;396:16-21. [<DOI>](#).
12. Dan-Hua X, Jian-Xi Z, Lin L, Yi Y, Xi-Lian W, 1 福州大学化学化工学院, 胶体与界面化学研究所, 福州 350108;, 1 Institute of Colloid and Interface Chemistry, College of Chemistry and Chemical Engineering, Fuzhou University, Fuzhou, Fujian, 350108, P. R. China;, et al. A Highly Viscoelastic Anionic Wormlike Micellar System. *Acta Physico-Chimica Sinica*. 2013;29(07):1534-40. [<DOI>](#).
13. Yu H, Xu Z, Wang D, Chen X, Zhang Z, Yin Q, et al. Intracellular pH-activated PEG-b-PDPA wormlike micelles for hydrophobic drug delivery. *Polym Chem*. 2013;4(19):5052. [<DOI>](#).
14. Khalil RA, Saadoon FA. Effect of presence of benzene ring in surfactant hydrophobic chain on the transformation towards one dimensional aggregate. *Journal of Saudi Chemical Society*. 2015 Jul;19(4):423-8. [<DOI>](#).
15. Khalil RA, Alsamarrai LH. The role of surfactants head group in the formation of self-assembled supramolecular aggregate. *Arab J Phys Chem*. 2015;2(1):7-13.
16. Fieber W, Scheklaikov A, Kunz W, Pleines M, Benczedi D, Zemb T. Towards a general understanding of the effects of hydrophobic additives on the viscosity of surfactant solutions. *Journal of Molecular Liquids*. 2021 May;329:115523. [<DOI>](#).
17. Tan G, Zou W, Weaver M, Larson RG. Determining threadlike micelle lengths from rheometry. *Journal of Rheology*. 2021 Jan;65(1):59-71. [<DOI>](#).
18. Pandya N, Rajput G, Janni DS, Subramanyam G, Ray D, Aswal V, et al. SLES/CMEA mixed surfactant system: Effect of electrolyte on interfacial behavior and microstructures in aqueous media. *Journal of Molecular Liquids*. 2021 Mar;325:115096. [<DOI>](#).
19. Mehringer J, Hofmann E, Touraud D, Koltzenburg S, Kellermeier M, Kunz W. Salting-in and salting-out effects of short amphiphilic molecules: a balance between specific ion effects and hydrophobicity. *Phys Chem Chem Phys*. 2021;23(2):1381-91. [<DOI>](#).
20. Khalil RA, Alsamarrai LH. Study The Effect Of Ethanol On The Formation Of The Wormlike Micelles For A Mixture Of Ionic Surfactants. *Ratio*. 2015;10(90):4344-89.
21. Shibaev AV, Aleshina AL, Arkharova NA, Orekhov AS, Kuklin AI, Philippova OE. Disruption of Cationic/Anionic Viscoelastic Surfactant Micellar Networks by Hydrocarbon as a Basis of Enhanced Fracturing Fluids Clean-Up. *Nanomaterials*. 2020 Nov 27;10(12):2353. [<DOI>](#).
22. Moitzi C, Freiberger N, Glatter O. Viscoelastic Wormlike Micellar Solutions Made from Nonionic Surfactants: Structural Investigations by SANS and DLS. *J Phys Chem B*. 2005 Aug 1;109(33):16161-8. [<DOI>](#).
23. Khalil R, Zarari A. Theoretical investigations for the behavior of hydrotropes in aqueous solution. *JOTCSA*. 2015;2(4):42-52. [<URL>](#).







## Utilization of Kiwi Peel Lignocellulose as Fillers in Poly(Lactic Acid) Films

Ece Sogut<sup>1\*</sup>  , Atif Can Seydim<sup>1</sup> 

<sup>1</sup>Suleyman Demirel University, Food Engineering Department, Isparta, 32260, Turkey

**Abstract:** Lignocellulosic structures extracted from agricultural wastes have great potential in re-designing sustainable packaging materials. In this study, the utilization of kiwifruit peels (KFP) (unt) and lignocellulosic structures extracted from KFP, which were alkali-treated (al), acid-treated (ac), and acetylated (ace), in poly(lactic acid) (PLA) films were investigated. Untreated and treated lignocellulosic structures were added to PLA film-forming solutions at 5% (w/w based on PLA). The film samples were characterized by their mechanical, water vapor permeability (WVP), FTIR, and optical properties. FTIR results presented that the acid treatment and acetylation have changed the chemical structure of KFP, which resulted in changes in intensities and peak shifts between 1400-1900 cm<sup>-1</sup>. WVP of the films containing KFP-based lignocellulosic structures was lower than control PLA films ( $p < 0.05$ ). The addition of KFP-based lignocellulosic structures increased the tensile strength and elastic modulus ( $p > 0.05$ ) compared to PLA control films. Films including acid-treated lignocellulosic structures had high opacity and relatively low lightness values ( $p < 0.05$ ). These results showed that adding lignocellulosic structures into PLA films is a promising method to improve the film properties.

**Keywords:** Kiwifruit peels, Lignocellulose, Modification, Poly(lactic acid)

**Submitted:** November 16, 2021. **Accepted:** February 03, 2022.

**Cite this:** Sogut E, Seydim AC. Utilization of Kiwi Peel Lignocellulose as Fillers in Poly(Lactic Acid) Films. JOTCSA. 2022;9(1):283-94.

**DOI:** <https://doi.org/10.18596/jotcsa.1024326>.

**\*Corresponding author. E-mail:** [ececagdassdu.edu.tr](mailto:ececagdassdu.edu.tr).

### INTRODUCTION

The rise in energy demand, the increase in carbon gas emissions, and the depletion of fossil-based sources have recently raised environmental concerns (1,2). The circular economy promotes the transition from petroleum-based materials to renewable materials and greener processes for obtaining energy and materials. Biowastes are an abundant and inexpensive source. Their complete utilization to extract added-value materials is an appealing option from an eco-friendly standpoint (2-5). Among the various biomasses, lignocellulosic biomass accounts for nearly 70% of total plant biomass (4). Thus, the environmental problems and depletion of fossil resources have increased interest in green and sustainable chemistry, which focuses on lignocellulose-based materials as a promising, abundant, and renewable resource for different

materials (6-8). The main constituents found in lignocellulosic structures are cellulose (homopolymer), hemicelluloses (heteropolymer), and lignin (aromatic polymers) (7-9). To convert them into various bio-based compounds, individual fractions could be recovered from lignocellulosic biomass (10).

Researchers have used pre-treatments to separate these main structures (lignin, hemicellulose) from lignocellulosic structures, modify, improve their reactivity by extracting those valuable constituents, and change degrees of crystallization and polymerization (11-15). Alkaline or acid hydrolysis has been widely used as a chemical pretreatment technique (16,17). Among the various pre-treatments, alkaline de-lignification destroys the lignin structure and breaks linkages between lignin and carbohydrate to make the latter more

accessible (18). Hydrothermal treatments are high-capacity treatments for hemicellulose solubilization while also producing cellulose and lignin-rich structures that are open to being treated to extract these components (19,20). Besides, acetylation has been used to plasticize the cellulosic fibers, substituting hydroxyl groups with acetyl groups to make the material more hydrophobic, stabilize the material against water, and enhance the degradation and stability (21). Ozone treatment is another biomass pretreatment method in which it oxidizes the structure to remove lignin and hemicellulose (22).

The use of lignocellulosic structures as fillers for bio-based polymers has gained popularity due to their better mechanical strength, wide range of availability, and being suitable for various chemical structure-based modifications (23–28). Many studies have examined the incorporation of agro-wastes into natural biopolymers such as starch, protein, cellulose, poly(lactic) acid (PLA), and polyhydroxy butyrate (PHB) to create bio-based plastics (23,26,29–31). Among biopolymers, PLA has been vastly studied due to its easily processed structure, having similar characteristics to conventional plastics, intrinsic biodegradability and biocompatibility, compostability, thermoplastic nature, and outstanding mechanical performance (32). However, to widen the application of PLA-based materials, PLA has been studied to modify its structure by various alternative methods such as blending with other polymers, reactive extrusion, using crosslinking agents or chain extender, chemical or physical modifications, and use of reinforcing agents including inorganic fillers and natural fibers (33–36). Among these applications, the addition of lignocellulosic structures such as corncob (37), yerba mate (32,38), bamboo, switchgrass (39), nanofibers from lignocellulose biomass (40) into PLA has also been gained attention by researchers.

Fruit peels, such as kiwifruit peels, are from the agro-food industry with promising potential as an appropriate raw material for use in a biorefinery (7). Kiwifruit processing creates wastes with bio-active properties of various sectors such as cosmetic, food, and pharmaceutical industries due to their bioactive molecules having health-promoting properties (41–44). After extracting active compounds (kaempferol and quercetin derivatives) from kiwifruit peel, the obtained solid fraction is primarily composed of lignocellulosic structures (45). Incorporating lignocellulosic structures obtained from agro-wastes like kiwifruit peel as reinforcements typically lowers cost and water uptake while increasing mechanical strength (46). Arrieta et al. (38) studied the effect of lignocellulosic-based mate nanoparticles extracted from yerba mate residue on the properties of PLA films. They reported enhanced thermal stability, increased flexibility, processability, UV light

blocking effect, and an appropriate disintegration in compost. However, interfacial adhesion between PLA and natural fibers extracted from agro-wastes is one of the most important issues (37). Generally, weak interaction between PLA and lignocellulosic structures has been reported in the literature (47–49). Thus, research on the addition of modified lignocellulosic structures to improve the adhesion in thermoplastics/lignocellulose composites are gaining interest.

The food industry has been commercializing the kiwi fruit in diverse processed forms, even though the kiwi fruit is commonly consumed as fresh (50). Therefore, the byproducts such as the peel of kiwi fruit have been increasing and are still under-explored (51). However, a great interest in these byproducts has increased due to their high concentration of bioactive molecules (52). The characterization of kiwi fruit byproducts has been studied by many researchers (51); however, the valorization of these byproducts as fillers in biopolymers is required more studies to confirm their utilization. Besides, it has been reported that the direct use of these fillers might result in incompatibility problems, which chemical modifications on lignocellulosic structures could recover. PLA reinforcement with various chemically modified lignocellulosic fibers has been rarely studied. Thus, this study aimed to examine the valorization of kiwifruit peels in PLA films as fillers followed by different pre-treatments including alkali, acetylation, and acid treatments, and further evaluate regarding mechanical, water vapor permeability (WVP), Fourier transform infrared spectroscopy (FTIR), and optical properties, whether to determine the potential of kiwifruits byproduct in the food packaging applications.

## MATERIALS AND METHODS

### Materials

Kiwi fruits (KF) were provided from a local producer in Isparta (Turkey) and peeled to collect kiwi fruit peels (KFP). KFPs were then dried at 60 °C for 24 h and ground with a high-speed blender. After screening the obtained particles with suitable meshes, particles smaller than 300 µm in size were used in the experiments. Homogenized KFPs were coded as “unt” and stored at 4°C until use. Poly(lactic acid) (PLA) (4032D; molecular weight of 80,000-100,000 g/mol, 1.25 g/cm<sup>3</sup> of specific gravity, melt flow index of 5.89 g/10 min) was from NatureWorks LLC (Minnetonka, MN, USA) and other chemicals including sulfuric acid (H<sub>2</sub>SO<sub>4</sub>), ethanol, sodium hydroxide (NaOH), chloroform, glacial acetic acid, and magnesium nitrate (Mg(NO<sub>3</sub>)<sub>2</sub>) were purchased from Sigma-Aldrich (St. Louis, Missouri, USA).

### Extraction of Cellulose-Rich Structures from Kiwi Peels and Characterization

The extraction steps of cellulose-rich structures from KFPs are shown in Figure 1.

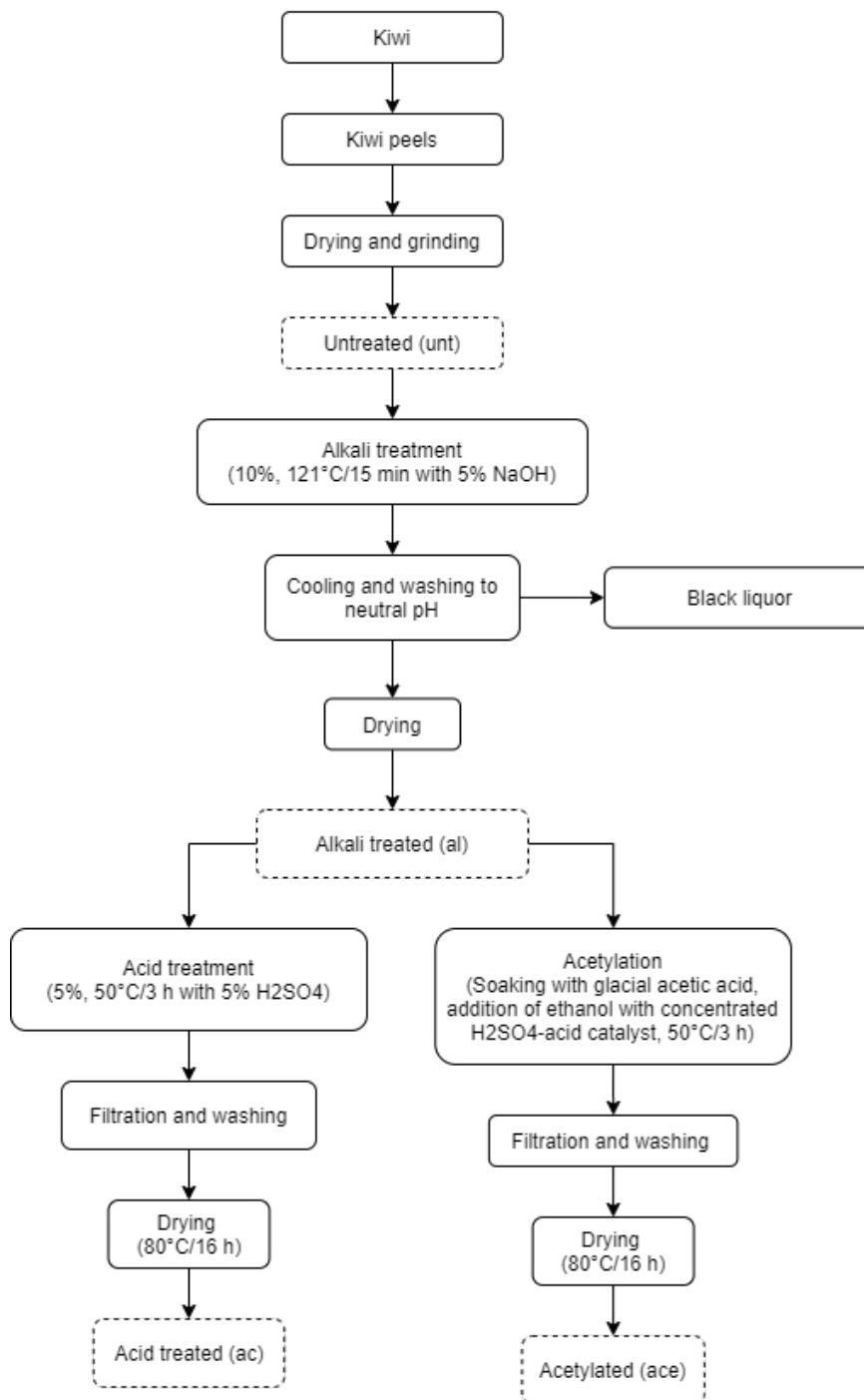


**Figure 1:** Schematic representation of extraction steps.

KFPs were de-lignified in an alkaline medium using NaOH at 5% (w/w) with a liquid: solid ratio of 10% (w/w) at 121 °C for 15 min. Black liquor was separated by filtration followed by washing to neutral pH. The filtrate was dried and coded as alkali-treated (al). The alkali-treated solid part was then modified by acid treatment (ac) and acetylation (ace) (53). Acid-treated samples were

obtained after subjecting the alkali-treated solid part to H<sub>2</sub>SO<sub>4</sub> (5%, w/w) at a liquid: solid ratio of 5% (w/w) at 50°C for 3 h. After mild hydrolysis, the filtrate was washed several times and dried for 24 h at 80 °C. The acetylation reaction was performed by soaking the alkali-treated solid part in glacial acetic acid. The reaction was carried out by adding ethanol and concentrated H<sub>2</sub>SO<sub>4</sub> (acid catalyst) at 50 °C for

3 h. After washing with water several times, the filtrate was obtained and dried for 24 h at 80 °C. The al-, ac-, and ace-treated KFP-based fillers were

stored at 4 °C until use. The obtained cellulose-rich structures from kiwi peels are shown in Figure 2.

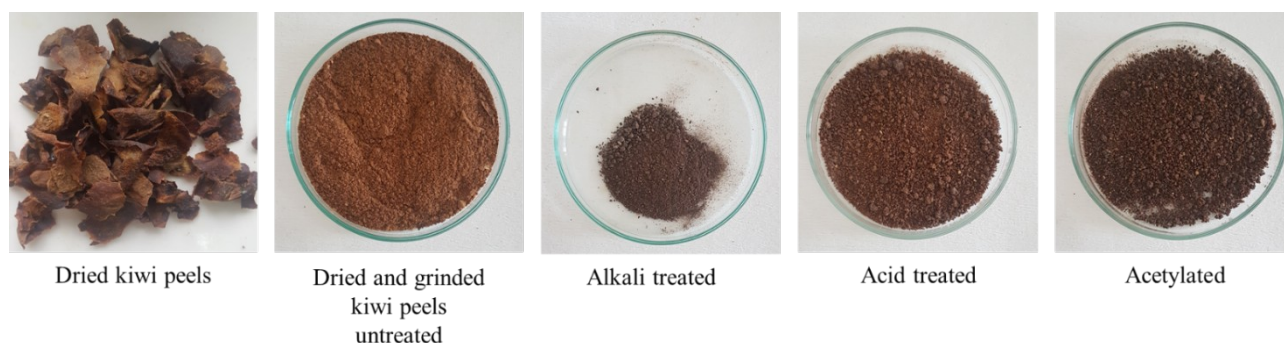


**Figure 2:** Pictures of extracted structures.

Lignin and cellulose contents of dried KFPs (unt) and extracted cellulose-rich structures were determined according to Sogut and Cakmak's methods (54). The Fourier transform infrared (FTIR) spectra, ranging from  $500\text{ cm}^{-1}$  to  $4000\text{ cm}^{-1}$ , for KFPs (unt) and extracted cellulose-rich structures were obtained by Spectrum Two FTIR spectrometer (Perkin Elmer, USA) with an attenuated total reflectance (ATR) module.

#### Preparation of PLA films

PLA at 6% (w/w) was dissolved in chloroform and poured on Teflon-coated Petri dishes. Reinforced film samples were obtained by mixing KFP-based

fillers at 5% (w/w) with PLA film-forming solution. Homogeneous film-forming solutions were cast and dried at room temperature. The pouring amount of film-forming solution was adjusted to control the film thickness. All film samples were conditioned at 25 °C and 53% relative humidity (RH) for one week before characterization analyses. PLA film, which did not include any filler, was named control film. Other film samples were called PLA-unt, PLA-al, PLA-ac, and PLA-ace for PLA films, including unt, al, ac, and ace, respectively (Figure 3). The thickness of six randomly selected points was measured by a digital micrometer (Quantu-Mike IP65, Mitutoyo, Japan,  $\pm 0.001\text{ mm}$ ).

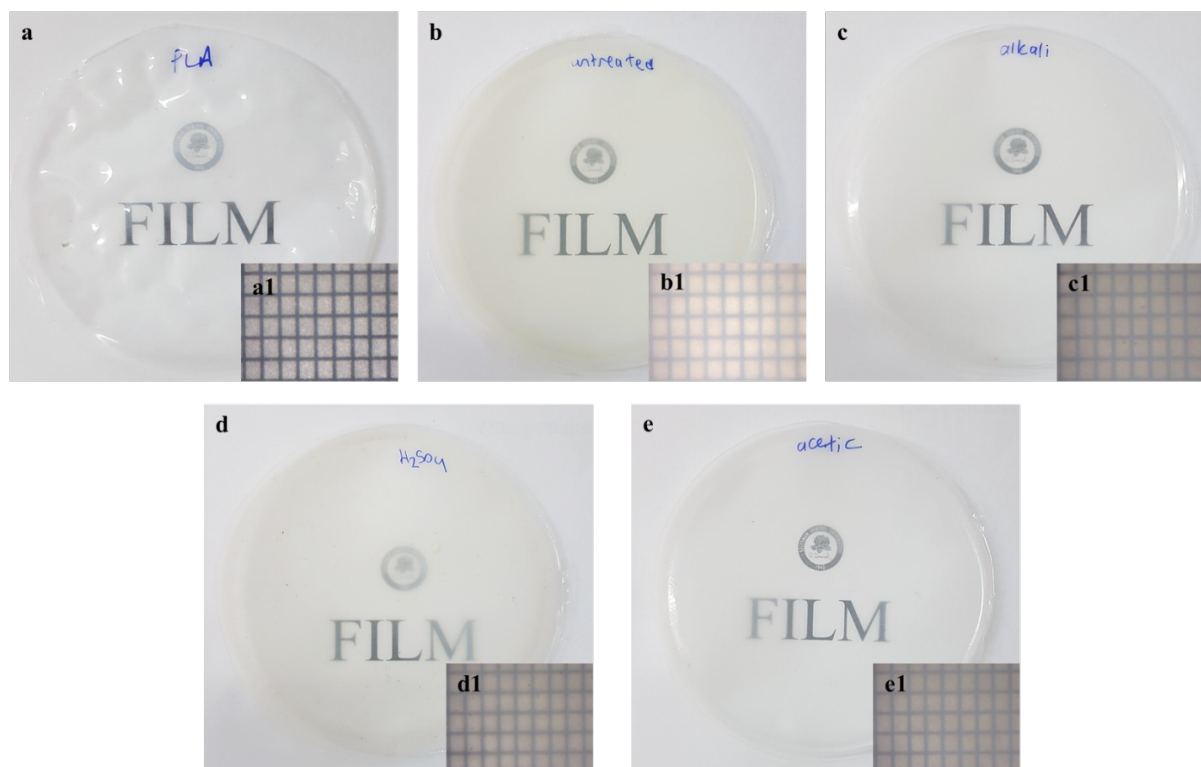


**Figure 3:** Pictures of film samples (a=PLA, b=PLA-unt, c=PLA-al, d=PLA-ac, e=PLA-ace and number 1 denotes images taken under a stereomicroscope (Carl Zeiss Stemi 5800, Oberkochen Germany) processed with Zeiss Zen (blue edition) software and with the scale of 0.1 mm)

## Characterization of the Film Samples

### *Fourier transform infrared (FTIR) spectroscopy*

FTIR spectra of film samples were recorded using Spectrum Two FTIR spectrometer (Perkin Elmer, USA) equipped with a horizontal ATR module, which was recorded from 500  $\text{cm}^{-1}$  to 4000  $\text{cm}^{-1}$  at 25 °C (with a resolution of 4  $\text{cm}^{-1}$ ).

### *Mechanical properties and water vapor permeability (WVP) of film samples*

The mechanical properties, tensile strength (TS), and elongation-at-break values (E) were determined by the ASTM standard method D882 (55). Films were mounted in the film-extension grips of the universal testing machine (Lloyd LR5, AMETEK, Inc, UK) and stretched at 50  $\text{mm}\cdot\text{min}^{-1}$ .

The WVP of films was determined according to the E96/E96M-16 gravimetric method (56). Film samples were exposed to 100% RH, and the permeability measurements were performed by weighing the cups periodically (every 1.5 h for 48 h) at 25°C.

### *Optical properties of film samples*

The opacity of film samples was determined using the absorption spectrum of the film sample (1×4 cm rectangular film strips) between 400 nm and 800 nm by a UV-visible spectrophotometer (Shimadzu,

UV-1601, Japan). The opacity was expressed as absorbance units per film thickness ( $\text{AU}\cdot\text{nm}\cdot\text{min}^{-1}$ ). The transmittance values were obtained at 450 nm as percent transmittance with a UV-visible spectrophotometer (Shimadzu, UV-1601, Japan).

The color of the prepared films was determined by a Minolta Chroma Meter (CR-400, Konica Minolta, Inc., Japan). CIE L\* (lightness), a\* (red-green) and b\* (yellow-blue) coordinates in the color space were recorded by using a white standard calibration plate (Y=92.7, x=0.3160, y=0.3321) as the background for color measurement of the films.

### Statistical Analysis

An analysis of variance (ANOVA) and Tukey's multiple comparison tests were used to find the differences between film samples at a 95% confidence level. The statistical analysis was performed using Minitab 17 software (Minitab Inc., Brandon, UK). Three observations were performed for each sample, and each experiment was replicated three times.

## RESULTS AND DISCUSSION

### Properties of kiwi fruit peels

The cellulose and lignin contents of untreated and treated kiwi peels are shown in Table 1.

**Table 1:** Lignin and cellulose contents of extracted structures.

Sample	Cellulose (%)	Lignin (%)
Untreated	13.66±2.22 <sup>c</sup>	29.93±7.74 <sup>a</sup>
Alkali treated	37.03±2.66 <sup>b</sup>	19.28±1.46 <sup>a</sup>
Acid treated	65.28±4.49 <sup>a</sup>	16.35±1.77 <sup>a</sup>
Acetylated	35.93±6.27 <sup>b</sup>	19.90±5.38 <sup>a</sup>

<sup>a-c</sup> Different superscripts in the same column are significantly different ( $p<0.05$ ).

It was observed that untreated KFP consisted of 13.66±2.22 and 29.93±7.74% cellulose and lignin, respectively. After the alkali treatment, cellulose content increased while lignin content decreased, showing the partial removal of lignin constituents. The same trend was also observed in acid treatment and acetylation, which might be due to the functionalization of lignocellulosic structures by reacting with cellulosic -OH groups. The acetylation process might also modify the fiber structure,

causing an increase in plasticization and a reduction in the water affinity of cellulose (57). Similarly, Narender and Priya Dasan (58) and Kocaman and Ahmetli (53) observed a reduction in lignin concentration after acid treatment and acetylation of coir pith and hazelnut shells, respectively.

The FTIR spectra of KFP and treated KFPs are shown in Figure 4.

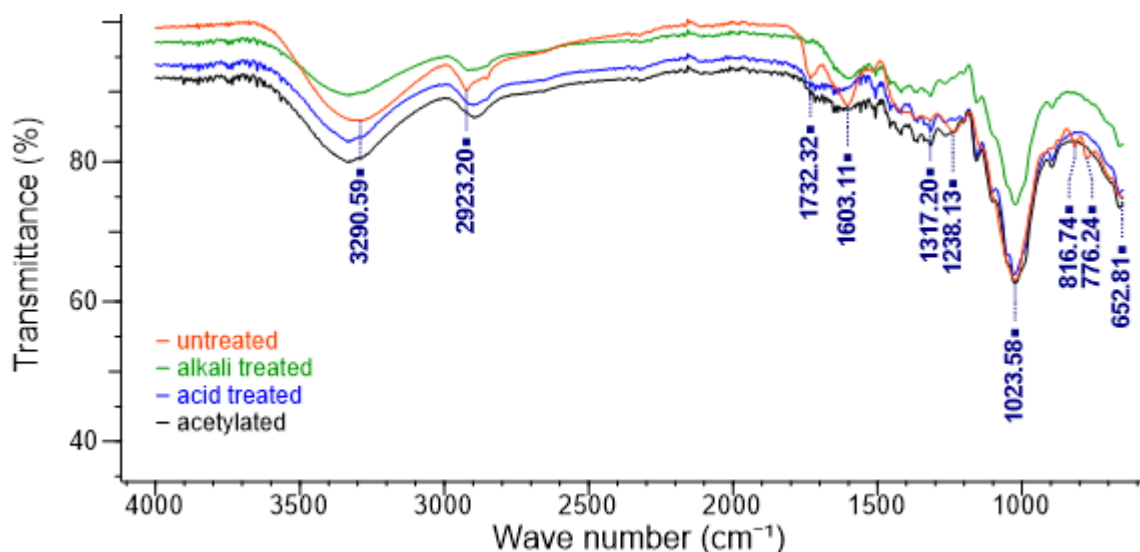


**Figure 4:** FTIR spectra of untreated, alkali-treated, acid-treated, and acetylated kiwi peels.

The peaks found at  $3300\text{ cm}^{-1}$ ,  $1600\text{ cm}^{-1}$ , and  $1700\text{ cm}^{-1}$  belong to the O-H stretching, the aromatic C=C stretching, and the unconjugated C=O groups stretching. The peaks found at  $1220\text{ cm}^{-1}$  are also assigned to the C-O stretching in lignin rings. The peak at  $900\text{--}1100\text{ cm}^{-1}$  belongs to the cellulosic linkages, and the changes in the intensity of these peaks are associated with the changes in cellulose levels after the treatments. The disappearance of peaks around  $1700\text{--}1800\text{ cm}^{-1}$  observed after the chemical treatments can be related to the decline in or the removal of hemicellulose-based structures. Besides, the intensity of peaks at  $1220\text{ cm}^{-1}$  was lower than the

untreated KFP structures, which can be correlated with the reduction in lignin concentration due to the chemical treatments. The band at  $1245\text{ cm}^{-1}$  might be observed due to the presence of the acetate groups. Similar behavior was observed by Sreekala et al. (59) for oil palm fiber and Kocaman (60) for apricot kernel shells after various chemical modifications.

#### Properties of film samples

The thickness, water vapor permeability (WVP), and mechanical properties of film samples are shown in Table 2.

**Table 2:** Thickness, water vapor permeability (WVP), and mechanical properties (TS, E) of film samples.

Sample	Thickness ( $\mu\text{m}$ )	WVP ( $\text{g}\cdot\text{mm}\cdot\text{kPa}^{-1}\cdot\text{h}^{-1}\cdot\text{m}^{-2}$ )	TS (MPa)	E (%)
PLA	$113\pm 15^a$	$0.15\pm 0.05^a$	$19.55\pm 1.88^a$	$4.32\pm 0.19^a$
PLA-unt	$150\pm 20^a$	$0.12\pm 0.01^b$	$21.44\pm 1.66^a$	$3.98\pm 0.53^a$
PLA-al	$128\pm 35^a$	$0.11\pm 0.03^b$	$27.55\pm 7.81^a$	$4.79\pm 0.61^a$
PLA-ac	$150\pm 21^a$	$0.11\pm 0.02^b$	$29.67\pm 5.25^a$	$4.92\pm 0.62^a$
PLA-ace	$128\pm 38^a$	$0.10\pm 0.01^b$	$26.14\pm 4.38^a$	$4.70\pm 0.25^a$

<sup>a-b</sup> Different superscripts in the same column are significantly different ( $p < 0.05$ ).

The thickness of film samples slightly increased with the addition of fillers; however, the fillers did not significantly affect the thickness of film samples. The highest thickness values were observed in PLA-unt and PLA-ac film samples due to less compatibility and lower interaction between the CH film matrix and the filler.

The addition of KPF-based fillers into PLA films significantly lowered the WVP of film samples, and the lowest values were found in PLA-ace film sample ( $p < 0.05$ ). The dispersion of fiber particles within the film matrix might affect the diffusion way of water molecules by changing the polarity of polymer and the path length of water molecules (61). Similar

results were observed by Khalil et al. (62), who studied the effect of bamboo fibers on the thermo-mechanical properties of carrageenan films, and Valdés García et al. (63) used almond skin residues to improve the properties of PCL films.

The application of different chemical treatments had various effects on the mechanical properties of film samples. Compared to neat PLA films, TS and E values increased after alkali treatment and modifications made by acetylation and acid treatment. The PLA films, including untreated KFP, also showed an increase in TS while a reduction was observed in elongation. The differences between untreated fiber added PLA film and PLA films,



including alkali-treated and modified KFP, might be due to increased cellulose content and improved adhesive characteristics obtained after chemical treatments (64). Acid-treated kiwi peels had the highest cellulose concentration, followed by alkali-treated and acetylated samples, while untreated peels had the lowest cellulose concentration. The presence of high cellulose fiber content might favor the interfacial adhesion between PLA and filler, resulting in better interactions with higher tensile strength. The addition of untreated peels had lower TS values, showing the modification improved the filler-matrix adhesion at the interface through the reaction with end groups of PLA (65). The direct use of lignocellulosic structures in polymeric matrices results in poor compatibility, requiring modifications to obtain a larger surface area for better interactions between filler and polymer (66). The chemical modifications used in the experiments

might substitute the hydroxyl groups of peels with other functional groups depending on the used method, making the fiber more hydrophobic and thus enhancing the TS of polymer (21).

Similarly, Kocaman et al. (64) also reported enhanced mechanical properties for biobased composite materials when chemically modified coconut waste particles were incorporated. The elongation at break is related to the flexibility of polymer chains; thus, an inverse effect is expected between TS and elongation. However, in this study, both TS and E values increased with fillers. The presence of lignin could also contribute to the plasticization of PLA due to the lignin-PLA bonding at the interphase regions (26).

The optical properties of film samples are shown in Table 3.

**Table 3:** Optical properties of film samples.

Sample	$L^*$	$a^*$	$b^*$	Transmittance (%)	Opacity (AU nm/ $\mu$ m)
PLA	96.33 $\pm$ 0.27 <sup>a</sup>	0.14 $\pm$ 0.03 <sup>a</sup>	1.82 $\pm$ 0.11 <sup>c</sup>	47.85 $\pm$ 6.70 <sup>a</sup>	4.42 $\pm$ 0.32 <sup>a</sup>
PLA-unt	91.72 $\pm$ 1.30 <sup>b</sup>	0.63 $\pm$ 1.23 <sup>a</sup>	11.19 $\pm$ 2.15 <sup>a</sup>	27.58 $\pm$ 2.01 <sup>ab</sup>	4.99 $\pm$ 0.30 <sup>a</sup>
PLA-al	91.42 $\pm$ 1.93 <sup>b</sup>	1.28 $\pm$ 0.60 <sup>a</sup>	6.11 $\pm$ 1.37 <sup>b</sup>	27.80 $\pm$ 7.33 <sup>ab</sup>	4.23 $\pm$ 0.18 <sup>a</sup>
PLA-ac	92.05 $\pm$ 1.80 <sup>b</sup>	1.40 $\pm$ 0.76 <sup>a</sup>	7.86 $\pm$ 1.74 <sup>b</sup>	24.40 $\pm$ 4.34 <sup>b</sup>	4.26 $\pm$ 0.41 <sup>a</sup>
PLA-ace	93.49 $\pm$ 0.49 <sup>ab</sup>	0.66 $\pm$ 0.29 <sup>a</sup>	4.80 $\pm$ 0.60 <sup>bc</sup>	29.10 $\pm$ 1.67 <sup>ab</sup>	4.97 $\pm$ 0.89 <sup>a</sup>

<sup>a-c</sup> Different superscripts in the same column are significantly different ( $p < 0.05$ ).

PLA control film had the high  $L^*$  value indicating its brightness and transparency, while its  $a^*$  and  $b^*$  values were close to zero. The lightness of films, including untreated and alkali-treated KFPs was the lowest, followed by acid-treated and acetylated KFP added PLA films ( $p < 0.05$ ). The  $a^*$  and  $b^*$  values significantly increased with the addition of fillers as indicative of a red, yellowish/brown coloration, which is due to the typical color of KFPs. This behavior was also reflected as a significant decrease in transmittance and a significant increase in

opacity. The lowest value was measured for the PLA-ac film, which might be due to the weak dispersion of the acid-treated lignin within the PLA matrix. The low transmittance values demonstrated the potential applicability of these films as UV-blocking films mainly for light-sensitive products (67). Similar behavior was observed by Wang et al. (68) for PLA and grafted PLA films, including lignin.

The FTIR spectra of film samples are shown in Figure 5.

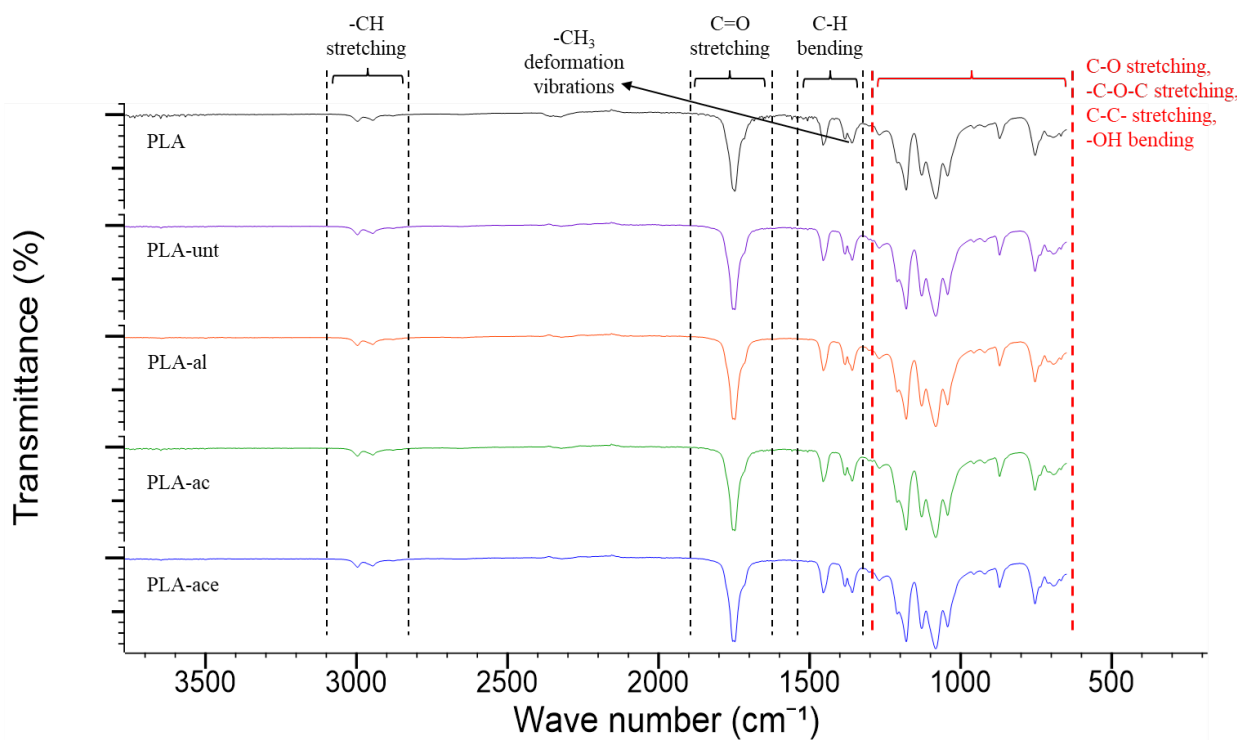


**Figure 5:** FTIR spectra of film samples.

The major peaks of PLA showed in Figure 5 are at  $1750\text{ cm}^{-1}$  assigned to the  $\text{-C=O}$  stretching vibration of the ester group, and the peaks between  $1300\text{-}1400\text{ cm}^{-1}$  corresponded to the asymmetric and symmetric  $\text{-CH}_3$  deformation vibrations, respectively. The other peaks identified between  $800$  and  $1300\text{ cm}^{-1}$  are related to the  $\text{-C-O-C}$ -stretching of the ester groups, the  $\text{C-O}$  stretching, the  $\text{-OH}$  bending, and the  $\text{-C-C-}$  stretching of the amorphous phase (69). Iglesias Montes et al. (70) observed similar FTIR spectrums for PLA bilayer films containing cellulose nanocrystals or lignin nanoparticles. The structure of PLA films did not vary with the addition of KFP-based fillers, as confirmed by any differences in FTIR spectra compared to those of neat PLA films. Opposite to these results, Nair et al. (26) found considerable interactions between the nanocellulose fibrils with high lignin content and PLA film matrix, which might be due to the differences in lignin particle size having an impact on particle-matrix interface adhesion.

## CONCLUSION

Lignocellulosic structures were extracted from KFPs by alkali treatment and alkali combined chemical treatments such as acetylation and acid treatment. It was observed that the lignin concentration decreased while the cellulose concentration increased after alkali treatment and chemical modifications of lignocellulosic structures extracted from KFPs. The obtained structures were then added to the PLA film-forming solutions to enhance the

PLA film properties as a food packaging material. The WVP, TS, and elongation of PLA films were enhanced with alkali-treated and alkali combined chemically modified structures. However, no significant changes in the chemical structure of PLA upon the addition of various KFP-based fibers as confirmed by FTIR spectra. In conclusion, alkali treatment and different modifications were found to have the potential to modify the lignocellulosic structures extracted from agricultural wastes to be used as fillers in the polymeric matrix for the improvement of film properties.

## CONFLICT OF INTEREST

The authors declare that there is no conflict of interest.

## ACKNOWLEDGMENTS

This study was conducted at Suleyman Demirel University Food Engineering Department Laboratories. Special thanks to Oguz Sogut for lignin characterization.

## REFERENCES

1. Dragone G, Kerssemakers AAJ, Driessen JLSP, Yamakawa CK, Brumano LP, Mussatto SI. Innovation and strategic orientations for the development of advanced biorefineries. *Bioresource Technology*. 2020 Apr;302:122847. <DOI>.
2. Ubando AT, Felix CB, Chen W-H. Biorefineries in circular bioeconomy: A comprehensive review. *Bioresource*

- Technology. 2020 Mar;299:122585. <DOI>.
3. Gullón B, Gullón P, Eibes G, Cara C, De Torres A, López-Linares JC, et al. Valorisation of olive agro-industrial by-products as a source of bioactive compounds. *Science of The Total Environment*. 2018 Dec;645:533-42. <DOI>.
  4. de Hoyos-Martínez PL, Erdocia X, Charrier-El Bouhtoury F, Prado R, Labidi J. Multistage treatment of almonds waste biomass: Characterization and assessment of the potential applications of raw material and products. *Waste Management*. 2018 Oct;80:40-50. <DOI>.
  5. Terzioğlu P, Güney F, Parin FN, Şen İ, Tuna S. Biowaste orange peel incorporated chitosan/polyvinyl alcohol composite films for food packaging applications. *Food Packaging and Shelf Life*. 2021 Dec;30:100742. <DOI>.
  6. Liu C, Hu J, Zhang H, Xiao R. Thermal conversion of lignin to phenols: Relevance between chemical structure and pyrolysis behaviors. *Fuel*. 2016 Oct;182:864-70. <DOI>.
  7. Morales A, Gullón B, Dávila I, Eibes G, Labidi J, Gullón P. Optimization of alkaline pretreatment for the co-production of biopolymer lignin and bioethanol from chestnut shells following a biorefinery approach. *Industrial Crops and Products*. 2018 Nov;124:582-92. <DOI>.
  8. Terzioğlu P, Parin FN, Sicak Y. Lignin Composites for Biomedical Applications: Status, Challenges and Perspectives. In: Sharma S, Kumar A, editors. *Lignin* [Internet]. Cham: Springer International Publishing; 2020 [cited 2022 Feb 5]. p. 253-73. (Springer Series on Polymer and Composite Materials). ISBN: 978-3-030-40663-9. <URL>.
  9. Laurichesse S, Avérous L. Chemical modification of lignins: Towards biobased polymers. *Progress in Polymer Science*. 2014 Jul;39(7):1266-90. <DOI>.
  10. Dávila I, Gullón B, Labidi J, Gullón P. Multiproduct biorefinery from vine shoots: Bio-ethanol and lignin production. *Renewable Energy*. 2019 Nov;142:612-23. <DOI>.
  11. Kumar P, Barrett DM, Delwiche MJ, Stroeve P. Methods for Pretreatment of Lignocellulosic Biomass for Efficient Hydrolysis and Biofuel Production. *Ind Eng Chem Res*. 2009 Apr 15;48(8):3713-29. <DOI>.
  12. Kothari R, Singh DP, Tyagi VV, Tyagi SK. Fermentative hydrogen production—An alternative clean energy source. *Renewable and Sustainable Energy Reviews*. 2012 May;16(4):2337-46. <DOI>.
  13. Guo F, Fang Z, Xu CC, Smith RL. Solid acid mediated hydrolysis of biomass for producing biofuels. *Progress in Energy and Combustion Science*. 2012 Oct;38(5):672-90. <DOI>.
  14. Quéméneur M, Hamelin J, Barakat A, Steyer J-P, Carrère H, Trably E. Inhibition of fermentative hydrogen production by lignocellulose-derived compounds in mixed cultures. *International Journal of Hydrogen Energy*. 2012 Feb;37(4):3150-9. <DOI>.
  15. Wulf C, Kaltschmitt M. Life cycle assessment of biohydrogen production as a transportation fuel in Germany. *Bioresource Technology*. 2013 Dec;150:466-75. <DOI>.
  16. Cheng Y-S, Zheng Y, Yu CW, Dooley TM, Jenkins BM, VanderGheynst JS. Evaluation of High Solids Alkaline Pretreatment of Rice Straw. *Appl Biochem Biotechnol*. 2010 Nov;162(6):1768-84. <DOI>.
  17. Zhang J, Ma X, Yu J, Zhang X, Tan T. The effects of four different pretreatments on enzymatic hydrolysis of sweet sorghum bagasse. *Bioresource Technology*. 2011 Mar;102(6):4585-9. <DOI>.
  18. Kim JS, Lee YY, Kim TH. A review on alkaline pretreatment technology for bioconversion of lignocellulosic biomass. *Bioresource Technology*. 2016 Jan;199:42-8. <DOI>.
  19. Dávila I, Gordobil O, Labidi J, Gullón P. Assessment of suitability of vine shoots for hemicellulosic oligosaccharides production through aqueous processing. *Bioresource Technology*. 2016 Jul;211:636-44. <DOI>.
  20. Morales A, Labidi J, Gullón P. Hydrothermal treatments of walnut shells: A potential pretreatment for subsequent product obtaining. *Science of The Total Environment*. 2021 Apr;764:142800. <DOI>.
  21. Silva NGS, Maia TF, Mulinari DR. Effect of Acetylation with Perchloric Acid as Catalyst in Sugarcane Bagasse Waste. *Journal of Natural Fibers*. 2021 Feb 9;1-15. <DOI>.
  22. Sun Y, Cheng J. Hydrolysis of lignocellulosic materials for ethanol production: a review. *Bioresource Technology*. 2002 May;83(1):1-11. <DOI>.
  23. Thakur VK, Thakur MK, Raghavan P, Kessler MR. Progress in Green Polymer Composites from Lignin for Multifunctional Applications: A Review. *ACS Sustainable Chem Eng*. 2014 May 5;2(5):1072-92. <DOI>.
  24. Spiridon I, Leluk K, Resmerita AM, Darie RN. Evaluation of PLA-lignin bioplastics properties before and after accelerated weathering. *Composites Part B: Engineering*. 2015 Feb;69:342-9. <DOI>.
  25. Klapiszewski Ł, Bula K, Sobczak M, Jesionowski T. Influence of Processing Conditions on the Thermal Stability and Mechanical Properties of PP/Silica-Lignin Composites. *International Journal of Polymer Science*. 2016;2016:1-9. <DOI>.
  26. Nair SS, Chen H, Peng Y, Huang Y, Yan N. Polylactic Acid Biocomposites Reinforced with Nanocellulose Fibrils with High Lignin Content for Improved Mechanical, Thermal, and Barrier Properties. *ACS Sustainable Chem Eng*. 2018 Aug 6;6(8):10058-68. <DOI>.
  27. Yang W, Fortunati E, Dominici F, Giovanale G, Mazzaglia A, Balestra GM, et al. Effect of cellulose and lignin on disintegration, antimicrobial and antioxidant properties of PLA active films. *International Journal of Biological Macromolecules*. 2016 Aug;89:360-8. <DOI>.
  28. Terzioğlu P, Parin FN. Polyvinyl alcohol-corn starch-lemon peel biocomposite films as potential food packaging.

- Celal Bayar University Journal of Science. 2020;16(4):373-8.
29. Holmgren A, Brunow G, Henriksson G, Zhang L, Ralph J. Non-enzymatic reduction of quinone methides during oxidative coupling of monolignols: implications for the origin of benzyl structures in lignins. *Org Biomol Chem*. 2006;4(18):3456. [<DOI>](#).
30. Graupner N. Application of lignin as natural adhesion promoter in cotton fibre-reinforced poly(lactic acid) (PLA) composites. *J Mater Sci*. 2008 Aug;43(15):5222-9. [<DOI>](#).
31. Brodin M, Vallejos M, Opedal MT, Area MC, Chinga-Carrasco G. Lignocellulosics as sustainable resources for production of bioplastics—A review. *Journal of Cleaner Production*. 2017 Sep;162:646-64. [<DOI>](#).
32. Beltrán FR, Arrieta MP, Gaspar G, de la Orden MU, Martínez Urreaga J. Effect of Iignocellulosic Nanoparticles Extracted from Yerba Mate (*Ilex paraguariensis*) on the Structural, Thermal, Optical and Barrier Properties of Mechanically Recycled Poly(lactic acid). *Polymers*. 2020 Jul 29;12(8):1690. [<DOI>](#).
33. Beltrán FR, Gaspar G, Dadras Chomachayi M, Jalali-Arani A, Lozano-Pérez AA, Cenis JL, et al. Influence of addition of organic fillers on the properties of mechanically recycled PLA. *Environ Sci Pollut Res*. 2021 May;28(19):24291-304. [<DOI>](#).
34. Beltrán FR, Infante C, de la Orden MU, Martínez Urreaga J. Mechanical recycling of poly(lactic acid): Evaluation of a chain extender and a peroxide as additives for upgrading the recycled plastic. *Journal of Cleaner Production*. 2019 May;219:46-56. [<DOI>](#).
35. Beltrán FR, de la Orden MU, Martínez Urreaga J. Amino-Modified Halloysite Nanotubes to Reduce Polymer Degradation and Improve the Performance of Mechanically Recycled Poly(lactic acid). *J Polym Environ*. 2018 Oct;26(10):4046-55. [<DOI>](#).
36. Arrieta M, Samper M, Aldas M, López J. On the Use of PLA-PHB Blends for Sustainable Food Packaging Applications. *Materials*. 2017 Aug 29;10(9):1008. [<DOI>](#).
37. Faludi G, Dora G, Renner K, Móczó J, Pukánszky B. Biocomposite from polylactic acid and lignocellulosic fibers: Structure-property correlations. *Carbohydrate Polymers*. 2013 Feb;92(2):1767-75. [<DOI>](#).
38. Arrieta MP, Peponi L, López D, Fernández-García M. Recovery of yerba mate (*Ilex paraguariensis*) residue for the development of PLA-based bionanocomposite films. *Industrial Crops and Products*. 2018 Jan;111:317-28. [<DOI>](#).
39. Xie J, Hse C-Y, Shupe TF, Hu T. Physicochemical characterization of lignin recovered from microwave-assisted delignified lignocellulosic biomass for use in biobased materials. *J Appl Polym Sci*. 2015 Oct 20;132(40):1-7. [<DOI>](#).
40. Mohammadlinejhad S, Almasi H, Esmaili M. Physical and release properties of poly(lactic acid)/nanosilver-decorated cellulose, chitosan and lignocellulose nanofiber composite films. *Materials Chemistry and Physics*. 2021 Aug;268:124719. [<DOI>](#).
41. Latocha P. The Nutritional and Health Benefits of Kiwiberry (*Actinidia arguta*) – a Review. *Plant Foods Hum Nutr*. 2017 Dec;72(4):325-34. [<DOI>](#).
42. Richardson DP, Ansell J, Drummond LN. The nutritional and health attributes of kiwifruit: a review. *Eur J Nutr*. 2018 Dec;57(8):2659-76. [<DOI>](#).
43. Chamorro F, Carpena M, Nuñez-Estevéz B, Prieto MA, Simal-Gandara J. Valorization of Kiwi by-Products for the Recovery of Bioactive Compounds: Circular Economy Model. *Proceedings*. 2020 Nov 9;70(1):9. [<DOI>](#).
44. Pinto D, Delerue-Matos C, Rodrigues F. Bioactivity, phytochemical profile and pro-healthy properties of *Actinidia arguta*: A review. *Food Research International*. 2020 Oct;136:109449. [<DOI>](#).
45. Almeida D, Pinto D, Santos J, Vinha AF, Palmeira J, Ferreira HN, et al. Hardy kiwifruit leaves (*Actinidia arguta*): An extraordinary source of value-added compounds for food industry. *Food Chemistry*. 2018 Sep;259:113-21. [<DOI>](#).
46. Sun Y, Yang L, Lu X, He C. Biodegradable and renewable poly(lactide)-lignin composites: synthesis, interface and toughening mechanism. *J Mater Chem A*. 2015;3(7):3699-709. [<DOI>](#).
47. Bax B, Müssig J. Impact and tensile properties of PLA/Cordenka and PLA/flax composites. *Composites Science and Technology*. 2008 Jun;68(7-8):1601-7. [<DOI>](#).
48. Bledzki AK, Jaszkievicz A, Scherzer D. Mechanical properties of PLA composites with man-made cellulose and abaca fibres. *Composites Part A: Applied Science and Manufacturing*. 2009 Apr;40(4):404-12. [<DOI>](#).
49. Petinakis E, Yu L, Edward G, Dean K, Liu H, Scully AD. Effect of Matrix-Particle Interfacial Adhesion on the Mechanical Properties of Poly(lactic acid)/Wood-Flour Micro-Composites. *J Polym Environ*. 2009 Jun;17(2):83-94. [<DOI>](#).
50. Zhu C, Gong Q, Li J, Zhang Y, Yue J, Gao J. Research progresses of the comprehensive processing and utilization of kiwifruit. *Storage and Process*. 2013;13(1):57-62.
51. Dias M, Caleja C, Pereira C, Calhelha RC, Kostic M, Sokovic M, et al. Chemical composition and bioactive properties of byproducts from two different kiwi varieties. *Food Research International*. 2020 Jan;127:108753. [<DOI>](#).
52. Wojdyło A, Nowicka P, Oszmiański J, Golis T. Phytochemical compounds and biological effects of *Actinidia* fruits. *Journal of Functional Foods*. 2017 Mar;30:194-202. [<DOI>](#).
53. Kocaman S, Ahmetli G. Effects of Various Methods of Chemical Modification of Lignocellulose Hazelnut Shell Waste on a Newly Synthesized Bio-based Epoxy Composite. *J Polym Environ*. 2020 Apr;28(4):1190-203. [<DOI>](#).

54. Sogut E, Cakmak H. Utilization of carrot (*Daucus carota* L.) fiber as a filler for chitosan based films. *Food Hydrocolloids*. 2020 Sep;106:105861. [<DOI>](#).
55. Anonymous. Standard Test Method for Tensile Properties of Thin Plastic Sheeting [Internet]. ASTM International; 2002. [<URL>](#).
56. Anonymous. Standard test methods for water vapor transmission of materials: E96/E96M- 16. American Society for Testing and Materials Standard; 2016.
57. Nam TH, Ogihara S, Tung NH, Kobayashi S. Effect of alkali treatment on interfacial and mechanical properties of coir fiber reinforced poly(butylene succinate) biodegradable composites. *Composites Part B: Engineering*. 2011 Sep;42(6):1648-56. [<DOI>](#).
58. Narendar R, Priya Dasan K. Chemical treatments of coir pith: Morphology, chemical composition, thermal and water retention behavior. *Composites Part B: Engineering*. 2014 Jan;56:770-9. [<DOI>](#).
59. Sreekala M, Kumaran M, Joseph S, Jacob M, Thomas S. Oil palm fibre reinforced phenol formaldehyde composites: influence of fibre surface modifications on the mechanical performance. *Applied Composite Materials*. 2000;7(5):295-329.
60. Kocaman S. Preparation and characterization of natural waste reinforced epoxy resin matrix composites modified with different chemicals. *Uluslararası Muhendislik Arastirma ve Gelistirme Dergisi*. 2019 Jan 31;11(1):77-86. [<DOI>](#).
61. Khalil H, Tye Y, Saurabh C, Leh C, Lai T, Chong E, et al. Biodegradable polymer films from seaweed polysaccharides: A review on cellulose as a reinforcement material. *Express Polymer Letters*. 2017;11(4):244-65.
62. Abdul Khalil HPS, Che Mohamad HCI, Khairunnisa AR, Owolabi FAT, Asniza M, Rizal S, et al. Development and characterization of bamboo fiber reinforced biopolymer films. *Mater Res Express*. 2018 Jul 24;5(8):085309. [<DOI>](#).
63. Valdés García A, Ramos Santonja M, Sanahuja AB, Selva M del CG. Characterization and degradation characteristics of poly( $\epsilon$ -caprolactone)-based composites reinforced with almond skin residues. *Polymer Degradation and Stability*. 2014 Oct;108:269-79. [<DOI>](#).
64. Kocaman S, Karaman M, Gursoy M, Ahmetli G. Chemical and plasma surface modification of lignocellulose coconut waste for the preparation of advanced biobased composite materials. *Carbohydrate Polymers*. 2017 Mar;159:48-57. [<DOI>](#).
65. Wang N, Zhang C, Weng Y. Enhancing gas barrier performance of polylactic acid/lignin composite films through cooperative effect of compatibilization and nucleation. *J Appl Polym Sci*. 2021 Apr 15;138(15):50199. [<DOI>](#).
66. Kabir MM, Wang H, Lau KT, Cardona F. Chemical treatments on plant-based natural fibre reinforced polymer composites: An overview. *Composites Part B: Engineering*. 2012 Oct;43(7):2883-92. [<DOI>](#).
67. Kim Y, Suhr J, Seo H-W, Sun H, Kim S, Park I-K, et al. All Biomass and UV Protective Composite Composed of Compatibilized Lignin and Poly (Lactic-acid). *Sci Rep*. 2017 Apr;7(1):43596. [<DOI>](#).
68. Wang N, Zhang C, Weng Y. Enhancing gas barrier performance of polylactic acid/lignin composite films through cooperative effect of compatibilization and nucleation. *J Appl Polym Sci*. 2021 Apr 15;138(15):50199. [<DOI>](#).
69. Muller J, Casado Quesada A, González-Martínez C, Chiralt A. Antimicrobial properties and release of cinnamaldehyde in bilayer films based on polylactic acid (PLA) and starch. *European Polymer Journal*. 2017 Nov;96:316-25. [<DOI>](#).
70. Iglesias Montes ML, Luzi F, Dominici F, Torre L, Cyras VP, Manfredi LB, et al. Design and Characterization of PLA Bilayer Films Containing Lignin and Cellulose Nanostructures in Combination With Umbelliferone as Active Ingredient. *Front Chem*. 2019 Mar 26;7:157. [<DOI>](#).







## Phytochemical Screening, Antioxidant and Anticancer Activities of *Euphorbia hyssopifolia* L. against MDA-MB-231 Breast Cancer Cell Line

Asseel Azaat\*<sup>1</sup> , Georget Babojian<sup>1</sup> , Nizar Issa<sup>1</sup> 

<sup>1</sup>Damascus University, College of Sciences, Damascus, Syria.

**Abstract:** *Euphorbia hyssopifolia* L. is an annual herb producing toxic latex. To our knowledge, this study is the first one that focuses on accurately identifying the bioactive compounds in *E. hyssopifolia* and evaluating its antioxidant and anti-breast cancer activities. Phytochemical qualitative screening tests were performed. Total phenolic contents (TPC) and total flavonoid contents (TFC) were determined by Folin Ciocalteu and Aluminum chloride methods, respectively. Bioactive compounds in *E. hyssopifolia* latex were identified by using GC-MS analysis. Antioxidant activity was evaluated using DPPH and ABTS assays, and anticancer activity of latex against MDA-MB-231 breast cancer cell line was studied using flow cytometry methods. Results revealed the presence of flavonoids, tannins, alkaloids, diterpenes, steroids, and cardiac glycosides in the plant, whereas saponins were absent. Latex outperformed methanolic 70% extract in terms of TPC and TFC ( $39.52 \pm 0.36$  mg GAE/g E and  $28.66 \pm 0.10$  mg RE/g E, respectively). GC-MS analysis of *E. hyssopifolia* latex resulted in the identification of 26 compounds, of which triterpenoids constitute 67.0172%, followed by lupeol (23.7089%) and betulin (14.0098%). According to the reference studies, most of the compounds found in latex have many biological activities. Latex outperformed all extracts and ascorbic acid in terms of antioxidant activity ( $IC_{50} = 0.029$  mg/mL for DPPH,  $IC_{50} = 0.001$  mg/mL for ABTS). Flow cytometry methods revealed that *E. hyssopifolia* latex induced cell cycle arrest at G1 phase (61%) and apoptosis (21.93%) of MDA-MB-231 cells after treating with latex at 10  $\mu$ g/mL for 24 hours. However, more studies should be performed to explore bioactive compounds in *E. hyssopifolia* and determine the underlying mechanism of its latex anti-breast cancer effects.

**Keywords:** *Euphorbia hyssopifolia*, apoptosis, *Euphorbiaceae*, necrosis, anticancer.

**Submitted:** November 10, 2021. **Accepted:** February 03, 2022.

**Cite this:** Azaat A, Babojian G, Issa N. Phytochemical Screening, Antioxidant and Anticancer Activities of *Euphorbia hyssopifolia* L. against MDA-MB-231 Breast Cancer Cell Line. JOTCSA. 2022;9(1):295–310.

**DOI:** <https://doi.org/10.18596/jotcsa.1021449>.

**\*Corresponding author. E-mail:** [Asseel7777@hotmail.com](mailto:Asseel7777@hotmail.com)

### INTRODUCTION

The genus *Euphorbia* belongs to *Euphorbiaceae*, the sixth largest family among flowering plants. It includes about 2100 species, and it is the most diverse genus of spermatophytes on the Earth. Species of *Euphorbia* are widely represented in the Mediterranean Basin, the Middle East, South Africa, and Southern USA (1-3).

Members of this genus are characterized by the production of a milky irritant latex produced by laticiferous vessels. Latex is a complex mixture of proteins, starch, sugars, alkaloids, tannins, oils, resins, and gums. It serves as a defense material and prevents herbivorous insects from feeding (4).

There are 45 species and 6 varieties of *Euphorbia* in Syria, except for the species studied in this research, most of which are herbaceous (5).



*Euphorbia hyssopifolia* L. is an annual herb commonly found in the tropical and sub-tropical regions of Africa and America, and is often found growing along road sides and in fields, erect or suberect, 25.89 ± 2.75 cm height, usually glabrous. Leaves opposite with serrated margin and obovate shape. Cyathia axillary and terminal, single or in small cymes, glands 4, yellow-green, appendages white or pale pink. Capsule triangular, ovoid, seeds are blackish, each side has 3 or 4 transverse furrows, caruncle being absent (6,7).

*E. hyssopifolia* was registered for the first time in the flora of Syria in 2018. It produces latex which is a health hazard to humans and livestock. Direct contact of latex with the eye may cause blindness. It is known to contain phenolic compounds which are inhibitory to seed germination and seedling growth as well as bacteria. This latex has also diuretic and purgative effects. It was used to treat respiratory infections and to induce bronchial relaxation in asthma. The juice is said to remove warts and the leaves can be boiled with *Phyllanthus niruri* to make tea for the treatment of gonorrhoea (8-10).

Phytochemical screening of the plant revealed the presence of alkaloids, flavonoids, carbohydrates, vitamin A, reducing sugars, saponins, glycosides, and steroidal aglycone. It also contains mono and sesquiterpenes, triterpenes, and steroids (11,12).

Few studies have demonstrated the toxic effects of *E. hyssopifolia*. One study revealed the genotoxic effect of its ethanolic extracts on HepG2 cells. Another study pointed out that its aqueous extract has toxic effects on the normal structure and functions of the liver and the heart of albino rats (12,13).

Breast cancer is one of the most common cancers that affects about 12% of women in the world. Despite advances in chemotherapy, breast carcinoma treatment is still a great challenge in the clinical therapy (14). Therefore, breast cancer should be at the forefront of medicinal plant research.

Up today, no study focused on accurately identifying the bioactive compounds in *E. hyssopifolia* and evaluating its antioxidant and anti-breast cancer activities.

This study aims to perform qualitative screening (flavonoids, tannins, alkaloids, saponins, diterpenes, and steroids), quantitative screening (total phenolic and flavonoid contents), identification of bioactive compounds in *E. hyssopifolia* using GC-MS analysis, and study its antioxidant and anticancer activities on MDA-MB-231 breast cancer cell line.

## MATERIALS AND METHODS

### Chemicals and Reagents

All solvents used in this study were of analytical grade and purchased from Merck. All other chemicals, including standard compounds (gallic acid and rutin), reagents and cell culture chemicals were purchased from Sigma-Aldrich.

### Plant Materials

*E. hyssopifolia* was collected from Al-Bramka Zone (33°30'37.1"N, 36°16'56.7"E) in Damascus Governorate in September 2019 and 2020. The plants were identified by Prof. Babojian, Botany Department, Sciences College, Damascus University, Damascus, Syria.

### Latex Collection

Crude white milky latex was obtained through cutting and squeezing the stems of the fresh plants, then it was dried in an oven at 45 °C up to constant weight (15). Dried latex was stored in a freezer at -20 °C until use.

It should be noted that dried latex was re-dissolved in DMSO when total phenolic and flavonoid contents were determined, and when DPPH and ABTS assays were performed.

It is also useful to point out that latex used in flow cytometry methods to study its anticancer activity on breast cancer cells was not dried and was kept wet in freezer at -20 °C until use.

### Preparation of the Extracts

Different extracts (aqueous, methanolic 70%, ethyl acetate, and *n*-hexane extracts) were prepared using maceration method; 40 g of powdered aerial parts were separately extracted in 400 mL of the organic solvents by maceration (3 times for 72 hours; re-extracted every 24 hours) at room temperature as mentioned in (16). After filtration, the solvents were removed using a rotary evaporator under reduced pressure and kept in a freezer at -20 °C.

The ethyl acetate and *n*-hexane extracts were re-dissolved in DMSO when total phenolic and flavonoid contents methods, and DPPH and ABTS assays were performed, whereas aqueous and methanolic 70% extracts were re-dissolved in their solvents.

### Preparation of Latex Extract for GC-MS Analysis

Methanol (99.9%, 5 mL) was added to 500 µL of latex and kept in the shaker for 24 hours at room temperature. The sample was centrifuged at 3000 rpm for 10 min and filtered. The supernatant was concentrated to volume of 100 µL and kept in the freezer at -20 °C until use.

### Phytochemical Qualitative Screening Tests

#### Test of flavonoids

a) Shinoda test: 2 to 3 mL of the extract and small pieces of metallic magnesium were added into a small porcelain lid, followed by careful dropwise addition of concentrated HCl. Appearance of purple color indicates the presence of flavonoids (17).

b) Alkaline Test: Method of (18) was applied with some modifications. 2 to 3 mL of the extract and few drops of 5% NaOH were added into a test tube. The appearance of intense yellow color that became colorless on addition of few drops of dilute HCl indicates the presence of flavonoids.

#### Test of tannins

Few drops of 5% ferric chloride reagent were added to the extract. Formation of an intense green or black color indicates the presence of tannins (19).

#### Test of alkaloids

a) Wagner's Test: 1 mL of each extract was mixed with equal volumes of Wagner's reagent (Iodine in potassium iodide). Formation of reddish brown precipitate indicates the presence of alkaloids.

b) Hager's test: To 2 mL of each extract, few drops of Hager's (Saturated picric acid solution) reagent were added. Presence of alkaloids was indicated by formation of a bright yellow-colored precipitate.

c) Mayer's Reagent: 1 mL of each extract was mixed with few drops of Mayer's reagent (Potassium Mercuric Iodide Solution). Formation of light yellow precipitate indicates the presence of alkaloids (20).

#### Test of saponins

Approximately 200 mg of each extract was shaken with 5 mL of distilled water in a test tube and heated on water bath to boil. Presence of saponins

was indicated by formation of strong and stable foam (21).

#### Test of diterpenes

3 mL of each extract was mixed with 3 mL of 10% copper acetate solution (note that the concentration is specific to the research). Presence of diterpenes was indicated by formation of green color (22).

#### Test of steroids

Salkowski's test: 2 mL of extract were mixed with 2 mL of chloroform and 2 mL concentrated sulfuric acid was added carefully. Formation of red color in the chloroform layer indicates the presence of steroids (23).

#### Test of cardiac glycosides

Extract (2 mL) was treated with 2 mL glacial acetic acid and few drops of  $\text{FeCl}_3$ . A brown color ring indicates the presence of positive test (24).

### Phytochemical Quantitative Screening Methods

TPC of the extracts and latex was determined by Folin Ciocalteu method (26). 1 mL of the sample was combined with 4 mL of 2%  $\text{Na}_2\text{CO}_3$  and 4.8 mL of the sample solvent (water for aqueous extract, methanol 70% for methanolic 70% extract and DMSO for ethyl acetate and *n*-hexane extracts and latex). 0.2 mL of 2 M Folin-Ciocalteu reagent (Sigma-Aldrich) was added to the mixture and mixed thoroughly. After incubation for 60 min in the dark, absorbance at 760 nm was measured by UV-visible spectrophotometer (Optizen, Mecasys- Korea). Sample solvent was used as a blank. Total phenolic content was determined as milligrams of gallic acid equivalents per gram of sample (GAE mg/gE) using a standard calibration curve between 0 to 300 ppm (Figure 1). Total phenolic contents of samples were determined in triplicate. Data were expressed as mean  $\pm$  standard deviation (SD).

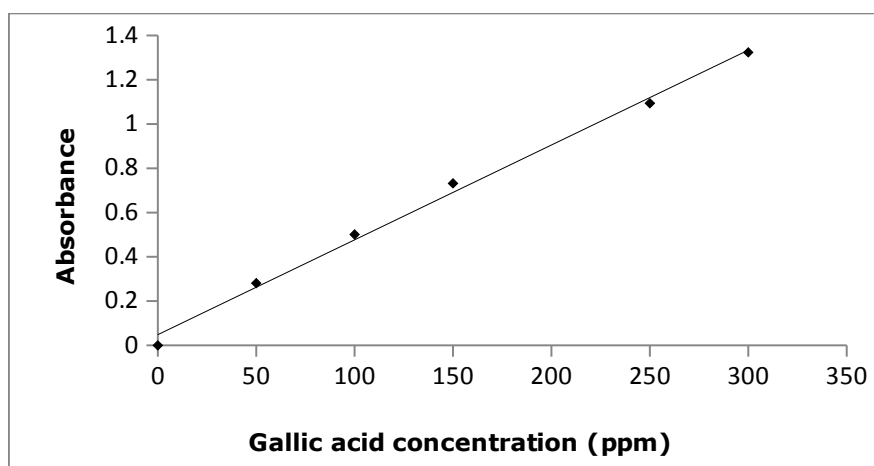


Figure 1: Standard calibration curve of gallic acid.

### TFC

Aluminum chloride colorimetric method was used for determination of flavonoids with some modifications (26). Briefly, 0.75 mL of sample was mixed with the same volume of the sample solvent (as we did in TPC determination), 1.5 mL of 2% aluminum chloride, and 6 mL of 5% potassium acetate were added. After incubation for 40 min in the dark, the absorbance of the reaction mixture was measured

at 415 nm spectrophotometrically. Sample solvent was used as a blank. Total flavonoid content was determined as milligrams of rutin equivalents per gram of sample (RE mg/gE) using a standard calibration curve between 0 to 150 ppm (Figure 2). Total flavonoid contents of samples were determined in triplicate. Data were expressed as mean  $\pm$  standard deviation (SD).

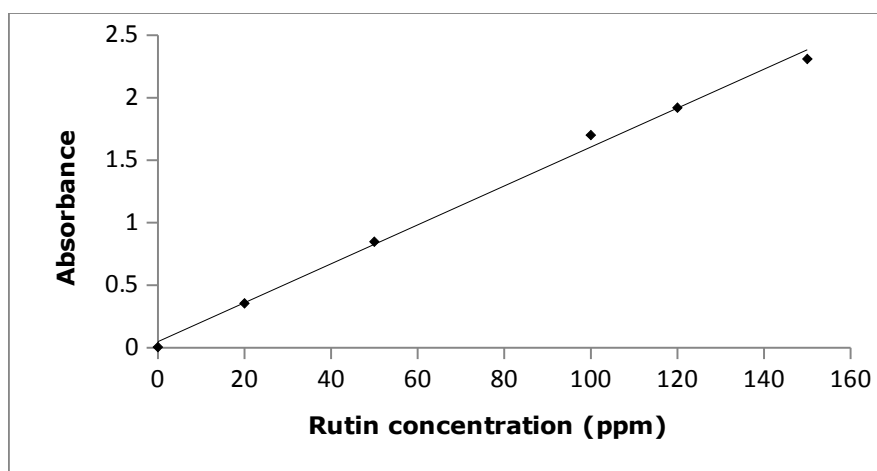


Figure 2: Standard calibration curve of rutin.

### Gas Chromatography-Mass Spectroscopy (GC-MS) Analysis of Latex

Methanolic extract of latex was subjected to GC-MS for the identification of bioactive volatile compounds. GC-MS analysis of the samples was carried out using Agilent series A7890 with nonpolar HB-5 MS column (30 m, 0.25 mm, 0.25  $\mu$ m). Helium was used as the carrier gas and the temperature programming was set with initial oven temperature at 80  $^{\circ}$ C, increased at 8  $^{\circ}$ C/min to 200  $^{\circ}$ C and held for 1 minute, and the final temperature of the oven was 300  $^{\circ}$ C and held for 20 minutes. 1  $\mu$ L sample was injected with splitless mode, ionization potential 70 eV, and a scan range of 50 to 550 amu. The total running time for a sample was 52 minutes. The chemical components of the extract were identified by comparing the retention times of chromatographic peaks with NIST Library to relative retention indices.

### Antioxidant Activity Assays

#### DPPH (2,2-diphenyl-1-picrylhydrazyl) assay

The free radical scavenging activities of extracts and latex on the DPPH radical were measured using the method described by (27). 0.3 mL of tested samples at different concentrations was added to 3 mL of DPPH solution (45  $\mu$ g/100 mL of ethanol). The

sample solvent (water for aqueous extract, methanol 70% for methanolic 70% extract, and DMSO for ethyl acetate and *n*-hexane extracts and latex) was used as a blank. After the mixture was shaken and left at room temperature for 30 min, the absorbance was measured at 517 nm with a spectrophotometer. The results were compared to ascorbic acid which was prepared as standard with different concentrations from 0 to 0.1 mg/mL (Figure 3). The antioxidant activity of the tested samples was calculated by determining the decrease in absorbance at different concentrations by using the following equation:

$$\text{DPPH scavenging effect (\%)} = \left[ \frac{(A_1 - A_2)}{A_1} \right] \times 100$$

Where:

- $A_1$  = the absorbance of the control reaction.
- $A_2$  = the absorbance in the presence of the sample.

The  $IC_{50}$  value, defined as the amount of antioxidant necessary to decrease the initial DPPH concentration by 50%, was calculated from the results and used for comparison.

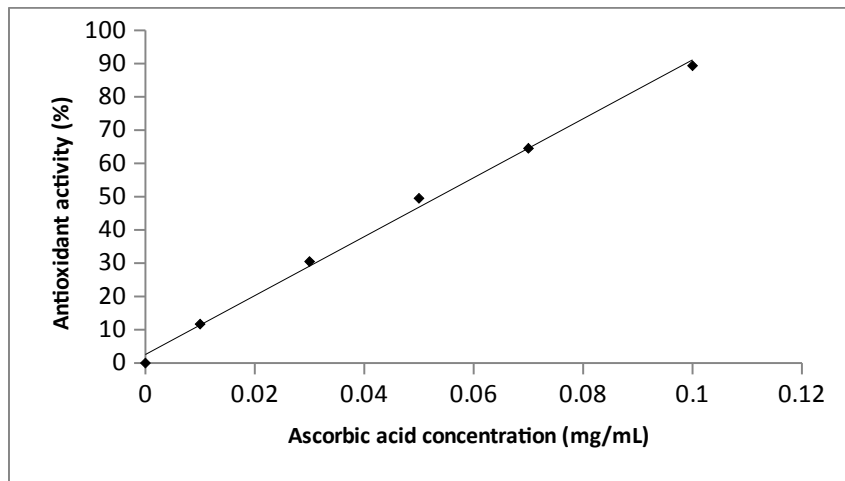


**Figure 3:** Standard calibration curve for antioxidant activity of ascorbic acid using DPPH assay.

*ABTS (2,2'-Azino - bis (3-ethylbenzoline-6-sulfonic acid)) assay*

The free radical scavenging activities of extracts and latex on the ABTS radical were measured using the method described by (28). The radical cation was prepared by mixing 7 mM ABTS stock solution with 2.45 mM potassium persulfate (1/1, v) and leaving the mixture for 4-16 h until the reaction was complete and the absorbance was stable. The ABTS<sup>+</sup> solution was diluted with ethanol to an absorbance of 0.700 ± 0.05 at 734 nm for measurements. The photometric assay was performed by adding 0.9 mL of ABTS<sup>+</sup> solution to 0.1 mL of tested samples and mixing for 45 sec, measurements were taken at 734 nm after 15 minutes. The results were compared to ascorbic acid which was prepared as standard with different concentrations from 0 to 0.015 mg/mL (Figure 4).

The sample solvent (as we did in DPPH assay) was used as a blank. The antioxidant activity of the tested samples was calculated by determining the decrease in absorbance at different concentrations by using the following equation:

$$\text{ABTS scavenging effect (\%)} = \left[ \frac{(A_1 - A_2)}{A_1} \right] \times 100$$

Where:

- A<sub>1</sub> = the absorbance of the control reaction.
- A<sub>2</sub> = the absorbance in the presence of the sample.

The IC<sub>50</sub> value was calculated from the results and used for comparison.

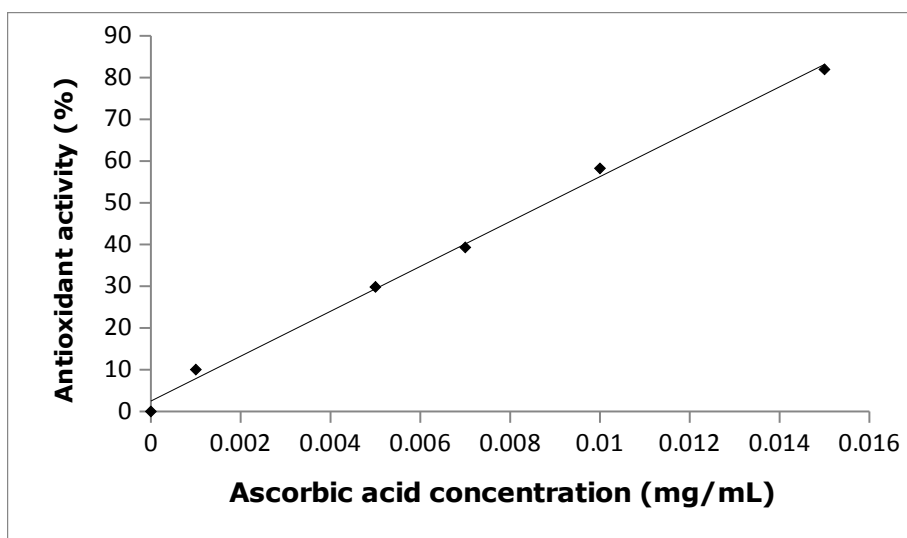


**Figure 4:** Standard calibration curve for antioxidant activity of ascorbic acid using ABTS assay.

### Anticancer Activity of *E. hyssopifolia* Latex against MDA-MB-231 Breast Cancer Cell Line

This part of the research was performed in Atomic Energy Commission of Syria, Biotechnology Department.

#### Cell culture

MDA-MB-231 cells were purchased from ATCC. The cells were seeded in a six-well culture plate and grown in a humidified incubator (95%) at 37 °C with 5% CO<sub>2</sub>. The cell culture medium was RPMI 1640 supplemented with 10% FBS and 1% penicillin/streptomycin. All cell culture chemicals were purchased from Sigma-Aldrich.

#### Cell cycle analysis by flow cytometry

Cell cycle analysis was performed by PI-based measurements of cell DNA content using flow cytometry. Cells were treated with various concentrations of latex (dissolved in DMSO) for 24 hours, followed by collection of both attached and detached cells. The pellet was rinsed twice with cold PBS and cells were fixed in 70% ice-cold ethanol overnight at 20 °C. Fixed cells were then washed twice with PBS, and DNA was stained with PI (Sigma-Aldrich) staining solution (20 µL of cell suspension were added to 2 mL of staining solution) and incubated in the dark for 5 minutes. Flow cytometry analysis was carried out using BD FACSCalibur Flow Cytometer.

#### Annexin V/PI apoptosis assay

Cells were cultured (1x10<sup>6</sup> cells/mL) overnight in 25 cm<sup>2</sup> cell culture flasks. Then, cells were treated with various concentrations of latex (dissolved in DMSO) for 24 hours. After treatment, both adherent and detached cells were collected and rinsed twice with cold PBS. The cell pellet was resuspended in 1 mL of annexin-binding buffer and incubated with 5 µL of Annexin V-FITC and 5 µL of PI for 15 minutes. The cells were analyzed by flow cytometry and data were analyzed using CellQuest Program. Data sets were expressed as mean ± standard deviation (SD).

#### Statistical Analysis

Experiments were performed in triplicate. Data were analyzed by SPSS software (version 22) using one-way ANOVA, LSD test. P<0.05 was considered statistically significant.

## RESULTS AND DISCUSSION

### Phytochemical Qualitative Screening of Secondary Metabolites

The results of phytochemical screening of *E. hyssopifolia* extracts showed that the plant contains flavonoids, tannins, alkaloids, diterpenes, steroids,

and cardiac glycosides, whereas saponins were absent. Methanolic 70% extract was the richest in secondary metabolites, especially of flavonoids and tannins. On the other hand, alkaloids were found with a moderate presence in the aqueous extract. It is also noted that ethyl acetate extract was the poorest in secondary metabolites; it contains cardiac glycosides only. However, our results are similar to the study (11) which revealed that leaves of the plant contain flavonoids, tannins, alkaloids, and other secondary metabolites, except for the presence of saponins; the study indicated that they were present in the plant leaves, while they were absent in our extracts. This may be due to the difference in the environment of the plant.

Another study (12) indicated the presence of flavonoids and steroids in the ethanolic extract of the plant, which were present also in our methanolic 70% extract (Table 1).

### Extraction Yield, Determination of Total Phenolic and Flavonoid Contents

No studies were found focused on the detection of diterpenes and cardiac glycosides in *E. hyssopifolia*. However, *Euphorbiaceae* (in all its genera) is known to contain diterpenes (29).

Results showed that maximum yield was obtained for aqueous extract (13.66% ± 3.37), followed by methanolic 70% extract (10.63% ± 0.12), ethyl acetate extract (2.80 ± 0.50), *n*-hexane extract (1.50% ± 0.26), and latex (0.05% ± 0.01). It is clear that yield of aqueous extract and methanolic 70% extract are significantly higher than other samples, and the yield of latex was the lowest (Table 2).

As for TPC and TFC, the extracts took the same order that they took in the results of the extraction yield; aqueous extract was the richest of these compounds (42.19 ± 0.70 GAE mg/g E for TPC, 35.71 ± 0.21 RE mg/g E for TFC), followed by methanolic 70% extract, ethyl acetate extract, and *n*-hexane extract. The surprising result is that the latex took the second order after the aqueous extract and outperformed significantly the methanolic 70% extract. TPC and TFC of latex were 39.52 ± 0.36 GAE mg/g and 28.66 ± 0.10 RE mg/g E respectively, even though it had the lowest yield (0.05% ± 0.01) (Table 2).

**Table 1:** Phytochemical screening of *E. hyssopifolia* extracts.

Extract	Flavonoids		Tannins	Alkaloids			Saponins	Diterpenes	Steroids	Cardiac glycosides
	NaOH	Shinoda		Wagner	Hager	Mayer				
Aqueous	++	++	+	++	++	++	-	+	-	-
MeOH 70%	+++	+++	+++	-	+	+	-	+	++	+
Ethyl acetate	-	-	-	-	-	-	-	-	-	++
<i>n</i> -hexane	-	-	-	+	+	+	-	-	-	+

–: absent, +: present, ++: moderately present, +++: abundantly present.

**Table 2:** Extraction yield, total phenolic (TPC) and flavonoid (TFC) contents of *E. hyssopifolia*.

Sample (extract/latex)	Yield extraction/Latex (%)	TPC (GAE mg/g E)	TFC (RE mg/g E)
Aqueous extract	13.66 ± 3.37	42.19 ± 0.70	35.71 ± 0.21
Methanolic 70% extract	10.63 ± 0.12	30.88 ± 0.21	17.95 ± 0.17
Ethyl acetate extract	2.80 ± 0.50	0.72 ± 0.05	0.31 ± 0.04
<i>n</i> -hexane extract	1.50 ± 0.26	0.45 ± 0.07	0.11 ± 0.02
Latex	0.05 ± 0.01	39.52 ± 0.36	28.66 ± 0.10

Each value is represented as mean ± SD (n = 3).

To our knowledge, there is no study determining the phenolic and flavonoid contents of *E. hyssopifolia* so far. By comparing our results with those of other *Euphorbia* species, differences were observed. One of these studies determined extraction yield, TPC and TFC in aqueous, methanolic, and ethyl acetate extracts of aerial parts of three *Euphorbia* species namely *E. hirta* L., *E. heterophylla* L. and *E. convolvuloides* Hochst. ex Benth.

Results showed that the yield of aqueous and methanolic extracts was higher significantly than that of ethyl acetate extracts. The values closest to ours are those of *E. convolvuloides*; yield extractions of aqueous, methanolic, and ethyl acetate extracts were 12.25%, 15.83%, and 3.29%, respectively.

The study also revealed that methanolic extracts of the three *Euphorbia* species possessed the highest TFC and TPC except the aqueous extract of *E. heterophylla* yielded the highest TPC (141.90 ± 3.34 mg GAE/g). TPC and TFC of ethyl acetate extracts were differed greatly between the three species; TPC values ranged from 29.61 ± 0.44 to 31.41 ± 0.53 mg GAE/g, whereas TFC values ranged from 3.44 ± 0.46 to 22.36 ± 0.32 mg RE/g (30).

Another study performed in Pakistan showed that ethanolic 50% extract of *E. dracunculoides* had the highest TPC and TFC; 17.35 ± 0.62 mg GAE/g and 7.57 ± 0.42 mg RE/g respectively, whereas *n*-hexane extract had the lowest values; 8.21 ± 0.49

mg GAE/g for TPC and 4.18 ± 0.25 mg RE/g for TFC (31).

Reflecting on our results and those of previous studies, it is clearly noted that extracts with high polarity (aqueous and alcoholic extracts) have higher yield extraction, TPC and TFC compared to extracts with lower polarity.

This is due to the fact that phenolic compounds constitute the largest share of secondary metabolites in plants (32), and they are generally highly soluble in alcohols, except for gallic, cinnamic, and coumaric acids prefer water, dichloromethane, and acetone, respectively (33). However, TPC and TFC in plants varies according to the species, environmental factors, and extraction methods.

*E. hyssopifolia* latex contained a relatively high TPC (39.52 ± 0.36 mg GAE/g E) and TFC (28.66 ± 0.10 RE mg/g E) compared to other *Euphorbia* species. For reference, a study has shown that TPC and TFC of methanolic extract of *E. tirucalli* latex were 10.50 ± 1.20 mg GAE/g E and 4.30 ± 0.50 mg catechin equivalent/g E respectively (34).

#### GC-MS Analysis of *E. hyssopifolia* Latex

The present study has identified 26 compounds in *E. hyssopifolia* latex, distributed as follows: triterpenoids (67.017%), phenolic compounds (11.281%), fatty acids and their derivatives (4.187%), steroids (2.647%), sesquiterpenes (0.778%), and other compounds (14.0895%) (Figure 5, Table 3).

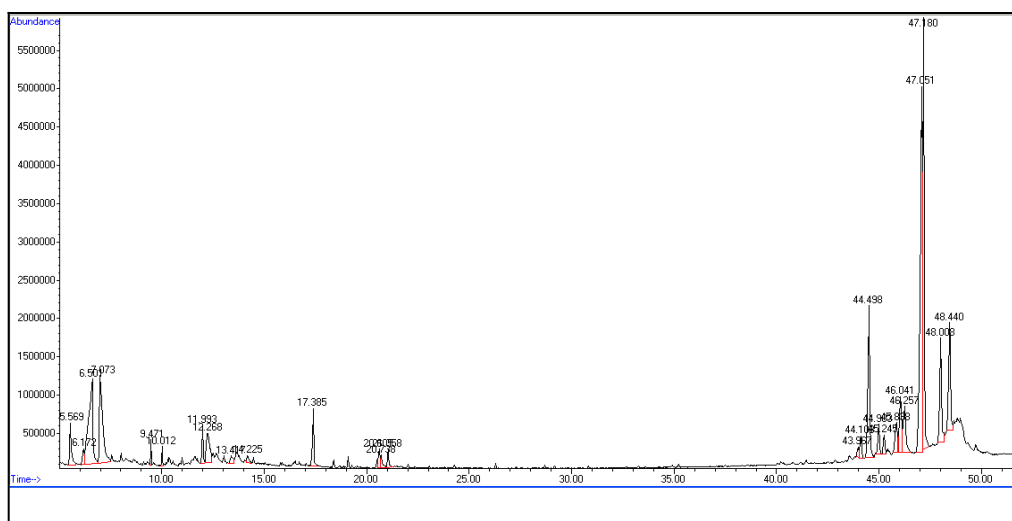


**Figure 5:** GC-MS chromatogram of methanolic extract of *E. hyssopifolia* latex.



Most of the compounds found in latex have many biological activities. Here, we highlight the major compounds. Lupeol, a pentacyclic triterpenoid, is the most abundant compound in latex (23.7089%). It has antioxidant, antimicrobial, anti-inflammatory, anti-tumor, and anti-cancer activities (35,36).

Betulin is the second major compound in latex (found at 14.0098%). It is also a pentacyclic triterpenoid and has anti-tumor and anti-HPV (Herpes simplex virus) activities (37,38). Lanosterol is a triterpenoid found in latex at 7.6304%, and it has antioxidant activity (39).

**Table 3:** Screening of the compounds identified in methanolic extract of *E. hyssopifolia* latex.

No.	Compound nature	Area %	RT	Compound name
1	Pentacyclic triterpenoid	1.9872	5.5667	2,3-Dihydro-3,5-dihydroxy-6-methyl-4-pyran-4-one
2	Carboxylic acid	0.8068	6.1713	Benzoic acid
3	Organic compound	9.9094	6.4978	4-Hydroxydihydro-2(3H)-furanone
4	Phenolic compound	8.3532	7.0746	Pyrocatechol
5	Sesquiterpene	0.4061	9.4719	$\beta$ -Caryophyllen
6	Sesquiterpene	0.3718	10.0139	$\alpha$ -Caryophyllene
7	Organic compound	1.1950	11.9942	1-Chlorocyclohexene
8	Phenolic compound	2.9273	12.2652	p-Hydroxybenzoic acid
9	Organic compound	0.6092	13.4187	5-Methyl-3-hexyn-2-ol
10	Organic compound	0.4465	14.2247	7-Methyl-Z-tetradecen-1-ol acetate
11	Saturated fatty acid	2.1633	17.3864	Palmitic acid
12	Monounsaturated fatty acid	0.7225	20.6036	cis-Vaccenic acid
13	Monounsaturated fatty acid	0.6664	20.7356	Oleic acid
14	Saturated fatty acid	0.6354	21.0553	Stearic acid
15	Steroid	0.4331	43.9649	Ergosta-7,22-dien-3.beta.-ol
16	Organic compound	1.1226	44.1108	Garcinielliptone FC
17	Tetracyclic triterpenoid	7.6304	44.4999	Lanosterol
18	Sterol	1.3322	44.9794	Obtusifoliol
19	Steroid	0.8822	45.2435	Ergosta-5,7-dien-3.beta.-ol
20	Triterpenoid of the sterol class	1.9876	45.841	Cycloartenol
21	Pentacyclic triterpenol	3.4377	46.0425	$\alpha$ -Amyrin
22	triterpenoid of the sterol class	3.3992	46.2580	Cycloartenol acetate
23	Pentacyclic triterpenoid	23.7089	47.0501	Lupeol
24	Pentacyclic triterpenoid	14.0098	47.1821	Betulin
25	Pentacyclic triterpenol	5.1167	48.0091	$\beta$ -Amyrin acetate
26	Triterpene alcohol	5.7397	48.4398	cycloartenylferulate

Pyrocatechol was the most abundant phenolic compound (found at 8.3532%), and it was not previously recorded in other *Euphorbia* species. A study revealed that it has antioxidant and anti-breast cancer activity (40,41). GC-MS analysis showed the presence of another phenolic compound found at (2.9273%), which is p-hydroxybenzoic acid. A study has shown that it has antioxidant activity (42). Cycloartenol and its derivatives are triterpenoids present often in *Euphorbia* species, and they were found in *E. hyssopifolia* latex. Cycloartenol was found at 1.9876%. It has antioxidant, anti-inflammatory, and anti-tumor activities (43,44). It should be noted that "Cycloartenyl ferulate" (found at 5.7397%) was not previously recorded in other *Euphorbia* species, and it has antioxidative, anti-allergic, anti-inflammatory, and anti-cancer activities (45). GC-MS analysis also showed the presence of other triterpenes commonly found in *Euphorbia* species, such as, amyryns and their derivatives.  $\alpha$ -amyryn (a pentacyclic triterpene) was found at 3.4377%. It has antioxidant, analgesic, and anti-inflammatory activities (46,47).  $\beta$ -amyryn acetate was found at 5.1167%. It has antioxidant, anticonvulsant, anti-inflammatory, and

antinociceptive activities (48). Garcinielliptone FC, a derivative of benzophenone, was found in *E. hyssopifolia* latex at 1.1226%. It was not previously recorded in other *Euphorbia* species. It has antioxidant, anti-leishmaniasis and anti-colorectal cancer activities (49-51).

#### Antioxidant Activity Using DPPH and ABTS Assays

It is known that a decrease in IC<sub>50</sub> value indicates an increase in the antioxidant activity of the sample. The results of DPPH and ABTS assays appear to be compatible, as both assays indicate that latex significantly outperformed all extracts and ascorbic acid; IC<sub>50</sub> values of it were 0.029 mg/mL and 0.001 mg/mL in DPPH and ABTS assays, respectively, noting that IC<sub>50</sub> of ascorbic acid was 0.053 mg/mL and 0.008 mg/mL in DPPH and ABTS assays, respectively. The results of both assays also converge in that methanolic 70% extract came in the second order after latex, noting that its IC<sub>50</sub> was equal to that of ascorbic acid in ABTS assay (0.008 mg/mL), whereas *n*-hexane extract was the least capable of scavenging free radicals (Table 4).

**Table 4:** Antioxidant activity of extracts and latex of *E. hyssopifolia*.

Sample (extract/latex)	IC <sub>50</sub> using DPPH Assay (mg/mL)	IC <sub>50</sub> using ABTS Assay (mg/mL)
aqueous extract	0.313	0.018
methanolic 70% extract	0.080	0.008
ethyl acetate extract	0.193	0.022
<i>n</i> -hexane extract	2.078	0.081
latex	0.029	0.001
ascorbic acid	0.053	0.008

On the other hand, DPPH and ABTS assays differed in the order of ethyl acetate and aqueous extracts in terms of their ability to scavenge free radicals. IC<sub>50</sub> of ethyl acetate extract was lower in DPPH assay (0.193 mg/mL), that is, it was better than the aqueous extract which had IC<sub>50</sub> of 0.313 mg/mL, while the order of the two extracts was reversed in ABTS assay; IC<sub>50</sub> values were 0.018 mg/mL and 0.022 mg/mL for the aqueous extract and ethyl acetate extract, respectively (Table 4).

Latex's great ability to scavenge free radicals is due to its phenolic and flavonoid contents which are relatively high as previously mentioned. TPC and TFC were 39.52 ± 0.36 GAE mg/g and 28.66 ± 0.10 RE mg/g E respectively (Table 2). It is also due to its content of phenolic and non-phenolic antioxidants that appeared as a result of GC-MS analysis, which are: pyrocatechol, p-hydroxybenzoic acid (phenolic compounds), lupeol, lanosterol, cycloartenol, cycloartenyl ferulate,  $\alpha$ -amyryn,  $\beta$ -amyryn acetate, and garcinielliptone FC (non-phenolic compounds). The high effectiveness of

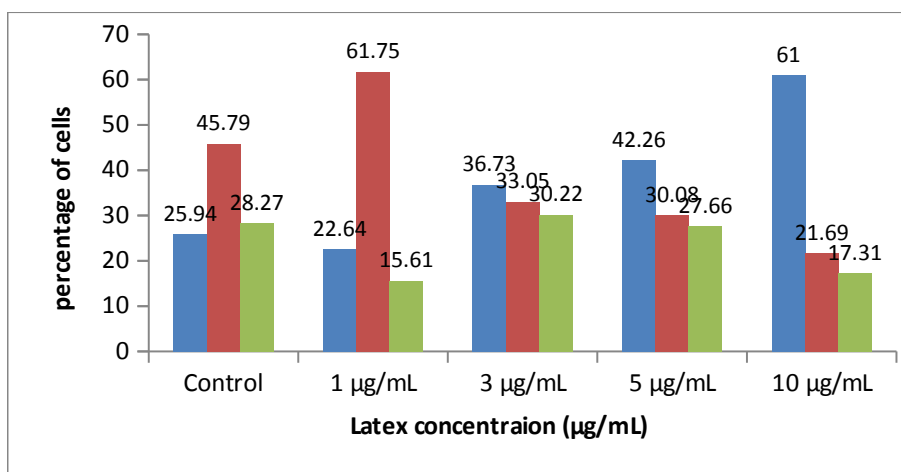
methanolic 70% extract in scavenging free radicals is due to its TPC and TFC which were 30.88 ± 0.21 GAE/g E and 17.95 ± 0.17 RE/g E, respectively (Table 2). It is noted that the aqueous extract was the richest of these compounds, but it was not the best as an anti-oxidant (Table 4), which indicates that there is not always a direct relationship between TPC and TFC on the one hand and the antioxidant activity on the other hand. Ethyl acetate and *n*-hexane extracts showed low free radical scavenging ability (Table 4). Referring to Table 1, it is noted that they were poor in bioactive compounds, as Table 2 showed that they contained negligible amounts of total phenols and flavonoids, and therefore flavonoids and tannins did not appear in results of phytochemical qualitative screening (Table 1). However, these results indicate that latex has the highest antioxidant activity, and statistical study confirmed this result.

**Anticancer Activity of *E. hyssopifolia* Latex against MDA-MB-231 Breast Cancer Cell Line**

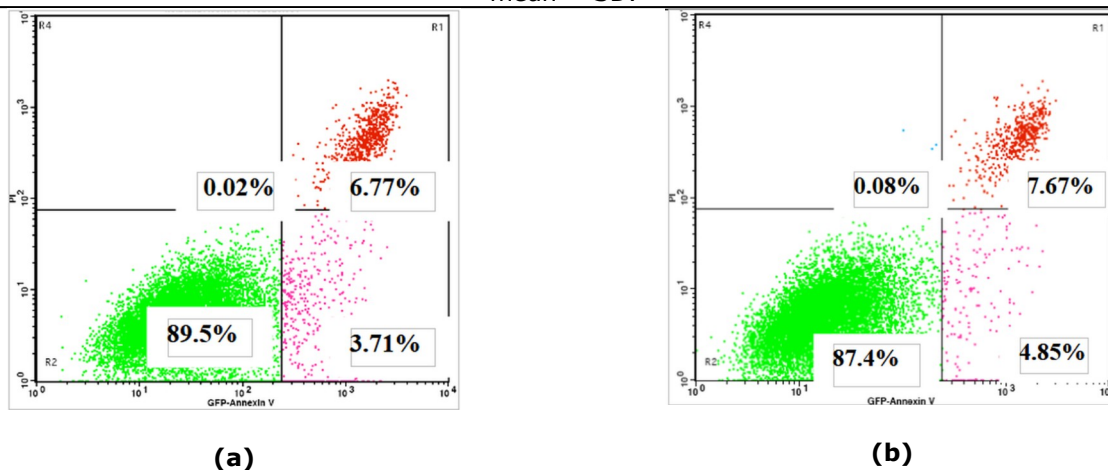
*Cell cycle analysis*

MDA-MB-231 cells were treated with various concentrations of *E. hyssopifolia* latex (1, 3, 5, and 10 µg/mL) for 24 hours. It should be noted that the mentioned concentrations depend on wet weight of latex. Figure 6 showed that the treatment of MDA-MB-231 cells with latex caused a concentration-dependent cell cycle arrest at G1 phase. The percentages of cells in G1 phase increased as a result of the treatment with concentrations (1, 3, 5, and 10) µg/mL by 0.87, 1.42, 1.63, and 2.35 times respectively compared to the percentage of G1 cells in untreated cells (control). In contrast, the percentages of cells in S phase decreased after treatment with the mentioned concentrations by

0.74, 1.38, 1.52, and 2.11 times, respectively, compared to the percentage of cells in S phase in the control. The percentages of cells in G2/M phase also decreased after treatment with the same concentrations by 1.81, 1.06, 0.97, and 1.63 times, respectively, compared to the percentage of cells in G2/M phase in the control. Thus, we conclude that the best results were obtained when cells were treated with a concentration of 10 µg/mL; so that the percentage of cells reached 61% in G1 phase, 21.69% in S phase and 17.31% in G2/M phase. The statistical study confirmed this result; there were significant differences in G1 phase and S phase between the concentration of 10% and other concentrations (Figure 6). These data suggest that treatment with latex induced cell cycle arrest at G1 phase.



**Figure 6:** Bar graphs representing cell cycle analysis in cells treated with latex. Data are represented as mean ± SD.



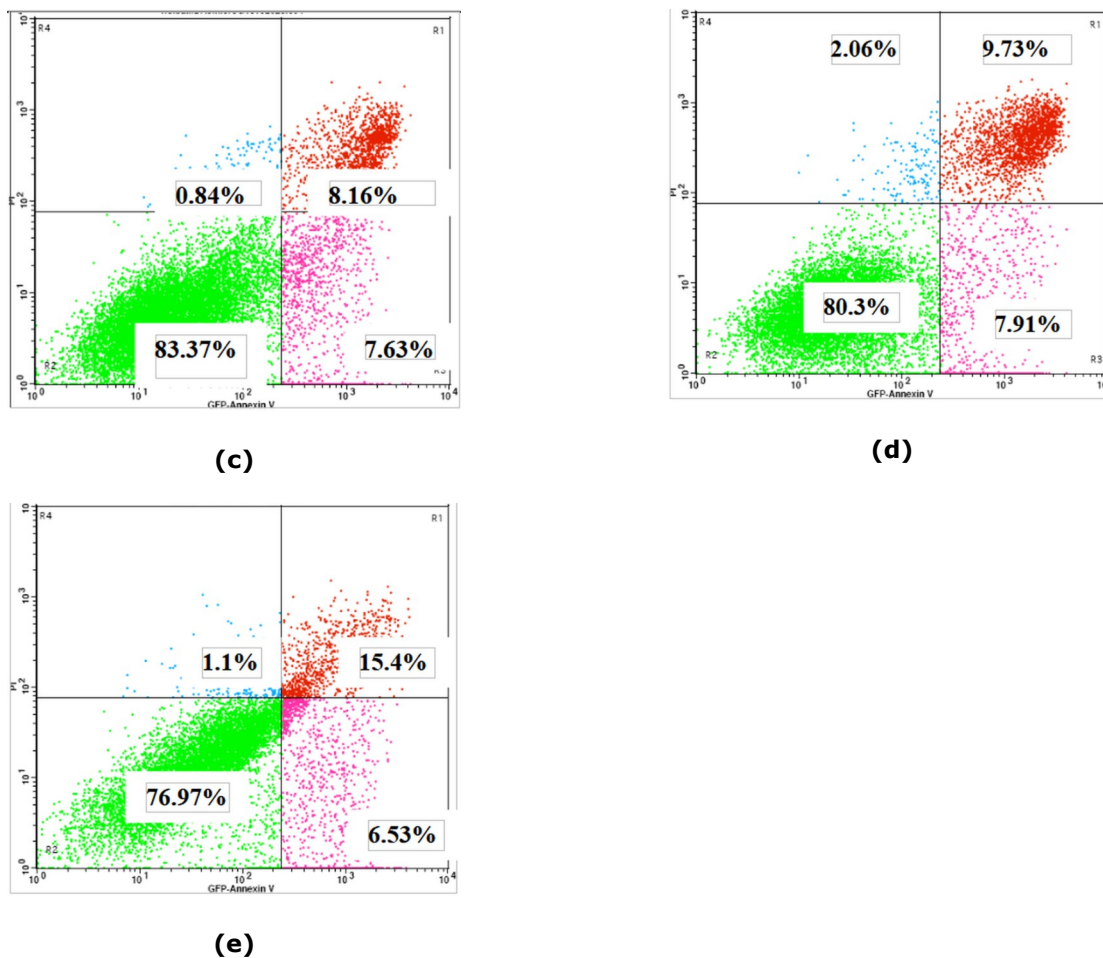


**Figure 7:** Fraction of viable, apoptotic, and necrotic MDA-MB-231 cells treated with different concentrations of latex for 24 h. a: control cells, b: cells treated with 1  $\mu\text{g/mL}$ , c: cells treated with 3  $\mu\text{g/mL}$ , d: cells treated with 5  $\mu\text{g/mL}$ , e: cells treated with 10  $\mu\text{g/mL}$ .

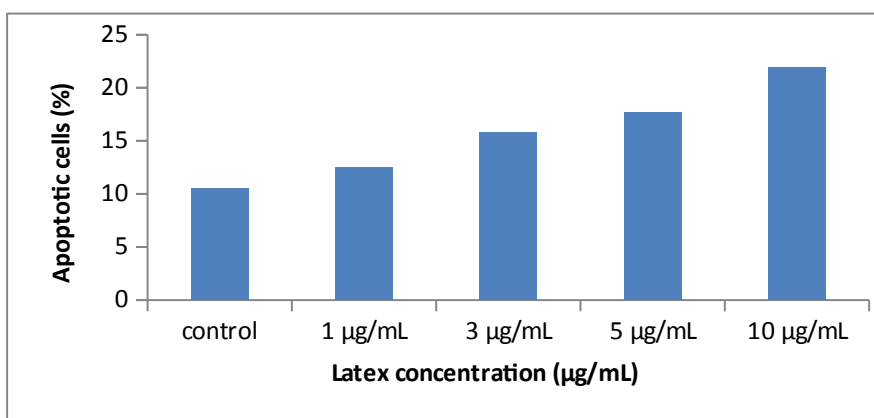


**Figure 8:** Apoptotic cells treated with *E. hyssopifolia* latex. Data are represented as mean  $\pm$  SD.

Annexin V-FITC/PI assay confirmed that latex was able to induce apoptosis. As shown in Figures 6 and 7, cells treated with different concentrations of latex (1, 3, 5, and 10)  $\mu\text{g/mL}$  showed increasing of percentage of apoptotic cells by 1.19, 1.51, 1.68, and 2.09 times respectively compared to the percentage of apoptotic cells in control.

*Annexin V/PI apoptosis assay*

Particularly, cells were treated with different concentrations of *E. hyssopifolia* latex (1, 3, 5, 10 µg/mL) for 24 hours, and the double staining Annexin V /PI allowed to measure the percentage of live, apoptotic, and necrotic cells.

Figure 7 shows the percentages of apoptotic cells induced by treatment of MDA-MB-231 cells at different concentrations (0, 1, 3, 5, and 10) µg/mL of *E. hyssopifolia* latex for 24 hours. It was also observed that the percentage of necrotic cells increased, especially when treated with concentrations 5 and 10 µg/mL, reaching 2.06% and 1.1%, respectively. However, these percentages are relatively low compared to the percentages of apoptosis. Thus, treatment with a concentration of 10 µg/mL is better than treatment with a concentration of 5 µg/mL, because it resulted more apoptotic cells (21.93%) and less necrotic cells (1.1%), which in turn is better than treatment with the rest of the concentrations. The statistical study confirmed our results (Figure 8). The presence of necrotic cells after treatment with latex is due to the fact that *Euphorbia* species generally contain compounds that induce necrosis (52). The results of treatment with latex appear to be good. This is due to its content of compounds that have anti-cancer activity shown by GC-MS analysis, foremost of which are lupeol (found at 23.7089%) and pyrocatechol (found at 8.3532%) (Table 3). A study showed that lupeol acts as an anticancer agent against MCF-7 breast cancer cells by inducing apoptosis (53). Another study showed that pyrocatechol was able to induce DNA damage, apoptosis and G1 cell cycle arrest in MCF-7 and MDA-MB-231 breast cancer cells (41). Based on the results of the present and previous studies that evaluated anti-cancer activity of *Euphorbia* species against MDA-MB-231 breast cancer cells, it was found that *E. hyssopifolia* latex was able to induce apoptosis in a good percentage (21.93%) after treatment with a relatively low concentration (10 µg/mL), noting that the concentration would be less if latex was dried, and within a short period (24 hours). Also, the percentage of necrotic cells was relatively low in our study (1.1%). For reference, the effect of a hydroalcoholic extract of the aerial parts of *E. szovitsii* on MDA-MB-231 breast cancer cells was studied. Results revealed that treatment with this extract increased the percentage of cells in G1 phase and decreased in S phase with increasing concentration. The study also found that treating cells with concentration of 50 µg/mL for 24 hours induced apoptosis of 20.65% and necrosis of 0.58% compared to the control (54). By comparing the results of this study with ours, it is clear that the percentages of apoptotic and necrotic cells are similar, but the concentration used in our study is lower.

**CONCLUSION**

The current study showed that *E. hyssopifolia* contains flavonoids, tannins, alkaloids, diterpenes, steroids, and cardiac glycosides, whereas saponins were absent. Methanolic 70% extract was the richest in secondary metabolites, especially flavonoids and tannins. The maximum yield extraction was obtained for aqueous extract, and it had the highest TPC and TFC. Latex significantly outperformed methanolic 70% extract in terms of TPC and TFC, even though it had the lowest yield. GC-MS analysis led to the identification of 26 bioactive compounds in *E. hyssopifolia* latex, of which triterpenoids constitute 67.0172%, led by lupeol and betulin. Latex had strong antioxidant activity which outperformed significantly ascorbic acid and all extracts, which indicates that latex is an excellent source of antioxidants. *E. hyssopifolia* latex induced cell cycle arrest at G1 phase and apoptosis of MDA-MB-231 cells after treatment for 24 hours at relatively low concentrations. However, more studies should be performed to isolate and purify bioactive compounds in *E. hyssopifolia*, as well as to determine the underlying mechanism its latex anti-breast cancer effects.

**CONFLICT OF INTEREST**

Authors have no conflicts of interest to disclose.

**ACKNOWLEDGEMENTS**

All the authors are thankful to Dr. Adnan Ikhtiar (main researcher in Biotechnology Department in Atomic Energy Commission of Syria) for his support and encouragement.

**REFERENCES**

1. Mabberley DJ. The plant book. Cambridge: Cambridge University Press; 1997.
2. Prenner G, Rudall PJ. Comparative ontogeny of the cyathium in *Euphorbia* (Euphorbiaceae) and its allies: exploring the organ flower inflorescence boundary. *American Journal of Botany*. 2007;94(10):1612-29. <DOI>.
3. Muthu C, Ayyanar M, Raja N, Ignacimuthu S. Medicinal plants used by traditional healers in Kancheepuram District of Tamil Nadu, India. *Journal of Ethnobiology and Ethnomedicine*. 2006;2(1):43. <DOI>.
4. Kitajima S, Kamei K, Taketani S, Yamaguchi M, Kawai F, Komatsu A, et al. Two chitinase-like proteins abundantly accumulated in latex of mulberry show insecticidal activity. *BMC Biochemistry*. 2010;11(1):6. <DOI>.
5. Mouterde P. Tome II. In: *Nouvelle flore du Liban et de la Syrie*. Beyrouth: Éd. de l'Impr. Catholique; 1966. p. 475-98.

6. Bolaji AO, Olojede CB, Famurewa AA, Faluyi JO. Morphological and cytological studies of *Euphorbia hyssopifolia* L. and *Euphorbia heterophylla* L. from Ile-Ife, Nigeria. *Nigerian Journal of Genetics*. 2014;28(2):15–8. <DOI>.
7. Ma J-S, Gilbert M. 4. *Euphorbia hyssopifolia* Linnaeus, *Syst. Nat.*, ed. 10. 2: 1048. 1759. *Flora of China*; FOC. 2016;11:289–93. <URL>
8. Babojian G. Recordation of *Euphorbia hyssopifolia* L. (Euphorbiaceae) a new alien Species for Flora of Syria. *Damascus University Journal for Basic Sciences*. 2018;34(1):121–47.
9. Abo KA. Characterisation of ingenol: an inflammatory diterpene from some Nigerian *Euphorbia* and *Elaeophorbia* species. *African Journal of Medicine and Medical Sciences*. 1994;23(2):161–3.
10. Adedapo AA, Abatan MO, i Olorunsogo OO. Toxic effects of some plants in the genus *Euphorbia* on haematological and biochemical parameters of rats. *Veterinarski Arhiv*. 2004;74(1):53–62.
11. Igwenyi IO, Agwor AS, Nwigboji IU, Agbafor KN, Offor CE. Proximate Analysis, Mineral and Phytochemical Composition of *Euphorbia Hyssopifolia*. *IOSR Journal of Dental and Medical Sciences*. 2014;13(6):41–3. <DOI>.
12. Araújo S de S, Fernandes TCC, Cardona YT, Almeida PM de, Marin-Morales MA, dos Santos AV, et al. Cytotoxic and genotoxic effects of ethanolic extract of *Euphorbia hyssopifolia* L. on HepG2 cells. *Journal of Ethnopharmacology*. 2015;170:16–9. <DOI>.
13. Igwenyi I, Nwachukwu N, Mba O, Offor CE, Aja P, Ugwu O. Hepatotoxicity effects of aqueous extract of *Euphorbia hyssopifolia* on selected tissues of albino rats. *Fermentation Technology and Bioengineering*. 2011;2:7–10.
14. McGuire A, Brown J, Malone C, McLaughlin R, Kerin M. Effects of Age on the Detection and Management of Breast Cancer. *Cancers*. 2015;7(2):908–29. <DOI>.
15. Bigoniya P, Shukla A, Singh CS. Dermal irritation and sensitization study of *Euphorbia neriifolia* latex and its anti-inflammatory efficacy. *International Journal of Phytomedicine*. 2010;2:3. <DOI>.
16. Yener İ, Ertaş A, Yılmaz MA, Tokul Ölmez Ö, Köseoğlu Yılmaz P, Yeşil Y, et al. Characterization of the Chemical Profile of *Euphorbia* Species from Turkey by Gas Chromatography–Mass Spectrometry (GC-MS), Liquid Chromatography–Tandem Mass Spectrometry (LC-MS/MS), and Liquid Chromatography–Ion Trap–Time-of-Flight–Mass Spectrometry (LC-IT-TOF-MS) and Chemometric Analysis. *Analytical Letters*. 2019;52(7):1031–49. <DOI>.
17. Shashikala M, Shah M, Pande M. Determination of Total Phenols and Flavonoid Content of *Bryonia laciniosa* by Spectrophotometric Method. *Journal of Chemical and Pharmaceutical Research*. 2018;10(12):30–4.
18. Borah R, Biswas SP. Tulsi (*Ocimum sanctum*), excellent source of phytochemicals. *International Journal of Environment, Agriculture and Biotechnology*. 2018;3(5):1732–8. <DOI>.
19. Gonfa T, Teketle S, Kiros T. Effect of extraction solvent on qualitative and quantitative analysis of major phyto-constituents and in-vitro antioxidant activity evaluation of *Cadaba rotundifolia* Forssk leaf extracts. Yildiz F, editor. *Cogent Food & Agriculture*. 2020;6(1):1853867. <DOI>.
20. Archana P, Samatha T, Mahitha B, Chamundeswari NR. Preliminary phytochemical screening from leaf and seed extracts of *Senna alata* L. Roxb-an ethno medicinal plant. *Int J Pharm Biol Res*. 2012;3(3):82–9.
21. Tadesse G, Reneela P, Dekebo A. Isolation and characterization of natural products from *Helinus mystachnus* (Rhamnaceae). *J Chem Pharm Res*. 2012;4(3):1756–62.
22. Das SS. Studies on Qualitative Determination of Phytochemical Constituents and Antimicrobial Activities of Five Mangrove Plants. In: *Mangroves of Indian Sundarban: Ecological, Biochemical and Molecular Aspects*. Lulu Publication; 2021. p. 31.
23. Kumar Bargah R. Preliminary test of phytochemical screening of crude ethanolic and aqueous extract of *Moringa pterygosperma* Gaertn. *Journal of Pharmacognosy and Phytochemistry*. 2015;4(1):07–9.
24. Sawant RS, Godghate AG. Qualitative phytochemical screening of rhizomes of *Curcuma longa* Linn. *International Journal of Science, Environment and Technology*. 2013;2(4):634–41.
25. AlHafez M, Kheder F, AlJoubbeh M. Polyphenols, flavonoids and (-)-epigallocatechin gallate in tea leaves and in their infusions under various conditions. *Nutrition & Food Science*. 2014;44(5):455–63. <DOI>.
26. Karimi A, Mohammadi-Kamalabadi M, Rafieian-Kopaei M, Amjad L, Salimzadeh L. Determination of antioxidant activity, phenolic contents and antiviral potential of methanol extract of *Euphorbia spinidens* Bornm (Euphorbiaceae). *Tropical Journal of Pharmaceutical Research*. 2016;15(4):759. <DOI>.
27. Saka F Al, Karabet F, Daghestani M, Soukkarieh C. Composition, in vitro antioxidant and antileishmanial activities of *Vitex agnus-castus* L. and *Thymus syriacus* boiss. *Essential Oils*. *International Journal of ChemTech Research*. 2015;8(8):53–60.
28. Re R, Pellegrini N, Proteggente A, Pannala A, Yang M, Rice-Evans C. Antioxidant activity applying an improved ABTS radical cation decolorization assay. *Free Radical Biology and Medicine*. 1999;26(9–10):1231–7. <DOI>.
29. Evans FJ, Taylor SE. Pro-Inflammatory, Tumour-Promoting and Anti-Tumour Diterpenes of the Plant Families Euphorbiaceae and Thymelaeaceae. In: *Fortschritte der Chemie organischer Naturstoffe/Progress in the Chemistry of Organic Natural Products*. 1983. p. 1–99. <DOI>.



30. Mahomoodally MF, Dall'Acqua S, Sinan KI, Sut S, Ferrarese I, Etienne OK, et al. Phenolic compounds analysis of three Euphorbia species by LC-DAD-MSn and their biological properties. *Journal of Pharmaceutical and Biomedical Analysis*. 2020;189:113477. <DOI>.
31. Majid M, Khan MR, Shah NA, Haq IU, Farooq MA, Ullah S, et al. Studies on phytochemical, antioxidant, anti-inflammatory and analgesic activities of Euphorbia dracunculoides. *BMC Complementary and Alternative Medicine*. 2015;15(1):349. <DOI>.
32. Dai J, Mumper RJ. Plant Phenolics: Extraction, Analysis and Their Antioxidant and Anticancer Properties. *Molecules*. 2010;15(10):7313–52. <DOI>.
33. Galanakis CM, Goulas V, Tsakona S, Manganaris GA, Gekas V. A Knowledge Base for The Recovery of Natural Phenols with Different Solvents. *International Journal of Food Properties*. 2013;16(2):382–96. <DOI>.
34. Abdel-Aty AM, Hamed MB, Salama WH, Ali MM, Fahmy AS, Mohamed SA. Ficus carica, Ficus sycomorus and Euphorbia tirucalli latex extracts: Phytochemical screening, antioxidant and cytotoxic properties. *Biocatalysis and Agricultural Biotechnology*. 2019;20:101199. <DOI>.
35. Guo M-B, Wang D-C, Liu H-F, Chen L-W, Wei J-W, Lin Y, et al. Lupeol against high-glucose-induced apoptosis via enhancing the anti-oxidative stress in rabbit nucleus pulposus cells. *European Spine Journal*. 2018;27(10):2609–20. <DOI>.
36. Gallo MBC, Sarachine MJ. Biological activities of lupeol. *Int J Biomed Pharm Sci*. 2009;3(1):46–66.
37. Zhao J, Li R, Pawlak A, Henklewska M, Sysak A, Wen L, et al. Antitumor Activity of Betulinic Acid and Betulin in Canine Cancer Cell Lines. *In Vivo*. 2018;32(5):1081–8. <DOI>.
38. Shamsabadipour S, Ghanadian M, Saeedi H, Rahimnejad MR, Mohammadi-Kamalabadi M, Ayatollahi SM, et al. Triterpenes and Steroids from Euphorbia denticulata Lam. With Anti-Herpes Simplex Virus Activity. *Iranian Journal of Pharmaceutical Research: IJPR*. 2013;12(4):759–67.
39. Delinassios G. UVA-induced oxidative stress and DNA damage in human skin cells and photoprotection by antioxidant compounds. *King's College London (University of London)*; 2012.
40. Kosobutskii VS. Pyrocatechol and its derivatives as antioxidants and prooxidants. *Russian Journal of General Chemistry*. 2014;84(5):839–42. <DOI>.
41. Vazhappilly CG, Hodeify R, Siddiqui SS, Laham AJ, Menon V, El-Awady R, et al. Natural compound catechol induces DNA damage, apoptosis, and G1 cell cycle arrest in breast cancer cells. *Phytotherapy Research*. 2021;35(4):2185–99. <DOI>.
42. Velika B, Kron I. Antioxidant properties of benzoic acid derivatives against Superoxide radical. *Free Radicals and Antioxidants*. 2012;2(4):62–7. <DOI>.
43. Sawale JA, Patel JR, Kori ML. Antioxidant Properties of Cycloartenol Isolated from Euphorbia neriifolia Leaves. *Indian Journal of Natural Products*. 2019;33(1):60–4.
44. Zhang Z-L, Luo Z-L, Shi H-W, Zhang L-X, Ma X-J. Research advance of functional plant pharmaceutical cycloartenol about pharmacological and physiological activity. *Zhongguo Zhong Yao Za Zhi= Zhongguo Zhongyao Zazhi= China Journal of Chinese Materia Medica*. 2017;42(3):433–7.
45. Hong G-L, Liu J-M, Zhao G-J, Wang L, Liang G, Wu B, et al. The reversal of paraquat-induced mitochondria-mediated apoptosis by cycloartenyl ferulate, the important role of Nrf2 pathway. *Experimental Cell Research*. 2013;319(18):2845–55. <DOI>.
46. Romero-Estrada A, Maldonado-Magaña A, González-Christen J, Bahena SM, Garduño-Ramírez ML, Rodríguez-López V, et al. Anti-inflammatory and antioxidative effects of six pentacyclic triterpenes isolated from the Mexican copal resin of Bursera copallifera. *BMC Complementary and Alternative Medicine*. 2016;16(1):422. <DOI>.
47. Simão da Silva KAB, Paszcuk AF, Passos GF, Silva ES, Bento AF, Meotti FC, et al. Activation of cannabinoid receptors by the pentacyclic triterpene  $\alpha,\beta$ -amyrin inhibits inflammatory and neuropathic persistent pain in mice. *Pain*. 2011;152(8):1872–87. <DOI>.
48. Duke JA. *Dr. Duke's Phytochemical and Ethnobotanical Databases*. 1992.<URL>.
49. Júnior JSC, Ferraz ABF, Feitosa CM, Cito A, Freitas RM, Saffi J. Evaluation of antioxidant effects in vitro of garcinielliptone FC (GFC) isolated from Platania insignis Mart. *Journal of Medicinal Plants Research*. 2011;5(2):293–9.
50. Costa Júnior JS, de Almeida AAC, Ferraz A de BF, Rossatto RR, Silva TG, Silva PBN, et al. Cytotoxic and leishmanicidal properties of garcinielliptone FC, a prenylated benzophenone from Platania insignis. *Natural Product Research*. 2013;27(4–5):470–4. <DOI>.
51. Won S-J, Lin T-Y, Yen C-H, Tzeng Y-H, Liu H-S, Lin C-N, et al. A novel natural tautomeric pair of garcinielliptone FC suppressed nuclear factor  $\kappa$ B and induced apoptosis in human colorectal cancer cells. *Journal of Functional Foods*. 2016;24:568–78. <DOI>.
52. Huerth KA, Hawkes JE, Meyer LJ, Powell DL. The Scourge of the Spurge Family—An Imitator of Rhus Dermatitis. *Dermatitis*. 2016;27(6):372–81. <DOI>.
53. Pitchai D, Roy A, Ignatius C. In vitro evaluation of anticancer potentials of lupeol isolated from Elephantopus scaber L. on MCF-7 cell line. *Journal of Advanced Pharmaceutical Technology & Research*. 2014;5(4):179. <DOI>.
54. Asadi-Samani M, Rafeian-Kopaei M, Lorigooini Z, Shirzad H. The effect of Euphorbia szovitsii Fisch. & C.A.Mey extract on the viability and the proliferation of MDA-MB-231 cell line. *Bioscience Reports*. 2019;39(1):1–8. <DOI>.



